

Norkhairunnisa Mazlan
S.M. Sapuan
R.A. Ilyas *Editors*

Advanced Composites in Aerospace Engineering Applications

 Springer

Advanced Composites in Aerospace Engineering Applications

Norkhairunnisa Mazlan • S. M. Sapuan
R. A. Ilyas
Editors

Advanced Composites in Aerospace Engineering Applications

 Springer

Editors

Norkhairunnisa Mazlan
Department of Aerospace Engineering
Universiti Putra Malaysia
Serdang, Malaysia

S. M. Sapuan
Department of Mechanical &
Manufacturing engineering
Universiti Putra Malaysia
Serdang, Selangor, Malaysia

R. A. Ilyas
Department of Chemical & Energy
Engineering
Universiti Teknologi Malaysia, Centre for
Advanced Composite Materials (CACM)
Universiti Teknologi Malaysia
Selangor, Malaysia

ISBN 978-3-030-88191-7

ISBN 978-3-030-88192-4 (eBook)

<https://doi.org/10.1007/978-3-030-88192-4>

© The Editor(s) (if applicable) and The Author(s), under exclusive license to Springer Nature Switzerland AG 2022

This work is subject to copyright. All rights are solely and exclusively licensed by the Publisher, whether the whole or part of the material is concerned, specifically the rights of translation, reprinting, reuse of illustrations, recitation, broadcasting, reproduction on microfilms or in any other physical way, and transmission or information storage and retrieval, electronic adaptation, computer software, or by similar or dissimilar methodology now known or hereafter developed.

The use of general descriptive names, registered names, trademarks, service marks, etc. in this publication does not imply, even in the absence of a specific statement, that such names are exempt from the relevant protective laws and regulations and therefore free for general use.

The publisher, the authors and the editors are safe to assume that the advice and information in this book are believed to be true and accurate at the date of publication. Neither the publisher nor the authors or the editors give a warranty, expressed or implied, with respect to the material contained herein or for any errors or omissions that may have been made. The publisher remains neutral with regard to jurisdictional claims in published maps and institutional affiliations.

This Springer imprint is published by the registered company Springer Nature Switzerland AG
The registered company address is: Gewerbestrasse 11, 6330 Cham, Switzerland

Contents

1	Advanced Polymer Composite for Aerospace Engineering Applications	1
	Natasha Ramli, Norkhairunnisa Mazlan, Yoshito Ando, Khalina Abdan, and Zulkiflle Leman	
2	Impact Studies of Hybrid Nanocomposites in Aerospace Application	23
	G. Balaganesan, N. K. Gupta, and R. Velmurugan	
3	High Strain Rate Studies of Polymer and Hybrid Nanocomposites for Aerospace Application	55
	S. Gurusideswar, R. Velmurugan, and R. Sarathi	
4	Design Methodologies for Composite Structures in Aircraft Engines	93
	Prakash Jadhav	
5	Machining Effects of Fibrous Composites and Related Stacks for Aerospace Applications	109
	Jinyang Xu, J. Paulo Davim, and Ming Chen	
6	Advanced Potential Hybrid Biocomposites in Aerospace Applications: A Comprehensive Review	127
	Muhammad Farhan, M. T. Mastura, Shahid Pervez Ansari, Muhammed Muaz, Mohammad Azeem, and S. M. Sapuan	
7	Resin-Injection Repair of Damaged Composites in Aerostructures: Finite Element Modelling of the Effects of Vent Holes in Carbon Fibre-Reinforced Composite Laminates	149
	Z. Y. D. Lim, W. L. Lai, H. Saeedipour, and K. L. Goh	
8	Studies on Magnesium Alloy: Composites for Aerospace Structural Applications	163
	B. Vijaya Ramnath, D. Kumaran, J. Melvin Antony, M. Rama Subramanian, and S. Venkatram	

9	An Overview of the Natural/Synthetic Fibre-Reinforced Metal-Composite Sandwich Structures for Potential Applications in Aerospace Sectors	177
	Lin Feng Ng, Kathiravan Subramaniam, and Noordiana Mohd Ishak	
10	Experimental Investigation of Surface Integrity Aspects and Recast Layer Formation for the Wire_{EDM} of Al/ZrO_{2(p)}-MMC Suitable for Aerospace Industries	195
	Sanjeev Kr. Garg, Alakesh Manna, and Ajai Jain	
11	Material Characterization of Alloy for Aerospace Application: Effect of Laser Power on the Co-axially Deposited T64 Alloy and Cu	225
	M. F. Erinsho, E. T. Akinlabi, and K. O. Oladosu	
12	Optimization of Reinforcement Parameters and Turning Conditions for Improving Surface Quality of Hybrid Al-SiC-Red Mud Composite for Automotive and Aerospace Components	237
	Amit Chauhan, Jaswinder Singh, and Saroj Bala	
13	Thermal Characterization of Graphitized Carbon Nanotube-Reinforced Ti64 Nanocomposites Synthesized by Field-Assisted Sintering Technique for Fuselage and Wing Box Applications	263
	Adewale Oladapo Adegbenjo, Mary Ajimegoh Awotunde, Tien-Chien Jen, and Johan Herman Potgieter	
14	Hybrid Biocomposites: Utilization in Aerospace Engineering	281
	Emel Kuram	
15	Molding of Carbon-Epoxy Composite Prepregs for Applications in Aerospace Industries	303
	Raghu Raja Pandiyan Kuppusamy, Santoshi Mohanta, and Swati Neogi	
16	Recent Advancements in Advanced Composites for Aerospace Applications: A Review	319
	Mohammad Azad Alam, H. H. Ya, S. M. Sapuan, Othman Mamat, Bisma Parveez, Mohammad Yusuf, Faisal Masood, and R. A. Ilyas	
17	Flexural and Impact Properties of Flax/Kevlar and Jute/Carbon Hybrid Fibers-Reinforced PLA Nanocomposites for Aircraft Interior Applications	341
	A. L. A'Liya, S. Nur Aqilah, Norkhairunnisa Mazlan, and R. Natasha	
18	Evolution of Aerospace Composite Materials	367
	Norkhairunnisa Mazlan, T. Chai Hua, S. M. Sapuan, and R. A. Ilyas	

19 Cooling Curve Thermal Analysis of Al-20% Mg₂Si-xB₄C Hybrid Composites for Aerospace Applications 387
 Kee Heng Raymond Ling, Hamidreza Ghandvar,
 Tuty Asma Abu Bakar, and Ying Ci Wee

20 Microstructural Characterization, Mechanical Properties, and Sliding Wear Behavior of Al-20% Mg₂Si-xB₄C Hybrid Composites of the Aircraft Body 405
 Shu Sin Teh, Nur Shazwani Ghazali, Hamidreza Ghandvar,
 and Tuty Asma Abu Bakar

21 Hybrid Composites for Very Large Lightweight Wind Turbine Blades: Structural and Materials Aspects 421
 Hande Yavuz

22 Influence of Scanning Speed on the Laser Metal Deposition of Ti-6Al-4V and Mo for Aerospace Application 435
 M. F. Erinosh, E. T. Akinlabi, and K. O. Oladosu

23 Carbon Nanomaterial-Carbon Fiber Hybrid Composite for Lightweight Structural Composites in the Aerospace Industry: Synthesis, Processing, and Properties 445
 Abhishek K. Pathak and Sanjay R. Dhakate

24 Advanced Composite in Aerospace Applications: Opportunities, Challenges, and Future Perspective 471
 M. R. M. Asyraf, R. A. Ilyas, S. M. Sapuan, M. M. Harussani,
 H. M. Hariz, J. M. Aiman, Danish Mahmood Baitaba, M. R. Sanjay,
 M. R. Ishak, Norkhairunnisa Mazlan, Shubham Sharma,
 Mohammad Azad Alam, and Mochamad Asrofi

Index 499

Chapter 1

Advanced Polymer Composite for Aerospace Engineering Applications



Natasha Ramli, Norkhairunnisa Mazlan, Yoshito Ando, Khalina Abdan,
and Zulkiflre Leman

1 Introduction

Composite material is a mixture of two or more different materials used to combine the best characteristics or impart a new set of features that none of the constituent materials could have achieved independently. The propeller for earlier “flying machines” developed by Wright brothers includes natural composite materials such as wood. The wood installation was done by aligning the wood grain in the direction that required high strength and stiffness. About 54 years ago, Dowty observed large-size composite propeller could significantly reduce the noise and erosion problem when lowering the propeller tip speed above 200 ms^{-1} in seawater (McCarthy et al., 1994). In the late 1960s, with the discovery of carbon fibers, composite materials were applied on military aircraft on a demonstration basis. The weight saving of

N. Ramli

Laboratory of Biocomposite, Institute of Tropical Forestry and Forest Products (INTROP),
Universiti Putra Malaysia, Serdang, Selangor, Malaysia

N. Mazlan (✉)

Institute of Nanoscience & Nanotechnology (ION2), Universiti Putra Malaysia,
Serdang, Selangor, Malaysia

Department of Aerospace Engineering, Faculty of Engineering, Universiti Putra Malaysia,
Serdang, Selangor, Malaysia

Aerospace Malaysia Research Center (AMRC), Universiti Putra Malaysia,
Serdang, Selangor, Malaysia

e-mail: norkhairunnisa@upm.edu.my

Y. Ando

Department of Biological Functions and Engineering, Graduate School of Life Science and
Systems Engineering, Kyushu Institute of Technology, Fukuoka, Japan

e-mail: yando@life.kyutech.ac.jp

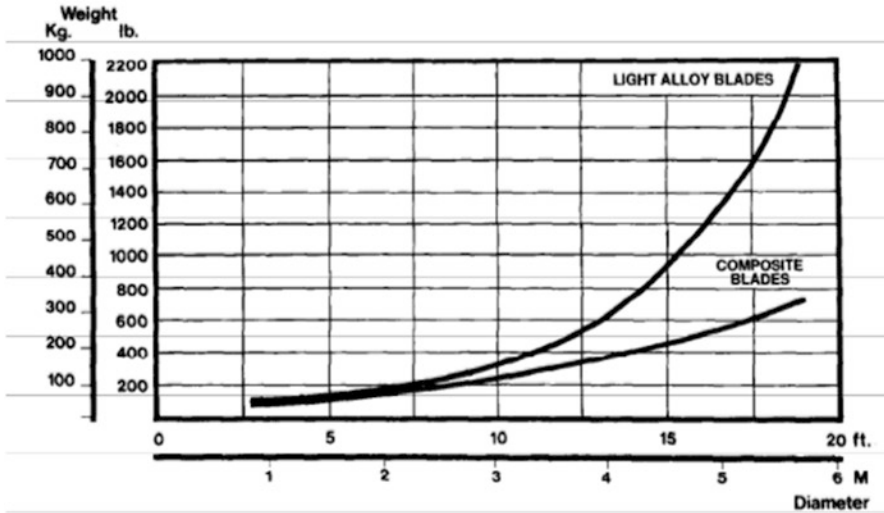


Fig. 1.1 Comparison in weight between light alloy blades and composite blades (McCarthy et al., 1994)

composite over light alloy materials replaced the conventional materials for primary aircraft structure (Fig. 1.1). The aluminum alloys, titanium alloys (Williams & Boyer, 2020), high-strength steels, and composites were the most regularly used commercial aircraft structural materials, accounting for more than 90% of the weight of airframes (Mansor et al., 2019). To demonstrate the weight savings, the A310 primary structure was constructed entirely of carbon composite, saving approximately 400 kg above aluminum alloy. Then, the A320 implemented the composites on both primary and secondary structures, which account for a weight reduction of 800 kg. Composites and modern molds also tailor the needs to improve aerodynamic performance by altering the aeroelasticity of the aircraft.

Nowadays, with the advancement in manufacturing and technology, the composite design was employed with high-strength reinforcing fibers coupled with computer-aided analysis to provide a better design of composite materials. A proper selection criterion for reinforcing fiber and matrix, lay-up method, and produced composite quality must be carefully regulated to achieve high toughness composite.

K. Abdan

Laboratory of Biocomposite, Institute of Tropical Forestry and Forest Products (INTROP), Universiti Putra Malaysia, Serdang, Selangor, Malaysia

Department of Biological and Agricultural Engineering, Faculty of Engineering, Universiti Putra Malaysia, Serdang, Selangor, Malaysia

e-mail: khalina@upm.edu.my

Z. Leman

Department of Mechanical and Manufacturing Engineering, Faculty of Engineering, Universiti Putra Malaysia, Serdang, Selangor, Malaysia

e-mail: zleman@upm.edu.my

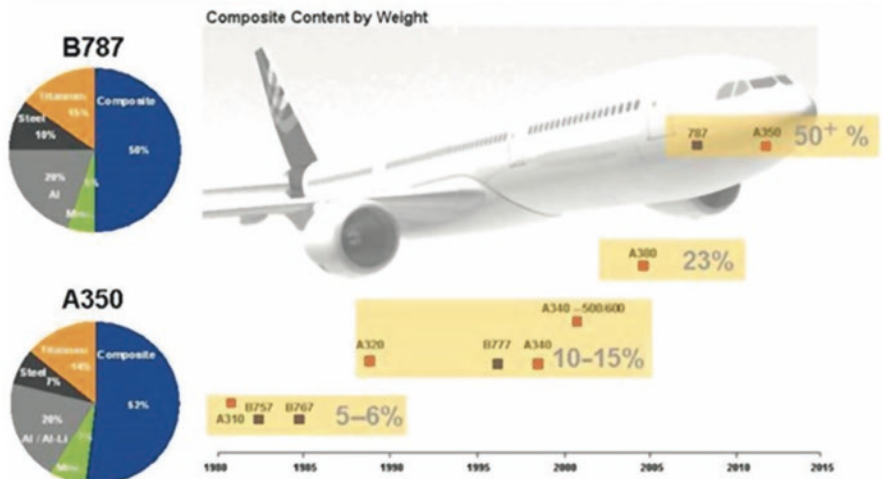


Fig. 1.2 Material distribution for Boeing 787. Source: Figure reproduced with copyright permission from Giurgiutiu (2015)

Furthermore, employing new sophisticated software to simulate composite properties using finite element analysis (FEA) saved time and was pleasant. According to Soutis (2015), it takes less than 3 weeks for the engineers to analyze the composite strength for an aircraft using FEA compared to 6 months with conventional analysis.

Polymer composite materials have been utilized extensively to construct the Eurofighter jet’s wings, fuselage, flaperons, and rudder. The rigid epoxy wings account for 75% of the jet’s total external surface (Redazione, 2018). In general, CFRP makes up around 40% of Eurofighter’s structural components. Other European fighter jets have polymer composite by weights of between 20 and 25%: for example, the Dassault Rafale has a composite by weight of 26%, while the Saab Gripen has a composite by weight of between 20 and 25%. It is worth noting that the use of composite materials in commercial transport aircraft is particularly beneficial because it results in a lighter airframe, which improves fuel economy and, as a result, cheaper operating costs (Muhammad et al., 2021). Airbus was the first commercial jet manufacturer to utilize composite material to design and construct the rudder on its A300 and A310 aircraft as early as 1983. It also uses the same composite materials for the tail fin in 1985. When composite fins were employed, around 2000 pieces, excluding the fasteners that employed metal fins, were reduced to less than 100. Reduction in parts resulted in a decrease in the total weight and production costs. The A310 elevator was built with a honeycomb core and CFRP faceplate (Muhammad et al., 2021). The success of the A310 has been applied to the design and construction of the A320’s whole tail structure, including fuselage, spoilers, ailerons, wheel doors, and nacelles. On the other hand, the door panels were made of glass fiber-reinforced plastic (GFRP). Thus, the A320 airframe consisted of 28% of composite materials.

The Boeing 787 Dreamliner (Timmis et al., 2015) and the Airbus A350 XWB (Marsh, 2016) were among the first commercial aircraft to use a considerable amount of composite materials. Figure 1.2 shows the material distribution for Boeing 787. The Boeing 787 makes superior composite materials in its airframe and primary structure than any previous Boeing commercial airplane (Wang et al., 2020). In order to develop a lightweight composite aircraft structure, the Boeing engineers determined the optimum composite material for particular applications around the airframe by conducting the design process without preconceived ideas. The ideation process results in an airframe containing almost half of plastic-reinforced carbon fiber and other composites. Compared to conventional aluminum designs, this solution provides weight savings of 20% on average. The aircraft fuselage was made entirely of composite materials. Production of each fuselage barrel eliminates the use of more than 50,000 fasteners as in conventional aircraft. In terms of strength, Lu (2010) added that the strength of the aluminum alloy is about 600 MPa, while the strength of unidirectional carbon/epoxy can reach up to 1724 MPa. This indicates that the strength of the composite materials was about three times stronger than the aluminum alloy. With high strength properties and lightweight features, the flight range can be extended due to fuel efficiency. Lu (2010) also added the sweptback wings on 787 made of malleable composite and allowed aircraft to be more aerodynamic, which revolutionized air travel to a new level.

The composite materials consist of a mixture of integrated materials created depending on the desired properties. The composite material's properties are superior to the individual materials from which it is built. Typically, composite material for aircraft is made of a high-strength fibrous material embedded in a resin. The composite fiber architectures were arranged in laminate to provide the strength and stiffness properties specifically designed to meet aircraft requirements. The engineering composite can be developed from individual layers, either woven mat or randomly aligned fibers (e.g., carbon, glass, aramid) embedded in a host polymer matrix (e.g., phenolic, polyester, epoxy) laminated layer by layer for the final structure to be constructed. The description for the laminate composite structure depends on the arrangement of fiber angle (Saravanakumar et al., 2021). In addition, the laminated nature of high-performance composite materials helps the manufacturer tailor optimal mechanical properties by orienting the primary load paths in the direction of the fiber (Alavudeen et al., 2015). Other advantages of fiber-reinforced plastics make the FRP composites increasingly attractive in the renewable energy market, such as the relative simplicity of producing complex shapes (Hadigheh & Kashi, 2018) and their excellent fatigue (Pitarresi et al., 2019) and corrosion resistance (Ray & Rathore, 2015).

The benefit of the composite materials' excellent strength and stiffness properties was evident in the lightweight and robust aircraft structural design (Li et al., 2020). Furthermore, air transport's fuel demand will increase due to increased passengers, long-haul flights, and more payloads. Thus, designing aircraft structures with lightweight composite materials would improve aircraft performance by reducing drag, increasing speed, and fuel savings. Reduction in fuel consumption is important for long-distance flight because the engine burns most of the fuel during

takeoff while more fuel is needed. It is estimated that every kilogram of weight lost saves about 2900 L of fuel each year (Soutis, 2015). Furthermore, lesser airframe weight leads to lower drag and boosts the fuel efficiency for a given cargo.

The aviation industry accounts for around 2% of all human-induced CO₂ emissions and 12% of all transportation-related emissions (Khalili et al., 2019). Low fuel efficiency is a double whammy for every airline's company. The utilization of a high amount of fuel will result in rising greenhouse gas emissions, contributing to global warming (Zhao et al., 2019). Then, an increase in fuel usage will subsequently increase the operational costs (Tanzil et al., 2021). With the restriction in traveling during the pandemic situation, the fuel price spikes tremendously, which will affect the airline fuel bill.

2 Advanced Polymer Composite

Many polymer composites are replacing the conventional metal materials in aircraft structures. The main reason for using polymer is to bind the reinforcing materials and preserved the reinforcement geometry. In addition, it must be efficient to carry the load and transfer it from one fiber to another so that each fiber will proportionally share the same load. On top of that, polymers offer significant weight-saving properties over metal and require less maintenance. Therefore, aircraft can spend more time in the air rather than maintenance at the hangar. In addition, polymer materials have good vibration and thermal properties. Moreover, the polymer materials also have good damage tolerance and environment degradation from erosion or corrosion. Figure 1.3 shows the polymer materials in general. The synthetic polymer is suitable for high service temperature and high structural performance applications. There are three types of polymer which are thermoset, thermoplastic, and elastomer. With concern on the environment, especially on climate change, global warming pollution due to fossil fuel burning, and lack of fossil fuel in the future, the biobased polymer was used to make biocomposite for the consideration in interior parts in aircraft. The biobased polymer is produced from natural sources, and it can be easily degradable and disposed of in the environment. Figure 1.4 shows the application of polymer composite materials on the Airbus A380 aircraft structure.

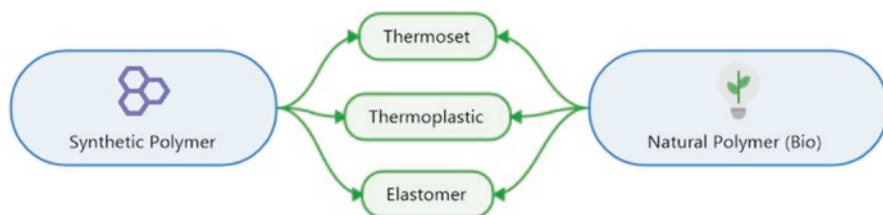


Fig. 1.3 Polymer classification

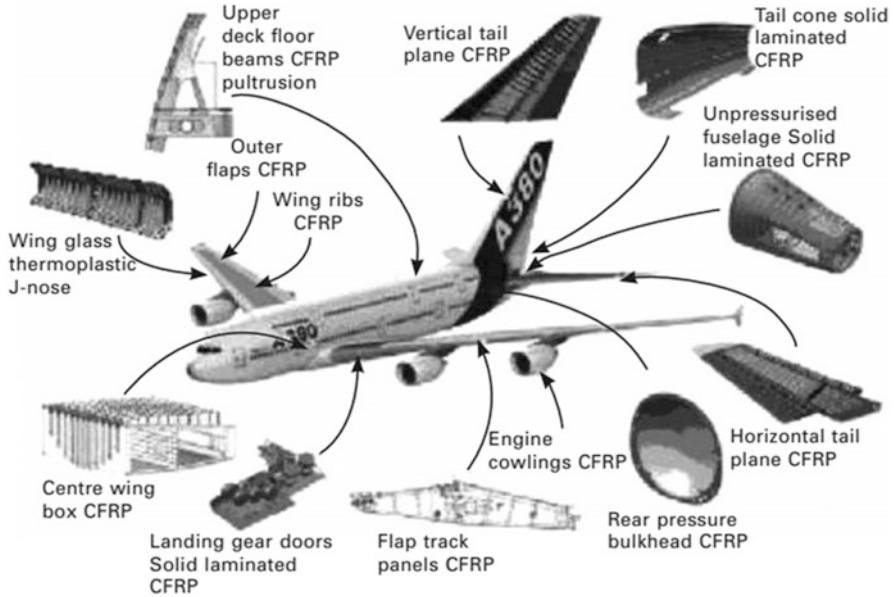


Fig. 1.4 Schematic showing components constructed from composite materials on the Airbus A380 (courtesy of Airbus). Source: Figure reproduced with copyright permission from Hamerton and Mooring (2012)

2.1 Thermoset Composite

Early wooden framed aircraft in 1940 was bonded with urea-formaldehyde, which is extensively used to bind the balsa composite engineered structure to make de Havilland aircraft. The invention of urea-formaldehyde at that time was to overcome the possibility of aluminum shortage. There were many challenges to the development of high-performance polymer, which is driven by the cold war and space race that raised the bar higher for the development of new materials. The thermoset composite has been used for about 50 years in commercial aircraft structures. Because of its design versatility, ease of curing with a wide range of initiators and curing agents, and low curing temperature, epoxy resin has dominated the aerospace industry. Figure 1.5 shows the properties of the high-performance thermoset polymers for aerospace applications.

Thermoset polymer is obtained by non-reversible hardening and forms a rigid three-dimensional crosslinking network. Thus, it cannot be remelted and reshaped. This allows the thermoset polymer to maintain its desired properties even after prolonged exposure to various environmental conditions. The backbone structure of high-performance thermoset polymers is aromatic or heterocyclic, and it is bridged with a range of flexible groups such as ether, sulfone, isopropylidene, and others. The most common thermoset polymer is epoxy, polyester, and vinyl ester. The curing process for the thermoset composite was usually done in an autoclave

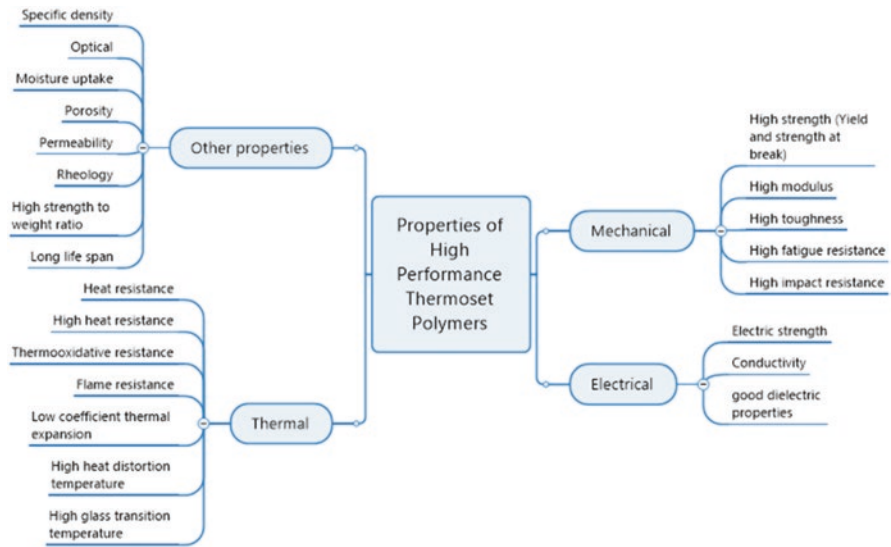


Fig. 1.5 Properties of high-performance thermoset polymers

to ensure the completed curing process and obtained optimum mechanical and thermal properties. Heat is required to ensure the crosslinking process is completed within the composite microstructure and to boost the composite’s macroscale strength. After that, pressure up to 8 bar is applied together with the heat in the autoclave to remove voids and trapped air and speed up the polymerization process. The advantage of using an autoclave is lack of toxic emission compared to the open molding process. Thermoset matrices produce robust composites with excellent fatigue resistance (Struzziero et al., 2019). On the other hand, they are highly brittle and have a low impact toughness. Thermoset composites are often cured thermally (often using an autoclave) at elevated temperatures above 100 °C in aerospace applications, with a post-cure frequently used to provide optimum thermal and mechanical qualities.

Table 1.1 shows the tensile and flexural properties of several fiber-reinforced thermoset polymer composites. Different fiber orientations, fiber content, and number of plies may affect the overall properties of the engineered composite. Variety types of engineered fibers such as glass, carbon, and kevlar were reinforced in thermoset composite. Carbon fibers (CF) with high strength and modulus have a diameter of 5–6 m and are made up of small crystallites of “turbostratic” graphite, an allotropic type of carbon. The attractiveness of using carbon fiber-reinforced thermoset polymer is attributed to their excellent mechanical strength, durability, high fatigue resistance, chemically inert, and lightweight, which results in energy savings. Bismaleimide (BMI) is another type of epoxy resin that is used widely in aircraft. Kamiyama et al. (2018) show that CF/BMI composite was less damaged due to lightning strikes than CF/epoxy composite. The thermal decomposition for CF/BMI composite starts at 370 °C rather than CF/epoxy composite, which starts at

Table 1.1 Tensile and flexural properties of fiber-reinforced thermoset polymer composite

	Thermoset composite composition	Fiber orientation (fiber content)	Tensile strength (MPa)	Tensile modulus (GPa)	Flexural strength (MPa)	Flexural modulus (GPa)	Reference
1.	CF/epoxy (3 plies)—epoxy Araldite	0°, 90°, 0° (60%)	1117	65.5	1016	45.7	Rahmani et al. (2013)
2.	CF/epoxy (3 plies)—epoxy Lionbond	0°, 90°, 0° (60%)	1043.8	60.66	1265.7	51.32	Rahmani et al. (2014)
3.	CF/epoxy (3 plies)—epoxy Araldite	0°	806	724	56	46	Hiremath et al. (2020)
4.	CF/epoxy added with 0.5 wt% silane	(58%)	1961	129.72	1420.61	102.47	Yang et al. (2013)
5.	T800 CF/epoxy—Araldite	(60%)	~680	~665	~554	~525	Muralidhara et al. (2020)
6.	3K carbon/epoxy (3 plies)	(70%)	—	—	~1130	~1075	He and Gao (2015)
7.	3K carbon/epoxy (8 plies) tested at 70 °C	—	719	52.5	—	—	Sun et al. (2021)
8.	CF/epoxy	(42.25 vol%)	89.54	12.83	—	—	Ma et al. (2016)
9.	Kevlar 49/epoxy (8 plies)	—	~400	~390	—	—	Haijuan et al. (2018)
10.	Glass/epoxy (8 plies)	(70%)	~290	70.36 ± 0.33	—	—	Reis et al. (2012)
11.	Glass/epoxy (4 plies)	(0/90/30/—60)	382.5 ± 35.45	—	—	—	Nareesh et al. (2018)
12.	Carbon/epoxy (4 plies)	(0/90/30/—60)	451.7 ± 17.65	—	—	—	Aslan and Daricik (2016)
13.	E-glass/epoxy (8 plies)	145°/0° ₂ /—45°/90° ₂ (65%)	239.47	—	426.03	—	Erden et al. (2010)
14.	Glass/polyester added with 3 wt% siloxane (6 plies)	(37%)	395.8 ± 23.9	18.0 ± 3.0	399.4 ± 22.4	18.8 ± 0.7	Hemanth et al. (2017)
15.	Glass/epoxy	—	40.53	3.117	177.37	11.09	El-Wazery et al. (2017)
16.	Glass/polyester	—	28.87	2.406	102.27	6.391	—
17.	Glass/polyester	(60%)	78.83	—	119.23	—	—

280 °C. High onset temperatures indicate better thermal stability of the composite materials.

The prospective uses of self-healing thermoset composites in the aerospace area have sparked interest in aerospace applications. The use of a combination of epoxy properties, such as good interfacial adhesion between thermoset polymer and reinforcement fibers, excellent mechanical and thermal properties, and the addition of self-mending functionalities of fillers by physical and chemical means, was found to improve the performance of the material (Paolillo et al., 2021).

2.2 Thermoplastic Composite

Thermoplastics and related composites are becoming more important as a primary material for aircraft’s internal and external structures as technology progresses. Thermoplastic polymers can be remelted and recycle compared to the non-reversible thermoset polymer. When heated, they become molten and solidify as they cool. Given the growing demand for novel aviation materials and the restrictions on heavy and combustible materials, thermoplastic composites are projected to play a significant role in aircraft manufacture in the future. As shown in the thermoplastic triangle, the high-performance engineering thermoplastic was suitable for aerospace applications (Fig. 1.6). High-temperature plastic and extreme-temperature plastic are categorized under high-performance engineering thermoplastic. In terms of

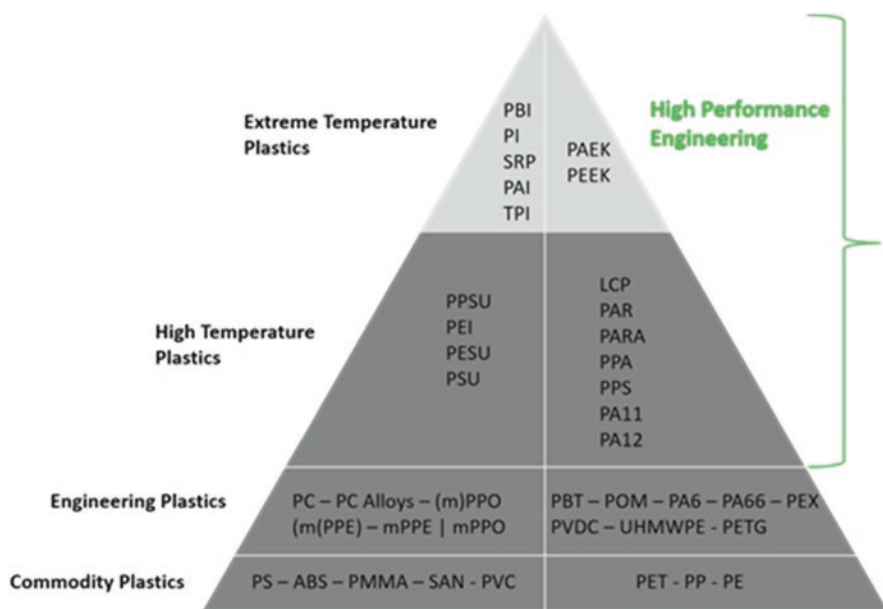


Fig. 1.6 Different types of thermoplastic in the market (Barile et al., 2020)

manufacturing, the processing of thermoplastic components is substantially faster than that of thermosets because the thermoplastic is fully polymerized, and the out-of-autoclave (OOA) technique allows for cost savings. Therefore, the aerospace-grade polymer is not only weight saving but also should be cost-effective (Ínal et al., 2021).

Thermoplastic composites have a high strength-to-weight ratio and contribute significantly to airplane weight reduction (Butt et al., 2019). Recently, the rise in using the thermoplastic composite for aerospace parts and components was due to its recyclability potential (Bing et al., 2020). In addition, thermoplastic composite can survive extreme temperatures, and the maintenance cycle can be shortened (Tatsumi et al., 2019). Furthermore, the thermoplastic composite was reliable over the thermoset composite by combining its high mechanical capabilities with minimum fire, smoke, and toxicity emissions. Thus, some metallic and thermoset composite parts were replaced with the engineered thermoplastic composite materials (Teplýk et al., 2020).

The utilization of thermoplastic composites for aerospace parts and components has increased dramatically in the last few years (Sudhin et al., 2020). However, the selection of materials for the aircraft interior cabin should be prioritized to maximize passenger safety and comfort while still meeting the Federal Aviation Administration's stringent regulations (FAA). When exposed to fire, the cabin material must have high strength, excellent fire, smoke, and toxicity (FST) and low volatile organic compound (VOC) release. Thousands of pounds of engineered materials are used for each aircraft in the overhead panels, floors, fairings, panels, overhead storage, beverage trucks, and many more (Fig. 1.7). The majority of the inside cabin panels are made of thermoplastic materials, which have a superior surface finish, resistant to damage, thermal and fire-resistant (Vos & Ebeling, 2010; Lapeña-Rey et al., 2015; Martin et al., 2017), have good scratch resistance (Müller, 2013), and have a lightweight property (Smith et al., 2018).

Although thermoset composites are widely used in aerospace applications, they have some flaws, such as lack of reusability, longer processing times, and higher processing costs. The advantages of the engineered thermoplastic composites include lightweight, an indefinite shelf life, low moisture absorption, excellent thermal stability and chemical resistance, high toughness and damage tolerance, solvent resistance, and a low dielectric constant, and they can be an alternative over the thermoset composite and revolutionize the aerospace industries (Barile et al., 2019). Figure 1.8 shows the advantages of utilizing thermoplastic composite materials for aircraft.

2.3 *Biocomposite*

Biocomposites from renewable materials such as natural fibers and biopolymers emerge in the aerospace industry as future aircraft materials. Lightweight, high specific stiffness, high strength, low electrical conductivity, easily bondable, good

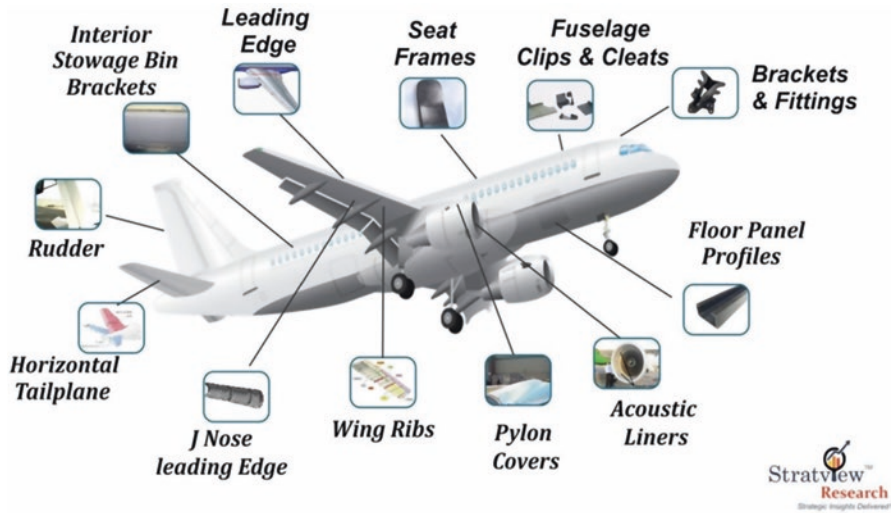


Fig. 1.7 Thermoplastic applications in aircraft. Figure reproduced with permission from (Stratview Research, 2021)

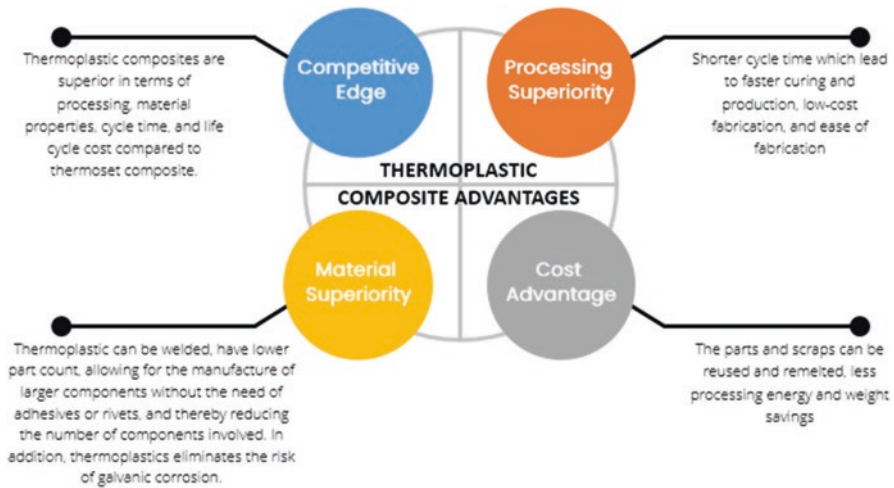


Fig. 1.8 Advantages of thermoplastic composite in aerospace industry

fatigue resistance, internal energy storage and release, low thermal expansion, easily molded to complex shapes, and design flexibility are just a few of the benefits of sustainable biocomposite (Roy et al., 2020). The raw materials of biocomposite come from natural sources. Natural fibers can be obtained from animals, plants, or mineral sources. The biopolymer can be processed from a biological origin such as plant oil, biomass, or biowaste. Figure 1.9 shows the classification of the biocomposite materials related to their degradability. Reinforcing the natural fiber with

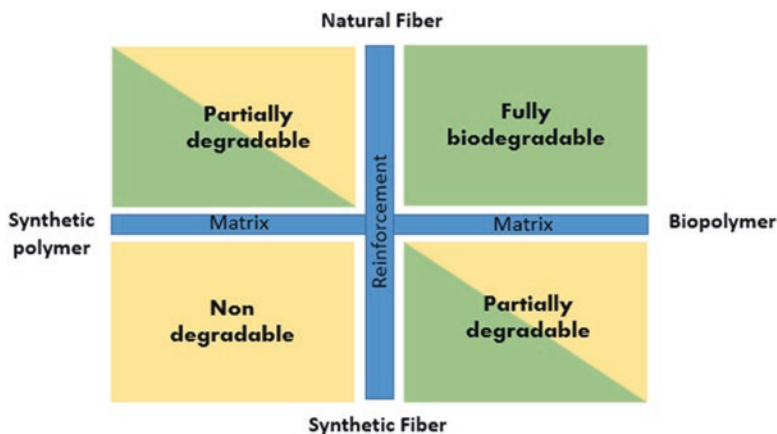


Fig. 1.9 Classification of biocomposite materials

biopolymer will produce biocomposite, which is fully degradable. However, reinforcing either natural fiber in synthetic polymer or synthetic fiber in biopolymer will produce biocomposite with partially degradable characteristics.

For aerospace applications, biocomposite materials could be applied in the interior cabin and cargo components in which emphasis must be given in developing biocomposites that can fulfill the stringent requirement of flammability, smoke density, and toxicity (FST) by the Federal Aviation Administration (FAA). For the primary and secondary structures, the biocomposite must have possessed high durability with improved mechanical performance. In addition, the biocomposite also can be used to make auxiliary materials for aerospace applications. Thus, the prospects for using biocomposite for aircraft parts seem promising; nevertheless, developing biofibers for aviation requires extensive testing and validation, and the research is still in its early stages. Bachmann et al. (2018) researched ECO-COMPASS, which focuses on developing renewable materials for aircraft interior and secondary structure under Horizon 2020 research and innovation actions (RIA). They stated that the proposed biocomposite materials should be mechanically and thermally efficient and also able to withstand the stress, risk of fire, lightning, and moisture uptake.

Jute, kenaf, coir, flax, and bamboo are common natural fibers used to make biocomposite materials where cost and strength are the most important considerations. Table 1.2 shows some basic properties of natural fiber. The primary chemical compositions existed in the natural fiber are cellulose, hemicellulose, and lignin. Although natural fibers have a vast range of chemical compositions, practically all natural fibers are hydrophilic. According to Väisänen et al. (2016), high linearity and crystallinity of cellulose microfibrils reduce the hydrophilicity of cellulose even though it is rich with hydroxyl (-OH) groups. The free -OH groups which existed on the microfibrils are still capable of absorbing a significant amount of water. Poor compatibility between natural fiber and polymer matrix due to differences in surface nature may lead to poor stress transfer in biocomposite when the load is applied.

Table 1.2 Basic properties of natural fiber (Väisänen et al., 2016; Petroudy, 2017; Silva et al., 2021)

Fiber	Density (g/cm ³)	Microfibrillar angle (degrees)	Tensile strength (MPa)	Elastic modulus (GPa)	Elongation at break (%)
Jute	1.3–1.5	8	200–770	20–55	2.0–3.0
Sisal	1.5	10–25	100–800	9–22	3.0–7.0
Kenaf	1.4–1.5	7.1	930	53	1.6
Coir	1.2	30–49	180	4–6	30.0
Flax	1.5	6–10	350–1040	28–70	2.0–4.0
Hemp	1.5	50–90	690	30–70	1.5–4.0
Bamboo	0.6–1.1	40–60	140–230	11–17	4.0–7.0

Thus, treatment on natural fibers is necessary to improve the adhesion properties between natural fiber and polymer matrix. In addition, surface treatment is necessary to improve the intrinsic natural fiber properties.

Figure 1.10 shows the relationship between microfibrillar angle (MFA) and tensile modulus for various natural fibers. The fiber stiffness is inversely related to MFA. Lau et al. (2018) investigated the effects of MFA on the tensile strength of the natural fibers. The elongation at break increases with microfibrillar angle. The larger the MFA, the higher the failure strain, as shown in sisal fiber. Other parameters of natural fibers may affect the composite properties such as fiber geometry, fiber orientation, pore structure, wettability, moisture absorption, and wettability.

The potential of natural fiber for radome applications has been discussed by Ilyas et al. (2019). Glass fiber-reinforced plastic was used in radome applications because it provides radio-frequency (RF) transparency in which the RF field can penetrate without heating. They reviewed that hybrid kenaf/glass fiber reinforcement in the epoxy composite is possible to reduce the composite weight and provide a better low dielectric constant for radome. The development of high-performance epoxy biocomposite based on rice husk for coating on air duct has been investigated by Karthigairajan et al. (2020). The addition of rice husk in epoxy was found to lower the thermal conductivity significantly and reduce the water uptake with the inclusion of only 2 vol% of silane-treated rice husk. Thus, coating of silane-treated rice husk-reinforced epoxy composite was suggested to be a better potential coating by providing longer lifetime to air duct to prevent welding crack initiation.

Liu et al. (2018) have developed an acoustic panel for aircraft propeller made of laminated hybrid ramie/glass-reinforced phenolic composite. Ramie exhibits strong specific stiffness and high strength properties. They observed that the flammability behavior of the produced biocomposite was acceptable and had the potential to be used for aircraft interior applications. Zin et al. (2019) investigated the fabrication technique of pineapple leaf fiber (PALF) hybrid biocomposite using an automated spray-up process. They found an improvement in tensile strength with low variation of the hybrid biocomposite. The synergistic effect between superior glass fiber properties and high strength (PALF) improves the tensile strength properties up to 71.86 MPa compared to single reinforcement of PALF composite, which is only 26.14 MPa. This hybrid PALF/glass biocomposite was suggested to be an alternative for interior aircraft applications.

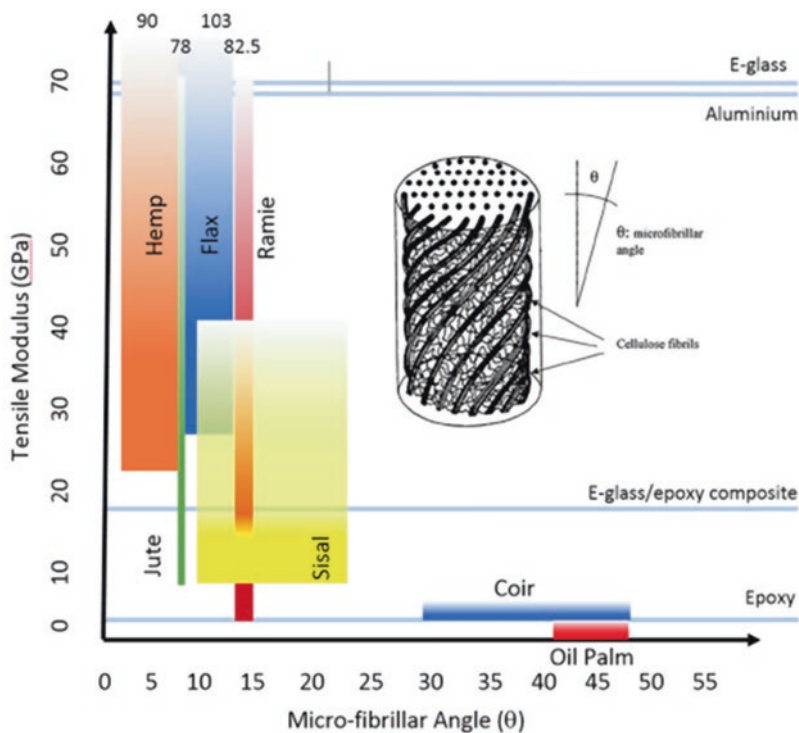


Fig. 1.10 Relationship between micro-fibrillar angle and tensile modulus of various natural fibers (Lau et al., 2018)

2.4 Geopolymer Composite

Geopolymer is another class of materials, and it is an interesting alternative material to existing ceramic and polymer matrix. Geopolymer is an inorganic polymer binder that is formed from the reaction between aluminosilicate materials and activated with a highly alkaline solution. The starting raw materials are rich with aluminosilicate sources found from ash derived from industrial, agricultural, and geological wastes. A typical liquid alkaline activator such as sodium hydroxide sodium silicate or a combination of these can be employed to process aluminosilicate. The desired characteristics of the generated geopolymer can be accomplished by designing the optimal mixing ingredients between aluminosilicates and activated alkali solutions. The production of high molecular structure from the geopolymerization process will form a geopolymer with excellent mechanical and thermal properties. It is feasible to control the properties of geopolymers by adjusting the Si/Al ratio. For example, the resultant mixture of Si/Al ratio of 3:1, for example, will generate a rigid end product. As a result, this mixture can be used to make concrete, cement, or a waste encapsulation medium. On the other hand, when the Si/Al ratio exceeds 3, the formulate geopolymer becomes less rigid and more flexible and has a

polymer-like behavior. However, care needs to be taken on the water content and composite thickness because high water content will delay the geopolymer composite curing process (Norkhairunnisa & Fariz, 2015).

Geopolymer has excellent thermal stability, low thermal conductivity, and excellent fire resistance with no smoke and emits toxicity during burning. The geopolymer composite offers high potential and is thermally stable at a temperature of about 800–1200 °C. According to Hron et al. (2018), geopolymer material shows low processing temperature, and the usable temperature was found to be higher than organic polymer.

The composite materials in an aircraft must comply with the Federal Aviation Regulations (FAR). Figure 1.11 shows the criteria on fire resistance material requirements by the Federal Aviation Administration (FAA). The rationale for using composites with fire-resistant and non-flammable properties is to give passengers and crew members more time to exit the plane after an accident by delaying the occurrence of a cabin flash fire or flashover. The escape time is crucial during aircraft fire incidents. Delaying fire escape during a fire will increase fatalities by suffocation due to toxic smoke inhalation within the burning cabin. Geopolymer materials are one of the alternative materials which are low cost, are environmentally friendly, have low density, and are fire-resistant.

Geopolymer is a potential material that can prevent fire hazards in the aircraft cabin. According to Lyon et al. (1997), geopolymer is not easily combustible as the time to flashover is infinity. Compared to other polymer composites, the time to flashover is around 12 min for thermoset and around 25 min for engineering plastic. Hron et al. (2018) investigated fiber-reinforced geopolymer composite, which is exposed to the operating fluids in the aircraft. They found that the tensile strength of the geopolymer composite increased to 25%, which indicates that the geopolymer composite can be considered to be applied in the extreme environment in the aircraft. The mechanical properties of unidirectional carbon fiber-reinforced geopolymer composite, which was prepared by ultrasonic-assisted slurry infiltration, were investigated by He et al. (2010). The high strength-to-weight ratio of carbon fiber can prevent catastrophic brittle failure of the geopolymer composites. Furthermore,



Fig. 1.11 Federal Aviation Administration (FAA) requirements on fire resistance

the heat treatment process in the range of 1100–1300 °C on the CF/geopolymer composite was found to improve the mechanical properties.

The use of lighter composite materials in aircraft construction can allow for greater payload and fuel savings. Thang et al. (2010) observed the flexural properties of the alumina nanofiber in carbon/geopolymer and basalt/geopolymer composites. They found that the addition of 1.0 wt% of alumina nanofiber improved the flexural strength of the fiber-reinforced geopolymer composite. The small amount of nanofiber is capable to exhibit reinforcing effects on the composite.

3 Future in Polymer Composite for Aerospace Applications

For the latest aircraft development, over 50% of the aircraft body was made of composite materials. Replacement of some parts or components of the conventional metal with composite materials reduces the aircraft weight, operating cost, and fuel saving and improves the flying performance. In addition, there are many advantages of composite materials, which are high strength-to-weight ratio, good fatigue and corrosion-resistant, better thermal stability, and ease to assemble. Besides focusing on weight saving, another reason was to make aircraft a safe travel mode. With improved composite materials and growth in technology, the number of fatal accidents can be reduced. Besides that, the traveling cost can be reduced with the innovative improvement of composite materials. Furthermore, with reduced weight structure, equipment such as inflight entertainment and extra legroom seats will make the flying experience more exciting and relaxing.

Nanotechnology development in composite materials is a way to reduce the weight by replacing some micron size filler with only a small concentration of nanofillers and providing better mechanical, thermal, and electrical properties. The nanocomposites can be incorporated into complex aircraft shapes, reducing waste generated during manufacture. The use of nanocomposites in various subsystems in the aircraft structure, particularly the self-healing capabilities of the polymer nanocomposite, revealed that the nanotechnology industry has a bright future (Guo et al., 2019). Polymer composite is lightweight and has insulation characteristics that can provide lightning strike protection and reduce aircraft accidents. The addition of conductive nanofillers, such as graphene, and carbon nanotube, in the polymer composite, can dissipate the lightning current and also function as a deicing heater element for the aircraft surface (Alemour et al., 2019). In addition, the wear and friction resistance at high operating temperatures in the aircraft were found to be reduced with the addition of nano-alumina in composite materials. Not only that, the vibration damping factors of the polymer nanocomposites filled carbon nanotube (CNT) were significantly reduced (Liang et al., 2009).

According to Wild et al. (2021), structural health monitoring (SHM) for aircraft structure is important to reduce catastrophic fatigue failure on aircraft. The fatigue behavior of carbon fiber-reinforced polymer (CFRP) depends on the interplanar

stress and strain of the lamina. The fatigue damage in the CFRP is very complex because it can occur through various mechanisms such as voids, matrix cracking, delamination, and fiber breakage. Thus, continuous inspection of the CFRP or fibrous polymer composite materials is crucial to identify the fatigue occurrence and overcome the current maintenance by SHM.

Many researches on reinforcement of agricultural waste fiber such as kenaf, ramie, and jute in polymer composite for aerospace applications are currently being conducted. Awareness on material sustainability, climate change, cost factor, and environmental pollution leads to widening the research scope on finding the potential application of biocomposite in aircraft components. The problem with the natural fiber is the variability of the fiber structure, which mainly consists of cellulose, hemicellulose, and lignin elements. In addition, the fiber surface is prone to water absorption due to the presence of hydroxyl groups which also makes it less compatible with the hydrophobic polymer. Even though many researches have been conducted on improving the natural fiber properties, more research needs to be conducted to ensure that the biocomposite complies with the FAR requirements.

4 Conclusion

Fiber-reinforced polymer composite materials have been widely used in aerospace. The important feature of polymer composite is high strength-to-weight ratio, durability, corrosion resistance, thermal stability, and many more. The lightweight feature on the aircraft can make the aircraft fly longer in the air and reduce the CO₂ emission in the air. The replacement of conventional metal alloys with polymer composite has tremendously reduced the number of fasteners that make conventional aircraft heavier than aircraft with a composite structure. Thermoset and thermoplastic are the major polymer types used in the aircraft structure, and both have similar performance characteristics when combined with engineered fiber. Thermoset has been used since the early development of aircraft composite materials. It is a non-reversible polymer with a high crosslink structure and forms a network with the reinforcing fibers to enhance the composite performance. Most of the thermoset composite fabrication was conducted using an autoclave. On the other hand, the thermoplastic polymer can be reversible and reshaped and is able to be recycled. The thermoplastic composite processing does not require autoclave, which leads to the flexibility and sustainability advantages in the manufacturing of aircraft parts. Besides that, research on natural fibers and biopolymers for aerospace applications is growing. Regarding the environmental concern on material sustainability and climate change, biocomposite was considered a future composite material for the aircraft interior. In addition, thermally stable and fire-resistant geopolymer composite materials of more than 1000 °C can also be a potential material for the interior or extreme environment in aircraft structures.

Acknowledgments The authors would like to thank the Department of Aerospace Engineering, Institute of Nanoscience and Nanotechnology (ION2), and Institute of Tropical Forestry and Forest Products (INTROP) in Universiti Putra Malaysia for the space and facilities to conduct the experiment on polymer composite. Special thanks are also given to Kyushu Institute of Technology (KyuTech), Japan, for the research collaboration in polymer composite materials.

References

- Alavudeen, A., Rajini, N., Karthikeyan, S., et al. (2015). Mechanical properties of banana/kenaf fiber-reinforced hybrid polyester composites: Effect of woven fabric and random orientation. *Materials and Design*, 66, 246–257. <https://doi.org/10.1016/j.matdes.2014.10.067>
- Alemour, B., Badran, O., & Hassan, M. R. (2019). A review of using conductive composite materials in solving lightning strike and ice accumulation problems in aviation. *Journal of Aerospace Technology and Management*, 11. <https://doi.org/10.5028/jatm.v11.1022>
- Aslan, Z., & Daricik, F. (2016). Effects of multiple delaminations on the compressive, tensile, flexural, and buckling behaviour of E-glass/epoxy composites. *Composites Part B: Engineering*, 100, 186–196. <https://doi.org/10.1016/j.compositesb.2016.06.069>
- Bachmann, J., Yi, X., Gong, H., et al. (2018). Outlook on ecologically improved composites for aviation interior and secondary structures. *CEAS Aeronautical Journal*, 9(3), 533–543. <https://doi.org/10.1007/s13272-018-0298-z>
- Barile, C., Casavola, C., & De Cillis, F. (2019). Mechanical comparison of new composite materials for aerospace applications. *Composites Part B: Engineering*, 162, 122–128. <https://doi.org/10.1016/j.compositesb.2018.10.101>
- Barile, M., Lecce, L., Iannone, M., et al. (2020). Thermoplastic composites for aerospace applications. In S. Pantelakis & K. Tserpes (Eds.), *Revolutionizing aircraft materials and processes* (pp. 87–114). Springer International Publishing. https://doi.org/10.1007/978-3-030-35346-9_4
- Bing, D. U., Liming, C. H. E. N., Houchang, L. I. U., et al. (2020). Resistance welding of glass fiber reinforced thermoplastic composite: Experimental investigation and process parameter optimization. *Chinese Journal of Aeronautics*, 33(12), 3469–3478. <https://doi.org/10.1016/j.cja.2020.02.018>
- Butt, J., Hewavidana, Y., Mohaghegh, V., et al. (2019). Hybrid manufacturing and experimental testing of glass fiber enhanced thermoplastic composites. *Journal of Manufacturing and Materials Processing*, 3(4), 96. <https://doi.org/10.3390/jmmp3040096>
- El-Wazery, M. S., El-Elamy, M. I., & Zoalfakar, S. H. (2017). Mechanical properties of glass fiber reinforced polyester composites. *International Journal of Applied Science and Engineering*, 14(3), 121–131.
- Erden, S. E. Ç. K. İ. N., Sever, K., Seki, Y., et al. (2010). Enhancement of the mechanical properties of glass/polyester composites via matrix modification glass/polyester composite siloxane matrix modification. *Fibers and Polymers*, 11(5), 732–737. <https://doi.org/10.1007/s12221-010-0732-2>
- Guo, Y., Zou, D., Zhu, W., et al. (2019). Infrared induced repeatable self-healing and removability of mechanically enhanced graphene–epoxy flexible materials. *RSC Advances*, 9(25), 14024–14032. <https://doi.org/10.1039/c9ra00261h>
- Giurgiutiu, V. (2015). *Structural health monitoring of aerospace composites*.
- Hadigheh, S. A., & Kashi, S. (2018). Effectiveness of vacuum consolidation in bonding fibre reinforced polymer (FRP) composites onto concrete surfaces. *Construction and Building Materials*, 187, 854–864. <https://doi.org/10.1016/j.conbuildmat.2018.07.200>
- Hamerton, I., & Mooring, L. (2012). The use of thermosets in aerospace applications. In *Thermosets* (pp. 189–227). Woodhead Publishing. <https://doi.org/10.1533/9780857097637.2.189>
- Haijuan, K., Hui, S., Jin, C., et al. (2018). Improvement of adhesion of kevlar fabrics to epoxy by surface modification with acetic anhydride in supercritical carbon dioxide. *Polymer Composites*, 40(S1), E920–E927. <https://doi.org/10.1002/pc.25100>

- He, H. W., & Gao, F. (2015). Effect of fiber volume fraction on the flexural properties of unidirectional carbon fiber/epoxy composites. *International Journal of Polymer Analysis and Characterization*, 20(2), 180–189. <https://doi.org/10.1080/1023666x.2015.989076>
- He, P., Jia, D., Lin, T., et al. (2010). Effects of high-temperature heat treatment on the mechanical properties of unidirectional carbon fiber reinforced geopolymer composites. *Ceramics International*, 36(4), 1447–1453. <https://doi.org/10.1016/j.ceramint.2010.02.012>
- Hemanth, R. D., Kumar, M. S., Gopinath, A., et al. (2017). Evaluation of mechanical properties of E-Glass and coconut fiber reinforced with polyester and epoxy resin matrices. *International Journal of Mechanical and Production Engineering Research and Development*, 7(5), 13–20. <https://doi.org/10.24247/ijmperdoct20172>
- Hiremath, N., Young, S., Ghossein, H., et al. (2020). Low cost textile-grade carbon-fiber epoxy composites for automotive and wind energy applications. *Composites Part B: Engineering*, 198, 108156. <https://doi.org/10.1016/j.compositesb.2020.108156>
- Hron, R., Kadlec, M., & Martaus, F. (2018). Mechanical properties of fibre reinforced geopolymer composites exposed to operating fluids. *Solid State Phenomena*, 278, 82–88. <https://doi.org/10.4028/www.scientific.net/ssp.278.82>
- Ilyas, R. A., Sapuan, S. M., Norizan, M. N., et al. (2019). Potential of natural fibre composites for transport industry: A review. *Prosiding Seminar Enau Kebangsaan, 2019*, 2–11.
- İnal, O., Akbolat, M. Ç., Soutis, C., et al. (2021). Toughening mechanisms in cost-effective carbon-epoxy laminates with thermoplastic veils: Mode-I and in-situ SEM fracture characterisation. *International Journal of Lightweight Materials and Manufacture*, 4(1), 50–61. <https://doi.org/10.1016/j.ijlmm.2020.07.003>
- Kamiyama, S., Hirano, Y., Okada, T., et al. (2018). Lightning strike damage behavior of carbon fiber reinforced epoxy, bismaleimide, and polyetheretherketone composites. *Composites Science and Technology*, 161, 107–114. <https://doi.org/10.1016/j.compscitech.2018.04.009>
- Karthigairajan, M., Nagarajan, P. K., Malarvannan, R. R., et al. (2020). Effect of silane-treated rice husk derived biosilica on visco-elastic, thermal conductivity and hydrophobicity behavior of epoxy biocomposite coating for air-duct application. *SILICON*, 1–10. <https://doi.org/10.1007/s12633-020-00772-z>
- Khalili, S., Rantanen, E., Bogdanov, D., et al. (2019). Global transportation demand development with impacts on the energy demand and greenhouse gas emissions in a climate-constrained world. *Energies*, 12(20), 3870. <https://doi.org/10.3390/en12203870>
- Lapeña-Rey, N., Gonzalez-Garcia, A. M., Martin-Alonso, P. P., et al. (2015). *Fire resistant sustainable aircraft interior panels*. U.S. Patent Application 14/591,855.
- Lau, K. T., Hung, P. Y., Zhu, M. H., et al. (2018). Properties of natural fibre composites for structural engineering applications. *Composites Part B: Engineering*, 136, 222–233. <https://doi.org/10.1016/j.compositesb.2017.10.038>
- Li, W., Guo, S., Giannopoulos, I. K., et al. (2020). Strength enhancement of bonded composite laminate joints reinforced by composite Pins. *Composite Structures*, 236, 111916. <https://doi.org/10.1016/j.compstruct.2020.111916>
- Liang, F., Tang, Y., Gou, J., et al. (2009). Multifunctional nanocomposites with high damping performance for aerospace structures. *ASME International Mechanical Engineering Congress and Exposition*, 43840, 267–273. <https://doi.org/10.1115/imece2009-12542>
- Liu, X., Yi, X., & Zhu, J. (2018). Bio-based epoxies and composites as environmentally friendly alternative materials. In *Thermosets* (pp. 621–637). Elsevier. <https://doi.org/10.1016/b978-0-08-101021-1.00019-8>
- Lu, B. (2010). The Boeing 787 dreamliner designing an aircraft for the future. *Journal of Young Investigators*, 4026, 34.
- Lyon, R. E., Balaguru, P. N., Foden, A., et al. (1997). Fire-resistant aluminosilicate composites. *Fire and Materials*, 21(2), 67–73. [https://doi.org/10.1002/\(sici\)1099-1018\(199703\)21:2%3C67::aid-fam596%3E3.0.co;2-n](https://doi.org/10.1002/(sici)1099-1018(199703)21:2%3C67::aid-fam596%3E3.0.co;2-n)
- Ma, Y., Zhang, Y., Sugahara, T., et al. (2016). Off-axis tensile fatigue assessment based on residual strength for the unidirectional 45 carbon fiber-reinforced composite at room temperature. *Composites Part A: Applied Science and Manufacturing*, 90, 711–723. <https://doi.org/10.1016/j.compositesa.2016.09.001>

- Mansor, M. R., Nurfaizey, A. H., Tamaldin, N., et al. (2019). Natural fiber polymer composites: Utilization in aerospace engineering. In *Biomass, biopolymer-based materials, and bioenergy* (pp. 203–224). Woodhead Publishing.
- Marsh, G. (2016). Composites consolidate in commercial aviation. *Journal of Reinforced Plastics, 60*(5), 302–305. <https://doi.org/10.1016/j.repl.2016.08.002>
- Martin, P. P., Gonzalez-Garcia, A., Lapena, N., et al. (2017). *Green aircraft interior panels*. U.S. Patent 9,782,944.
- McCarthy, R. F. J., Haines, G. H., & Newley, R. A. (1994). Polymer composite applications to aerospace equipment. *Composites Manufacturing, 5*(2), 83–93. [https://doi.org/10.1016/0956-7143\(94\)90059-0](https://doi.org/10.1016/0956-7143(94)90059-0)
- Muhammad, A., Rahman, M. R., Bains, R., et al. (2021). Applications of sustainable polymer composites in automobile and aerospace industry. In *Advances in sustainable polymer composites* (pp. 185–207). Woodhead Publishing. <https://doi.org/10.1016/b978-0-12-820338-5.00008-4>
- Müller, T. (2013). *Rear-illuminable aircraft interior component*. Airbus Operations GmbH, U.S. Patent 8, 501, 311.
- Muralidhara, B., Babu, S. K., & Suresha, B. (2020). Utilizing vacuum bagging process to prepare carbon fiber/epoxy composites with improved mechanical properties. *Materials Today: Proceedings, 27*, 2022–2028. <https://doi.org/10.1016/j.matpr.2019.09.051>
- Naresh, K., Shankar, K., & Velmurugan, R. (2018). Reliability analysis of tensile strengths using Weibull distribution in glass/epoxy and carbon/epoxy composites. *Composites Part B: Engineering, 133*, 129–144. <https://doi.org/10.1016/j.compositesb.2017.09.002>
- Norkhairunnisa, M., & Fariz, M. N. (2015). Geopolymer: A review on physical properties of inorganic aluminosilicate coating materials. *Materials Science Forum, 803*, 367–373. <https://doi.org/10.4028/www.scientific.net/msf.803.367>
- Paolillo, S., Bose, R. K., Santana, M. H., et al. (2021). Intrinsic self-healing epoxies in polymer matrix composites (PMCs) for aerospace applications. *Polymers, 13*(2), 201. <https://doi.org/10.3390/polym13020201>
- Petroudy, S. D. (2017). Physical and mechanical properties of natural fibers. In *Advanced high strength natural fibre composites in construction* (pp. 59–83). Woodhead Publishing. <https://doi.org/10.1016/b978-0-08-100411-1.00003-0>
- Pitarresi, G., Scalici, T., & Catalanotti, G. (2019). Infrared thermography assisted evaluation of static and fatigue Mode II fracture toughness in FRP composites. *Composite Structures, 226*, 111220. <https://doi.org/10.1016/j.compstruct.2019.111220>
- Rahmani, H., Najafi, S. H. M., & Ashori, A. (2014). Mechanical performance of epoxy/carbon fiber laminated composites. *Journal of Reinforced Plastics and Composites, 33*(8), 733–740. <https://doi.org/10.1177/0731684413518255>
- Rahmani, H., Najafi, S. H. M., Saffarzadeh-Matin, S., et al. (2013). Mechanical properties of carbon fiber/epoxy composites: Effects of number of plies, fiber contents, and angle-ply layers. *Polymer Engineering & Science, 54*(11), 2676–2682. <https://doi.org/10.1002/pen.23820>
- Ray, B. C., & Rathore, D. (2015). Environmental damage and degradation of FRP composites: A review report. *Polymer Composites, 36*(3), 410–423. <https://doi.org/10.1002/pc.22967>
- Redazione (2018). High-flying epoxies use of epoxy resins in aircraft design. Aviation Report.com. <http://en.aviation-report.com/high-flying-expoxies-use-of-epoxy-resins-in-aircraft-design/>
- Reis, J. M. L., Coelho, J. L. V., Monteiro, A. H., et al. (2012). Tensile behavior of glass/epoxy laminates at varying strain rates and temperatures. *Composites Part B: Engineering, 43*(4), 2041–2046. <https://doi.org/10.1016/j.compositesb.2012.02.005>
- Roy, P., Defersha, F., Rodriguez-Urbe, A., et al. (2020). Evaluation of the life cycle of an automotive component produced from biocomposite. *Journal of Cleaner Production, 273*, 123051. <https://doi.org/10.1016/j.jclepro.2020.123051>
- Saravanakumar, K., Suresh Kumar, C., & Arumugam, V. (2021). Damage monitoring of glass/epoxy laminates with different interply fiber orientation using acoustic emission. *Structural Health Monitoring, 17*(1). <https://doi.org/10.1177/1475921720939064>

- Silva, T. T. D., Silveira, P. H. P. M. D., Ribeiro, M. P., et al. (2021). Thermal and chemical characterization of Kenaf Fiber (*Hibiscus cannabinus*) reinforced epoxy matrix composites. *Polymers*, *13*(12), 2016. <https://doi.org/10.3390/polym13122016>
- Smith, J. T., Lasell, D. M., Daout, J. M., & Safran Seats USA LLC. (2018). *Thermoplastic composite components for commercial aircraft seats*. U.S. Patent Application 15/747,814.
- Soutis, C. (2015). Introduction: Engineering requirements for aerospace composite materials. In *Polymer composites in the aerospace industry* (pp. 1–18). Woodhead Publishing.
- Stratview Research. (2021). *Aerospace & defense thermoplastic composites market size, share, trend, forecast, & competitive analysis: 2021–2026*. SRAD156, p. 288.
- Sudhin, A. U., Remanan, M., Ajeesh, G., et al. (2020). Comparison of properties of carbon fiber reinforced thermoplastic and thermosetting composites for aerospace applications. *Materials Today: Proceedings*, *24*, 453–462. <https://doi.org/10.1016/j.matpr.2020.04.297>
- Sun, G., Zuo, W., Chen, D., et al. (2021). On the effects of temperature on tensile behavior of carbon fiber reinforced epoxy laminates. *Thin-Walled Structures*, *164*, 107769. <https://doi.org/10.1016/j.tws.2021.107769>
- Struzziero, G., Teuwen, J. J., & Skordos, A. A. (2019). Numerical optimisation of thermoset composites manufacturing processes: A review. *Composites Part A: Applied Science and Manufacturing*, *124*, 105499. <https://doi.org/10.1016/j.compositesa.2019.105499>
- Tanzil, A. H., Brandt, K., Wolcott, M., et al. (2021). Strategic assessment of sustainable aviation fuel production technologies: Yield improvement and cost reduction opportunities. *Biomass & Bioenergy*, *145*, 105942. <https://doi.org/10.1016/j.biombioe.2020.105942>
- Tatsumi, G., Ratoi, M., Shitara, Y., et al. (2019). Effect of lubrication on friction and wear properties of PEEK with steel counterparts. *Tribology Online*, *14*(5), 345–352.
- Teplyk, Y., Hapon, V., & Tuz, M. (2020). Thermoplastic materials-a new stage in the life of aircraft construction. *Proceedings of National Aviation University*, *84*(3).
- Thang, X. N., Kroisova, D., Louda, P., et al. (2010). Microstructure and flexural properties of geopolymer matrix-fibre reinforced composite with additives of alumina (Al₂O₃) nanofibres. In *International conference 7th-TEXSCI*, Czech Republic.
- Timmis, A. J., Hodzic, A., Koh, L., et al. (2015). Environmental impact assessment of aviation emission reduction through the implementation of composite materials. *International Journal of Life Cycle Assessment*, *20*(2), 233–243. <https://doi.org/10.1007/s11367-014-0824-0>
- Väisänen, T., Haapala, A., Lappalainen, R., et al. (2016). Utilization of agricultural and forest industry waste and residues in natural fiber-polymer composites: A review. *Waste Management*, *54*, 62–73. <https://doi.org/10.1016/j.wasman.2016.04.037>
- Vos, S. F., & Ebeling, T. A. (2010). *Thermoplastic composite material with improved smoke generation, heat release, and mechanical properties*. U.S. Patent Application 12/220,410.
- Wang, Y., Nuzzo, S., Zhang, H., et al. (2020). Challenges and opportunities for wound field synchronous generators in future more electric aircraft. *IEEE Transactions on Transportation Electrification*, *6*(4), 1466–1477. <https://doi.org/10.1109/tte.2020.2980189>
- Wild, G., Pollock, L., Abdelwahab, A. K., et al. (2021). The need for aerospace structural health monitoring: A review of aircraft fatigue accidents. *International Journal of Prognostics and Health Management*, *12*(3). <https://doi.org/10.36001/ijphm.2021.v12i3.2368>
- Williams, J. C., & Boyer, R. R. (2020). Opportunities and issues in the application of titanium alloys for aerospace components. *Metals*, *10*(6), 705. <https://doi.org/10.3390/met10060705>
- Yang, J., Xiao, J., Zeng, J., et al. (2013). Matrix modification with silane coupling agent for carbon fiber reinforced epoxy composites. *Fibers and Polymers*, *14*(5), 759–766. <https://doi.org/10.1007/s12221-013-0759-2>
- Zhao, F., Liu, F., Liu, Z., et al. (2019). The correlated impacts of fuel consumption improvements and vehicle electrification on vehicle greenhouse gas emissions in China. *Journal of Cleaner Production*, *207*, 702–716. <https://doi.org/10.1016/j.jclepro.2018.10.046>
- Zin, M. H., Abdan, K., Mazlan, N., et al. (2019). Automated spray up process for pineapple leaf fibre hybrid biocomposites. *Composites Part B: Engineering*, *177*, 107306. <https://doi.org/10.1016/j.compositesb.2019.107306>

Chapter 2

Impact Studies of Hybrid Nanocomposites in Aerospace Application



G. Balaganesan, N. K. Gupta, and R. Velmurugan

1 Introduction

Composite materials of polymer matrix reinforced with fibers like glass, carbon, and Kevlar are widely used in aerospace, automotive, marine, and other mechanical industries due to their superior mechanical properties and light weight. The structures are subjected to complex loading systems within static or dynamic conditions. The dynamic loads produce excessive vibration when subjected to impact loading. It is important to understand the dynamic response of these structures at various modes of vibration and behavior of these structures for energy absorption (Velmurugan & Balaganesan, 2011). The use of composites for energy absorption in impact loading has received much attention (Zinoviev & Ermakov, 1994). Since the use of these materials increases day by day and systems becoming complex, newer materials are developed or additional fillers are added in the matrix to improve the performance of the composites (Aymerich et al., 2011). Suriani et al. (2021a, b) summarized that the flammability and tensile properties of natural fiber-reinforced fire-retardant epoxy composites are reduced when the fiber volume contents are increased at the optimal loading of 20%. It is understood from the literature that polymer-based composites reinforced with small amount of nanoscale fillers improve the mechanical and thermal properties of polymer matrix materials (Mohan et al., 2006). Further the addition of nanofillers in fiber-reinforced plastics has also

G. Balaganesan

Department of Mechanical Engineering, Indian Institute of Technology Madras, Chennai, India

N. K. Gupta

Department of Applied Mechanics, Indian Institute of Technology Delhi, New Delhi, India

R. Velmurugan (✉)

Department of Aerospace Engineering, Indian Institute of Technology Madras, Chennai, India

e-mail: ramanv@iitm.ac.in

yielded improvement in impact and other mechanical properties of laminates (Vijay Kumar et al., 2019a, b). Nanocomposites are nanoscale fillers reinforced with composite materials, wherein one of the phases has geometry of less than 100 nm. The addition of nanofillers such as ceramic particles, nanotubes, nanofibers, whiskers, etc. improves the matrix properties of the fiber-reinforced polymer composites (Wetzela et al., 2003). Nurazzi et al. (2021) reviewed the application of carbon nanotube-reinforced composite application in various fields. It is expected that the interfacial properties of polymers containing nano-particles are largely influenced by the nanofillers due to high surface area between polymer and nanofillers. Nanocomposites differ from fiber-reinforced composites due to their high surface-to-volume ratio of the reinforcing phase in the matrix (Sun et al., 2009). Ilyas et al. (2021) presented the development and conducted studies on PLA-based natural fiber bio-composites over the last decade. Their work reviews recent PLA-derived bio-composite research related to PLA synthesis and biodegradation and its properties, processes, challenges, and prospects. Sandwiching of composite laminates by adding core material improvises the stiffness with an increase in volume of the sandwich structures (Alsubari et al., 2021). Nurazzi et al. (2021) reviewed on the influence of utilizing various natural fibers as an alternative material to Kevlar fabric for armor structure system. Their work focuses on the effect of layering and sequencing of natural fiber fabric in the composites to advance the current armor structure system. Omran et al. (2021) studied on how the reinforcement of micro- and nanocellulose can yield a material with improved performance. They have featured the performances, limitations, and possible areas of improvement to fit into the broader range of engineering applications.

2 Experiments

2.1 Materials

The WRM glass fibers of 610 gsm, Owens Corning made, are used as reinforcement for preparing the laminates. Huntsman-made epoxy LY556 and Hardener HY951 are used as matrix system. The nanoclay Garamite 1958 purchased from Southern Clay Products, USA, is used as filler. The percentage of filler varied from 1 to 5 weight percentage of matrix.

Figure 2.1 shows the SEM image of un-separated clay particles in micron size. The clay in micron size is a formation of millions of nanoscale clay platelets. The nanoscale clay is separated during dispersion with matrix system by using mechanical shear mixer which is discussed in the latter part of this chapter.

The EDAX report for the elements in clay particles is seen in Fig. 2.2, and the corresponding weight percentage of various elements is given in Table 2.1. The first peak in Fig. 2.2 corresponds to “C” carbon. It is not due to clay; carbon indicated the tap, which is pasted on the crucible to hold the sample. Silica, magnesium, and alumina are the major elements present in the clay.

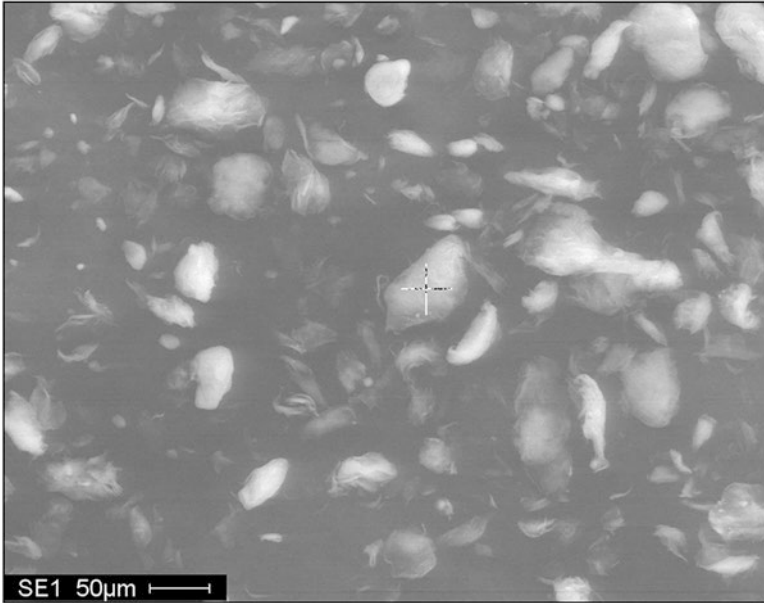


Fig. 2.1 SEM image of un-separated clay particles

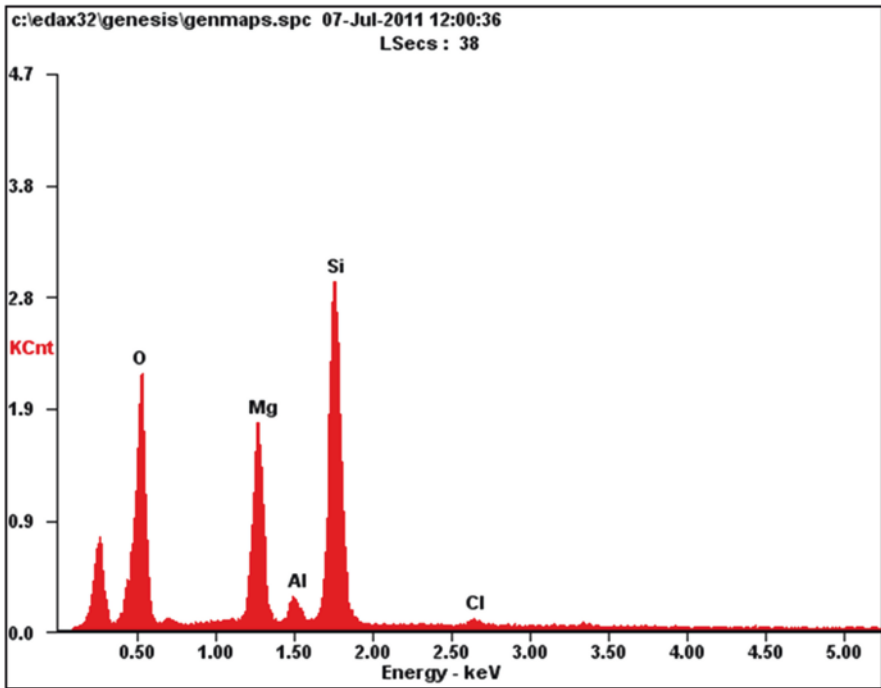


Fig. 2.2 Elements present in nanoclay

Table 2.1 Percentage of elements present in nanoclay

Element	Weight %	Atomic weight %
<i>O</i>	52.46	64.71
<i>Mg</i>	17.33	14.07
<i>Al</i>	02.42	01.77
<i>Si</i>	27.26	19.16
<i>Cl</i>	00.52	00.29

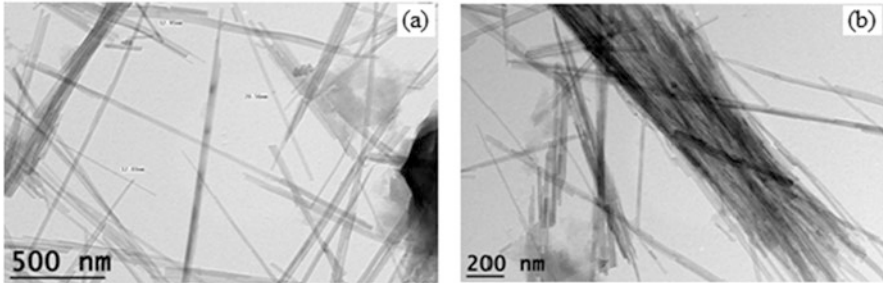
**Fig. 2.3** TEM image of (a) nanoclay (b) a bunch of clay layers

Figure 2.3(a) shows the TEM image of the nanoclay. The cross section of the clay is in few nanometers and the length is in micron size. Figure 2.3(b) shows the TEM image of a bunch of clay layers. The clay has high aspect ratio which acts as secondary fibers when reinforced with matrix.

2.2 Dispersion of Nanofillers and Fabrication of Specimens

Figure 2.4 shows the dispersion mechanisms of nanoplatelets in polymer. If the bunches of platelets are shear apart, the result of mixing is the un-separated platelets in polymer matrix which leads to agglomeration. If the individual platelet is peel apart, the result of mixing is the well-dispersed platelets in polymer matrix which leads to exfoliation. Shear mixing process is used to disperse the nanoclay of 1–5 wt. % in the epoxy matrix. A roller is used for better infiltration of resin in the fiber layers. Numbers of layers are changed for various thickness values of the laminates. Figure 2.5 shows the hand lay-up process used for the preparation of nanocomposite laminates. After 3 h, the laminate is placed in a mold and kept under pressure in a compression molding machine for a period of 3 h. The compression molding machine used to prepare the laminates is shown in Fig. 2.6. The laminates are prepared with three, five, and eight layers of glass fibers with 0°/90° orientation of thickness 2 mm, 3 mm, and 5 mm, respectively. The cured laminates are cut into 300 mm × 300 mm size and holes are made for mounting the laminates in the fixture.

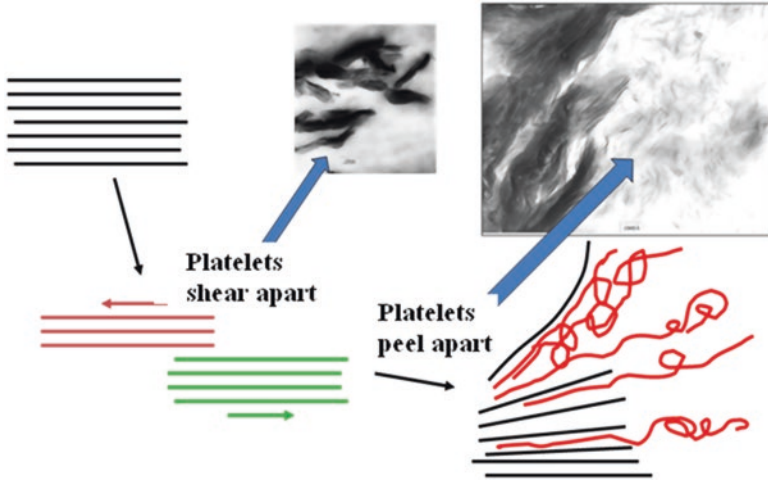


Fig. 2.4 Dispersion mechanisms of nanoplatelets in polymer

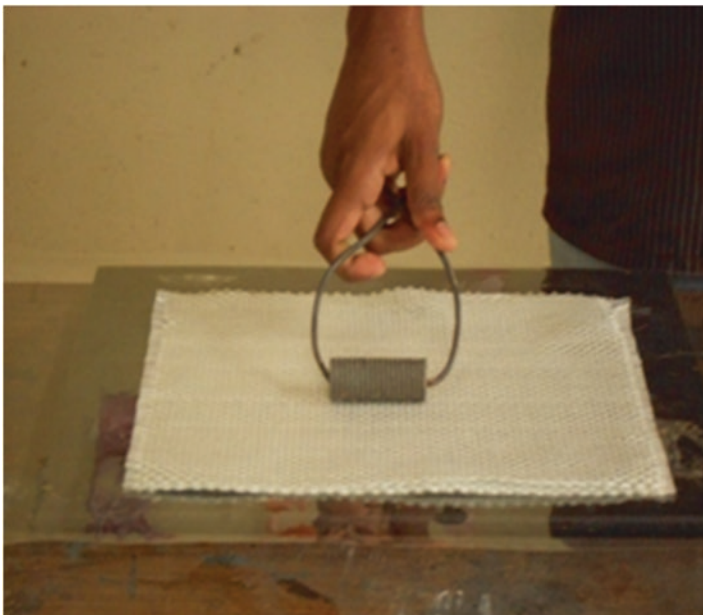


Fig. 2.5 Preparation of laminates using hand lay-up process

Figure 2.7 shows the single-stage gas gun used for conducting impact testing. A range of impact velocities are obtained by varying the pressure of air in the chamber of gas gun. The air pressure in the chamber is monitored by a pressure gauge. The



Fig. 2.6 Compression molding machine used for making laminates

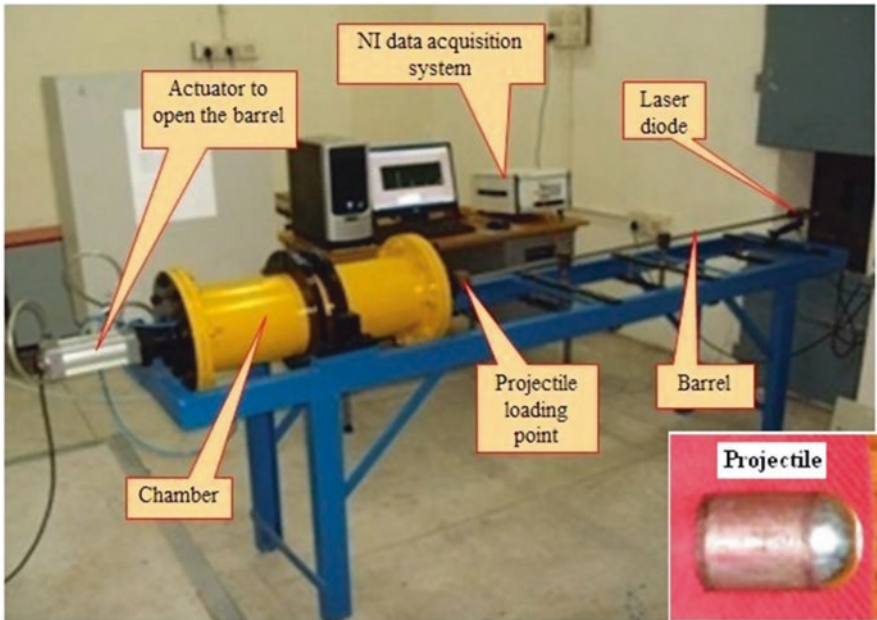


Fig. 2.7 Gas gun experimental setup used for impact loading

projectile is made using mild steel with a spherical nose of diameter 9.5 mm and mass 7.6 g. A shock accelerometer is used to find the response of laminates during impact. The velocity of projectile is measured using laser-photodiode system. High-speed camera is also used to predict initial and residual velocity of projectile.

3 Energy Absorbed by the Laminates in Impact Loading

The laminates are subjected to impact at different velocities to predict ballistic limit. The damage modes of the laminates are analyzed for below and above ballistic limit. The energy dissipated by the laminates subjected to velocities which are below the ballistic limit is in the form of vibration, delamination, and failure of matrix in the delaminated area.

For above ballistic limit and during penetration, the majority of the projectile energy is absorbed in deformation due to the secondary fibers. In addition to the energy absorbed due to deflection, the laminate also absorbs energies in delamination, fiber fracture, and perforation. The impact of the projectile results in the formation of a cone on the back face of the composite through the propagation of a transverse wave as shown in Fig. 2.8. On impact, the primary fibers in the composite, i.e., fibers directly impacted by the projectile, are strained to tensile failure. The secondary fibers in the composite, i.e., fibers that are not directly impacted by the projectile, undergo deformation due to the formation of cone. The deformation of

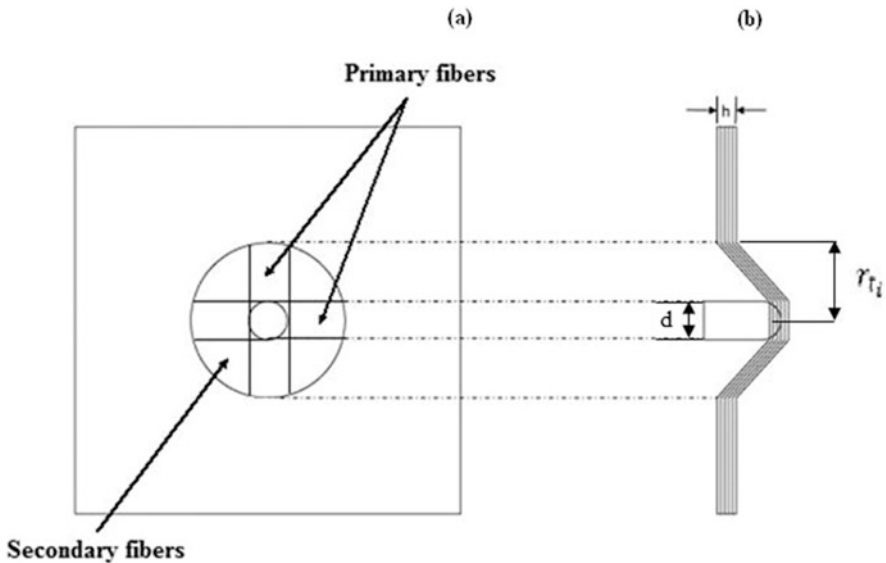


Fig. 2.8 Deformation of a composite laminate during ballistic impact by a projectile. (a) Plane of the back face. (b) Side view

the laminate is elastic and the composite reverts back substantially to its original shape after the impact is over, with only a small damage area where the fibers are failed. A portion of initial kinetic energy of the projectile is absorbed due to delamination and matrix crack, which is observed experimentally (Velmurugan & Balaganesan, 2013).

3.1 Energy Absorbed by the Laminates in Below Ballistic Limit

During the impact of projectile into the target, in the area of contact of projectile, a localized deformation around the impact region and global deflection away from the point of impact have occurred, which result in plane compression in the front face and tension in the rear face of the laminate. The deflection of the laminate in the direction of projectile movement causes strain in the fibers and matrix (Balaganesan & Khan, 2016). As the velocity of impact is well within ballistic limit, the strain in the fibers is below the failure strain. This causes the rebound of the projectile as well as vibration of the laminate. The stress waves propagate in radial direction. These stress values exceed interlaminar shear stress, and hence there is possibility for failure in the matrix and at the lamina interfaces. The initial failure occurring in a laminate due to projectile impact is matrix crack. Interlaminar shear strength of the laminate decreases due to matrix crack which further leads to delamination. The energy dissipated in deflection and then vibration and delamination and in matrix crack is discussed below.

The energy absorbed by the laminates during vibration is calculated based on its total potential energy when subjected to impact loading (Sun & Potti, 1996).

The total potential energy at the beginning of vibration is given by the expression:

$$E_v = \frac{1}{2} kx^2 \quad (2.1)$$

where k is the stiffness of the laminates obtained from static penetration test and x is the deflection at the center of the laminate which is also the point of impact. The amplitude at the center is obtained from the correlation between the amplitude at the location of accelerometer and impact point.

The amplitude at the center of the laminates is obtained for laminates by the following expressions which are predicted experimentally. For the laminates,

$$x_{c2} = 3.789A_{accln} + 0.220 \quad (2.2)$$

In Eq. (2) x_{c2} is the amplitude or deflection at the center and A_{accln} is the amplitude at the location of accelerometer for the laminate.

The maximum amplitude at the location of the accelerometer is calculated from the following expression:

$$Acc = A_{accln} \omega^2 \quad (2.3)$$

In the above expression, A_{cc} is the maximum amplitude of acceleration and ω is the angular velocity which is obtained from the accelerometer signal and A_{accln} is the maximum displacement.

The total energy of the projectile is given by:

$$E_T = \frac{1}{2} mV^2 \quad (2.4)$$

where m is the mass of the projectile and V is the velocity of the projectile.

The area of delamination (A_{delam}) is measured from the impacted laminates. The energy due to delamination is given by:

$$E_{delam} = A_{delam} G_{IIc} \quad (2.5)$$

where G_{IIc} is the critical strain energy release rate in mode II which is obtained from three-point bending of end notched flexural specimen (Morais, 2004).

The area undergoing matrix crack is the same as the delamination area. The energy due to matrix crack is given by:

$$E_{matcrack} = A_{delam} E_{mt} hV_m \quad (2.6)$$

where E_{mt} is the energy absorbed by matrix cracking per unit volume calculated from tensile test results of neat epoxy and clay-dispersed epoxy specimens, h is the thickness of the laminates, and V_m is the volume fraction of the matrix.

3.2 Energy Absorbed by the Laminates in Above Ballistic Limit

The kinetic energy of a moving projectile of mass m , with a velocity V , is given by:

$$\text{Kinetic energy} = \frac{1}{2} mV^2 \quad (2.7)$$

After perforation of the target, the velocity of the projectile becomes " V_r ."

$$\text{Residual kinetic energy} = \frac{1}{2} mV_r^2 \quad (2.8)$$

The energy lost by the projectile during perforation E_L is given by:

$$E_L = \frac{1}{2} m(V^2 - V_r^2) \quad (2.9)$$

Thus, the total energy absorbed by target laminate (Naik et al., 2006) is given by:

$$E_{\text{tot}} = E_{\text{frac}} + E_{\text{def}} + E_{\text{mc}} + E_{\text{delam}} + E_{\text{matcrack}} \quad (2.10)$$

where E_{frac} is the energy absorbed due to tensile failure of fiber, E_{def} is the energy absorbed due to deformation of secondary fiber, E_{mc} is the energy absorbed due to the formation of moving cone, E_{delam} is the energy absorbed due to delamination, and E_{matcrack} is the matrix crack energy.

Ballistic limit is given by:

$$V_o = \sqrt{\frac{2}{m} E_{\text{tot}}} \quad (2.11)$$

During the ballistic impact event, the longitudinal and transverse waves propagate along the radial direction. The transverse wave is responsible for cone formation on the rear side of plate. The radius of the cone depends on the time Δt , which is from the beginning of the impact to the instant when the fiber is broken or the projectile is stopped. The transverse wave velocity is given by:

$$C_t = \sqrt{\frac{G_{23}}{\rho}} \quad (2.12)$$

where G_{23} is the shear modulus and ρ is the density of the laminate.

And plastic wave at the front propagates at the velocity of:

$$C_p = \sqrt{\frac{1}{\rho} \left(\frac{d\sigma}{d\varepsilon} \right)_\varepsilon} \quad (2.13)$$

If the impact event for the failure is divided into a number of small instants, then at i th instant, the time is given by t_i . At that time the transverse wave has traveled to a distance r_{ti} and the plastic wave has traveled to a distance r_{pi} . The distances of r_{ti} and r_{pi} after time $t_i = i\Delta t$ are:

$$r_{ti} = C_t i\Delta t \quad (2.14)$$

$$r_{pi} = C_p i\Delta t \quad (2.15)$$

The strain in fiber changes with reference to change in distance from impact point. At the impact point, stress and strain are maximum and decrease along the length of the fiber. At i th time interval, the strain at the point of impact is given by:

$$\varepsilon_i = \left\{ \frac{(d/2) + \sqrt{(r_{ti} - (d/2))^2 + z_i^2} - r_{pi}}{f^{(r_{pi}/d)} - 1} \right\} \left\{ \frac{\ln f}{d} \right\} \quad (2.16)$$

where f is transmission factor, Z_i is distance moved by the projectile, and d is failed width of the fibers, respectively. If the variation of strain in the fibers is known, the

energy absorption by various failure mechanisms like failure of primary fibers and deformation of secondary fibers can be found.

In the beginning of the first interval of time, the entire energy is in the form of kinetic energy of the projectile. This energy is later shared by different failure mechanisms, projectile kinetic energy, and kinetic energy of the moving cone. Considering the energy balance at the end of i th time interval:

$$KE_o = E_{P_i} + E_{mci} + E_{frac(i-1)} + E_{def(i-1)} + E_{delam(i-1)} + E_{matcrack(i-1)} \quad (2.17)$$

where KE_o is the initial kinetic energy of projectile and E_{P_i} and E_{mci} are projectile and moving cone energies at i th instant of time. Rearranging the terms,

$$\frac{1}{2}mV_o^2 - E_{(i-1)} = \frac{1}{2}(m + M_{C_i})V_i^2 \quad (2.18)$$

where m and V_o are the mass and initial velocity of the projectile and M_{C_i} is the mass of moving cone at i th time interval.

$$E_{(i-1)} = E_{frac(i-1)} + E_{def(i-1)} + E_{delam(i-1)} + E_{matcrack(i-1)} \quad (2.19)$$

The energies shared in each time interval are explained in the following sections. The above energy is for $(i - 1)$ th time interval. From Eq. (2.18) the velocity of projectile at the end of i th time interval is obtained by the following equation:

$$V_i = \sqrt{\frac{\frac{1}{2}mV_o^2 - E_{(i-1)}}{\frac{1}{2}(m + M_{C_i})}} \quad (2.20)$$

If the projectile velocity is calculated at the beginning and at the end of i th time interval, then the deceleration of the projectile during impact can be found. It is given by:

$$d_{c_i} = \frac{(V_{(i-1)} - V_i)}{\Delta t} \quad (2.21)$$

The distance traveled by the projectile z_i up to i th time interval is given by:

$$z_i = \sum_{n=0}^{n=i} \Delta z_n \quad (2.22)$$

$$\Delta z_i = \left(V_{(i-1)} \Delta t - \frac{1}{2} d_{c_i} (\Delta t)^2 \right) \quad (2.23)$$

The above iteration is repeated till the target fails due to projectile impact and complete perforation takes place. The velocity at the end is called residual velocity of the projectile.

3.3 Energy Absorbed in Various Failure Modes

3.3.1 Energy Absorbed in Tensile Failure of Primary Fibers

The fibers in the impact point undergo tensile failure due to stretching of the target radially. This tensile failure of the fibers absorbs a portion of the incident energy (Pushparaja et al., 2018). If the strain of a fiber reaches the failure strain in tension, then it fails. The entire length of the fiber under the point of impact is not strained. When the strain in fiber reaches failure strain, energy is absorbed due to tensile failure.

The stress-strain curve of the nanocomposite specimen is shown in Fig. 2.9(a). The strain variation in the fibers from the impact point is shown in Fig. 2.9(b). The strain at a distance “ r ” from the impact point is given by $\varepsilon(r)$. The strain $\varepsilon(r)$ is given by the expression:

$$\varepsilon(r) = \varepsilon_0 f^{x/d} \quad (2.24)$$

where ε_0 is the failure strain at the point of impact.

Consider an element of length and cross section area in the failure zone is $A = dh$, at a distance r from the impact point. The strain energy of the element at any distance r from impact point is the product of the volume of the element and the area under the stress-strain curve.

The energy absorbed up to a strain of $\varepsilon(r)$ is given by:

$$\text{Energy absorbed} = A dr \int_0^{\varepsilon(r)} \sigma(\varepsilon) d\varepsilon \quad (2.25)$$

where $\sigma(\varepsilon)$ is the stress-strain function curve shown in Fig. 2.9(a).

The total energy absorbed due to tensile failure is given by:

$$E_{\text{frac}} = dh \int_0^r \left(\int_{\varepsilon=0}^{\varepsilon(r)=\varepsilon_0 f^{r/d}} \sigma(\varepsilon) d\varepsilon \right) dr \quad (2.26)$$

where ε_0 is the ultimate strain limit and $\sigma(\varepsilon)$ is the stress function.

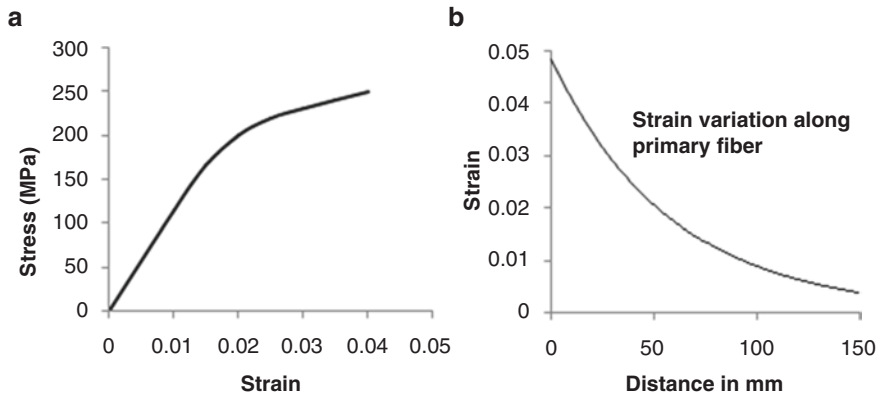


Fig. 2.9 (a) Stress-strain curve for the nanocomposite specimens and (b) strain variation in a primary fiber from the impact point

3.3.2 Energy Absorbed in Elastic Deformation of Secondary Fibers

The fibers in deformed zone are subjected to variation in strain according to their position from the point of impact. The fibers close to impact point experience a strain equal to the strain in the fiber subjected to tensile failure. The fibers which are far away from the impact point are strained to the least (Balaganesan et al., 2017; Pushparaja et al., 2017a, b). The energy absorbed by the secondary fibers of the laminate per unit volume (E_{defv}) is the area under the stress-strain curve up to elastic limit (Naik et al., 2006).

$$E_{\text{defv}} = \int_0^{\varepsilon_{s_i}} \sigma_s(\varepsilon_s) d\varepsilon_s \quad (2.27)$$

Consider a circular element in the secondary fibers as shown in Fig. 2.10, at a radius of “ r ” and thickness of “ dr .”

The volume of the circular element (dV) is given by:

$$dV = h \{2\pi r - 4d\} dr \quad (2.28)$$

where h is thickness of the laminate. Also, the stress and strain variation in the ring is according to its position from the impact point. The fibers near to the projectile, at a radius “ $d/2$,” are subjected to failure strain, and the fibers away from the impact point are based on the distance of the transverse wave “ r_i .” The energy due to the deformation of secondary fibers is given by:

$$E_{\text{defi}} = \int_{\frac{d}{2}}^{r_i} \left(\int_0^{\varepsilon_{s_i}} \sigma_s(\varepsilon_s) d\varepsilon_s \right) h \{2\pi r - 4d\} dr \quad (2.29)$$

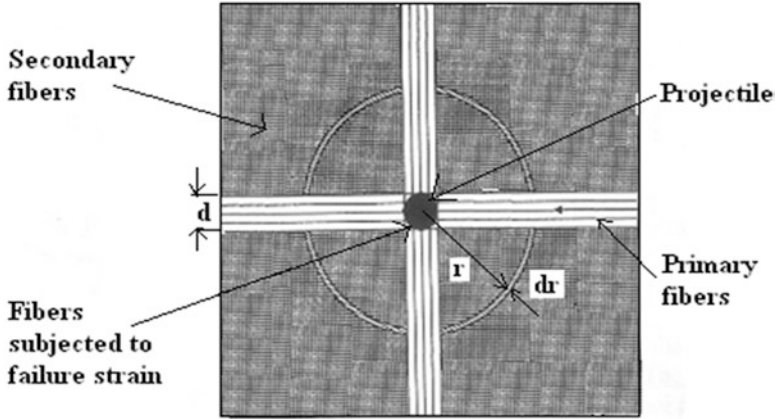


Fig. 2.10 Fiber area analysis for the nanocomposite plates (front view)

In the above expression the boundary conditions for the variation in strain, with distance from the impact point, $\epsilon = \epsilon_0$ at $r = \frac{d}{2}$ and $\epsilon = 0$ at $r = r_i$.

3.3.3 Energy Absorbed Due to Kinetic Energy of the Moving Cone

The mass of the moving cone at the i th time interval is given by:

$$M_{C_i} = \pi r_i^2 h \rho \tag{2.30}$$

where ρ is the density of the laminate.

The energy absorbed by the moving cone is:

$$E_{mci} = \frac{1}{2} M_{C_i} V_i^2 \tag{2.31}$$

Where M_{ci} is mass of moving cone and V_i is velocity of moving and it is assumed that moving cone and projectile move at the same velocity.

3.3.4 Energy Absorbed in Delamination

The area undergoing delamination in the conical region at i th time interval is given by:

$$\text{Damaged Area} = \pi \left(r_{di}^2 - r_{(di-1)}^2 \right) \tag{2.32}$$

where r_d is the radius of damaged zone.

The energy absorbed during i th time interval is given by:

$$\Delta E_{\text{delam}} = \pi \left(r_{di}^2 - r_{(di-1)}^2 \right) G_{IIc} \quad (2.33)$$

where G_{IIc} is the critical strain energy release rate in mode II. The total energy absorbed in delamination is given by:

$$E_{\text{delam}} = \sum_{n=0}^{n=i} \Delta E_{\text{delam}} \quad (2.34)$$

3.3.5 Energy Absorbed in Matrix Crack

The area undergoing matrix crack is the same as the delamination area. At i th time interval the area of matrix crack energy is given by:

$$\Delta E_{\text{matcrack}} = \pi \left(r_{di}^2 - r_{(di-1)}^2 \right) E_{\text{mt}} h V_m \quad (2.35)$$

where E_{mt} is the energy absorbed by matrix cracking per unit volume and V_m is the volume fraction of the matrix.

The total energy absorbed due to matrix crack is given by:

$$E_{\text{matcrack}} = \sum_{n=0}^{n=i} \Delta E_{\text{matcrack}} \quad (2.36)$$

4 Results and Discussions

4.1 Energy Absorbed by the Laminates at Below Ballistic Limit

The vibration energy is calculated based on initial deflection and stiffness values of the laminates as given in Eq. (2.1) (Balaganesan et al., 2015). The initial projectile energies are 4.65 J, 9.5 J, 16.05 J, and 25.55 J for the impact velocities of 35 m/s, 50 m/s, 65 m/s, and 82 m/s, respectively. Figure 2.11 shows the vibration, delamination, and matrix crack energies of the three-layer laminate with and without clay, when subjected to impact velocity of 50 m/s which is below the ballistic limit. The vibration energy of laminate without clay when subjected to impact energy of 9.5 J is 2.99 J. For the same energy input, for the laminate with 3% clay, the vibration energy is 3.62 J which is 21% higher than the laminate without clay. The energy absorption in vibration is decreasing for 4% and 5% of clay in the matrix. But still the values are higher than the laminates without clay. When the laminates without clay are subjected to impact loading, the energy absorption in delamination is higher

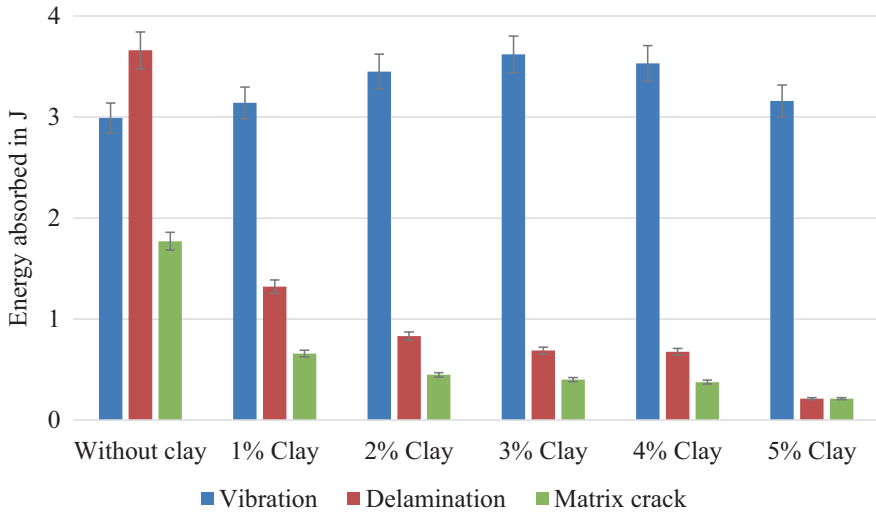


Fig. 2.11 Energy absorbed by the three-layer laminates when subjected to impact velocity of 50 m/s

than the energy absorption in vibration. In nanocomposites, delamination and matrix crack energies are decreasing with clay up to 5%. This is due to minimum failure of laminate in delamination due to the dispersion of clay (Velmurugan & Balaganesan, 2013). The total energy absorbed by the laminate without clay is 8.42 J, in which the vibration energy is 2.99 J, delamination energy is 3.66 J, and matrix crack energy is 1.77 J. In nanocomposite with 3% clay, the corresponding values are 4.72 J, 3.62 J, 0.69 J, and 0.41 J, respectively. Energy dissipation in vibration is higher in nanocomposites due to the increase in surface area between matrix and nanofiller interface (Mohan et al., 2006). Also the presence of clay controls the damage of the laminates in impact loading. The reason for this statement is due to the fact that the clay acts as secondary reinforcement and interlayers have better bonding strength by creating nano-level interlocking mechanism. Many researchers attempted with nanomaterial to enhance impact resistance of composites. In their study utilized the function of nanocellulose to modify the properties of nano-silica shear thickening fluid and mix with Kevlar fabrics for impact resistance. The application of nanocellulose was reported by researchers that nanocellulose enhances the steady state and dynamic property of the shear thickening fluid during impact. With only 0.2% of nanocellulose, the impact resistance of the composites is enhanced with almost no tear cross section reported on the fracture surface.

Figure 2.12 corresponds to energy absorption of three-layer laminates when subjected to impact velocity of 82 m/s. Corresponding projectile energy is 25.55 J. The energy absorption in laminate without clay due to vibration is 6.46 J. The laminate with 3% clay absorbs 9.61 J of energy in vibration which is 50% higher than the laminate without clay. The delamination and matrix crack energies are less than the energy absorbed in vibration for the laminates with and without clay. When the

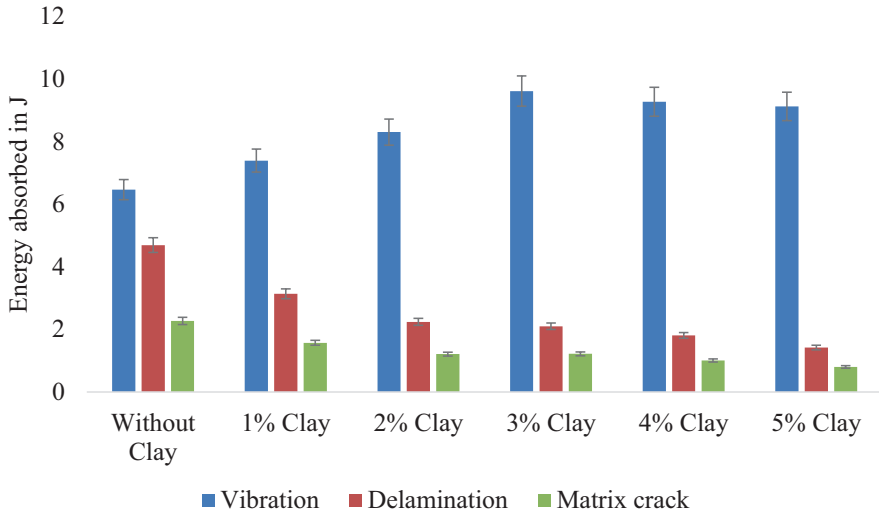


Fig. 2.12 Energy absorbed by the three-layer laminates when subjected to impact velocity of 82 m/s

laminates subjected to below ballistic velocity, the maximum amount of energy of projectile is consumed due to deformation and the laminate is subjected to elastic strain. After rebounding of projectile, the elastic energy stored by the laminate is dissipated in the form of vibration. Also there is no failure of fibers in majority of below ballistic impact events. Hence, the energy absorbed by delamination and matrix crack for the nanocomposites are less than that of laminate without clay. The delamination energy of laminate with 3% clay is less than 50% of the laminate without clay. The matrix crack energy for laminate with 3% clay is about 50% of laminate without clay.

4.2 Energy Absorbed by the Laminates at Above Ballistic Limit

Figure 2.13 shows the plot for initial velocity versus the residual velocity of the three-layer laminates with and without clay. The laminate without clay is perforated at 101.84 m/s and the laminate with 2% clay is perforated at 122.32 m/s, the increase is about 20%. Laminate with 3% clay shows an improvement of 22% compared to laminate without clay. Laminate with 5% clay is perforated at 129.51 m/s, where the increase in velocity is about 27%. It is observed that the improvement is better for laminates with clay up to 2%, and thereafter the improvement is only marginal. The laminates are tested for the velocities of 135 m/s, 140 m/s, and 145 m/s which are above the ballistic limit. In all the cases, the laminates without clay show higher residual velocities than the laminates with 1–5% clay. The decrease in residual

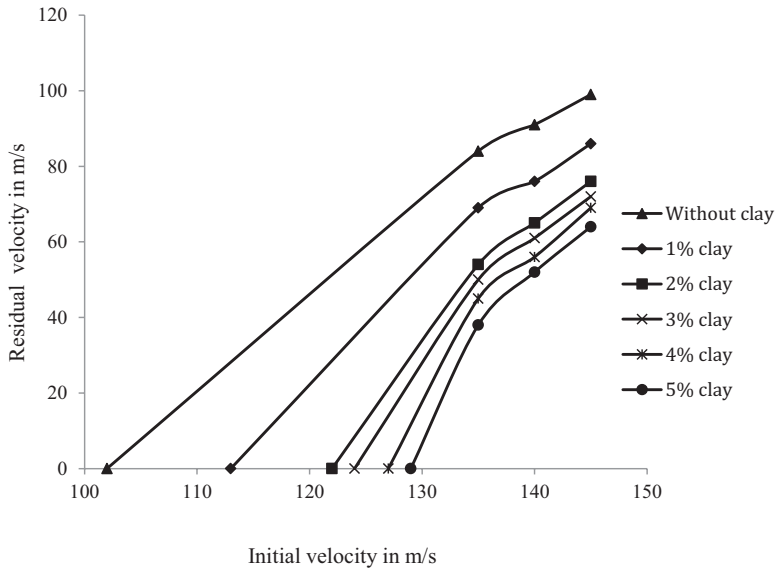


Fig. 2.13 Initial velocity vs. residual velocity for the laminates

velocity is high for the laminate with 5% clay when compared to laminate without clay. The decreases in percentage of residual velocity for laminates with 2%, 3%, 4%, and 5% clay when subjected to velocity of 135 m/s are 35%, 40%, 46%, and 55%, respectively, when compared to the laminates without clay. Clay dispersion up to 2% offers high resistance to perforation. When the laminates are subjected to a velocity of 140 m/s, the decreases in percentage for the laminates with 2%, 3%, 4%, and 5% clay are 29%, 33%, 38%, and 43%, respectively. The corresponding values for the velocity of 145 m/s and the decrease in percentage of residual velocities are 23%, 27%, 30% and 35%, respectively. It is observed that as the initial velocity of projectile increases, the decrease in percentage of residual velocity decreases. The presence of clay in matrix creates more surface-level interactions between nanofiller and polymer matrix. The energy of the projectile is consumed by nanofiller in vibration within the matrix, bending and twisting within the matrix system (Velmurugan et al., 2013). These mechanisms enhance resistance and better energy dissipation capability of nanocomposite laminates.

Lee et al. (2014) have observed that the multilayer graphene has several times greater specific penetration energy than its steel counterpart. In order to take that as advantage, Naveen et al. (2019) have reported similar results by adding graphene nanoplatelets to improvise the matrix strength of the epoxy resin and reinforced with Kevlar/*Cocos nucifera* sheath composites. However, the results showed the decrement in energy absorption and ballistic limit due to improvement in interfacial interaction between fiber and graphene nanoplatelets. This enhancement is inappropriate to absorb and dissipate the kinetic energy of the projectile. In contrary, Ge

et al. (2018) observed in their research that the addition of only 0.5 vol% graphene oxide incorporated in epoxy resin-reinforced 30 vol% ramie fabric showed increment in ballistic absorption energy. Graphene oxide has been known as one of the graphene-based nanomaterials synthesized from graphite through oxidation process.

4.3 Delamination Area of the Laminates

Impact on target laminate makes delamination which is separation of adjacent layers. Suriani et al. (2021a, 2021b) discussed the delamination as composite laminates failure when subjected to impact load. Due to high interlaminar stress associated with the normal very-low through-thickness intensity, this phenomenon can occur. Figure 2.14 shows the variation in delamination area for the laminates, with and without clay, when subjected to impact velocities which are below and above the ballistic limit. The delamination area of the laminate without clay is 2823 mm² at 110 m/s and the ballistic limit is about 102 m/s. The delamination area for the laminate with 5% clay is 3253 mm² which is 15% higher than the laminate without clay. When the laminate without clay is subjected to 135 m/s impact velocity, the delamination area is 2310 mm² which is less when compared to 110 m/s impact velocity. The delamination area for the laminate with 5% clay is 4328 mm² which is 87% higher than the laminate without clay. The absorption of energy is saturated for velocities above 135 m/s for the laminate with clay.

It seems that for velocities which are below the ballistic limit of 102–110 m/s, the damage area in the laminate without clay is higher, and as % clay increases the delamination area becomes smaller. However, for velocities which are above the ballistic limit (102–110 m/s), the laminate without clay has not much resistance to impact and projectile penetrates easily and creates smaller damage area. But

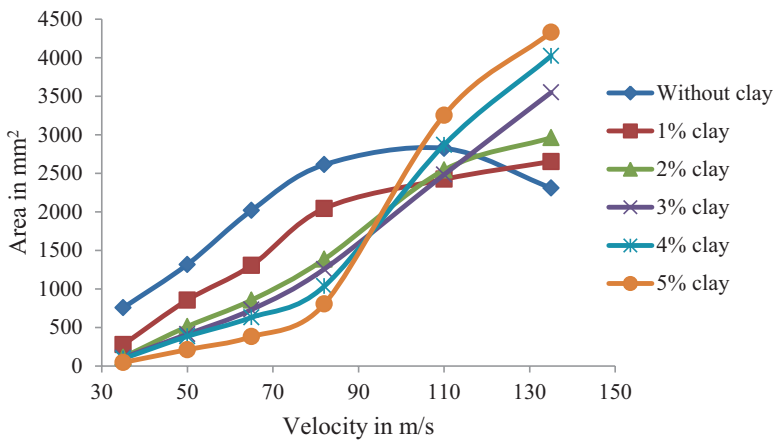


Fig. 2.14 Delamination area of the laminates when subjected to different velocities of impact

laminates with clay show higher resistance around the impacted area and more materials in the region absorb energy, and hence the damage area is larger and this is consistently true as the % of clay increases. This is due to nano-reinforcement in matrix which supports for better interlayer strength. The velocity near the ballistic limit acts as threshold energy and forces to break the interfacial nanoscale bonding to initiate the damage. Pereira et al., (2000) found that the addition of graphene oxide in epoxy matrix reveals superior ballistic properties with the presence of 30 vol% ramie fabric. The energy absorption of ramie fabric/0.5 vol% graphene oxide epoxy nanocomposites is 23.4% higher compared to Kevlar alone. Therefore, the researchers claimed that the novel ramie fabric-reinforced graphene oxide incorporated epoxy nanocomposites as a promising material for the second layer in a ceramic front multi-layered ballistic armor for ballistic application. Despite using natural fiber reinforced with nanomaterials for advance ballistic properties, the application of biomaterial like nanocellulose also has been reported. Shear thickening fluid was known for its superior performance for ballistic and bulletproof applications.

Figure 2.15 shows the images for delamination area of the laminates with and without clay during perforation at impact velocity 135 m/s. The laminates without clay and with clay up to 5% are perforated at this velocity. Figure 2.15(a) corresponds to the laminate without clay. Figure 2.15(b)–(f) corresponds to the delamination area of the laminate with clay from 1% to 5%. It is seen that as the clay percentage increases, increase in delamination area is observed for the laminates with clay up to 5% when compared to the laminate without clay. The failure of fibers is seen in the center of the delaminated area. This is observed for the laminates with and without clay.

The sequence of images captured by a high-speed camera (Phantom V611) during perforation of projectile in a three-layer laminate without clay is presented in Fig. 2.16. The images are captured at 28000 fps and the time between each frame is 36 μ s. The impact event captured for 329 μ s is presented in 18 frames in the figure. The initial velocity of projectile based on the frames 1 to 3 is 134.5 m/s. Penetration takes place between frames 3 and 4. Moving cone is seen in frames 5 and 6. Petal formation is observed around the projectile in frames 7–10. In frame 12, the separation of layers is observed and this may lead to delamination. The broken parts of matrix and fibers are flying behind the projectile which is seen in frames 12–18. Also, the modal vibration and stress waves of the laminate are seen from frames 14 to 18. The frequency of laminates during vibration after penetration of projectile matches the higher resonance frequency levels of the laminate. Also, the separation of layers makes the layers to vibrate at different amplitudes and the stress waves travel from point of impact to boundary. Some researchers worked on the hybridization of nanoscale reinforcement incorporated in the fiber-reinforced polymer composites as the middle layer in a laminate. Many researchers have investigated the effect of adding various nanofillers such as graphene, carbon nanotube, nanoclay, and nanocellulose ranging 0.01–5 wt. % on the mechanical properties of fiber-reinforced polymer nanocomposites. Graphene-based materials have replaced the usage of aramid fabric-based body armor.

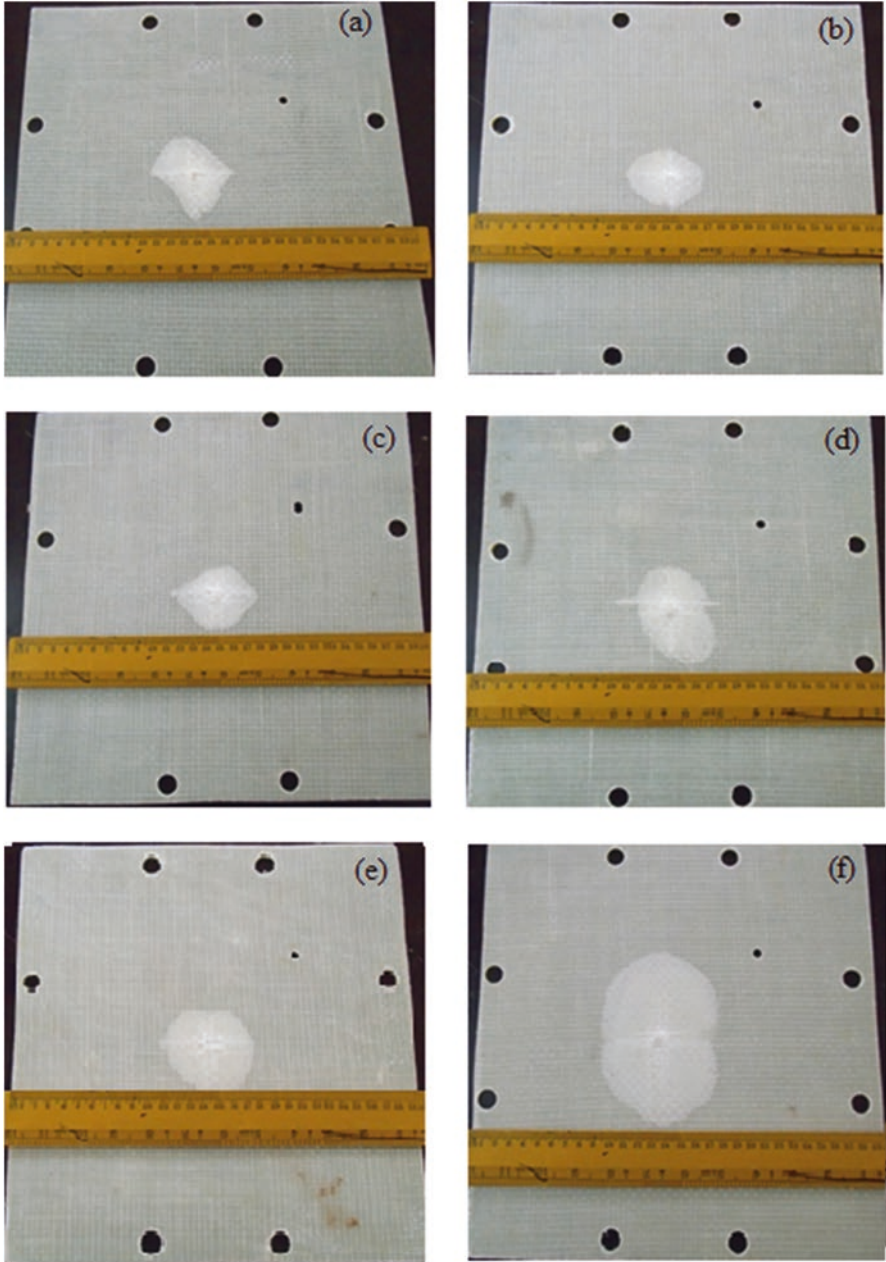


Fig. 2.15 Rear face of the three-layer laminate when subjected to impact velocity of 135 m/s (a) without clay, (b) 1% clay, (c) 2% clay, (d) 3% clay, (e) 4% clay, and (f) 5% clay (Balaganesan & Velmurugan, 2015)

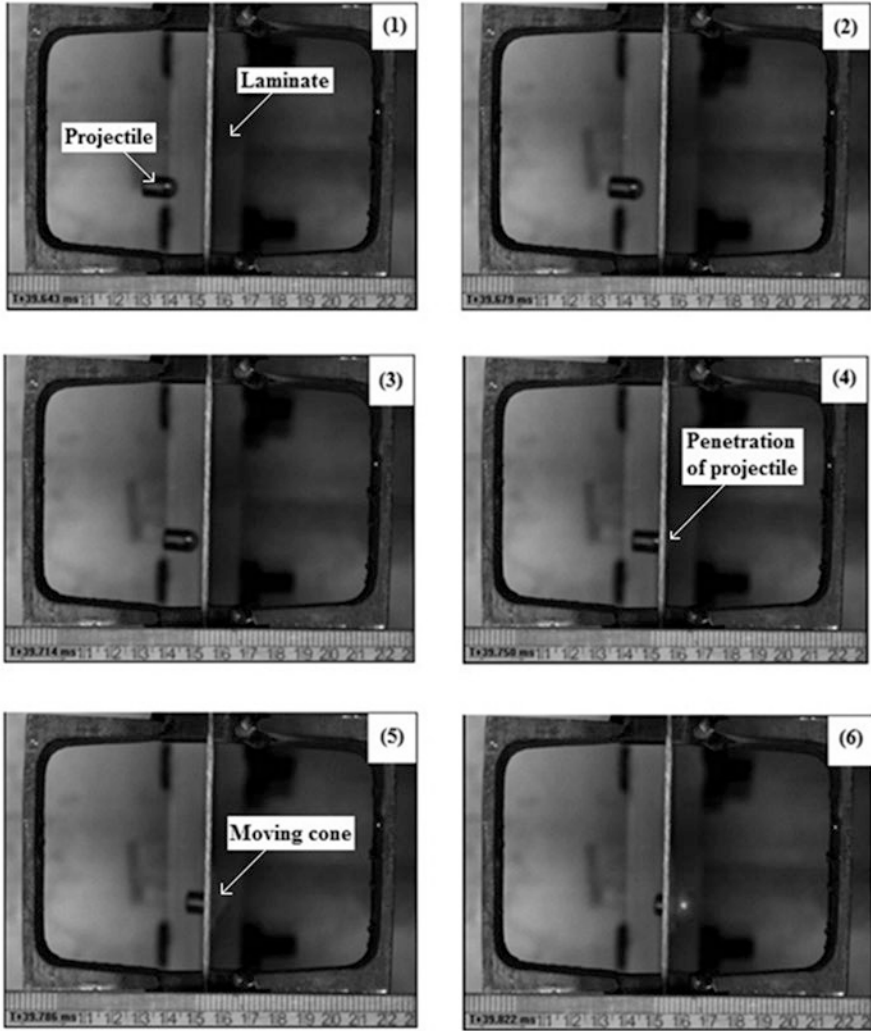


Fig. 2.16 High-speed camera images for the laminate without clay during perforation (Balaganesan et al., 2014)

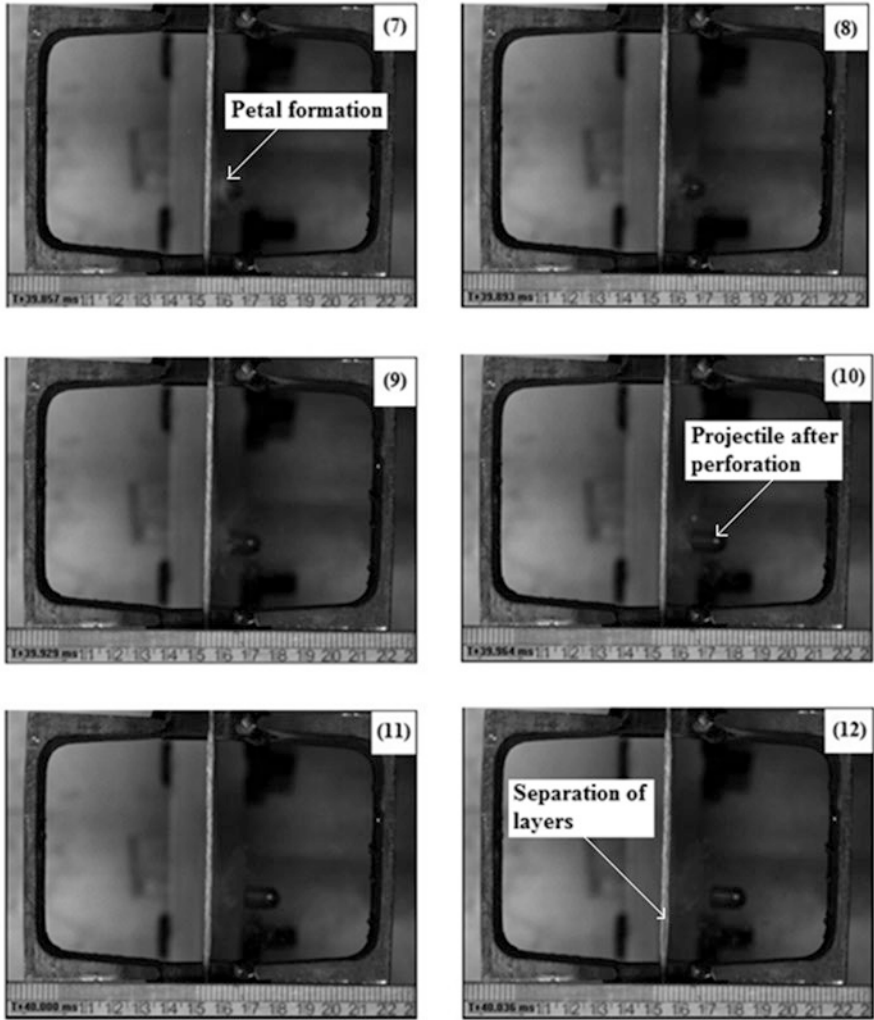


Fig. 2.16 (continued)

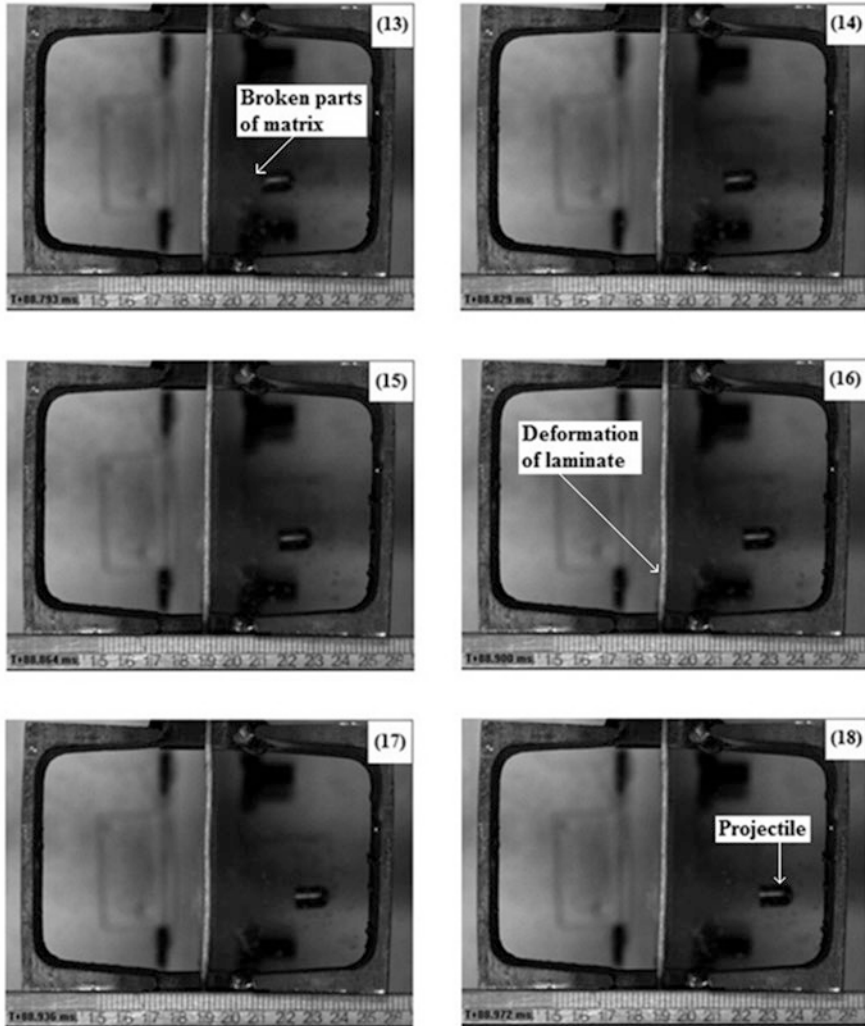


Fig. 2.16 (continued)

4.4 Energy Absorbed by the Laminate in Various Failure Modes

Figure 2.17 shows the results for the projectile energy and the energy absorbed during perforation by the laminate without clay at 99.8 m/s which is the ballistic velocity. The corresponding initial energy of the projectile is 37.8 J. At the end of the perforation, the velocity of the projectile has become zero; hence, the kinetic energy of the moving cone also becomes zero. In other forms of failure energies, the energy due to the deformation of secondary fiber is maximum, and it is about 72% of the

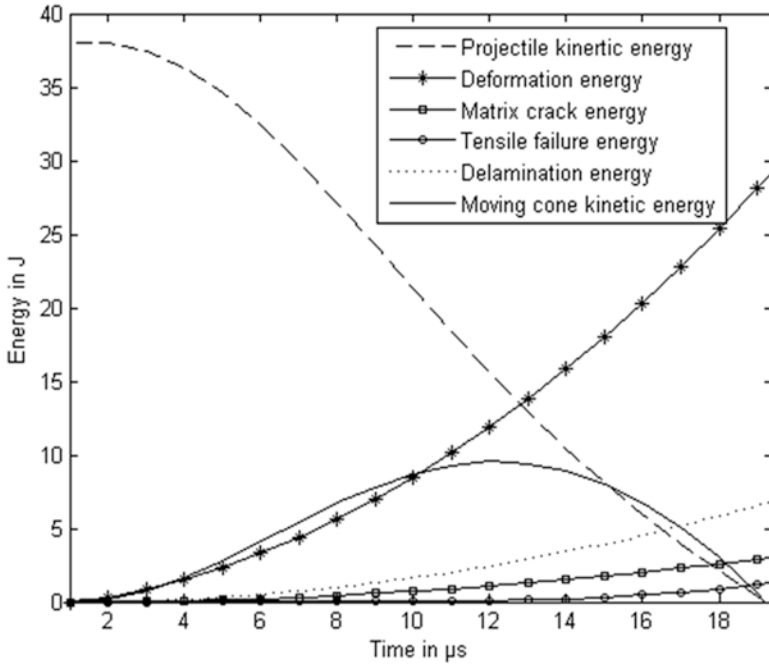


Fig. 2.17 Different modes of energy for three-layer laminate without clay when subjected to 99.8 m/s (ballistic limit)

projectile energy. This is due to elastic stretching of the secondary fibers of the laminate. The delamination energy, matrix crack, and tensile failure energies are 16%, 7.5%, and 3%, respectively. The time taken for complete perforation is 19 μs.

Figure 2.18 shows the energy absorption for the three-layer laminate with 1% clay. The initial energy of the projectile is 46.4 J and the velocity of the projectile is 110.5 m/s. The energy absorption is 22.7% higher than the laminate without clay. The delamination, matrix crack, and tensile failure energies are higher when compared to laminate without clay, but the corresponding percentage of energy absorption is marginally less for deformation and marginally high for matrix crack, delamination, and tensile failure. The duration for the ballistic event is about 20 μs.

The energy absorption for the laminate with 2% clay is shown in Fig. 2.19. The energy absorption at ballistic velocity is 54.5 J which is about 44% higher than the laminate without clay. There is not much variation in percentage of deformation of secondary fibers and matrix crack energies when compared to laminate without clay. The percentage of tensile failure energy is 20% higher than the laminate without clay. The percentage of delamination energy is 6% higher than the laminate without clay.

Figure 2.20 corresponds to laminate with 3% clay, which absorbs 48% higher energy than the laminate without clay. The energies absorbed in deformation of secondary fibers, delamination, matrix crack, and tensile failure are 70.4%, 17.7%, 6.9%, and 3.1%, respectively, of the initial energy of the projectile. The time taken for complete penetration of the projectile on target is 19 μs.

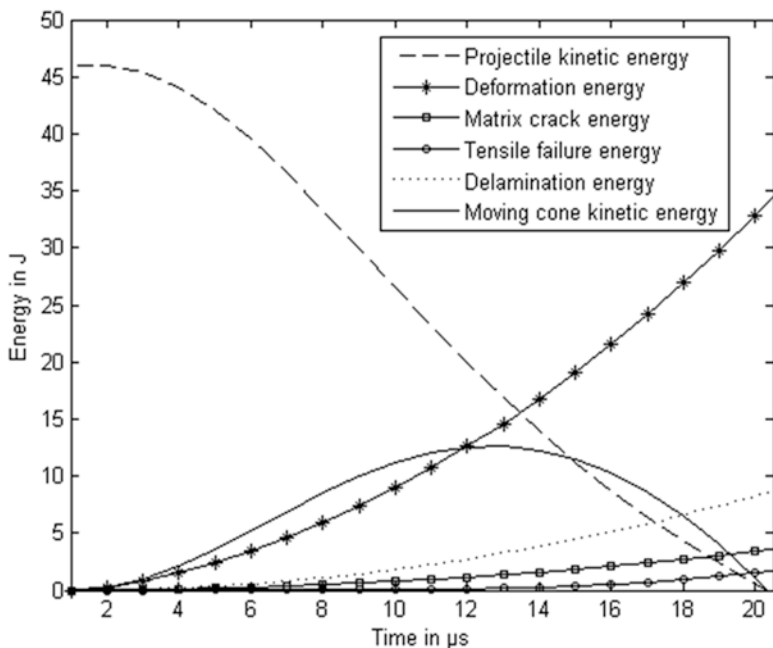


Fig. 2.18 Different modes of energy for three-layer laminate with 1% clay when subjected to 110.5 m/s (ballistic limit)

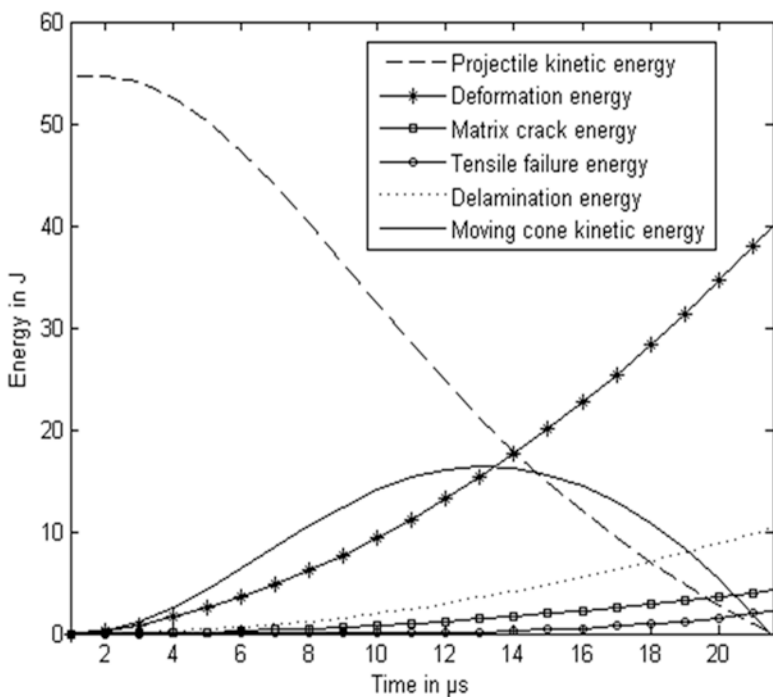


Fig. 2.19 Different modes of energy for three-layer laminate with 2% clay when subjected to 119.8 m/s (ballistic limit)

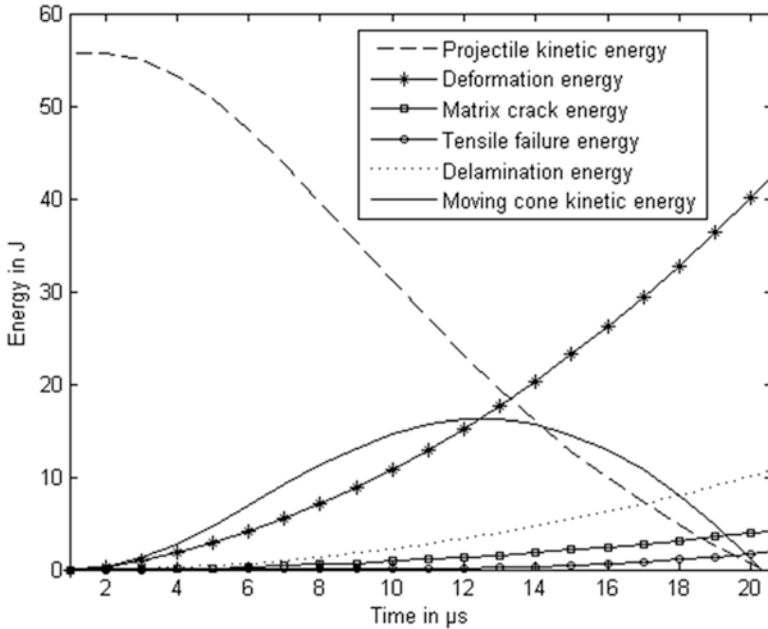


Fig. 2.20 Different modes of energy for three-layer laminate with 3% clay when subjected to 122.3 m/s (ballistic limit)

Figure 2.21 shows the energy absorption for the laminate with 4% clay. The initial energy of the projectile is 59.2 J and the velocity of the projectile is 124.3 m/s. The energy absorption is 56.7% higher than the laminate without clay. The energy absorption for the laminate with 5% clay is shown in Fig. 2.22. The duration for complete perforation is 22 μs . The ballistic limit is 125.1 m/s and the corresponding energy absorption is 61.9 J. It is observed that the laminate with 5% clay absorbs 64% higher energy than the laminate without clay. The energies absorbed in deformation of secondary fibers, delamination, matrix crack, and tensile failure are 70.6%, 16.7%, 7.2%, and 3.9%, respectively. In all the cases, there is not much variation in the percentages of individual failure mode energies.

4.5 Comparison of Energy Absorbed in Analytical Method with Experiments

The experimental results for ballistic limits based on projectile energy are compared with analytical results of failure mode energies of the laminates with and without clay. Figure 2.23 shows the comparison of results for energy absorbed by the laminates with and without clay in analytical method and experiments. The improvement in ballistic limit is observed in laminates with clay up to 5%. The laminate

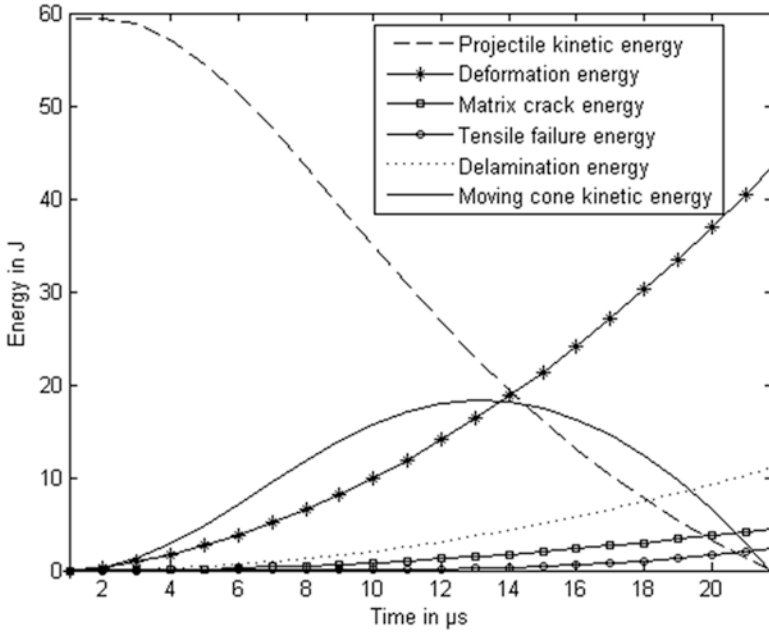


Fig. 2.21 Different modes of energy for the laminate with 4% clay when subjected to 124.3 m/s (ballistic limit)

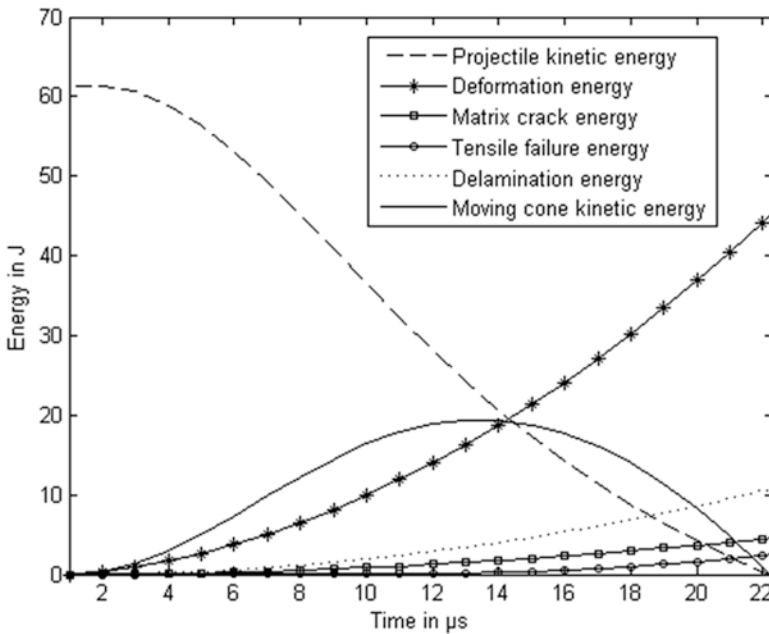


Fig. 2.22 Different modes of energy for the laminate with 5% clay when subjected to 125.1 m/s (ballistic limit)

Fig. 2.23 Comparison of experimental results with summation of failure modes of energy calculated analytically for the laminates at the ballistic limit

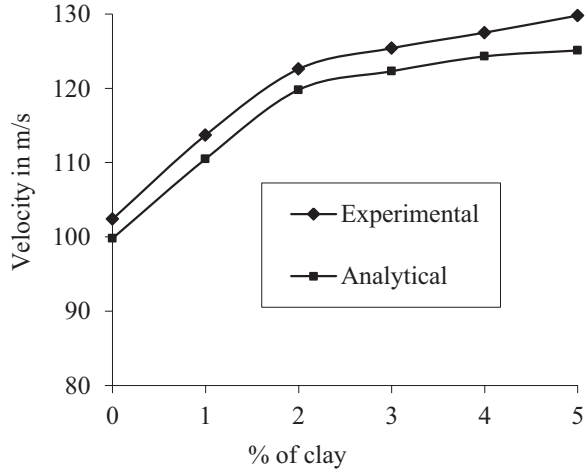


Table 2.2 Comparison of model results with experimental results for the laminates subjected to impact velocities above the ballistic limit

Laminate	Experimental results		Analytical results	
	Initial velocity (m/s)	Residual velocity (m/s)	Initial velocity (m/s)	Residual velocity (m/s)
Without clay	129.1	51.3	130	52.6
1% clay	130.6	47.9	130	49.5
2% clay	131.4	45.1	130	46.8
3% clay	130.9	42.7	130	44.2
4% clay	129.5	41.8	130	43.4
5% clay	129.0	37.7	130	38.5

with 5% clay shows 27% improvement in ballistic limit when compared to laminate without clay. The error between analytical and experimental results is less than 5%.

The total energy absorption is analyzed for the impact velocities which are above the ballistic limit. The results of analytically calculated velocity values for initial and residual velocity are compared with the experimental results. Table 2.2 shows the comparisons for three-layer laminates with and without clay subjected to impact velocity of 130 m/s which is above the ballistic limit. There is some variation in experimental initial velocities which is due to marginal change in pressure of air in the gas gun chamber and other testing conditions. The variation is observed to be less than 2% in all the cases. The residual velocities of analytical model results are having good agreement with experimental results for the laminates with and without clay. As the percentage of clay increases, there is a decrease in residual velocity which is due to absorption of energy by higher surface interaction between nano-filler and matrix. The decrease is observed for the laminates with clay up to 5%. The difference between the analytical residual velocity and experimental residual velocity is less than 5%.

5 Conclusions

The conclusions from the study for energy absorbed by the nanocomposite laminates subjected to velocities which are below the ballistic limit are as follows:

- The projectile energy is absorbed and dissipated by the laminate in the form of vibration and failure due to delamination and matrix crack.
- The energy absorption in vibration for impact velocities which are below the ballistic limit is higher than the energy absorption due to delamination and matrix crack in nanocomposite.
- The presence of clay in matrix increases the energy absorption capacity of the laminates in vibration. The laminates with 3% clay show maximum increase in energy absorption in vibration when compared to the laminate without clay. The laminate with 3% clay when subjected to 82 m/s absorbs energy in vibration 50% higher than that in the laminate without clay.
- Dispersion of clay in the matrix decreases the energy absorption of the laminates with clay up to 5% in delamination and matrix crack for the impact velocities which are below the ballistic limit. The laminate with 5% clay when subjected to 82 m/s absorbs energy in delamination and matrix crack 50% less than that in the laminate without clay.
- The projectile energy absorbed by the laminate when subjected to impact for above ballistic velocity is in the form of deformation due to the secondary fibers, delamination, matrix crack, and tensile failure of primary fibers.
- The presence of clay in the matrix increases the ballistic performance of the nanocomposites when compared to composites without clay. The increase in ballistic limit is observed with increase in clay up to 5%. The ballistic limit of the laminate with 5% clay is 27% higher than the laminate without clay.
- The energy absorption of the nanocomposites is higher than the laminates without clay. The increase in energy absorption is observed with increase in clay up to 5%. For the laminate with 5% clay when subjected to impact velocity of 135 m/s, the increase in energy absorption is 50% higher than the laminate without clay.
- The delamination area is high for the nanocomposites when the laminates are subjected to impact velocities which are above the ballistic limit. The delamination area for the laminate with 5% clay when subjected to impact velocity of 135 m/s is 87% higher than the laminate without clay.
- The analytical model predicts the change in projectile energy with reference to time during perforation of the laminates and the energy absorbed by the laminates in failure modes which include deformation of secondary fibers, delamination, matrix crack, and tensile failure of primary fibers.
- The energy absorbed by deformation is about 70% in all the cases at ballistic limit.
- The increase in energy absorption is observed for the laminates with clay up to 5%. This trend is similar to that in experiments.
- Ballistic limit obtained from analytical calculation is validated with experimental results and good agreement is found.

Acknowledgments The authors acknowledge the Aeronautics Research and Development Board (ARDB), India, for the financial support provided to carry out this research.

References

- Alsbari, S., Zuhri, M. Y. M., Sapuan, S. M., Ishak, M. R., Ilyas, R. A., & Asyraf, M. R. M. (2021). Potential of natural fiber reinforced polymer composites in sandwich structures: A review on its mechanical properties. *Polymers*, 3, 423. <https://doi.org/10.3390/polym13030423>
- Aymerich, F., Dalla Via, A., & Quaresimin, M. (2011). Energy absorption capability of nano modified glass/epoxy laminates. *Procedia Engineering*, 10, 780–785.
- Balaganesan, G., & Khan, V. C. (2016). Energy absorption of repaired composite laminates subjected to impact loading. *Journal of Composites: Part B*, 98, 39–48.
- Balaganesan, G., & Velmurugan, R. (2015). Vibration and energy dissipation of nanocomposite laminates for below ballistic impact loading. *Latin American Journal of Solids and Structures*, 12, 2259–2280. <https://doi.org/10.1590/167978251703>
- Balaganesan, G., Velmurugan, R., Srinivasan, M., Gupta, N. K., & Kanny, K. (2014). Energy absorption and ballistic limit of nanocomposite laminates subjected to impact loading. *International Journal of Impact Engineering*, 74, 57–66. <https://doi.org/10.1016/j.ijimpeng.2014.02.017>
- Balaganesan, G., Velmurugan, R., & Kanny, K. (2015). Dynamic response of nanocomposite laminates during low, medium and high velocity impact loading. *Frontier in Aerospace Engineering*, 4(2), 56–69. <https://doi.org/10.12783/fae.2015.0402.03>
- Balaganesan, G., Pushparaja, M., Velmurugan, R., & Gupta, N. K. (2017). Impact loading on nanocomposites in thermal environment. *Procedia IUTAM*, 23, 210–219. <https://doi.org/10.1016/j.piutam.2017.06.022>
- Ge, Z., Yang, L., Xiao, F., Wu, Y., Yu, T., Chen, J., Lin, J., & Zhang, Y. (2018). Graphene family nanomaterials: Properties and potential applications in dentistry. *Int. J. Biomater.*, 2018, 1539678. <https://doi.org/10.1155/2018/1539678>
- Ilyas, R. A., Sapuan, S. M., Harussani, M. M., Hakimi, M. Y. A. Y., Haziq, M. Z. M., Atikah, M. S. N., Asyraf, M. R. M., Ishak, M. R., Razman, M. R., Nurazzi, N. M., Norraahim, M. N. F., Abral, H., & Asrofi, M. (2021). Polylactic Acid (PLA) biocomposite: Processing, additive manufacturing and advanced applications. *Polymers*, 8, 1326. <https://doi.org/10.3390/polym13081326>
- Lee, J. H., Loya, P. E., Lou, J., & Thomas, E. L. (2014). Dynamic mechanical behavior of multi-layer graphene via supersonic projectile penetration. *Science*, 346(6213), 1092–1096. <https://doi.org/10.1126/science.1258544>
- Mohan, T. P., Ramesh Kumar, M., & Velmurugan, R. (2006). Mechanical and barrier properties of epoxy polymer filled with nanolayered silicate clay particles. *Journal of Materials Science*, 41, 2929–2937.
- Mohd Nurazzi, N., Asyraf, M. R. M., Khalina, A., Abdullah, N., Sabaruddin, F. A., Kamarudin, S. H., Ahmad, S.'b., Mahat, A. M., Lee, C. L., Aisyah, H. A., Norraahim, M. N. F., Ilyas, R. A., Harussani, M. M., Ishak, M. R., & Sapuan, S. M. (2021). Fabrication, functionalization, and application of carbon nanotube-reinforced polymer composite: An overview. *Polymers*, 7, 1047. <https://doi.org/10.3390/polym13071047>
- Morais, A. B. (2004). Analysis of mode II interlaminar fracture of multidirectional laminates. *Compos Part A*, 35, 51–57.
- Naik, N. K., Srirao, P., & Reddy, B. C. K. (2006). Ballistic impact behavior of woven fabric composites: Formulation. *International Journal of Impact Engineering*, 32, 1521–1552.
- Naveen, J., Jawaid, M., Zainudin, E. S., Sultan, M. T. H., & Yahaya, R. (2019). Effect of graphene nanoplatelets on the ballistic performance of hybrid Kevlar/Cocos nucifera sheath-reinforced epoxy composites. *Textile Research Journal*, 89.
- Nurazzi, N. M., Asyraf, M. R. M., Khalina, A., Abdullah, N., Aisyah, H. A., Rafiqah, S. A., Sabaruddin, F. A., Kamarudin, S. H., Norraahim, M. N. F., Ilyas, R. A., & Sapuan, S. M. (2021).

- A review on natural fiber reinforced polymer composite for bullet proof and ballistic applications. *Polymers*, 4, 646. <https://doi.org/10.3390/polym13040646>
- Omran, A. A. B., Mohammed, A. A. B. A., Sapuan, S. M., Ilyas, R. A., Asyraf, M. R. M., Koloor, R., Seyed, S., & Petrú, M. (2021). Micro- and nanocellulose in polymer composite materials: A review. *Polymers*, 2, 231. <https://doi.org/10.3390/polym13020231>
- Pereira, A. C., Lima, A. M., Cristyne, L., Oliveira, M. S., Costa, U. O., Bruno, W., Bezerra, A., Monteiro, S. N., Jesus, R., & Rodriguez, S. (2000). Ballistic performance of ramie fabric reinforcing graphene oxide-incorporated epoxy matrix composites. *Polymers*, 12, 2711.
- Pushparaja, M., Balaganesan, G., & Velmurugan, R. (2017a). Frangibility study of natural fiber reinforced composite laminates. *Key Engineering Materials*, 725, 88–93. <https://doi.org/10.4028/www.scientific.net/KEM.725.88>
- Pushparaja, M., Balaganesan, G., Velmurugan, R., & Gupta, N. K. (2017b). Energy absorption characteristics of Carbon/Epoxy nano filler dispersed composites. *Procedia Engineering*, 173, 175–181. <https://doi.org/10.1016/j.proeng.2016.12.055>
- Pushparaja, M., Reddy, N., Shankar, K., Velmurugan, R., & Balaganesan, G. (2018). High velocity impact damage investigation of carbon/epoxy/clay nanocomposites using 3D computed tomography. *Materials Today: Proceedings*, 5(9), 16946–16955. <https://doi.org/10.1016/j.matpr.2018.04.098>
- Sun, C. T., & Potti, S. V. (1996). A simple model to predict residual velocities of thick composite laminates subjected to high velocity impact. *International Journal of Impact Engineering*, 18, 339–353.
- Sun, L., Gibson Ronald, F., Gordaninejad, F., & Suhr, J. (2009). Energy absorption capability of nano composites: A review. *Composites Science and Technology*, 69, 2392–2409.
- Suriani, M. J., Rapi, H. Z., Ilyas, R. A., Petrú, M., & Sapuan, S. M. (2021a). Delamination and manufacturing defects in natural fiber-reinforced hybrid composite: A review. *Polymers*, 8, 1323. <https://doi.org/10.3390/polym13081323>
- Suriani, M. J., Radzi, F. S. M., Ilyas, R. A., Petrú, M., Sapuan, S. M., & Ruzaidi, C. M. (2021b). Flammability, tensile, and morphological properties of oil palm empty fruit bunches fiber/pet yarn-reinforced epoxy fire retardant hybrid polymer composites. *Polymers*, 8, 1282. <https://doi.org/10.3390/polym13081282>
- Velmurugan, R., & Balaganesan, G. (2011). Modal analysis of pre and post impacted nano composite laminate. *Latin American Journal of Solids and Structures*, 8, 9–26. <https://doi.org/10.1590/S1679-78252011000100002>
- Velmurugan, R., & Balaganesan, G. (2013). Energy absorption characteristics of glass/epoxy nano composite laminates by impact loading. *International Journal of Crashworthiness*, 18(1), 82–92.
- Velmurugan, R., & Balaganesan, G. (2011). Modal analysis of pre and post impacted nano composite laminate. *Latin American Journal of Solids and Structures*, 8, 9–26. <https://doi.org/10.1590/S1679-78252011000100002>
- Vijay Kumar, V., Balaganesan, G., Kong Yoong, J. L., Esmaeely Neisiany, R., Surendran, S., & Ramakrishna, S. (2019a). A review of recent advances in nanoengineered polymer composites. *Polymers*, 11, 644. <https://doi.org/10.3390/polym11040644>
- Vijay Kumar, V., Ramakrishna, S., Kong Yoong, J. L., Esmaeely Neisiany, R., Surendran, S., & Balaganesan, G. (2019b). Electrospun nanofiber interleaving in fiber reinforced composites—Recent trends. *Material Design & Processing Communications*, 1, e24. <https://doi.org/10.1002/mdp2.24>
- Wetzela, B., Frank, H., & Ming, Q. Z. (2003). Epoxy nano composites with high mechanical and tribological performance. *Composites Science and Technology*, 63, 2055–2067.
- Zinoviev, P. A., & Ermakov, Y. N. (1994). *Energy dissipation in composite materials*. Technomic Publishing Company.

Chapter 3

High Strain Rate Studies of Polymer and Hybrid Nanocomposites for Aerospace Application



S. Gurusideswar, R. Velmurugan, and R. Sarathi

1 Introduction

Traditionally, polymers have been added with natural or synthetic fillers in order to enhance their mechanical, thermal and electrical properties and also to reduce the cost. They are extensively used in aerospace, automotive, defence and electronics industries. It is proved that the dispersion of nanosized fillers with a larger aspect ratio in polymers leads to dramatic improvement in properties. Among all the potential fillers, clay or layered silicates have been widely used because of their natural abundance, easy availability, high aspect ratio, low cost and environment-friendly nature. Clay/polymer nanocomposites show tremendous enhancement in a wide range of engineering properties and this recent technology can now be applied commercially. The mechanical properties of most of the polymers and its matrix composites are sensitive to strain rates, and in many practical cases, they are subjected to dynamic loadings, which require prior knowledge of dynamic mechanical properties to prevent catastrophic failure during its service. In practical scenarios, the composite structures undergo high-velocity impact loadings (Nurazzi et al., 2021; Suriani et al., 2021). A few examples are collision, crash landing, rigid body impact on a structure, bird impact on jet engine compressor rotating blades, automotive

S. Gurusideswar

Department of Aerospace Engineering, SRM Institute of Science and Technology,
Chennai, India

Department of Aerospace Engineering, Indian Institute of Technology Madras, Chennai, India

R. Velmurugan (✉)

Department of Aerospace Engineering, Indian Institute of Technology Madras, Chennai, India
e-mail: ramanv@iitm.ac.in

R. Sarathi

Department of Electrical Engineering, Indian Institute of Technology Madras, Chennai, India

vehicle components, satellite solar panel, ship hull structures, shock loads, bomb blasts, etc. In order to understand the dynamic behaviour of epoxy, glass/epoxy and its clay nanocomposites, the current research work focuses on the strain rate effects (low and high) of these composites.

Most of the thermoset resins are inherently brittle, which restricts its performance to many structural applications. In general, polymers are being incorporated with micro fillers, such as calcium carbonate, glass beads, mica and talc, in order to enhance their performance. However, it is often reported that the addition of these fillers has certain drawbacks such as an increase in weight, brittleness and opacity (Pavlidou & Papaspyrides, 2008). It is also reported that the properties of those materials can be customized by changing the weight fraction, shape and size of the fillers. A further enhancement in performance can be achieved by adding fillers in the nanometre range, which have a high aspect ratio (Tjong, 2006). The addition of fillers in polymers for which at least one dimension of the dispersed particles is in the nanometre range (<100 nm) is known as nanocomposites. Nanocomposites are considered as one of the classes of nanomaterials, where nanofillers are dispersed in the matrix phase.

Many researchers (Pavlidou & Papaspyrides, 2008; Azeez et al., 2013; Kotal & Bhowmick, 2015; Clifton et al., 2020; Sanusi et al., 2020; Omran et al., 2021; Alsubari et al., 2021; Mohd Nurazzi et al., 2021; Suriani et al., 2021) have devoted themselves to the field of “nanocomposites”, mainly focusing on manufacturing, characterization, fracture mechanism, wear resistance and so on. In actual scenario, polymeric materials and their composites are subjected to dynamic loading and high strain rate deformation in a wide range of aerospace applications. Also, simulation of composite structures under high strain rate deformation requires a clear identification of the strain rate effect on the material behaviour. Hence, high strain rate studies are important, which is not reported in the above-mentioned literature.

Very few literature report the dynamic mechanical responses of this kind of nanocomposites due to the difficulty of high strain rate testing and data interpretation. It is noted that the viscoelastic nature of polymers exhibits significant rate dependence in its stress–strain responses. The effect of the strain rate on the mechanical properties of epoxy nanocomposites was rarely studied, and the data is very limited (Guo & Li, 2007). Chen et al. (2002) modified the split-Hopkinson tension bar (SHTB) to obtain the dynamic stress–strain responses (2.5×10^{-3} – $1.2 \times 10^3 \text{ s}^{-1}$) of epoxy resin and polymethyl methacrylate (PMMA) in compression and tension loadings. They observed that the tensile stress–strain response of both epoxy and PMMA polymer differs significantly from compressive response. Gilat et al. (2007) investigated the mechanical response of two different epoxy resins at different strain rates of 5×10^{-5} , 2, and 450 – 700 s^{-1} in shear and tensile loadings and found that the maximum stress is the same for intermediate and high strain rate testing and lower for low strain rate testing. Evora and Shukla (2003) employed direct ultrasonication technique for fabricating polyester/TiO₂ nanocomposites and observed that the presence of TiO₂ nanoparticles had a significant effect on quasi-static fracture toughness and dynamic modulus and no marked effect on ultimate strength at high strain rate (2000 s^{-1}). Roland et al. (2007)

studied the effects of strain rates ($0.06\text{--}573\text{ s}^{-1}$) on tensile properties for an elastomeric polyurea using a drop weight test instrument and found an increase in stiffness and failure stress and a decrease in failure strain with increasing strain rate. Guo and Li (2007) studied the quasi-static and dynamic compression behaviour of $\text{SiO}_2/\text{epoxy}$ nanocomposites at different strain rates ($10^{-4}\text{--}10^4\text{ s}^{-1}$) using desktop split-Hopkinson pressure bar (SHPB) and found that the nanocomposites are sensitive to loading rate and nanoparticle dispersion. Zebarjad and Sajjadi (2008) investigated the effect of nano-sized calcium carbonate and strain rate (0.1 s^{-1}) on the tensile properties of high-density polyethylene (HDPE) and concluded that strain-rate sensitivity of HDPE decreased with the addition of nanofillers. Xiao (2008) carried out the dynamic tensile test using a servo-hydraulic machine on different polymers. Fu et al. (2009) performed dynamic tensile tests (1750 s^{-1}) on polycarbonate using a split-Hopkinson tension bar (SHTB) system and found that the tensile behaviour of polycarbonate is dependent on the strain rate. Raisch and Möglinger (2010) discussed the modification of the clamps of a servo-hydraulic tensile testing machine to achieve a strain rate of 670 s^{-1} and observed that both tensile modulus and tensile yield stress increase logarithmically with the strain rate. Cao et al. (2010) studied the effect of strain rate on the tensile response of polycarbonate over a wide range of strain rates ($0.001\text{ s}^{-1}\text{--}1700\text{ s}^{-1}$) using the servo-hydraulic machine, a moderate strain testing apparatus and split Hopkinson tension bar and observed that the material is highly sensitive to strain rate. They also proposed a viscoelastic constitutive model to describe the stress–strain response of polycarbonate over a wide range of strain rates. All the above studies are carried out on different polymers at high strain rates. The motivation of this work is to study the effect of medium strain rates on epoxy/clay nanocomposites, which is not reported in the literature.

Composites are generally rate sensitive. Many researchers reported that glass/epoxy composites have shown an increase in tensile modulus and strength as strain rate increases (Lifshitz & Rotem, 1972; Armenàkas & Sciammarella, 1973; Davies & Magee, 1975). Several techniques were developed to study the rate sensitivity of composites for a wide range of strain rates such as conventional loading frame, servo-hydraulic testing machine, drop mass setup and SHPB technique. Daniel et al. (1981) developed a method called expanding ring technique for testing and characterizing graphite/epoxy composites at strain rates in the regime of $100\text{--}500\text{ s}^{-1}$. Kawata et al. (1981) introduced SHPB technique for tensile testing of composites at high strain rates. Harding and Welsh (1983) and Staab and Gilat (1995) modified the SHPB for dynamic testing of composites. Hayes and Adams (1982) studied the strain rate effects of glass/epoxy and graphite/epoxy composites using a pendulum impactor. Hamouda and Hashmi (1998) discussed several techniques for obtaining the mechanical behaviour of composite materials under impact loading at high strain rates. Jacob et al. (2004) reviewed the strain rate dependence of mechanical properties of composite materials. Majzoobi et al. (2007) achieved strain rates up to $10,000\text{ s}^{-1}$ using flying wedge apparatus for testing composites.

In literature, many studies employed SHPB apparatus for high strain rates, which works in a high strain rate range and it is expensive. It was found that the

experimental techniques to determine tensile properties at medium range strain rates of $1\text{--}100\text{ s}^{-1}$ are not well established (Xiao, 2008). The conventional servo-hydraulic machine is restricted to lower strain rates ($<10\text{ s}^{-1}$), due to its inertial effects of the load cell and grips. The drop mass test setup is inexpensive and it can accommodate different specimen geometries and strain rates. Lifshitz (1976) studied the tensile strength under dynamic loading of glass/epoxy composites using an instrumented drop weight apparatus, and failure stresses were found to be 20–30% higher than the static values; however, failure strain and modulus were the same for static and dynamic loadings. Groves et al. (1993) studied the high strain rate effects between 0.0001 s^{-1} and 2660 s^{-1} for carbon fibre-reinforced polymer composites and found an unexpected exponential-like increase in strength and modulus beyond strain rates of 10 s^{-1} due to high-intensity stress waves. They also observed changes in the fracture propagation pattern. The setup is made for compression loading and limited to 10 s^{-1} due to high-intensity stress waves. In the current work, a drop mass tower with specimen fixture is designed and fabricated for tensile loading and can accommodate strain rates up to 500 s^{-1} . Barré et al. (1996) studied the dynamic response ($10^{-1}\text{--}10^1\text{ s}^{-1}$) of glass phenolic/polyester composites and found that the tensile modulus and strength tend to increase with strain rate. It was reported that the use of falling weight tup leads to vibration waves, which are superimposed on the load curve. Okoli (2001) carried out tensile, shear and bending tests to measure energy absorbed to failure of a material by instrumented impact tester on glass/epoxy composites at increasing strain rates. He found an increase in tensile, shear and flexural energy of 17%, 5.9% and 8.5%, respectively, for the strain rates from 0.0106 s^{-1} to 2.72 s^{-1} per decade of increase in the log of strain rate. The instrumented impact tester is restricted to a velocity of 4 m/s for flexural impact. The strain rate effects on tensile properties in the range of low strain rates ($0.00017\text{--}0.00830\text{ s}^{-1}$) and medium strain rates ($0.1\text{--}20\text{ s}^{-1}$) were carried out using a low-speed tensile testing machine and servo-hydraulic machine. Pardo et al. (2002) investigated the tensile behaviour of glass/polyester composites at different strain rates using the hydraulic testing machine and found an increase in tensile properties. A maximum of 20 m/s (approximately 100 s^{-1}) was reported. Shokrieh and Omid (2009) investigated the dynamic response of glass/epoxy composites at different strain rates using a servo-hydraulic testing machine equipped with a special jig and fixture. They found an increase of 52% in tensile strength, 12% in tensile modulus, 10% in failure strain and 53% in absorbed failure energy as the strain rate increased from 0.001 to 100 s^{-1} . Though servo-hydraulic testing apparatus with a jig and fixture can accommodate medium strain rates, it restricts the strain rate to 160 s^{-1} and it is also expensive. Also, it is reported that servo-hydraulic equipment suffers from system ringing (noise) effects. The present study provides a cost-effective solution to tensile testing and can accommodate a wide range of intermediate strain rates. Brown et al. (2010) studied the effects of strain rate ($10^{-3}\text{--}10^2\text{ s}^{-1}$) on the tensile, compression and shear properties of glass/polypropylene composites using drop weight tower and found an increase in tension and compression properties, but a decrease in shear properties with increasing strain rate. The modified instrumental falling weight drop tower using a specially designed fixture was

employed to get an intermediate strain rate of 70 s^{-1} on dynamic tensile study of glass/polypropylene composites. The current study focuses on dynamic tensile studies on epoxy and glass/epoxy composites with nanofillers, which is required for aircraft and automobile structural applications. Li and Liu (2015) studied the compressive and tensile behaviour of carbon composites using drop weight impact tester with large impacting mass and achieved constant strain rate by employing a shaper material. An affordable testing technique utilizing drop weight impact tester was proposed for characterizing carbon composites at low strain rates. Perogamvros et al. (2016) employed a modified drop tower to achieve medium strain rates ($1\text{--}200 \text{ s}^{-1}$) and validated the experimental results using an explicit finite element code. In recent times, digital image correlation (DIC) technique has been widely accepted and employed in the field of experimental mechanics for the estimation of strain fields on composite surfaces, and the Young's modulus can be calculated from the strain data (Pan, 2018; Janeliukstis & Chen, 2021). Powell et al. (2017) studied the dynamic response ($0.0001\text{--}200 \text{ s}^{-1}$) of unidirectional and woven carbon fibre-reinforced composites using standard uniaxial frame and an intermediate-to-high-speed testing system with 3D digital image correlation system. Elmahdy and Verleysen (2019) investigated the strain rate sensitivity ($0.003\text{--}645 \text{ s}^{-1}$) of woven basalt and glass epoxy composites in tension using split-Hopkinson pressure tension bar and high-speed stereo digital image correlation technique. They observed that both basalt and glass composites show an increase in tensile properties in comparison with quasi-static loading. Naresh et al. (2020) investigated the strain rate dependence of glass and carbon fibre-reinforced polymer (FRP) composites for different stacking sequences using drop mass setup and digital image correlation technique. They observed an increment in tensile strength and modulus and a decrement in percentage of failure strain for both glass and carbon composites from quasi-static loading to a strain rate of 542 s^{-1} . They also carried out scanning electron microscopy (SEM) fractography on fractured specimens under the modes of failure at high strain rates. Kim et al. (2021) employed digital image correlation method to quantify the fracture characteristics for polypropylene composites. Weng et al. (2021) studied the shear properties of carbon fibre-reinforced composites under dynamic loading using a high-speed tensile testing system and digital image correlation technique. They also investigated different modes of shear failure for composite specimen under various strain rates.

From the comprehensive summary of published investigations, it is noted that studies on intermediate strain rate regime are rarely reported. It is suggested that the drop tower apparatus with digital image correlation (DIC) technique optical devices is suitable for medium strain rate tensile testing. Hence, in this work an attempt is made to study the effect of strain rates from quasi-static to several hundred per second on the tensile properties of epoxy/clay and glass/epoxy/clay nanocomposites with the application of drop mass system and non-contact DIC technique. The purpose is to improve the performance of polymer and its composites by adding nanoclay as a filler material in high strain rate applications.

2 Materials and Methods

2.1 Materials

A medium viscous unmodified liquid diglycidylether of bisphenol A (DGEBA) epoxy resin was used for the current work, and the commercial name of the resin is Araldite® LY 556. A low viscous unmodified aliphatic-type triethylenetetramine (TETA) was used as a curing agent and the commercial name of the curing agent is Aradur® HY 951. Both the resin and the curing agent were procured from Huntsman Advanced Materials (Belgium). It is advisable to mix the epoxy and the curing agent in a gentle manner to achieve a homogeneous solution and also to avoid air bubbles during curing. E-glass-type fibre of 610 gsm with woven-roving mat (WRM) architecture was procured from M/s. Sakthi Fibres (India) and used as the primary reinforcement for the fabrication of composites. Modified montmorillonite clay (GARAMITE®-1958) was procured from BYK-Chemie GmbH, Germany (formerly Rockwood Additives), and used as a secondary reinforcement for the fabrication of nanocomposites.

2.2 Specimen Preparation

Clay levels of 1.5, 3.0 and 5.0 wt% were chosen to fabricate epoxy/clay nanocomposites. The required amount of clay was first preheated at 50 °C for 2 h to avoid agglomeration due to moisture content, and subsequently the epoxy was preheated at 50 °C for 2 h to reduce the viscosity. The primary dispersion was carried out through mechanical stirring technique and the secondary dispersion was carried out using an ultrasonicator for 10 min. The required amount of curing agent (TETA) was then added to the epoxy/clay mixture and mixed properly to prevent air bubbles, as the epoxy/clay mixture and curing agent were at different viscosities. The epoxy mixture was kept in a vacuum oven at 50 °C for 5 min to remove air voids. A glass mould of dimension 300 × 300 mm was used. Rubber beadings were used to maintain a 3 mm constant thickness all around the mould plates and the wax was used as a releasing agent. The solution was poured into the mould and left for curing at room temperature for 24 h.

Glass/epoxy nanocomposites with clay levels of 1.5, 3.0 and 5.0 wt% were fabricated using hand lay-up technique followed by compression moulding technique. A thin layer of epoxy/organoclay mixture was coated with a brush on an aluminium plate. Then the epoxy/organoclay mixture was impregnated into the WRM glass fibre with the assistance of hand roller to ensure uniform wetting of fibres. The laminates were cured at room temperature and kept in the compression moulding equipment for complete curing.

2.3 Testing Techniques

In general, six different types of testing systems are employed to study the strain rate effects of a material. They are as follows:

1. Conventional screw drive load frame ($<0.1 \text{ s}^{-1}$)
2. Servo-hydraulic system ($0.1\text{--}100 \text{ s}^{-1}$)
3. Drop mass test setup ($100\text{--}1000 \text{ s}^{-1}$)
4. Split-Hopkinson pressure bar ($100\text{--}10^4 \text{ s}^{-1}$)
5. Expanded ring (10^4 s^{-1})
6. Flyer plate ($>10^5 \text{ s}^{-1}$)

The SHPB apparatus can be employed for high strain rate testing in the region of $100\text{--}10,000 \text{ s}^{-1}$. However, it cannot be used in the medium strain rate range ($1\text{--}100 \text{ s}^{-1}$). Servo-hydraulic machines can cover medium strain rates; however, they are not affordable due to its high cost and also it may lead to a system ringing phenomenon. In order to overcome these issues, a drop mass test apparatus is chosen to cover the medium strain rate range for the current work. The drop mass test setup comprises a drop mass tower, specimen fixture, load sensor and data acquisition system (Fig. 3.1).

The guide rods, made up of induction-hardened chrome alloy (CK 45) with a tensile strength of 630 MPa, are used to guide the elevator or impactor unit. The impactor unit, which holds the electromagnet and drop mass, has a linear bearing assembly to enable smooth sliding motion along the two guide rods. The entire drop mass unit can be lifted by an electric motor to a required height. The drop tower is designed for low energy and low-velocity applications, and it can be used to achieve a maximum velocity of 8.5 m/s using 25 kg drop mass, which is computed from where the mass can be dropped. Figure 3.2 shows a typical photograph of specimen fixture. It has two grips, where the specimen is clamped at each end between steel grips. The top grip is directly bolted through the load cell to the fixed carriage. A moving carriage is supported by the lower grip and is guided by three steel rods. The drop tower striker imparts a load on the moving carriage which loads the specimen in tension through the lower grip as it travels downward. To get reliable stress data, an integrated circuit piezoelectric (ICP)-type load sensor is employed to acquire load data at the high-speed environment. It is noted that quartz-type load sensors are recommended for dynamic force applications. However, it cannot be used for static applications. A maximum load of 2224 N can be achieved with the given load sensor.

2.4 High-Speed Digital Image Correlation (DIC) Technique

DIC is a non-interferometric optical technique and it is considered as a powerful and flexible tool to get reliable strain data. It is based on digital image processing and numerical computing and it was first developed by a group of researchers at the University of South Carolina in the 1980s. In literature (Pan et al., 2009), digital

Fig. 3.1 Photograph of drop mass tower with specimen fixture (Gurusideswar et al., 2016), copyright 2021. Reproduced with permission from Elsevier Ltd.

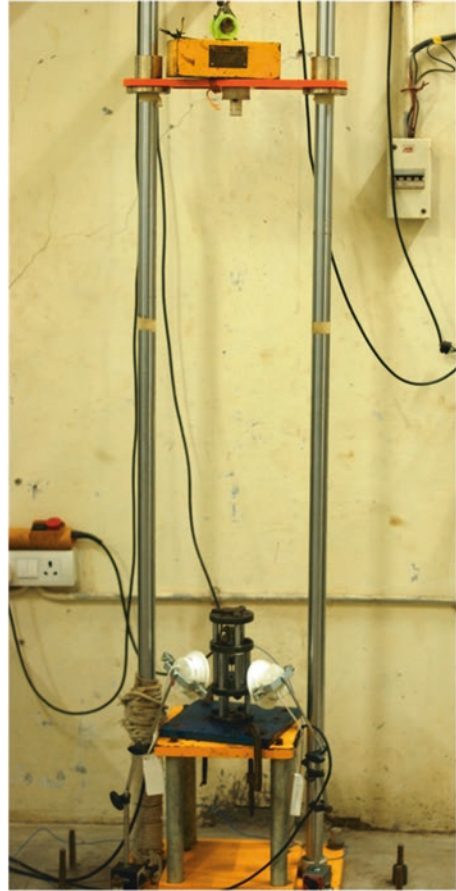
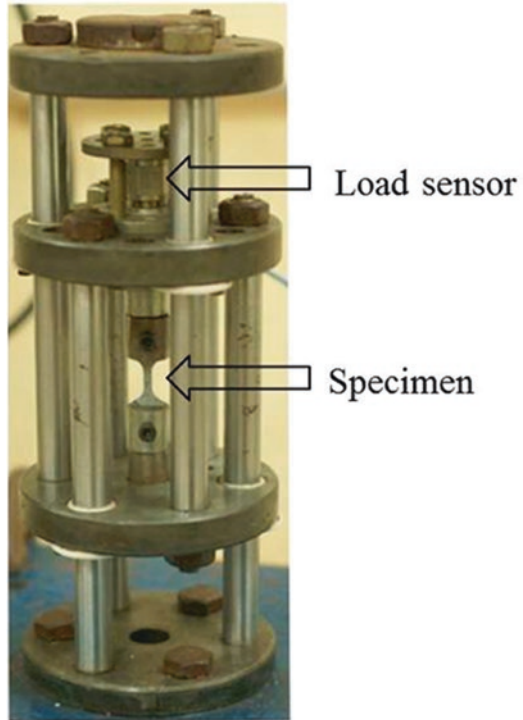


image correlation technique is denoted using different names such as non-contact strain measurement technique, digital speckle correlation method (DSCM), computer-aided speckle interferometry (CASI), electronic speckle photography (ESP) and texture correlation. The basic principle of 2D DIC for the measurement of displacement (strain) involves tracking the movement of points between the two recorded images before and after loading. To achieve this, a virtual grid of subsets of a selected size and shape consisting of pixel grey value distributions is superimposed on the artificially sprayed surface pattern. The purpose of choosing a subset rather than a pixel is to have a wider range of grey-level intensities, which helps to distinguish it from other subsets and to identify it in a unique manner. The processing involves calculation of the average greyscale intensity over the subset of the reference image and deformed image (after loading) and correlating them. In general, the 2D DIC method comprises the following principles:

1. Preparation of specimen (speckle pattern)
2. Recording the images of specimen before and during loading till failure

Fig. 3.2 Photograph of in-house designed specimen fixture assembly (Gurusideswar et al., 2017), copyright 2021. Reproduced with permission from Elsevier Ltd.



3. Post-processing the recorded images using a computer program (image correlation algorithm)

It is noted that the strain measurement accuracy of 2D DIC relies more on the quality of imaging, perfection of loading systems and the selection of post-processing parameters (Pan et al., 2009). From trial runs, the following DIC parameters were optimized and chosen for high strain rate experiments to get accurate and reliable data using the 2D DIC technique:

1. Guarantee parallelism between the CCD camera and the specimen surface
2. 12 W concealed LED lamps
3. 50 mm focal length lens
4. 15 cm distance between the camera and the specimen surface
5. Manual speckle pattern using pen marker to obtain high contrast
6. 128×128 pixels to achieve 100,000 fps
7. 19–25 subset size range

In this work, a Phantom[®] V611 camera was employed to capture images at a high speed. It has a widescreen 1280×800 CMOS sensor, which enables it to capture moving targets. A maximum of 6242 frames per second can be achieved at its full resolution, whereas a maximum of 680,000 fps can be achieved at a reduced resolution (128×8 pixels) and also it is possible to achieve 1,000,000 fps using the ‘fast option’.

3 Results and Discussion

3.1 High Strain Rate Sensitivity of Epoxy/Clay Nanocomposites

Tensile studies were carried out on the drop mass tower from heights of 0.5, 0.75 and 1 m, producing theoretical strain rates of 315, 385 and 445 s^{-1} , respectively. A drop mass of 0.5 kg was used. Figure 3.3 shows the variation of nominal strain rate versus drop mass height. The actual strain rate can be determined from strain histories, such as the one shown in Fig. 3.4. It is observed that the initial part of the strain–time curve is not truly indicative of the effective strain rate experienced by the specimen, and hence, the actual strain rates were thus determined from the gradient of the strain–time curves (Hsiao & Daniel, 1998; Brown et al., 2010). The averages of actual strain rates during the experiments at heights of 0.5, 0.75 and 1 m (3.1, 3.8 and 4.4 ms^{-1}) were 25, 41 and 53 s^{-1} , respectively. However, the actual strain rates are used in practice for the purpose of analysis. A significant increase in strain rate at about 75 μs could be due to local failure as the duration of impact is very short. An average decrease in strain to failure of 12%, 20% and 27% at 315, 385 and 415 s^{-1} , respectively, is observed for epoxy/clay nanocomposites with respect to quasi-static loading.

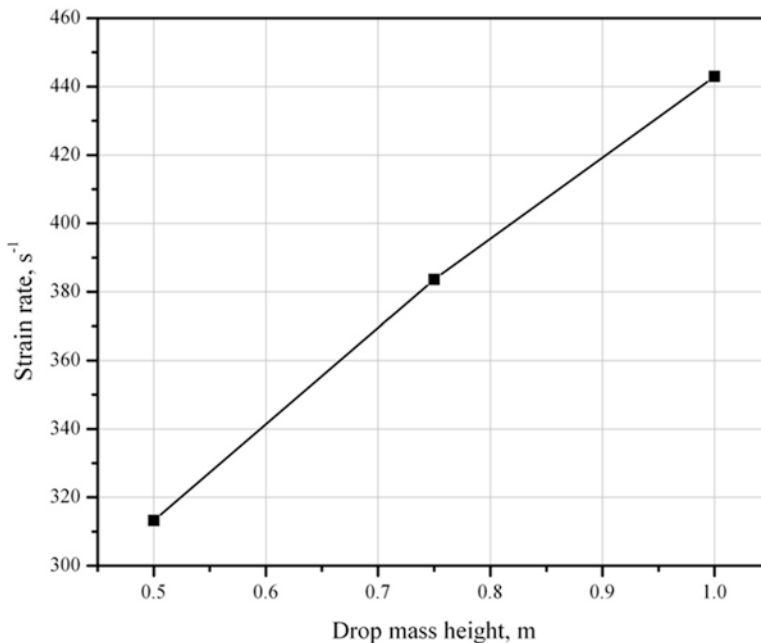


Fig. 3.3 Variation of strain rate versus drop mass height (Gurusideswar et al., 2017), copyright 2021. Reproduced with permission from Elsevier Ltd.

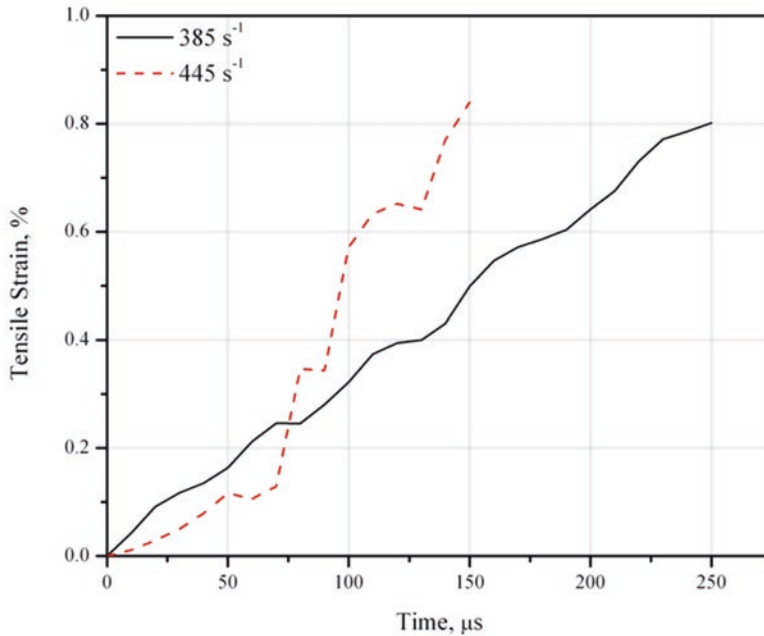


Fig. 3.4 Strain histories of 3.0 wt% clay/epoxy nanocomposites at strain rates of 385 s^{-1} and 445 s^{-1} (Gurusideswar et al., 2016), copyright 2021. Reproduced with permission from Elsevier Ltd.

Figure 3.5a and b shows load and strain histories for 1.5 wt% clay nanocomposites at dynamic loading (385 s^{-1}). The specimen failed at 550 N and the corresponding strain is 1.2% at a drop mass height of 0.75 m, which corresponds to the strain rate of 385 s^{-1} .

Figure 3.6a shows stress–strain responses for 1.5 wt% clay nanocomposites at quasi-static and dynamic loadings. At 0.75 m drop mass height corresponding to the strain rate of 385 s^{-1} , the stress–strain behaviour is different from quasi-static results. It showed increasing slope and strength with the increase of strain rate. Similar observations are shown in Fig. 3.6b, for the stress–strain behaviour of 3.0 wt% clay nanocomposites at a strain rate of 445 s^{-1} relative to quasi-static loading.

Gilat et al. (2007) reported that the strain rate effects could be explained by the shape of stress–strain curves. At high strain rates, deformation during the test involves only short-range intermolecular interactions between polymer chains without appreciable change in the intramolecular configuration (shape) of the large polymer chains (due to the short duration of testing). At lower strain rates, molecular motions are fast enough to allow changes in the intramolecular configuration during the test.

Figure 3.7 shows the strain contour plots of 3.0 wt% clay/epoxy nanocomposites at a strain rate of 315 s^{-1} at different time steps. The longitudinal strain (ϵ_{yy}) distribution at $t_0 + 130 \mu\text{s}$ corresponding to a load value of 84 N is shown in Fig. 3.7a.

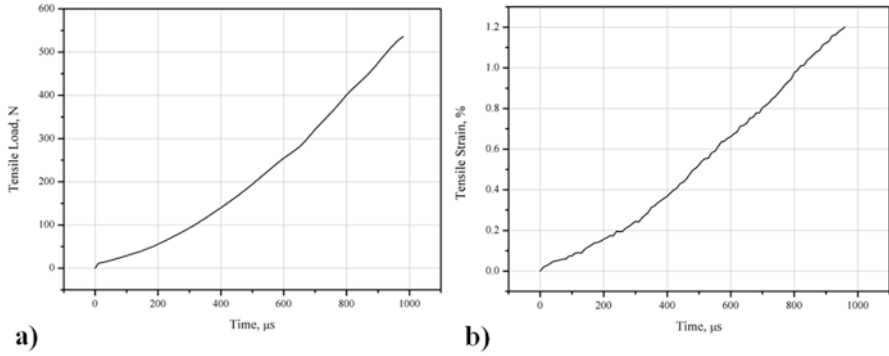


Fig. 3.5 (a) Load and (b) strain histories of 1.5 wt% clay/epoxy nanocomposites at a strain rate of 385 s^{-1}

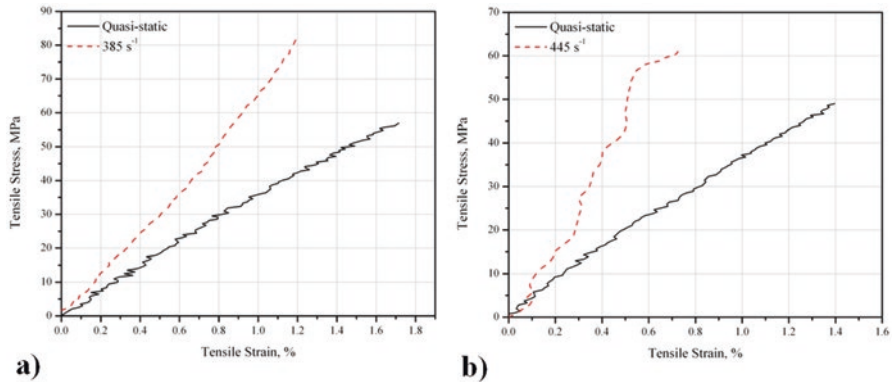


Fig. 3.6 Stress–strain responses of (a) 1.5 wt% and (b) 3.0 wt% clay/epoxy nanocomposites (Gurusideswar et al., 2016), copyright 2021. Reproduced with permission from Elsevier Ltd.

Similarly, Fig. 3.7b shows strain distribution at $t_0 + 330 \mu\text{s}$ corresponding to a load value of 327 N. The maximum strain value of 2.36% at $t_0 + 530 \mu\text{s}$ (467 N) is observed in Fig. 3.7c just before the fracture. Figure 3.7d shows the typical brittle fracture of nanocomposite specimen at $t_0 + 560 \mu\text{s}$. The variation in strain could be due to the non-uniform clay distribution and need not be because of bending load. This could be validated from the strain contour plot of glass/epoxy composites (Fig. 3.17), in which the strain is uniform across the specimen width.

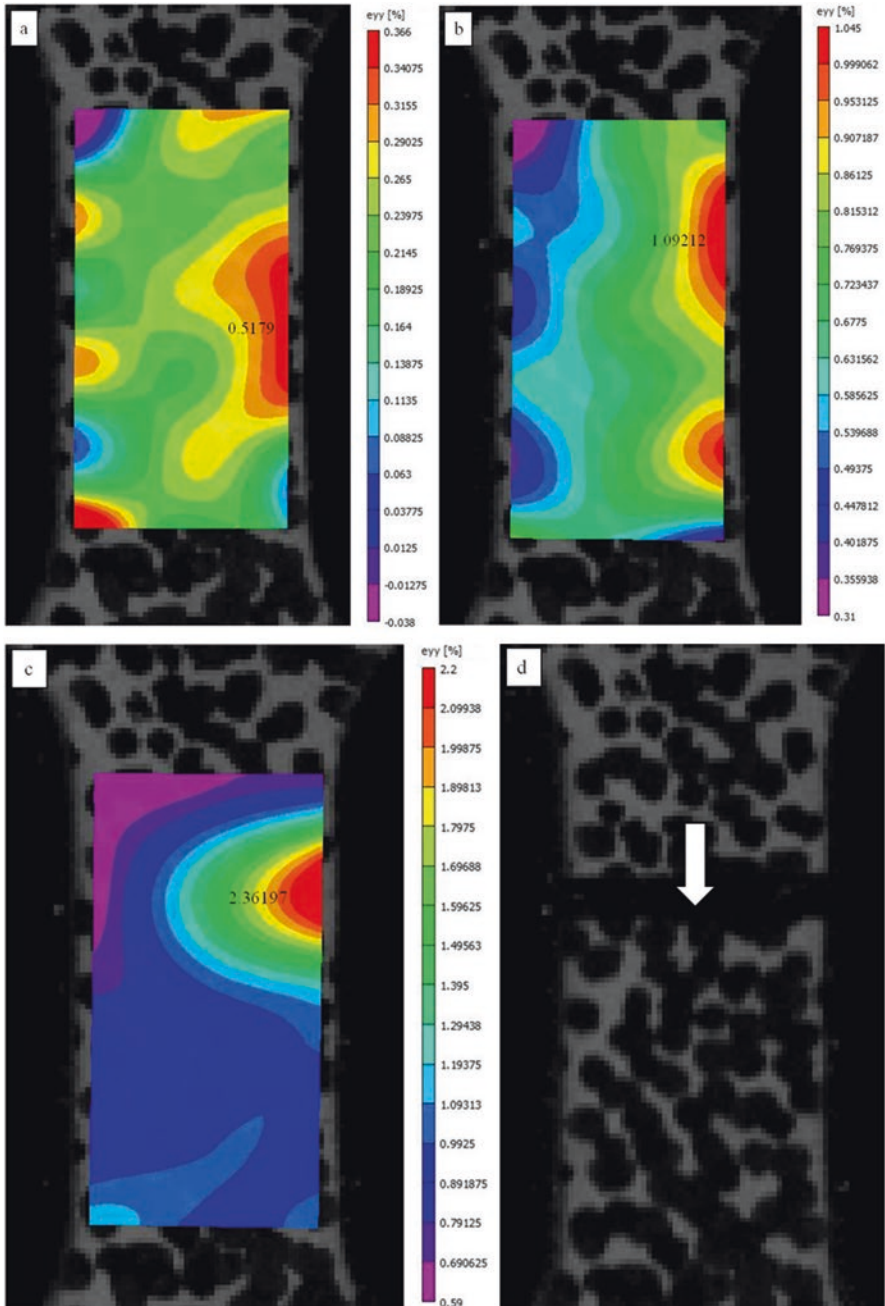


Fig. 3.7 Strain contour plots of 3.0 wt% clay/epoxy nanocomposites at a strain rate of 315 s^{-1} (a) $t_0 + 130 \mu\text{s}$, (b) $t_0 + 330 \mu\text{s}$, (c) $t_0 + 530 \mu\text{s}$ and (d) $t_0 + 560 \mu\text{s}$ (Gurusideswar et al., 2016), copyright 2021. Reproduced with permission from Elsevier Ltd.

3.2 Effect of High Strain Rate on Tensile Properties of Epoxy

Figure 3.8 illustrates the effect of strain rate on the tensile modulus on a logarithmic scale. The elastic modulus is calculated by considering the initial slope of the strain–strain response of the material. The VIC 2D software gives the average strain values along the chosen gauge area. The tensile modulus (3.54 GPa) significantly increases up to 77% (6.25 GPa) at the highest strain rate for the neat epoxy system. The same trend is followed for epoxy/clay nanocomposites. An increase of 90%, 83% and 89% in tensile modulus is observed from quasi-static to the highest strain rate of 445 s^{-1} (1 m drop mass height) for 1.5 wt%, 3.0 wt% and 5.0 wt% of clay loadings, respectively. The maximum increase (90%) in modulus is observed for 1.5 wt% clay loading at the strain rate of 445 s^{-1} .

The tensile modulus and tensile strength are quite sensitive to high strain rates. Figure 3.9 illustrates the effect of strain rate on the tensile strength on a logarithmic scale. The tensile strength (39 MPa) of neat epoxy follows a similar trend, just like the tensile modulus, with an increase of 41% (55 MPa). Buckley et al. (2001) performed tensile tests on three different thermosetting resins and found an increase in modulus of 62%, a marginal increase in maximum stress of 11% and a reduction in failure strain of 41% with increasing strain rate (2000 s^{-1}) for unmodified diglycidylether of bisphenol A (DGEBA) epoxy resin.

The tensile modulus, strength and failure strain at various strain rates are presented in Table 3.1 for the neat epoxy system, 1.5, 3.0 and 5.0 wt% clay loading, respectively. The increase in tensile modulus and strength is commonly described by the viscoelastic nature of the polymeric matrix (Buckley et al., 2001; Shokrieh & Omid, 2009), i.e. stiffening with increased rate of loading. An increase of 50%, 45% and 25% in tensile strength is observed from quasi-static loading to the highest strain rate of 445 s^{-1} (1 m drop mass height) for 1.5, 3.0 and 5.0 wt% clay loadings, respectively, in contrast to quasi-static strain rate. The maximum increase of 50% in

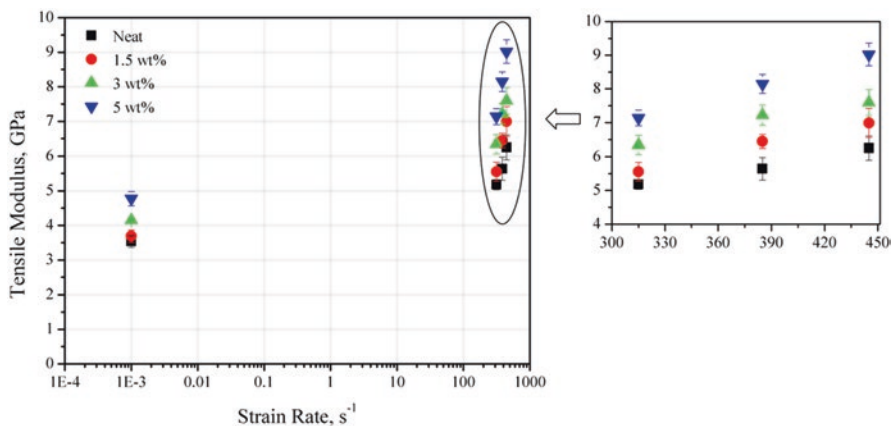


Fig. 3.8 Effect of high strain rate on tensile modulus of epoxy and its clay nanocomposites

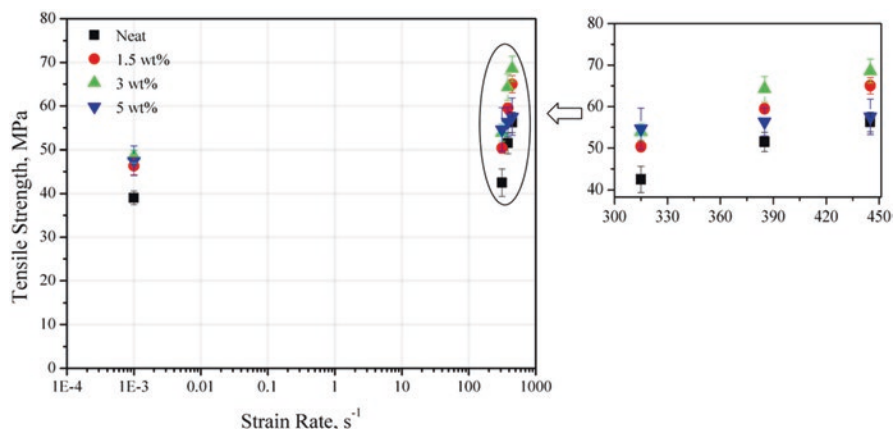


Fig. 3.9 Effect of high strain rate on tensile strength of epoxy and its clay nanocomposites

Table 3.1 Effect of high strain rate on tensile properties of epoxy and its clay nanocomposites

Clay content wt%	Drop mass height m	Strain rate s^{-1}	Tensile modulus GPa	Tensile strength MPa	Tensile strain %
Neat	Quasi-static	0.001	3.54 ± 0.16	39 ± 1.56	1.039 ± 0.014
	0.5	315	5.18 ± 0.15	42.5 ± 3.15	0.974 ± 0.008
	0.75	385	5.64 ± 0.33	51.47 ± 2.32	0.928 ± 0.009
	1	445	6.25 ± 0.35	56.24 ± 2.32	0.852 ± 0.021
1.5	Quasi-static	0.001	3.69 ± 0.18	46.3 ± 1.99	1.2 ± 0.056
	0.5	315	5.56 ± 0.27	50.38 ± 1.1	1.031 ± 0.018
	0.75	385	6.45 ± 0.21	65.86 ± 1.18	0.977 ± 0.022
	1	445	7 ± 0.43	69.36 ± 1.97	0.903 ± 0.016
3	Quasi-static	0.001	4.15 ± 0.07	48.5 ± 1.41	1.396 ± 0.038
	0.5	315	6.34 ± 0.28	53.88 ± 1.97	1.264 ± 0.017
	0.75	385	7.22 ± 0.31	66.79 ± 3.03	1.035 ± 0.004
	1	445	7.6 ± 0.39	70.54 ± 2.89	0.95 ± 0.056
5	Quasi-static	0.001	4.77 ± 0.21	47.5 ± 3.37	1.25 ± 0.059
	0.5	315	7.14 ± 0.23	54.64 ± 4.98	0.986 ± 0.061
	0.75	385	8.15 ± 0.28	56.33 ± 3.36	0.926 ± 0.019
	1	445	9.02 ± 0.34	59.53 ± 4.27	0.85 ± 0.052

strength is observed for 1.5 wt% clay loading at the strain rate of $445 s^{-1}$. From the results, it is found that the tensile modulus of epoxy/clay nanocomposites is more sensitive to strain rates compared to tensile strength. An average of 27% decrease in failure strain is found as strain rate increases for epoxy/clay nanocomposites.

3.2.1 Effect of Clay on Tensile Properties of Epoxy

The stress–strain responses (Fig. 3.10) of epoxy and its clay nanocomposite at a strain rate of 385 s^{-1} reveal that addition of clay leads to brittle failure.

The high specific surface area (of the order of $800\text{ m}^2/\text{g}$) of nanoclay shows dramatic improvements in modulus even at a low content in an epoxy matrix. It is found that the tensile modulus of the clay nanocomposites increases monotonically with increasing clay content. In general, the improvement in elastic modulus is ascribed to the good dispersion of nanosized clay particles and good interfacial adhesion between the particles and the epoxy matrix so that the mobility of polymer chains is restricted under loading (Yasmin et al., 2003; Velmurugan & Mohan, 2004; Wang et al., 2006; Guo & Li, 2007; Zainuddin et al., 2010). From Fig. 3.11, an increment of 35% in tensile modulus is achieved with the addition of 5.0 wt% of clay in epoxy at quasi-static loading. At the highest strain rate (445 s^{-1}), 45% increase in tensile modulus is observed with the addition of 5.0 wt% of clay in epoxy.

Figure 3.12 shows the percentage variation in tensile modulus due to the addition of clay in epoxy at quasi-static and dynamic loadings. 5.0 wt% clay/epoxy samples show maximum improvement in tensile modulus at all strain rates. The combined effect of high strain rate (445 s^{-1}) and clay (1.5 wt%) in tensile modulus is found to be 98% when compared with a neat epoxy system tested at quasi-static loading.

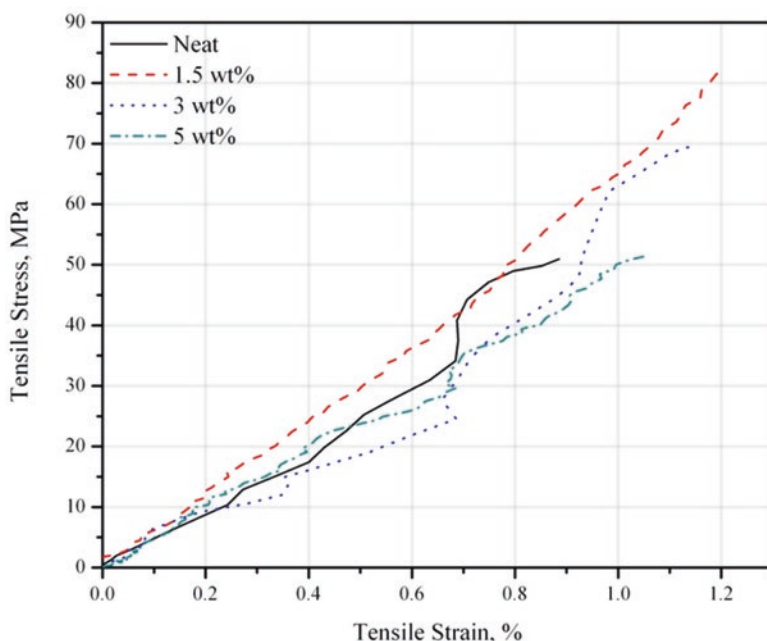


Fig. 3.10 Stress–strain responses of epoxy and its clay nanocomposites at a strain rate of 385 s^{-1}

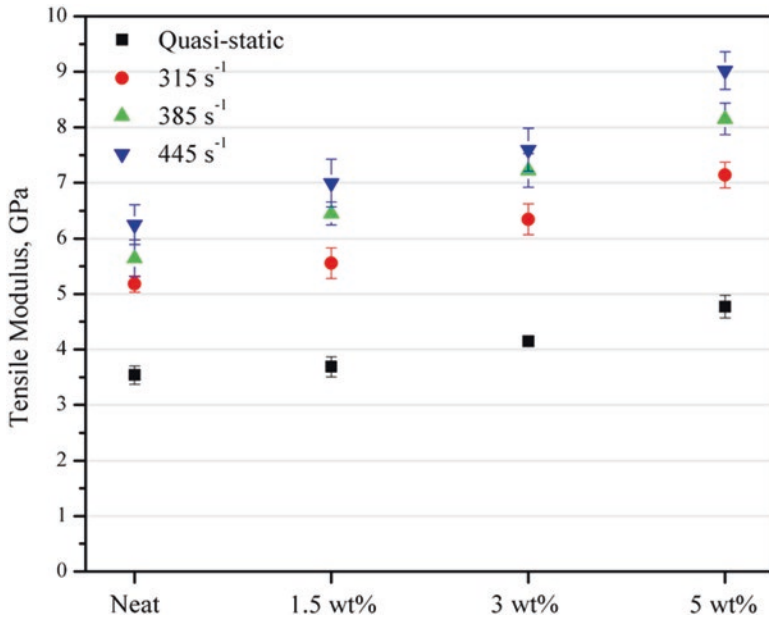


Fig. 3.11 Effect of clay in epoxy on tensile modulus for various high strain rates

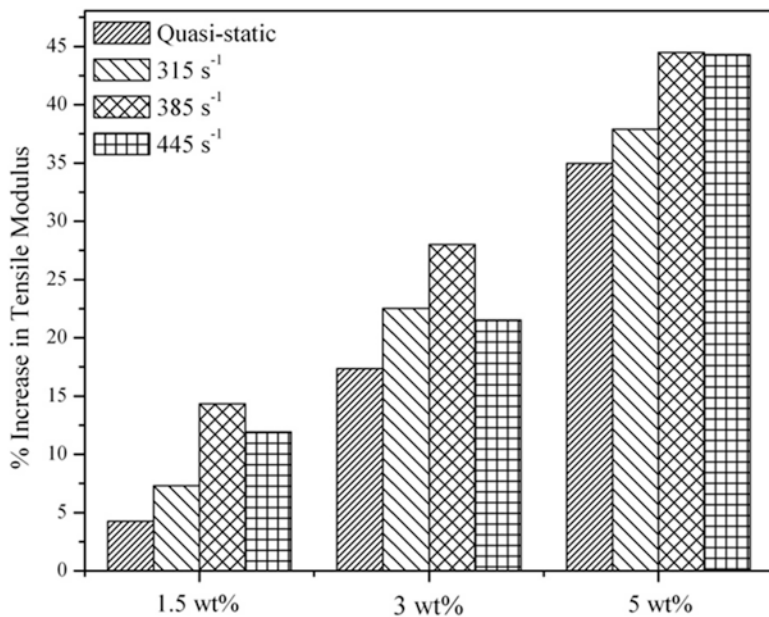


Fig. 3.12 Percentage increase in tensile modulus for various clay loadings in epoxy at quasi-static and dynamic loadings

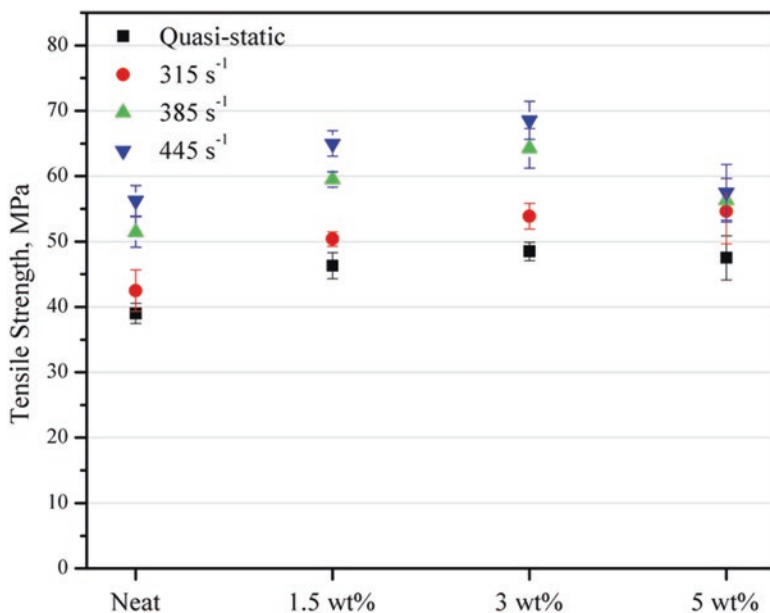


Fig. 3.13 Effect of clay in epoxy on tensile strength for various high strain rates

Figure 3.13 shows the effect of clay on tensile strength at quasi-static and dynamic loadings and the optimal clay loading is found to be 3.0 wt%. An increment of 25% in tensile strength is observed with the addition of clay at quasi-static loading. At the highest strain rate (445 s⁻¹), a 27% increase in tensile strength is observed with the addition of clay in epoxy. The decrease in tensile strength is found at 5.0 wt% clay loading, which could be due to the microvoids and also increased brittleness of the system on addition of clay (Yasmin et al., 2003; Liu et al., 2005; Qi et al., 2006).

Figure 3.14 shows the percentage variation in tensile strength due to the addition of clay in epoxy at quasi-static and dynamic loadings. 3.0 wt% clay/epoxy samples show maximum improvement in strength at all strain rates. The combined effect of high strain rate (445 s⁻¹) and clay (1.5 wt%) on the tensile strength is found to be an increase of 67% when compared with a neat epoxy system tested at quasi-static loading.

3.3 High Strain Rate Sensitivity of Glass/Epoxy Hybrid Nanocomposites

Dynamic tensile studies were performed in the drop mass tower with a drop mass of 1 kg. Similar to epoxy/clay nanocomposites, three different heights were chosen, viz. 0.5 m, 0.75 m and 1 m, corresponding to high strain rates of 315 s⁻¹, 385 s⁻¹ and

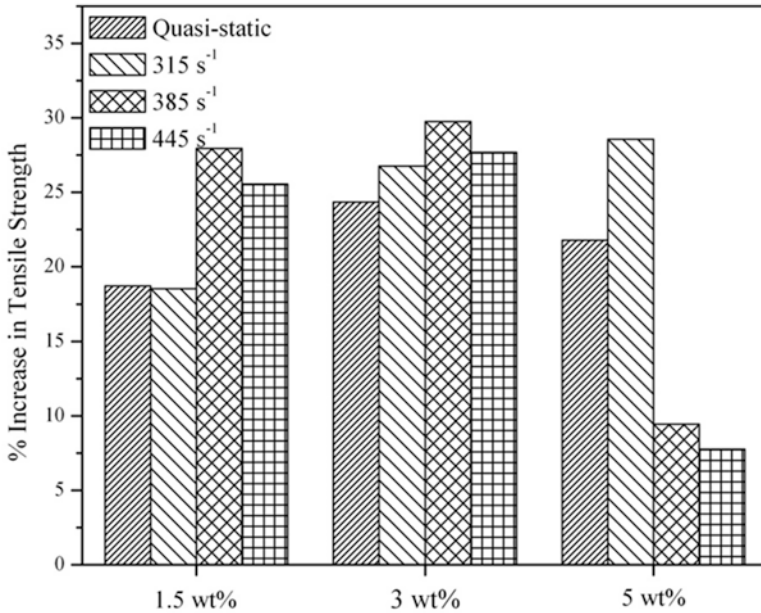


Fig. 3.14 Percentage increase in tensile strength for various clay loadings in epoxy at quasi-static and dynamic loadings

445 s⁻¹, respectively, to study the strain rate effects of glass/epoxy composites and its clay nanocomposites (1.5, 3.0 and 5.0 wt%). At quasi-static loading, the stress–strain behaviour is approximately linearly elastic up to the maximum stress point of 315 MPa followed by a sudden failure at a strain of 2.5% (Fig. 3.15).

Figure 3.16 shows the strain histories of 1.5 wt% and 5.0 wt% glass/epoxy/clay nanocomposites tested at drop heights of 0.5 m and 1 m. For 1.5 wt% clay loading, the specimen failed at 2% (1800 μs) and 1.8% (600 μs) under strain rates of 315 s⁻¹ and 445 s⁻¹, respectively. It is observed that the initial slope of the strain history is not a true indication of the effective strain rate experienced by the material, and hence, the actual strain rates are determined from the gradient of the strain–time curves (Hsiao & Daniel, 1998). The averages of actual strain rates determined at heights of 0.5, 0.75 and 1 m were 24, 41 and 52 s⁻¹, respectively. However, the actual strain rates are used in practice for analysis. In general, the nominal or theoretical strain rate can be calculated by dividing the gauge length of the specimen to the cross-head speed (here, it is drop mass velocity).

Figure 3.17 shows the strain contour plots of 1.5 wt% clay/glass/epoxy nanocomposites at a strain rate of 315 s⁻¹. A strain localization is observed just before the failure, which indicates the physical phenomena and not due to DIC parameters. The longitudinal strain (ϵ_{yy}) distribution at $t_0 + 460 \mu\text{s}$ corresponding to a load value of 283 N is shown in Fig. 3.17a. Similarly, Fig. 3.17b shows strain distribution at $t_0 + 1460 \mu\text{s}$ corresponding to a load value of 1080 N.

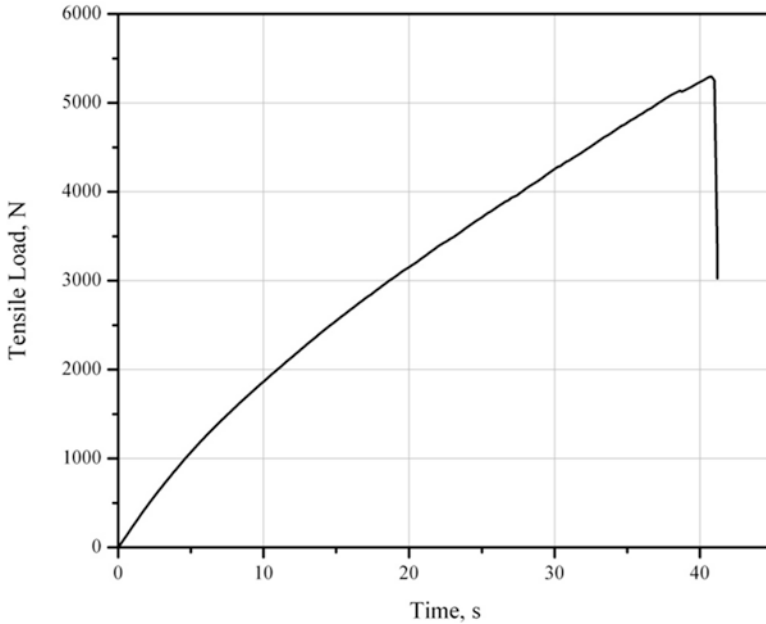


Fig. 3.15 A typical load history of glass/epoxy composite at quasi-static loading

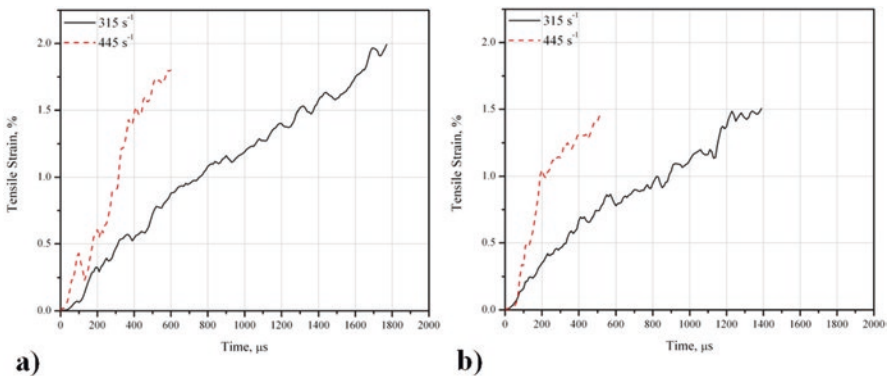


Fig. 3.16 Strain histories of (a) 1.5 wt% and (b) 5.0 wt% clay/glass/epoxy nanocomposites for various high strain rates (Gurusideswar et al., 2017), copyright 2021. Reproduced with permission from Elsevier Ltd.

Figure 3.18 shows the stress–strain response for neat glass/epoxy and 5.0 wt% glass/epoxy/clay nanocomposites at quasi-static and dynamic loading. The stress–strain behaviour shows increasing slope and strength and decreasing strain with the increase of strain rate. The strain rate effects of polymers can be explained by the shape of the stress–strain curves (Gilat et al., 2007).

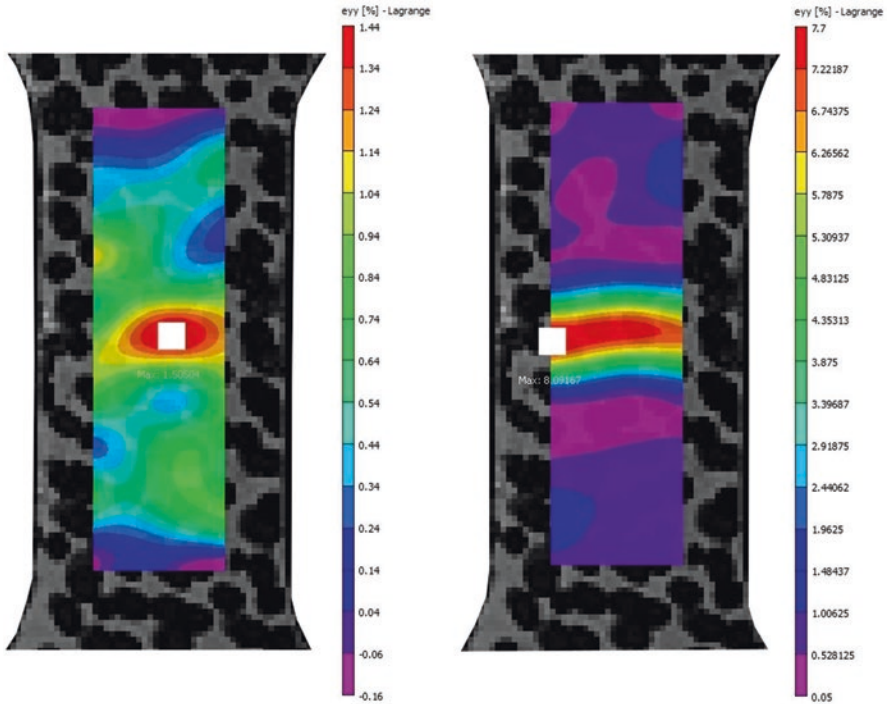


Fig. 3.17 Strain contour plots of 1.5 wt% clay/glass/epoxy nanocomposites at a strain rate of 315 s^{-1} (Gurusideswar et al., 2017), copyright 2021. Reproduced with permission from Elsevier Ltd.

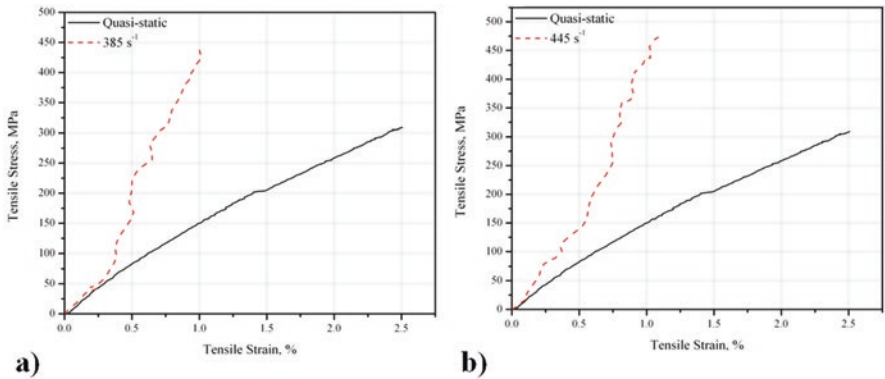


Fig. 3.18 Stress–strain response of (a) neat and (b) 5.0 wt% glass/epoxy composite at quasi-static and dynamic loadings

3.3.1 Effect of High Strain Rate on Tensile Properties of Glass/Epoxy

The tensile modulus, strength and strain to failure at various high strain rates are presented in Table 3.2 for neat glass/epoxy, 1.5, 3.0 and 5.0 wt% glass/epoxy/clay nanocomposites, respectively. It is observed that the tensile modulus is relatively sensitive to high strain rates.

The variation of tensile modulus and strength with the log of strain rate (Fig. 3.19) shows a sharp upward deviation in the high strain rate region, which confirms the strain rate sensitivity of the material. The values of tensile modulus and tensile strength of glass/epoxy composites obtained at low strain rates (10^{-4} – 10^{-1} s $^{-1}$) are also included in Fig. 3.19 for comparison.

Figure 3.20 shows load histories of 1.5 wt% and 3.0 wt% glass/epoxy/clay nanocomposites at high strain rates (315–445 s $^{-1}$). 3.0 wt% clay samples show a higher load of 1550 N, whereas 1.5 wt% clay samples show 1400 N at the highest strain rate of 445 s $^{-1}$.

Figure 3.21 illustrates the effect of strain rate on the tensile modulus of glass/epoxy/clay nanocomposites. The tensile modulus (18.09 GPa) increases significantly by 106% (37.31 GPa) for the highest strain rate of neat glass/epoxy composites. The same trend is followed for glass/epoxy/clay nanocomposites. An increase of 150%, 173% and 158% in tensile modulus is observed from quasi-static to the highest strain rate of 445 s $^{-1}$ for 1.5, 3.0 and 5.0 wt% clay loadings, respectively.

Figure 3.22 illustrates the effect of strain rate on the tensile strength of glass/epoxy/clay nanocomposites. The tensile strength is relatively sensitive to high strain rates. The tensile strength (314.9 MPa) increases up to 67% (526 MPa) for the strain

Table 3.2 Effect of high strain rate on tensile properties of glass/epoxy/clay nanocomposites

Clay content wt%	Drop mass height m	Strain rate s $^{-1}$	Tensile modulus GPa	Tensile strength MPa	Tensile strain %
Neat	Quasi-static	0.001	18.09 ± 0.17	314.9 ± 0.71	2.507 ± 0.02
	0.5	315	28.58 ± 1.36	421.7 ± 10.1	2.272 ± 0.212
	0.75	385	34.81 ± 3.13	476.9 ± 20.2	1.942 ± 0.225
	1	445	37.31 ± 2.06	526.1 ± 15.8	1.798 ± 0.023
1.5	Quasi-static	0.001	19.65 ± 0.18	343.2 ± 3.1	1.693 ± 0.04
	0.5	315	32.61 ± 2.99	446.5 ± 8.1	1.746 ± 0.206
	0.75	385	40.75 ± 4.3	529.9 ± 21.6	1.635 ± 0.128
	1	445	45.2 ± 2.13	579.5 ± 14.4	1.476 ± 0.019
3	Quasi-static	0.001	20.13 ± 0.07	326.8 ± 2.8	1.771 ± 0.08
	0.5	315	33.05 ± 1.26	443.2 ± 6.3	1.663 ± 0.18
	0.75	385	43.07 ± 5.05	510.3 ± 21.5	1.54 ± 0.188
	1	445	49.36 ± 6.33	573.9 ± 29.8	1.131 ± 0.058
5	Quasi-static	0.001	19.35 ± 0.21	321.7 ± 3.7	1.894 ± 0.09
	0.5	315	29.65 ± 0.92	432.6 ± 4.7	1.599 ± 0.083
	0.75	385	40.36 ± 1.76	479.6 ± 17.2	1.513 ± 0.12
	1	445	46.69 ± 3.38	530.7 ± 18.5	1.087 ± 0.094

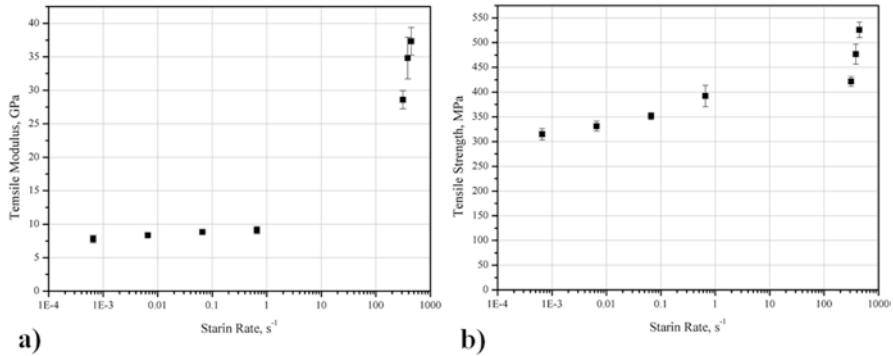


Fig. 3.19 Variation in (a) tensile modulus and (b) tensile strength with log of strain rate for glass/epoxy composites (Gurusideswar et al., 2017), copyright 2021. Reproduced with permission from Elsevier Ltd.

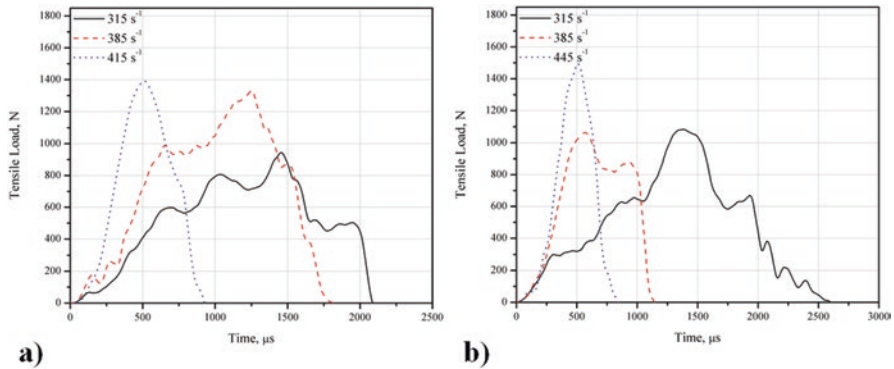


Fig. 3.20 Load histories of (a) 1.5 wt% and (b) 3.0 wt% clay/glass/epoxy nanocomposites for various high strain rates (Gurusideswar et al., 2017), copyright 2021. Reproduced with permission from Elsevier Ltd.

rate of 445 s^{-1} of neat glass/epoxy composites. A similar trend of increase in tensile strength with strain rate is in agreement with the findings of Okoli and Smith (2000). The increase in tensile strength and modulus is ascribed to the viscoelastic nature of the matrix, fibre–matrix interfacial properties, weaving type and geometry of the composites (Welsh & Harding, 1985; Brown et al., 2010). An increase of 69%, 76% and 65% in tensile strength is observed from quasi-static to the strain rate of 445 s^{-1} for 1.5, 3.0 and 5.0 wt% clay loadings, respectively.

From the results, it is observed that the stiffness of glass/epoxy/clay nanocomposites is more sensitive to strain rates compared to its tensile strength. On average, a 25% decrease in failure strain is found as strain rate increases for glass/epoxy/clay nanocomposites. Similar observations were observed by many researchers. Majzoobi et al. (2005) observed nearly 50% decrease of failure strain for $[\pm 60^\circ]$ glass/epoxy composites at 621 s^{-1} , and Ochola et al. (2004) observed a strain to

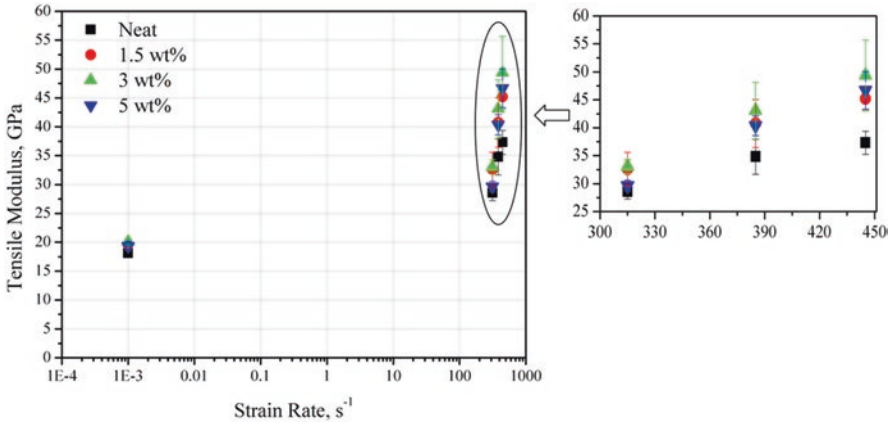


Fig. 3.21 Effect of high strain rate on tensile modulus of glass/epoxy/clay nanocomposites

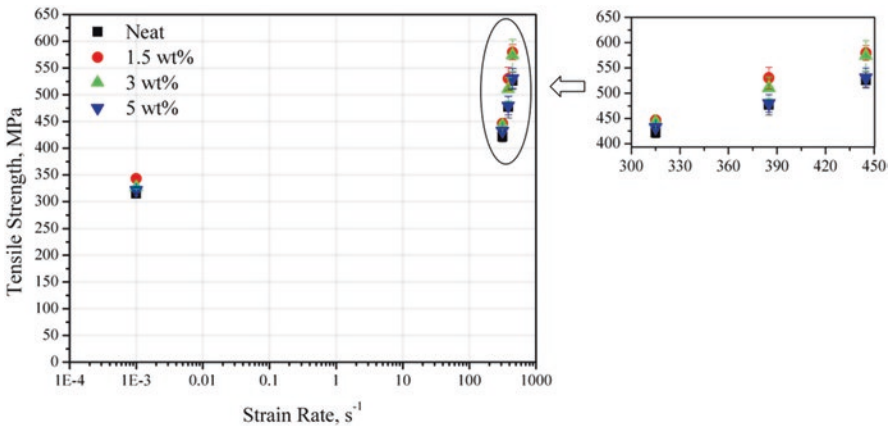


Fig. 3.22 Effect of high strain rate on tensile strength of glass/epoxy/clay nanocomposites

failure of 15% under compression loading at low strain rates (10^{-3} s^{-1}) and 4% at high strain rate of 450 s^{-1} for GFRP system. It is believed that due to rapid loading, the composite tends to be more brittle resulting in a lower strain to failure.

3.3.2 Effect of Clay on Tensile Properties of Glass/Epoxy

The addition of nanoclay makes the glass/epoxy nanocomposites fail in a brittle mode (Fig. 3.23) and leads to restriction of plastic deformations in the nanocomposites (Kornmann et al., 2005). From Fig. 3.24, an increment of 15% in tensile modulus is achieved with the addition of 3.0 wt% of clay in glass/epoxy at quasi-static loading. At high strain rate (445 s^{-1}), 25% increase in tensile modulus is observed

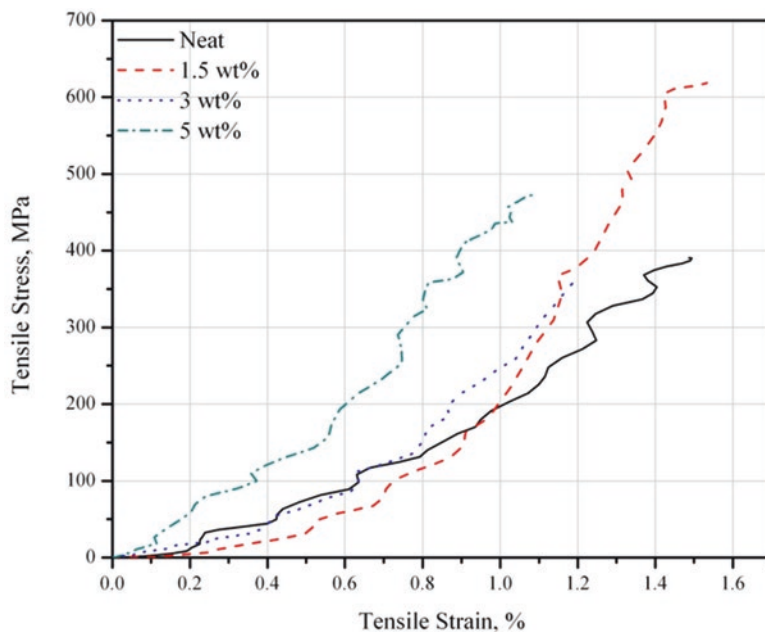


Fig. 3.23 Stress–strain responses of glass/epoxy and its clay nanocomposites at a strain rate of 445 s⁻¹ (Gurusideswar et al., 2017), copyright 2021. Reproduced with permission from Elsevier Ltd.

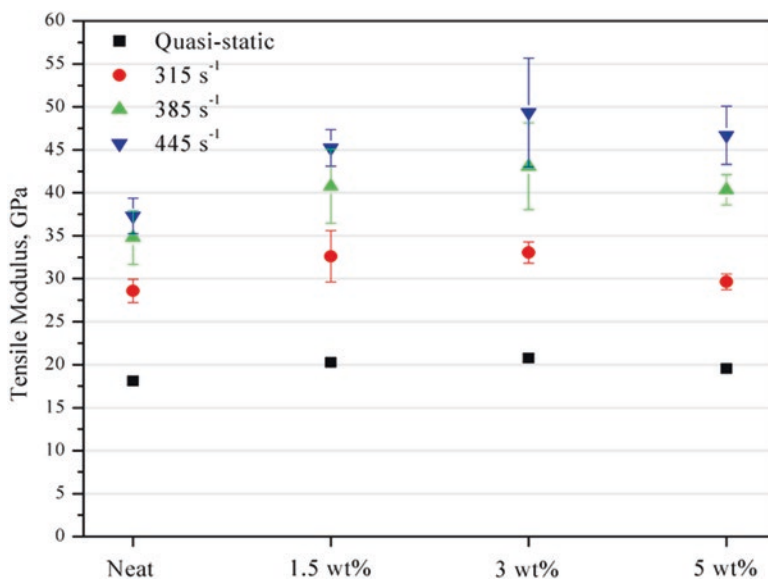


Fig. 3.24 Effect of clay on tensile modulus at different high strain rates

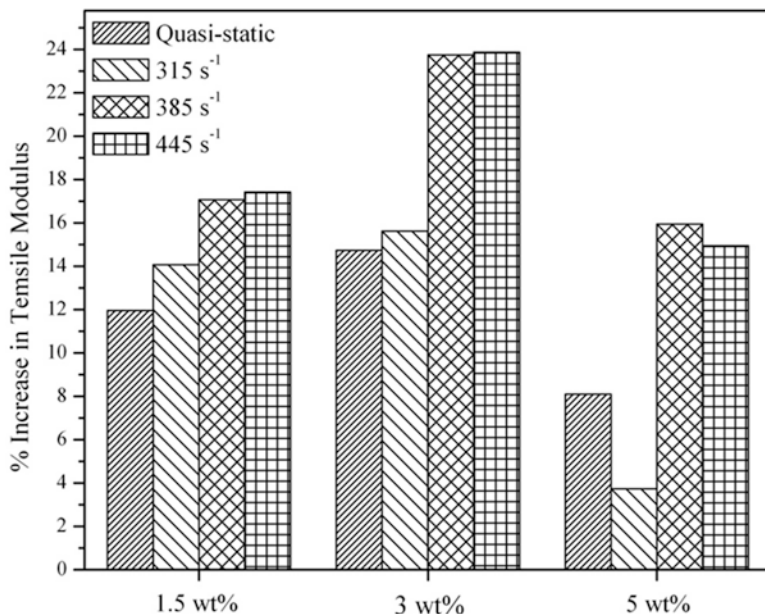


Fig. 3.25 Percentage increase in tensile modulus for various clay loadings in glass/epoxy at quasi-static and dynamic loadings (Gurusideswar et al., 2017), copyright 2021. Reproduced with permission from Elsevier Ltd.

with the addition of 3.0 wt% of clay in glass/epoxy composites. Similarly, a maximum increment of 24% and 16% in tensile modulus is found at strain rates of 385 s⁻¹ and 315 s⁻¹ by adding 3.0 wt% of clay in glass/epoxy composites. Similar findings are reported by many authors (Wu et al., 2002; Yasmin et al., 2006; Shi et al., 2009; Zainuddin et al., 2010). It is also noted that the microstructure of glass fibre/epoxy/clay restricts the mobility of the polymer in the interface between the fibre and epoxy or between the clay and epoxy in the glass/epoxy/clay nanocomposites. This allows better stress transfer to the fibres and leads to an improved stiffness at low strain values (Lin et al., 2006).

Figure 3.25 shows the percentage variation in tensile modulus due to the addition of clay in glass/epoxy at quasi-static and dynamic loadings. 3.0 wt% glass/epoxy/clay sample shows maximum improvement at all strain rates. The combined effect of high strain rate (445 s⁻¹) and clay (1.5 wt%) in tensile modulus is found to be 150% when compared with neat glass/epoxy composites tested at quasi-static loading.

Similarly, the tensile strength increases with increasing clay loading. Figure 3.26 shows the effect of clay on tensile strength at quasi-static and dynamic loadings. An increment of 9% in tensile strength is observed with the addition of 1.5 wt% clay at quasi-static loading. However, at higher clay loadings, the tensile strength decreases. The reason for the decrement could be the formation of clay agglomerations, which leads to stress concentration, thus causing premature failure and formation of

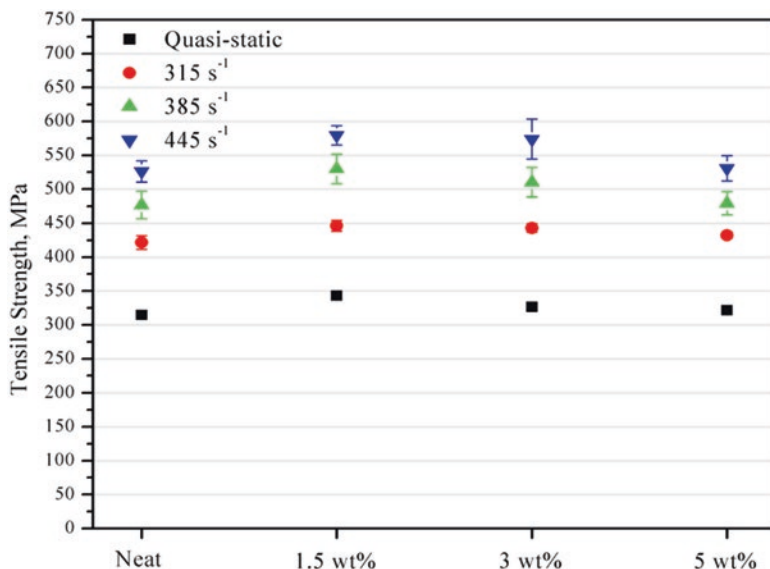


Fig. 3.26 Effect of clay on tensile strength for various strain rates

microvoids at higher clay loadings. At the highest strain rate (445 s^{-1}), 10% increase in tensile strength is observed with the addition of 1.5 wt% of clay in glass/epoxy composites. Similarly, a maximum increase of 11% and 6% in tensile strength is observed at strain rates of 385 s^{-1} and 315 s^{-1} by adding 1.5 wt% of clay in glass/epoxy composites.

Figure 3.27 shows the percentage variation in tensile strength due to the addition of clay in glass/epoxy at quasi-static and dynamic loadings. Optimal clay loading of 1.5 wt% is identified at quasi-static and dynamic tensile loadings. The combined effect of high strain rate (445 s^{-1}) and clay (1.5 wt%) in tensile strength is found to be 84% when compared with neat glass/epoxy composites tested at quasi-static loading.

3.4 Fractography

Fractography of the failed specimens was investigated using HR-SEM (Hitachi model S-4800) to study the effects of clay addition and high strain rate on tensile properties of epoxy and glass/epoxy composites. The SEM micrograph (Fig. 3.28) shows a smooth, glassy and featureless fracture surface for a neat epoxy specimens tested at quasi-static loading. This type of morphology indicates a typical brittle fracture behaviour of epoxy resin (Ratna et al., 2003; Zhou et al., 2006; Wang et al., 2006; Zainuddin et al., 2010).

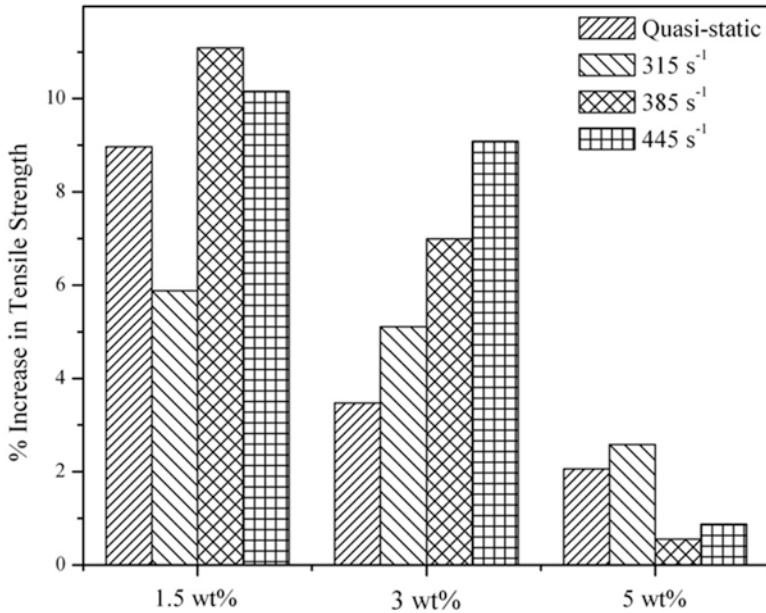


Fig. 3.27 Percentage increase in tensile strength for various clay loadings at quasi-static and dynamic loadings (Gurusideswar et al., 2017), copyright 2021. Reproduced with permission from Elsevier Ltd.

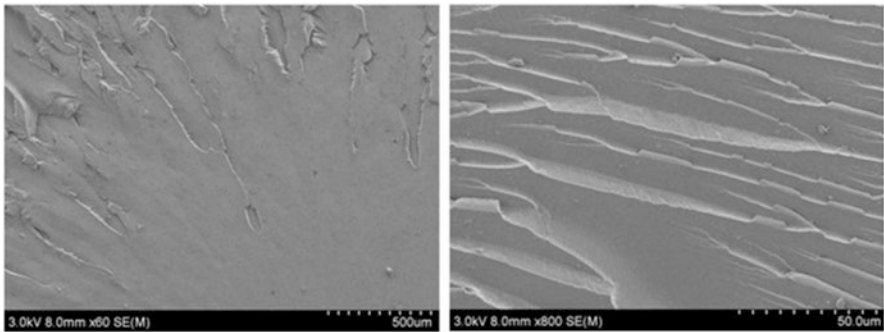


Fig. 3.28 SEM images of tensile fractured surfaces of neat epoxy at different magnifications in quasi-static loading (Gurusideswar et al., 2016), copyright 2021. Reproduced with permission from Elsevier Ltd.

The fracture surfaces of epoxy/clay nanocomposites (Fig. 3.29) show rough fractographic features, deep river markings and clay agglomerates. The increased surface roughness shows that the crack path is more distorted and difficult to propagate due to the presence of nanoclay (Wang et al., 2006). Also, cleavages are observed on fracture surfaces of epoxy and its clay nanocomposites. Deep cleavages are observed in neat epoxy specimens, whereas shallow cleavages are observed in

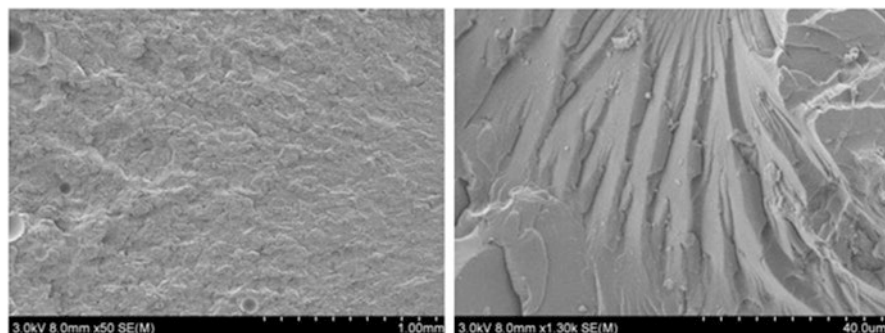


Fig. 3.29 Fractured surfaces of 1.5 wt% clay/epoxy nanocomposites at different magnifications in quasi-static loading (Gurusideswar et al., 2016), copyright 2021. Reproduced with permission from Elsevier Ltd.

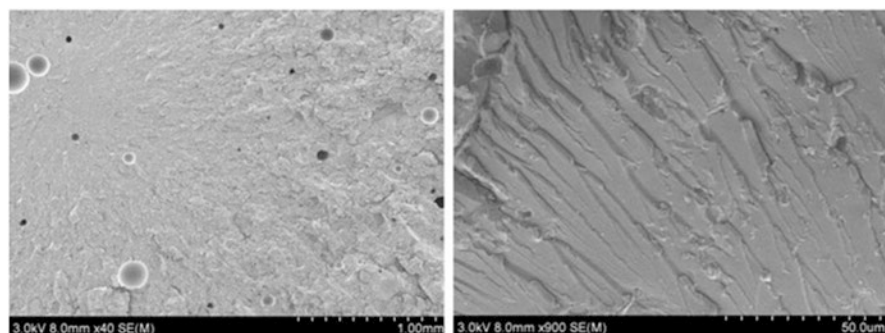


Fig. 3.30 Fractured surfaces of 3.0 wt% clay/epoxy nanocomposites at different magnifications in quasi-static loading (Gurusideswar et al., 2016), copyright 2021. Reproduced with permission from Elsevier Ltd.

epoxy/clay nanocomposite specimens. In addition, microvoids are observed in epoxy/clay nanocomposites containing higher clay content (Fig. 3.30), and also the failure mode is significantly changed as shown in Figs. 3.29 and 3.30. The failure is initiated at a localized domain which might be due to the presence of agglomerations of clay particles, and the crack initiation is caused by the stress concentration developed around the agglomerated particles leading to failure (Zainuddin et al., 2010).

It is observed that the roughness of the fracture surface has increased considerably at higher strain rates due to irregular deep cleavages, resulting in sudden failure (Shadlou et al., 2014). Similar to quasi-static testing, epoxy/clay nanocomposites exhibit rough fractographic features in dynamic tensile testing. Figure 3.31 shows the micrograph of neat epoxy at 385 s^{-1} , which resembles a typical cleavage fracture. With the addition of clay, the fracture surface shows secondary cracks and more and deeper river markings around the agglomerates.

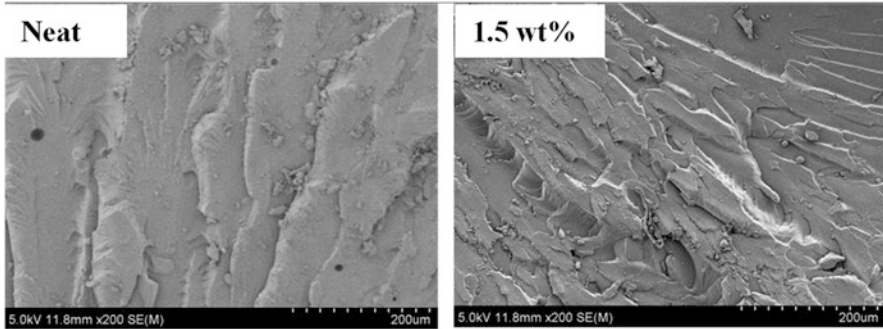


Fig. 3.31 Fractured surfaces of neat epoxy and its clay nanocomposites at a strain rate of 385 s^{-1} at low magnification (Gurusideswar et al., 2016), copyright 2021. Reproduced with permission from Elsevier Ltd.

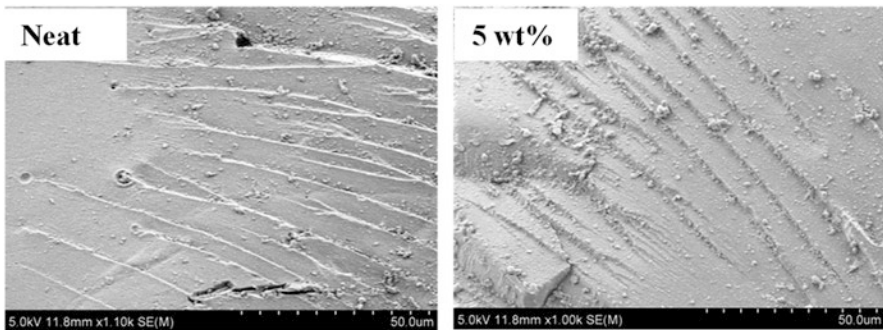


Fig. 3.32 Fractured surfaces of neat epoxy and its clay nanocomposites at a strain rate of 385 s^{-1} at high magnification (Gurusideswar et al., 2016), copyright 2021. Reproduced with permission from Elsevier Ltd.

The fracture surface of epoxy/clay nanocomposites at high magnification (Fig. 3.32) shows massive shear deformation. This indicates that during loading the stress concentration developed around the nanoparticles contributed to shear yielding of epoxy interlayers at the tip of the propagating crack (Ratna et al., 2003). Cavities are observed in 3.0 wt% clay content (Fig. 3.33), and this might be due to entrapped voids or decohesion of clay agglomerations after failure (Yasmin et al., 2003; Liu et al., 2005; Qi et al., 2006). Also, the fracture surface of nanocomposites with 5.0 wt% of clay content confirms that the formation of microvoids was due to the debonding of clay nanoparticles from the matrix.

Similar to epoxy/clay nanocomposites, fractography of the failed specimens was investigated using HR-SEM (Hitachi model S-4800) to study the effects of clay addition and high strain rate on tensile properties of glass/epoxy composites. Figure 3.34 shows fibre–matrix interactions of different clay loadings at quasi-static loading. From Fig. 3.34, it is observed that the fibres are de-bonded from the matrix and fibre breaking is the dominant mode of failure for neat glass/epoxy, which

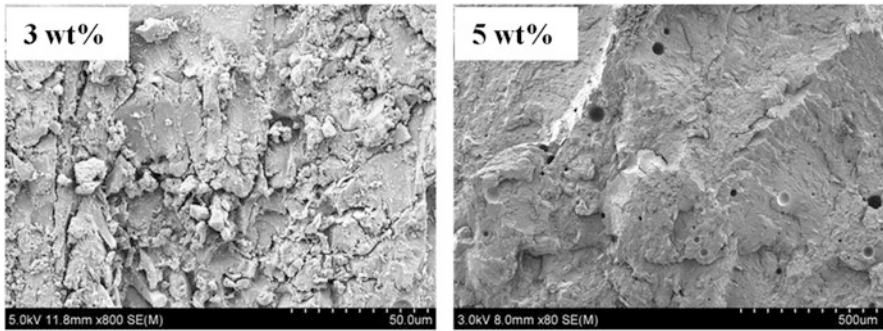


Fig. 3.33 SEM micrographs of 3.0 wt% and 5.0 wt% clay/epoxy nanocomposites reveal microvoids at different magnifications (Gurusideswar et al., 2016), copyright 2021. Reproduced with permission from Elsevier Ltd.

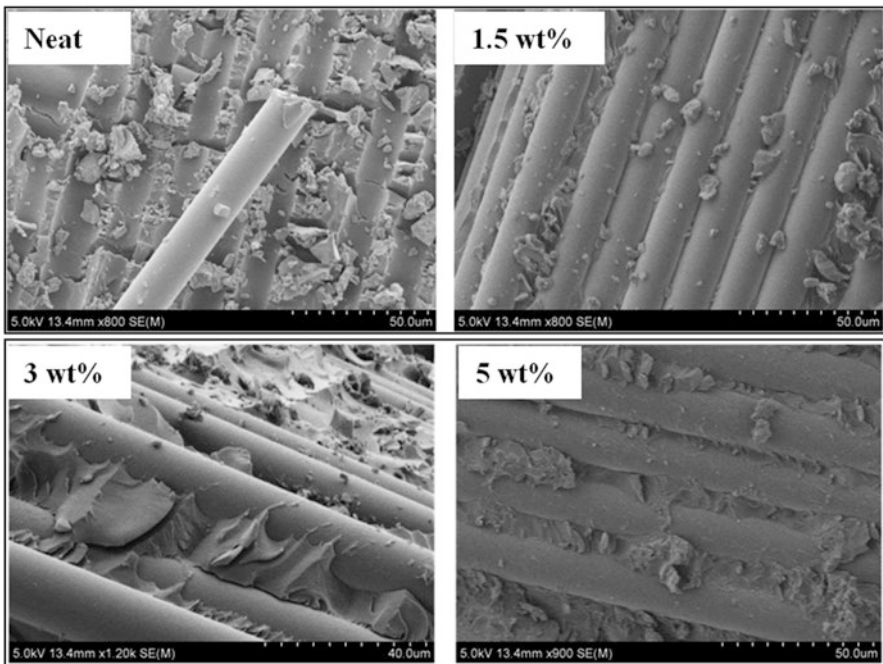


Fig. 3.34 Fibre matrix interaction of glass/epoxy and its clay nanocomposites (Gurusideswar et al., 2017), copyright 2021. Reproduced with permission from Elsevier Ltd.

indicates poor adhesion between fibre and matrix. In the case of glass/epoxy composites with clay, it is clearly observed that the surface of the fibres is rougher and the fibres have good bonding with the matrix (Chowdhury et al., 2006; Shi et al., 2009; Khan et al., 2011). Figure 3.34 shows good wettability between matrix and fibre of 1.5 wt% and 3.0 wt% clay loadings. This could be due to the particular

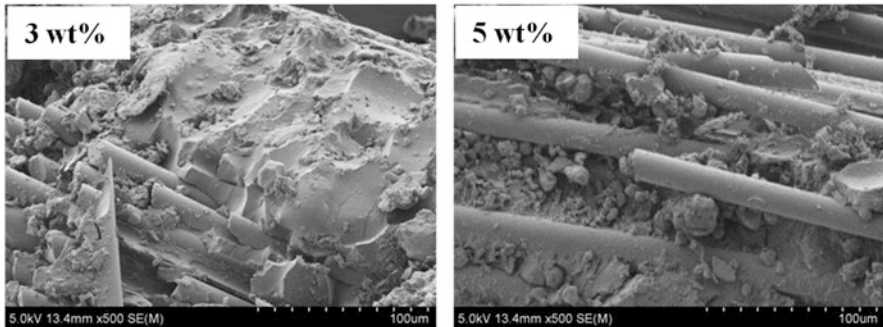


Fig. 3.35 Fracture surfaces of glass/epoxy/clay nanocomposites show matrix agglomeration (Gurusideswar et al., 2017), copyright 2021. Reproduced with permission from Elsevier Ltd.

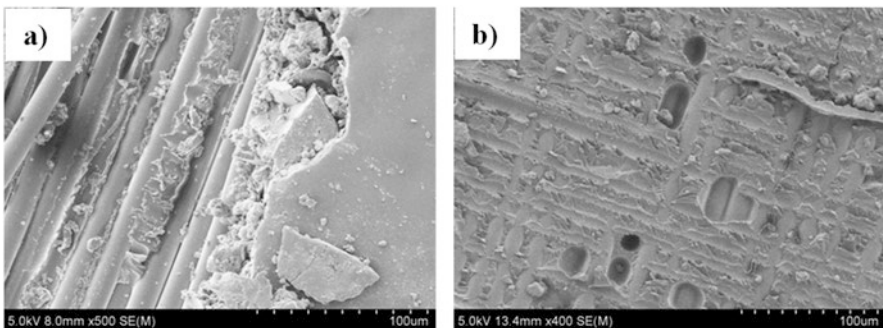


Fig. 3.36 SEM micrographs of (a) matrix damage and (b) minor agglomerations (Gurusideswar et al., 2017), copyright 2021. Reproduced with permission from Elsevier Ltd.

affinity of the nanoclay with the glass fibre surface. It is explained by Kornmann et al. (2005) that both fibres and clay are inorganic materials functionalized at the surface with organic molecules, which lead to polarity match between their respective surfaces.

At higher clay loadings (Fig. 3.35), coarse surface and matrix agglomeration are observed in the fibre–matrix interface region resulting in improved interfacial bonding strength (Haque et al., 2003). The increase in clay loading prevents the free volume of nanoparticles from moving around and the cross-link density of the epoxy is increased leading to a tendency to form clay clusters or agglomerates (Lam et al., 2005). Quaresimin and Varley (2008) found a similar morphology for 3.0 wt% nanomodified epoxy laminate and stated an improved local energy dissipation for the nanomodified laminates.

Figure 3.36 shows matrix damage and agglomeration of neat and 1.5 wt% clay glass/epoxy nanocomposites, respectively. The rough fracture surface induced by the addition of clay indicates the enhanced interfacial bonding of the clay with matrix and the clay with fibre, which results in improvement in tensile modulus. The

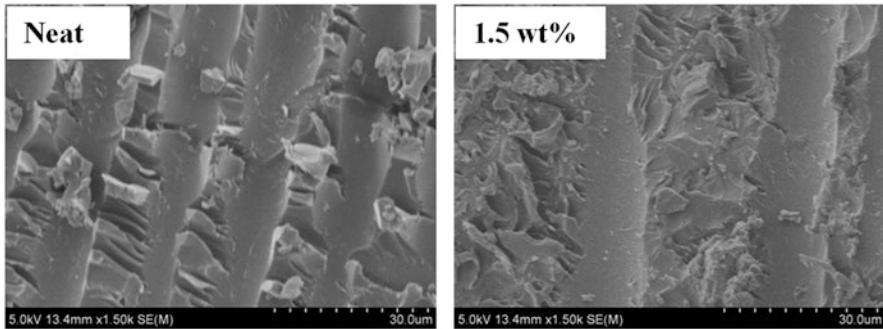


Fig. 3.37 SEM micrographs show fibre pull-outs at a strain rate of 445 s^{-1} (Gurusideswar et al., 2017), copyright 2021. Reproduced with permission from Elsevier Ltd.

microvoids and the clay agglomeration at higher clay loadings lead to a decrease in tensile strength.

It is noted that the fibre pull-outs are dominant with increasing strain rates (Fig. 3.37). Also, the interfacial debonding becomes more severe with increasing strain rate. Staab and Gilat (1995) observed significant changes in the fracture surface appearance as a function of strain rate, and Shokrieh and Omidi (2009) also reported significant changes in the fracture surface with the increase in strain rate by visually inspecting the failed specimens of glass/epoxy composites.

4 Conclusions

The prime objective of this research work was to study the strain rate effects of epoxy, glass/epoxy and its clay nanocomposites. Composite materials are widely used in aerospace structures, automotive industry and marine structures, and in many instances, they are subjected to high-velocity dynamic loadings, which require prior knowledge of dynamic mechanical properties to prevent catastrophic failure at high loading rates. Numerous literatures on high strain rate effects for epoxy and glass/epoxy composites using split-Hopkinson pressure bar (SHPB) have been reported earlier. But the strain rate effects of composites in the medium range ($100\text{--}1000 \text{ s}^{-1}$) are rarely reported. Hence, the high strain rate effects of epoxy, glass/epoxy and its clay nanocomposites are considered for the current research work and investigated.

Dynamic tensile studies were conducted on epoxy/clay and glass/epoxy/clay nanocomposites, using a drop mass setup equipped with in-house fabricated specimen fixture assembly and a high-speed camera. Data obtained from this method filled a gap between conventional testing machines and SHPB measurements. The effects of the strain rate and clay on the tensile behaviour of epoxy resin and glass/epoxy composite were investigated over a wide range of strain rates. A non-contact

strain measurement technique (DIC) using the high-speed camera was employed to capture the full-field strain measurement in the dynamic environment. Quasi-static and dynamic experiment results show that the tensile behaviour of epoxy/clay nanocomposites is dependent on the strain rate. When the strain rate increases from 0.008 to 445 s⁻¹, the tensile modulus (+67%) and tensile strength (+45%) increased for the neat epoxy system and the modulus (106%) and strength (+67%) for neat glass/epoxy composite. A similar trend is observed for epoxy, glass/epoxy and its clay nanocomposites. The presence of clay in epoxy and glass/epoxy composite plays a significant role during dynamic loading. Microscopic observations of the fracture surface showed that the surface becomes rougher with the increase in strain rate. The fracture surfaces of epoxy and glass/epoxy composites were studied using SEM to understand the strain rate effects. The roughness of the fracture surface for epoxy is increased at higher strain rates, leading to irregular cleavages and deeper valleys; these signify sudden fractures. In the case of glass/epoxy, with increasing strain rate, fracture path covers the entire gauge region and an extensive debonding of fibres from the matrix is observed.

Material behaviour at high strain rates obtained through experimental methods can be used for validation of proposed material models, and the future scope of this work is focused on the development of test standards for the determination of dynamic mechanical properties.

References

- Alsubari, S., Zuhri, M. Y. M., Sapuan, S. M., et al. (2021). Potential of natural fiber reinforced polymer composites in sandwich structures: A review on its mechanical properties. *Polymers*, *13*, 423. <https://doi.org/10.3390/polym13030423>
- Armenàkas, A. E., & Sciammarella, C. A. (1973). Response of glass-fiber-reinforced epoxy specimens to high rates of tensile loading. *Experimental Mechanics*, *13*, 433–440. <https://doi.org/10.1007/bf02324887>
- Azeez, A. A., Rhee, K. Y., Park, S. J., & Hui, D. (2013). Epoxy clay nanocomposites—Processing, properties and applications: A review. *Composites Part B: Engineering*, *45*, 308–320. <https://doi.org/10.1016/j.compositesb.2012.04.012>
- Barré, S., Chotard, T., & Benzeggagh, M. L. (1996). Comparative study of strain rate effects on mechanical properties of glass fibre-reinforced thermoset matrix composites. *Composites Part A: Applied Science and Manufacturing*, *27*, 1169–1181.
- Brown, K. A., Brooks, R., & Warrior, N. A. (2010). The static and high strain rate behaviour of a commingled E-glass/polypropylene woven fabric composite. *Composites Science and Technology*, *70*, 272–283. <https://doi.org/10.1016/j.compscitech.2009.10.018>
- Buckley, C. P., Harding, J., Hou, J. P., et al. (2001). Deformation of thermosetting resins at impact rates of strain. Part I: Experimental study. *Journal of the Mechanics and Physics of Solids*, *49*, 1517–1538. [https://doi.org/10.1016/S0022-5096\(00\)00085-5](https://doi.org/10.1016/S0022-5096(00)00085-5)
- Cao, K., Ma, X., Zhang, B., et al. (2010). Tensile behavior of polycarbonate over a wide range of strain rates. *Materials Science and Engineering A*, *527*, 4056–4061. <https://doi.org/10.1016/j.msea.2010.03.088>
- Chen, W., Lu, F., & Cheng, M. (2002). Tension and compression tests of two polymers under quasi-static and dynamic loading. *Polymer Testing*, *21*, 113–121. [https://doi.org/10.1016/S0142-9418\(01\)00055-1](https://doi.org/10.1016/S0142-9418(01)00055-1)

- Chowdhury, F. H. H., Hosur, M. V. V., & Jeelani, S. (2006). Studies on the flexural and thermomechanical properties of woven carbon/nanoclay-epoxy laminates. *Materials Science and Engineering A*, 421, 298–306. <https://doi.org/10.1016/j.msea.2006.01.074>
- Clifton, S., Thimmappa, B. H. S., Selvam, R., & Shivamurthy, B. (2020). Polymer nanocomposites for high-velocity impact applications-A review. *Composites Communications*, 17, 72–86. <https://doi.org/10.1016/j.coco.2019.11.013>
- Daniel, I. M., LaBedz, R. H., & Liber, T. (1981). New method for testing composites at very high strain rates. *Experimental Mechanics*, 21, 71–77. <https://doi.org/10.1007/bf02325199>
- Davies, R. G., & Magee, C. L. (1975). The effect of strain-rate upon the tensile deformation of materials. *Journal of Engineering Materials and Technology, Transactions of the ASME*, 97, 151–155. <https://doi.org/10.1115/1.3443275>
- Elmahdy, A., & Verleysen, P. (2019). Tensile behavior of woven basalt fiber reinforced composites at high strain rates. *Polymer Testing*, 76, 207–221. <https://doi.org/10.1016/j.polymertesting.2019.03.016>
- Evora, V. M. F., & Shukla, A. (2003). Fabrication, characterization, and dynamic behavior of polyester/TiO₂ nanocomposites. *Materials Science and Engineering A*, 361, 358–366. [https://doi.org/10.1016/S0921-5093\(03\)00536-7](https://doi.org/10.1016/S0921-5093(03)00536-7)
- Fu, S., Wang, Y., & Wang, Y. (2009). Tension testing of polycarbonate at high strain rates. *Polymer Testing*, 28, 724–729. <https://doi.org/10.1016/j.polymertesting.2009.06.002>
- Gilat, A., Goldberg, R. K., & Roberts, G. D. (2007). Strain rate sensitivity of epoxy resin in tensile and shear loading. *Journal of Aerospace Engineering*, 20, 75–80. [https://doi.org/10.1061/\(asce\)0893-1321\(2007\)20:2\(75\)](https://doi.org/10.1061/(asce)0893-1321(2007)20:2(75))
- Groves, S., Sanchez, R., Lyon, R., & Brown, A. (1993). High strain rate effects for composite materials. In *Eleventh Volume: Composite materials—Testing and design*. ASTM International.
- Guo, Y., & Li, Y. (2007). Quasi-static/dynamic response of SiO₂-epoxy nanocomposites. *Materials Science and Engineering A*, 458, 330–335. <https://doi.org/10.1016/j.msea.2007.02.011>
- Gurusideswar, S., Velmurugan, R., & Gupta, N. K. (2016). High strain rate sensitivity of epoxy/clay nanocomposites using non-contact strain measurement. *Polymer*, 86, 197–207. <https://doi.org/10.1016/j.polymer.2015.12.054>
- Gurusideswar, S., Velmurugan, R., & Gupta, N. K. (2017). Study of rate dependent behavior of glass/epoxy composites with nanofillers using non-contact strain measurement. *International Journal of Impact Engineering*, 110, 324–337. <https://doi.org/10.1016/j.ijimpeng.2017.05.013>
- Hamouda, A. M. S., & Hashmi, M. S. J. (1998). Testing of composite materials at high rates of strain: Advances and challenges. *Journal of Materials Processing Technology*, 300, 327–336. [https://doi.org/10.1016/s0924-0136\(97\)00436-6](https://doi.org/10.1016/s0924-0136(97)00436-6)
- Haque, A., Shamsuzzoha, M., Hussain, F., & Dean, D. (2003). S2-glass/epoxy polymer nanocomposites: Manufacturing, structures, thermal and mechanical properties. *Journal of Composite Materials*, 37, 1821–1837. <https://doi.org/10.1177/002199803035186>
- Harding, J., & Welsh, L. M. (1983). A tensile testing technique for fibre-reinforced composites at impact rates of strain. *Journal of Materials Science*, 18, 1810–1826. <https://doi.org/10.1007/BF00542078>
- Hayes, S. V., & Adams, D. F. (1982). Rate sensitive tensile impact properties of fully and partially loaded unidirectional composites. *Journal of Testing and Evaluation*, 10, 61–68. <https://doi.org/10.1520/jte10234j>
- Hsiao, H. M., & Daniel, I. M. (1998). Strain rate behavior of composite materials. *Composites Part B: Engineering*, 29, 521–533. [https://doi.org/10.1016/S1359-8368\(98\)00008-0](https://doi.org/10.1016/S1359-8368(98)00008-0)
- Jacob, G. C., Starbuck, J. M., Fellers, J. F., et al. (2004). Strain rate effects on the mechanical properties of polymer composite materials. *Journal of Applied Polymer Science*, 94, 296–301. <https://doi.org/10.1002/app.20901>
- Janeliukstis, R., & Chen, X. (2021). Review of digital image correlation application to large-scale composite structure testing. *Composite Structures*, 271, 114143. <https://doi.org/10.1016/j.compstruct.2021.114143>

- Kawata K, Hondo A, Hashimoto S, et al (1981) Dynamic behavior analysis of composite materials.
- Khan, S. U., Iqbal, K., Munir, A., & Kim, J. K. (2011). Quasi-static and impact fracture behaviors of CFRPs with nanoclay-filled epoxy matrix. *Composites Part A: Applied Science and Manufacturing*, 42, 253–264. <https://doi.org/10.1016/j.compositesa.2010.11.011>
- Kim, M., Park, T. Y., & Hong, S. (2021). Experimental determination of the plastic deformation and fracture behavior of polypropylene composites under various strain rates. *Polymer Testing*, 93, 107010. <https://doi.org/10.1016/j.polymertesting.2020.107010>
- Kornmann, X., Rees, M., Thomann, Y., et al. (2005). Epoxy-layered silicate nanocomposites as matrix in glass fibre-reinforced composites. *Composites Science and Technology*, 65, 2259–2268. <https://doi.org/10.1016/j.compscitech.2005.02.006>
- Kotal, M., & Bhowmick, A. K. (2015). Polymer nanocomposites from modified clays: Recent advances and challenges. *Progress in Polymer Science*, 51, 127–187.
- Lam, C. K., Cheung, H. Y., Lau, K. T., et al. (2005). Cluster size effect in hardness of nanoclay/epoxy composites. *Composites Part B: Engineering*, 36, 263–269. <https://doi.org/10.1016/j.compositesb.2004.09.006>
- Li, G., & Liu, D. (2015). Low strain rate testing based on drop weight impact tester. *Experimental Techniques*, 39, 30–35. <https://doi.org/10.1111/j.1747-1567.2012.00862.x>
- Lifshitz, J. M. (1976). Impact strength of angle ply fiber reinforced materials. *Journal of Composite Materials*, 10, 92–101. <https://doi.org/10.1177/002199837601000108>
- Lifshitz, J. M., & Rotem, A. (1972). Longitudinal tensile failure of unidirectional fibrous composites. *Journal of Materials Science*, 7, 861–869. <https://doi.org/10.1007/BF00550433>
- Lin, L.-Y., Lee, J.-H., Hong, C.-E., et al. (2006). Preparation and characterization of layered silicate/glass fiber/epoxy hybrid nanocomposites via vacuum-assisted resin transfer molding (VARTM). *Composites Science and Technology*, 66, 2116–2125. <https://doi.org/10.1016/j.compscitech.2005.12.025>
- Liu, W., Hoa, S. V., & Pugh, M. (2005). Organoclay-modified high performance epoxy nanocomposites. *Composites Science and Technology*, 65, 307–316. <https://doi.org/10.1016/j.compscitech.2004.07.012>
- Majzoobi, G. H., Barton, D C, & Ramezani, M. (2007). Stress wave effects in the flying edge high strain rate tensile testing device. *The Journal of Strain Analysis for Engineering Design*, 42, 507–516. <https://doi.org/10.1243/03093247JSA289>
- Majzoobi, G. H., Saniee, F. F., & Bahrami, M. (2005). A tensile impact apparatus for characterization of fibrous composites at high strain rates. *Journal of Materials Processing Technology*, 162–163, 76–82. <https://doi.org/10.1016/j.jmatprotec.2005.02.182>
- Mohd Nurazzi, N., Asyraf, M. R. M., Khalina, A., et al. (2021). Fabrication, functionalization, and application of carbon nanotube-reinforced polymer composite: An overview. *Polymers*, 13, 1047. <https://doi.org/10.3390/polym13071047>
- Naresh, K., Shankar, K., Velmurugan, R., & Gupta, N. K. (2020). High strain rate studies for different laminate configurations of bi-directional glass/epoxy and carbon/epoxy composites using DIC. *Structure*, 27, 2451–2465. <https://doi.org/10.1016/j.istruc.2020.05.022>
- Nurazzi, N. M., Asyraf, M. R. M., Khalina, A., et al. (2021). A review on natural fiber reinforced polymer composite for bullet proof and ballistic applications. *Polymers*, 13, 646. <https://doi.org/10.3390/polym13040646>
- Ochola, R. O., Marcus, K., Nurick, G. N., & Franz, T. (2004). Mechanical behaviour of glass and carbon fibre reinforced composites at varying strain rates. *Composite Structures*, 63, 455–467. [https://doi.org/10.1016/S0263-8223\(03\)00194-6](https://doi.org/10.1016/S0263-8223(03)00194-6)
- Okoli, O. I. (2001). The effects of strain rate and failure modes on the failure energy of fibre reinforced composites. *Composite Structures*, 54, 299–303. [https://doi.org/10.1016/S0263-8223\(01\)00101-5](https://doi.org/10.1016/S0263-8223(01)00101-5)
- Okoli, O. I., & Smith, G. F. (2000). High strain rate characterization of a glass/epoxy composite. *Journal of Composites Technology and Research*, 22, 3–11. <https://doi.org/10.1520/ctr10619j>
- Omran, A. A. B., Mohammed, A. A. B. A., Sapuan, S. M., et al. (2021). Micro- and nanocellulose in polymer composite materials: A review. *Polymers*, 13, 231. <https://doi.org/10.3390/polym13020231>

- Pan, B. (2018). Digital image correlation for surface deformation measurement: Historical developments, recent advances and future goals. *Measurement Science and Technology*, 29, 082001. <https://doi.org/10.1088/1361-6501/aac55b>
- Pan, B., Qian, K., Xie, H., & Asundi, A. (2009). Two-dimensional digital image correlation for in-plane displacement and strain measurement: A review. *Measurement Science and Technology*, 20, 062001. <https://doi.org/10.1088/0957-0233/20/6/062001>
- Pardo, S., Baptiste, D., Décobert, F., et al. (2002). Tensile dynamic behaviour of a quasi-unidirectional E-glass/polyester composite. *Composites Science and Technology*, 62, 579–584. [https://doi.org/10.1016/S0266-3538\(01\)00152-X](https://doi.org/10.1016/S0266-3538(01)00152-X)
- Pavlidou, S., & Papaspyrides, C. D. (2008). A review on polymer-layered silicate nanocomposites. *Progress in Polymer Science (Oxford)*, 33, 1119–1198.
- Perogamvros, N., Mitropoulos, T., & Lampeas, G. (2016). Drop tower adaptation for medium strain rate tensile testing. *Experimental Mechanics*, 56, 419–436. <https://doi.org/10.1007/s11340-015-0112-3>
- Powell, L. A., Luecke, W. E., Merzkirch, M., et al. (2017). High strain rate mechanical characterization of carbon fiber reinforced polymer composites using digital image correlations. *SAE International Journal of Materials and Manufacturing*, 10, 138–146. <https://doi.org/10.4271/2017-01-0230>
- Qi, B., Zhang, Q. X., Bannister, M., & Mai, Y. W. (2006). Investigation of the mechanical properties of DGEBA-based epoxy resin with nanoclay additives. *Composite Structures*, 75, 514–519. <https://doi.org/10.1016/j.compstruct.2006.04.032>
- Quaresimin, M., & Varley, R. J. (2008). Understanding the effect of nano-modifier addition upon the properties of fibre reinforced laminates. *Composites Science and Technology*, 68, 718–726. <https://doi.org/10.1016/j.compscitech.2007.09.005>
- Raisch, S. R., & Möglinger, B. (2010). High rate tensile tests—Measuring equipment and evaluation. *Polymer Testing*, 29, 265–272. <https://doi.org/10.1016/j.polymertesting.2009.11.010>
- Ratna, D., Becker, O., Krishnamurthy, R., et al. (2003). Nanocomposites based on a combination of epoxy resin, hyperbranched epoxy and a layered silicate. *Polymer*, 44, 7449–7457. <https://doi.org/10.1016/j.polymer.2003.08.035>
- Roland, C. M., Twigg, J. N., Vu, Y., & Mott, P. H. (2007). High strain rate mechanical behavior of polyurea. *Polymer*, 48, 574–578. <https://doi.org/10.1016/j.polymer.2006.11.051>
- Sanusi, O. M., Benelfellah, A., & Aït Hocine, N. (2020). Clays and carbon nanotubes as hybrid nanofillers in thermoplastic-based nanocomposites—A review. *Applied Clay Science*, 185, 105408.
- Shadlou, S., Ahmadi-Moghadam, B., & Taheri, F. (2014). The effect of strain-rate on the tensile and compressive behavior of graphene reinforced epoxy/nanocomposites. *Materials & Designing*, 59, 439–447. <https://doi.org/10.1016/j.matdes.2014.03.020>
- Shi, Y., Kanny, K., & Jawahar, P. (2009). Hybrid Nanocomposites: Processing and Properties. *Advanced Composite Materials*, 18, 365–379. <https://doi.org/10.1163/156855109X434757>
- Shokrieh, M. M., & Omid, M. J. (2009). Tension behavior of unidirectional glass/epoxy composites under different strain rates. *Composite Structures*, 88, 595–601. <https://doi.org/10.1016/j.compstruct.2008.06.012>
- Staab, G. H., & Gilat, A. (1995). High strain rate response of angle-ply glass/epoxy laminates. *Journal of Composite Materials*, 29, 1308–1320. <https://doi.org/10.1177/002199839502901003>
- Suriani, M. J., Rapi, H. Z., Ilyas, R. A., et al. (2021). Delamination and manufacturing defects in natural fiber-reinforced hybrid composite: A review. *Polymers*, 13, 1323. <https://doi.org/10.3390/polym13081323>
- Tjong, S. C. (2006). Structural and mechanical properties of polymer nanocomposites. *Materials Science and Engineering R: Reports*, 53, 73–197.
- Velmurugan, R., & Mohan, T. P. (2004). Room temperature processing of epoxy-clay nanocomposites. *Journal of Materials Science*, 9, 7333–7339.
- Wang, L., Wang, K., Chen, L., et al. (2006). Preparation, morphology and thermal/mechanical properties of epoxy/nanoclay composite. *Composites Part A: Applied Science and Manufacturing*, 37, 1890–1896. <https://doi.org/10.1016/j.compositesa.2005.12.020>

- Welsh, L. M., & Harding, J. (1985). *Dynamic tensile response of unidirectionally-reinforced carbon epoxy and glass epoxy composites* (pp. 1517–1531). Metallurgical Soc Inc.
- Weng, F., Fang, Y., Ren, M., et al. (2021). Effect of high strain rate on shear properties of carbon fiber reinforced composites. *Composites Science and Technology*, 203. <https://doi.org/10.1016/j.compscitech.2020.108599>
- Wu, C. L., Zhang, M. Q., Rong, M. Z., & Friedrich, K. (2002). Tensile performance improvement of low nanoparticles filled-polypropylene composites. *Composites Science and Technology*, 62, 1327–1340. [https://doi.org/10.1016/S0266-3538\(02\)00079-9](https://doi.org/10.1016/S0266-3538(02)00079-9)
- Xiao, X. (2008). Dynamic tensile testing of plastic materials. *Polymer Testing*, 27, 164–178. <https://doi.org/10.1016/j.polymertesting.2007.09.010>
- Yasmin, A., Abot, J. L., & Daniel, I. M. (2003). Processing of clay/epoxy nanocomposites by shear mixing. *Scripta Materialia*, 49, 81–86. [https://doi.org/10.1016/S1359-6462\(03\)00173-8](https://doi.org/10.1016/S1359-6462(03)00173-8)
- Yasmin, A., Luo, J. J., Abot, J. L., & Daniel, I. M. (2006). Mechanical and thermal behavior of clay/epoxy nanocomposites. *Composites Science and Technology*, 66, 2415–2422. <https://doi.org/10.1016/j.compscitech.2006.03.011>
- Zainuddin, S., Hosur, M. V., Zhou, Y., et al. (2010). Experimental and numerical investigations on flexural and thermal properties of nanoclay–epoxy nanocomposites. *Materials Science and Engineering: A*, 527, 7920–7926. <https://doi.org/10.1016/j.msea.2010.08.078>
- Zebarjad, S. M., & Sajjadi, S. A. (2008). On the strain rate sensitivity of HDPE/CaCO₃ nanocomposites. *Materials Science and Engineering A*, 475, 365–367. <https://doi.org/10.1016/j.msea.2007.05.008>
- Zhou, Y., Pervin, F., Biswas, M. A., et al. (2006). Fabrication and characterization of montmorillonite clay-filled SC-15 epoxy. *Materials Letters*, 60, 869–873. <https://doi.org/10.1016/j.matlet.2005.10.042>

Chapter 4

Design Methodologies for Composite Structures in Aircraft Engines



Prakash Jadhav

1 Introduction

Fiber-reinforced composites are well known for their specific strength and specific stiffness properties. Due to these important properties, the composites are always the most sought-after material in the field of aerospace engineering. As far as the aircraft engine is concerned, there were practical difficulties which were preventing the manufacturers to implement the use of composites in the engine for a long time. Eventually however, due to innovation in toughened resins, it was possible to make strong and stiffer fiber-reinforced composites and hence the manufacturers started incorporating the composites into the aeroengines. As far as the low-temperature region of the engine is concerned, the manufacturers are already able to introduce composite components in it now like fan blade, fan platform, and the low-pressure compressor blades, which resulted in the huge weight savings. It also in turn resulted in overall cost savings. Figure 4.1 shows the general aircraft engine cross section where you can identify the region where composite components are being introduced, i.e. fan and low-pressure compressor. The fan sucks in huge amount of air, part of which is compressed through the low-pressure compressor and followed by high-pressure compressor. Compressed air is burnt in combustion chamber and then exhaust gases are thrown out of the nozzle once it passes through the turbines. The fan allows part of the air that is sucked in to pass through the bypass ducts to create more thrust. Figure 4.2 shows the big composite fan blade by the manufacturer GE Ltd., which is located right at the frontal face of the engine. As shown in Fig. 4.2, the blade is made of carbon epoxy material and the leading edge is covered by a titanium metal cap to protect it. The aerodynamic shape of the blade helps increase the efficiency. This blade has been in use for the last 20 years. Figure 4.3 shows the

P. Jadhav (✉)

Mechanical Engineering Department, SRM University AP, Guntur, Andhra Pradesh, India

e-mail: Prakash.j@srmmap.edu.in

© The Author(s), under exclusive license to Springer Nature Switzerland AG 2022

N. Mazlan et al. (eds.), *Advanced Composites in Aerospace Engineering*

Applications, https://doi.org/10.1007/978-3-030-88192-4_4

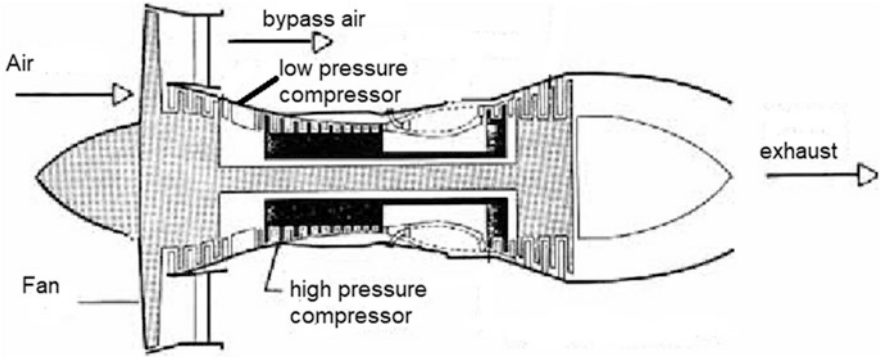


Fig. 4.1 Aircraft section view showing low-pressure compressor and fan region

Fig. 4.2 Composite fan blade



composite fan platform developed by engine manufacturers. This is a part which holds the fan blade and connects it to the rotating hub of the central shaft of the engine. This is also made using the carbon composite material. Figure 4.4 shows the composite compressor blade developed by the engine manufacturers to be used in the low-pressure compressor area of the engine. The compressor blade is also called as booster blade as it helps boost the pressure of the inlet air. Most of these components are made of carbon fiber-toughened epoxy composites due to high strength and high stiffness requirements.

Although basic innovation was already done and implemented for composite fan blade by manufacturers before 2000, there are a few researchers who worked on the improvement of composite components in the aircraft engine. Composite



Fig. 4.3 Composite fan platform

Fig. 4.4 Composite compressor blade



compressor blades were evaluated for the vibration criteria, and it was shown that they can meet the criteria successfully (Wollmann et al., 2017). The effect of stacking sequence in the composite fan blade was studied and it was found that the 0/45/0/-45 ply layup shows the least chance of failure through simulation results, i.e. margins to failure plots (Xiao et al., 2017). Structural design and analysis procedures that are followed by the manufacturers recently are also discussed and presented (Amoo, 2013). One such attempt discusses the use of sandwich composite fan blade replacing the metal blade, and by doing that 72% weight saving was demonstrated without affecting the mechanical performance (Coroneos & Gorla, 2012).

A NASA study indicates that ply-by-ply composite blade for aeroengines can be built, and it is proved through the simulation that it will sustain the loading successfully (Abumeri et al., 2004). Enhanced numerical simulation capability was demonstrated through the advanced bird strike analysis of composite blades and deformation/damage characterization methodologies were developed (Nishikawa et al., 2011). It was a big challenge to redesign these engine components with composite materials and to prove the feasibility of it for the stress, frequency, and other bird strike requirements. Some researcher teams have worked for many years on incorporating the composite components in aircraft engine (Scott Finn et al., 2009, Scott Finn et al., 2010). While working on these improvement ideas, a method was devised to design lab-level coupons with the proposed improvement feature built inside the coupon and apply appropriate loads and boundary conditions to it. These coupon models were built in the finite element code with parametric abilities so that multiple trials were conducted and analyzed. Based on the results, promising coupon candidates were shortlisted and recommended for further experimental evaluation. Promising coupon designs were then fabricated and tested under appropriate boundary condition. Based on experimental results and earlier modeling results, further shortlisting of designs was done and the improvement features under consideration were implemented on actual blade for further testing and evaluation. This was the broader philosophy that was used here for the most improvement ideas with minor changes in case-to-case basis. All those improvement ideas and the efforts to prove them are described below. Please note that this is an industry work and there is no precedence of it in the literature, nor did any prior publications related to it except the few patents and publications (Jadhav et al., 2015; Jadhav, 2020a, b; Jadhav, 2021a, b, c; Jadhav-Yella, 2021, Shim et al., 2012).

2 Composite Fan Blade

Many ideas on the improvement of current carbon composite fan blade design for the purpose of higher aero-efficiency or lesser weight or any other improvements are presented here. One by one, all these ideas and the way they are proved to be feasible are described below. The main design criteria for the composite fan blade are of course the survival or damage tolerance under bird strike loading. For all the studies here, carbon fiber epoxy composite prepreg material (IM7-8551) is used and specimens were made using hand layup with autoclave curing process. The layups mostly consist of 0 and 45° oriented fibers.

2.1 Ply Drop Design in Fan Blade

In order to study the effect of the presence of single ply drop or multiple ply drops inside the composite fan blade, various designs of coupons were made based on layups or ply drop locations (Jadhav et al., 2015; Jadhav, 2020a, b). They were

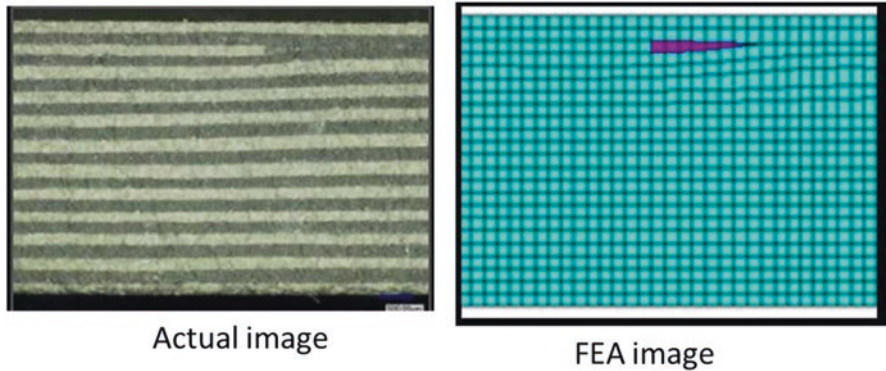


Fig. 4.5 Real coupon with a ply drop and FEA model of the same coupon

tested in different boundary conditions like flexure or four-point bend test for assessing the behavior of ply drop(s) under tensile or compressive loading, interlaminar shear test to assess the behavior of ply drop(s) under interlaminar shear loading, and finally multiple ply drop location study using cantilever test. The issue here is it is suspected that the blades fail in delamination mode under bird strike and the reason could be crack initiation due to delamination at the ply drop locations (Jadhav, 2020a, b). Figure 4.5 shows one design of coupon with single ply drop located near the surface of the specimen and the same thing duplicated in a FEA model. Based on the modeling results and test results of similar coupons (with and without ply drop), strain allowable is extracted from the data which are shown in Table 4.1. It shows the comparative strain levels at which every coupon fails, normalizing the strain level to the one in baseline coupon without ply drop. It shows how coupons fail early due to the presence of single or multiple ply drops for different cases as compared to the coupons without any ply drop (in some cases the difference in failure strain is as high as 17% as seen in Table 4.1). In the case of the multiple ply drop coupons, they were built inside the coupons near the surface so that under cantilever type of boundary condition, top and bottom surfaces and the ply drops nearby are subjected to tensile or compressive stresses. Multiple ply drops have a tendency to allow jumping of the crack from one ply drop to another and in turn helping the delamination (Fig. 4.6).

2.2 Embedded Foam Inserts in Fan Blade

In order to reduce the weight of the fan blades, it was proposed to introduce the lightweight foam insert to be embedded inside the solid carbon composite blade (like an embedded pocket) (Jadhav, 2020a, b; Ashely et al. 2016). As usual, various coupons were designed, modeled, analyzed, fabricated, and tested in staggered four-point bend boundary condition as shown in Fig. 4.7. As shown in the figure,

Table 4.1 Strain allowable for the presence of ply drops

Coupon case	Test configuration	Failure mode	Strain allowable (normalized)
Baseline without ply drop	Short beam shear	Interlaminar shear	1%
Baseline without ply drop	4-point bend	Compressive fiber breakage	1%
Single ply drop	Short beam shear	Interlaminar shear	0.94%
Single ply drop	4-point bend	ILS + compressive fiber breakage	0.94%
Multiple ply drop fiber direction transverse to length	Cantilever	ILS	0.83%
Multiple ply drop-fiber direction parallel to length	Cantilever	ILS	0.95%

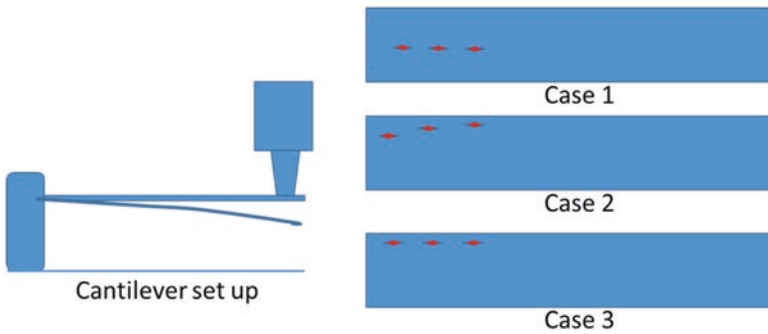


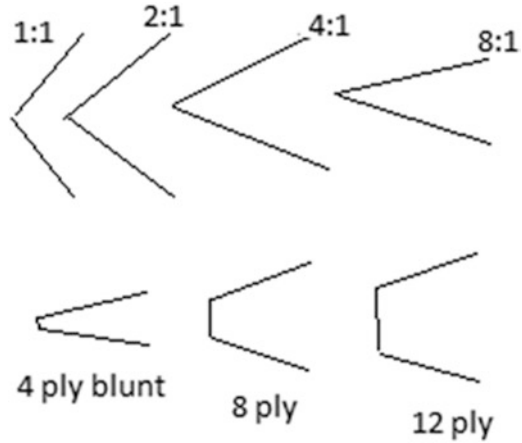
Fig. 4.6 Cantilever type of tests to see the effect of ply drop locations



Fig. 4.7 Coupon test set up with embedded foam insert

foam insert ends up having two sharp edges at the two ends which are the probable locations for stress concentration inside the coupons, and hence foam tip designs need to be altered as shown in Fig. 4.8. The tapering slope of the tip of the foam inserts is changed and analyzed in four different ways as shown (1:1, 2:1, 4:1, 8:1). The flat blunting level of the tip is changed and analyzed in three more ways as shown (4 ply, 8 ply, and 12 ply). Here blunting the tip means, instead of having tapered sharp corner at the end, the composite plies are arranged in such a way that

Fig. 4.8 Foam tip—possible designs



they end up together at the corner resulting in a blunted corner (blunting level changes with number of plies ending together). When the effect of one parameter is studied, others were kept constant. Statistical analysis was also performed by setting up DOE to study the inter-parameter effects.

Figure 4.9 shows the result summary of all the possible foam insert design cases, while monitoring the interlaminar shear stress level near the tip of foam in each design. As can be seen, there are some promising cases where interlaminar shear stress level goes down to a great extent. As the interlaminar stress levels are low, there is a lesser possibility of crack originating at the tip locations, and hence these geometries/designs are recommended to be used when the lightweight foam inserts need to be designed/incorporated in the carbon composite fan blade.

2.3 *Passive Morphing in Fan Blade*

As the composite fan blades are subjected to the different level of loading cases like takeoff, cruise, or landing, the efficiency requirements are different at different times. At takeoff, the fan needs to rotate at higher rpm and generate more thrust as compared to the cruise condition where thrust requirement is lower. Aerodynamic shape of the blade has to be changed in order to efficiently generate enough thrust. In order to achieve the different efficiency requirements at different situations, it is proposed here to design a composite fan blade with asymmetric layup which will allow the fan blade to change its shape at different loading levels to achieve the desired efficiency (Jadhav, 2021a; Shim et al., 2013; Kray et al., 2013). This is based on the fact that the cured composites with asymmetric layups can twist and warp on application of loading. As shown in Fig. 4.10, the target change in deviation angle of blade (camber) with respect to its original position due to in-built asymmetric layup and change in loading condition is 10° . This 10° requirement is

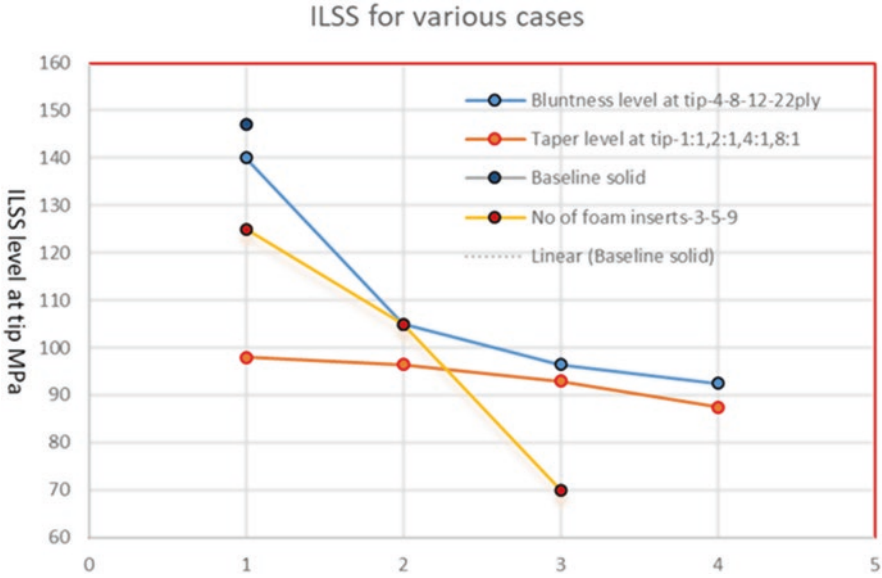


Fig. 4.9 Result summary of different foam insert analysis cases

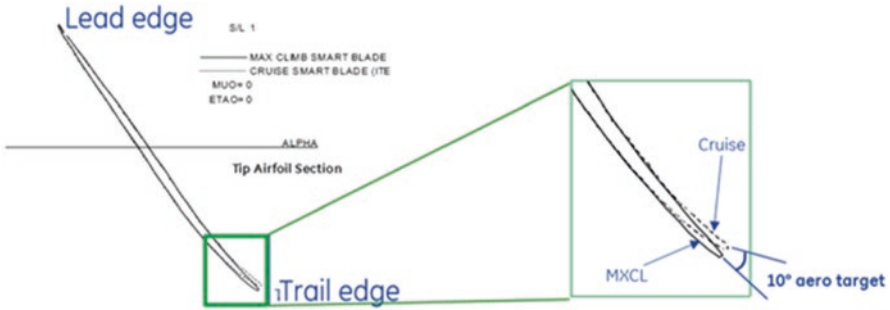


Fig. 4.10 Camber change—allowable change in angle

computed by back-calculating the changes required in chordwise blade shape for different thrust requirements like takeoff or cruise. Figure 4.11 shows the ABD matrix of the laminated composite in which the highlighted coupling coefficients need to be maximized to provide for more twist and warp. A code was written in MATLAB and optimization routine was executed to find out layups which will generate maximum coupling coefficients. Using these layups, panel level and blade models were studied in FEA to find out the amount of camber they generate.

As can be seen in Table 4.2, panel-level entitlement of camber seems like about 4° max. Using these optimized layups, blade-level analysis was run. As the blade thickness is higher and also it varies along the chord and span, the actual entitlement of the camber is much less, like in the range of 0.85° which does not provide the

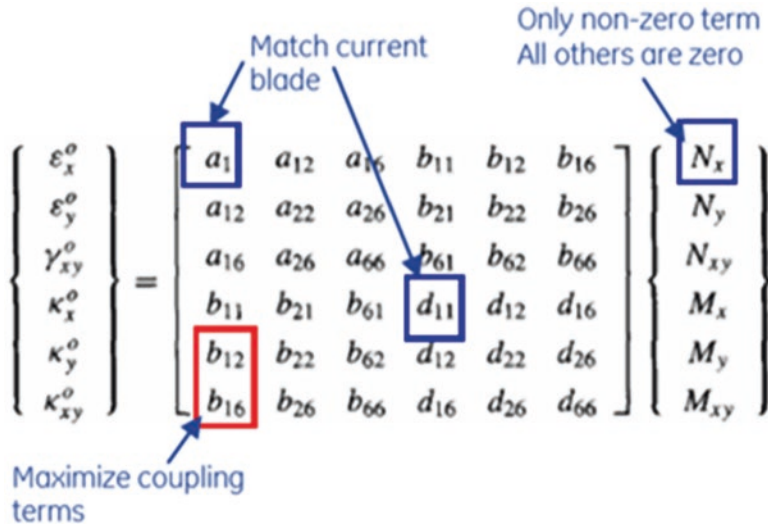


Fig. 4.11 Optimization of the coupling coefficients

Table 4.2 Amount of camber for different optimized layups in composite panel

Layup	Coupling coefficient optimized	Avg camber angle (°)		$\Delta\theta$
		$N_x = 19 \text{ N/mm}$	$N_x = 24 \text{ N/mm}$	
[30,-30, 0,45,0,90]	$\uparrow b_{12} \downarrow b_{16} \downarrow b_{11}$	3.43	4.51	1.08
[-45,30,-45,45,-45,-30]	$\uparrow b_{12} \uparrow b_{16} \downarrow b_{11}$	1.66	2.16	0.52
[-45,30,-45,45,-45,-30]	$\uparrow b_{12} \uparrow b_{16} \downarrow b_{11}$ (other tip)	6.29	8.28	1.99
[-30,45,-45,45,90,30]	$\uparrow(b_{12} + (-b_{16})), \downarrow b_{11}$	12.7	16.59	3.89
[-30,-45,45,30,90,0]	$\uparrow(b_{12} + (-b_{16}) + b_{11})$	8.2	10.76	2.56
[-30,-45,45,90,45,90]	$\uparrow(b_{12} + (-b_{16}) + b_{11})$	13.02	17.05	4.03

required amount of change in the shape of the blade to have a significant effect of efficiency. However, active excitation idea like using the embedded piezoceramic layers inside the carbon composite blade does give higher amount of camber (Kray et al., 2013), and hence, it is recommended to be used for this purpose. An issue in using the active morphing technologies is the realistic difficulty to embed the excitation mechanical elements inside the solid composite blade which may weaken the blades by creating the hot spots to promote the delamination.

2.4 Fan Blade with Wavy Edges

To increase the aero-efficiency of the composite fan blades, it is proposed to use the wavy edge shape on the trailing edge of the fan blades (Jadhav, 2021b). However, the wavy edges create big notch-shaped cutouts on the trailing edge and its effect on

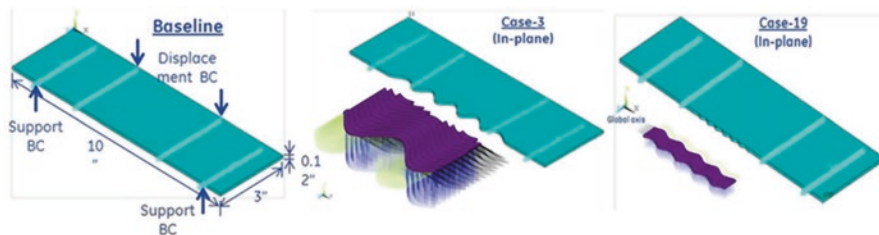


Fig. 4.12 Plate-level models with embedded wavy edge mimicking the trailing edge

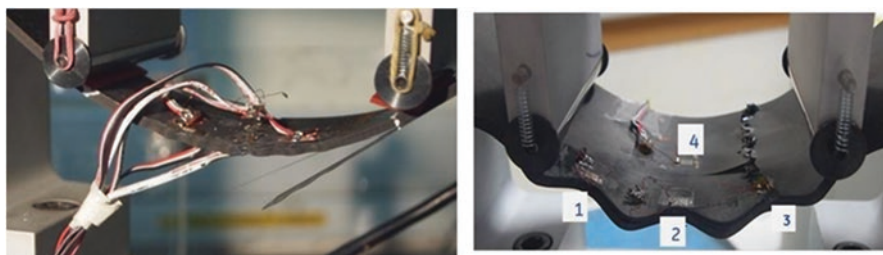


Fig. 4.13 Plate-level testing under flexure conditions to study the effect of notches

structural behavior needs to be studied. Various wavy shape geometries were incorporated on the edges of plate models in FEA as well as plate-level coupons (Figs. 4.12 and 4.13). Figure 4.12 shows three coupons, one baseline with flat edges, the other with a typical wavy feature design incorporated on one edge, and the third with another wavy feature incorporated on one edge. Overall length, width, and thickness of all coupons are the same. Figure 4.13 shows one of the coupons (with wavy feature on one edge) being tested in four-point bend boundary condition. It shows strain gauge locations and also the fiber breakage on compression side and delamination type of failure on tension side. The coupons with wavy notches were fabricated using hand layup/autoclave and tested under four-point bend conditions to study the strain level near the notch tips. The test and FEA results help understand the notch effect, and using these results, characteristic distance “a” is computed as shown in Table 4.3 (distance from the bottom-most point of notch to the point where the stress level matches that of the plate without any notch). A characteristic distance “a” from the edge can be computed or obtained using some preliminary experimental test data for wavy edge and baseline flat edge specimens along with FEA analysis of similar coupons, and can be successfully used to predict the failure load for any new such designs with notched/wavy edges. This can really help reduce the efforts of modifying the blade designs, by eliminating most of the blade making and testing cost, and of course the savings in time.

Table 4.3 Characteristic distance which defines the typical notch geometry and its effect

Case	Distance in mm
Case 3	0.5
Case 19	0.4325
STE 15	0.425
STE 17	0.4325

Fig. 4.14 Typical compressor blade

3 Composite Compressor Blade

It is proposed here to replace the current metal compressor blade with the laminated carbon composite one to further reduce the weight of the compressor assembly (N.J. Kray et al., 2019; Jadhav, 2021c). The typical compressor blade is shown in Fig. 4.14. The main design criterion here for the compressor blades is the survival under the bird strike loading. The pieces of bird do enter through the gaps between frontal fan blades and then hit the compressor blade. Again here, the representative composite plates were designed and fabricated as per the desired layups and the geometry. These plates were tested under bird strike loading in a test center at the National Aerospace Lab, Bangalore. Similarly, the bird strike analysis was performed in the explicit dynamic FEA software LS-Dyna on similar plate models (as shown in Fig. 4.15). Figure 4.15 shows a cylindrical-shaped object (Eulerian bird) sliding over the plate as it is given the vertical and horizontal

Fig. 4.15 Typical plate-level bird strike analysis

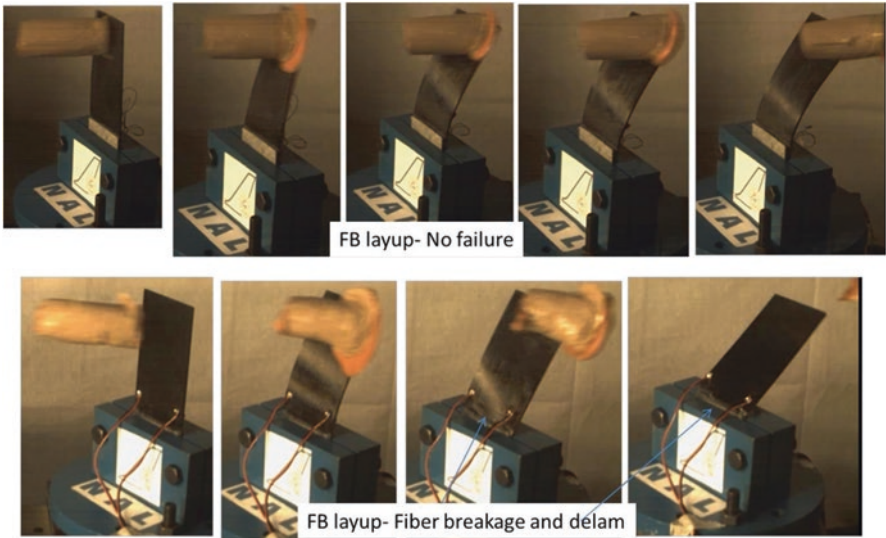
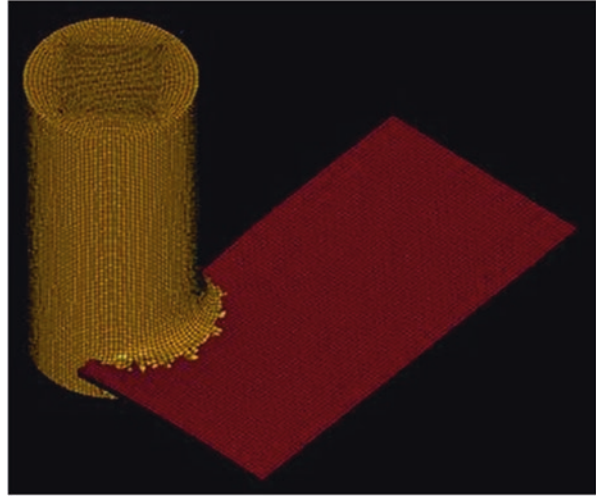


Fig. 4.16 Typical plate-level bird strike test

velocity input. Automatic node-to-surface contact was used with hourglass control settings. Bird elements undergo a huge amount of strain as they hit and slide over the composite plate before failing and disappearing. The typical response of the composite plate to the gelatin bird impact is shown in Fig. 4.16. The bird strike facility at the National Aerospace Lab was used and the gelatin birds were shot using a big pneumatic gun on a target (which is a composite plate fixed in a vice at some angle to the bird's traveling direction). As seen in the picture, the bird was

Table 4.4 Strain allowable for composite plate under bird strike

Bird velocity	FEA max longitudinal strain		FEA max interlaminar strain
	Tension	Compression	
65 m/s (no failure)	2.28	1.95	2.49
75 m/s (fiber breakage/delamination)	2.49	2.14	2.81
85 m/s (fiber breakage/delamination)	2.88	2.31	3.41
Strain allowable	2.4	2.0	>2.5

hit and then slides over the plate before getting thrown off elsewhere. The velocity at which the bird is impacting the composite plate is varied, and based on the experimental results and similar FEA results, the strain allowable is computed. Table 4.4 shows the strain allowable computation—tension, compression, and interlaminar shear strain allowable for the composite under consideration under bird strike loading. At around 75 m/s bird velocity, composite plate seems to fail in fiber breakage and/or delamination mode. Depending upon the angle which plate makes to the bird’s traveling direction or whether it’s a direct impact or offset impact (part of the bird outside the boundary of the plate), failure mode varies (fiber breakage or delamination). By going into FEA, the exact velocity and strain level at which composite fails can be obtained. The strain allowable for a particular composite layups and particular velocity/boundary condition can be used to design the composite compressor blade. It will reduce the bunch of testing efforts and time by using mostly FEA and few coupon tests only instead of expensive blade tests.

4 Composite Fan Platform

Designing a composite fan platform is comparatively easy, as it can be modeled as a solid geometry and the average properties of composites (smeared) can be assigned to the elements assuming that the platform behaves almost like an isotropic material. Initially it started with the use of chopped fiber composite for the platform and modeling its behavior using static structural analysis. Please note that here in this case, the loading is mostly static structural type and easy to analyze. Bird strike design criteria do not apply here as the bird is hitting only the fan blade, while the fan platform is near the hub and takes only the static mounting load. Although chopped fiber composite was meeting the static load design criteria, still after the development of 3D woven composites, the focus has shifted there. The 3D woven composites were tried out for this application using the FEA modeling, with average properties to be used as input. It served the purpose and this new composite material perfectly works fine for platform application.

5 Summary and Conclusion

The main objective of this work is to develop simple methodologies or techniques or procedures to design, develop, and incorporate the composite applications into the aircraft engine parts. As explained above, various methodologies were tried out here. The fundamental concept is to simplify the part into the testable coupon/plate shape and simplify the boundary condition into the testable configuration. While doing this, an extra care is taken so that the simplified boundary condition does mimic the actual boundary condition up to a reasonable extent. For achieving this, the simulation results of actual parts in FEA are used and part deflections/stress patterns under actual loads are studied. Even for bird strike cases, actual videos of part deflecting under real bird strike loads are studied, and based on that appropriate boundary conditions for test coupons are decided. There may be a question like, how can we relate the static coupon test results with dynamically loaded actual blade test results? Enough validation is done to prove this correlation. With appropriate boundary conditions and appropriate design of test coupons, a strong correlation was established between the coupon-level static test results and blade-level actual test results. Time and again this methodology was used and proved to be reasonably good enough to continue designing composite parts this way.

One thing to be noted here is that due to exceptionally odd part designs and loads/boundary conditions for the aircraft engine parts, the standard ASTM testing couldn't be used in many cases. As can be seen, for every particular part design and development case, a unique test setup was created and used for the coupon or subelement-level validation.

To summarize the work, various new design iterations were tried to either incorporate the use of composites into the aircraft engine parts or improve the design of existing composite parts. The strain allowable for the presence of single and multiple drops inside the existing composite fan blade is computed for the applicable load and boundary conditions using simple methods. New designs for the multiple ply drops were suggested to avoid the stress concentrations which may lead to delamination. Use of lightweight foam insert inside the existing composite fan blade is enabled by coming up with the appropriate design/geometry of the insert along with suggestions of suitable laminate layups near the insert tips. Morphing/shape changing capability of existing composite fan blade was evaluated using a simple technique, and it was demonstrated that passive morphing may not generate enough degree of morphing, but instead of that active morphing may work as expected. The effect of notches on the trailing edge of existing composite fan blades was computed using simple coupon failure criteria technique, and an easy way to predict the notch effect for various new designs was devised.

The use of composite compressor blade is evaluated using simple methodology under appropriate loads/boundary conditions and proved to be capable to be used in the aircraft engine. A simple subelement-level coupon testing with appropriate test setup can achieve the expected result. Strain allowable for a particular material and

a typical design of compressor blade was obtained. Finally, composite fan platform feasibility was proven using a simple subelement model analysis technique.

Based on the simple techniques developed, new ideas were proven and patents were filed. Some of the ideas were implemented into the products. The bottom line is that simple and effective methods can be developed to prove the feasibility of the use of the laminated composite parts in the aircraft engine.

Acknowledgments The author would like to thank all the teammates who directly or indirectly helped complete these projects.

References

- Abumeri, G. H., Kuguoglu, L. H., & Chamis, C. C. (2004). *Composite fan blade design for advanced engine concept*. NASA/TM-2004-212943.
- Amoo, L. M. (2013). On the design and structural analysis of jet engine fan blade structures. *Progress in Aerospace Science*, 60, 1–11.
- Ashely, S. R., Lin, W., Schilling, J., Shim, D. J., Gemeinhardt, G. C., & Prakash, K. J. (2016). *Hybrid turbine blade including multiple insert sections*. US Patent US 9309772B2.
- Coroneos, R. M., & Gorla, R. S. R. (2012). Structural analysis and optimization of a composite fan blade for future aircraft engine. *Int. J. Turbo Jet Engines*, 29(3), 131–164.
- Finn, S. R., Rengarajan, G., Crall, D. W., & Prentice, I. (2009). *Reinforced fan blade*. US patent no US7575417B2.
- Finn, S. R., Young, C. D., & Finnigan, P. M. (2010). *Fan containment casings and methods of manufacture*. US Patent, 7713021B2.
- Jadhav, P. (2020a). Effect of ply drop on aerospace composite structures. *Key Engineering Materials*, 847, 46–51.
- Jadhav, P. (2020b). Innovative designs of embedded foam inserts in aerospace composite structures. *Materials Today Proceedings*, 21(part 2), 1164–1168.
- Jadhav, P. (2021a). Passive morphing in aerospace composite structures. *Key Engineering Materials*, in press.
- Jadhav, P. (2021b). Failure criteria for composite blades with wavy edge in aerospace applications. *Lecture notes in mechanical engineering*. https://doi.org/10.1007/978-981-16-0673-1_9.
- Jadhav, P. (2021c). Feasibility of Composite Compressor Blade using Sub-element Level Bird Strike Tests and Analysis. *Lecture note in mechanical engineering*, in press.
- Jadhav, P., & Yella, G. L. (2021). Design and optimization of hybrid interface joint in a composite fan blade of aircraft engine. *IOP Material Science and Engineering*, 1126.
- Jadhav, P., Li, Z., et al. (2015). Ply drop in composite structures-evaluation of strain allowable. In *Proceedings of COMTEST Conference, IMDEA*, Spain.
- Kray, N. J., Prentice, I., Breeze-Stringfellow, A., Shim, D. J., & Gemeinhardt, G. C. (2013). *Embedded actuators in composite airfoils*. US Patent US 2013-0302168A1.
- Kray, N. J., Gemeinhardt, G. C., Jadhav, P., Klei, D. E., Nandula, P., & Subramanian, S. (2019). *Composite compressor blade and method of assembling*. US Patent 10247014 B2.
- Nishikawa, M., Hemmi, K., & Takeda, N. (2011). Finite element formulation for modeling composite plates subjected to soft body, high velocity impact for application to bird strike problem of composite fan blades. *Composite Structures*, 93, 1416–1423.
- Shim, D.-J., Finn, S., Kray, N. J., Karafillis, A. P., Hasting, W. H., & Hegeman, A. (2012). *Method and apparatus for a structural outlet guide vane*. US Patent US8177513B2.
- Shim, D.-J., Finn, S. R., Kray, N. J., Sinha, V. K., Jadhav, P. K., & Zheng, L. (2013). *Fan Blade*. US Patent US 2013/02875588A1.

- Wollmann, T., Modler, N., Dannemann, M., Langkamp, A., Nitschke, S., & Filippatos, A. (2017). Design and testing of composite compressor blades with focus on the vibration behavior, composite part A. *Applied Science and Manufacturing*, 92, 183–189.
- Xiao, J., Chen, Y., Zhu, Q., Lee, J., & Tingting, M. A. (2017). A general ply design for aero engine composite fan blade. In *Proceeding of ASME Turbo Expo Technical conference*. <https://doi.org/10.1115/GT2017-64377>.

Chapter 5

Machining Effects of Fibrous Composites and Related Stacks for Aerospace Applications



Jinyang Xu, J. Paulo Davim, and Ming Chen

1 Introduction

Over recent decades, the aerospace manufacturing sectors are seeking the use of lightweight materials to fabricate advanced aircraft structures favoring the energy saving and system improvement (Bonnet et al., 2015; Xu et al., 2016). This is motivated by the ecological requirements for minimizing the fuel consumption as well as for economic reasons like low operating costs, long maintenance cycles, and large ranges of aircraft with high passenger numbers (reduction of life-cycle cost) (Brinksmeier et al., 2011). Under such circumstances, fibrous composites emerge and significantly impact the material distribution in modern industries (Alsubari et al., 2021; Mohd Nurazzi et al., 2021; Nurazzi et al., 2021). Since the engineering materials possess unique mechanical/physical properties such as high specific strength/modulus, excellent corrosion and fatigue resistance, etc., they become very attractive for aerospace applications (Abrão et al., 2007; Liu et al., 2012; Amir et al., 2019; Geier et al., 2019).

Fibrous composites are characterized by the presence of the fiber-phase reinforcement impregnated with the matrix base, being the aerospace-grade materials extensively used in modern airplanes. They are often fabricated with polymer matrix, which can be either thermosetting polymers or thermoplastic polymers. The thermoset polymers have the property of becoming permanently hard and rigid when heated or cured, while the thermoplastic polymers entail the linear chain of the molecular structures, so they can be recycled and reused when heated (Ahmad et al., 2019; Xu et al., 2020a, b). The thermoplastic polymer shows a high sensitivity

J. Xu (✉) · M. Chen
School of Mechanical Engineering, Shanghai Jiao Tong University, Shanghai, China
e-mail: xujinyang@sjtu.edu.cn

J. P. Davim
Department of Mechanical Engineering, University of Aveiro, Aveiro, Portugal

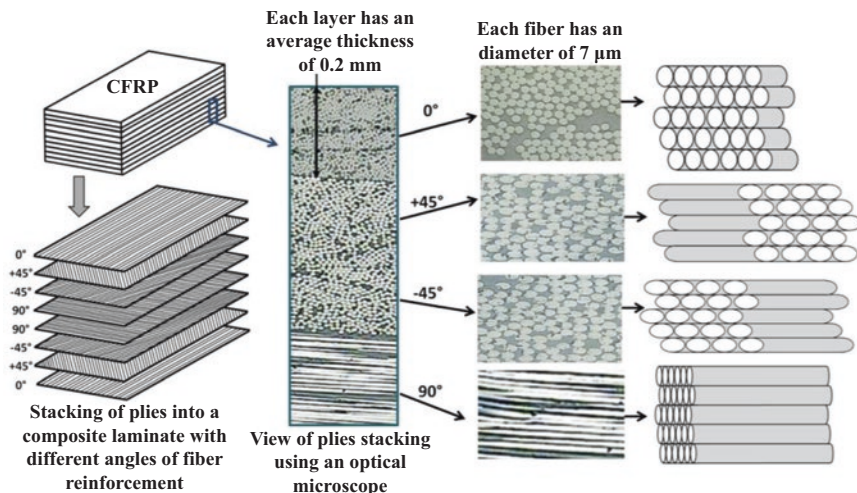


Fig. 5.1 An example of a multidirectional fibrous composite laminate. Reproduced with copyright permission from Mondelin et al. (2010)

to the process temperature and is prone to glass transition failure. With respect to the reinforcing fibers, they can be laid up in the matrix following several different configurations. Two typical examples are unidirectional tapes and fabric weaves. The difference between the two types of layup lies in the fact that there is only one fiber direction on the plane surface for the unidirectional tape, while for the fabric weave, the two fiber directions are cross-coupled and are perpendicular to each other, where the first direction is called the warp direction and the second direction is named the weft direction. Additionally, there is also the existence of multidirectional fiber-reinforced composites, such as the symmetric layup or the nonsymmetric layup composites. Both types of composites are made up of various fiber plies with different orientations. Figure 5.1 shows the typical layup of one multidirectional fibrous composite laminate fabricated following different fiber alignments (Mondelin et al., 2010). The composite laminate is shown to contain eight plies, and there is a symmetrical surface among the layers, so it is a quasi-isotropic fibrous composite.

In fibrous composites, the reinforcing fibers are often hard, stiff, and strongly dispersed in the composite with impregnated matrix base (Callister & Rethwisch, 2007; Aamir et al., 2019). Their main functions are to offer the main properties of the composite material and to withstand the applied loads, while the matrix base aims to act as a binder by surrounding the reinforcement, transfer the loads, and protect the fibers from damage (Xu et al., 2016). The matrix also provides ductility and prevents crack propagation from one fiber to another (Mallick, 2007). Therefore, fibers resist tension, the matrix opposes shear, and together, both act to resist compression, reflecting the overall properties of the composites (Callister & Rethwisch, 2007). Additionally, the composite properties are also determined by the fiber volume fraction, the fiber/matrix type, and the fiber orientation configuration. Since the

reinforcing fibers and the matrix base exhibit different levels of properties, the fibrous composites are generally heterogeneous in architecture. Moreover, fiber orientation is also a critical factor making the fibrous composite show an anisotropic behavior. For instance, the material yields the highest properties (e.g., the strength, stiffness) along the fiber orientation direction but shows the lowest properties toward the transverse direction. Such fiber-orientation-dependent behaviors guarantee the excellent designability and applicability of the composite material.

Moreover, fibrous composites can be used in conjunction with metallic alloys such as titanium or aluminum alloys to form hybrid composite structures in order to obtain enhanced properties and improved functionalities (Xu & El Mansori, 2016a; Xu et al., 2016, 2019a). As such, these materials are taking a prominent position in modern aerospace applications. For instance, carbon fiber-reinforced polymer (CFRP) composites are often employed in the aircraft wing boxes, horizontal and vertical stabilizers, and wing panels (Soutis, 2005). Glass fiber-reinforced polymer (GFRP) composites are mainly used in the fairings, storage room doors, landing gear doors, and passenger compartments (Gay et al., 2003; Soutis, 2005). Fiber metal laminates (FMLs) are applied in the wing structures and fuselages (Sinmazçelik et al., 2011; Liu et al., 2012). Figures 5.2 and 5.3 show the material distribution in the new-generation Boeing 787 Dreamliner and the Airbus A380 airplane, respectively. The composites and related stacks have occupied over 50% of all the materials used in the Boeing 787 Dreamliner. Moreover, fibrous composites like CFRPs have been applied in various types of load-carrying components in the Airbus A380 such as outer flaps, flap track panels, floor beams for upper deck, etc.

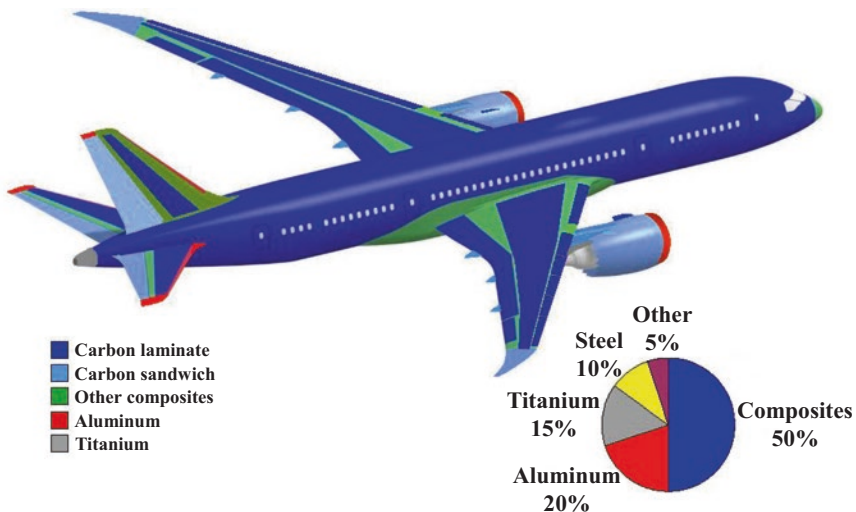


Fig. 5.2 The material distribution of the Boeing 787 Dreamliner. Reproduced with copyright permission from The Boeing Company

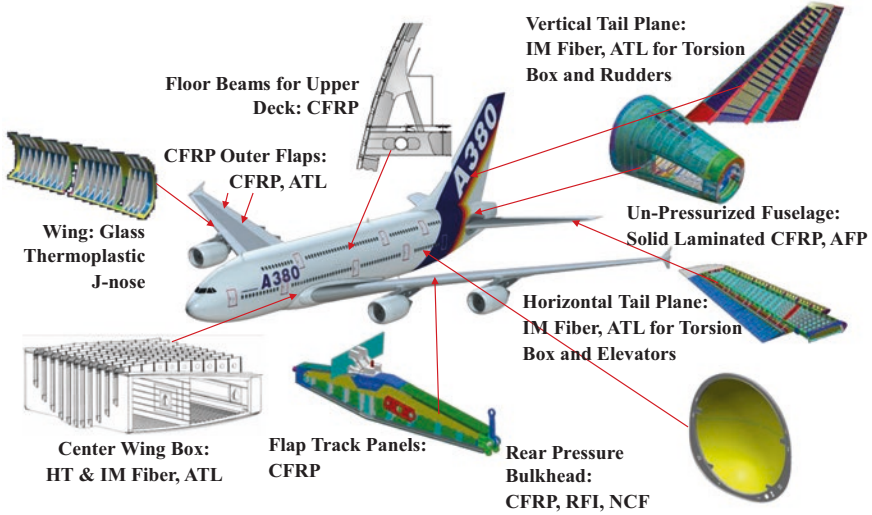


Fig. 5.3 The material distribution of the Airbus A380 airplane. Reproduced with copyright permission from The Airbus Company

Even though the fibrous composites and their related stacks obtain widespread applications, secondary manufacturing operations such as trimming, milling, and drilling are still required to produce desired dimensional accuracy and qualified surface quality before the final aircraft applications. However, machining of fibrous composites and their related stacks is very challenging compared with the cutting of conventional isotropic materials such as metals and steels (Xu et al., 2019a, 2021). The event is firmly associated with the fiber-orientation-dependent machinability of the composite material, which results in the disparate removal modes in relation to the fiber layup. As such, it complicates the composite separation and brings difficulties in generating excellent surface morphologies. Particular issues are poor surface quality, leading to a large number of part rejections and rapid tool wear, resulting in high machining costs. For the surface quality attributes, interlaminar delamination is critical as it is irreparable and determines the final composite part acceptance (Hocheng & Tsao, 2003, 2005; Abrão et al., 2007). Additionally, some other quality-associated issues such as fiber pullouts, fiber splintering, resin loss, and surface cavities can be prevalent during the composite machining processes.

Moreover, rapid tool wear is another decisive challenge for the high-quality cutting of fibrous composites as the reinforcing fibers cause severe abrasions and erosions onto the tool surfaces because of their high hardness and high abrasiveness. To improve the composite machinability, it is essential to understand the cutting mechanisms of the materials. The present chapter attempts to address the cutting-associated issues for fibrous composites and to discuss their complexity behind the machining operations. It emphasizes the technical problems occurring when machining aerospace-grade composites and the corresponding possible solutions.

Aspects including the chip removal mechanisms, cutting forces, machining temperatures, surface quality, and wear modes were analyzed. Some perspectives regarding future developments in the research field of composites machining are outlined.

2 Chip Removal Mechanisms

The cutting mechanisms of fibrous composites are more complicated than those of conventional metallic alloys since the composite separation modes are fiber-orientation-dependent. Details of the chip removal process for each unidirectional fibrous composite having a specific fiber orientation are discussed in this subsection. Figure 5.4 shows the chip separation process for a 0° fiber-reinforced composite (Iliescu et al., 2010). In this case, the cutting direction is parallel to the fiber direction, and the machining configuration is orthogonal cutting. Since the tool rake angle equals zero, both the tool rake face and the tool tip attack the composite laminates simultaneously. Then the tool advancement causes compression stresses initiated at the interface of two adjacent layers, and consequently, microcracks are generated to separate the fiber plies. Additionally, the tool rake face causes a cantilever bending, which leads to the buckling of the 0° fibers, as well as the fiber cracking. Therefore, the material removal is initiated by the cantilever bending of fiber bundles ahead of the tool. Then the interfacial debonding occurs firstly, followed by the fiber fracture toward the cross section. When the cracks reach the fiber-free surfaces, or the stress reaches the ultimate fiber strength limit, fibers are broken from the tool rake face, resulting in the complete chip formation. Note that in the parallel cutting relation, the cut composite surfaces are very fine, containing very little damage or failure.

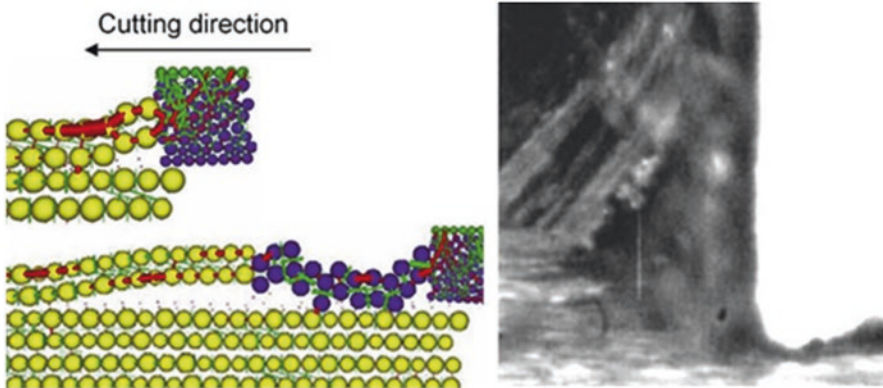


Fig. 5.4 Chip separation process in the orthogonal cutting of a 0° unidirectional fibrous composite. Reproduced with copyright permission from Iliescu et al. (2010)

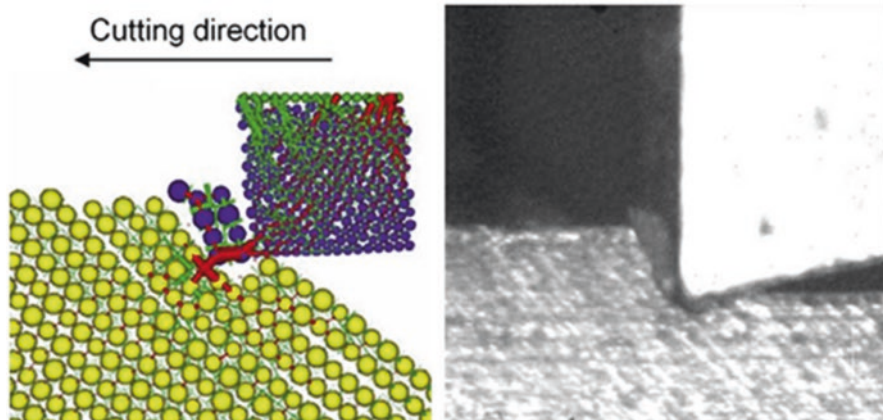


Fig. 5.5 Chip separation process in the orthogonal cutting of a 45° unidirectional fibrous composite. Reproduced with copyright permission from Iliescu et al. (2010)

Concerning the 45° unidirectional fibrous composite, the cutting relation shown in Fig. 5.5 can be considered as along the fiber direction (Iliescu et al., 2010). In this case, the fiber orientation angle is within $0\text{--}90^\circ$. Since the cutting tool has a 0° rake angle, both the tool tip and the tool rake face cut the composite material simultaneously. With the tool advancement, the tool rake face tends to bend the composite layers, causing the stress concentration at the tool tip region. Then microcracks initiate at the tool tip and develop quickly toward the fiber cross section. With the ongoing tool advancement, interlaminar cracking initiates along the fiber/matrix interface, leading to the debonding failure. Finally, when the crack reaches the fiber-free surface, chips are separated from the composite base. Note that for this type of fiber orientation, there are two procedures responsible for the fiber fracture. The first is the shear-induced fracture toward the fiber cross section, and the second is the interfacial debonding along the fiber/matrix interface leading to the complete chip separation. Consequently, the shear plane for the fiber separation is parallel to the fiber direction, producing the triangular chip shape as depicted in the right image of Fig. 5.5.

In terms of the 90° unidirectional fibrous composite, the cutting relation belongs to the vertical cutting configuration. The machining speed is perpendicular to the fiber direction, as shown in Fig. 5.6 (Iliescu et al., 2010). In this cutting relation, the tool-chip contact length depends on the tool rake angle. The tool rake face tends to cause high compression stresses inside the composite layers; then, microcracks are initiated across the fiber axis. When the cracks reach the fiber-free surfaces, the fibers fracture at the cross-sectional area. The interlaminar debonding also takes place with the tool advancement, and the fibers tend to separate toward the vertical fiber direction, resulting in complete chip removal. Additionally, the tool induces cantilever bending of the unidirectional fibers, causing certain degrees of fiber buckling damage. Moreover, since the cutting load is perpendicular to the fiber/matrix interface, the tool leads to severe interfacial debonding damage and interlaminar

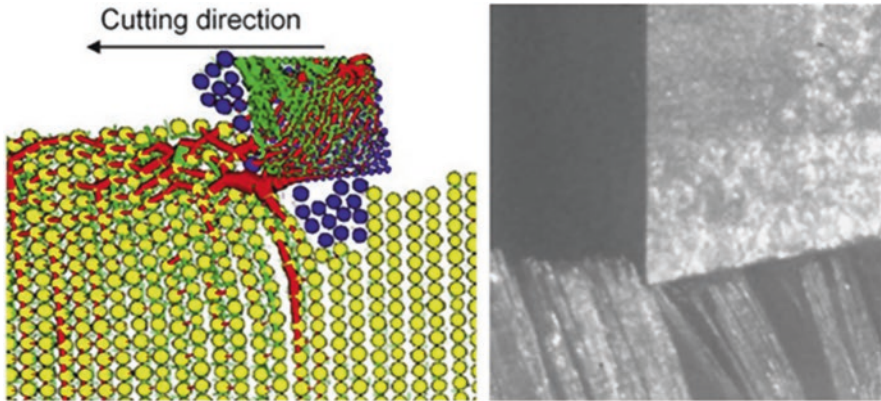


Fig. 5.6 Chip separation process in the orthogonal cutting of a 90° unidirectional fibrous composite. Reproduced with copyright permission from Iliescu et al. (2010)

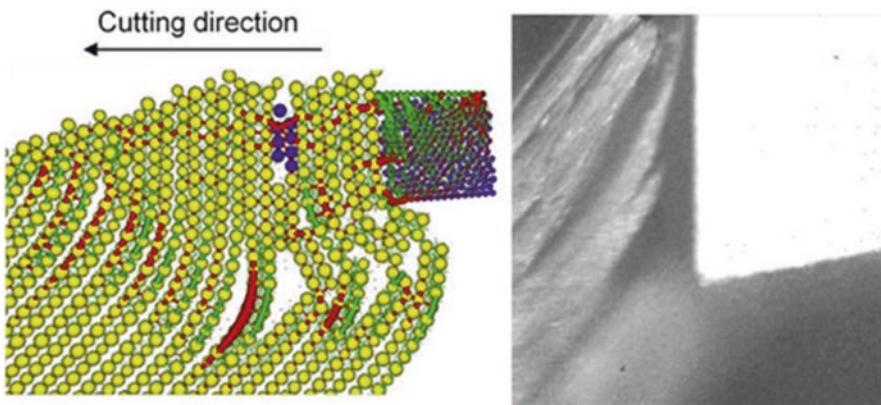


Fig. 5.7 Chip separation process in the orthogonal cutting of a 135° unidirectional fibrous composite. Reproduced with copyright permission from Iliescu et al. (2010)

delamination of the composite, particularly when the tool edge tends to cut off the laminate. The cut surface morphologies are very poor, containing a lot of defects or machining damage such as cracking, cavities, fiber pullouts, and splintering. Note that since the tool rake face has a larger contact area with the uncut fibers, it tends to result in much higher values of cutting forces. Moreover, since the vertical fibers are broken randomly on different cross-sectional surfaces, the cut surface morphologies of the 90° plies are much poorer compared with those gained along fiber cutting relations. Therefore, the vertical cutting relation should be avoided in order to guarantee better surface quality.

Finally, Fig. 5.7 shows the chip separation process of a 135° fibrous composite (Iliescu et al., 2010). In the against fiber cutting relation, the tool rake face firstly contacts the uncut fibers, causing bending stresses of the uncut fibers, resulting in

the shear stress occurring at the fiber cross section. This action causes the interlaminar delamination or interfacial debonding of the fiber/matrix system under the bending load. Many cracks inside the fiber/matrix interface are produced containing different damage depths. Severe interfacial cracking and debonding are found on the composites being cut off. These cracks are the consequences of the bending-induced shear stresses and the cantilever effects during the chip removal process. On the other hand, the tool tip attacks the fibers leading to the shear stress of the fibers. Therefore, if the shear and bending stresses caused by the tool rake face reach the ultimate fiber strength, fibers are separated with a lower root thickness. Otherwise, if the fibers fail when the shear stresses induced by the tool tip reach the ultimate fiber strength, the resected chips tend to have a larger root thickness. Therefore, under this condition, the machined surfaces are more inferior, containing various cutting-induced defects as the chips are separated with different root thicknesses. The interlaminar debonding becomes prevalent, leading to much deeper cracking of the composite subsurface.

For the composite-related stacks, the chip separation mode can be considered as a combination of both the brittle fracture and the elastoplastic deformation, which leads to the powdery and continuous chip formation. Previous studies have indicated that apart from the composite fiber orientation, the cutting sequence strategy also affects the cutting mechanisms for the hybrid composite structures (Xu & El Mansori, 2016b; Xu et al., 2016, 2019a, b). Generally, machining from the fibrous composite to the metallic alloy benefits the chip breakage of the stack material under the orthogonal cutting configuration (Xu & El Mansori, 2017; Xu et al., 2019a, b), while cutting from the metallic alloy to the composite favors the machinability improvement of the stacks under the drilling operations due to the avoided scratching effects of the chip ejection onto the composite hole walls (Xu & El Mansori, 2016a; Xu et al., 2019b).

3 Cutting Forces and Temperatures

Cutting forces/temperatures are critical physical phenomena produced at the tool-chip and tool-work interfaces following the chip removal of fibrous composites. They are the essential indexes to reflect the machinability grade of a composite material as they directly affect the quality of cut surfaces and the extent of tool wear. Due to the anisotropy of the composite materials, the cutting force magnitudes vary significantly depending on the used fiber cutting angle. Higher values of cutting forces are typically produced for fibrous composites when a higher obtuse fiber cutting angle is used (Bhatnagar et al., 1995; Wang et al., 1995; Wang & Zhang, 2003). Additionally, process parameters such as cutting speed, depth of cut, and feed rate also affect the variations of cutting forces for the aerospace-grade composites. In most cases, high cutting speeds, low depths of cut, as well as low feed rates are found to benefit the reduction of the composite machining forces (Ben Soussia et al., 2014). In terms of the drilling processes, the thrust force has an inherent

correlation with the drilling-induced delamination for the fibrous composites and their related stacks. It is believed that there is a critical thrust force (CTF) below which no delamination takes place (Hocheng & Tsao, 2005). Moreover, besides the cutting speed and the feed rate, tool geometries also influence the thrust forces when drilling fibrous composites. For instance, the modification of drill chisel edges, the decrease of drill point angles, as well as the use of functionally designed tool structures can reduce the drilling thrust values and consequently the drilling-induced delamination extents. This is evidenced by the widespread use of special drill bits such as multifaceted drills, step drills, candlestick drills, and core drills for the drilling of aerospace-grade composites to decrease the thrust forces and the delamination damage (Hocheng & Tsao, 2003).

With respect to the machining temperature, it also plays a decisive role in the machinability of fibrous composites and their related stacks. Typically, a high magnitude of machining temperatures signifies an increased risk of glass transition for the composite material. Since the glass transition is an irreparable failure and once it occurs, the composite properties are significantly degraded. The temperature values should be minimized as far as possible during the composite separation process. Even though the temperature magnitudes are often much lower than the glass transition temperature during the fibrous composite cutting, much higher temperature values can be promoted when machining metallic-composite stacks such as the CFRP/Ti6Al4V sandwiches (Xu et al., 2020d). This is due to the high cutting temperature produced in the metal cutting that transfers onto the composite phase resulting in the glass transition of the polymer matrix. The process parameters such as the cutting speed and the feed rate are widely confirmed as the key factors influencing the generation of machining temperatures. In general, low cutting speeds and high feed rates are found to favor the decrease of the drilling temperatures for fibrous composites. However, for the drilling of metallic-composite stacks, the cutting sequence strategy may also affect the development of the cutting temperature. To reduce the machining temperatures for fibrous composites and their related stacks, a careful section of cutting parameters and cutting sequences is of vital importance (Xu et al., 2019d, 2020d, 2021).

Since both the cutting forces and the machining temperatures are detrimental to the composite manufacturing processes, great endeavors should be made to optimize process parameters, design functional tools, as well as select reasonable cutting sequence strategies.

4 Surface Quality Characteristics

The surface quality is a comprehensive factor characterizing the overall conditions of cut workpiece surfaces. It is firmly associated with the coupling effects of chip removal modes and cutting conditions such as the machining environments, the cutting speed, the depth of cut, the feed rate, the tool-work system, etc. For the surface quality attributes, delamination is one of the most critical damages existing within

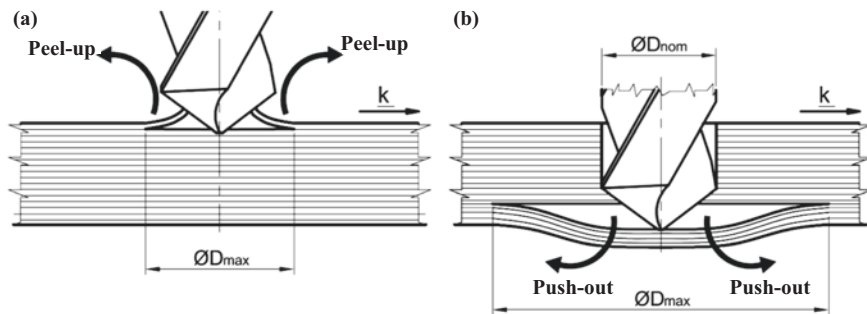


Fig. 5.8 Schematic illustrations of (a) the peel-up and (b) the push-out delamination modes. Reproduced with copyright permission from Geier et al. (2019)

the machined composite surfaces, which signifies the interlaminar debonding of neighboring fiber plies (Xu et al., 2018; Suriani et al., 2021). The delamination damage is a force-related failure that consists of two types of formation modes, as shown schematically in Fig. 5.8 (Geier et al., 2019). The first mode is the peel-up delamination which is caused by the cantilever effects of the drill edges as they come in contact with the composite plies firstly. The second mode is called the push-down delamination, which is induced by the thrust force acting onto the last plies of the fiber layers leading to the debonding failure. Since delamination damage is irreparable, it accounts for approximately 60% of all part rejections for fibrous composites (Davim et al., 2007; Davim, 2009). Therefore, delamination is the most critical damage mode that needs to be carefully controlled to improve the composite machinability.

Apart from the critical delamination damage, fiber pullouts, uncut fibers, uncut resin, and breakout are also critical issues for the surface quality attributes of fibrous composites. For instance, the fiber pullout or fiber splintering signifies the extrusion of fibers due to the non-effective cutting of fibers. This is very similar to the conditions of uncut fibers residing around a hole circumference. This type of defect may affect the dimensional accuracy of a cut fibrous composite surface. However, the defect can be eventually removed if a finish operation is carried out. Moreover, the damage of breakout signifies the undesired separation of the fibers or the matrix, which significantly affects the integrity of cut composite surfaces. Sometimes, this damage is a crucial reason for the formation of surface cavities due to the loss of matrix or fibers. Figure 5.9 shows the macroscopic images of a cut fibrous composite hole at the entrance side (Turki et al., 2014). The observations indicate that different types of machining-induced defects are promoted around the hole circumference after the drilling of fibrous composites such as spalling, uncut fibers, and irreparable delamination. The damage formation is firmly associated with the anisotropic machinability of fibrous composites. Herein, spalling is a term used to describe the process that occurs when flakes are separated from some type of larger body of material. In machining composites, the spalling is mainly caused by the excessive separation of the fibers or the matrix base, leaving the cavities onto the

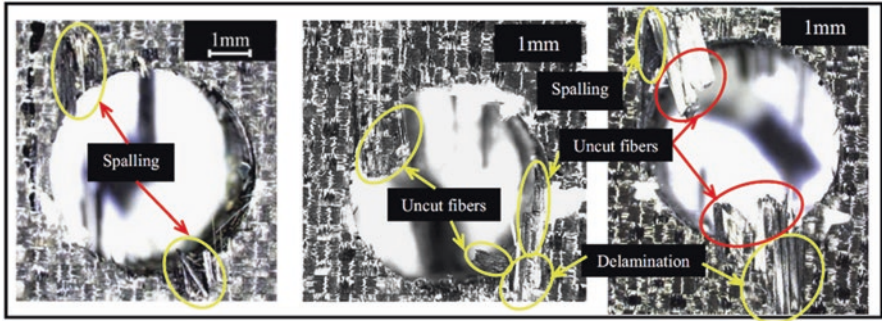


Fig. 5.9 Macroscopic observations of a cut fibrous composite hole at the entrance side. Reproduced with copyright permission from Turki et al. (2014)

composite surface. Uncut fibers are undesired material segments remaining onto the cut composite surface, which can be removed following a deburring operation. It is worth noting that the drilling-induced defects for fibrous composite holes often exhibit a symmetric distribution law along the hole circumference due to the fiber-orientation-dependent machinability of the composites (Xu et al., 2013, 2017; Turki et al., 2014, 2017). Moreover, most of the machining-associated defects are formed under the against fiber cutting relations owing to the poor chip separation process encountered when cutting a high-fiber angle-oriented composite.

Concerning the composite-related stacks (e.g., CFRP/Ti6Al4V sandwiches), the cut surfaces may include the damage promoted from both the metallic alloy and the interface, in addition to the composite phase defects (Xu et al., 2016, 2019b). In general, the hybrid composite stacks show much poorer machinability than individual fibrous composites, and consequently, a variety of cutting-induced damage becomes prevalent during the material removal. The interlaminar delamination inside the composite phase and the cracking occurring at the interface zone are considered critical issues when drilling hybrid composite stacks. According to previous investigations, the effective way to guarantee excellent surface quality for composite-related stacks is to select a reasonable cutting sequence strategy, adopt optimal process parameters, and use functionally designed cutting tools. Moreover, special attention should be paid to minimizing the stack interface damage when dealing with the machining of composite-related stacks.

5 Tool Wear Modes

Apart from the machining-induced defects, rapid tool wear is another critical concern when machining fibrous composites and their related stacks. Due to the high abrasiveness of reinforcing fibers, progressive abrasion wear in the form of edge blunting or dulling has been confirmed as the dominant wear mode governing the machining of fibrous composites (Faraz et al., 2009; Rawat & Attia, 2009; Wang

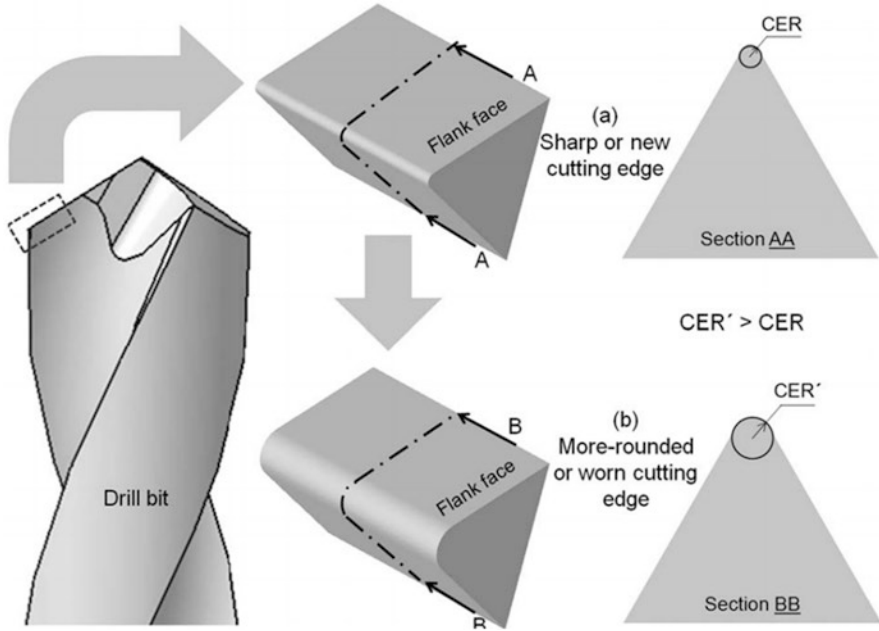


Fig. 5.10 Cutting-edge rounding (CER): (a) sharp cutting edge and (b) rounded cutting edge. Reproduced with copyright permission from Faraz et al. (2009)

et al., 2013; Xu et al., 2019c). For instance, during the drilling operation, the chip separation is carried out within the primary drill edge zone, so the drill edge wear is a key concern when dealing with the machining of composites. Since the instantaneous cutting speed of each drill edge segment varies with its position relative to the drill tip, the edge segment far away from the drill tip involves the highest speed. In contrast, the drill tip entails zero cutting speed. Therefore, the wear extents exerted onto the drill edge segments are different (Xu et al., 2020c). As shown in Fig. 5.10 (Faraz et al., 2009), the phenomenon of an enlargement of the edge radius after the drilling of fibrous composites is visible. Before the machining process, the cutting-edge radius (CER) is very small, while after the drilling of the composites, the CER increases significantly. This is due to the high abrasiveness of the reinforcing fiber which dulls and blunts the sharpness of the drill edges, leading to the increased edge radius. As the drill edges come in contact with fibrous composites, the high hardness fibers may abrade significantly the edge surfaces, leading to the dulling of cutting edges. As the tool-chip contact length is very small, the wear-affected zone is very narrow being close to the drill edges. As such, the phenomena of crater wear are not very significant. Therefore, the abrasion wear in the form of edge rounding represents the characteristic wear mode dominating the drilling processes of fibrous composites.

To verify the phenomenon of abrasion wear and edge rounding wear in the drilling of composites, Fig. 5.11 shows the wear morphologies of the two types of drills

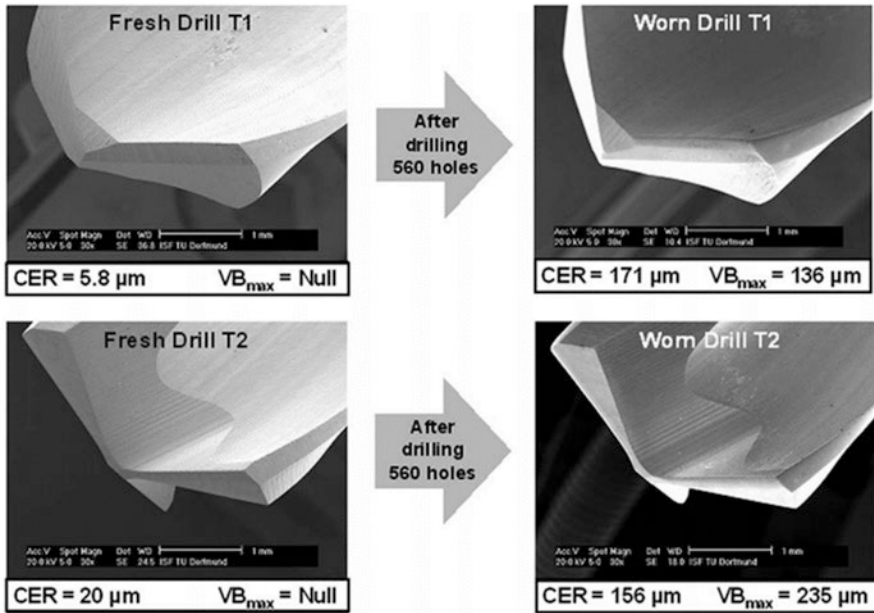


Fig. 5.11 SEM photographs: sharp cutting edges and smoothly rounded edges. Reproduced with copyright permission from Faraz et al. (2009)

after drilling a certain number of composite holes. The left two images of Fig. 5.11 show the SEM morphologies of the two fresh drills. The drills differ in both original CER values and geometrical structures. The right two images of Fig. 5.11 depict the wear morphologies after drilling 560 composite holes. It is evident that drilling fibrous composites entails the enlargement of the CER value. For the first drill (T1), the CER value has increased nearly 30 times compared with the original one, while for the second drill (T2), the CER value increases probably 7.8 times compared with the original one. By contrast, the flank wear and crater wear are insignificant from the SEM observations. The above results verify the dominance of the cutting-edge rounding wear during the drilling of fibrous composites. Note that there is no clear evidence of drill crater wear following the drilling of fibrous composites, which is contrary to the machining of conventional metals and steels. This is because, during the composites machining, the chips are separated by the brittle fracture rather than the elastoplastic deformation. Therefore, the tool-chip contact length is too narrow to form the crater wear signatures onto the drill rake faces. As such, crater wear is not identified during the composite machining. Additionally, besides the commonly observed abrasion wear, the high abrasiveness of fibers may cause the deterioration of the tool edges as well as the microchipping failure when the concentrated stresses at the drill edge segment exceed the tool's ultimate strength. The deterioration of cutting edges is mainly in the form of changes of the edge shapes, resulting from the cumulative effects of tool abrasion wear. By contrast, microchipping is a partial

failure and fracture of tool edges, being the critical factor leading to the tool rejection.

In the case of machining composite-related stacks, the operating wear mode can be considered as the coupling effects of abrasion wear resulting from the composite cutting and the adhesion wear arising from the metallic alloy machining (Park et al., 2011; Wang et al., 2014; Xu & El Mansori, 2017). Therefore, the cutting tools may undergo a very rapid wear rate compared to the cutting of individual fibrous composites due to the cumulative wear impacts. In most cases, adhesion wear from the metal cutting operates as the critical factor leading to premature tool failures such as microchipping or edge fracture. Finally, it should be noted that both the tool wear modes and the tool failures are affected by a broad spectrum of factors such as the applied machining parameters and the workpiece properties. To effectively control the wear progression following the machining of fibrous composites, a careful selection of specialized tool geometries and superior tool materials is of great importance.

6 Conclusions

In the modern aerospace industries, mechanical machining has become an inevitable process for fibrous composites and their related stacks before their eventual industrial applications. However, these aerospace-grade composites are extremely difficult to machine due to their inherent anisotropy and heterogeneity. Precision machining of these materials with high quality is facing considerable challenges in the aerospace manufacturing community owing to the serious cutting-induced damage and rapid tool wear. The present chapter has addressed the machinability issues associated with aerospace-grade composites machining, and the following conclusions are drawn:

- The machinability of fibrous composites is anisotropic and fiber-orientation-dependent, being the key characteristics of the materials due to their fiber-orientation-dependent properties. As such, the fiber orientation plays a decisive role in the material separation for fibrous composites. To improve the machinability of aerospace-grade composites, the machinists have to arrange carefully the fiber cutting angle during the material removal process.
- Cutting forces and machining temperatures are critical factors that significantly affect the machinability of aerospace-grade composites. Most of the cutting-induced damage is related to the force/temperature effects during the composite machining. The use of functional tool geometries and optimal cutting parameters can effectively reduce the cutting forces and machining temperatures.
- The surface quality of fibrous composites is rather difficult to guarantee due to the poor machinability of the materials. Delamination, uncut fibers, fiber splintering, and surface cavities are the main damage modes for the cut surfaces of aerospace-grade composites. Machining of metallic-composite stacks entails

surface damage promoted from both the composite/metallic phases and the interface zone.

- Machining of fibrous composites involves abrasion wear in the form of edge rounding and dulling. In the case of machining composite-related stacks, the operating wear mode can be considered as the coupling effects of abrasion wear resulting from the composite cutting and adhesion wear arising from the metallic alloy machining. Moreover, the key failure modes of tools for the machining of aerospace-grade composites are the microchipping or edge fracture due to the cumulative wear effects or the stress concentration at the tool edge segments.
- To improve the machinability and quality of aerospace-grade composites, a careful selection of fiber orientations, cutting parameters, and tool geometries should be undertaken in future research. Additionally, designing functional cutting tools should take the composite chip removal and damage formation mechanisms into consideration. Finally, the manufacturing sectors need to develop more reliable cutting techniques capable of realizing the high-quality and delamination-free machining of aerospace-grade composites and their related stacks.

Acknowledgments This work was supported by the National Natural Science Foundation of China (Grant No. 51705319).

References

- Aamir, M., Tolouei-Rad, M., Giasin, K., et al. (2019). Recent advances in drilling of carbon fiber-reinforced polymers for aerospace applications: A review. *International Journal of Advanced Manufacturing Technology*, 105, 2289–2308.
- Abrão, A. M., Faria, P. E., Rubio, J. C. C., et al. (2007). Drilling of fiber reinforced plastics: A review. *Journal of Materials Processing Technology*, 186, 1–7.
- Ahmad, F., Manral, A., & Bajpai, P. K. (2019). Machining of thermoplastic composites. In P. K. Rakesh & I. Singh (Eds.), *Processing of green composites* (pp. 107–123). Springer Singapore.
- Alsubari, S., Zuhri, M. Y. M., Sapuan, S. M., et al. (2021). Potential of natural fiber reinforced polymer composites in sandwich structures: A review on its mechanical properties. *Polymers*, 13, 423.
- Ben Soussia, A., Mkaddem, A., & El Mansori, M. (2014). Rigorous treatment of dry cutting of FRP—Interface consumption concept: A review. *International Journal of Mechanical Sciences*, 83, 1–29.
- Bhatnagar, N., Ramakrishnan, N., Naik, N. K., et al. (1995). On the machining of fiber reinforced plastic (FRP) composite laminates. *International Journal of Machine Tools and Manufacture*, 35, 701–716.
- Bonnet, C., Poulachon, G., Rech, J., et al. (2015). CFRP drilling: Fundamental study of local feed force and consequences on hole exit damage. *International Journal of Machine Tools and Manufacture*, 94, 57–64.
- Brinksmeier, E., Fangmann, S., & Rentsch, R. (2011). Drilling of composites and resulting surface integrity. *CIRP Annals - Manufacturing Technology*, 60, 57–60.
- Callister, W. D., & Rethwisch, D. G. (2007). *Materials science and engineering: An introduction*. Wiley.
- Davim, J. P. (2009). *Drilling of composite materials*. Nova Science Publishers.

- Davim, J. P., Rubio, J. C., & Abrao, A. M. (2007). A novel approach based on digital image analysis to evaluate the delamination factor after drilling composite laminates. *Composites Science and Technology*, 67, 1939–1945.
- Faraz, A., Biermann, D., & Weinert, K. (2009). Cutting edge rounding: An innovative tool wear criterion in drilling CFRP composite laminates. *International Journal of Machine Tools and Manufacture*, 49, 1185–1196.
- Gay, D., Hoa, S. V., & Tsai, S. W. (2003). *Composite materials design and applications*. CRC Press.
- Geier, N., Davim, J. P., & Szalay, T. (2019). Advanced cutting tools and technologies for drilling carbon fibre reinforced polymer (CFRP) composites: A review. *Composites Part A: Applied Science and Manufacturing*, 125, 105552.
- Hocheng, H., & Tsao, C. C. (2003). Comprehensive analysis of delamination in drilling of composite materials with various drill bits. *Journal of Materials Processing Technology*, 140, 335–339.
- Hocheng, H., & Tsao, C. C. (2005). The path towards delamination-free drilling of composite materials. *Journal of Materials Processing Technology*, 167, 251–264.
- Iliescu, D., Gehin, D., Iordanoff, I., et al. (2010). A discrete element method for the simulation of CFRP cutting. *Composites Science and Technology*, 70, 73–80.
- Liu, D., Tang, Y., & Cong, W. L. (2012). A review of mechanical drilling for composite laminates. *Composite Structures*, 94, 1265–1279.
- Mallick, P. K. (2007). *Fiber-reinforced composites: Materials, manufacturing, and design*. CRC Press.
- Mohd Nurazzi, N., Asyraf, M. R. M., Khalina, A., et al. (2021). Fabrication, functionalization, and application of carbon nanotube-reinforced polymer composite: An overview. *Polymers*, 13, 1047.
- Mondelin, A., Furet, B., & Rech, J. (2010). Characterisation of friction properties between a laminated carbon fibres reinforced polymer and a monocrystalline diamond under dry or lubricated conditions. *Tribology International*, 43, 1665–1673.
- Nurazzi, N. M., Asyraf, M. R. M., Khalina, A., et al. (2021). A review on natural fiber reinforced polymer composite for bullet proof and ballistic applications. *Polymers*, 13, 646.
- Park, K. H., Beal, A., Kim, D., et al. (2011). Tool wear in drilling of composite/titanium stacks using carbide and polycrystalline diamond tools. *Wear*, 271, 2826–2835.
- Rawat, S., & Attia, H. (2009). Wear mechanisms and tool life management of WC-Co drills during dry high speed drilling of woven carbon fibre composites. *Wear*, 267, 1022–1030.
- Sinmazçelik, T., Avcu, E., Bora, M. Ö., et al. (2011). A review: Fibre metal laminates, background, bonding types and applied test methods. *Materials and Design*, 32, 3671–3685.
- Soutis, C. (2005). Fibre reinforced composites in aircraft construction. *Progress in Aerospace Science*, 41, 143–151.
- Suriani, M. J., Rapi, H. Z., Ilyas, R. A., et al. (2021). Delamination and manufacturing defects in natural fiber-reinforced hybrid composite: A review. *Polymers*, 13, 1323.
- Turki, Y., Habak, M., Velasco, R., et al. (2014). Experimental investigation of drilling damage and stitching effects on the mechanical behavior of carbon/epoxy composites. *International Journal of Machine Tools and Manufacture*, 87, 61–72.
- Turki, Y., Habak, M., Velasco, R., et al. (2017). Highlighting cutting mechanisms encountered in carbon/epoxy composite drilling using orthogonal cutting. *International Journal of Advanced Manufacturing Technology*, 92, 685–697.
- Wang, X. M., & Zhang, L. C. (2003). An experimental investigation into the orthogonal cutting of unidirectional fibre reinforced plastics. *International Journal of Machine Tools and Manufacture*, 43, 1015–1022.
- Wang, D. H., Ramulu, M., & Arola, D. (1995). Orthogonal cutting mechanisms of graphite/epoxy composite. Part I: Unidirectional laminate. *International Journal of Machine Tools and Manufacture*, 35, 1623–1638.
- Wang, X., Kwon, P. Y., Sturtevant, C., et al. (2013). Tool wear of coated drills in drilling CFRP. *Journal of Manufacturing Processes*, 15, 127–135.

- Wang, X., Kwon, P. Y., Sturtevant, C., et al. (2014). Comparative tool wear study based on drilling experiments on CFRP/Ti stack and its individual layers. *Wear*, *317*, 265–276.
- Xu, J., & El Mansori, M. (2016a). Experimental study on drilling mechanisms and strategies of hybrid CFRP/Ti stacks. *Composite Structures*, *157*, 461–482.
- Xu, J., & El Mansori, M. (2016b). Numerical studies of frictional responses when cutting hybrid CFRP/Ti composite. *International Journal of Advanced Manufacturing Technology*, *87*, 657–675.
- Xu, J., & El Mansori, M. (2017). Wear characteristics of polycrystalline diamond tools in orthogonal cutting of CFRP/Ti stacks. *Wear*, *376-377*, 91–106.
- Xu, J., An, Q., Cai, X., et al. (2013). Drilling machinability evaluation on new developed high-strength T800S/250F CFRP laminates. *International Journal of Precision Engineering and Manufacturing*, *14*, 1687–1696.
- Xu, J., Mkaddem, A., & El Mansori, M. (2016). Recent advances in drilling hybrid FRP/Ti composite: A state-of-the-art review. *Composite Structures*, *135*, 316–338.
- Xu, J., An, Q., & Chen, M. (2017). An experimental investigation on cutting-induced damage when drilling high-strength T800S/250F carbon fiber-reinforced polymer. *Proceedings of the Institution of Mechanical Engineers, Part B: Journal of Engineering Manufacture*, *231*, 1931–1940.
- Xu, J., Li, C., Mi, S., et al. (2018). Study of drilling-induced defects for CFRP composites using new criteria. *Composite Structures*, *201*, 1076–1087.
- Xu, J., El Mansori, M., Chen, M., et al. (2019a). Orthogonal cutting mechanisms of CFRP/Ti6Al4V stacks. *International Journal of Advanced Manufacturing Technology*, *103*, 3831–3851.
- Xu, J., El Mansori, M., Voisin, J., et al. (2019b). On the interpretation of drilling CFRP/Ti6Al4V stacks using the orthogonal cutting method: Chip removal mode and subsurface damage formation. *Journal of Manufacturing Processes*, *44*, 435–447.
- Xu, J., Li, C., Chen, M., et al. (2019c). An investigation of drilling high-strength CFRP composites using specialized drills. *International Journal of Advanced Manufacturing Technology*, *103*, 3425–3442.
- Xu, J., Li, C., Chen, M., et al. (2019d). A comparison between vibration assisted and conventional drilling of CFRP/Ti6Al4V stacks. *Materials and Manufacturing Processes*, *34*, 1182–1193.
- Xu, J., Huang, X., Chen, M., et al. (2020a). Drilling characteristics of carbon/epoxy and carbon/polyimide composites. *Materials and Manufacturing Processes*, *35*, 1732–1740.
- Xu, J., Huang, X., Davim, J. P., et al. (2020b). On the machining behavior of carbon fiber reinforced polyimide and PEEK thermoplastic composites. *Polymer Composites*, *41*, 3649–3663.
- Xu, J., Ji, M., & Chen, M. (2020c). On the quantitative analysis of drill edge wear when machining CFRP/Ti6Al4V stacks. *International Journal of Advanced Manufacturing Technology*, *108*, 1463–1472.
- Xu, J., Li, C., Chen, M., et al. (2020d). On the analysis of temperatures, surface morphologies and tool wear in drilling CFRP/Ti6Al4V stacks under different cutting sequence strategies. *Composite Structures*, *234*, 111708.
- Xu, J., Chen, M., Davim, J. P., et al. (2021). A review on the machinability of aerospace-grade CFRP/titanium stacks. *Advanced Materials Letters*, *12*, 21011591.

Chapter 6

Advanced Potential Hybrid Biocomposites in Aerospace Applications: A Comprehensive Review



Muhammad Farhan, M. T. Mastura, Shahid Pervez Ansari,
Muhammed Muaz, Mohammad Azeem, and S. M. Sapuan

1 Introduction

1.1 Hybrid Biocomposites

There is a persistent demand for lightweight materials with superior strength and toughness for use in aerospace applications for several purposes. To meet this requirement, polymer matrix-based composite materials were created. Biocomposites are used in different applications including aircrafts, automobiles, biomedical industry, sporting equipment, helmets and household furnishings.

M. Farhan (✉)

Department of Mechanical Engineering, Faculty of Engineering and Technology, Integral University, Lucknow, India
e-mail: mufarhan@iul.ac.in

M. T. Mastura

Faculty of Mechanical and Manufacturing Engineering Technology, Universiti Teknikal Malaysia Melaka, Melaka, Malaysia

S. P. Ansari

Z. H. College of Engineering and Technology, Department of Applied Chemistry, Faculty of Engineering and Technology, Aligarh Muslim University, Aligarh, India

M. Muaz

Z. H. College of Engineering and Technology, Department of Mechanical Engineering, Faculty of Engineering and Technology, Aligarh Muslim University, Aligarh, India

M. Azeem

Department of Mechanical Engineering, Faculty of Engineering, Universiti Teknologi Petronas, Seri Iskandar, Perak, Malaysia

Hybrid biocomposites are a type of biocomposites in which the matrix or reinforcing phase is biodegradable (Idicula et al., 2005; Narnaware et al., 2015; Rajesh et al., 2018; Mohd Nurazzi et al., 2019; Aisyah et al., 2021; Alsubari et al., 2021; Nurazzi et al., 2021).

Green composites are biodegradable biocomposites in which both phases (reinforcing phase and matrix phase) are biodegradable. Generally, biodegradable components of biocomposites are often sourced from nature. Frequently mentioned natural fibres and fillers used as reinforcements are banana, sisal rice straw, coir, hemp, clays, wood flour, coir shell and natural biodegradable matrices such as starch, polylactic acid, soy, coir shell, etc. (Jacob et al., 2006; Ramesh et al., 2013; Silva et al., 2013; Sathishkumar et al., 2017; Saxena & Gupta, 2019; Ilyas et al., 2019a, 2020a, b, 2021; Syafiq et al., 2020; Jumaidin et al., 2021; Punia Bangar et al., 2021).

One of the several ways used to minimize the brittleness of carbon fibre composites and produce improved toughness qualities was to hybridize them with fibres of different nature (Swolfs et al., 2015). In hybrids, the reinforcement mix is chosen in such a way that each component's qualities are essentially distinct. Deviations may develop as a result of a synergistic impact, such as a positive or negative hybrid impact (less than the expected) (Nurazzi et al., 2020; Rozilah et al., 2020; Alsubari et al., 2021). Hybrid biocomposites are biocomposites with two or more reinforcing elements in a single matrix. The reinforcements might come in a variety of physical forms. Fibres with other fibres, fibres with particle fillers, two types of particle fillers, layered fibrous mats, and so on are some of the conceivable combinations. Figure 6.1 shows an overview of hybrid biocomposites, as well as other types of composites.

The hybrid biocomposites widely used in the phenomenon of hybridization for high-performance fibres such as carbon, Kevlar and basalt have been extensively examined, while biodegradable reinforcement-based hybrid biocomposites have received less attention. Natural fibres and fillers were combined with man-made reinforcements by researchers. Only a few research studies have been published in which both the reinforcing and reinforcing phases are made of biodegradable fibres. This study will look at hybrid biocomposites, which are composites with at least one biodegradable fibre or filler as a reinforcement (Singh & Mukhopadhyay, 2020).

S. M. Sapuan

Advanced Engineering Materials and Composites Research Centre (AEMC), Department of Mechanical and Manufacturing Engineering, Universiti Putra Malaysia, Serdang, Selangor, Malaysia

Laboratory of Biocomposite Institute of Tropical Forestry and Forest Products (INTROP), Universiti Putra Malaysia, Serdang, Selangor, Malaysia

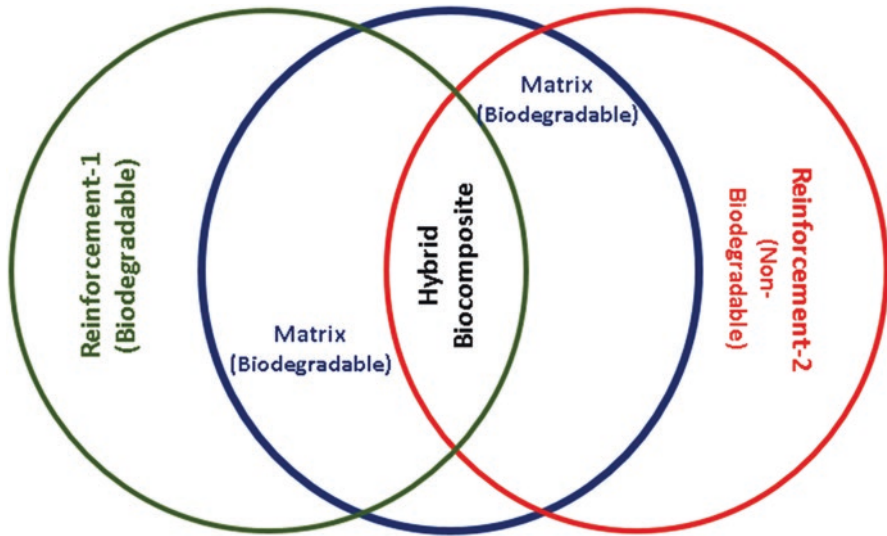


Fig. 6.1 Representation of hybrid biocomposites

2 Reinforcements and Matrices of Hybrid Biocomposites

2.1 Reinforcing Phases of Hybrid Biocomposites

Phases that reinforce each other the usage of several forms of biodegradable reinforcements in hybrid biocomposites have been described by researchers. Almost all of the documented reinforcements come from nature, and the majority of them contain cellulose as the primary component. Hybrid composites with two reinforcing phases were reported by the majority of researchers. There are a few publications till now that report more than two reinforcing phases. Some researchers (Otto et al., 2017; Pradhan & Acharya, 2021) have described studies with three reinforcing stages. The usage of particle fillers in hybrid biocomposites has also been reported to be restricted. Researchers have mostly utilized fibres in the form of fibrous webs, both woven and non-woven, as reinforcements.

Various types of natural fibres are investigated in conjunction with man-made or natural fibres, while research on hybrid biocomposites including both natural and man-made reinforcements is dominated by those containing one natural and one man-made fibre. Glass fibres in various physical forms make up a significant component of these man-made fibres, which are employed as one of the ingredients. There are additional studies on particle filler-based hybrid biocomposites. Coir and kenaf fibres were combined with wood flour (Yao et al., 2012; Yahaya et al., 2017). In epoxy resin, fly ash was used as a filler with jute fibres. Carbon black was mixed with pineapple leaf fibres in a natural rubber matrix. However, particulate-based

Table 6.1 Recent advances with different reinforcements used in hybrid biocomposites (Singh & Mukhopadhyay, 2020)

Reinforcements	References
Fibres	
Glass	Gangil et al. (2020), Ramesh et al. (2013), Birat et al. (2015), Rout et al. (2001), Petrucci et al. (2015), Leman et al. (2008), Sreekumar et al. (2012), Rout et al. (2001)
Bamboo	Cai et al. (2021), Samanta et al. (2015)
Flax	Petrucci et al. (2015), Santulli et al. (2005), Prabhakaran et al. (2014), Zhang et al. (2020), Ahmed et al. (2013), Živković et al. (2017), Ravandi et al. (2019), Papa et al. (2020), Fiore et al. (2017), Petrucci et al. (2015)
Hemp	Ridzuan et al. (2017), Halimatul et al. (2019)
Coir	Sathishkumar et al. (2017), Boujmal et al. (2018)
Silk	Jawaid et al. (2013), Faezipour et al. (2016)
OPEFB	Kadem et al. (2018)
Pineapple	Idicula et al. (2006)
Banana	Rajesh et al. (2018), Idicula et al. (2005), Silva et al. (2013), Boopalan et al. (2013), Idicula et al. (2005), Sanjay et al. (2017)
Sisal	Idicula et al. (2005), Gupta and Srivastava (2016), Sathishkumar et al. (2017), Ramesh et al. (2013), Silva et al. (2013), Jacob et al. (2006), Aslan et al. (2018), Idicula et al. (2005), Jacob et al. (2006)
Kenaf	Atiqah et al. (2017), Yahaya et al. (2017), Sivakumar et al. (2018), Sathishkumar et al. (2017)
Oil palm fibre	Jawaid et al. (2013), Sreekumar et al. (2012), Ishak et al. (1998), Jacob et al., (2006)
Cotton	Sathishkumar et al. (2017), Athijayamani et al. (2010), Alsina et al. (2005)
Lyocell	Idicula et al. (2006)
Seaweed	Sapuan and Ilyas (2018)
Palmyra	Nunna et al. (2012)
Baggase	Boujmal et al. (2018), Saw et al. (2011)
Particulate filler	
Clay	Qaiss et al. (2015), Essabir et al. (2017)
Wood flour	Jawaid et al. (2013), Faezipour et al. (2016)
Fly ash	Raghavendra et al. (2016)
Coconut shell	Dhakal et al. (2018)
Flour silica	Gonçalves et al. (2014)
Cornhusk	Kwon et al. (2014)

fillers are used in a smaller percentage of research. Table 6.1 summarizes the various types of fibres and fillers that were employed as reinforcements (Yantaboot & Amornsakchai, 2017).

Another part of Table 6.1 shows that the bulk of literature on hybrid biocomposites contains fibres, with the majority of them containing one reinforcement in the form of glass in a fibrous form. In hybrid biocomposites, there have been just a few research on the use of particle fillers.

2.2 Matrix Phase of Hybrid Biocomposites

The bulk of the above-mentioned reinforcements have been reinforced with thermoset matrices. The use of polyester and epoxy-based resins in natural fibre-based hybrid composites is well documented in the literature (Nurazzi et al., 2019; Kumar et al., 2020; Suriani et al., 2021a, b, c, d). Other thermoset resins such as phenol formaldehyde and novolac, on the other hand, have been reported. Thermoset resin is thought to be able to efficiently saturate the fibres, resulting in improved penetration into the fibrous web and layers. It might be the reason why thermoset resins have been employed so extensively in natural fibre-based hybrid composites so far. There are also a few investigations using thermoplastic resins such polypropylene, polyethylene, thermoplastic natural rubber and soybean oil (Sanjay & Yogesha, 2016). Table 6.2 lists the many types of matrices utilized in hybrid biocomposites, as well as the research that have reported on them. In comparison to thermoplastic polymers, thermoset resins have been employed more frequently as a matrix in hybrid biocomposites, as shown in Table 6.2. The most common matrix phase is epoxy-based resins. Epoxy resins are a prominent kind of thermoset composite matrix. The resin, modifiers and cross-linking agent can be used to customize the properties of cured epoxy resin to obtain specific performance characteristics. There are various properties for which epoxies are favoured as a resin.

Epoxies have extremely good chemical resistance, particularly in alkaline conditions. It provides excellent adherence to a wide range of surfaces. In terms of mechanical qualities, they feature a mix of high tensile, compressive and flexural strengths. Shrinkage in thermoset resins is frequently a source of concern. On cure,

Table 6.2 Different matrices used in hybrid biocomposites (Singh & Mukhopadhyay, 2020)

Matrices	References
Thermoset	
Epoxy resin	Fiore et al. (2017), Sanjay and Yogesha (2018), Jawaid et al. (2013), Gupta and Srivastava (2016), Ramesh et al. (2013), Gonçalves et al. (2014)
Modified epoxy resin	Saw et al. (2011), Rozman et al. (2013), Vijaya Ramnath et al. (2015)
Polyester	Atiqah et al. (2019), Rout et al. (2001), Idicula et al. (2006)
Natural rubber	Jacob et al. (2006)
Phenolic resin	Bach et al. (2017), Raj et al. (2017)
Banana	Sathishkumar et al. (2017), Reddy (2019), Vijaya Ramnath et al. (2015)
Kenaf	Sathishkumar et al. (2017)
Soybean oil matrix	Santulli (2007)
Thermoplastic	
Polypropylene	Qaiss et al. (2015), Birat et al. (2015), Aslan et al. (2018), Rozman et al. (2013)
PLA	Battegazzore et al. (2019), Kwon et al. (2014)
Polyethylene	Boujmal et al. (2018), Essabir et al. (2017)

the epoxies showed very little shrinking. Epoxies are useful in areas where electrical insulation is required. They are also corrosion resistant. When compared to other thermoset materials, their fatigue strength is better.

3 Natural Fibre-Reinforced Polymer Composite

Natural fibre polymer composite consists of natural fibres as reinforced material and polymer as matrix (Ayu et al., 2020; Aiza Jaafar et al., 2021). These two materials are compounded together to obtain superior material properties and replace the traditional materials. Natural fibre in polymer composite can be classified into three main categories which are plant-based fibre, animal-based fibre and mineral-based fibre. As shown in Fig. 6.2, plant-based fibres are extracted from different parts of the plant such as bast, fruit, seed and leaf. Kenaf, hemp, jute, flax, ramie and roselle are the fibres that are collected from the outer layers of the plant stem. Coconut coir fibre is an example of the fibre is that collected from the fruit where it is extracted from the outer layers of the internal crust of the coconut. Kapok and cotton fibres are the examples of fibres that are collected from the seed of the plant. Banana and pineapple leaf fibres are the most found fibres that are extracted from the leaf of the plant. Generally, all the natural fibres that are plant-based type are known as cellulose fibres as they contain a high percentage of cellulose. Plant-based fibres also contain hemicellulose, lignin, pectin and wax as these chemical compositions exhibit the material properties of the fibres. Animal-based fibres are mostly found in the application of medical tools where this type of fibres can be degraded in the human body without adverse toxicity. Animal-based fibres also known as protein-based fibres primarily contained a series of amino acid and peptide chains. Similar with the plant-based fibres, animal-based fibres are collected from different parts of animal such as hair, feathers, cocoon and skin. Wool and keratin are the examples of the fibres that are collected from the hair or fur of the animals. Silk is one of the fibrous proteins that is produced by moth, spider and scorpion and consists of glycine, alanine and serine. With good mechanical properties and hydrophobic properties, silk is mostly found in tissue scaffold applications. Collagen is another type of protein-based fibres where it is collected from the skin, tendon, cartilage, bone and internal organs of animals containing repeating amino acid chain. Generally, these animal-based fibres are preferable in the selection of biomaterials due to its low cost

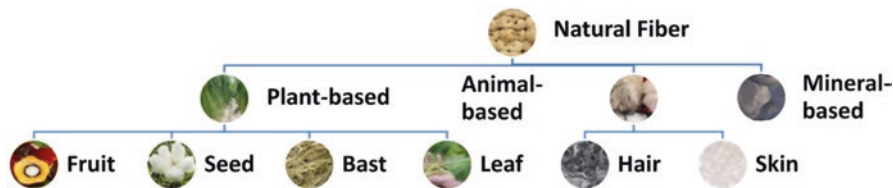


Fig. 6.2 Types of natural fibres

and biocompatibility in medical application. Mineral-based fibre is a solid substance that is not made by an organism, and it is naturally occurred with definite chemical composition and has a systematic and repeating pattern of internal structure. On earth, plenty of mineral resources varied based on their mineral formulae. Each mineral material is unique, and a complex method could classify the type of mineral materials. A mineral is a type of material that has a wide range of species that is modified based on the weathering process and geologic conditions. Consequently, the chemical and mineral content of the fibres are different from location to location. Mineral-based fibres are preferable in producing fibre-reinforced concrete composite because of their low cost of production, good deformation properties and improved crack resistance and concrete durability. Basalt fibre that contains SiO_2 , Al_2O_3 , MgO , CaO , Fe_2O_3 and FeO is mostly found to be reinforced in a polymer composite material. Other mineral fibres that are used as reinforced materials in polymer composites are kaolinite, amosite, actinolite and tremolite.

Numerous studies on natural fibre-reinforced polymer composites have been conducted by past researchers. These studies include the exploration of the benefits of natural fibre-reinforced polymer composites and the investigation on how to counteract the weakness of the composites. Generally, the applications of natural fibre-reinforced polymer composites are mostly due to the sustainable properties of the materials. The application of natural fibre-reinforced polymer composites could reduce plastic consumption, especially in product design parts. Having a substitute to traditional plastic applications with biodegradable materials like natural fibre-reinforced polymer composite is a best way to reduce the consumption of non-renewable materials and save the life of more creatures on earth, especially those that live in the ocean. In a life cycle analysis of the natural fibre-reinforced polymer composite, this type of materials exhibits lower toxicity and lower harmful emission for the whole of their life compared with synthetic fibre composites and neat polymer materials. Moreover, natural fibre-reinforced polymer composites may improve the properties of the traditional materials used in various types of applications such as automotive, defence technology and food packaging. In automotive applications, Yahaya et al. (2017) studied on non-woven kenaf and hybrid non-woven/woven kenaf fabric for application on PROTON Saga FL car door map pocket. The hybrid composite is found to be lighter and has better tensile and flexural strength compared with neat polypropylene, and the composite is suitable for automotive door map pocket. In another study, Sanjay and Yogesha (2016) reviewed the application of natural fibre composites by renowned automotive manufacturer such as Mercedes-Benz, Audi and Toyota. Mercedes-Benz used epoxy matrix with jute addition in its 1996 vehicles for door panel, Audi launched A2 midrange car which used polyurethane reinforced with flax/sisal material mixture for the door trim panels, and Toyota car interior is made by developed eco-plastic made from sugarcane. Fogorasi and Barbu (2017) found that natural fibre-reinforced polymer composites have low density with weight reduction up to 10–30% and also their possible application for new production technologies and materials, and their favourable processing properties for lower tool usage. Natural fibre-reinforced polymer composites also have good mechanical and acoustic properties. In safety aspect, the composites give huge

benefits due to their high stability and less splintering, providing a high standard of passive safety during collision or burning. Meanwhile in health aspect, the composites produce less harmful emission compared to glass fibre during the production.

Natural fibre-reinforced polymer composites are more compatible in additive manufacturing process compared to subtractive manufacturing process. Compression moulding, hand lay-up, extrusion and hot press are the most found manufacturing processes used by the engineers in fabricating the composites. Gupta et al. (2019) suggested hot press method to make composite by mixing the hemp non-woven mats with polypropylene fibres for various fibre volume fractions. For specimen preparation, Atiqah et al. (2019) used hand lay-up method to fabricate kenaf fibre with thermoset and used pre-gel coat during moulding process to produce good surface finish. Ferdous and Sarwar Hossain (2017) stated that the techniques used to manufacture biocomposite based on existing composite material processing techniques are press moulding, hand lay-up, filament winding, extrusion, injection moulding and compression moulding, but the majority of current biocomposite materials are based on thermoplastics processed by compounding and extrusion. Dashtizadeh et al. (2017) reviewed that hand lay-up and compression moulding methods are used for coir pith, nylon fabric and epoxy hybrid composite development.

4 Hybridization of Fibre-Reinforced Composites

Polymer matrix composites are made from two components: (1) polymer matrix and (2) reinforcing materials. In general, the polymer matrix is mainly chosen from elastomer and thermoplastic and thermoset polymers. At the same time, the reinforcing materials are either natural fibres or synthetic fibres used in the polymer matrix composites (PMCs). During the synthesis of any desired PMC, selecting a reinforcing material with desired properties is a serious challenge for scientists, engineers and manufacturers in various industries. The critical attributes of reinforcing materials are their economic-ecological balance and performance. Being economical, eco-friendly (biodegradable) and lightweight are few benefits of natural fibres. Due to the rising demands and stringent regulatory limits to operate, the natural fibres are preferred over synthetic fibres. However, synthetic fibres can be used as when required due to their excellent performance and durability (Gangil et al., 2020) (Sapuan et al., 2019).

A new trend to utilize two types of fibres to prepare PMCs (hybrid composites) with desired properties has recently attracted interest in the field of materials science and engineering. The hybrid composites offer the benefits of both the fibres being used to reinforce the matrix. Therefore, the hybrid composites yield superior properties than PMCs based on a single type of fibre. In general, hybrid composites refer to composites wherein the matrix contains two or more reinforcing materials. All the components play an important role to yield the desired properties in the hybrid composites. Matrix is the founding component and plays an important role

in corrosion, resistance for chemicals and temperature, damage tolerance, etc.; the fibres act as reinforcing materials and play an important role to provide strength, stiffness and impact behaviour of the hybrid composites. The type/form of the fibres also affects the composite properties (Sapuan et al., 2019).

It has been reported that for automotive parts, thermoplastic composites reinforced with continuous fibres are better suited because of their excellent mechanical properties. Unlike synthetic fibre-reinforced composites, natural fibre composites offer slightly inferior properties compared to the glass fibre-based polymer composites. Therefore, to bridge this gap, the concept of hybridization of fibres (natural and synthetic) opted for improved mechanical properties for structural and semi-structural applications. It also helped to the reduction of cost and weight of the hybrid composites. It was observed that the hybrid composites yielded a balance of desired mechanical properties, economy and environment. As the different components play their roles, it is said that the synergetic effect of two types of fibres (natural/synthetic) causes a balance of mechanical properties and economy.

Therefore, hybridization may be termed as the reinforcement of natural and synthetic fibres with the matrix. It helps to reduce the usage of synthetic fibres and improve the properties of composites. The following are few important situations and reasons for the enhancement of the mechanical properties of hybrid composites over single component composites (Gupta & Deep, 2019; Boopalan et al., 2013).

Condition 1. Fibres of different diameters but same length: Different diameters increase the effective area for fibre-matrix adhesion, which favours uniform stress transfer.

Condition 2. Fibres with different modulus: The properties like stiffness and load bearing capacity are enhanced due to the presence of fibres of high modulus, while on the other hand, the low modulus fibre offers better damage tolerance at low cost.

Condition 3. Fibres with different elongation at break: As suggested by the situation, if load is applied to the hybrid composite, the fibres of lower elongation will break first followed by the load transfer to the fibres of higher elongation without the failure of the matrix.

4.1 Cellulosic/Synthetic Fibre (Hybrid)-Reinforced Biocomposites

Biopolymer composites refer to all those composites which have at least one bio-based or biodegradable constituent. Biocomposites may be classified into two groups: (1) partial biodegradable and (2) complete biodegradable biocomposites, depending on their constituents (matrix and fibres). The partially biodegradable biocomposites are made of bio-based/biodegradable matrices and synthetic fibres/non-biodegradable fibres (e.g. epoxy, polyester polyethylene, polypropylene, etc.) as reinforcement materials. The completely biodegradable/biocomposites are made of bio-based/biodegradable components which are derived either from renewable

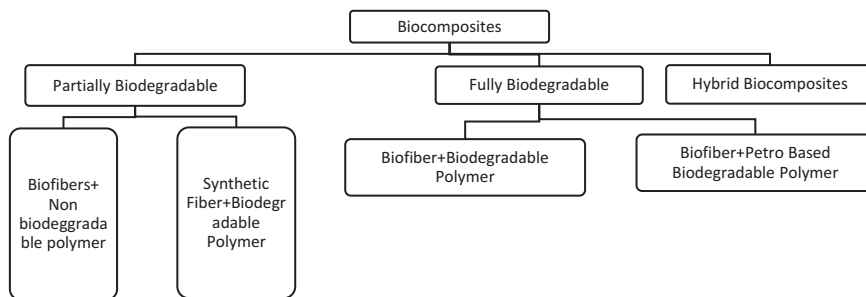


Fig. 6.3 Classification of biocomposites (Drzal et al., 2013)

biopolymer (cellulosic/starch-based plastics) or petroleum-based biodegradable polymers (e.g. polyester amides). In other terms, this classification suggests that the completely biodegradable composites (wherein the two components are completely biodegradable) will decompose and go back to the environment at the end of their life. The partially biodegradable composites (wherein one component is completely biodegradable and the other is non-biodegradable) do not exhibit 100% biodegradability. This classification does not suggest any idea of time, rate and amount of degradation. It only indicates that a biocomposite is fully/partially biodegradable at the end of its life. A schematic of the classification of biocomposites is presented in Fig. 6.3 (Rout et al., 2001; Manyatshe et al., 2020).

The main factors which play a significant role to yield the desired properties to the manufactured products from hybrid composite are as below:

1. Selection of materials (fibre and matrix): It depends primarily on the desired application.
2. The technique of preparation: It depends mainly on the type of fibre/matrix and working space (indoor/outdoor).
3. Fibre-matrix interaction: It is mainly controlled/manipulated by pre-treating the fibres or using coupling agents.

Cellulose is mainly found in the plant cell wall and the most abundant natural organic polymer on earth (Ilyas et al., 2018, 2019b; Ahmad Ilyas et al., 2019; Jumaidin et al., 2020; Omran et al., 2021). It offers good durability and strength. The structure of cellulose varies from highly ordered, microcrystalline region to less ordered, amorphous region. It gets hydrolyzed with acidic treatment and can also degrade on exposure to chemicals. On the other hand, hemicellulose, the second largest biomolecules, has much shorter chains and lower degree of polymerization than cellulose. As these are major components of many natural fibres, we will discuss some critical findings related to them (Bahrami et al., 2020).

In cellulosic fibre-based hybrid biocomposites, hybrid arrangement inhibits moisture absorption into the biocomposites as the voids are filled up due to the packed arrangement of fibres during the formation of hybrid biocomposites. The hydrophilic nature of cellulosic fibres and the capillary action cause increased intake

of water when these materials are soaked into the water, which results in the swelling of fibres. As a result, dimensional variation can occur in the composites, which finally affects their mechanical properties. Lignocellulosic fibres are also hydrophilic and incompatible to hydrophobic polymeric matrices and this causes poor adhesion between fibres and matrices; it makes the dispersion of fibres in the polymeric matrices difficult. Researchers studied composites of cellulosic fibres with polypropylene, polyethylene and polystyrene and found that the inadequate distribution of fibres results in their aggregation into knotted masses, leading to composites with poor final properties. Several methods have been reported to improve filler dispersion and interfacial interaction between filler and matrix. Cellulosic fibres exhibit low thermal stability which limits its processing to some techniques and its applications at lower temperatures. The low thermal stability increases the possibility of cellulosic degradation and the possibility of emissions of volatile materials that could adversely affect the composite properties. Processing temperatures are thus limited to about 200 °C, although it is possible to use a higher temperature for short periods (Nisini et al., 2017; Ishak et al., 1998; Jawaid & Abdul Khalil, 2011).

In cellulosic hybrid biocomposites, the properties (physical and mechanical) of the biocomposites are governed by the size of fibres, amount of fibres, orientation of fibres, extent of intermingling of the two fibres and the interfacial interaction between the fibres and matrix.

Most of the studies on cellulosic fibre hybrid composites are mainly related to their mechanical properties, effects of coupling agents, chemical treatments, etc. (Gao et al., 2003). Recently, Shahzad and Nasir (2017) have reported hybrid laminated biocomposites with enhanced mechanical properties. Figure 6.4 shows the bridging structure formed between cellulose nanocrystal (CNC) and cellulose nanofibre (CNF) arranged alternately. This configuration is advantageous; both the ductile and the brittle phases are present in the composite. The CNF, due to its high ductility, offers mechanical buffering in an alternating pattern and prevents the formation and propagation of cracks in the brittle layer of CNC. Additionally, the CNF layer establishes a strong network of hydrogen bonds with CNC layer which

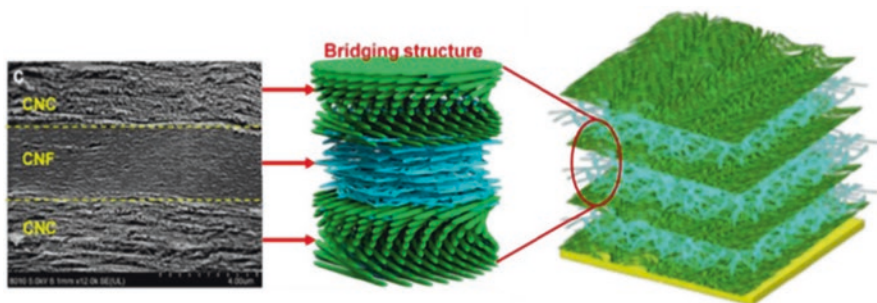


Fig. 6.4 Schematic of chiral nematic cellulose nanofibre/random cellulose nanofibre (CNC-CNF) biocomposite with an alternating sequence of layers and corresponding SEM image of layer. Adapted from (Shahzad & Nasir, 2017)

subsequently optimizes the load transfer property and enhances the strength and toughness of the biocomposites. Such biocomposites may find their application in soft robotics and calorimetric sensors.

5 Natural Fibre/Synthetic Fibre (Hybrid)-Reinforced Polymer Composites

We have discussed in our previous section that the mechanical properties of most of the natural fibres or their composites are inferior compared to that of synthetic fibres/composites. Also reported are some inherent challenges like poor dimensional stability, moisture absorption capacity, low thermal resistance and most importantly, adhesion of the natural fibres with the polymer matrix. Hybridization of natural fibres with synthetic fibres in the polymer matrix is considered as a promising option to overcome the disadvantages of natural fibres. The incorporation of synthetic fibres would improve the overall mechanical properties due to their poor water absorption capacity, dimensional stability, good interaction with polymer matrix, etc., owing to their relatively superior mechanical properties, negligible moisture absorption and compatibility with polymer. A comparative list of the mechanical properties of some natural fibres and synthetic fibres is given in Table 6.3. Glass fibres, carbon fibres and aramid fibres are the most important and widely used synthetic fibres for the manufacture of natural fibre/synthetic fibre hybrid composites. Though the hybrid composites exhibit superior mechanical properties compared to natural fibre-polymer composite, they are traded with biodegradability (Eichhorn et al., 2010).

The industrial applications of hybrid composites have slowly but steadily taken a good pace. The commonly used natural fibres for the purpose are bamboo fibres, coir fibre and jute fibre. Structural materials like wall (interior/exterior) of buildings, emergency shelters, deck, offshore deck platforms, insulated panels, roofing panels, etc. are generally made from hybrid composites. In 2010, Bachtiar et al. studied kenaf-glass hybrid epoxy composites and suggested their applications in car bumper beam materials. Tensile strength and modulus of hybrid composites were found to be higher than the typical car bumper beam material. Likewise, in 2015, Birat et al. (2015) reported a balance of properties (impact, strength, flow and heat deflection) desired for various automotive components. These reports are quite favourable and suggest the considerable potential of these materials in various industrial applications.

However, hybridization of natural fibres with synthetic fibres has some associated issues which need to be considered before the hybridization process. These are reinforcing efficiency of the two fibres (the hybrid effect discussed earlier), moisture content of natural fibres, dispersion of natural fibres in the matrix, fibre/matrix interface, thermal stability of natural fibres and biodegradability of the composites (Zhang et al., 2020).

Table 6.3 Mechanical and physical properties of natural fibres and synthetic fibres

Fibre	Coir	Cotton	E-glass	Flax	Hemp	Jute	Kenaf	Kevlar	Nettle	Ramie	Sisal	Wool	Alfa	Carbon	Harakeke	Silk	Feather	Wool
Density (g cm ⁻³)	1.15–1.46	1.5–1.6	2.55	1.5	1.5	1.3–1.49	–	1.44	–	1.55	1.45	1.3	1.4	1.78	1.3	1.3	0.9–3.3	1.3
Diameter (µm)	100–460	12–38	<17	40–600	25–500	25–200	–	–	–	–	50–200	–	1.5–2.4	5–7	4.2–5.8	–	–	–
Length (mm)	1.2	10–60	Continuous	5–900	5–55	1.5–120	–	–	–	900–1200	–	38–152	350	–	4–5	Continuous	10–30	38–152
Tensile strength (MPa)	131–220	287–800	2000–3400	345–1500	690	393–800	930	3000	650	400–938	468–1627	50–315	188–308	3400–4800	440–990	100–1500	100–203	50–315
Stiffness/Young's modulus (GPa)	4–6	5.5–12.6	70–73	27.6	70	13–26.5	53	60	38	61.4–128	34.5–82.5	2.3–5	18–25	240–425	14–23	5–25	3–10	2.3–5
Specific tensile strength	110–180	190–530	800–1400	230–1220	1.47	300–610	–	–	–	270–620	362–610	38–242	134–220	–	338–761	100–1500	112–226	38–242
Specific Young's modulus (GPa/g cm ⁻³)	3.3–5	3.7–8.4	29	18–53	370–740	7.1–39	–	–	–	29–85	6.7–20	1.8–3.8	13–18	–	11–25	4–20	3.3–11	1.8–3.8
Failure strain (%)	15–30	3.0–10	2.5	1.2–3.2	39–47	1.5–1.8	–	–	–	2.0–3.8	2.0–2.5	13.2–35	1.5–2.4	–	4.2–5.8	15–60	6.9	13.2–35
Elongation at break (%)	15–40	7–8	2.5	2.7–3.2	1.6	1.16–1.5	1.6	2.5–3.7	1.7	1.2–3.8	1.6	–	–	1.4–1.8	–	–	–	–

The effects of hybridization have been elaborated on in previous sections. It can be said that the natural fibre-synthetic fibre hybrid composites exhibit hybrid impact in terms of their improved mechanical properties. The natural fibres absorb moisture from their surroundings due to their hydrophilic nature, but synthetic fibres exhibit inhibition of moisture absorption. The hydrophilic nature of natural fibres does not favour proper adhesion with polymer matrix. It can be overcome by hybridization of the natural fibres and synthetic fibres as the synthetic fibres are more compatible with polymer matrix and resistant to absorption of moisture. Natural fibres also exhibit lower thermal stability, which can be overcome by hybridization with synthetic fibres, which are thermally more stable. In terms of biodegradability, due to the presence of synthetic fibres, the biodegradability of the hybrid composites is reduced (Jawaid & Thariq, 2018).

6 Application of Hybrid Biocomposites in Aerospace Sector

Recent couple of decades have witnessed a steep growth in the aerospace sector which can easily be gauged from the exponential rise in air travellers and the number of satellites launched in space in the same period. This calls for better technological advancements in every aspect ranging from material procurement to manufacturing capabilities. The responsibility rests on the shoulders of engineers and researchers working on the frontline. The success of an air-/spacecraft relies to a much extent on the materials used for its manufacturing. A material is deemed good for aerospace industry if it is light and strong at the least. However, in recent times there are concerns which have gained importance and should be addressed on a priority basis. One is the noise generated from the aerospace vehicles and the other is the environmental degradation due to material manufacturing, and the disposal in the later stage (Scheff et al., 2020). The use of lightweight materials gained much popularity due to aerospace applications. It is known that majority of the aerospace industries relies on metals such as aluminium due to its high strength-to-weight characteristics. However, the use of metals is discouraged due first to the environmental factors and second to the high cost associated with them. There is an urge to explore alternatives that are cheaper, stronger, environmentally friendly and widely available in abundance. To this end hybrid biocomposites are being looked upon as a material of great potential for aerospace applications. A significant amount of research in recent years has shown that a large amount of aerospace structures can be made with materials derived from sources of biological origin. Many of the lightweight modern aircrafts have been made possible just because of the developments in composite materials. Hybrid biocomposites can be used inside the fuselage of the passenger aeroplanes that will not only reduce the acoustic signature from the engine and from the surrounding airflow but will also be cheap and eco-friendly (Winter et al., 2020).

Hybrid biocomposites have found application in the development of sound-absorbing materials which can potentially be used in the construction of anechoic chambers. Anechoic chambers are widely used in aerospace industry for free field testing of noise generated by aircrafts and rocket nozzles. Some of the earlier

studies have shown that natural materials such as wood and coconut coir have good sound-absorbing characteristics and are suitable for making anechoic chambers (Ward et al., 2021) (Bhatnagar, 2006).

7 Direction and Future Applications of Hybrid Biocomposites for Advanced Applications

It is a well-established finding that several limitations are associated with biocomposites composed of a single natural fibre in a matrix. Many such problems can be addressed by the method of hybridization. A hybrid biocomposite, which consists of more than one biodegradable reinforcement material, exhibits extraordinary favourable properties. The most important aspect is that their properties can be tailored according to the requirement. Various such properties which cannot be imparted in a simple biocomposites can be imparted by developing hybrid biocomposites. Therefore, hybrid biocomposites have great scope in various crucial applications in future. Although such applications include aerospace sector, automobiles, sports accessories, furniture, civil structural components, etc., the most attracting and demanding applications are in the field of aerospace. Several applications in the aerospace industry need highly specific requirements which can be fulfilled by the hybrid biocomposites. The most important property of an aerial vehicle is that it should be as lighter in weight as possible. However, the reduction in weight cannot be made responsible for reduction in other crucial properties. For instance, the strength of such structures cannot be sacrificed at any cost. Lightweight unmanned aerial vehicle is one of the application areas where the hybrid biocomposites are attracting the researchers. The lightweight structure of the vehicle must have the desired strength compatible with unfavourable conditions. These criteria can be easily fulfilled while selecting proper reinforcement materials and arranging them in a proper fashion. There are several biodegradable materials which serve the purpose satisfactorily as described in the previous sections. Another application associated with the aerospace industry is the development of soundproof structures for passenger aircrafts. For unmanned vehicles, soundproofing is not essential. The concept of air taxi is also coming to be in effect in the very near future. Significant investments and research are being conducted in the area of urban air mobilities (Ward et al., 2021; Winter et al., 2020). Safe, quiet and efficient aircrafts will make the dream true (Scheff et al., 2020). Hybrid biocomposites are exhibiting the features favourable for such applications.

8 Conclusion

Hybrid biocomposites have shown great potential in aerospace applications. Conventional materials which are being used in such applications must be replaced necessarily with the hybrid biocomposites as far as environmental issues are

concerned. It requires the research to be shifted towards the development of such hybrid biocomposites having required properties. Such combination of the properties, which cannot be achieved in a single conventional material, can be achieved in a properly designed hybrid biocomposites. The addition of more solid fibre or composite filler typically increases the mechanical overall characteristics, which is evident. The effect is sometimes referred to as a positive hybrid effect for hybrid biocomposites. Likewise, a degrading impact is referred to as the negative hybrid effect for a certain characteristic since it is added to weak fibre or filler. On the other hand, the synthetic fibres are non-biologically degradable, offer certain dangers to health and are more expensive, heavier and non-recycling. The path forward will be the hybridization of polymer composites with natural or synthetic matrix strengthened by natural or synthetic reinforcements.

In the near future, great scope exists for the research and development in this direction. Biodegradable matrix, two or more reinforcement materials, their orientation and stacking sequence, etc. are important parameters and must be taken into consideration judiciously. Their proper selection tailors the characteristics of the composites making them suitable for aerospace application. The research described in this chapter demonstrates that hybrid biocomposites are very promising as alternative materials for developing environmentally friendly materials.

Acknowledgement The authors thank Aligarh Muslim University, India, and Universiti Putra Malaysia for providing the facilities to carry out this research with technical support in writing this chapter. They are grateful to Dr. R.A. Ilyas of UTM, Malaysia, for his guidance throughout the chapter. The authors also thank Dr. Mohd Shadab Khan of Integral University, India, for his advice and fruitful discussions.

References

- Ahmad Ilyas, R., Mohd Sapuan, S., Ibrahim, R., et al. (2019). Sugar palm (*Arenga pinnata* (Wurmb.) Merr) cellulosic fibre hierarchy: A comprehensive approach from macro to nano scale. *Journal of Materials Research and Technology*, 8, 2753–2766. <https://doi.org/10.1016/j.jmrt.2019.04.011>
- Ahmed, E. M., Aggor, F. S., Awad, A. M., & El-Aref, A. T. (2013). An innovative method for preparation of nanometal hydroxide superabsorbent hydrogel. *Carbohydrate Polymers*, 91, 693–698. <https://doi.org/10.1016/j.carbpol.2012.08.056>
- Aisyah, H. A., Paridah, M. T., Sapuan, S. M., et al. (2021). A comprehensive review on advanced sustainable woven natural fibre polymer composites. *Polymers (Basel)*, 13, 471. <https://doi.org/10.3390/polym13030471>
- Aiza Jaafar, C. N., Zainol, I., Ishak, N. S., et al. (2021). Effects of the liquid natural rubber (LNR) on mechanical properties and microstructure of epoxy/silica/kenaf hybrid composite for potential automotive applications. *Journal of Materials Research and Technology*, 12, 1026–1038. <https://doi.org/10.1016/j.jmrt.2021.03.020>
- Alsina, O. L. S., de Carvalho, L. H., Ramos Filho, F. G., & D’Almeida, J. R. M. (2005). Thermal properties of hybrid lignocellulosic fabric-reinforced polyester matrix composites. *Polymer Testing*, 24, 81–85. <https://doi.org/10.1016/j.polymertesting.2004.07.005>

- Alsubari, S., Zuhri, M. Y. M., Sapuan, S. M., et al. (2021). Potential of natural fiber reinforced polymer composites in sandwich structures: A review on its mechanical properties. *Polymers (Basel)*, *13*, 423. <https://doi.org/10.3390/polym13030423>
- Aslan, M., Tufan, M., & Küçükömeroğlu, T. (2018). Tribological and mechanical performance of sisal-filled waste carbon and glass fibre hybrid composites. *Composites: Part B*. <https://doi.org/10.1016/j.compositesb.2017.12.039>
- Athijayamani, A., Thiruchitrabalam, M., Manikandan, V., & Pazhanivel, B. (2010). Mechanical properties of natural fibers reinforced polyester hybrid composite. *International Journal of Plastics Technology*, *14*, 104–116. <https://doi.org/10.1007/s12588-009-0016-0>
- Atiqah, A., Jawaid, M., Ishak, M. R., & Sapuan, S. M. (2017). Moisture absorption and thickness swelling behaviour of sugar palm fibre reinforced thermoplastic polyurethane. *Procedia Engineering*, *184*, 581–586. <https://doi.org/10.1016/j.proeng.2017.04.142>
- Atiqah, A., Chandrasekar, M., Kumar, T. S. M., et al. (2019). *Characterization and interface of natural and synthetic hybrid composites characterization and interface of natural and synthetic hybrid composites*. Elsevier Ltd.
- Ayu, R. S., Khalina, A., Harmaen, A. S., et al. (2020). Characterization study of empty fruit bunch (EFB) fibers reinforcement in poly(butylene) succinate (PBS)/starch/glycerol composite sheet. *Polymers (Basel)*, *12*, 1571. <https://doi.org/10.3390/polym12071571>
- Bach, M. R., Chalivendra, V. B., Alves, C., & Depina, E. (2017). Mechanical characterization of natural biodegradable sandwich materials. *Journal of Sandwich Structures and Materials*, *19*, 482–496. <https://doi.org/10.1177/1099636215622143>
- Bahrami, M., Abenojar, J., & Martínez, M. Á. (2020). Recent progress in hybrid biocomposites: Mechanical properties, water absorption, and flame retardancy. *Materials (Basel)*, *13*, 5145. <https://doi.org/10.3390/ma13225145>
- Battegazzore, D., Abt, T., Maspoch, M. L., & Frache, A. (2019). Multilayer cotton fabric bio-composites based on PLA and PHB copolymer for industrial load carrying applications. *Composites. Part B, Engineering*, *163*, 761–768. <https://doi.org/10.1016/j.compositesb.2019.01.057>
- Bhatnagar A (2006) Lightweight ballistic composites: Military and law-enforcement applications.
- Birat, K., Panthapulakkal, S., Kronka, A., et al. (2015). Hybrid biocomposites with enhanced thermal and mechanical properties for structural applications. *Journal of Applied Polymer Science*, *132*. <https://doi.org/10.1002/app.42452>
- Boopalan, M., Niranjana, M., & Umapathy, M. J. (2013). Study on the mechanical properties and thermal properties of jute and banana fiber reinforced epoxy hybrid composites. *Composites. Part B, Engineering*, *51*, 54–57. <https://doi.org/10.1016/j.compositesb.2013.02.033>
- Boujmal, R., Kakou, C. A., Nekhlaoui, S., et al. (2018). Alfa fibers/clay hybrid composites based on polypropylene. *Journal of Thermoplastic Composite Materials*, *31*, 974–991. <https://doi.org/10.1177/0892705717729197>
- Cai, S., Yang, K., Xu, Y., et al. (2021). Structure and moisture effect on the mechanical behavior of a natural biocomposite, buffalo horn sheath. *Composites Communications*, *26*, 100748. <https://doi.org/10.1016/j.coco.2021.100748>
- Dhakar, H. N., Ismail, S. O., Ojo, S. O., et al. (2018). Abrasive water jet drilling of advanced sustainable bio-fibre-reinforced polymer/hybrid composites: A comprehensive analysis of machining-induced damage responses. *International Journal of Advanced Manufacturing Technology*, *99*, 2833–2847. <https://doi.org/10.1007/s00170-018-2670-x>
- Drzal, L. T., Mohanty, A. K., & Misra, M. (2013). Bio-composite materials as alternatives to petroleum-based composites for automotive applications. *Magnesium*, *40*, 1.3–1.2.
- Eichhorn, S. J., Dufresne, A., Aranguren, M., et al. (2010). Review: Current international research into cellulose nanofibres and nanocomposites. *Journal of Materials Science*, *45*, 1–33. <https://doi.org/10.1007/s10853-009-3874-0>
- Essabir, H., Jawaid, M., Quaiss, A., & Bouhfid, R. (2017). Mechanical and thermal properties of polypropylene reinforced with doum fiber: Impact of fibrillation. In M. Jawaid, S. Sapuan, & O. Allothman (Eds.), *Green biocomposites. Green energy and technology* (pp. 255–270). Springer.

- Faezipour, M., Shamsi, R., Ashori, A., et al. (2016). Hybrid composite using recycled polycarbonate/waste silk fibers and wood flour. *Polymer Composites*, 37, 1667–1673. <https://doi.org/10.1002/pc.23339>
- Fiore, V., Scalici, T., Sarasini, F., et al. (2017). Salt-fog spray aging of jute-basalt reinforced hybrid structures: Flexural and low velocity impact response. *Composites. Part B, Engineering*, 116, 99–112. <https://doi.org/10.1016/j.compositesb.2017.01.031>
- Gangil, B., Ranakoti, L., Verma, S., et al. (2020). Natural and synthetic fibers for hybrid composites. *Hybrid Fiber Compos Mater Manuf Process Eng*, 1–15.
- Gao, P. X., Ding, Y., & Wang, Z. L. (2003). Crystallographic orientation-aligned ZnO nanorods grown by a tin catalyst. *Nano Letters*, 3, 1315–1320. <https://doi.org/10.1021/nl034548q>
- Gonçalves, J. A. V., Campos, D. A. T., Oliveira, G., et al. (2014). Mechanical properties of epoxy resin based on granite stone powder from the Sergipe fold-and-thrust belt composites. *Materials Research*, 17, 878–887. <https://doi.org/10.1590/S1516-14392014005000100>
- Gupta, M., & Deep, V. (2019). Effect of water absorption and stacking sequences on the properties of hybrid sisal/glass fibre reinforced polyester composite. *Proceedings of the Institution of Mechanical Engineers, Part L*, 233, 2045–2056. <https://doi.org/10.1177/1464420718811867>
- Gupta, M. K., & Srivastava, R. K. (2016). A review on characterization of hybrid fibre reinforced polymer composite. *American Journal of Polymer Science & Engineering*, 4, 1–7.
- Halimatul, M. J., Sapuan, S. M., Jawaid, M., et al. (2019). Effect of sago starch and plasticizer content on the properties of thermoplastic films: Mechanical testing and cyclic soaking-drying. *Polimery*, 64, 32–41. <https://doi.org/10.14314/polimery.2019.6.5>
- Idicula, M., Malhotra, S. K., Joseph, K., & Thomas, S. (2005). Dynamic mechanical analysis of randomly oriented intimately mixed short banana/sisal hybrid fibre reinforced polyester composites. *Composites Science and Technology*, 65, 1077–1087. <https://doi.org/10.1016/j.compscitech.2004.10.023>
- Idicula, M., Boudenne, A., Umadevi, L., et al. (2006). Thermophysical properties of natural fibre reinforced polyester composites. *Composites Science and Technology*, 66, 2719–2725.
- Ilyas, R. A., Sapuan, S. M., & Ishak, M. R. (2018). Isolation and characterization of nanocrystalline cellulose from sugar palm fibres (Arenga Pinnata). *Carbohydrate Polymers*, 181, 1038–1051. <https://doi.org/10.1016/j.carbpol.2017.11.045>
- Ilyas, R. A., Sapuan, S. M., Ibrahim, R., et al. (2019a). Effect of sugar palm nanofibrillated cellulose concentrations on morphological, mechanical and physical properties of biodegradable films based on agro-waste sugar palm (Arenga pinnata(Wurmb.) Merr) starch. *Journal of Materials Research and Technology*, 8, 4819–4830. <https://doi.org/10.1016/j.jmrt.2019.08.028>
- Ilyas, R. A., Sapuan, S. M., Ishak, M. R., & Zainudin, E. S. (2019b). Sugar palm nanofibrillated cellulose (Arenga pinnata (Wurmb.) Merr): Effect of cycles on their yield, physic-chemical, morphological and thermal behavior. *International Journal of Biological Macromolecules*, 123, 379–388. <https://doi.org/10.1016/j.ijbiomac.2018.11.124>
- Ilyas, R. A., Sapuan, S. M., Atiqah, A., et al. (2020a). Sugar palm (Arenga pinnata [Wurmb.] Merr) starch films containing sugar palm nanofibrillated cellulose as reinforcement: Water barrier properties. *Polymer Composites*, 41, 459–467. <https://doi.org/10.1002/pc.25379>
- Ilyas, R. A., Sapuan, S. M., Ibrahim, R., et al. (2020b). Thermal, biodegradability and water barrier properties of bio-nanocomposites based on plasticised sugar palm starch and nanofibrillated celluloses from sugar palm fibres. *Journal of Biobased Materials and Bioenergy*, 14, 234–248. <https://doi.org/10.1166/jbmb.2020.1951>
- Ilyas, R. A., Sapuan, S. M., Harussani, M. M., et al. (2021). Polylactic acid (PLA) biocomposite: Processing, additive manufacturing and advanced applications. *Polymers (Basel)*, 13, 1326. <https://doi.org/10.3390/polym13081326>
- Ishak, Z. A. M., Aminullah, A., Ismail, H., & Rozman, H. D. (1998). Effect of silane-based coupling agents and acrylic acid based compatibilizers on mechanical properties of oil palm empty fruit bunch filled high-density polyethylene composites. *Journal of Applied Polymer Science*, 68, 2189–2203. [https://doi.org/10.1002/\(SICI\)1097-4628\(19980627\)68:13<2189::AID-APP16>3.0.CO;2-V](https://doi.org/10.1002/(SICI)1097-4628(19980627)68:13<2189::AID-APP16>3.0.CO;2-V)

- Jacob, M., Varughese, K. T., & Thomas, S. (2006). Dielectric characteristics of sisal–oil palm hybrid biofibre reinforced natural rubber biocomposites. *Journal of Materials Science*, 41, 5538–5547. <https://doi.org/10.1007/s10853-006-0298-y>
- Jawaid, M., & Abdul Khalil, H. P. S. (2011). Cellulosic/synthetic fibre reinforced polymer hybrid composites: A review. *Carbohydrate Polymers*, 86, 1–18. <https://doi.org/10.1016/j.carbpol.2011.04.043>
- Jawaid, M., & Thariq, M. (2018). *Sustainable composites for aerospace applications*. Elsevier.
- Jawaid, M., Abdul Khalil, H. P. S., Hassan, A., et al. (2013). Effect of jute fibre loading on tensile and dynamic mechanical properties of oil palm epoxy composites. *Composites. Part B, Engineering*, 45, 619–624. <https://doi.org/10.1016/j.compositesb.2012.04.068>
- Jumaidin, R., Khiruddin, M. A. A., Asyul Sutan Saidi, Z., et al. (2020). Effect of cogon grass fibre on the thermal, mechanical and biodegradation properties of thermoplastic cassava starch biocomposite. *International Journal of Biological Macromolecules*, 146, 746–755. <https://doi.org/10.1016/j.ijbiomac.2019.11.011>
- Jumaidin, R., Diah, N. A., Ilyas, R. A., et al. (2021). Processing and characterisation of banana leaf fibre reinforced thermoplastic cassava starch composites. *Polymers (Basel)*, 13, 1420. <https://doi.org/10.3390/polym13091420>
- Kadem, S., Irinislimane, R., & Belhaneche-Bensemra, N. (2018). Novel biocomposites based on sunflower oil and alfa fibers as renewable resources. *Journal of Polymers and the Environment*, 26, 3086–3096. <https://doi.org/10.1007/s10924-018-1196-5>
- Kumar, T. S. M., Chandrasekar, M., Senthilkumar, K., et al. (2020). Characterization, thermal and antimicrobial properties of hybrid cellulose nanocomposite films with in-situ generated copper nanoparticles in tamarindus indica nut powder. *Journal of Polymers and the Environment*, 1–10. <https://doi.org/10.1007/s10924-020-01939-w>
- Kwon, H.-J., Sunthornvarabhas, J., Park, J.-W., et al. (2014). Tensile properties of kenaf fiber and corn husk flour reinforced poly(lactic acid) hybrid bio-composites: Role of aspect ratio of natural fibers. *Composites. Part B, Engineering*, 56, 232–237. <https://doi.org/10.1016/j.compositesb.2013.08.003>
- Leman, Z., Sapuan, S. M., Azwan, M., et al. (2008). The effect of environmental treatments on fiber surface properties and tensile strength of sugar palm fiber-reinforced epoxy composites. *Polymer - Plastics Technology and Engineering*, 47, 606–612. <https://doi.org/10.1080/03602550802059451>
- Manyatshe, A., Balogun, M. O., Nkambule, T. T. I., et al. (2020). Chemical modification of sugarcane bagasse with chitosan for the removal of phosphates in aqueous solution. *AIP Conference Proceedings*, 2289. <https://doi.org/10.1063/5.0028378>
- Mohd Nurazzi, N., Khalina, A., Sapuan, S. M., & Ilyas, R. A. (2019). Mechanical properties of sugar palm yarn/woven glass fiber reinforced unsaturated polyester composites: Effect of fiber loadings and alkaline treatment. *Polimery/Polymers*, 64, 665. <https://doi.org/10.14314/polimery.2019.10.3>
- Narnaware, P. H., Surose, R. G., & Gaikwad, S. V. (2015). Current status and the future potentials of renewable energy in India-A review. *International Journal on Advanced Science, Engineering and Information Technology*, 2321–9009.
- Nisini, E., Santulli, C., & Liverani, A. (2017). Mechanical and impact characterization of hybrid composite laminates with carbon, basalt and flax fibres. *Composites. Part B, Engineering*, 127, 92–99. <https://doi.org/10.1016/j.compositesb.2016.06.071>
- Nunna, S., Chandra, P. R., Shrivastava, S., & Jalan, A. K. (2012). A review on mechanical behavior of natural fiber based hybrid composites. *Journal of Reinforced Plastics and Composites*, 31, 759–769.
- Nurazzi, N. M., Khalina, A., Sapuan, S. M., et al. (2019). Thermal properties of treated sugar palm yarn/glass fiber reinforced unsaturated polyester hybrid composites. *Journal of Materials Research and Technology*. <https://doi.org/10.1016/j.jmrt.2019.11.086>
- Nurazzi, N. M., Khalina, A., Sapuan, S. M., et al. (2020). Thermal properties of treated sugar palm yarn/glass fiber reinforced unsaturated polyester hybrid composites. *Journal of Materials Research and Technology*, 9, 1606–1618. <https://doi.org/10.1016/j.jmrt.2019.11.086>

- Nurazzi, N. M., Asyraf, M. R. M., Khalina, A., et al. (2021). A review on natural fiber reinforced polymer composite for bullet proof and ballistic applications. *Polymers (Basel)*, *13*, 646. <https://doi.org/10.3390/polym13040646>
- Omran, A. A. B., Mohammed, A. A. B. A., Sapuan, S. M., et al. (2021). Micro- and nanocellulose in polymer composite materials: A review. *Polymers (Basel)*, *13*, 231. <https://doi.org/10.3390/polym13020231>
- Otto, G. P., Moisés, M. P., Carvalho, G., et al. (2017). Mechanical properties of a polyurethane hybrid composite with natural lignocellulosic fibers. *Composites. Part B, Engineering*, *110*, 459–465. <https://doi.org/10.1016/j.compositesb.2016.11.035>
- Papa, I., Ricciardi, M., Antonucci, V., et al. (2020). Comparison between different non-destructive techniques methods to detect and characterize impact damage on composite laminates. *Journal of Composite Materials*, *54*, 617–631. <https://doi.org/10.1177/0021998319864411>
- Petrucci, R., Santulli, C., Puglia, D., et al. (2015). Impact and post-impact damage characterisation of hybrid composite laminates based on basalt fibres in combination with flax, hemp and glass fibres manufactured by vacuum infusion. *Composites. Part B, Engineering*, *69*, 507–515. <https://doi.org/10.1016/j.compositesb.2014.10.031>
- Prabhakaran, S., Krishnaraj, V., Kumar, M. S., & Zitoune, R. (2014). Sound and vibration damping properties of flax fiber reinforced composites. *Procedia Engineering*, *97*, 573–581. <https://doi.org/10.1016/j.proeng.2014.12.285>
- Pradhan, S., & Acharya, S. K. (2021). Solid particle erosive wear behaviour of Eulaliopsis binata fiber reinforced epoxy composite. *Proceedings of the Institution of Mechanical Engineers, Part J*, *235*, 830–841. <https://doi.org/10.1177/1350650120931645>
- Punia Bangar, S., Nehra, M., Siroha, A. K., et al. (2021). Development and characterization of physical modified pearl millet starch-based films. *Food*, *10*, 1609. <https://doi.org/10.3390/foods10071609>
- Quaiss, A., Bouhfid, R., & Essabir, H. (2015). Effect of processing conditions on the mechanical and morphological properties of composites reinforced by natural fibres. In *Manufacturing of natural fibre reinforced polymer composites* (pp. 177–197). Springer International Publishing.
- Raghavendra, G., Ojha, S., Acharya, S. K., & Pal, S. K. (2016). A comparative analysis of woven jute/glass hybrid polymer composite with and without reinforcing of fly ash particles. *Polymer Composites*, *37*, 658–665. <https://doi.org/10.1002/pc.23222>
- Raj, F. M., Nagarajan, V. A., & Elsi, S. S. (2017). Mechanical, physical and dynamical properties of glass fiber and waste fishnet hybrid composites. *Polymer Bulletin*, *74*, 1441–1460. <https://doi.org/10.1007/s00289-016-1783-3>
- Rajesh, M., Singh, S. P., & Pitchaimani, J. (2018). Mechanical behavior of woven natural fiber fabric composites: Effect of weaving architecture, intra-ply hybridization and stacking sequence of fabrics. *Journal of Industrial Textiles*, *47*, 938–959. <https://doi.org/10.1177/1528083716679157>
- Ramesh, M., Palanikumar, K., & Reddy, K. H. (2013). Comparative evaluation on properties of hybrid glass fiber-sisal/jute reinforced epoxy composites. *Procedia Engineering*, *51*, 745–750. <https://doi.org/10.1016/j.proeng.2013.01.106>
- Ravandi, M., Kureemun, U., Banu, M., et al. (2019). Effect of interlayer carbon fiber dispersion on the low-velocity impact performance of woven flax-carbon hybrid composites. *Journal of Composite Materials*, *53*, 1717–1734. <https://doi.org/10.1177/0021998318808355>
- Reddy, N. (2019). Composites from coir fibers. In *Sustainable applications of coir and other coconut by-products* (pp. 141–185). Springer International Publishing.
- Ridzuan, M. J. M., Majid, M. S. A., Afendi, M., et al. (2017). Effect of elevated temperature on the tensile strength of Napier/glass-epoxy hybrid reinforced composites. *AIP Conference Proceedings*, *1902*, 020062.
- Rout, J., Misra, M., Tripathy, S. S., et al. (2001). The influence of fibre treatment on the performance of coir-polyester composites. *Composites Science and Technology*, *61*, 1303–1310. [https://doi.org/10.1016/S0266-3538\(01\)00021-5](https://doi.org/10.1016/S0266-3538(01)00021-5)
- Rozilah, A., Jaafar, C. N. A., Sapuan, S. M., et al. (2020). The effects of silver nanoparticles compositions on the mechanical, physiochemical, antibacterial, and morphology properties of sugar palm starch biocomposites for antibacterial coating. *Polymers (Basel)*, *12*, 2605. <https://doi.org/10.3390/polym12112605>

- Rozman, H. D., Shannon-Ong, S. H., Azizah, A. B., & Tay, G. S. (2013). Preliminary study of non-woven composite: Effect of needle punching and kenaf fiber loadings on non-woven thermoplastic composites prepared from Kenaf and Polypropylene Fiber. *Journal of Polymers and the Environment*, 21, 1032–1039. <https://doi.org/10.1007/s10924-013-0599-6>
- Samanta, S., Muralidhar, M., Singh, T. J., & Sarkar, S. (2015). Characterization of mechanical properties of hybrid Bamboo/GFRP and Jute/GFRP composites. *Materials Today: Proceedings*, 2, 1398–1405. <https://doi.org/10.1016/j.matpr.2015.07.059>
- Sanjay, M. R., & Yogesha, B. (2016). Studies on mechanical properties of jute/E-glass fiber reinforced epoxy hybrid composites. *Journal of Minerals and Materials Characterization and Engineering*, 04, 15–25. <https://doi.org/10.4236/jmmce.2016.41002>
- Sanjay, M., & Yogesha, B. (2018). Studies on hybridization effect of jute/kenaf/E-glass woven fabric epoxy composites for potential applications: Effect of laminate stacking sequences. *Journal of Industrial Textiles*, 47, 1830–1848. <https://doi.org/10.1177/1528083717710713>
- Sanjay, M. R., Madhu, P., Jawaid, M., et al. (2017). Characterization and properties of natural fiber polymer composites: A comprehensive review. *Journal of Cleaner Production*, 172, 566–581. <https://doi.org/10.1016/j.jclepro.2017.10.101>
- Santulli, C. (2007). Impact properties of glass/plant fibre hybrid laminates. *Journal of Materials Science*, 42, 3699–3707. <https://doi.org/10.1007/s10853-006-0662-y>
- Santulli, C., Janssen, M., & Jeronimidis, G. (2005). Partial replacement of E-glass fibers with flax fibers in composites and effect on falling weight impact performance. *Journal of Materials Science*, 40, 3581–3585. <https://doi.org/10.1007/s10853-005-2882-y>
- Sapuan, S. M., & Ilyas, R. A. (2018). Characterization of sugar palm nanocellulose and its potential for reinforcement with a starch-based composite. *Sugar Palm Biofibers, Biopolym Biocomposites*, 189–220. <https://doi.org/10.1201/9780429443923-10>
- Sapuan, S. M., Sahari, J., Ishak, M. R., & Sanyang, M. L. (2019). *Sugar palm biofibers, biopolymers, and biocomposites*. First. CRC Press (Taylor & Francis Group)LLC.
- Sathishkumar, T., Naveen, J., Navaneethkrishnan, P., et al. (2017). Characterization of sisal/cotton fibre woven mat reinforced polymer hybrid composites. *Journal of Industrial Textiles*, 47, 429–452. <https://doi.org/10.1177/1528083716648764>
- Saw, S. K., Sarkhel, G., & Choudhury, A. (2011). Dynamic mechanical analysis of randomly oriented short bagasse/coir hybrid fibre-reinforced epoxy novolac composites. *Fibers and Polymers*, 12, 506–513. <https://doi.org/10.1007/s12221-011-0506-5>
- Saxena, M., & Gupta, M. (2019). Mechanical, thermal, and water absorption properties of hybrid wood composites. *Proceedings of the Institution of Mechanical Engineers, Part L*, 233, 1914–1922. <https://doi.org/10.1177/1464420718798661>
- Scheff, S., Friedman-Berg, F., Shively, J., & Carter, A. (2020). Human factors challenges in urban air mobility. *Proceedings of the Human Factors and Ergonomics Society Annual Meeting*, 64, 179–182. <https://doi.org/10.1177/1071181320641044>
- Shahzad, A., & Nasir, S. U. (2017). Mechanical properties of natural fiber/synthetic fiber reinforced polymer hybrid composites. In M. Jawaid, S. Sapuan, & O. Allothman (Eds.), *Green biocomposites. Green energy and technology* (pp. 355–396). Springer.
- Silva, L., Panzera, T., Velloso, V., et al. (2013). Statistical design of polymeric composites reinforced with banana fibres and silica microparticles. *Journal of Composite Materials*, 47, 1199–1210. <https://doi.org/10.1177/0021998312446499>
- Singh, V. K., & Mukhopadhyay, S. (2020). Hybrid biocomposites. *Indian Journal of Fibre & Textile Research*, 45, 224–246.
- Sivakumar, D., Ng, L. F., Lau, S. M., & Lim, K. T. (2018). Fatigue life behaviour of Glass/Kenaf woven-ply polymer hybrid biocomposites. *Journal of Polymers and the Environment*, 26, 499–507. <https://doi.org/10.1007/s10924-017-0970-0>
- Sreekumar, P. A., Agoudjil, B., Boudenne, A., et al. (2012). Transport properties of polyester composite reinforced with treated sisal fibers. *Journal of Reinforced Plastics and Composites*, 31, 117–127. <https://doi.org/10.1177/0731684411431971>
- Suriani, M., Sapuan, S., Ruzaidi, C., et al. (2021a). Flammability, morphological and mechanical properties of sugar palm fiber/polyester yarn-reinforced epoxy hybrid biocomposites with magnesium hydroxide flame retardant filler. *Textile Research Journal*, 004051752110086. <https://doi.org/10.1177/00405175211008615>

- Suriani, M. J., Radzi, F. S. M., Ilyas, R. A., et al. (2021b). Flammability, tensile, and morphological properties of oil palm empty fruit bunches fiber/pet yarn-reinforced epoxy fire retardant hybrid polymer composites. *Polymers (Basel)*, *13*, 1282. <https://doi.org/10.3390/polym13081282>
- Suriani, M. J., Rapi, H. Z., Ilyas, R. A., et al. (2021c). Delamination and manufacturing defects in natural fiber-reinforced hybrid composite: A review. *Polymers (Basel)*, *13*, 1323. <https://doi.org/10.3390/polym13081323>
- Suriani, M. J., Zainudin, H. A., Ilyas, R. A., et al. (2021d). Kenaf fiber/pet yarn reinforced epoxy hybrid polymer composites: Morphological, tensile, and flammability properties. *Polymers (Basel)*, *13*, 1532. <https://doi.org/10.3390/polym13091532>
- Swolfs, Y., McMeeking, R. M., Verpoest, I., & Gorbatikh, L. (2015). The effect of fibre dispersion on initial failure strain and cluster development in unidirectional carbon/glass hybrid composites. *Composites. Part A, Applied Science and Manufacturing*, *69*, 279–287. <https://doi.org/10.1016/j.compositesa.2014.12.001>
- Syafiq, R., Sapuan, S. M., Zuhri, M. Y. M., et al. (2020). Antimicrobial activities of starch-based biopolymers and biocomposites incorporated with plant essential oils: A review. *Polymers (Basel)*, *12*, 2403. <https://doi.org/10.3390/polym12102403>
- Vijaya Ramnath, B., Sharavanan, R., Chandrasekaran, M., et al. (2015). Experimental determination of mechanical properties of banana jute hybrid composite. *Fibers and Polymers*, *16*, 164–172. <https://doi.org/10.1007/s12221-015-0164-0>
- Ward, K. A., Winter, S. R., Cross, D. S., et al. (2021). Safety systems, culture, and willingness to fly in autonomous air taxis: A multi-study and mediation analysis. *Journal of Air Transport Management*, *91*, 101975. <https://doi.org/10.1016/j.jairtraman.2020.101975>
- Winter, S. R., Rice, S., & Lamb, T. L. (2020). A prediction model of Consumer's willingness to fly in autonomous air taxis. *Journal of Air Transport Management*, *89*, 101926. <https://doi.org/10.1016/j.jairtraman.2020.101926>
- Yahaya, R., Sapuan, S. M., Jawaid, M., et al. (2017). Review of kenaf reinforced hybrid biocomposites: Potential in defence applications. *Current Analytical Chemistry*, *14*, 226–240. <https://doi.org/10.2174/1573411013666171113150225>
- Yantaboot, K., & Amornsakchai, T. (2017). Effect of preparation methods and carbon black distribution on mechanical properties of short pineapple leaf fiber-carbon black reinforced natural rubber hybrid composites. *Polymer Testing*, *61*, 223–228. <https://doi.org/10.1016/j.polymertesting.2017.05.026>
- Yao, J., Hu, Y., & Lu, W. (2012). Performance research on coir fiber and wood debris hybrid boards. *BioResources*, *7*, 4262–4272.
- Zhang, X., Xiong, R., Kang, S., et al. (2020). Alternating stacking of nanocrystals and nanofibers into ultrastrong chiral biocomposite laminates. *ACS Nano*, *14*, 14675–14685. <https://doi.org/10.1021/acsnano.0c06192>
- Živković, I., Fragassa, C., Pavlović, A., & Brugo, T. (2017). Influence of moisture absorption on the impact properties of flax, basalt and hybrid flax/basalt fiber reinforced green composites. *Composites. Part B, Engineering*, *111*, 148–164. <https://doi.org/10.1016/j.compositesb.2016.12.018>

Chapter 7

Resin-Injection Repair of Damaged Composites in Aerostructures: Finite Element Modelling of the Effects of Vent Holes in Carbon Fibre-Reinforced Composite Laminates



Z. Y. D. Lim, W. L. Lai, H. Saeedipour, and K. L. Goh

1 Introduction

1.1 Composites

A composite material is created by physically merging two or more materials. The resulting material may create superior structural properties than those by the individual materials (Katnam et al., 2013; Agarwal & Broutman, 2015). The individual materials used for creating the new composite material locally retain its own properties (Campbell, 2010; Katnam et al., 2013). Generally, composite materials constitute two material phases; they are (1) the reinforcement phase and (2) the matrix phase (Agarwal & Broutman, 2015). The reinforcement materials in the form of fibres or particles are spatially bound by the matrix materials to form composites. The composite material properties depend on the (1) materials of the reinforcement and the matrix, (2) distribution of the reinforcement in the matrix, and (3) interaction between the reinforcement and matrix materials (Agarwal & Broutman, 2015).

Z. Y. D. Lim · W. L. Lai · K. L. Goh (✉)

Faculty of Science, Agriculture and Engineering, Newcastle University, Newcastle, UK

NUIS, Newcastle University in Singapore, Singapore, Singapore

e-mail: kheng-lim.goh@ncl.ac.uk

H. Saeedipour

Republic Polytechnic, Singapore, Singapore

1.2 *Fibres*

Our research focused on fibre-polymer composite materials. The fibres can be categorised into continuous or discontinuous fibres. The continuous fibres have high aspect ratios (length to diameter ratio), while the discontinuous fibres have small aspect ratios (Campbell, 2010; Agarwal & Broutman, 2015). Figure 7.1 shows the alignment of the continuous fibres that can be in (a) unidirectional, (b) woven, and (c) roving arrangements (Campbell, 2010, Agarwal & Broutman, 2015). Depending on the design of the composite material, the continuous fibres embedded in the matrix can be fabricated into laminates (Agarwal & Broutman, 2015). The alignment of the discontinuous fibres is random either in the form of (d) chopped or (e) mat (Campbell, 2010; Agarwal & Broutman, 2015; Goh, 2017). The discontinuous fibres can be embedded or suspended in the matrix (Campbell, 2010; Agarwal & Broutman, 2015; Goh, 2017).

1.3 *Laminates*

A single lamina or ply can be stacked to form a laminate (Campbell, 2010; Aisyah et al., 2021). Figure 7.2(a) shows a schematic of several unidirectional lamina layups in the same fibre directions (0°) to create a unidirectional laminate (Campbell, 2010). Generally, a unidirectional laminate is strong and stiff along the fibre direction (0°) but weak in the transverse direction (90°); therefore, it is important that the matrix alone can carry loads in the transverse direction (Campbell, 2010). Typically, the tensile strength of the matrix is lower than that of a fibre (Campbell, 2010; Agarwal & Broutman, 2015; Alsubari et al., 2021). In order to enhance the laminate's mechanical properties, the lamina can be orientated and stacked up at different angles (Campbell, 2010; Agarwal & Broutman, 2015). Figure 7.2(b) shows a schematic of the quasi-isotropic layup to create a laminate. The lamina layup is

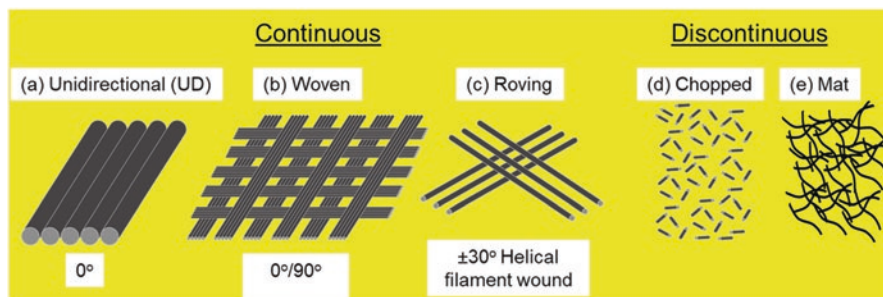


Fig. 7.1 Continuous and discontinuous fibres to be embedded into matrix to form composite materials (Campbell, 2010). The continuous fibres can be aligned in (a) unidirectional, (b) woven, and (c) roving. The discontinuous fibres can be in the form of chopped and mat

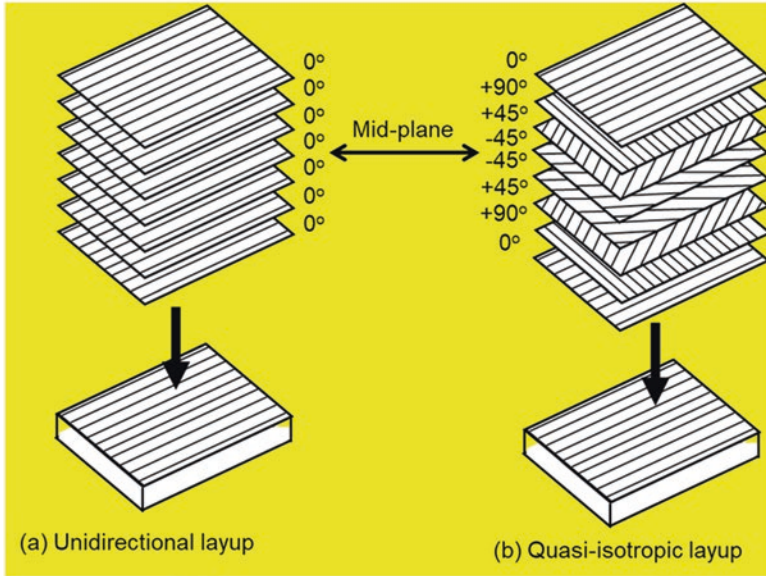


Fig. 7.2 Different layup to create laminates (Campbell, 2010). (a) Unidirectional layup where the unidirectional lamina was stacked up in the same orientation. (b) Quasi-isotropic layup where the unidirectional lamina was stacked up in different orientations

different in fibre orientation (in the sequence of 0° , 90° , $+45^\circ$, -45°) and the orientation of the lamina is mirrored at the mid-plane of the laminate thickness. The different fibre orientation of the lamina allows load distribution along the fibre direction in a laminate (Campbell, 2010; Agarwal & Broutman, 2015; Aisyah et al., 2021).

1.4 Fundamental Relationship of the Laminate Properties

The rule of mixture can be used to estimate the longitudinal modulus (E_{11}) and longitudinal tensile strength (σ_{11}) when the applied load is parallel to the direction of the fibres (0°) (see Fig. 7.2(a)) (Campbell, 2010). The longitudinal modulus can then be expressed as:

$$E_{11} = E_f V_f + E_m V_m \tag{7.1}$$

where E_f is the fibre stiffness, V_f is the volume fraction of the fibre, E_m is the matrix stiffness, and V_m is the volume fraction of the matrix.

The composite strength σ_{11} can be estimated using the rule of mixture expressed as:

$$\sigma_{11} = \sigma_f V_f + \sigma_m V_m \tag{7.2}$$

where σ_f and σ_m are the fibre and matrix strength of the laminate, respectively.

To determine the transverse laminate properties, namely, the transverse modulus (E_{22}) (90° to the fibre direction), Poisson's ratio (ν_{12}), and shear modulus (G_{12}) by using the rule of mixture (Campbell, 2010), the equations can be expressed as:

$$\frac{1}{E_{22}} = \frac{V_f}{E_f} + \frac{V_m}{E_m} \quad (7.3)$$

$$\nu_{12} = \nu_f V_f + \nu_m V_m \quad (7.4)$$

$$\frac{1}{G_{12}} = \frac{V_f}{G_f} + \frac{V_m}{G_m} \quad (7.5)$$

The classical lamination theory (CLT) was used to derive the stress and strain in composite laminates (Agarwal & Broutman, 2015). The ABD stiffness matrix (Eq. 7.6) was used to characterise the mechanical behaviour of the laminates by correlating the cross-sectional loads and moments to the mid-plane strains and curvature of the laminates (Agarwal & Broutman, 2015). The extensional stiffness matrix [A] relates the resultant forces to the strain at the mid-plane of the laminate. The bending stiffness matrix [D] relates the resultant moments to the plate curvature at the mid-plane of the laminates. The coupling stiffness matrix in the plate constitutive equation signifies coupling between the extension and bending of the laminate. As the laminate experiences in-plane deformation that leads to mid-plane strain, it not only results in normal and shear forces but also twisting and bending.

$$ABD = \begin{bmatrix} A & B \\ B & D \end{bmatrix} \quad (7.6)$$

1.5 Impact Damage

Carbon fibre-reinforced polymer (CFRP) composites have been heavily utilised for many aircraft structural applications (viz. radome, fuselage, cowling, wings, fairings, and others) (Dodt, 2011). However, when in service, the CFRP aerostructures are prone to damage resulting from impact by foreign object debris (e.g. tool drop during maintenance, kick-up of stones during taxiing of aircraft or moving off from runway) or environmental conditions (e.g. hailstorm) (Cantwell & Morton, 1991; Katnam et al., 2013). The types of damage can be classified by the speed of the projectile or object impacting the composite structure. They are low-velocity (1–10 m/s), medium-velocity (11–50 m/s), high-velocity (51–2000 m/s), and hyper-velocity (2001–5000 m/s) impact damage (Cantwell & Morton, 1991; Safri et al., 2014). Generally, the mechanical properties of a composite structure are degraded when damage occurs (Sohn et al., 2000), resulting in the reduction of the structural

mechanical properties that may not be able to bear the structural loads under operating conditions and compromise the safety of the user (Sohn et al., 2000).

Our research focuses on low-velocity impact damage (LVID). The damaged structure of LVID was hidden in the CFRP structure, therefore also known as barely visible impact damage (BVID) (Tarpani et al., 2006). Recent research found that BVID in CFRP laminates features several types of failure modes, namely, delamination between ply, fibre fracture, fibre pull-out, matrix cracks, and transverse shear failure in the fibres and matrix (Lai et al., 2020, 2021b; Lai, 2021). The structural failure mechanism could potentially affect the mechanical properties of the CFRP laminates and also affect the material characteristics being able to regulate the transfer of stress from the bulk to the fibre level (Goh, 2017).

1.6 Repair Method

The Federal Aviation Administration (FAA) and aircraft manufacturers (viz. Airbus and Boeing) have prescribed several repair methods to repair the damaged structures back to their original conditions (B787-81205-Z0210-00, 2012; FAA-H-8083-31, 2012). Before repair, the damaged structures were assessed using non-destructive testing (NDT) methods (e.g. ultrasonic testing and infrared thermography). The purpose of NDT is to evaluate whether the size of the damage is within the acceptable damage tolerance for repair as specified by the FAA and the aircraft manufacturers (Poudel et al., 2015). Of note, the aircraft maintenance, repair, and overhaul (MRO) centres preferred to repair the damaged structures because scrapping and replacing the damaged parts are costly for the MRO centres and the airlines (Poudel et al., 2015).

A repair method known as resin injection was prescribed by the FAA and the aircraft manufacturers to repair the BVID-type damage (B787-81205-Z0210-00, 2012, FAA-H-8083-31, 2012). The resin-injection method is an ideal solution to be used for repairing BVID-type damage, as other repair techniques (viz. patch, scarf, and stepped method) require higher material use for creating a new patch and higher labour cost to prep for the repair due to the precise machining needs (Katnam et al., 2013; Slattery et al., 2016).

The resin-injection method requires drilling of several holes within the BVID sites of the CFRP laminates, followed by injecting the resins into the damaged sites (Thunga et al., 2014; Lai et al., 2017; Saeedipour et al., 2017; Rahman et al., 2019; Lai, 2021). A resin-injection hole (RH) is created at the centre of the BVID site for introducing adhesive into the crack network, and four to six vent holes (VHs) were created at the periphery within the BVID for driving air and debris out of the crack network from the VHs (Thunga et al., 2014; Lai et al., 2020, 2021b). However, creating holes by mechanical drilling removed useful materials that could result in a decrease in material strength (Soutis et al., 1991; Lai et al., 2020, 2021b; Lai, 2021).

This study focuses on assessing the effects on the mechanical behaviour of 24-ply CFRP laminates with different numbers of VHs (viz. 4, 5, and 6) by finite

element analysis (FEA). The CFRP laminates with different hole setups were subjected to in-plane compression load, and the results of the stress-field pattern were compared to the pristine CFRP laminates with no holes.

2 Finite Element Analysis

A full-size FEA model of a rectangular 24-ply CFRP laminate has been developed in ANSYS following the specifications listed in Table 7.1. The connections between one lamina to another were predefined as bonded. The model was meshed with quadratic tetrahedral elements. The FEA models were solved using a software (ANSYS Mechanical).

The boundary conditions applied to the CFRP laminate model were derived based on the in-plane compression testing (Fig. 7.3(a)) that was employed in an experimental study (Lai et al., 2020, 2021b). The three types of boundary conditions have been set up for the FEA model (Fig. 7.3(b)); they are (1) fixed support at the base of the CFRP laminates, (2) frictionless support at the two long edges (sides) of the CFRP laminates, and (3) load applied (~100 kN of load to fracture the pristine CFRP laminate that was derived from experimental testing) on the top of the CFRP laminates.

Figure 7.3(c) shows the schematics of the different hole setups in the CFRP laminates, which include (1) no hole, (2) one RH, and (3) one RH with different numbers of VHs (n_{VH}), namely, 4, 5, and 6 VHs. For the position of RH, the hole was placed at the centre of the CFRP laminates. To determine the position of the VHs, the RH-to-VH distance was set to 25 mm, and the orientation of VHs was set to $360^\circ/n_{\text{VH}}$ which was equally spaced around the periphery of a 50-mm-diameter circle. The RH-to-VH distance was set to mimic the BVID size of 50 mm diameter in the CFRP laminates after impact damage (Lai et al., 2020, 2021b; Lai, 2021). The placement of holes (RH and VHs) was typically arranged for resin-injection repair procedures derived from several literatures (Thunga et al., 2014; Slattery et al.,

Table 7.1 Specifications of the CFRP laminates

Specifications	Descriptions
Number of plies	24
Laminate size	160 mm (length) \times 100 mm (width) \times 4 mm (thickness)
Laminate layup	Quasi-isotropic
Stacking sequence and ply orientations	WF, +45, -45, 90, 0, +45, -45, 90, 0, +45, -45, 90 // 90, -45, +45, 0, 90, -45, +45, 0, 90, -45, +45, WF
First and last ply	3 K twill carbon fibre prepreg, 300 gsm, model 3KTX300
Inter-ply	12 K uni-directional carbon fibre prepreg, 150 gsm, model UDX150
Laminate properties	$E_{11} = 16.53$ GPa; $E_{22} = 9.73$ GPa $\nu_{12} = 0.188$ $G_{12} = 5.28$ GPa

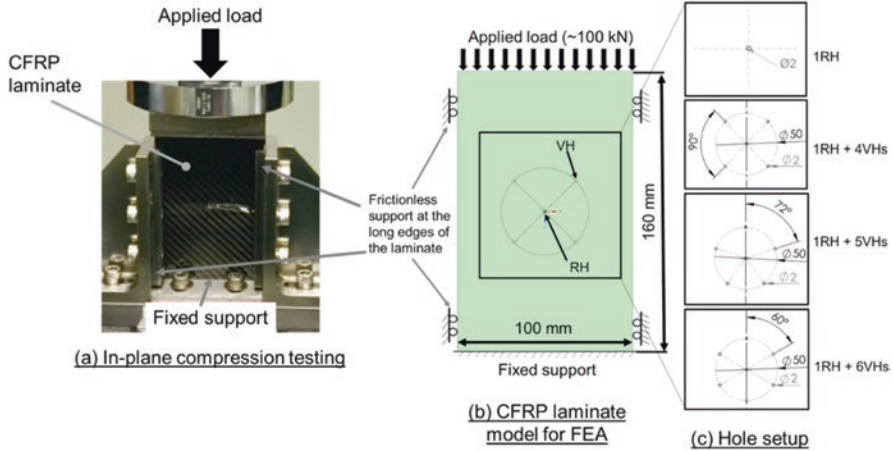


Fig. 7.3 FEA model of the CFRP laminate. (a) The boundary conditions were derived based on in-plane compression testing that was conducted in an experimental study. (b) Schematic of the FEA model showing the boundary conditions applied, with reference to the in-plane compression testing. Fixed support was applied to the base of the laminate. Frictionless support was applied to the two long sides of the laminate. A load of 100 kN was applied on the top of the laminate. (c) Hole setup in the CFRP laminate (Lai et al., 2020, 2021b)

2016; Lai et al., 2020, 2021b). All circular holes were created at 2 mm diameter, through the thickness of the laminate (open/through hole).

3 Results

The stress patterns (Figs. 7.4, 7.5, 7.6, 7.7, and 7.8) on the CFRP laminate with different hole setups were derived using the FEA. The different hole setups in the CFRP laminates include (a) no hole, (b) 1 RH, (c) 1 RH and 4 VHs, (d) 1 RH and 5 VHs, and (e) 1 RH and 6 VHs. The FEA model has successfully meshed with quadratic tetrahedral mesh and its sizes were refined around the hole (fine mesh), resulting in approximately seven million elements and 15 million nodes.

The images in the figures show the stress pattern in the (1) CFRP laminates, (2) magnified view of all the holes, (3) magnified view of the stress pattern around the RH, and (4) cross-sectional view of the RH revealing stresses around a hole. The stress (σ) around the holes was illustrated by a spectrum of colours where the higher σ region was indicated by bright colours such as red, orange, and yellow, and the least σ region was indicated by cooler colours such as blue.

Figure 7.4 shows the FEA result of the pristine CFRP laminate with no holes. The result showed that when a load was applied onto the laminates, the σ occurred in the laminate was uniformly distributed (no geometrical discontinuity) throughout the laminate. It was observed that the σ reduced at the base of the laminate where the fixed support constraint was applied.

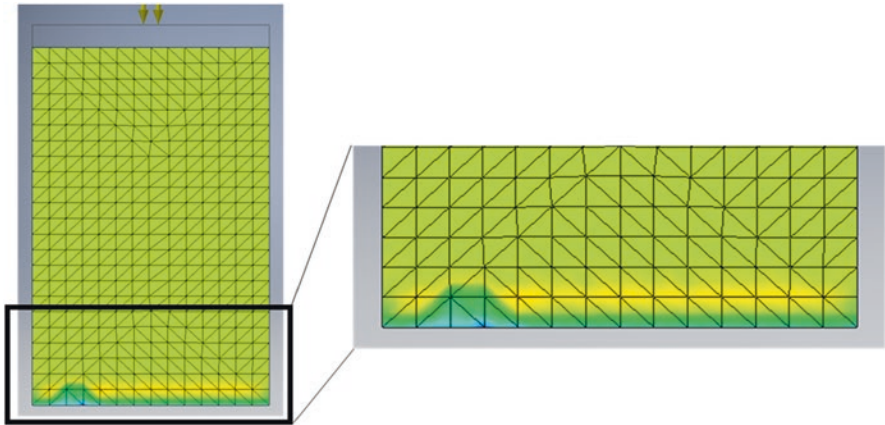


Fig. 7.4 Stress pattern on pristine CFRP laminates. The σ was uniformly distributed in the CFRP laminates. The σ reduced at the base of the laminate where the fixed support was constrained

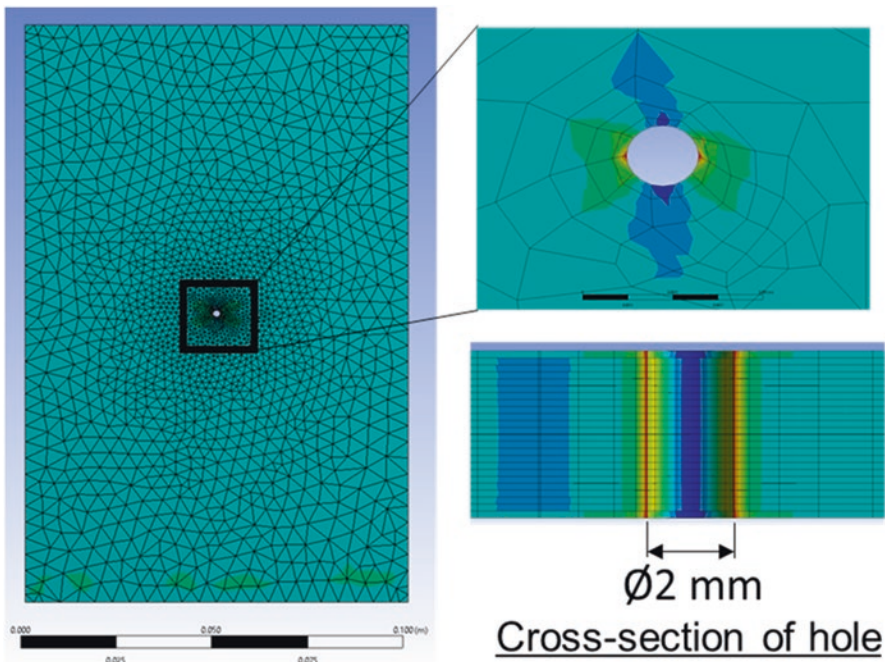


Fig. 7.5 Stress pattern on pristine CFRP laminates with 1 RH. Magnified view and cross-sectional view on the right showing the σ pattern around the RH. High σ occurred at the hole wall in the transverse direction of the applied load

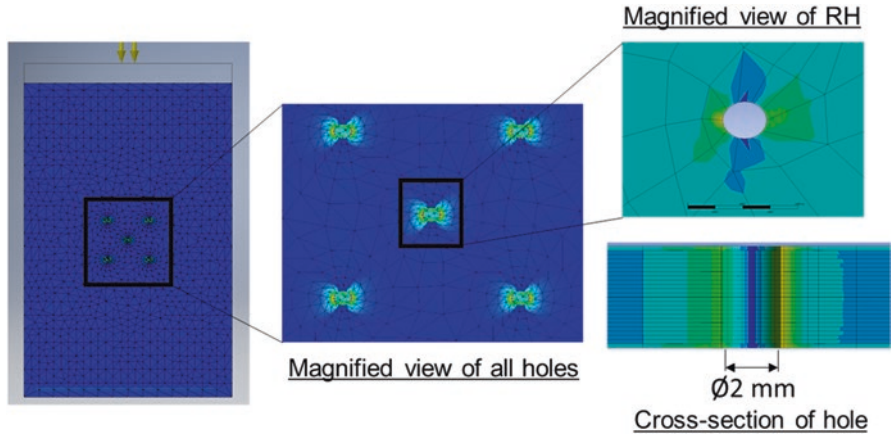


Fig. 7.6 Stress pattern on pristine CFRP laminates with 1 RH and 4 VHs. Magnified view and cross-sectional view on the right showing the σ pattern around the holes. High σ occurred at the hole wall in the transverse direction to the applied load. There is no sign of interaction in the σ field patterns between the RH-to-VH and VH-to-VH

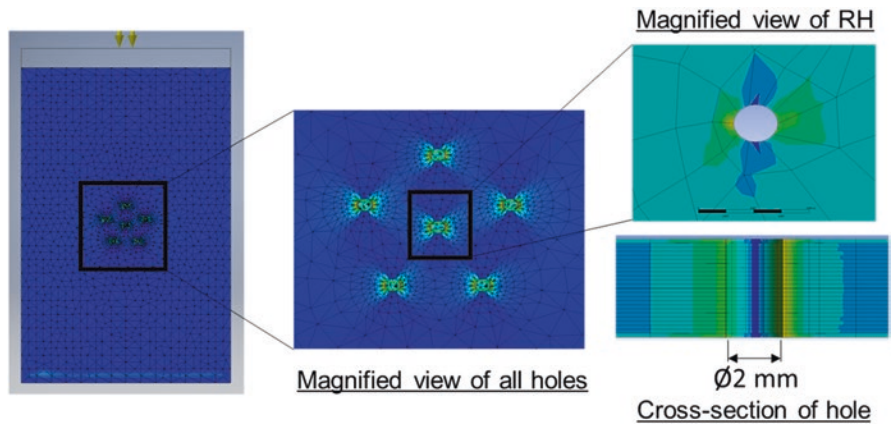


Fig. 7.7 Stress pattern on pristine CFRP laminates with 1 RH and 5 VHs. Magnified view and cross-sectional view on the right showing the σ pattern around the holes. High σ occurred at the hole wall in the transverse direction to the applied load. There is no sign of interaction in the σ field patterns between the RH-to-VH and VH-to-VH

Figure 7.5 shows the FEA result of the pristine CFRP laminate with 1 RH. When a hole is present in the CFRP structure (Fig. 7.4(b)), the σ decreases and converges along with the increasing distance from the hole (Soutis et al., 1991). High σ is observed at the wall of the hole. The high σ occurs at the hole wall in the transverse direction to the applied load direction (see the images showing the magnified view and the cross-sectional view of the stress pattern around the hole). The cross-sectional image shows that the σ decreases with increasing distance away from the

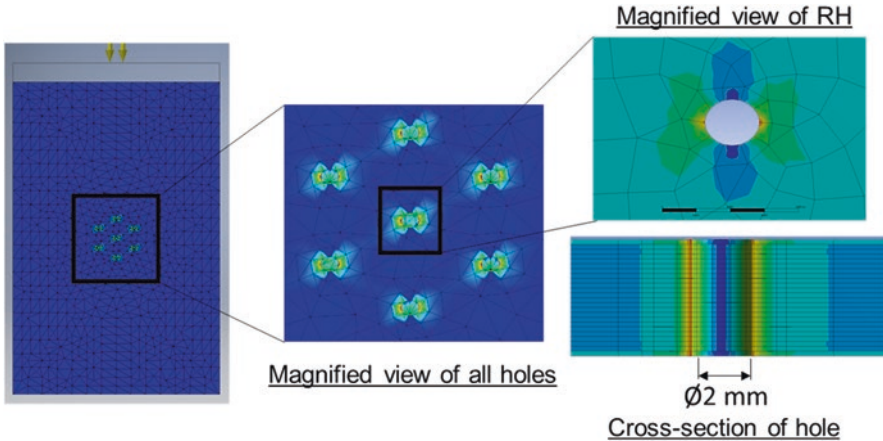


Fig. 7.8 Stress pattern on pristine CFRP laminates with 1 RH and 6 VHs. Magnified view and cross-sectional view on the right showing the σ pattern around the holes. High σ occurred at the hole wall in the transverse direction to the applied load. There is no sign of interaction in the σ field patterns between the RH-to-VH and VH-to-VH

hole. Also, larger σ field pattern occurs around the hole wall at the first and the last lamina. The σ does not vary through the depth profile of the hole in the pristine laminate between the first and the last lamina.

Figure 7.6 shows the FEA result of the pristine CFRP laminate with 1 RH and 4 VHs. Regardless of the positional of holes, the magnified view of all holes showed that the σ decreases with the increasing distance from the hole. High σ was observed at the wall of the hole. The high σ occurs at the hole wall in the transverse direction to the applied load direction (see the magnified view and the cross-sectional view of the stress pattern around the holes). The cross-sectional image showed that the σ decreases with increasing distance away from the hole. Also, larger σ field pattern occurred around the hole wall at the first and the last lamina. The σ does not vary through the depth profile of the hole in the pristine laminate between the first and the last lamina. Furthermore, there is no sign of σ field patterns interacting or connecting in the CFRP laminates between the RH-to-VH and VH-to-VH (orientation of VH-to-VH about 90° apart from the RH).

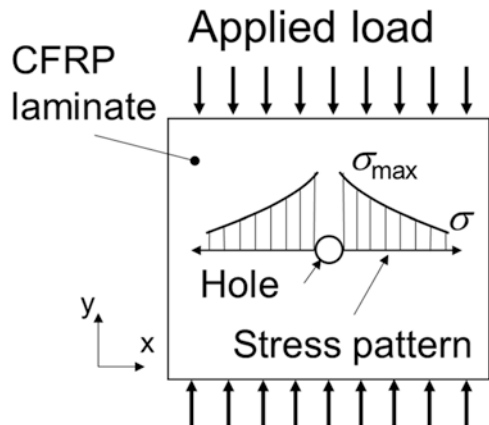
Figure 7.7 shows the FEA result of the pristine CFRP laminate with 1 RH and 5 VHs. Regardless of the position of holes, the magnified view of all holes showed that the σ decreases with the increasing distance from the hole. High σ was observed at the wall of the hole. The high σ occurs at the hole wall in the transverse direction to the applied load direction (see the magnified view and the cross-sectional view of the stress pattern around the holes). The cross-sectional image shows that the σ decreases with increasing distance away from the hole. Also, larger σ field pattern occurred around the hole wall at the first and the last lamina. The σ does not vary through the depth profile of the hole in the pristine laminate between the first and the last lamina. Furthermore, there is no sign of σ field patterns interacting or

connecting in the CFRP laminates between the RH-to-VH and VH-to-VH (orientation of VH-to-VH about 72° apart from the RH).

Figure 7.8 shows the FEA result of the pristine CFRP laminate with 1 RH and 6 VHs. Regardless of the positional of holes, the magnified view of all holes showed that the σ decreases with the increasing distance from the hole. High σ was observed at the wall of the hole. The high σ occurs at the hole wall in the transverse direction to the applied load direction (see the magnified view and the cross-sectional view of the stress pattern around the holes). The cross-sectional image showed that the σ decreases with increasing distance away from the hole. Also, larger σ field pattern occurred around the hole wall at the first and the last lamina. The σ does not vary through the depth profile of the hole in the pristine laminate between the first and the last lamina. Furthermore, there is no sign of σ field patterns interacting or connecting in the CFRP laminates between the RH-to-VH and VH-to-VH (orientation of VH-to-VH about 60° apart from the RH).

In general, regardless of hole setups, the results showed that the peak stress (σ_{max}) occurred at the hole walls and σ decreases with increasing distance away from the hole (see Fig. 7.9). Figure 7.10(a) shows the result from the FEA and an experimental study, the CFRP laminates fractured at the hole in the transverse direction of the applied load (Lai et al., 2020, 2021a, b; Lai, 2021). As observed, the results from the FEA are in agreement with the experimental study where high σ occurred at the hole wall in the transverse direction of the applied load (Lai, 2021, Lai et al., 2021a, b). From the cross-sectional view of the hole, it can be observed that a larger σ field pattern occurs around the hole wall at the first and the last lamina. The σ field pattern around the hole between the first and the last lamina does not vary along with the depth profile of the hole. The σ field pattern around the hole was in agreement with the results from an experimental study (Lai, 2021, Lai et al., 2021a, b). In several other experimental studies (Hocheng & Tsao, 2005; Lai et al., 2020, 2021a, b), the results showed that drilling-related defects, namely, peel-up failure, occurred at the entry of hole (first lamina) and push-out failure occurred at the exit of the hole (last lamina) (see Fig. 7.10(b)). Such failure modes at the hole entry and exit may result

Fig. 7.9 Schematic of stress pattern around a hole when the CFRP laminate is subjected to in-plane compressive load. The σ_{max} occurred at the hole walls and the σ decreases with increasing distance away from the hole



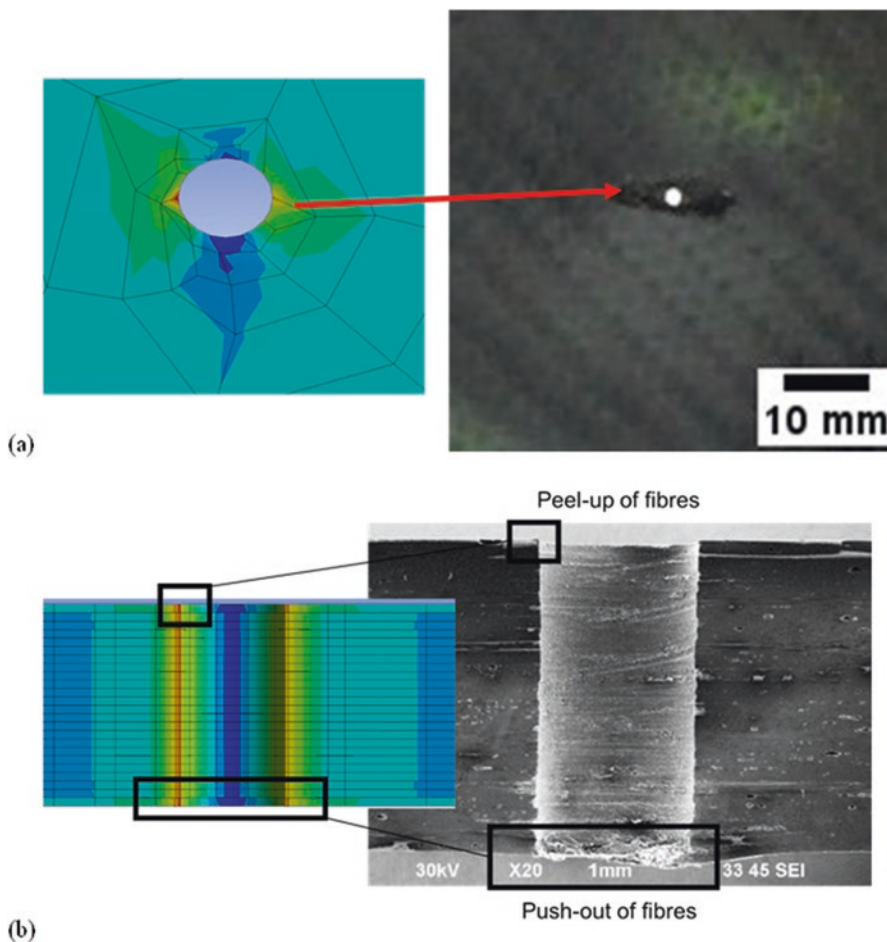


Fig. 7.10 FEA results of stress patterns (left) and images of failure modes around a hole from an experimental study (Lai, 2021, Lai et al., 2021a, b). (a) FEA model shows that high σ occurred at the hole wall in the transverse direction to the applied load (left). A high-resolution image shows that micro-buckling occurred at the hole wall in the transverse direction to the applied load (right). (b) Cross-sectional view of the FEA model revealing the σ pattern of the depth profile of the hole (left). High-resolution scanning electron micrograph showing the peel-up and push-out failure at the entry and exit of the hole, respectively

in higher σ when an in-plane load was applied to the laminate. The aforementioned experimental results were in agreement with our FEA that shows larger σ field pattern around the hole between the first and the last lamina.

A different number of VHs was set up following the resin-injection protocol for repairing the damaged laminates. When a CFRP laminate is subjected to an applied load, the drilling-related defects around the holes could propagate from one hole to another (Soutis et al., 1991). Saint-Venant's theory states that the changes in σ

become negligible when the distances from the hole are larger than the hole diameter ($D = 2r$, where r denotes the radius of a hole) (Pilkey, 2005). The σ increases when the distance between holes is smaller than the hole diameter, and this effect is referred to as hole-to-hole interaction.

4 Conclusions

An investigation on the stress patterns around holes in CFRP laminates has been conducted using the FEA method. Holes were set up in different configurations, namely, 4, 5, and 6 VHs, accompanied with 1 RH to mimic the hole setups employed for the resin-injection method to repair the damaged CFRP laminates. The FEA results on the stress patterns for the different number of VHs present in CFRP laminates were in agreement with the experimental results published elsewhere (Lai et al., 2020, 2021a, b).

After completion of the computational work in this research, the FEA results showed no sign of σ field patterns interacting between holes in the CFRP laminates with different n_{VH} , and the hole-to-hole distance exceeded 12 times the hole diameter. It is concluded that the outcomes of the stress patterns and the interaction between holes were in good agreement with the results reported elsewhere which stated that hole-hole interaction had ceased when the spacing between two holes exceeded four times the hole diameter (Soutis et al., 1991; Lai et al., 2020, 2021a, b; Lai, 2021).

The continuance to the next step of this research is to simulate BVID in the CFRP laminates, followed by studying the mechanical response of the damaged CFRP laminates at the vicinity of different numbers of VHs.

Acknowledgements We thank Professor Geoffrey Gibson (visiting professor to Newcastle University) and Dr. Eugene Wong for useful discussion on drilling holes in CFRP laminates used for the composite repair application, during the early part of the study. This work was supported by the Singapore Ministry of Education (MOE2013-TIF-1-G-068).

References

- Agarwal, B. D., & Broutman, L. J. (2015). *Analysis and performance of fiber composites*. Wiley.
- Aisyah, H. A., Paridah, M. T., Sapuan, S. M., Ilyas, R. A., Khalina, A., Nurazzi, N. M., Lee, S. H., & Lee, C. H. (2021). A comprehensive review on advanced sustainable woven natural fibre polymer composites. *Polymers (Basel)*, 13(3).
- Alsubari, S., Zuhri, M. Y. M., Sapuan, S. M., Ishak, M. R., Ilyas, R. A., & Asyraf, M. R. M. (2021). Potential of natural fiber reinforced polymer composites in sandwich structures: A review on its mechanical properties. *Polymers (Basel)*, 13(3).
- B787-81205-Z0210-00. (2012). *Boeing 787-8 structural repair manual*. The Boeing Company 13(B787-81205-Z0210-00).
- Campbell, F. C. (2010). *Introduction to composite materials*. ASM International.

- Cantwell, W. J., & Morton, J. (1991). The impact resistance of composite materials—A review. *Composites*, 22(5), 347–362.
- Dodt, T. (2011). *Introducing the 787—Effect on major investigations and interesting tidbits*. The Boeing Company.
- FAA-H-8083-31. (2012). *Aviation maintenance technician handbook—Airframe*. United States Department of Transportation, Federal Aviation Administration.
- Goh, K. L. (2017). *Discontinuous-fibre reinforced composites*. Springer London.
- Hocheng, H., & Tsao, C. C. (2005). The path towards delamination-free drilling of composite materials. *Journal of Materials Processing Technology*, 167(2–3), 251–264.
- Katnam, K. B., Da Silva, L. F. M., & Young, T. M. (2013). Bonded repair of composite aircraft structures: A review of scientific challenges and opportunities. *Progress in Aerospace Sciences*, 61, 26–42.
- Lai, W. L. (2021). *Repair of damaged carbon fibre reinforced polymer composite laminates-Resin-injection method*. Doctor of Philosophy PhD, Newcastle University.
- Lai, W. L., Cheah, A. Y. H., Ruiz, R. C. O., Lo, N. G. W., Kuah, K. Q. J., Saeedipour, H., & Goh, K. L. (2017). A simple portable low-pressure healant-injection device for repairing damaged composite laminates. *International Journal of Mechanical Engineering Education*, 45(4), 360–375.
- Lai, W. L., Saeedipour, H., & Goh, K. L. (2020). Mechanical properties of low-velocity impact damaged carbon fibre reinforced polymer laminates: Effects of drilling holes for resin-injection repair. *Composite Structures*, 235, 1–10.
- Lai, W. L., Saeedipour, H., & Goh, K. L. (2021a). Dataset on open/blind hole-hole interaction in barely visible impact damaged composite laminates. *Data Brief*, 34, 106607.
- Lai, W. L., Saeedipour, H., & Goh, K. L. (2021b). Experimental assessment of drilling-induced damage in impacted composite laminates for resin-injection repair: Influence of open/blind hole-hole interaction and orientation. *Composite Structures*, 271.
- Pilkey, W. D. (2005) *Formulas for stress, strain, and structural matrices*. Second Edn. Hoboken, New Jersey: John Wiley & Sons, Inc.
- Poudel, A., Mitchell, K. R., Chu, T. P., Neidigk, S., & Jacques, C. (2015). Non-destructive evaluation of composite repairs by using infrared thermography. *Journal of Composite Materials*, 50(3), 351–363.
- Rahman, M. A. A. S. B., Lai, W. L., Saeedipour, H., & Goh, K. L. (2019). Cost-effective and efficient resin-injection device for repairing damaged composites. *Reinforced Plastics*, 63(3), 156–160.
- Saeedipour, H., Lai, W. L., Wong, E. W. L., Goh, K. L., & Gibson, A. G. (2017). Smart restoration of internal defects in damaged composite aerostructures. *JEC Composites Magazine*, 70–73.
- Safri, S. N. A., Sultan, M. T. H., Yidris, N., & Mustapha, F. (2014). Low velocity and high velocity impact test on composite materials—A review. *The International Journal of Engineering and Science (IJES)*, 3(9), 50–60.
- Slattery, P. G., McCarthy, C. T., & O'Higgins, R. M. (2016). Development of a novel cyanoacrylate injection repair procedure for composites. *Composite Structures*, 153, 1–11.
- Sohn, M. S., Hu, X. Z., Kim, J. K., & Walker, L. (2000). Impact damage characterization of carbon fibre/epoxy composites with multi-layer reinforcement. *Composites Part B: Engineering*, 31(8), 681–691.
- Soutis, C., Fleck, N. A., & Curtis, P. T. (1991). Hole-hole interaction in carbon fibre/epoxy laminates under uniaxial compression. *Composites*, 22(1), 31–38.
- Tarpani, J. R., Milan, M. T., Spinelli, D., & Bose, W. W. (2006). Mechanical performance of carbon-epoxy laminates. Part II: Quasi-static and fatigue tensile properties. *Materials Research*, 9(2), 121–130.
- Thunga, M., Bauer, A., Obusek, K., Meilunas, R., Akinc, M., & Kessler, M. R. (2014). Injection repair of carbon fiber/bismaleimide composite panels with bisphenol E cyanate ester resin. *Composites Science and Technology*, 100, 174–181.

Chapter 8

Studies on Magnesium Alloy: Composites for Aerospace Structural Applications



B. Vijaya Ramnath, D. Kumaran, J. Melvin Antony, M. Rama Subramanian, and S. Venkatram

1 Introduction

Aluminum metal matrix composites replace a lot of conventional materials in automotive, aerospace, and marine industries due to their improved mechanical properties, namely, very high strength-to-weight ratio, superior wear resistance, greater stiffness, better fatigue resistance, and controlled coefficient of thermal expansion. Among various aluminum composites, AZ63 magnesium alloys reinforced with silicon carbide play a vital role in various applications like aerospace and automobile for their great mechanical properties.

Silicon carbide has high mechanical properties such as high strength, greater stiffness, better wear, and creep resistance, and so it is used in a wide array of applications like automobile, aerospace, etc. By investigating the effects of freezing temperature and ceramic fraction on the mechanical properties of the composites, without paying attention to the effect of the sintering additive, we can determine that the material is structurally suitable for this research project (Hong et al., 1993; Shaga et al., 2016).

Magnesium alloys also have great specific strengths and low coefficient of thermal expansion along with good wear resistance, but cannot provide for the rising demands in the industries. When they are made into a composite with the addition of SiC at varying wt.% in the mixture of epoxy resin and hardener which acts as the bonding agent in the fabrication of the said composite, its mechanical properties are

B. Vijaya Ramnath (✉) · D. Kumaran · J. Melvin Antony
Department of Mechanical Engineering, Sri Sai Ram Engineering College,
Chennai, Tamil Nadu, India

M. Rama Subramanian
Aveva Solutions, Hyderabad, Telangana, India

S. Venkatram
Kautex Corporation, Windsor, ON, Canada

greatly enhanced such that it could meet the standards for its applications in various industries (Ferkel & Mordike, 2001; Lan et al., 2004; Wang et al., 2010).

The ultrasonic waves are used to disperse the SiC into the nanocomposite at a molecular level in order to prevent micro-clusters of SiC in the fabricated composite. To prove its effectiveness, tensile test is taken to prove whether this process affects Mg-(2,4) Al-1Si-silicon carbide nanocomposite's mechanical properties (Cao et al., 2008a, b). Tensile properties of magnesium alloys are amplified using silicon carbide, but while increasing its yield strength its ductile properties are retained which was due to the increase in particle volume fraction and particle size (Milan & Bowen, 2004; Ghias & Vijaya Ramnath, 2015). Similar to tensile strength, its hardness factor is also elevated by combining these materials (Sinha et al., 2006; Sirahbizu Yigezu et al., 2013).

The addition of SiC on the higher wt.% improves the compressive properties of the base materials for both magnesium and aluminum alloys. While studying the deformation of the test material caused by compressive force, the SiC seems to have postponed the initiation of the cracks in the particle matrix interface by decreasing the intermolecular space which is now occupied by SiC micro-clusters, thus increasing its creep resistance (Matin et al., 2015; Hosseini Monazzah et al., 2017).

The process which is used in combining two or more materials in the production of composite materials is considered to be a very crucial step as it plays a significant role in the construction of the composite material's mechanical properties and incorporation of the internal molecular structure of the SiC-reinforced magnesium composite and Al-SiC composite where stir casting is used in the fabrication of these composites which showed improved properties when compared to the same composite fabricated using hand layup method (Poddar et al., 2007; Soltani et al., 2017).

Stir casting technique is employed in the manufacturing process of the composite material as it allows intermolecular bonding of the different materials that constitute the composite material and it is proven to improve the overall structure of the combined composite material (Idrisi & Mourad, 2019).

Impact behavior of the fabricated material is very important in the study of its particle cluster and matrix-reinforcement bonding. At the point of impact, a huge amount of energy is released or transferred, causing the sample to heat and reach higher temperatures which can affect its impact strength. In the case of silicon-reinforced aluminum alloy, the impact strength is decreased due to the presence of clusters of SiC which is already proven to decrease the ductility of the composite (Ozden et al., 2007).

Flexural modulus or flexural strength of the material is generated by conducting flexural tests which are generally done by laying the material horizontally over different points of contact and applying force between the points. It is seen that flexural load capacity is high for specimen 2 which has been treated with NaOH and high potential graphene. It is noted that fiber treatment increases flexural load-carrying capacity which is nothing but flexural strength of the fabricated composites (Ramnath et al., 2020).

The aluminum composite reinforced with carbon nanotubes (CNTs) is tested for its compression and chemical properties, and it is found that the compressive strength of the composite is greatly increased by the CNTs by providing an extra layer support for the total structure, whereas the hardness had no improvements compared to the increase in the weight percentage of the carbon nanotubes. In case the of nano-ferrous composite, it had been found that the addition of carbon nanotubes as reinforcement for iron which is the ferrous part of the composite material could lead to the increment of the mechanical properties of the composite without substantial increase in the weight of the composite (Parswajinan et al., 2014; Vijaya Ramnath et al., 2014b).

The effects of multi-walled carbon nanotubes which are used to reinforce aluminum is found by testing its mechanical and chemical properties, and it is found that there is an improvement in the compressive strength by forming a uniform layer of the same material (carbon) which provides structural support in between the layers, but no changes in hardness of the composite material. The mechanical properties of the aluminum metal matrix and silicon carbide are improved by adding carbon nanotubes by stir casting to improve the tensile properties as there is a molecular intermixing in the layers of both aluminum and carbon nanotubes (Parswajinan et al., 2015, 2018a).

The testing of the mechanical behavior of Fe-CNT metal matrix composite is determined to find the homogenous dispersion of the CNTs and its effects in the structural strength of the composite. The ball milling process is used to blend the CNT, liquid paraffin, and iron powder together and then hydraulic pressed. The sintered component called green specimen is created with varying composition of CNT which is proven to have high influence on the composite's mechanical properties as the sintering process helps in the quenching of the base metal, thus increasing its base structure (Vijaya Ramnath et al., 2014a; Parswajinan et al., 2018b).

2 Specimen Preparation

2.1 Materials

The main material of this composite fabrication is AZ63 magnesium alloy. The chemical composition of magnesium alloy is shown in Table 8.1.

The magnesium alloy was crushed into finer particles for better surface area interaction from the original bar purchased from the supplier in Chennai. The alloy is of silverish white in color similar to aluminum with a density of 1.81 g/cc.

Table 8.1 Chemical composition of AZ63 magnesium alloy (wt.%)

Composition	Magnesium (Mg)	Aluminum (Al)	Silicon (Si)
Weight percentage	90.7	6	0.3

Silicon carbide is a semiconductor with gray in color with the density of 3.2 g/cc which is purchased in a powdered form in Chennai. The SiC is used at varying wt.% for each sample in order to see the effect of the addition of SiC with magnesium alloys, having great specific strengths, low coefficient of thermal expansion, and good wear resistance; however, it cannot provide for higher demands in industries alone, so with the addition of SiC, its mechanical properties are greatly improved to meet the standards for its applications.

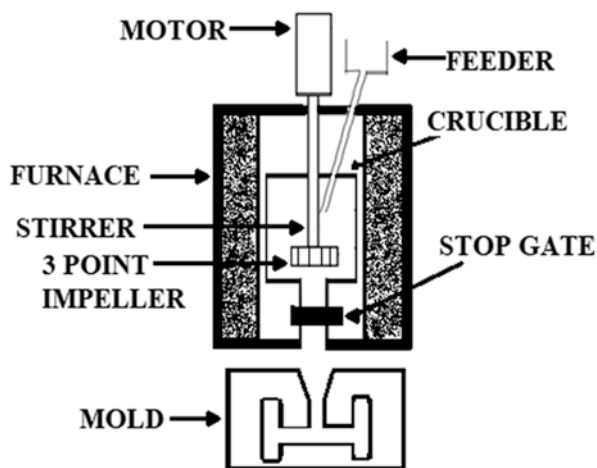
2.2 Stir Casting

Combining two or more materials in the production of composite materials is considered to be a very crucial step as it plays a significant role in the construction of the composite material's mechanical properties and incorporation of the internal molecular structure.

The stir casting process was used to fabricate the composites by varying weight percentage of silicon carbide (0.5, 1.0, 1.5, and 2.0 wt.%) with magnesium alloy. Stir casting technique as shown in Fig. 8.1 is employed in the manufacturing process of the composite material as it allows intermolecular bonding of different materials that constitute the composite material and it is proven to improve the overall structure of the combined composite material.

The stir casting apparatus consists of a motor which is connected to the three-point impeller which is used for greater contact area and stability during mixing via the stirrer. The melting point of the magnesium alloy is around 450–550 °C and is constantly mixed with the impeller at 450–500 rpm for 10–15 min. The addition of SiC with different wt.% is performed and the impeller rpm is increased to 550–600 with 15–20-min time interval which enables a uniform mixture of the magnesium alloy and SiC material. The pre-heated mold is used as a template for the fabricated

Fig. 8.1 Bottom pouring type stir casting furnace



composite with varying Si C wt.%, and the molten mixture is poured into the mold and left for 5–6 h to cool down at room temperature. Once cooled the composite is further processed for mechanical testing.

3 Testing of Composites

The following mechanical tests were performed in order to study the mechanical behavior of fabricated metal matrix composites.

3.1 Impact Test

The Izod impact test was performed in order to determine the toughness or the impact strength of the fabricated composites. The impact test is done as per the ASTM D256 standard as shown in Fig. 8.2, where each and all combinations of silicon carbide weight percentage specimens are cut with a V notch, and it is placed vertically on the test bed in which a known mass of a striker which is kept at a specified height is used to strike the composite specimen at the top of the specimen, followed by the movement of the indicator which is used to denote the impact resistance of the material.

3.2 Hardness Test

The hardness test was performed in order to evaluate the hardness or the ability of the composite material to prevent permanent indentation or scratches under the friction produced from external materials under contact. The hardness of the composite material was done using Vickers hardness methodology as per ASTM E92. Here the pyramid-shaped diamond indenter is used, which is applied with a known force at a

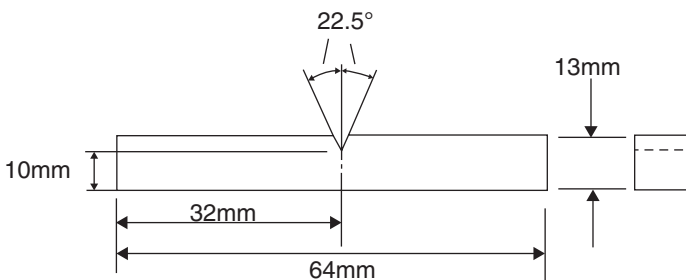


Fig. 8.2 Izod impact test specimen (ASTM: D256)

constant time period for all the compositions. Once the specified time is elapsed, the microscope is used to measure the diagonals. The Vickers hardness number is calculated by the ratio of applied force and area of indentation, respectively.

3.3 Double Shear Test

The double shear test is performed in order to evaluate the maximum shear stress that the composite can withstand before failure occurs. The double shear test is done using the universal testing machine, as per ASTM D5379 as shown in Fig. 8.3; here the sample is loaded into the double shear die and it is placed on the universal testing machine where the load is applied until the specimen shears into multiple pieces; since it is a double shear test, the specimen breaks into three pieces, the maximum force is calculated by the machine, and the graph is plotted for stress with respect to strain, respectively.

3.4 Flexural Test

The flexural test is performed in order to evaluate the flexure or bending strength which is used to determine the resistance offered for flexing or the stiffness of the composite material, respectively. The flexural strength is done using the universal testing machine as per ASTM D790 as shown in Fig. 8.4; here the sample is tested using central point loading, where the composite is placed on top of rollers supporting the base on both sides and another roller is placed on top of the composite where

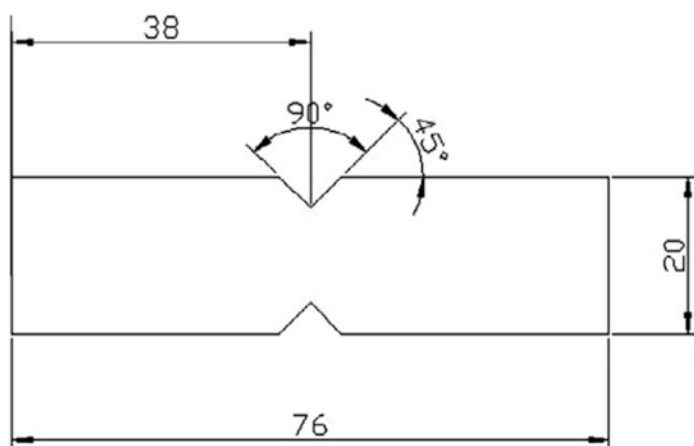


Fig. 8.3 Double shear test specimen (ASTM: D5379)

Fig. 8.4 Flexural test specimen (ASTM: D790)

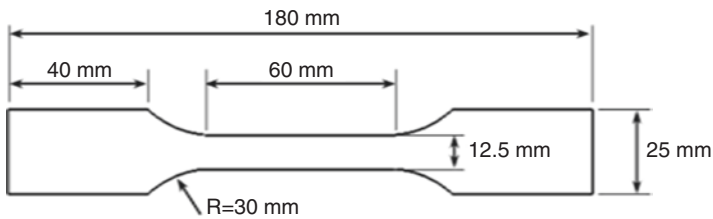
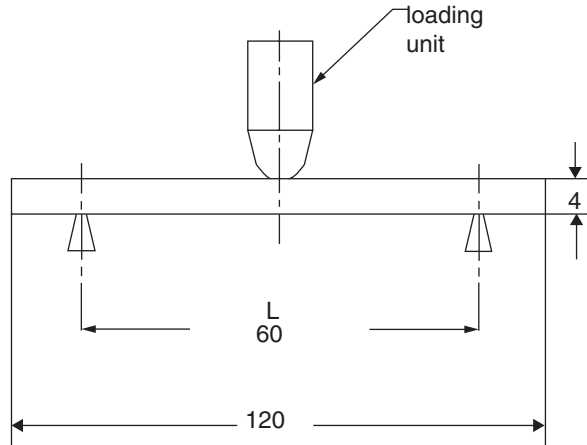


Fig. 8.5 Tensile test specimen (ASTM: E8)

the load is applied; the maximum force is calculated and the stress is plotted in the graph with respect to strain.

3.5 Tensile Test

The tensile test is performed in order to evaluate the maximum breaking load or the elongation of the material before it fails permanently under constant or irregular tension. The tensile test is done using a universal testing machine, as per ASTM E8 as shown in Fig. 8.5; here the sample is clamped using the jaws of the testing machine and the tension is applied; here one end of the bar is fixed stationarily and other end of the bar is pulled up with tension. During the performance of the test, necking can be observed and finally the bar breaks into two pieces, the maximum force is calculated, and the stress is plotted in the graph with respect to strain.

4 Results and Discussion

The results of performed mechanical tests are discussed here.

4.1 Impact Test

Izod impact test results are tabulated as shown in Table 8.2. The specimen with 0.5 wt.% SiC has the highest impact resistance. The SiC has excellent thermal shock resistance followed by the high temperature strength which evens out at the time of impact. The 2.0 wt.% SiC specimen which has the least impact resistance is due to the addition of SiC above the saturation point of the composite in the case of impact test. The 1.0 and 1.5 wt.% SiC specimens fall in between both the highest and lowest SiC weight percentage specimens, respectively.

The above result concludes that the sample with 0.5 wt.% SiC outperforms each and every specimen prepared of varying SiC weight percentage, which is 2.50 times better when compared directly with the 2.0 wt.% SiC specimen. The 1.0 and 1.5 wt.% SiC specimens can resist up to 1.5 and 2.0 times the impact value of 2.0 wt.% specimen, respectively.

4.2 Hardness Test

The hardness test results are tabulated as shown in Table 8.3. The fabricated composite is measured by Vickers hardness test. The specimen with 0.5 wt.% SiC has the highest hardness value due to the mechanical properties of SiC which is known for its high hardness and wear resistance properties. The 0.5 wt.% SiC is 1.087 times better when compared directly with the 1.5 wt.% SiC specimen. The 1.0 and 2.0 wt.% SiC specimens can resist up to 1.082 and 1.017 times the hardness value tested when compared with 1.5 wt.% SiC specimen.

4.3 Double Shear Test

The shear test results are plotted in the graph as shown in Fig. 8.6, followed by the results which are tabulated as shown in Table 8.4. The specimen with 1.5 wt.% SiC has the maximum force value of 8.95KN and stress of 69 N/mm², followed by the

Table 8.2 Result of impact test

Specimen	0.5 wt.% SiC	1.0 wt.% SiC	1.5 wt.% SiC	2.0 wt.% SiC	Standard deviation
Impact value (J)	10	6	8	4	2.58

Table 8.3 Result of hardness test

Specimen	0.5 wt.% SiC	1.0 wt.% SiC	1.5 wt.% SiC	2.0 wt.% SiC	Standard deviation
T1	37.5	35.1	34.8	35.8	1.21
T2	38	39.9	35.8	36.2	1.88
T3	39.7	39.7	35.3	35.8	2.40
Average	38.4	38.2	35.3	35.93	1.57

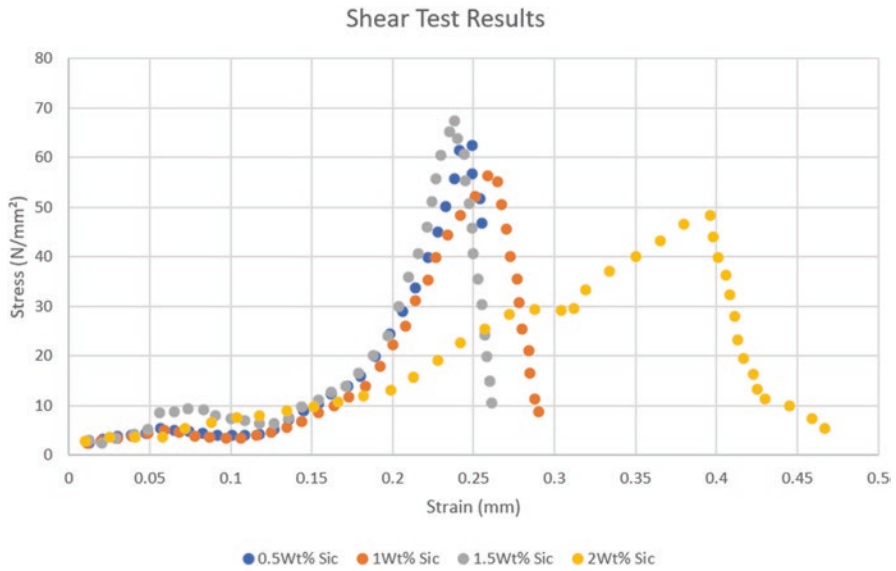


Fig. 8.6 Result of double shear test

2.0 wt.% SiC specimen which has the least maximum force of 7.35KN and stress of 49 N/mm², respectively.

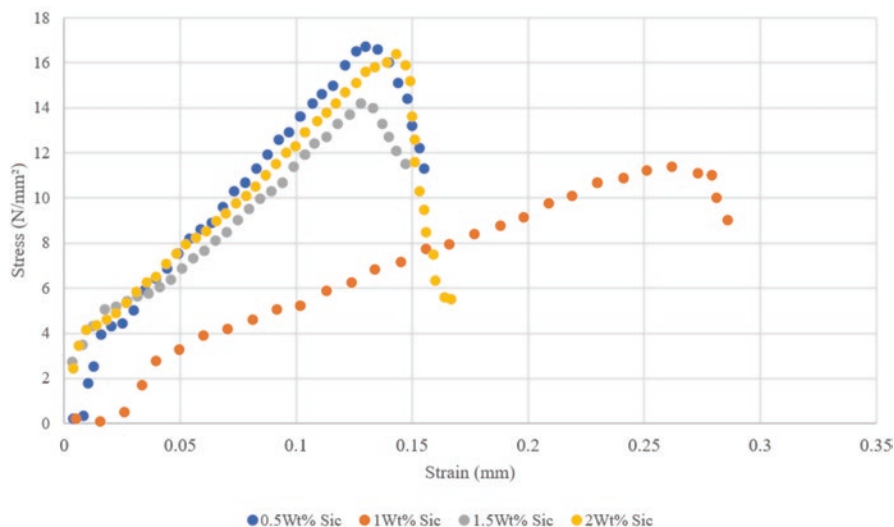
The 1.5 wt.% SiC is 1.21 times better when compared directly with the 2.0 wt.% SiC specimen due to the lightweight property of the magnesium alloy and high damping nature; the addition of 1.5 wt.% SiC had resulted the best saturation point for the third specimen. The 0.5 and 1.5 wt.% SiC specimens can resist a maximum force up to 1.14 and 1.11 times the shear value tested when compared with 2.0 wt.% SiC specimen.

4.4 Flexural Test

The flexural test results are plotted in the graph as shown in Fig. 8.7 and the results are tabulated as shown in Table 8.5. The specimen with 0.5 wt.% SiC has the highest maximum force value of 4.31KN and stress of 16.8 N/mm², followed by the 1.0 wt.% SiC specimen which has the least maximum force of 1.54KN and stress of 11.8 N/mm², respectively.

Table 8.4 Result of double shear test

Specimen	0.5 wt.% SiC	1.0 wt.% SiC	1.5 wt.% SiC	2.0 wt.% SiC	Standard deviation
Fmax (KN)	8.4	8.19	8.95	7.35	0.66
Stress (N/mm ²)	62	58	69	49	8.35

**Fig. 8.7** Result of flexural test

The magnesium alloy exhibits high stiffness and durability along with the high hardness property of silicon carbide combined together successfully resisting the flexural load applied during the flexural test period. The stress induced in the composite is maximum with the 0.5 wt.% SiC specimen which is achieved by minimum strain displacement of 0.125 mm.

The test results conclude that the sample with 0.5 wt.% SiC outperforms each and every specimen prepared of varying SiC weight percentage, which is 2.79 times better when compared directly with the 1.0 wt.% SiC specimen. The 1.5 and 2.0 wt.% SiC specimens can resist a maximum force up to 1.7 and 2.64 times the flexural value tested when compared with 1.0 wt.% SiC specimen.

4.5 Tensile Test

The tensile test results are plotted in the graph as shown in Fig. 8.8 and the results are tabulated as shown in Table 8.6. The specimen with 2.0 wt.% SiC has the highest maximum force value of 17.07 KN, followed by the 1.0 wt.% SiC specimen which has the least maximum force of 8.74 KN which proves that the addition SiC increases the composite tensile property as the addition of SiC restricts the plastic

Table 8.5 Result of flexural test

Specimen	0.5 wt.% SiC	1.0 wt.% SiC	1.5 wt.% SiC	2.0 wt.% SiC	Standard deviation
Fmax (KN)	4.31	1.54	2.62	4.08	1.30
Stress (N/mm ²)	16.8	11.8	14.2	16.3	2.28

Table 8.6 Tensile test

Specimen	0.5 wt.% SiC	1.0 wt.% SiC	1.5 wt.% SiC	2.0 wt.% SiC	Standard deviation
Fmax (KN)	14.85	8.74	13.97	17.07	3.53
UTS (Mpa)	110.69	86.19	104.31	107.8	11.02
Yield stress (Mpa)	104.76	81.18	89	97.14	10.18
%EL	7.6	5.4	7.6	7.6	1.10

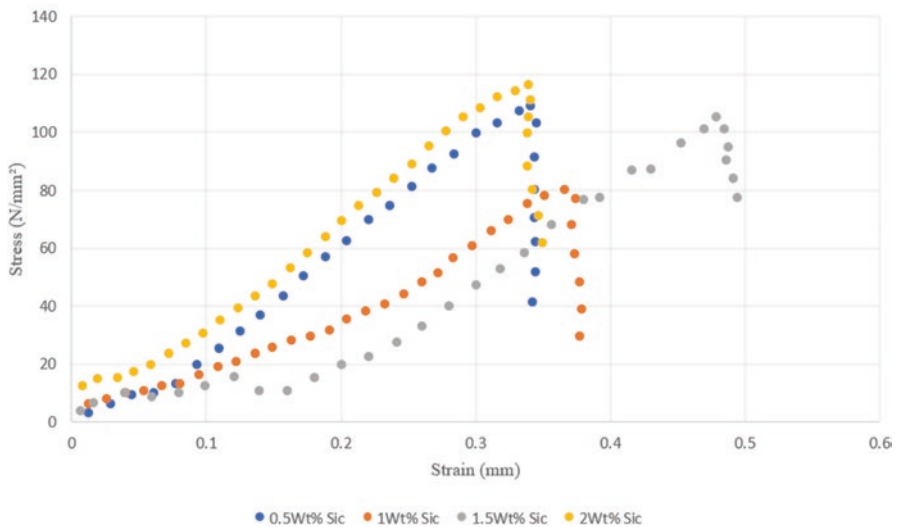


Fig. 8.8 Tensile test results

flow of force in Al matrix due to the uniform and compact distribution of the particles.

The tensile test result concludes that the uniform fusion of 2.0 wt.% SiC is 1.95 times better when compared directly with the 1.0 wt.% SiC specimen. The 0.5 and 1.5 wt.% SiC specimens can resist a maximum force up to 1.69 and 1.59 times the tensile value tested when compared with 1.0 wt.% SiC specimen, which proves that the proper distribution of even a small amount of SiC in the metal matrix can significantly increase the structural property of the composite.

The ultimate tensile strength and yield stress of the 0.5 wt.% SiC specimen outperforms the 2.0 wt.% SiC specimen with the difference of 2.89 and 7.62 MPa even though its maximum force was comparatively higher. The amount of stress

generated was the highest in the 2.0 wt.% SiC specimen which results in minimum amount of strain displacement of 0.333 mm which is possible due to the above reasons.

5 Conclusion

In this chapter AZ63 magnesium alloy-based metal matrix composites were fabricated by stir casting process with varying percentage of silicon carbides. It is found that the impact, hardness, and maximum force in flexural test were highest in the 0.5 wt.% SiC specimen; therefore, in order to get the maximum impact and hardness value, the addition of minimum amount of silicon carbide is recommended. The maximum force in shear and tensile test was achieved by 1.5 and 2.0 wt.% SiC specimen, respectively; therefore, in order to get the maximum shear and tensile force, the addition of maximum amount of silicon carbide is recommended.

References

- Cao, G., Kobliska, J., Konishi, H., & Li, X. (2008a). Tensile properties and microstructure of SiC nanoparticle-reinforced Mg-4Zn alloy fabricated by ultrasonic cavitation-based solidification processing. *Metallurgical and Materials Transactions A: Physical Metallurgy and Materials Science*, 39 A, 880–886. <https://doi.org/10.1007/s11661-007-9453-6>
- Cao, G., Konishi, H., & Li, X. (2008b). Mechanical properties and microstructure of SiC-reinforced Mg-(2,4) Al-1Si nanocomposites fabricated by ultrasonic cavitation-based solidification processing. *Materials Science and Engineering A*, 486, 357–362. <https://doi.org/10.1016/j.msea.2007.09.054>
- Ferkel, H., & Mordike, B. L. (2001). Magnesium strengthened by SiC nanoparticles. *Materials Science and Engineering A*, 298, 193–199.
- Ghias, A. S. A., & Vijaya Ramnath, B. (2015). Investigation of tensile property of aluminium SiC metal matrix composite. *Applied Mechanics and Materials*, 766–767, 252–256. <https://doi.org/10.4028/www.scientific.net/amm.766-767.252>
- Hong, S. I., Iip, G. T. G., & Lewandowski, J. J. (1993). Dynamic deformation behavior of Al-Zn-Mg-Cu alloy matrix composites reinforced with 20 Vol.% SiC. *Acta Metallurgica et Materialia*, 41(8), 2337–2351.
- Hosseini Monazzah, A., Pouraliakbar, H., Bagheri, R., & Seyed Reihani, S. M. (2017). Al-Mg-Si/SiC laminated composites: Fabrication, architectural characteristics, toughness, damage tolerance, fracture mechanisms. *Composites Part B: Engineering*, 125, 49–70. <https://doi.org/10.1016/j.compositesb.2017.05.055>
- Idrisi, A. H., & Mourad, A. H. I. (2019). Conventional stir casting versus ultrasonic assisted stir casting process: Mechanical and physical characteristics of AMCs. *Journal of Alloys and Compounds*, 805, 502–508. <https://doi.org/10.1016/j.jallcom.2019.07.076>
- Lan, J., Yang, Y., & Li, X. (2004). Microstructure and microhardness of SiC nanoparticles reinforced magnesium composites fabricated by ultrasonic method. *Materials Science and Engineering A*, 386, 284–290. <https://doi.org/10.1016/j.msea.2004.07.024>

- Matin, A., Saniee, F. F., & Abedi, H. R. (2015). Microstructure and mechanical properties of Mg/SiC and AZ80/SiC nano-composites fabricated through stir casting method. *Materials Science and Engineering A*, 625, 81–88. <https://doi.org/10.1016/j.msea.2014.11.050>
- Milan, M. T., & Bowen, P. (2004). Tensile and fracture toughness properties of SiCp reinforced Al alloys: Effects of particle size, particle volume fraction, and matrix strength. *Journal of Materials Engineering and Performance*, 775–783.
- Ozden, S., Ekici, R., & Nair, F. (2007). Investigation of impact behaviour of aluminium based SiC particle reinforced metal-matrix composites. *Composites Part A: Applied Science and Manufacturing*, 38, 484–494. <https://doi.org/10.1016/j.compositesa.2006.02.026>
- Parswajinan, C., Vijaya Ramnath, B., Elanchezhian, C., et al. (2014). Investigation on mechanical properties of nano ferrous composite. In *Procedia engineering* (pp. 513–521). Elsevier Ltd.
- Parswajinan, C., Vijaya Ramnath, B., Vetrivel, M., et al. (2015). Experimental investigation of mechanical and chemical properties of aluminium reinforced with MWCNT. *Applied Mechanics and Materials*, 766–767, 287–292. <https://doi.org/10.4028/www.scientific.net/amm.766-767.287>
- Parswajinan, C., Vijaya Ramnath, B., Abishek, S., et al. (2018a). Hardness and impact behaviour of aluminium metal matrix composite. In *IOP Conference Series: Materials Science and Engineering*. Institute of Physics Publishing.
- Parswajinan, C., Vijaya Ramnath, B., Vetrivel, M., et al. (2018b). Determination of mechanical behaviour of Fe-CNT MMC. In *Materials today: Proceedings* (pp. 1176–1185). Elsevier.
- Poddar, P., Srivastava, V. C., De, P. K., & Sahoo, K. L. (2007). Processing and mechanical properties of SiC reinforced cast magnesium matrix composites by stir casting process. *Materials Science and Engineering A*, 460–461, 357–364. <https://doi.org/10.1016/j.msea.2007.01.052>
- Ramnath, B. V., Gowtham, S., Melvin Antony, J., et al. (2020). Investigations of flexural and hardness behaviour of graphene composites. *IOP Conference Series: Materials Science and Engineering*. <https://doi.org/10.1088/1757-899X/954/1/012004>
- Shaga, A., Shen, P., Guo, R. F., & Jiang, Q. C. (2016). Effects of oxide addition on the microstructure and mechanical properties of lamellar SiC scaffolds and Al-Si-Mg/SiC composites prepared by freeze casting and pressure less infiltration. *Ceramics International*, 42, 9653–9659. <https://doi.org/10.1016/j.ceramint.2016.03.052>
- Sinha, S. K., Reddy, S. U., & Gupta, M. (2006). Scratch hardness and mechanical property correlation for Mg/SiC and Mg/SiC/Ti metal-matrix composites. *Tribology International*, 39, 184–189. <https://doi.org/10.1016/j.triboint.2005.04.017>
- Sirahbizu Yigezu, B., Mahapatra, M. M., & Jha, P. K. (2013). Influence of reinforcement type on microstructure, hardness, and tensile properties of an aluminum alloy metal matrix composite. *Journal of Minerals and Materials Characterization and Engineering*, 01, 124–130. <https://doi.org/10.4236/jmmce.2013.14022>
- Soltani, S., Azari Khosroshahi, R., Taherzadeh Mousavian, R., et al. (2017). Stir casting process for manufacture of Al–SiC composites. *Rare Metals*, 36, 581–590. <https://doi.org/10.1007/s12598-015-0565-7>
- Vijaya Ramnath, B., Elanchezhian, C., Jaivignesh, M., et al. (2014a). Evaluation of mechanical properties of aluminium alloy-alumina-boron carbide metal matrix composites. *Materials and Design*, 58, 332–338. <https://doi.org/10.1016/j.matdes.2014.01.068>
- Vijaya Ramnath, B., Parswajinan, C., Elanchezhian, C., et al. (2014b). Experimental investigation on compression and chemical properties of aluminium nano composite. In *Applied mechanics and materials* (pp. 7–10). Trans Tech Publications Ltd.
- Wang, Z. H., Wang, X. D., Zhao, Y. X., & Du, W. B. (2010). SiC nanoparticles reinforced magnesium matrix composites fabricated by ultrasonic method. *Transactions of Nonferrous Metals Society of China (English Edition)*, 20, s1029–s1032. [https://doi.org/10.1016/S1003-6326\(10\)60625-5](https://doi.org/10.1016/S1003-6326(10)60625-5)

Chapter 9

An Overview of the Natural/Synthetic Fibre-Reinforced Metal-Composite Sandwich Structures for Potential Applications in Aerospace Sectors



Lin Feng Ng, Kathiravan Subramaniam, and Noordiana Mohd Ishak

1 Introduction

A significant milestone has been achieved in the field of composite materials over the past few decades. The technological evolution has ignited the development of advanced composite sandwich materials, namely, fibre-metal laminates (FMLs), in the aerospace sectors. The initial intention of developing FMLs was to tackle the poor fatigue crack resistance of metal alloys in the aerospace sectors. Later, it was found that the coalescence of metal and composite layers results in excellent impact properties with a significant weight reduction. The reduction in the fatigue crack growth rate and the improvement in the impact properties of FMLs have made these materials the successor over their individual constituents. In fact, the search for high damage tolerance and toughness materials for aircraft structures is motivated by the new design philosophy as introduced by the Federal Aviation Administration (FAA) (Asundi & Choi, 1997). Therefore, the development of FMLs aims to meet the design philosophy as introduced by the FAA.

FMLs are in the category of composite sandwich laminates consisting of alternating layers of metal alloys and composites. The typical metal layers employed in FMLs are aluminium, titanium and magnesium. In addition to the excellent fatigue and impact properties of FMLs, the introduction of composite materials in the FMLs has led to weight saving. The weight reduction is particularly attractive to the aerospace sector as it could improve energy efficiency. The sandwich concept was

L. F. Ng (✉)

Centre for Advanced Composite Materials, School of Mechanical Engineering,
Faculty of Engineering, Universiti Teknologi Malaysia, Johor Bahru, Johor, Malaysia
e-mail: linfeng@utm.my

K. Subramaniam · N. M. Ishak

Centre for Advanced Research on Energy, Faculty of Mechanical Engineering, Universiti
Teknikal Malaysia Melaka, Melaka, Malaysia

initialised at the Delft University of Technology in 1978 (Mohammed et al., 2018). The first successfully developed FMLs were aramid fibre-reinforced aluminium laminate (ARALL). Later, glass fibre-reinforced aluminium laminate (GLARE) was developed in which the glass fibre prepreg was used to supersede aramid fibre in FMLs to improve the overall performance. An attempt had been made to incorporate carbon fibre in the FMLs, but it was realised that the combination of aluminium alloys and carbon fibre results in galvanic corrosion. Galvanic corrosion is an electrochemical process happening when two dissimilar conductive materials are exposed to an electrolyte. In FMLs, the carbon fibre and aluminium can be electrically connected through the free edges of the laminates in the presence of an electrolyte, having a high risk of galvanic corrosion (Hamill et al., 2018). In this context, glass fibre is non-conductive, and thus the combination of glass fibre and aluminium will not result in galvanic corrosion. Since glass fibre-reinforced composites are not vulnerable to galvanic corrosion, they may serve as an insulating layer between carbon fibre-reinforced composites and aluminium layers (Ireland et al., 2012). Overall, GLARE has been considered the most successful FMLs throughout the years. GLARE is mainly applied for the primary aircraft structures such as fuselage and wing skin (Alderliesten & Homan, 2006).

The impact damages to the structures, which are due to the runway debris and hail strikes, are always the main concerns in aerospace industries. The impact velocity in some cases can be up to 100 m/s. Thus, GLARE has specifically been optimised to improve its impact resistance. To date, the impact resistance of GLARE with various lay-ups has been extensively studied. Over the years, it had been concluded that GLARE could resist impact load more effectively compared to monolithic aluminium alloys. Abdullah et al. (2015) stated that FMLs based on glass fibre-reinforced epoxy exhibit superior impact resistance over aluminium alloys and carbon fibre-based laminates. Furthermore, GLARE also performs better than monolithic aluminium in resisting the fatigue load due to its sandwich configuration. Truthfully, the excellent fatigue performance of FMLs is mainly attributed to the fibre bridging mechanism where part of the load is transferred to the fibre, reducing the stress intensity factor and therefore lowering the fatigue crack propagation rate.

Despite the conventional FMLs showing outstanding characteristics, the long processing time and the high production cost have limited their use in a wide variety of structural applications. Generally, conventional FMLs are prepared through the autoclave process, which provides uniform structure and limited or zero void content in FMLs. Minimising the void content ensures the optimum mechanical performance of FMLs as the structural components in the aerospace sectors. Nevertheless, the autoclave process requires high cost due to the long processing time and tool preparation (Ramaswamy Setty et al., 2011). Therefore, alternative manufacturing process such as vacuum-assisted resin transfer moulding (VARTM) has been developed. This process requires a lower production cost than autoclave, but the quality of the product could not be achieved as high as the autoclave process. This issue remains a challenge among the research communities to develop a manufacturing

method that could duplicate the performance of the autoclave process at a lower production cost.

The continuous rise of environmental awareness and consciousness has ignited an effort to implement cellulosic plant fibres in fibre-reinforced composites and FMLs. Plant fibres consist of cellulosic and non-cellulosic chemical contents such as lignin, hemicellulose, pectin, wax and impurities (Omran et al., 2021). It is well-known that plant fibres have demonstrated some attractive properties such as low density, biodegradability, low energy consumption and high specific properties. The high specific properties of plant fibres are especially promising for improving the energy efficiency of the aircraft without compromising the mechanical performance. Nonetheless, plant fibres also possess some demerits which retard the use of natural fibres in primary structural applications. Quality variation, low thermal stability, poor compatibility with polymer matrices and high moisture uptake are the known drawbacks of plant fibres (Alsubari et al., 2021; Ilyas et al., 2021; Nurazzi et al., 2021; Suriani et al., 2021a). Moreover, the plant fibres also demonstrate significantly lower mechanical strength than synthetic fibres. Among the approaches to improve the mechanical strength and the interfacial adhesion of plant fibre-based composites are the addition of nanofillers and the implementation of chemical treatments. The addition of fillers such as carbon nanotubes improves the mechanical performance of polymeric materials for several structural applications (Mohd Nurazzi et al., 2021). Various treatment methods have been established to enhance the interfacial bonding and reduce the moisture uptake of plant fibres. Apart from the addition of nanofillers and chemical treatments, the hybridisation concept has also been proposed to develop materials having balance in the mechanical properties and environmental friendliness. It is believed that the hybridisation concept could reduce the stress on the aerospace industries to search for lightweight, high damage tolerance and high toughness materials with the consideration of environmental friendliness. The current focus has been shifted towards the use of thermoplastic polymers and natural fibres.

2 Hybridisation Concept

Composite materials are composed of two or more phases with a boundary between components (Suriani et al., 2021b). They have shown various outstanding benefits for structural components (Ng et al., 2020). Hybridisation is the advancement in the field of composite materials with the aim of compensating the disadvantages of one fibre with the advantages of the other fibre. The hybridisation concept is the current focus in the composite field due to its several favourable characteristics. It can be defined as the incorporation of multiple types of fibres within the single matrix, allowing greater freedom to obtain the desired properties according to certain engineering applications. Hybridisation may include both natural and synthetic fibres in composite laminates and FMLs. The incorporation of natural and synthetic fibres imparts their respective advantages to the resulting hybrid composite materials,

achieving the balance in the eco-friendliness and acceptable mechanical properties. In addition to the fibre-matrix compatibility, fibre size, fibre orientation and the compatibility between multiple types of reinforcements also have a decisive effect on the mechanical properties of composite materials.

In hybrid composites, the hybridisation effect is more significant when the multiple types of fibres are strain compatible. Generally, the mechanical properties of hybrid composites are intermediate between their respective non-hybrid composites. Arpitha et al. (2017) reported that the mechanical properties of sisal/glass fibre-reinforced hybrid composites were in between their respective non-hybrid sisal and glass fibre-reinforced composites. Sanjay and Yogesha (2018) revealed similar findings where the mechanical properties of jute/kenaf/glass fibre-reinforced hybrid composites were intermediate between the non-hybrid composites. The incorporation of high-strength fibre in the composites tends to improve the mechanical properties. In certain cases, the mechanical properties of hybrid composites could be greater than non-hybrid composites (Sapuan et al., 2020; Ramlee et al., 2019; Rafiqzaman et al., 2016). Hence, it could be foreseen that hybrid composites could have great potential to be used for structural applications in aerospace industries.

3 Standardised FMLs in Aerospace Sectors

Contemporary metallic alloys, particularly aluminium alloys, have been widely utilised in aerospace sectors over the past decades. Aluminium alloys have shown their high strength-to-weight ratio characteristic, and thus, they have gained popularity for a wide variety of structural applications. FMLs have been part of the third evolution materials in aerospace industries, which are developed to tackle the poor fatigue resistance of monolithic metals. However, it was also found that FMLs display excellent impact properties. Thus, the combination of metallic alloys and composite materials can resolve the poor fatigue performance of metallic alloys and also weak impact properties of composite materials. ARALL has been the first generation of FMLs consisting of aramid/epoxy prepreg and aluminium alloys. In order to further improve the mechanical properties of FMLs, glass fibre was incorporated in the FMLs to replace aramid fibre. Besides ARALL and GLARE, carbon fibre-reinforced aluminium laminate (CARALL) was also developed due to the high stiffness characteristic of carbon fibre. Nevertheless, the consolidation of aluminium alloys and carbon fibre leads to galvanic corrosion, which deteriorates the mechanical properties of CARALL. Therefore, carbon fibre is generally isolated from aluminium alloys to avoid galvanic corrosion. In comparison with GLARE and ARALL, CARALL is still considered a novice, which is not widely used in industries. Figure 9.1 shows the classification of standardised FMLs in aerospace sectors.

The standardised FMLs can be further classified into different grades, which are based on their fibre orientations, the number of fibre layers and types of aluminium. As can be seen in Fig. 9.1, GLARE and ARALL are sub-divided into six and four

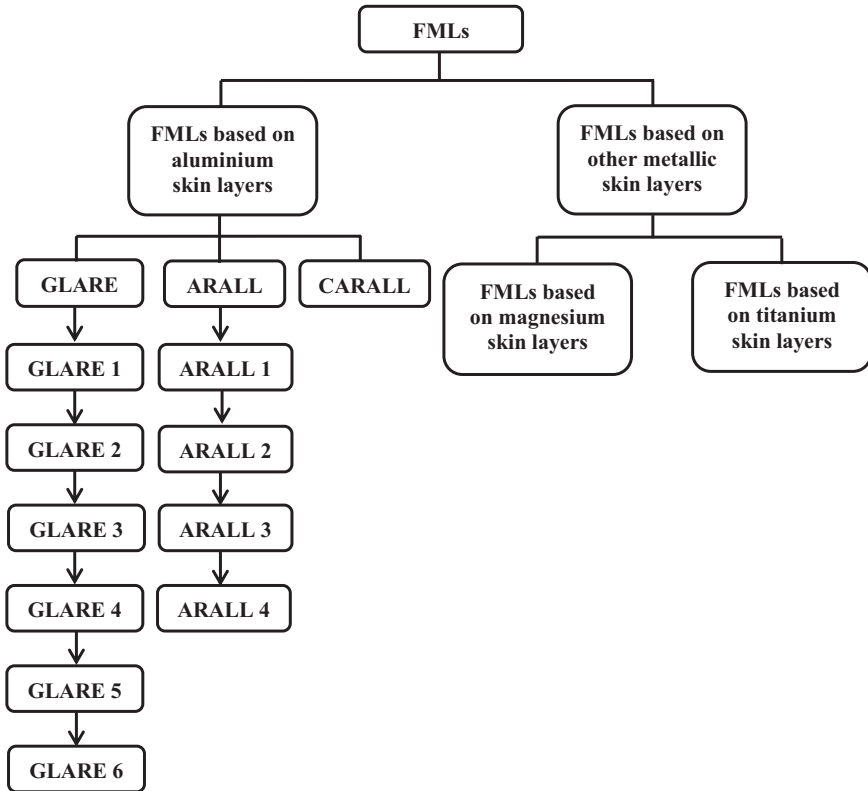


Fig. 9.1 Classification of standardised FMLs. (Reprinted with permission from Feng & Malingam, 2019)

grades, respectively. The majority of GLARE consist of aluminium 2024-T3 with an average thickness of 0.2–0.5 mm. However, the fibre orientation and the number of fibre layers may vary in each grade of GLARE. On the contrary, the fibre orientation and the number of fibre layers remain the same in ARALL. Each grade of ARALL has different types of aluminium alloy. For example, ARALL 1 consists of aramid prepreg bonded with aluminium 7075-T6; however, aluminium 2024-T3 is employed for ARALL 2. Apart from the FMLs based on aluminium alloys, titanium and magnesium alloys have also been used to form FMLs. Unlike aluminium-based FMLs which are widely used in aerospace sectors, titanium-based FMLs are primarily used in shipbuilding, military applications and off-shore industries because of their excellent corrosion resistance (Gorynin, 1999). When exposed to oxygen and air, the oxide layer formed on the titanium alloys acts as a protective layer against corrosion. This oxide layer on titanium surface is even more durable than that of aluminium alloys (Golaz et al., 2013). It should be emphasised that titanium alloys and carbon fibre have well electro-compatibility, and thus the galvanic-related issues could be avoided. Due to the superior fatigue and impact properties of FMLs,

they have been proposed to be used in the automotive industries. In order to widen the application of FMLs in other sectors, the production cost of FMLs needs to be greatly reduced so as to gain acceptance by the industries.

In fact, these standardised FMLs have common disadvantages such as long processing time, poor inter-laminar fracture toughness and difficulty in repairing. Thus, an attempt has been made to replace the thermoset polymer with thermoplastic polymer in FMLs. Thermoplastic-based FMLs offer several benefits, including short processing time, ease of forming into complex shapes and excellent inter-laminar fracture toughness. Numerous research studies have been conducted on the mechanical properties of thermoplastic-based FMLs (Feng et al., 2020; Subramaniam et al., 2019; Ng et al., 2017; Cortes & Cantwell, 2007; Reyes & Kang, 2007). In this context, polypropylene (PP) is one of the most attractive thermoplastic polymers used in both composite and FMLs. PP has been commonly used as the polymer matrix for FMLs based on glass and carbon fibre-reinforced composites in aerospace and automotive industries (Gresham et al., 2006; Mosse et al., 2006). The low-density and low-cost characteristics make PP polymer extensively utilised as matrix material in composites and FMLs.

4 The Manufacturing Process of FMLs

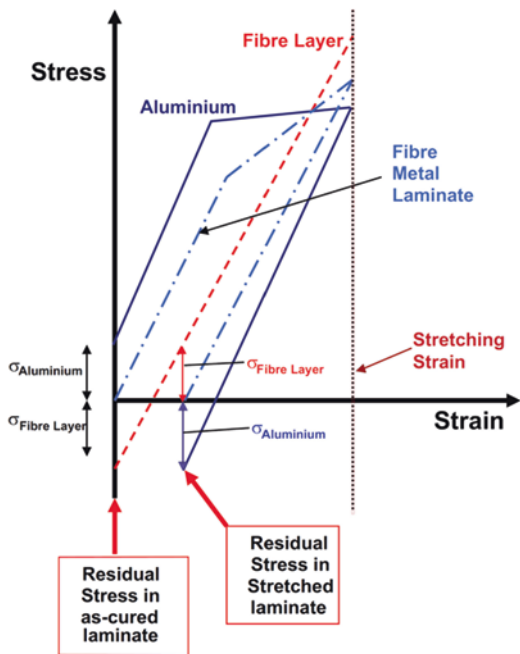
The manufacturing process of FMLs comprises three major steps, including the metal surface treatment, metal-composite consolidation and post-stretching. Each of the steps plays an essential role in developing FMLs at their optimum mechanical performance. Metal surface pre-treatment is regarded as a critical step that cannot be neglected before the metal-composite consolidation. This pre-treatment aims at improving the metal-composite adhesion through surface modification. Several techniques have been utilised in aerospace industries to improve the wettability of the metal surface, consequently improving the adhesion quality between the metal and the composites. Mechanical, chemical, electrochemical, coupling agent and dry surface treatment are those typical techniques used in aerospace industries.

As mentioned earlier, the autoclave process is often the technique being used to manufacture the standardised FMLs for primary structural applications in the aerospace sectors. FMLs are formed by stacking the thin metal sheets with composite prepreg alternatively and then cured at a temperature of 120 °C and pressure of up to 6 bar (Botelho et al., 2006). The purpose of maintaining high temperature and pressure during the autoclave process is to eliminate the void content in FMLs, allowing the quality of FMLs to meet the stringent standards established by the manufacturers. Void content is one of the critical elements that need to be controlled and minimised since the formation of the voids at the metal-composite interfaces results in delamination. At present, the autoclave process is the only production method for FMLs, which guarantees the high quality of the materials for the aerospace industries (Dariushi et al., 2019). However, the high processing cost of the autoclave technique has limited the use of FMLs to other engineering applications.

In addition to the high processing cost, it was found that the exposure of FMLs to the elevated temperatures and thermal cyclic load in the autoclave undermines their mechanical properties (Müller et al., 2016; da Costa et al., 2012). Therefore, several manufacturing techniques, which are more economical and affordable, have been proposed, including VARTM, resin infusion technique and resin transfer moulding (RTM). Unfortunately, these out-of-autoclave techniques are not able to replicate the high performance of the autoclave process. The inability of out-of-autoclave techniques to control the high temperature and pressure entails non-uniformity of the laminates and formation of voids. The void content of FMLs manufactured using out-of-autoclave techniques is relatively high, which leads to the poor mechanical properties of the materials.

The consolidation of FMLs is followed by post-stretching to purge the residual stress in the FMLs. The thermal expansion coefficients of the metal and composite layers are different, resulting in the unfavourable residual stress in the metal and composite layers. This residual stress adversely affects the fatigue resistance of FMLs. The increased crack opening and stress concentration factor resulting from the residual stress deteriorate the fatigue resistance of FMLs (Khan et al., 2009). Accordingly, post-stretching is vital to reverse the residual stress in FMLs, thereby recovering the optimum fatigue resistance of the FMLs. The post-stretching mechanism of FMLs is demonstrated in Fig. 9.2. During the post-stretching of FMLs, the metal layers are stretched into plastic deformation at a small percentage, whereas the fibre layer remains in the elastic region. The post-stretching converts the residual tensile stress in the aluminium to compressive stress. It had been shown that the

Fig. 9.2 Representation of post-stretching process in stress-strain curves. (Reprinted with permission from Khan et al., 2009)



post-stretching process is indeed beneficial to the fatigue properties of FMLs. Lin et al. (1991) reported that GLARE and CARALL exhibited outstanding fatigue crack resistance after being subjected to the post-stretching process. The last step in the manufacturing process of FMLs is the inspection of any defects which could result in a detrimental effect on the mechanical properties.

5 Surface Pre-treatment of FMLs

FMLs encompass superior mechanical properties only when the metal-composite adhesion has reached an acceptable level. The metal-composite adhesion should be strong enough to allow the fibre bridging effect to take place in FMLs. In this regard, surface pre-treatment is the key factor that has a decisive effect on the mechanical properties of FMLs. The treatment modifies the wettability, surface morphology and surface energy of the metal sheets, thereby promoting the strong bonding between the metal and composite layers (Sinmazçelik et al., 2011; Kim et al., 2003). As mentioned earlier, several types of surface pre-treatment methods can be applied to the metal layers. Generally, the combination of several surface pre-treatment methods is commonly practised in aerospace industries to guarantee the superior metal-composite adhesion. Figure 9.3 shows the classification of metal surface pre-treatments for adhesive bonding.

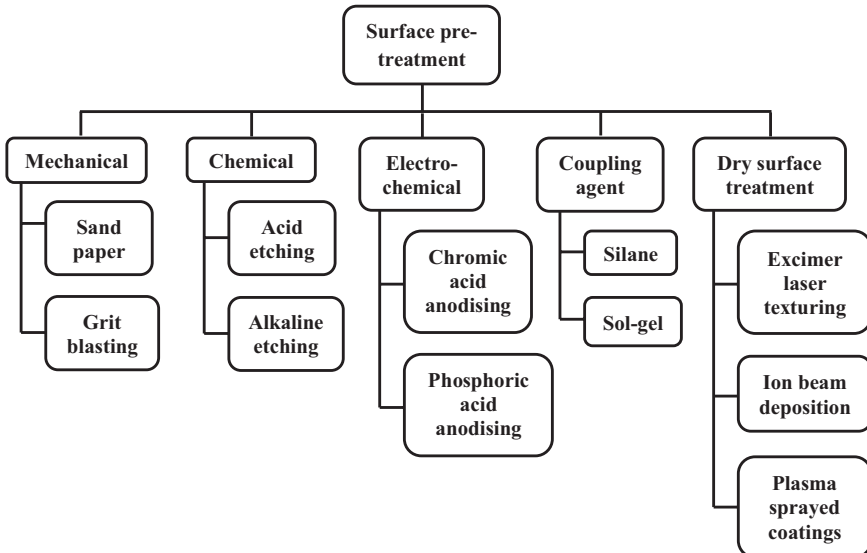


Fig. 9.3 Classification of the surface pre-treatments for adhesive bonding

5.1 Mechanical Surface Treatment

Among the surface treatment techniques, mechanical surface treatment is one of the most widely applied techniques owing to its simplicity (Mandracci et al., 2016). In mechanical treatment, the process of roughening metal sheets is performed using abrasive paper, grit blasting or shot peening technology. The mechanical surface treatment produces a macro-roughened surface and eliminates the contaminants on the metal surface. This treatment results in physico-chemical and surface energy changes. Consequently, the wettability of the metal surface is greatly improved. In addition to abrasive paper, grit blasting is another advanced mechanical surface treatment technique that ensures the metal surface is free from contaminants and increases the surface roughness for a firm adhesion between metal sheets and composites. Grit blasting is conducted by spraying a continuous stream of abrasive particles such as sand or alumina to the metal surface to create a rough surface. Figure 9.4 shows the three-dimensional (3-D) profile of steel surface before and after grit blasting. It can be observed that the surface roughness of steel after grit blasting, as shown in Fig. 9.4(a), is apparently higher than non-treated steel, as shown in Fig. 9.4(b). The selection of the types of abrasive particles highly depends on the substrate materials. Generally, the abrasive particles used in grit blasting should be harder than the substrate materials for abrasion purpose. Bresson et al. (2012) stated that it is highly recommended that the surface of metal sheets should be subjected to grit blasting prior to the adhesive bonding. Ng et al. (2019) concluded that the mechanical surface-treated aluminium laminates had higher lap shear strength than untreated aluminium laminates. Degreasing using a solvent such as acetone is usually carried out before the adhesive bonding to eliminate the contaminants or residues, which could hamper the development of chemical bonds.

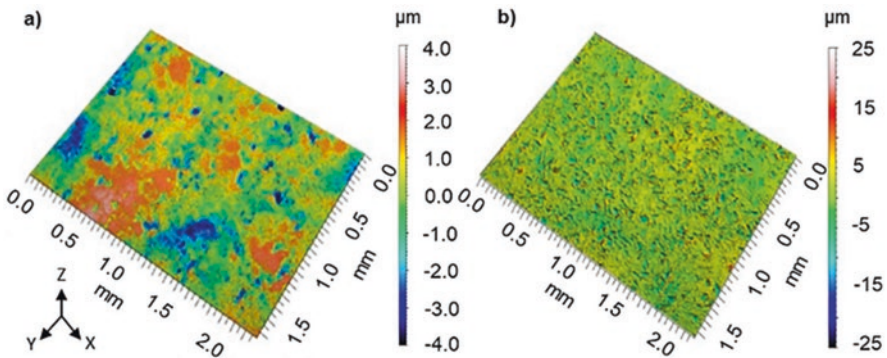
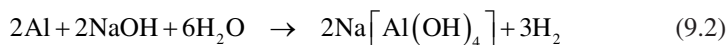


Fig. 9.4 3-D surface profile. (a) Grit blasting. (b) Non-treated. (Reprinted with permission from Santhanakrishnan Balakrishnan et al., 2019)

5.2 Chemical Treatment

Although mechanical surface treatment can improve the surface roughness of metal sheets, it may not guarantee the excellent metal-composite adhesion level as achieved by chemical treatment. Gonzalez-Canche et al. (2018) evaluated the interfacial adhesion of FMLs using different surface treatments techniques, including degreasing, mechanical surface treatment and chemical treatment. They concluded that the metal sheets subjected to the chemical treatment had the highest wettability and surface roughness compared to degreasing and mechanical surface treatment. As a result, metal-composite interfaces had the highest shear strength after being subjected to chemical treatments. Moreover, chemically treated FMLs possessed the highest tensile properties in comparison with the degreased and mechanical surface-treated FMLs. Among chemical surface treatments, chromic-sulphuric acid etching is the most widely applied chemical for metal surface treatment (Critchlow & Brewis, 1996). Chromic-sulphuric acid etching involves the immersion of the metal into the solution consisting of sulphuric acid and potassium dichromate.

Chemical treatments often include both acid and alkaline treatments to obtain the desired results. Aluminium is a passive metal that has been widely used to combine with composite materials to form FMLs. This metal tends to react with oxygen and moisture content in the atmosphere to form aluminium oxide (Al_2O_3) at the aluminium surface. It is essential to remove the weak oxide layer on the metal surface and substitute it with a new and stable oxide layer. Alkaline etching using sodium hydroxide (NaOH) has been a recognised oxide removing technique for aluminium alloys (Hu et al., 2019). Besides removing the oxide layer on the aluminium surface, alkaline etching also modifies the surface topography, which eventually improves the metal-composite adhesion level. The reaction between aluminium alloys and sodium hydroxide (NaOH) can be represented by chemical Eqs. (9.1) and (9.2).

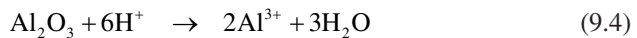
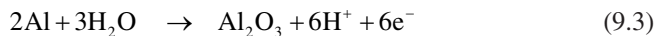


As shown in Eqs. (9.1) and (9.2), both aluminium and its oxide layer react with NaOH, leading to the formation of sodium aluminate. The subsequent chromic-sulphuric acid etching eventually generates a new and stable oxide layer that can promote strong and durable adhesive bonds (Bishopp, 2005). Generally, the acid/alkaline etching of metal alloys is followed by electrochemical treatment.

5.3 *Electrochemical Treatment*

It has been found that electrochemical treatment is able to improve the interfacial adhesion in FMLs significantly. Still, the performance of this treatment depends on various factors such as temperature, electrolyte concentration and voltage. Therefore, the temperature, electrolyte concentration and voltage should be carefully controlled to obtain the desired results. Xu et al. (2016) revealed that the optimal parameters in the anodising process could increase the surface energy of aluminium alloys, resulting in the maximum adhesion strength between aluminium and epoxy. Khan et al. (2017) performed a peel test on surface-treated CARALL. It was found that the electrochemical treatment further improved the peak force and fractured energy of CARALL when compared to those of CARALL with mechanical and chemical surface treatment only.

The alkaline/acid pre-treatment is often scarce for certain non-bonded area where corrosion may occur. Hence, electrochemical treatment is necessary to develop a durable protective layer with high wear and corrosion resistance on the metal surface before the coalescence of metal to composite layers. Anodising is often used in the electrochemical treatment, which gives a thin and ductile oxide layer to the metal layers. Chromic, oxalic, phosphoric and sulphuric acids are commonly used in the anodising process (Elabar et al., 2017). However, chromic-acid anodising (CAA) and phosphoric acid anodising (PAA) are the two most preferable electrochemical treatments in the aerospace industries. Through the anodising process on the metal surface, the corrosion susceptibility of the metal is greatly reduced. The reduction in corrosion susceptibility is attributed to the formation of a regular and uniform oxide layer with a high level of micro-roughness on the metal surface. The overall process of electrochemical treatment of aluminium can be expressed in Eqs. (9.3) and (9.4) (Wang et al., 2014; Vrublevsky et al., 2005). Due to the uniform pits formed during the anodising, polymer matrix can infiltrate into the pits of the aluminium surface, providing a mechanical anchoring effect at the metal-composite interfaces. The mechanical anchoring effect endows the FMLs with excellent metal-composite adhesion.



5.4 *Coupling Agent*

Silane is regarded as the coupling agent which is commonly applied to improve metal-composite adhesion. Silane is a bi-functional molecule that could simultaneously react with the metal sheets and polymer matrices, forming strong chemical bonds with organic and inorganic layers. Indeed, silane can promote strong

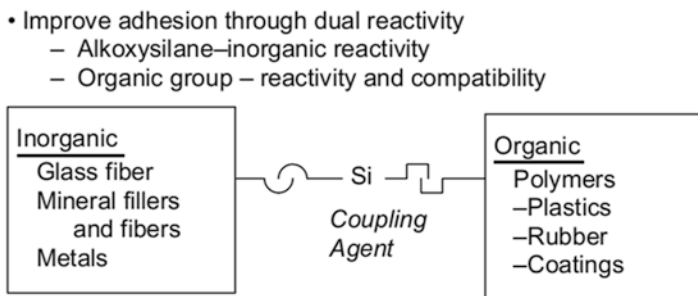


Fig. 9.5 The bridging of silane coupling agent between inorganic and organic substances. (Reprinted with permission from Ebnesajjad, 2014)

adhesion between inorganic metal layers and polymers by providing a bridging effect at the interface region. During the silane coupling agent treatment, the alkoxy groups of silane are hydrolysed to yield reactive silanol groups, and the aluminium sheets are soaked into the silane solution. The silanol groups form covalent bonds with the hydroxyl groups of aluminium sheets (Da Ponte et al., 2015). Meanwhile, the other end of the silanol groups remains available to form covalent bonds with the polymers. The bridging of silane coupling agent between inorganic and organic substances is presented in Fig. 9.5.

Apart from improving the adhesion at the metal-composite interface, silane coupling agent treatment can also reduce the rate of hydration of aluminium surface, and therefore, the metal-composite adhesion can be very stable in a humid environment. The penetration of moisture into the interfaces could weaken the adhesion and lead to physical detachment. Thus, the improvement in the resistance against hydrolysis resulting from the silane coupling agent is pivotal to ensure an excellent quality of the chemical bonding. Besides, the corrosion resistance of the metal-composite interfaces can be enhanced through the silane coupling agent treatment. Fedel et al. (2009) reported that the silane coupling agent could promote good adhesion between metal and polymer as well as provide a barrier effect against the oxygen and water. Sol-gel coating is also being used in aerospace applications to avoid corrosion which may lead to the delamination of FMLs. Furthermore, sol-gel coating for the aluminium sheets can prevent the occurrence of galvanic corrosion in CARALL.

5.5 Dry Surface Treatment

There are several types of dry surface treatments that have been developed for aluminium sheets. Excimer laser texturing, ion beam enhanced deposition (IBED) and plasma-sprayed coatings are grouped into dry surface treatment. Similar to the silane coupling agent, the dry surface treatment can reduce the use of toxic chromate-based treatments that negatively affects the environment. Excimer laser texturing

has been shown to have a profound effect on bond strength and durability. This laser texturing alters the surface morphology and microstructure of the metal surface, leading to improved bond strength and durability. Laser texturing offers the flexibility to control the processing parameters. Hence, it is possible to have greater control on the surface topography of the metals at micro- or nano-scales (Dinca et al., 2015; Maressa et al., 2015). Galantucci et al. (1996) reported that the excimer laser texturing on the aluminium and carbon fibre-reinforced composites improved the bond strength.

IBED, also known as ion beam assisted deposition (IBAD), is a surface treatment that cleans and alters the surface by sputtering with high-energy argon ions in a vacuum environment (Sinmazçelik et al., 2011). This approach focuses on the non-equilibrium inter-diffusion and the formation of nucleation sites at the interfaces by low-energy ion bombardment to enhance the adhesion (Loh et al., 1987). Plasma-sprayed coatings are also used as the surface pre-treatment method to improve the adhesion strength. Plasma-sprayed coating is a very versatile technique for the deposition of a wide range of materials, including metals, ceramic and composites. This process is performed by heating the materials, typically in powder, to the molten state, which is then projected towards the substrate at high velocity. The molten state of the materials and the high velocity impart excellent adhesion strength to the substrate (Davis et al., 1997).

6 Potential Applications of Hybrid FMLs

The contemporary FMLs have been involved in aerospace and marine applications. FMLs are primarily based on aluminium alloys and synthetic fibre-based composites in the aerospace industries. GLARE based on S-2 glass fibre/epoxy prepreg and aluminium alloys is currently being used for the primary aircraft structures such as the fuselage and wing skin materials. Similar to GLARE, ARALL finds its application in aerospace industries for the wing skin panels and the cargo door (Alderliesten, 2009). In contrast, CARALL is generally used as the impact absorber for helicopter struts and aircraft seats (Vlot & Gunnink, 2001). The most attractive feature of CARALL is the high stiffness of carbon fibre, which offers a superior fibre bridging effect to the laminates, resulting in a very low crack growth rate.

Considering the environmental friendliness of the materials without significantly compromising the mechanical properties, FMLs incorporated with both natural and synthetic fibres have shown their promising features in the replacement of synthetic fibre-based FMLs in aerospace industries. The use of natural fibre to supersede synthetic fibre is not realistic because the mechanical strength of natural fibres is lower than synthetic fibres. Thus, the hybridisation concept is considered an alternative way to be applied in both fibre-reinforced composites and FMLs. By properly designing the hybrid composites in a judicious way, the natural/synthetic fibre-reinforced hybrid composites could have comparable mechanical properties to non-hybrid synthetic fibre-based composites.

In recent years, intensive research studies have been conducted to explore the potential of hybrid composites to identify the feasibility of natural fibres in engineering applications. The previous literature studies concluded that hybrid composites and FMLs could have comparable mechanical properties to the non-hybrid synthetic fibre-based composites and FMLs when the high-strength synthetic fibres were located at the outermost layers in the laminates (Feng et al., 2019a, b). This is because the outermost layers in the composite laminates are the primary load-bearing components (Ary Subagia et al., 2014; Idicula et al., 2010). This phenomenon is even more significant when the composite laminates are subjected to out-of-plane loadings. Therefore, it is envisaged that FMLs based on natural/synthetic fibre-reinforced hybrid composites could be the excellent candidate to be applied in aerospace industries for the primary or secondary aircraft structures as substitute to synthetic fibre-based FMLs. By partially replacing the synthetic fibre in FMLs, it is believed that the energy efficiency of the aircraft will be increased as the density of natural fibres is lower than that of the glass fibre.

7 Conclusions

The advanced sandwich laminates, FMLs, have been successfully developed and applied for the primary structures in aerospace industries over the past decades. In addition to the excellent fatigue crack resistance of FMLs, these advanced sandwich laminates also lead to weight-saving and high impact resistance compared to conventional metal alloys. In order to obtain FMLs with optimum mechanical properties, the autoclave technique is usually used to manufacture FMLs with minimum or zero void content. However, this technique results in a high processing cost which hampers the use of FMLs to other structural applications in aerospace industries. Out-of-autoclave methods have been developed as an alternative, but these methods often result in a certain amount of void in the sandwich laminates. Thus, this issue remains a challenge to the engineers, scientists and researchers to develop a manufacturing method which can produce FMLs with high quality at low cost. Surface pre-treatment is a critical step to ensure excellent metal-composite adhesive bonding in FMLs. A strong metal-composite adhesion allows the effective fibre bridging mechanism, thereby improving the fatigue crack resistance.

Hybridisation has become the central focus for composite materials, aiming at reducing the dependence on synthetic fibre in both composites and FMLs. The previous studies have attested that hybrid composites may possess comparable mechanical properties to non-hybrid composites. This idea can be extended to the FMLs in the aerospace sectors in order to improve the environmental friendliness of the materials. Since natural fibres exhibit lower density than glass fibre, the energy efficiency of air transportation could be enhanced as well. The replacement of non-hybrid synthetic fibre-based FMLs with hybrid FMLs could be achieved by proper material design. Therefore, further exploration of the natural/synthetic fibre-based

hybrid FMLs is necessary to tackle the obstacles such as fibre-matrix compatibility and high moisture uptake when incorporating natural fibres in FMLs.

References

- Abdullah, M. R., Prawoto, Y., & Cantwell, W. J. (2015). Interfacial fracture of the fibre-metal laminates based on fibre reinforced thermoplastics. *Materials and Design*, *66*, 446–452. <https://doi.org/10.1016/j.matdes.2014.03.058>
- Alderliesten, R. (2009). On the development of hybrid material concepts for aircraft structures. *Recent Patents on Engineering*, *3*, 25–38. <https://doi.org/10.2174/187221209787259893>
- Alderliesten, R., & Homan, J. (2006). Fatigue and damage tolerance issues of Glare in aircraft structures. *International Journal of Fatigue*, *28*, 1116–1123. <https://doi.org/10.1016/j.ijfatigue.2006.02.015>
- Alsubari, S., Zuhri, M. Y. M., Sapuan, S. M., et al. (2021). Potential of natural fiber reinforced polymer composites in sandwich structures: A review on its mechanical properties. *Polymers (Basel)*, *13*, 423. <https://doi.org/10.3390/polym13030423>
- Arpitha, G. R., Sanjay, M. R., Senthamaraiannan, P., et al. (2017). Hybridisation effect of sisal/glass/epoxy/filler based woven fabric reinforced composites. *Experimental Techniques*, *41*, 577–584. <https://doi.org/10.1007/s40799-017-0203-4>
- Ary Subagia, I. D. G., Kim, Y., Tijing, L. D., et al. (2014). Effect of stacking sequence on the flexural properties of hybrid composites reinforced with carbon and basalt fibers. *Composites. Part B, Engineering*, *58*, 251–258. <https://doi.org/10.1016/j.compositesb.2013.10.027>
- Asundi, A., & Choi, A. Y. N. (1997). Fiber metal laminates: An advanced material for future aircraft. *Journal of Materials Processing Technology*, *63*, 384–394. [https://doi.org/10.1016/S0924-0136\(96\)02652-0](https://doi.org/10.1016/S0924-0136(96)02652-0)
- Bishopp, J. (2005). Chapter 4: Surface pre-treatment for structural bonding. In P. Cognard (Ed.), *Handbook of adhesives and sealants* (pp. 163–214).
- Botelho, E. C., Silva, R. A., Pardini, L. C., & Rezende, M. C. (2006). A review on the development and properties of continuous fiber/epoxy/aluminum hybrid composites for aircraft structures. *Materials Research*, *9*, 247–256. <https://doi.org/10.1590/S1516-14392006000300002>
- Bresson, G., Jumel, J., Shanahan, M. E. R., & Serin, P. (2012). Strength of adhesively bonded joints under mixed axial and shear loading. *International Journal of Adhesion and Adhesives*, *35*, 27–35. <https://doi.org/10.1016/j.ijadhadh.2011.12.006>
- Cortes, P., & Cantwell, W. J. (2007). The impact properties of high-temperature fiber-metal laminates. *Journal of Composite Materials*, *41*, 613–632. <https://doi.org/10.1177/0021998306065291>
- Critchlow, G. W., & Brewis, D. M. (1996). Review of surface pre-treatments for aluminium alloys. *International Journal of Adhesion and Adhesives*, *16*, 255–275. [https://doi.org/10.1016/S0143-7496\(96\)00014-0](https://doi.org/10.1016/S0143-7496(96)00014-0)
- da Costa, A. A., da Silva, D. F. N. R., Travessa, D. N., & Botelho, E. C. (2012). The effect of thermal cycles on the mechanical properties of fiber-metal laminates. *Materials and Design*, *42*, 434–440. <https://doi.org/10.1016/j.matdes.2012.06.038>
- Da Ponte, G., Ghosh, A. K., Kakaroglou, A., et al. (2015). Adhesion improvement between epoxy and stainless steel using a silane coupling agent in an atmospheric plasma process. *Plasma Processes and Polymers*, *12*, 347–361. <https://doi.org/10.1002/ppap.201400106>
- Dariushi, S., Rezadoust, A. M., & Kashizadeh, R. (2019). Effect of processing parameters on the fabrication of fiber metal laminates by vacuum infusion process. *Polymer Composites*, *40*, 4167–4174. <https://doi.org/10.1002/pc.25277>
- Davis, G. D., Groff, G. B., & Zatorski, R. A. (1997). Plasma spray coatings as treatments for aluminum, titanium and steel adherends. *Surface and Interface Analysis*, *25*, 366–373. [https://doi.org/10.1002/\(SICI\)1096-9918\(199705\)25:5<366::AID-SIA245>3.0.CO;2-S](https://doi.org/10.1002/(SICI)1096-9918(199705)25:5<366::AID-SIA245>3.0.CO;2-S)

- Dinca, V., Alloncle, P., Delaporte, P., et al. (2015). Excimer laser texturing of natural composite polymer surfaces for studying cell-to-substrate specific response. *Applied Surface Science*, 352, 82–90. <https://doi.org/10.1016/j.apsusc.2015.02.141>
- Ebnesajjad, S. (2014). Adhesion promoters. In S. Ebnesajjad (Ed.), *Surface treatment of materials for adhesive bonding* (pp. 301–329).
- Elabar, D., La Monica, G. R., Santamaria, M., et al. (2017). Anodizing of aluminium and AA 2024-T3 alloy in chromic acid: Effects of sulphate on film growth. *Surface and Coatings Technology*, 309, 480–489. <https://doi.org/10.1016/j.surfcoat.2016.11.108>
- Fedel, M., Olivier, M., Poelman, M., et al. (2009). Corrosion protection properties of silane pre-treated powder coated galvanised steel. *Progress in Organic Coatings*, 66, 118–128. <https://doi.org/10.1016/j.porgcoat.2009.06.011>
- Feng, N. L., & Malingam, S. D. (2019). Monotonic and fatigue responses of fiber-reinforced metal laminates. In M. Jawaid, M. Thariq, & N. Saba (Eds.), *Mechanical and physical testing of biocomposites, fibre-reinforced composites and hybrid composites* (pp. 307–323). Woodhead Publishing.
- Feng, N. L., DharMalingam, S., Zakaria, K. A., & Selamat, M. Z. (2019a). Investigation on the fatigue life characteristic of kenaf/glass woven-ply reinforced metal sandwich materials. *Journal of Sandwich Structures and Materials*, 21, 2440–2455. <https://doi.org/10.1177/1099636217729910>
- Feng, N. L., Malingam, S. D., Subramaniam, K., et al. (2019b). The influence of fibre stacking configurations on the indentation behaviour of pineapple leaf/glass fibre reinforced hybrid composites. *Defence S and T Technical Bulletin*, 12, 113–123.
- Feng, N. L., Malingam, S. D., Ishak, N. M., & Subramaniam, K. (2020). Novel sandwich structure of composite-metal laminates based on cellulosic woven pineapple leaf fibre. *Journal of Sandwich Structures and Materials*. <https://doi.org/10.1177/1099636220931479>
- Galantucci, L. M., Gravina, A., Chita, G., & Cinquepalmi, M. (1996). Surface treatment for adhesive-bonded joints by excimer laser. *Composites. Part A, Applied Science and Manufacturing*, 27, 1041–1049. [https://doi.org/10.1016/1359-835X\(96\)88890-7](https://doi.org/10.1016/1359-835X(96)88890-7)
- Golaz, B., Michaud, V., Lavanchy, S., & Manson, J. A. E. (2013). Design and durability of titanium adhesive joints for marine applications. *International Journal of Adhesion and Adhesives*, 45, 150–157. <https://doi.org/10.1016/j.ijadhadh.2013.04.003>
- Gonzalez-Canche, N. G., Flores-Johnson, E. A., Cortes, P., & Carrillo, J. G. (2018). Evaluation of surface treatments on 5052-H32 aluminum alloy for enhancing the interfacial adhesion of thermoplastic-based fiber metal laminates. *International Journal of Adhesion and Adhesives*, 82, 90–99. <https://doi.org/10.1016/j.ijadhadh.2018.01.003>
- Gorynin, I. V. (1999). Titanium alloys for marine application. *Materials Science and Engineering A*, 263, 112–116. [https://doi.org/10.1016/s0921-5093\(98\)01180-0](https://doi.org/10.1016/s0921-5093(98)01180-0)
- Gresham, J., Cantwell, W., Cardew-Hall, M. J., et al. (2006). Drawing behaviour of metal-composite sandwich structures. *Composite Structures*, 75, 305–312. <https://doi.org/10.1016/j.compstruct.2006.04.010>
- Hamill, L., Hofmann, D. C., & Nutt, S. (2018). Galvanic corrosion and mechanical behavior of fiber metal laminates of metallic glass and carbon fiber composites. *Advanced Engineering Materials*, 20, 1700711. <https://doi.org/10.1002/adem.201700711>
- Hu, Y., Yuan, B., Cheng, F., & Hu, X. (2019). NaOH etching and resin pre-coating treatments for stronger adhesive bonding between CFRP and aluminium alloy. *Composites. Part B, Engineering*, 178, 107478. <https://doi.org/10.1016/j.compositesb.2019.107478>
- Iidicula, M., Joseph, K., & Thomas, S. (2010). Mechanical performance of short banana/sisal hybrid fiber reinforced polyester composites. *Journal of Reinforced Plastics and Composites*, 29, 12–29. <https://doi.org/10.1177/0731684408095033>
- Ilyas, R. A., Sapuan, S. M., Harussani, M. M., et al. (2021). Polylactic acid (pla) biocomposite: Processing, additive manufacturing and advanced applications. *Polymers (Basel)*, 13, 1326. <https://doi.org/10.3390/polym13081326>

- Ireland, R., Arronche, L., & La Saponara, V. (2012). Electrochemical investigation of galvanic corrosion between aluminum 7075 and glass fiber/epoxy composites modified with carbon nanotubes. *Composites. Part B, Engineering*, 43, 183–194. <https://doi.org/10.1016/j.compositesb.2011.08.001>
- Khan, S. U., Alderliesten, R. C., & Benedictus, R. (2009). Post-stretching induced stress redistribution in Fibre Metal Laminates for increased fatigue crack growth resistance. *Composites Science and Technology*, 69, 396–405. <https://doi.org/10.1016/j.compscitech.2008.11.006>
- Khan, F., Qayyum, F., Asghar, W., et al. (2017). Effect of various surface preparation techniques on the delamination properties of vacuum infused Carbon fiber reinforced aluminum laminates (CARALL): Experimentation and numerical simulation. *Journal of Mechanical Science and Technology*, 31, 5265–5272. <https://doi.org/10.1007/s12206-017-1019-y>
- Kim, M. C., Yang, S. H., Boo, J. H., & Han, J. G. (2003). Surface treatment of metals using an atmospheric pressure plasma jet and their surface characteristics. *Surface and Coatings Technology*, 174–175, 839–844. [https://doi.org/10.1016/S0257-8972\(03\)00560-7](https://doi.org/10.1016/S0257-8972(03)00560-7)
- Lin, C. T., Kao, P. W., & Yang, F. S. (1991). Fatigue behaviour of carbon fibre-reinforced aluminium laminates. *Composites*, 22, 135–141. [https://doi.org/10.1016/0010-4361\(91\)90672-4](https://doi.org/10.1016/0010-4361(91)90672-4)
- Loh, I.-H., Hirvone, J. K., Martin, J. R., et al. (1987). The promotion of metal/polymer adhesion by ion beam enhanced deposition. In *MRS proceedings* (pp. 241–246).
- Mandracci, P., Mussano, F., Rivolo, P., & Carossa, S. (2016). Surface treatments and functional coatings for biocompatibility improvement and bacterial adhesion reduction in dental implantology. *Coatings*, 6, 7. <https://doi.org/10.3390/coatings6010007>
- Maressa, P., Anodio, L., Bernasconi, A., et al. (2015). Effect of surface texture on the adhesion performance of laser treated Ti6Al4V alloy. *The Journal of Adhesion*, 91, 518–537. <https://doi.org/10.1080/00218464.2014.933809>
- Mohammed, I., Talib, A. R. A., Hameed Sultan, M. T., et al. (2018). Mechanical properties of fibre-metal laminates made of natural/synthetic fibre composites. *BioResources*, 13, 2022–2034. <https://doi.org/10.15376/biores.13.1.2022-2034>
- Mohd Nurazzi, N., Asyraf, M. R. M., Khalina, A., et al. (2021). Fabrication, functionalization, and application of carbon nanotube-reinforced polymer composite: An overview. *Polymers (Basel)*, 13, 1047. <https://doi.org/10.3390/polym13071047>
- Mosse, L., Compston, P., Cantwell, W. J., et al. (2006). The development of a finite element model for simulating the stamp forming of fibre–metal laminates. *Composite Structures*, 75, 298–304. <https://doi.org/10.1016/j.compstruct.2006.04.009>
- Müller, B., Hagenbeek, M., & Sinke, J. (2016). Thermal cycling of (heated) fibre metal laminates. *Composite Structures*, 152, 106–116. <https://doi.org/10.1016/j.compstruct.2016.05.020>
- Ng, L. F., Sivakumar, D. M., Zakaria, K. A., & Bin Selamat, M. Z. (2017). Fatigue performance of hybrid fibre metal laminate structure. *International Review of Mechanical Engineering*, 11, 61–68. <https://doi.org/10.15866/ireme.v11i1.10532>
- Ng, L. F., Sivakumar, D., Woo, X. J., et al. (2019). The effects of bonding temperature and surface roughness on the shear strength of bonded aluminium laminates using polypropylene based adhesive. *Journal of Advanced Manufacturing Technology*, 13, 113–127.
- Ng, L. F., Dhar Malingam, S., Selamat, M. Z., et al. (2020). A comparison study on the mechanical properties of composites based on kenaf and pineapple leaf fibres. *Polymer Bulletin*, 77, 1449–1463. <https://doi.org/10.1007/s00289-019-02812-0>
- Nurazzi, N. M., Asyraf, M. R. M., Khalina, A., et al. (2021). A review on natural fiber reinforced polymer composite for bullet proof and ballistic applications. *Polymers (Basel)*, 13, 646. <https://doi.org/10.3390/polym13040646>
- Omran, A. A. B., Mohammed, A. A. B. A., Sapuan, S. M., et al. (2021). Micro-and nanocellulose in polymer composite materials: A review. *Polymers (Basel)*, 13, 231. <https://doi.org/10.3390/polym13020231>
- Rafiquzzaman, M., Islam, M., Rahman, H., et al. (2016). Mechanical property evaluation of glass–jute fiber reinforced polymer composites. *Polymers for Advanced Technologies*, 27, 1308–1316. <https://doi.org/10.1002/pat.3798>

- Ramaswamy Setty, J., Upadhyaya, A. R., Dayananda, G. N., et al. (2011). Autoclaves for aerospace applications: Issues and challenges. *International Journal of Aerospace Engineering*, 2011, 985871. <https://doi.org/10.1155/2011/985871>
- Ramlee, N. A., Jawaid, M., Zainudin, E. S., & Yamani, S. A. K. (2019). Tensile, physical and morphological properties of oil palm empty fruit bunch/sugarcane bagasse fibre reinforced phenolic hybrid composites. *Journal of Materials Research and Technology*, 8, 3466–3474. <https://doi.org/10.1016/j.jmrt.2019.06.016>
- Reyes, G., & Kang, H. (2007). Mechanical behavior of lightweight thermoplastic fiber-metal laminates. *Journal of Materials Processing Technology*, 186, 284–290. <https://doi.org/10.1016/j.jmatprotec.2006.12.050>
- Sanjay, M. R., & Yogesha, B. (2018). Studies on hybridisation effect of jute/kenaf/E-glass woven fabric epoxy composites for potential applications: Effect of laminate stacking sequences. *Journal of Industrial Textiles*, 47, 1830–1848. <https://doi.org/10.1177/1528083717710713>
- Santhanakrishnan Balakrishnan, V., Obrosovo, A., Kuke, F., et al. (2019). Influence of metal surface preparation on the flexural strength and impact damage behaviour of thermoplastic FRP reinforced metal laminate made by press forming. *Composites. Part B, Engineering*, 173, 106883. <https://doi.org/10.1016/j.compositesb.2019.05.094>
- Sapuan, S. M., Aulia, H. S., Ilyas, R. A., et al. (2020). Mechanical properties of longitudinal basalt/woven-glass-fiber-reinforced unsaturated polyester-resin hybrid composites. *Polymers (Basel)*, 12, 1–14. <https://doi.org/10.3390/polym12102211>
- Sinmazçelik, T., Avcu, E., Bora, M. Ö., & Çoban, O. (2011). A review: Fibre metal laminates, background, bonding types and applied test methods. *Materials and Design*, 32, 3671–3685. <https://doi.org/10.1016/j.matdes.2011.03.011>
- Subramaniam, K., Dhar Malingam, S., Feng, N. L., & Bapokutty, O. (2019). The effects of stacking configuration on the response of tensile and quasi-static penetration to woven kenaf/glass hybrid composite metal laminate. *Polymer Composites*, 40, 568–577. <https://doi.org/10.1002/pc.24691>
- Suriani, M. J., Rapi, H. Z., Ilyas, R. A., et al. (2021a). Delamination and manufacturing defects in natural fiber-reinforced hybrid composite: A review. *Polymers (Basel)*, 13, 1323. <https://doi.org/10.3390/polym13081323>
- Suriani, M. J., Mohd Radzi, F. S., Ilyas, R. A., et al. (2021b). Flammability, tensile, and morphological properties of oil palm empty fruit bunches fiber/pet yarn-reinforced epoxy fire retardant hybrid polymer composites. *Polymers (Basel)*, 13, 1282. <https://doi.org/10.3390/polym13081282>
- Vlot, A., & Gunnink, W. (2001). *Fibre metal laminates: An introduction*. Netherlands Kluwer Acad.
- Vrublevsky, I., Parkoun, V., & Schreckenbach, J. (2005). Analysis of porous oxide film growth on aluminum in phosphoric acid using re-anodising technique. *Applied Surface Science*, 242, 333–338. <https://doi.org/10.1016/j.apsusc.2004.08.034>
- Wang, S., Zhai, B., & Zhang, B. (2014). The effect of the microstructure of porous alumina films on the mechanical properties of glass-fiber-reinforced aluminum laminates. *Composite Interfaces*, 21, 417–430. <https://doi.org/10.1080/15685543.2014.868692>
- Xu, Y., Li, H., Shen, Y., et al. (2016). Improvement of adhesion performance between aluminum alloy sheet and epoxy based on anodising technique. *International Journal of Adhesion and Adhesives*, 70, 74–80. <https://doi.org/10.1016/j.ijadhadh.2016.05.007>

Chapter 10

Experimental Investigation of Surface Integrity Aspects and Recast Layer Formation for the Wire_{EDM} of Al/ZrO_{2(p)}-MMC Suitable for Aerospace Industries



Sanjeev Kr. Garg, Alakesh Manna, and Ajai Jain

Abbreviations

PMMC	Powder-added metal matrix composite
$RL_{t\text{ avg}}$	Recast layer-average thickness
SG	Spark gap width
SR(Ra)	Surface-roughness-average height
SR(Rt)	Surface roughness total height
Wire _{EDM}	Wire-EDM
x_1, PW	Pulse width
x_2, TBP	Time between pulses
$x_3, SCMRV$	Servo control mean reference voltage
x_4, SPT	Short pulse time
x_5, WFR	Wire feed rate
x_6, WMT	Wire tension (mechanical)

S. K. Garg (✉)
Seth Jai Parkash Mukand Lal Institute of Engineering and Technology,
Radaur, Haryana, India

A. Manna
PEC University of Technology, Chandigarh, India

A. Jain
National Institute of Technology, Kurukshetra, Haryana, India

1 Introduction

Metal matrix composite (MMC) material properties can be controlled or varied to meet the requirements as per the design by selecting the different matrix materials and types of reinforcements and varying the microstructure of reinforcement and matrix material. These composite materials consist of a matrix made of metals such as aluminium, aluminium alloys, copper, copper alloys, magnesium, and magnesium alloys and added with ceramics (oxide, carbides) which act as the reinforcement to improve the mechanical properties. Powder-added MMC (PMMC) are the materials in which reinforcement in the form of powder is added in the metal matrix. PMMC have wide applications in space industries, electronic industries, bicycle parts, automobile parts, sports equipment and a variety of other applications. As per the available literature survey, Wire_{EDM} is an effective machining method suggested by various researchers to machine the PMMC (Vijayabhaskar & Rajmohan, 2017; Dey & Pandey, 2017; Pramanik & Littlefair, 2016; Jun et al., 2018; Pramanik et al., 2016).

In this chapter, Wire_{EDM} is utilized to machine the samples of Al/ZrO_{2(p)} MMC. Many researchers used various optimization techniques to obtain the optimal parametric combinations for optimum performance characteristics for Wire_{EDM} such as Taguchi (Selvakumar et al., 2018; Sharma et al., 2017; Ramamurthy et al., 2015; Raj & Prabhu, 2016; Kumar & Singh, 2016; Kandpal et al., 2017; Maher et al., 2016; Ma et al., 2018; Pramanik et al., 2016), grey relational and statistical analysis (Sharma et al., 2017; Chalisgaonkar & Kumar, 2014; Dey & Pandey, 2018; Khanna & Singh, 2014), response surface methodology (Garg et al., 2012, 2014, 2016; Shihab, 2018; Wang et al., 2017; Vijayabhaskar & Rajmohan, 2017; Senkathir et al., 2018; Sharma et al., 2015; Rao & Venkaiah, 2016), neural network (Saha et al., 2008), fuzzy logic (Kumar et al., 2018a, b), JAYA algorithm (Kumar et al., 2018a, b), Gaussian process regression (Zhang et al., 2002) and genetic algorithm (GA) (Kuriakose & Shunmugam, 2005).

Patil and Brahmankar (2010) conducted a study on Wire_{EDM} (model: Robofil 290) of Al 6061/Al₂O_{3p} MMC using coated brass wire (CuZn50) electrode. The authors examined the effect of electrical and non-electrical machining parameters on performance characteristics using Taguchi L₂₇ orthogonal array. They found that the volumetric fraction of reinforcement (10% and 22%), on-time, servo voltage and off-time were significant parameters for CV performance measure; on-time and volumetric fraction of reinforcement were found to be significant parameters for surface finish performance measure, while the on-time and volumetric fraction of reinforcement were significant parameters for spark gap width performance measure. The authors also found that Al₂O_{3p} particulates do not melt during machining and their availability changes the gap conditions and fluidity of matrix metal. Garg et al. (2010) reviewed the published work related with sinking EDM and Wire_{EDM} of MMC materials. They reported that majority of the research work was related to SiC added MMC, whereas limited research was reported on Al₂O₃ and other added/reinforced MMCs. The authors also reported that majority of the research work had

been published on optimization of machining parameters to obtain the optimum performance characteristics considering electrical process parameters and flushing pressure as non-electrical parameter only, and small work was published related to non-electrical parameters such as work piece rotation and electrode rotation. Further, many MMCs such as Al_2O_3 -reinforced MMC need to be investigated. Kumar et al. (2011) investigated Wire_{EDM} of Al 6063/SiCp MMC using brass wire electrode. Taguchi L_9 orthogonal array was used to design the experiment, and the effect of Wire_{EDM} parameters on MRR as well as SR was studied. The authors concluded that an increase in the volumetric ratio of SiC resulted in an increase in SR and a decrease in MRR. They also reported that there was a discrete localized pool/agglomeration of SiC particles in the microstructure of stir cast composite, indicating constraint of the process for attaining uniform microstructure. Shandilya et al. (2012) obtained parametric optimization during Wire_{EDM} of Al 6061/10% wt. SiC_p MMC (fabricated by liquid melt-stir casting technique) using RSM and analysed the machined surface. The authors found that fine surface finish was obtained using lower levels of process parameters, whereas craters and black patches arise on the machined surface when machining was done using higher levels of process parameters. Azhiri et al. (2014) applied Taguchi, adaptive neuro-fuzzy inference system and grey relational for optimization of Wire_{EDM} process while using gaseous media during machining of Al/SiC MMCs. The modification in the machine was done by incorporating a gas injector to provide air with high flow pressure of 0.2 MPa. The authors found that oxygen gas and brass wire result to higher cutting velocity. Further, they concluded that discharge current and on-time were the significant factors, whereas wire tension was a non-significant factor. Pramanik (2014) reviewed the developments in the non-traditional machining of MMCs. The author found that during Wire_{EDM} of particulate-reinforced MMCs, three different kinds of situations, i.e. particulate is fully inside the spark gap width, the particulate is partially available in un-melted material and partially in the intended path of the wire, and the particulate is partially in un-melted material and partially in melted material, might be available. The author also found that the presence of reinforced particulates affects the mechanism of Wire_{EDM} process. After some time, the material available underneath the particulate melts, which causes the separation of the particulate from its position. The author also revealed the availability of the recast layer, wire shifts and heat-affected zone during Wire_{EDM} of MMCs. Sharma et al. (2015) optimized the Wire_{EDM} responses during machining of Inconel 706. The authors concluded that the thickness of recast layer formed has direct relationship with the discharge energy generated during the process. Rao and Venkaiah (2016) studied the surface veracity aspects during Wire_{EDM} of Inconel 690. The authors investigated the parametric effect on responses such as surface roughness, average recast layer thickness and micro-hardness using RSM. Pramanik et al. (2016) investigated the effect of particulates reinforced in metal matrix on the Wire_{EDM} performance characteristics. They concluded that the reinforced particulates protect the matrix material to get melted and vaporized during machining being having the higher melting temperature causing reduction in the MRR. Vijayabhaskar and Rajmohan (2017) identified the optimum parametric combinations during Wire_{EDM} of Mg matrix composites

reinforced with nano-size particles of SiC using RSM. The authors analysed the effect of reinforced particles on the Wire_{EDM} responses and surface morphology. Dey and Pandey (2018) analysed the Wire_{EDM} performance characteristics of AA 6061/cenosphere composite and concluded that the availability of insulating particles caused the difference in the mechanism of the Wire_{EDM} process than that of the monolithic alloy and affect the formation of arc and melting during the process. Bisaria and Shandilya (2018) studied the Wire_{EDM} performance characteristics of Nimonic C-263 super-alloy. The authors observed that the obtained surface after Wire_{EDM} indicated the availability of craters, droplets of debris and porosity.

From the available literature survey, it is concluded that limited research work is reported on the investigation and analysis of surface veracity aspects including recast layer developed related to Wire_{EDM} of MMC. In this chapter, the surface veracity aspects and $RL_{t_{avg}}$ are analysed for the Wire_{EDM} of Al/ZrO_{2(p)}-MMC obtained surfaces using optimal parametric combination identified using grey relational analysis. The effect of different weight fraction of ZrO_{2(p)} on average recast layer thickness was also investigated during machining of different considered weight fractions of Al/ZrO_{2(p)}-MMCs.

2 Material and Methods

The commercially available Al alloy (AA2024) used as matrix material for casting of three different MMCs and particulates of ZrO₂ is used as a reinforcement material. The weight percentage of ZrO_{2(p)} is varied from 5% to 15% in steps of 5% in order to prepare cast samples of Al/5%wt. ZrO_{2(p)}, Al/10% wt. ZrO_{2(p)} and Al/15% wt. ZrO_{2(p)}-MMC, respectively. Tables 10.1 and 10.2 present the chemical composition of the commercially available Al alloy (AA 2024) and the properties of zirconium dioxide-reinforced particulates (ZrO₂), respectively.

Table 10.1 Chemical composition of aluminium alloy (AA 2024) used as metal matrix

Matrix	Cu	Si	Mg	Zn	Mn	Fe	Pb	Al
Al alloy (AA 2024)	3.13	0.82	0.84	0.15	0.48	0.02	0.01	Balance

Table 10.2 Properties of zirconia (ZrO₂)-reinforced particulates

Reinforcement	Density	Hardness	Modulus of elasticity	Fracture toughness
ZrO ₂	4.15 gcm ⁻³	1600 (HV)	380 (GPa)	12 (MPa m ^{1/2})

2.1 Casting of Al/ZrO_{2(p)} MMC Samples

The following steps are carried out to cast samples of Al/5%wt. ZrO_{2(p)}, Al/10% wt. ZrO_{2(p)} and Al/15% wt. ZrO_{2(p)}-MMC using liquid melt-stir casting:

- (a) Preheating of Al alloy: Carved pieces of Al alloy (AA2024) are preheated at 450 °C for 2 h before melting in the first furnace of capacity 1150 °C.
- (b) Melting of Al alloy: After preheating of Al alloy, furnace temperature is then raised to and above the liquidus temperature of Al alloy, i.e. 850 ± 10 °C, for melting Al ingot completely and is then cooled down just below the liquidus, i.e. 750 ± 10 °C, to keep the slurry in a semi-solid state. Hexachloroethane tablet is used as a degassing agent to remove any unwanted gases generated during melting of Al alloy.
- (c) Preheating of ZrO₂ particulates: Simultaneously with the melting of Al alloy, preheat the estimated amount of ZrO₂ particulates at 950 °C for 3–4 h using second furnace of capacity 1250 °C through another graphite crucible. Manual mixing of preheated ZrO₂ particulates is done during preheating for proper distribution of heat and equality of agitation of the hard particles.
- (d) Mixing of Al alloy and ZrO₂ particulates: After proper preheating, the ZrO₂ particulates are mixed with the molten metal matrix at 750 ± 10 °C by means of automated mechanical mixing equipment. Then crucible consisting of composite slurry, i.e. mixture of matrix and hard reinforced particles, is placed in the furnace at liquid state and continued mixing operation is carried out for 10 min at stirring rate of 200 rpm.
- (e) Preheating of metal mould: Permanent metal moulds (size 40 mm diameter × 100 mm long) made of IS-1079/3.15 mm thick steel sheet (Fig. 3.4) are fabricated and then coated with fire clay. Simultaneously with the mixing of Al alloy and ZrO₂ particulates, preheating of the fire clay-coated metal mould is done at temperature 400 °C, maintaining it for 2 h in the third furnace of capacity 550 °C.
- (f) Pouring of mixture of Al alloy and ZrO₂ particulates: Preheated and baked metallic mould is taken out from the furnace and held on a fixture for pouring the molten mixture. Then the melted mixture of Al alloy and ZrO₂ particulates is poured into the mould and allowed for solidification for 30 min.
- (g) Fettling of cast samples: Fettling of cast samples is done to obtain the samples of fabricated Al/ZrO_{2(p)}-MMC.

2.2 Solution Heat Treatment

The solution heat treatment process is a chain of operations as mentioned below used for Al alloy and Al/ZrO_{2(p)}-MMC samples.

- (a) Heating: Usually, solution heat treatment temperature is important and dependent on the type of alloy or MMC. Al alloy (AA 2024) and the fabricated Al/

ZrO₂-MMCs are heated in an induction furnace maintaining a temperature of 410 ± 5 °C for 8 h. The heated specimens are placed in an oil bath maintaining 250 ± 6 °C temperature. Oil bath (E3 make) is used for the solution heat treatment. It is to ensure that all specimens are thoroughly dry before placing them into an oil bath.

- (b) Soaking: Samples of three considered weight fractions of fabricated Al/ZrO_{2(p)}-MMC are soaked for 3 h.
- (c) Quenching: The quench bath temperature is maintained at 30 ± 5 °C and should contain sufficient amount of water while quenching. During quenching, parts should be agitated to make sure an even transfer of heat into the water.
- (d) Artificial aging: The temperature, i.e. 190 ± 2 °C, is maintained for 9 h during artificial aging of Al alloy (AA 2024) and the fabricated Al/ZrO_{2(p)}-MMC samples.

2.3 Measuring and Testing Equipment Used for Experimental Investigation

The details of measuring and testing equipment used for mechanical property testing and microstructural investigation of Al alloy (AA 2024) and three considered weight fractions of Al/ZrO_{2(p)}-MMC are as follows:

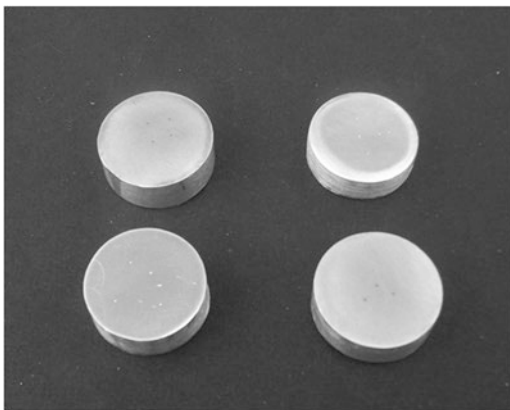
- (a) Digital Vernier Caliper: Digital vernier caliper (Baker) having least count 0.01 is used to measure the cast sample diameter and height. It is also used to measure the various dimensions of the specimens used for performing various tests.
- (b) Scanning Electron Microscope (SEM): Scanning electron microscope (ZEISS; model: EVO[®] MA15) is used for the microstructural investigation of three considered weight fractions of fabricated Al/ZrO_{2(p)}-MMC specimens with the help of SEM graphs. The microstructure of the different tensile test specimens' fractured surface is also investigated with the help of micrograph taken by SEM (JEOL; model: JSM 6610 LV).
- (c) Universal Testing Machine: The tensile strength of three considered weight fractions of fabricated Al/ZrO_{2(p)}-MMC specimens is investigated with the help of universal testing machine (Hounsfield; model: H25KS) having a 25 KN capacity.
- (d) Hardness Tester: Hardness of different weight percentage particulate-reinforced fabricated Al/ZrO_{2(p)}-MMC specimens is investigated using Brinell hardness tester (FIE) of 35 KN capacity.
- (e) Surface Roughness Tester: The machined surface roughness heights of three considered weight fractions of fabricated Al/ZrO_{2(p)}-MMC specimens are measured with the help of surface roughness tester (ZEISS, model: Surfcom 130A). The length of travel of the probe on the machine surface is 8 mm in order to measure the surface roughness average height (R_a) and total height (R_t) of different samples machined by utilizing different machining conditions.

2.4 Preparation of Samples for Testing

Specimens of Al alloy (AA 2024), Al/5%wt. $ZrO_{2(p)}$, Al/10% wt. $ZrO_{2(p)}$ and Al/15% wt. $ZrO_{2(p)}$ -MMC are prepared in order to investigate their mechanical properties, i.e. hardness and tensile strength. Machining of different cast samples is done by different steps of conventional machining, e.g. shaping, milling and grinding, so as to prepare the specimens for mechanical testing, microstructural investigation and WEDM operation. To make proper shape and size of the cast samples, conventional machines such as lathe, shaper and milling machines are also used. Grinders, dead smooth files, emery papers, abrasives (hand polishing) and smooth cloth are used to impart the proper smoothness to the machined surface. Different grades of emery papers such as P400, P800, P1200 and P1500 are temporarily fixed on the polishing machine to polish the surface of the specimens. Specimens of Al alloy (AA 2024), Al/5%wt. $ZrO_{2(p)}$, Al/10% wt. $ZrO_{2(p)}$ and Al/15% wt. $ZrO_{2(p)}$ -MMC, shown in Fig. 10.1, are prepared for hardness testing.

In order to investigate the yield strength and ultimate tensile strength, tensile test is performed on the specimen of Al alloy (AA 2024), Al/5%wt. $ZrO_{2(p)}$, Al/10%wt. $ZrO_{2(p)}$ and Al/15%wt. $ZrO_{2(p)}$ -MMC using universal testing machine (25 KN capacity). The dimensions of the specimen used for tensile test as per ASTM-E8M standard are shown in Fig. 10.2. Figure 10.3 shows the photographic view of Al alloy (AA 2024) and three considered weight fractions of Al/ $ZrO_{2(p)}$ -MMC specimens used for tensile test. Figure 10.4 shows the photographic view of the Al alloy and three considered weight fractions of Al/ $ZrO_{2(p)}$ -MMC specimens used for SEM test. The surfaces of samples are etched with Keller's etchant (2 mL hydrofluoric acid, 3 mL hydrochloric acid, 5 mL nitric acid and 190 mL distilled water) in order to properly expose and to obtain the proper SEM image. The obtained surfaces are also cleaned with acetone ($(CH_3)_2CO$) before taking SEM.

Fig. 10.1 Specimens for hardness testing



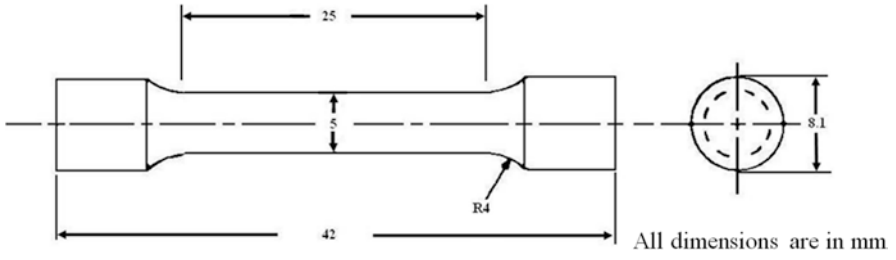


Fig. 10.2 Sketch of universal tensile testing specimen

Fig. 10.3 Specimens for universal tensile testing machine



Fig. 10.4 Specimens for scanning electron microscope

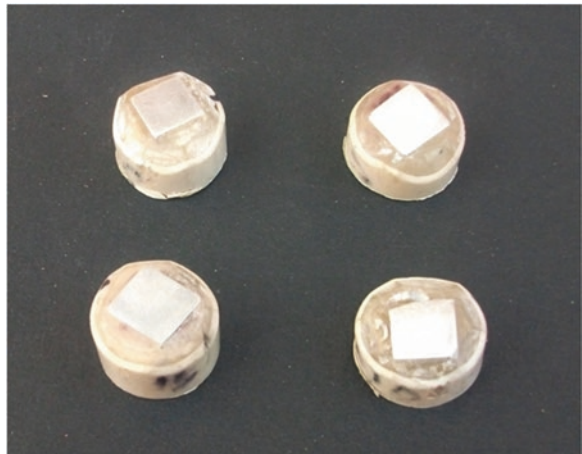


Table 10.3 Results of hardness test

Material (before heat treatment)	BHN	Material (after heat treatment)	BHN
Al alloy (AA 2024)	58	Al alloy (AA 2024) (T6)	126.2
Al/5% wt. ZrO _{2(p)} -MMC	91.2	Al/5% wt. ZrO _{2(p)} -MMC (T6)	132.4
Al/10% wt. ZrO _{2(p)} -MMC	98.6	Al/10% wt. ZrO _{2(p)} -MMC (T6)	138.7
Al/15% wt. ZrO _{2(p)} -MMC	104.5	Al/15% wt. ZrO _{2(p)} -MMC (T6)	143.8

2.5 Results of Hardness Test

This section presents the results of hardness test for Al alloy (AA 2024) and three considered weight fractions of Al/ZrO_{2(p)}-MMC. The Brinell hardness test is performed using 500 Kg load and using 10 mm diameter ball. The results of hardness tests are summarized in Table 10.3. From Table 10.3, it is concluded that the hardness of Al/5%wt. ZrO_{2(p)}-MMC is more than that of Al alloy (AA 2024) and it increases with an increase in weight percentage of ZrO₂-reinforced particulates. Further, it is also concluded that the hardness of solution heat-treated Al alloy (AA 2024) is more than that of non-treated Al alloy (AA 2024). Similarly, the hardness of solution heat-treated Al/5%wt. ZrO_{2(p)}, Al/10%wt. ZrO_{2(p)} and Al/15%wt. ZrO_{2(p)}-MMC specimens is more than that of non-treated Al/5%wt. ZrO_{2(p)}, Al/10%wt. ZrO_{2(p)} and Al/15%wt. ZrO_{2(p)}-MMC specimens. This is because copper fails to come out of solid solution and Al super-saturated with copper is locked into the single phase alloy state. Instead, over a period of days, these copper-rich compounds migrate to the metallic grain boundaries and they interfere with the movement between slip planes which results in a hardening effect.

2.6 Results of Tensile Test

The results of tensile tests are summarized in Table 10.4. From the results of tensile tests, it is clear that proof stress, maximum load and ultimate tensile strength of Al/5%wt. ZrO_{2(p)}-MMC are more than that of Al alloy (AA 2024) and these increase with the increase of weight percentage of reinforced particulates in the MMC. Further from Table 10.4, it is also clear that proof stress, maximum load and ultimate tensile strength of solution heat-treated specimens of Al alloy (AA 2024) and treated three considered weight fractions of reinforced particulate Al/ZrO_{2(p)}-MMC are more than that of non-treated specimens of Al alloy (AA 2024) and three considered weight fractions of reinforced particulate Al/ZrO_{2(p)}-MMC. During a review of the properties, it can be safely concluded that Al/ZrO_{2(p)}-MMC is suitable to manufacture the parts used in aerospace and satellite industries (Garg, 2015).

Central composite design and full-factorial methodology of RSM are utilized to obtain the experimentation setup with the help of Design-Expert® (8.0 version) software (Chua et al., 1993; Gaitonde et al., 2009). The selected design is better as it has no sensitivity for the missing data and suggested more runs than the other available

Table 10.4 Results of tensile test

Material	Strain	Ultimate tensile strength (MPa)	Proof stress (MPa)	Load (N)
Without solution heat treatment				
Al alloy (AA 2024)	0.07461	176.859	111.4682	3332.0514
Al/5% wt. ZrO _{2(p)} -MMC	0.06997	192.815	117.0831	3702.7073
Al/10% wt. ZrO _{2(p)} -MMC	0.06471	204.620	128.4356	3969.2305
Al/15% wt. ZrO _{2(p)} -MMC	0.05878	213.495	132.1191	4168.0818
With solution heat treatment				
Al alloy (AA 2024) (T6)	0.06479	419.984	246.9063	8107.574
Al/5% wt. ZrO _{2(p)} -MMC (T6)	0.05129	435.033	272.2419	8506.8298
Al/10% wt. ZrO _{2(p)} -MMC(T6)	0.04555	472.660	295.7679	9235.1945
Al/15% wt. ZrO _{2(p)} -MMC(T6)	0.04078	496.837	318.9779	9329.9512

Table 10.5 Process parameter range

S. No.	Wire _{EDM} parameters	Units	Range of the Wire _{EDM} parameters
			−1.57 to 1.57
1	Pulse width (x_1)	μs	0.36 to 1.14
2	Time between pulses (x_2)	μs	4.61 to 23.39
3	Servo control mean reference voltage (x_3)	Volts	11.52 to 58.48
4	Short pulse time (x_4)	μs	0.12 to 0.6
5	Wire feed rate(x_5)	m/min	4.87 to 11.13
6	Wire mechanical tension (x_6)	daN	0.43 to 1.37
Fixed parameters			
7	Workpiece thickness	10.2 mm	
8	Discharge current	0.5 Ampere	

designs which make this design more robust (Manual-Design-Expert®). Table 10.5 presents the machining input parameters along with their levels used to design and perform the set of experiments (Garg et al., 2013). The optimal parametric combinations are identified to obtain the multi-objective performance characteristics, i.e. minimum SG, minimum SR(R_s), minimum SR(R_r) and maximum MRR.

3 Experimental Results Obtained Using Response Surface Methodology

Experimental setup is designed using central composite design (CCD) and full-factorial approach of RSM as mentioned above and shown in Table 10.6 and a total of 86 runs is performed for experimental investigation. Table 10.7 shows the

Table 10.6 WireEDM process parameter levels for the experimental design

Run	PW	TBP	SPT	SCMRV	WFR	WMT	Run	PW	TBP	SPT	SCMRV	WFR	WMT
1	-1	-1	-1	-1	-1	-1	47	-1	1	1	1	-1	1
2	1	-1	-1	-1	-1	-1	48	1	1	1	1	-1	1
3	-1	1	-1	-1	-1	-1	49	-1	-1	-1	-1	1	1
-	-	-	-	-	-	-	-	-	-	-	-	-	-
-	-	-	-	-	-	-	-	-	-	-	-	-	-
-	-	-	-	-	-	-	59	-1	1	-1	1	1	1
10	1	-1	-1	1	-1	-1	60	1	1	-1	1	1	1
11	-1	1	-1	1	-1	-1	61	-1	-1	1	1	1	1
12	1	1	-1	1	-1	-1	-	-	-	-	-	-	-
-	-	-	-	-	-	-	-	-	-	-	-	-	-
-	-	-	-	-	-	-	69	0	0	-1.57	0	0	0
-	-	-	-	-	-	-	70	0	0	1.57	0	0	0
20	1	1	-1	-1	1	-1	-	-	-	-	-	-	-
21	-1	-1	1	-1	1	-1	-	-	-	-	-	-	-
22	1	-1	1	-1	1	-1	75	0	0	0	0	0	-1.57
-	-	-	-	-	-	-	76	0	0	0	0	0	1.57
-	-	-	-	-	-	-	-	-	-	-	-	-	-
-	-	-	-	-	-	-	-	-	-	-	-	-	-
30	1	-1	1	1	1	-1	82	0	0	0	0	0	0
31	-1	1	1	1	1	-1	83	0	0	0	0	0	0
32	1	1	1	1	1	-1	84	0	0	0	0	0	0
-	-	-	-	-	-	-	85	0	0	0	0	0	0
-	-	-	-	-	-	-	86	0	0	0	0	0	0

experimental results of performance characteristics obtained by setting the input process parameter as per experimental design by using brass wire electrode and dif-fused wire electrode during the machining of Al/5%wt.ZrO_{2(p)}-MMC. Figure 10.5 shows the workpiece after being machined by Wire_{EDM}. Mathematical models are developed using Design-Expert software as mentioned above which show the relationship between the input process parameters such as PW (x₁), TBP (x₂), SCMRV(x₃), SPT (x₄), WFR(x₅) and WMT(x₆) and the performance characteristics such as minimum SG, maximum MRR, minimum SR(R_a) and minimum SR(R_t) and expressed as Eqs. (10.1)–(10.4).

$$\begin{aligned}
 SG_{3B} = & 0.0121 + 0.0156x_1 - 0.0011x_2 - 0.0456x_3 + 0.00025x_4 - 0.00075x_5 + 0.0346x_6 \\
 & - 0.00006x_1x_2 - 0.005x_1x_3 - 0.00017x_1x_4 + 0.0002x_1x_5 + 0.002x_1x_6 + 0.0002x_2x_3 \\
 & + 0.000006x_2x_4 + 0.00004x_2x_5 - 0.00006x_2x_6 - 0.00006x_3x_4 + 0.002x_3x_5 - 0.021x_3x_6 \\
 & - 0.000013x_4x_5 - 1.0842E - 19x_4x_6 - 0.0035x_5x_6 - 0.00301x_1^2 + 0.000023x_2^2 + 0.0732x_3^2
 \end{aligned} \tag{10.1}$$

Table 10.7 Experimental results for performance characteristics (Al/5%wt. ZrO_{2(p)}-metal matrix composite)

Run	Results using brass wire electrode					Results using diffused wire electrode				
	CV _{SB}	SG _{SB}	MRR _{SB}	SR (R _a) _{SB}	SR (R _i) _{SB}	CV _{SD}	SG _{SD}	MRR _{SD}	SR (R _a) _{SD}	SR (R _i) _{SD}
1	4.556	0.016	12.976	0.802	4.193	5.069	0.012	14.028	0.972	4.187
2	6.525	0.021	19.244	1.789	5.181	6.375	0.022	18.930	1.645	5.432
3	5.312	0.018	15.344	1.385	4.345	5.423	0.018	15.665	1.418	4.834
–	–	–	–	–	–	–	–	–	–	–
–	–	–	–	–	–	–	–	–	–	–
11	4.024	0.017	11.542	2.121	5.875	4.627	0.015	13.085	2.337	6.125
12	4.616	0.019	13.427	1.634	5.028	4.325	0.019	12.581	1.685	5.039
13	5.012	0.023	14.984	2.343	6.128	5.214	0.022	15.482	2.447	4.734
–	–	–	–	–	–	–	–	–	–	–
–	–	–	–	–	–	–	–	–	–	–
28	4.322	0.018	12.485	1.684	4.938	4.155	0.018	12.002	1.633	4.868
29	5.035	0.028	15.561	2.125	5.644	5.326	0.027	16.353	2.235	5.997
30	6.500	0.030	20.352	2.274	5.989	6.754	0.030	21.147	2.307	6.132
–	–	–	–	–	–	–	–	–	–	–
–	–	–	–	–	–	–	–	–	–	–
51	4.524	0.020	13.251	1.186	4.789	4.823	0.019	14.029	1.205	4.489
52	5.688	0.022	16.890	1.342	4.482	5.454	0.022	16.195	1.447	4.629
53	5.765	0.025	17.468	1.365	4.465	5.373	0.026	16.389	1.409	4.598
–	–	–	–	–	–	–	–	–	–	–
–	–	–	–	–	–	–	–	–	–	–
68	5.073	0.018	14.654	1.213	4.375	5.422	0.017	15.552	1.376	4.598
69	5.346	0.023	15.982	1.685	4.893	5.696	0.022	16.914	1.805	4.901
70	7.598	0.027	23.329	2.434	6.385	7.345	0.028	22.700	2.664	5.094
–	–	–	–	–	–	–	–	–	–	–
–	–	–	–	–	–	–	–	–	–	–
84	6.661	0.023	19.914	1.886	5.236	6.469	0.022	19.209	1.747	5.131
85	6.804	0.021	20.066	2.087	5.526	7.055	0.020	20.664	1.981	5.014
86	7.127	0.019	20.731	2.634	6.896	7.344	0.019	21.362	2.436	6.212

$$\begin{aligned}
 1/\text{Sqrt}(\text{MRR}_{\text{SB}}) = & 0.495 - 0.212x_1 - 0.0083x_2 - 0.126x_3 - 0.0017x_4 - 0.005x_5 - 0.061x_6 \\
 & + 0.0014x_1x_2 - 0.0135x_1x_3 + 0.00086x_1x_4 - 0.0005x_1x_5 + 0.016x_1x_6 - 0.0017x_2x_3 \\
 & + 0.00005x_2x_4 + 0.00012x_2x_5 + 0.0014x_2x_6 - 0.0015x_3x_4 - 0.0041x_3x_5 - 0.006x_3x_6 \\
 & - 0.000649x_4x_5 - 0.000324x_4x_6 + 0.001081x_5x_6 + 0.067216x_1^2 + 0.000166x_2^2 + 0.17738x_3^2 \\
 & + 0.0000364x_4^2 + 0.000419x_5^2 + 0.01677x_6^2
 \end{aligned} \tag{10.2}$$

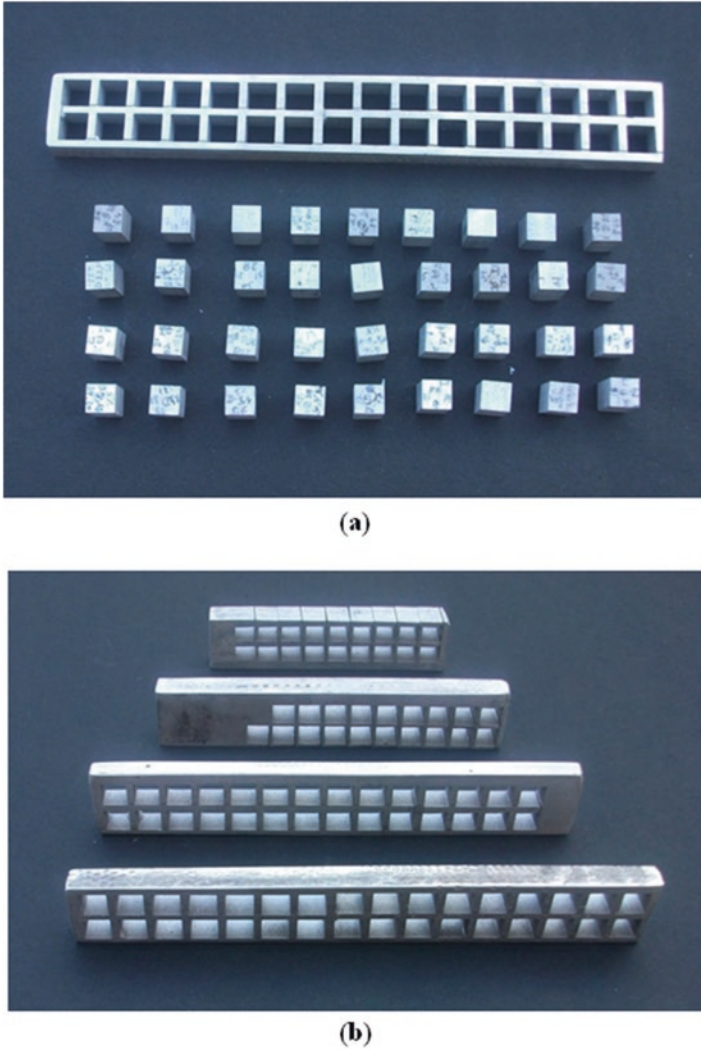


Fig. 10.5 Workpiece after being machined by wire electrical discharge machining

$$\begin{aligned}
 SR(R_a)_{5B} = & -2.302 + 3.2803x_1 + 0.092x_2 + 2.1315x_3 + 0.086x_4 - 0.1609x_5 + 1.861x_6 \\
 & 0.0536x_1x_2 + 0.23x_1x_3 - 0.0101x_1x_4 - 0.0165x_1x_5 + 0.0454x_1x_6 + 0.0616x_2x_3 \\
 & - 0.00128x_2x_4 + 0.0023x_2x_5 - 0.00021x_2x_6 - 0.0136x_3x_4 + 0.0364x_3x_5 + 1.0389x_3x_6 \\
 & + 0.00020x_4x_5 - 0.0078x_4x_6 - 0.1103x_5x_6 - 1.0777x_2^1 - 0.00240x_2^2 - 3.0844x_3^2 \\
 & - 0.00053x_4^2 + 0.0118x_5^2 - 0.7575x_6^2
 \end{aligned} \quad (10.3)$$

$$\begin{aligned}
1/\text{SR}(R_i)_{\text{SB}} = & 0.356 - 0.209x_1 - 0.0134x_2 + 0.0053x_3 - 0.004x_4 + 0.02118x_5 - 0.0055x_6 \\
& + 0.0032x_1x_2 - 0.014x_1x_3 + 0.0004x_1x_4 + 0.0043x_1x_5 + 0.0086x_1x_6 - 0.0044x_2x_3 \\
& + 0.00006x_2x_4 - 0.00019x_2x_5 - 0.00028x_2x_6 + 0.00045x_3x_4 + 0.00056x_3x_5 - 0.0587x_3x_6 \\
& - 0.00002x_4x_5 + 0.00084x_4x_6 + 0.0031x_5x_6 + 0.0569x_1^2 + 0.0004x_2^2 + 0.0433x_3^2 + 0.00002x_4^2 \\
& - 0.0014x_5^2 - 0.0095x_6^2
\end{aligned} \quad (10.4)$$

4 Multi-objective Optimization Using Grey Relational Analysis

The grey relational analysis (GRA) is used to obtain the multi-objective optimization of Wire_{EDM} parameters for machining of three considered weight fractions of Al/ZrO_{2(p)}-MMC. Multi-objective optimization theory using GRA is used for optimizing the parameters when only limited information is known. The GRA is simple, liable and efficient means (Deng, 1982, 1989) of assessing the optimum process parameter for machining Al/ZrO_{2(p)}-MMC and multi-objective optimization. The response table data shows the results for the optimal machining Wire_{EDM} parameters. The grey relational analysis establishes the relationship between components of the system, and if the relationship is higher, the obtained grey relational grade is large.

4.1 Pre-processing Data

The experimental results have been normalized (range 0–1), and pre-processing of this data step is known as the generation of grey relational data (Deng, 1982, 1989). The elements of each choice have been normalized using three different considerations such as larger-the-better, nominal-the-best and smaller-the-better. In the present investigation, material removal rate has been selected as the larger-the-better characteristic, whereas spark gap and surface roughness are selected as the smaller-the-better characteristics. For larger-the-better characteristics, Eq. (10.5) is used, and for smaller-the-better characteristics, Eq. (10.6) is used (Sharma & Yadava, 2012).

$$\text{The "larger – the – better" characteristic; } X_{ij} = \frac{y_{ij} - \min y_{ij}}{\max y_{ij} - \min y_{ij}} \quad (10.5)$$

$$\text{The "smaller – the – better" characteristic; } X_{ij} = \frac{\max y_{ij} - y_{ij}}{\max y_{ij} - \min y_{ij}} \quad (10.6)$$

where X_{ij} is the value obtained after GRA generation, $\min y_{ij}$ is the smallest value obtained for j th response and $\max y_{ij}$ is the largest value obtained for j th response.

4.2 Calculation of Grey Relational Coefficient

The grey relational coefficient can be calculated with the help of pre-processed data using Eq. (10.7) (Pawade & Joshi, 2011).

$$\xi(X_{0j}, X_{ij}) = \frac{\Delta_{\min} + \zeta \Delta_{\max}}{\Delta_{ij} + \zeta \Delta_{\max}} \quad (10.7)$$

where $\Delta_{ij} = |X_{0j} - X_{ij}|$; $\Delta_{\min} = \text{Min} \{ \Delta_{ij}, i = 1, 2, 3, \dots, m - 1, m; j = 1, 2, 3, \dots, n - 1, n \}$; $\Delta_{\max} = \text{Max} \{ \Delta_{ij}, i = 1, 2, 3, \dots, m - 1, m; \text{ and } j = 1, 2, 3, \dots, n - 1, n \}$; the distinguishing coefficient, ζ , is used to provide the compensation to the effect of the data series and is varied in the range between 0 and 1; however, usually, the value of ζ can be set to 0.5.

4.3 Calculation of Grey Relational Grade

The grey relational grade shows the levels of relationship that exist between the reference and the comparability sequence. The grey relational grade can be obtained by using Eq. (10.8) (Pawade & Joshi, 2011).

$$\gamma(X_{0j}, X_{ij}) = \frac{1}{n} \sum_{k=1}^n \xi(X_{0j}, X_{ij}) \quad (10.8)$$

The multi-objective optimization of the performances for the Wire_{EDM} of Al/5%wt. ZrO_{2(p)}-MMC using the experimental result of RSM is shown in Table 10.7. In the present investigation, performance characteristics MRR_{5B} and MRR_{5D} are considered as the larger-the-better characteristic and performance characteristics SG_{5B}, SG_{5D}, SR(R_a)_{5B}, SR(R_a)_{5D}, SR(R_t)_{5B} and SR(R_t)_{5D} are considered as the smaller-the-better characteristics. Experimental observations of RSM are converted into pre-processed data using the Eqs. (10.5) and (10.6). Table 10.8 shows the pre-processed data for the above-said performance characteristics. GRA coefficients for the performance characteristics are calculated from pre-processed data using Eq. (10.7). Table 10.8 also presents the GRA coefficients for the performance characteristics.

GRA grade presents the levels of relationship between the reference sequence and the comparability sequence and is calculated by utilizing Eq. (10.8), and the results of which are also shown in Table 10.8.

Table 10.8 Pre-processed data, grey relational coefficient and grey relational grade (Al/5%wt. ZrO_{2(p)}-metal matrix composite)

S.No.	Using brass wire electrode								
	Pre-processed data				Grey relational Coefficients				Grade
	SG _{5B}	MRR _{5B}	SR (R _a) _{5B}	SR (R _i) _{5B}	ξ SG _{5B}	ξ MRR _{5B}	ξ SR(R _a) _{5B}	ξ SR(R _i) _{5B}	
1	1	0.106	1	1	0.333	0.825	0.333	0.333	0.456
2	0.706	0.538	0.511	0.634	0.415	0.482	0.494	0.441	0.458
3	0.882	0.269	0.711	0.944	0.362	0.650	0.413	0.346	0.443
–	–	–	–	–	–	–	–	–	–
–	–	–	–	–	–	–	–	–	–
11	0.941	0.007	0.347	0.378	0.347	0.985	0.590	0.570	0.623
12	0.824	0.137	0.588	0.691	0.378	0.785	0.460	0.420	0.510
13	0.588	0.245	0.237	0.284	0.459	0.672	0.678	0.638	0.612
–	–	–	–	–	–	–	–	–	–
–	–	–	–	–	–	–	–	–	–
27	0.824	0.018	0.401	0.504	0.378	0.965	0.555	0.498	0.599
28	0.882	0.072	0.563	0.724	0.362	0.874	0.470	0.408	0.528
29	0.294	0.284	0.345	0.463	0.630	0.637	0.592	0.519	0.594
–	–	–	–	–	–	–	–	–	–
–	–	–	–	–	–	–	–	–	–
44	0.529	0.111	0.574	0.687	0.486	0.818	0.466	0.421	0.548
45	0.176	0.318	0.281	0.429	0.739	0.611	0.640	0.538	0.632
46	0.235	0.642	0.181	0.264	0.680	0.438	0.734	0.654	0.627
–	–	–	–	–	–	–	–	–	–
–	–	–	–	–	–	–	–	–	–
61	0.882	0.449	0.578	0.685	0.362	0.527	0.464	0.422	0.444
62	0.588	0.747	0.157	0.238	0.459	0.401	0.761	0.678	0.575
63	0.647	0.309	0.352	0.400	0.436	0.618	0.587	0.556	0.549
–	–	–	–	–	–	–	–	–	–
–	–	–	–	–	–	–	–	–	–
84	0.588	0.584	0.463	0.614	0.459	0.461	0.519	0.449	0.472
85	0.706	0.595	0.364	0.507	0.415	0.457	0.579	0.497	0.487
86	0.824	0.641	0.093	0	0.378	0.438	0.843	1	0.665

Response table (Table 10.9) shows the effect of each machining parameters on the performance characteristics considered together for multi-response optimization. Based on the results of the response table (Table 10.9), the optimal parametric combination for SG_{5B}, MRR_{5B}, SR(R_a)_{5B} and SR(R_i)_{5B} considered together for multi-objective optimization using brass wire electrode is A₅B₁C₅D₄E₅F₁. Similarly, optimal parametric combination for SG_{5D}, MRR_{5D}, SR(R_a)_{5D} and SR(R_i)_{5D} considered together for multi-response optimization using diffused wire electrode is A₄B₁C₅D₄E₅F₁.

Table 10.9 Response table (Al/5%wt. ZrO_{2(p)}-metal matrix composite)

Type of wire electrode	Parameter	Symbol used	Level 1 (-1.57)	Level 2 (-1)	Level 3 (0)	Level 4 (1)	Level 5 (1.57)	Max-min	Order
Brass	PW	A	0.467	0.521	0.516	0.531	0.579^a	0.112	4
	TBP	B	0.597^a	0.534	0.516	0.519	0.447	0.150	2
	SPT	C	0.487	0.511	0.514	0.541	0.603^a	0.116	3
	SCMRV	D	0.477	0.492	0.520	0.561^a	0.496	0.084	5
	WFR	E	0.559	0.534	0.513	0.518	0.560^a	0.047	6
	WMT	F	0.611^a	0.531	0.517	0.521	0.422	0.188	1
Diffused	PW	A	0.474	0.528	0.525	0.540^a	0.533	0.066	5
	TBP	B	0.610^a	0.538	0.522	0.529	0.452	0.158	3
	SPT	C	0.486	0.523	0.521	0.545	0.596^a	0.110	4
	SCMRV	D	0.510	0.502	0.524	0.565^a	0.516	0.063	6
	WFR	E	0.589	0.540	0.512	0.528	0.678^a	0.166	2
	WMT	F	0.663^a	0.536	0.522	0.532	0.406	0.257	1

^aSelected optimal value for each parameter

Table 10.10 Confirmation test results for multi-objective optimization (Al/5%wt. ZrO_{2(p)}-metal matrix composite)

S. No.	RSM mathematical model values				Experimental values				% of error			
	SG	MRR	SR (R _a)	SR (R _t)	SG	MRR	SR (R _a)	SR (R _t)	SG	MRR	SR (R _a)	SR (R _t)
1	Utilizing brass wire electrode and optimal parametric combination A ₅ B ₁ C ₅ D ₄ E ₅ F ₁											
	0.0342	20.624	2.518	5.844	0.034	20.824	2.437	5.537	0.584	2.42	0.82	0.83
2	Utilizing diffused wire electrode and optimal parametric combination A ₄ B ₁ C ₅ D ₄ E ₅ F ₁											
	0.0344	20.836	2.512	5.620	0.035	22.136	2.392	5.498	1.74	0.57	2.23	0.77

Table 10.11 Response table (Al/10%wt. ZrO_{2(p)}-metal matrix composite)

Type of wire electrode	Parameter	Symbol used	Level 1 (-1.57)	Level 2 (-1)	Level 3 (0)	Level 4 (1)	Level 5 (1.57)	Max-min	Order
Brass	PW	A	0.482	0.544	0.543	0.558	0.630^a	0.148	3
	TBP	B	0.598^a	0.560	0.544	0.542	0.497	0.100	5
	SPT	C	0.503	0.534	0.536	0.568	0.739^a	0.236	1
	SCMRV	D	0.455	0.512	0.549	0.591^a	0.521	0.136	4
	WFR	E	0.586	0.553	0.540	0.549	0.574^a	0.046	6
	WMT	F	0.620^a	0.555	0.546	0.547	0.421	0.200	2
Diffused	PW	A	0.362	0.406^a	0.379	0.402	0.395	0.044	5
	TBP	B	0.406	0.409^a	0.378	0.399	0.370	0.040	6
	SPT	C	0.369	0.397	0.376	0.411	0.449^a	0.080	3
	SCMRV	D	0.339	0.385	0.380	0.423^a	0.385	0.084	2
	WFR	E	0.424	0.410	0.373	0.398	0.444^a	0.071	4
	WMT	F	0.426^a	0.403	0.379	0.405	0.317	0.109	1

^aSelected optimal value for each parameter

Table 10.12 Confirmation test results for multi-response optimization (Al/15%wt. ZrO_{2(p)}-metal matrix composite)

S. No.	RSM mathematical model values				Experimental values				% of error			
	SG	MRR	SR (R _a)	SR (R _i)	SG	MRR	SR (R _a)	SR (R _i)	SG	MRR	SR (R _a)	SR (R _i)
Utilizing brass wire electrode and optimal parametric combination A ₅ B ₁ C ₅ D ₄ E ₅ F ₁												
1.	0.0317	18.131	2.755	5.958	0.032	17.867	2.66	6.014	0.9464	1.45607	3.44828	0.9399
Utilizing diffused wire electrode and optimal parametric combination A ₂ B ₂ C ₅ D ₄ E ₅ F ₁												
2.	0.0324	20.181	2.426	5.759	0.033	20.445	2.356	5.675	1.8519	1.3082	2.88541	1.45859

Table 10.13 Response table (Al/15%wt. ZrO_{2(p)}-metal matrix composite)

Type of wire electrode	Parameter	Symbol used	Level 1 (-1.57)	Level 2 (-1)	Level 3 (0)	Level 4 (1)	Level 5 (1.57)	Max-min	Order
Brass	PW	A	0.508	0.555	0.552	0.588	0.640^a	0.132	3
	TBP	B	0.513	0.585^a	0.559	0.558	0.488	0.097	6
	SPT	C	0.536	0.542	0.544	0.601	0.756^a	0.220	2
	SCMRV	D	0.483	0.531	0.556	0.612^a	0.575	0.129	4
	WFR	E	0.625	0.579	0.545	0.564	0.665^a	0.120	5
	WMT	F	0.671^a	0.576	0.555	0.567	0.415	0.257	1
Diffused	PW	A	0.51	0.542	0.549	0.587^a	0.551	0.077	6
	TBP	B	0.537	0.579^a	0.551	0.549	0.480	0.099	4
	SPT	C	0.506	0.527	0.540	0.601	0.737^a	0.231	1
	SCMRV	D	0.487	0.519	0.551	0.610^a	0.540	0.123	3
	WFR	E	0.572	0.570	0.542	0.559	0.637^a	0.095	5
	WMT	F	0.657^a	0.570	0.546	0.559	0.464	0.193	2

^aSelected optimal value for each parameter

Table 10.10 presents the confirmation test results of multi-response optimization corresponding to Wire_{EDM} of Al/5%wt. ZrO_{2(p)}-MMC. The % of error calculated using optimal values and experimental values of responses varies between 0.584 and 2.423, which is within the acceptance range, hence confirming the above-said multi-response optimization results.

The multi-objective optimization of the performance characteristics is based on grey relational analysis using the experimental result of RSM corresponding to Wire_{EDM} of Al/10%wt. ZrO_{2(p)}-MMC. Based on the results of the response table (Table 10.11), the optimal parametric combination for SG_{10B}, MRR_{10B}, SR(R_a)_{10B} and SR(R_i)_{10B} considered together for multi-objective optimization is A₅B₁C₅D₄E₅F₁. Similarly, the optimal parametric combination for SG_{10D}, MRR_{10D}, SR(R_a)_{10D} and SR(R_i)_{10D} considered together for multi-objective optimization is A₂B₂C₅D₄E₅F₁. That is, the optimal machining conditions for multi-response optimization using brass wire electrode are PW of 1.14 μs, TBP of 4.61 μs, SPT of 0.58 μs, SCMRV of 50 volts, WFR of 11.13 m/min and WMT of 0.43 daN, and the optimal machining conditions for multi-response optimization using diffused wire electrode are PW of

Table 10.14 Confirmation test results for multi-response optimization (Al/15%wt. ZrO₂-metal matrix composite)

S. No.	RSM mathematical model values				Experimental values				% of error			
	SG	MRR	SR (R _a)	SR (R _t)	SG	MRR	SR (R _a)	SR (R _t)	SG	MRR	SR (R _a)	SR (R _t)
1.	Utilizing brass wire electrode and optimal parametric combination A ₅ B ₂ C ₅ D ₄ E ₅ F ₁											
	0.0301	17.686	3.015	6.277	0.03	17.114	2.945	6.208	0.33223	3.2342	2.32172	1.09925
2.	Utilizing diffused wire electrode and optimal parametric combination A ₄ B ₂ C ₅ D ₄ E ₅ F ₁											
	0.0308	19.05	2.689	6.064	0.031	19.553	2.601	5.871	0.6494	2.6404	3.27259	3.18272

0.5 μs, TBP of 8 μs, SPT of 0.58 μs, SCMRV of 50 volts, WFR of 11.13 m/min and WMT of 0.43 daN.

Table 10.12 presents the confirmation test results of multi-response optimization corresponding to Wire_{EDM} of Al/10%wt. ZrO_{2(p)}-MMC. The % of error calculated using optimal values and experimental values of performances varies from 0.9399% to 3.448%, which is within the accepted range, hence confirming the multi-objective optimization results.

Similarly, the multi-response optimization results corresponding to Wire_{EDM} of Al/15% wt. ZrO_{2(p)}-MMC are also obtained. Response table (Table 10.13) shows the effect of each machining parameter on the above-said performance characteristics considered together for multi-objective optimization. Based on the results of the response table (Table 10.13), the optimal parametric combination for SG_{15B}, MRR_{15B}, SR(R_a)_{15B} and SR(R_t)_{15B} considered together for multi-objective optimization is A₅B₂C₅D₄E₅F₁. Similarly, the optimal parametric combination for SG_{15D}, MRR_{15D}, SR(R_a)_{15D} and SR(R_t)_{15D} considered together for multi-response optimization is A₄B₂C₅D₄E₅F₁.

Table 10.14 presents the confirmation test results corresponding to Wire_{EDM} of Al/15% wt. ZrO_{2(p)}-MMC. The % of errors calculated using optimal values and experimental values of performances varies from 0.3322% to 3.2725%, which is within the accepted range, hence confirming the multi-objective optimization results.

5 Surface Veracity and Recast Layer Analysis of Machined Samples

The surface veracity aspects that include microstructure examination as well as recast layer thickness are investigated for three considered weight fractions of Al/ZrO_{2(p)}-MMCs. The discharge energy impinged on the workpiece surface during Wire_{EDM} melts the material and debris are flushed away by the dielectric. Thus, thermal energy produced during Wire_{EDM} process causes fast heating, melting and vaporization, affecting the surface veracity of the machined surface. In the present

work, surface veracity is investigated for the machined surface that is obtained from optimal parametric combination suggested during single as well as multi-response optimization for performance characteristics, i.e. maximum MRR, minimum SR(R_a) and minimum SG. It is investigated with a view to identify its composition and surface defects, i.e. cracks, voids, craters and pockmarks, as well as to identify the average thickness of the recast layer deposited on the machined surface for different optimal parametric combinations.

The analysis of surface veracity aspects of the obtained surfaces after machining is carried out through SEM (model JSM-6610LV) that is coupled with an energy-dispersive X-ray (EDX) spectrometer. The Wire_{EDM} of material produces the recast layer which is extremely undesirable as the machined surface becomes susceptible to fatigue failure (Ekmekci, 2009; Jadam et al., 2019). The thickness of recast layer formed is not uniform so recast layer average thickness ($RL_{t,avg}$) is calculated using AxioVision (Release 4.8.2 SP2)[®] software.

The compositions of the machined surfaces are investigated through energy-dispersive X-ray (EDX) analysis. EDX is the technique that is used to identify the elemental composition of the machined specimens. The EDX spectrum contains the various peaks related to the energy level of the maximum received X-rays. The height of the peak in the spectrum shows the concentration of the element present in the specimen (Garg, 2015).

The following subsections present analysis of the machined surface microstructure and average recast layer thickness obtained after Wire_{EDM} of three considered weight fractions of Al/ZrO_{2(P)}-MMCs.

5.1 Surface Veracity and Recast Layer Analysis of Al/5% wt. ZrO_{2(P)}-MMC

Figure 10.6(a, b) shows SEM images of obtained surface after Wire_{EDM} of Al/5% wt. ZrO_{2(P)}-MMC and Fig. 10.6(c) shows the recast layer formed using optimum parametric combination for multi-response optimization. Figure 10.6(a, b) reveals the availability of droplets of debris, porosity, micro-cracks and shallow and deep craters in the obtained surface. The same was also reported by Nag et al. (2018), Kumar et al. (2018a, b). During Wire_{EDM} of Al/5% wt. ZrO_{2(P)}-MMC, wire deviation from its intended path usually happens when the electrode does not find any conductive path because of the presence of non-conductive ZrO_{2(P)}-reinforced particulates in the wire path. Thus, it leaves an oblique mark on the obtained surface. The same fact was also observed by Goswami and Kumar (2014), Kumar et al. (2018a, b). Figure 10.6(c) reveals that $RL_{t,avg}$ developed after Wire_{EDM} is 24.19 μ m. This is because the high value of SPT (0.6 μ s) and PW (1.0 μ s) along with the low value of TBP (4.61 μ s) generates higher discharge energy per unit time in the machining zone that causes more melting of workpiece material which leads to

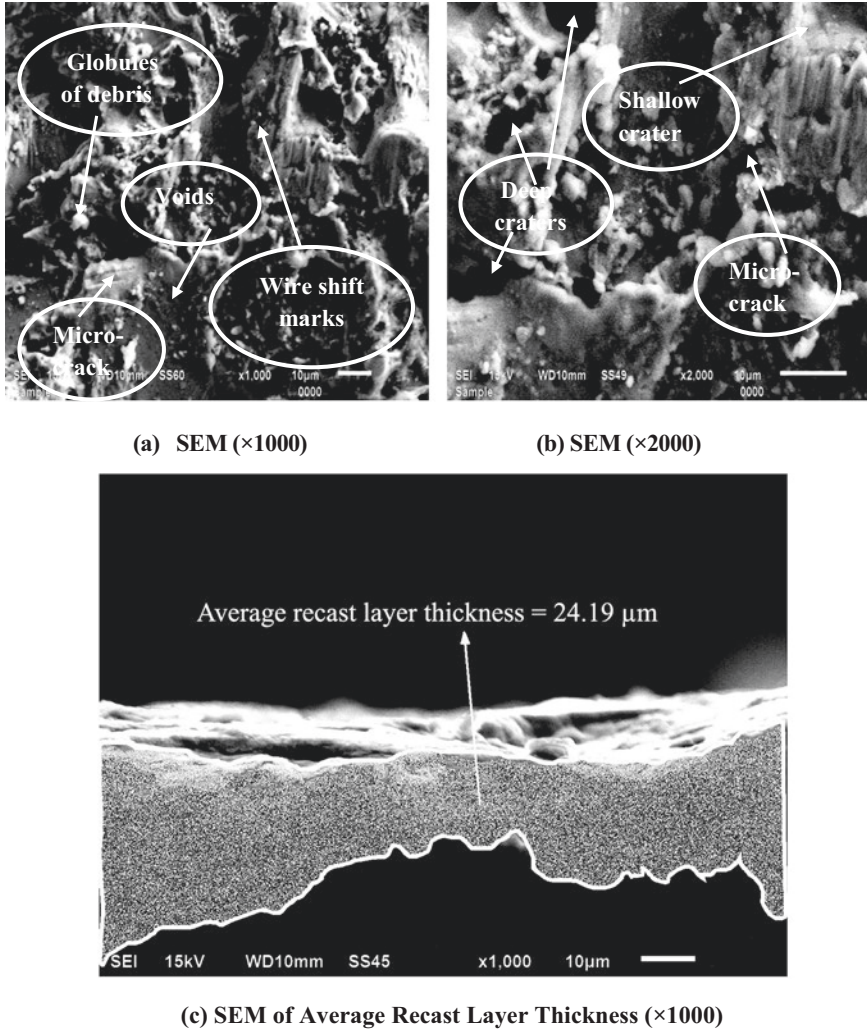


Fig. 10.6 (a–c) SEM images of Wire_{EDM} surface of Al/5% wt. ZrO_{2(P)}-MMC (PW = 1.00 μ s, TBP = 4.61 μ s, SPT = 0.60 μ s, SCMRV = 50.00 volts, WFR = 10.00 m/s, WMT = 0.43 daN). (a) SEM ($\times 1000$); (b) SEM ($\times 2000$); (c) SEM of average recast layer thickness ($\times 1000$)

the formation of thicker recast layer. This is in agreement with the findings reported by Kumar et al. (2018a, b), Yan et al. (2005) and Habib and Okada (2016). Figure 10.7 indicates the EDX analysis of the machined surface. It reveals that there is migration of Cu and Zn ions from electrode to the obtained surface. Further, chemical dissociation of dielectric medium causes the presence of O on the obtained surface.

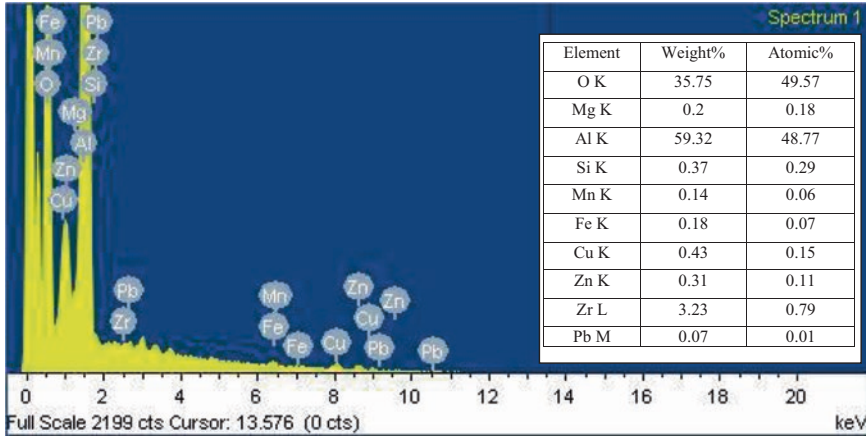


Fig. 10.7 EDX results for Wire_{EDM} machined sample of Al/5% wt. ZrO_{2(P)}-MMC

5.2 Surface Veracity and Recast Layer Analysis of Al/10% wt. ZrO_{2(P)}-MMC

Figures 10.8(a)–(c) and 10.9 show the SEM images and EDX analysis of Wire_{EDM} obtained surfaces of Al/10% wt. ZrO_{2(P)}-MMC using optimum parametric combinations for multi-objective optimization. Figure 10.8(a, b) shows the availability of pockmarks, droplets of debris, cracks, porosity and shallow craters in the obtained surface after Wire_{EDM}. Figure 10.8(c) shows RL_{t avg} developed after Wire_{EDM} is 20.90 μm.

Figure 10.9 indicates EDX results which show that there is migration of ions of Cu and Zn from electrode to the workpiece surface during machining. Comparison of Fig. 10.8(a, b) with Fig. 10.6(a, b) shows the presence of craters, droplets of debris, pockmarks, cracks and porosity in the machined surfaces of Al/10% wt. ZrO_{2(P)}-MMC and Al/5% wt. ZrO_{2(P)}-MMC. Further, RL_{t avg} (20.90 μm) for Al/10% wt. ZrO_{2(P)}-MMC is lesser as compared to RL_{t avg} (24.19 μm) for Al/5% wt. ZrO_{2(P)}-MMC micrographs shown in Fig. 10.6(c). This is due to the fact that the amount of ZrO_{2(P)}-reinforced particulates present in Al/10% wt. ZrO_{2(P)}-MMC is more as compared to Al/5% wt. ZrO_{2(P)}-MMC. Further, ZrO_{2(P)}-reinforced particulates have higher melting temperature as compared to Al alloy matrix (Shanmugam & Sahadevan, 2018). The MRR is also lower during Wire_{EDM} of Al/10% wt. ZrO_{2(P)}-MMC as compared to Al/5% wt. ZrO_{2(P)}-MMC (20.445 mm³/min. as compared to 22.136 mm³/min.). Moreover, the value of process parameter TBP (8.00 μs. as compared to 4.61 μs.) and WFR is more (11.13 m/s as compared to 10.00 m/s) which causes to produce lesser discharge energy during sparking and carries more heat from the sparking zone, respectively. Results of EDX confirm the presence of more Zr and O elements on the machined surface as shown in Fig. 10.9 as compared to the results of EDX shown in Fig. 10.7.

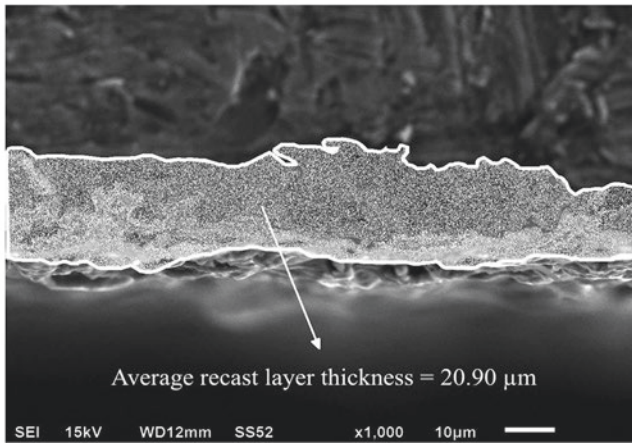
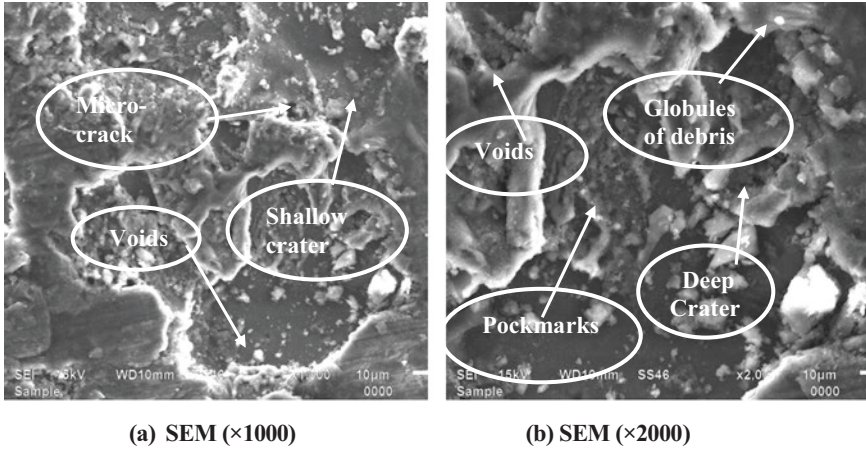


Fig. 10.8 (a–c) SEM of Wire_{EDM} surface of Al/10% wt. ZrO_{2(P)}-MMC (PW = 1.00 μs , TBP = 8.00 μs , SPT = 0.60 μs , SCMRV = 50.00 volts, WFR = 11.13 m/s., WMT = 0.43 daN). (a) SEM ($\times 1000$); (b) SEM ($\times 2000$); (c) SEM image of average recast layer thickness ($\times 1000$)

5.3 Surface Veracity and Recast Layer Analysis of Al/15% wt. ZrO_{2(P)}-MMC

Figure 10.10(a)–(c) and 10.11 show the SEM images and results of EDX for the Wire_{EDM} obtained surfaces of Al/15% wt. ZrO_{2(P)}-MMC corresponding to optimal parameters for multi-objective optimization. Figure 10.10(a, b) shows the

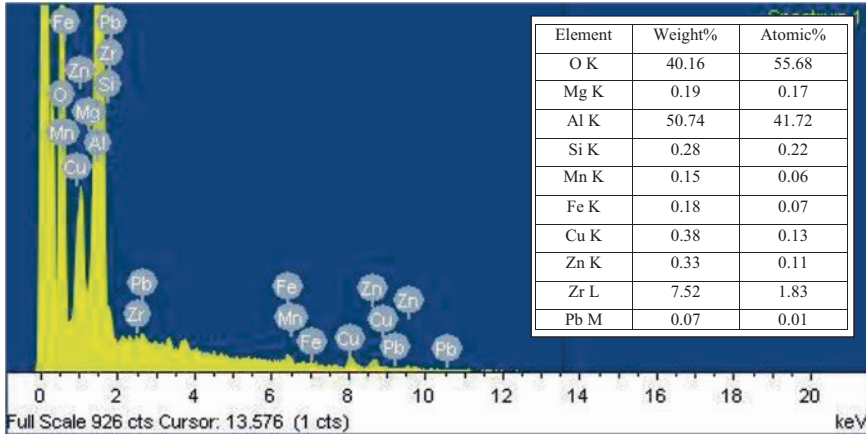


Fig. 10.9 EDX results for Wire_{EDM} machined sample of Al/10% wt. ZrO_{2(p)}-MMC

availability of pockmarks, craters, droplets of debris, cracks and craters on the obtained surface. Figure 10.10(c) shows that $RL_{t\text{ avg}}$ developed after Wire_{EDM} is 18.89 μm . Figure 10.7 indicates EDX analysis of the machined surface and reveals that there is migration of ions of Cu and Zn from electrode to the machined surface. Comparison of Fig. 10.10(a, b) with Fig. 10.8(a, b) and Fig. 10.6(a, b) reveals the presence of deep and shallow craters, pockmarks, droplets of debris, cracks and voids in machined surfaces of Al/15% wt. ZrO_{2(p)}-MMC, Al/10% wt. ZrO_{2(p)}-MMC and Al/5% wt. ZrO_{2(p)}-MMC. Further, $RL_{t\text{ avg}}$ (18.89 μm) for Al/15% wt. ZrO_{2(p)}-MMC is lesser as compared to $RL_{t\text{ avg}}$ 20.90 μm for Al/10% wt. ZrO_{2(p)}-MMC and 24.19 μm for Al/5% wt. ZrO_{2(p)}-MMC micrographs shown in Figs. 10.8(c) and 10.6(c), respectively. This is due to the fact that the amount of ZrO_{2(p)}-reinforced particulates present in Al/15% wt. ZrO_{2(p)}-MMC is more as compared to Al/10% wt. ZrO_{2(p)}-MMC and Al/5% wt. ZrO_{2(p)}-MMC. Further, ZrO_{2(p)}-reinforced particulates have higher melting temperature as compared to Al alloy matrix. Moreover, MRR is also lower during Wire_{EDM} of Al/15% wt. ZrO_{2(p)}-MMC as compared to Al/10% wt. ZrO_{2(p)}-MMC and Al/5% wt. ZrO_{2(p)}-MMC. Results of EDX confirm the presence of more Zr and O elements in the machined surface as shown in Fig. 10.11 as compared to the results of EDX shown in Fig. 10.9 and Fig. 10.7 for the Wire_{EDM} of Al/10% wt. ZrO_{2(p)}-MMC and Al/5% wt. ZrO_{2(p)}-MMC, respectively.

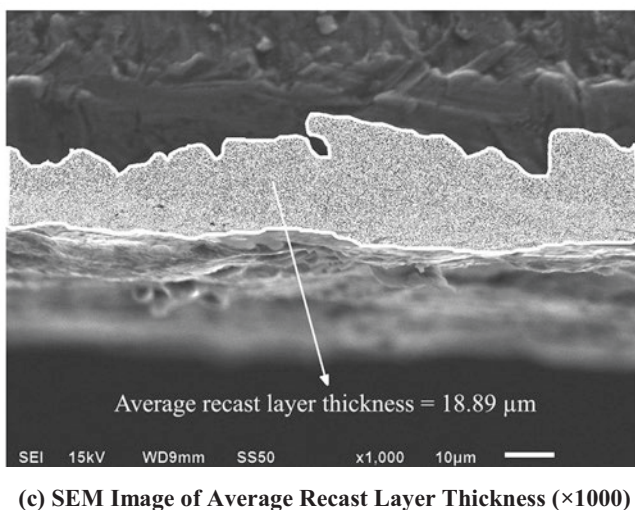
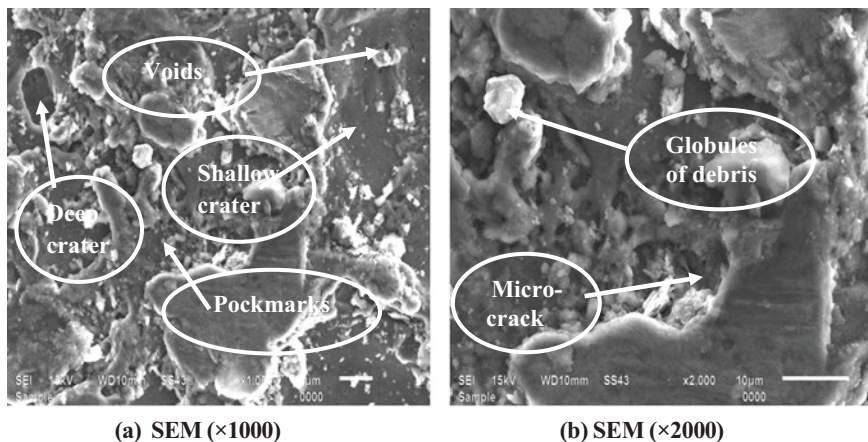


Fig. 10.10 (a–c) SEM of Wire_{EDM} of Al/15% wt. ZrO_{2(p)}-MMC (PW = 1.00 μs, TBP = 8.00 μs, SPT = 0.50 μs, SCMRV = 50.00 volts, WFR = 10.00 m/s, WMT = 0.43 daN). (a) SEM (×1000); (b) SEM (×2000); (c) SEM image of average recast layer thickness (×1000)

6 Conclusions

Based on the experimental investigation during Wire_{EDM} of three considered weight fractions of Al/ZrO_{2(p)}-MMCs, the safe conclusions drawn are mentioned below:

1. Wire_{EDM} machined surface reveals the presence of pockmarks, porosity, cracks, micro-voids, craters and droplets of debris.
2. Wire deviation from its intended path is identified during machining which leaves an oblique mark on the surface of Wire_{EDM} machined sample of Al/ZrO_{2(p)}-MMCs.

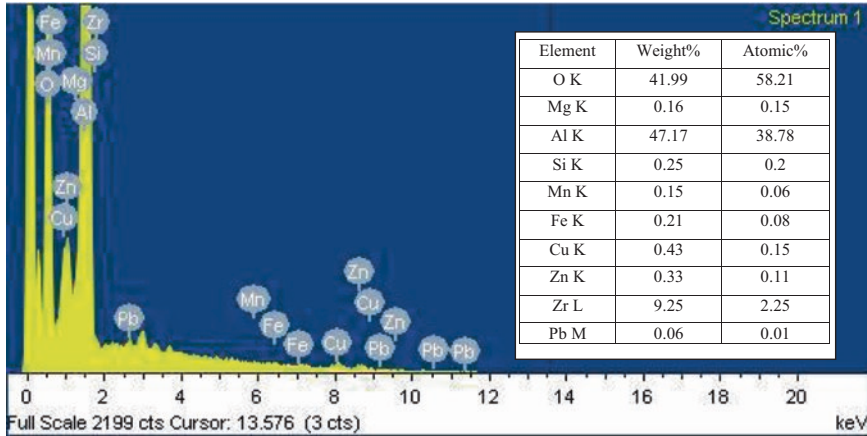


Fig. 10.11 EDX results for Wire_{EDM} machined sample of Al/15% wt. ZrO_{2(P)}-MMC

3. Migration of metallic ions (Cu and Zn ions) which are the constituents of electrode is observed as these are available on the surface of Al/ZrO_{2(P)}-MMC Wire_{EDM} machined samples.
4. The chemical dissociation of dielectric fluid causes the availability of oxygen on the surface of Al/ZrO_{2(P)}-MMCs Wire_{EDM} machined samples.
5. Lower values of input process parameters, i.e. pulse width and short pulse time and higher values of input process parameter time between pulses, are preferred for better surface veracity aspects and for lower recast layer thickness for the Wire_{EDM} of Al/ZrO_{2(P)}-MMCs.
6. The average recast layer thickness developed during Wire_{EDM} decreases as weight fraction of ZrO_{2(P)} increases in Al/ZrO_{2(P)}-MMC from 5 to 15%.

The authors believe that experimental investigation of surface veracity aspects and recast layer developed during Wire_{EDM} of Al/ZrO_{2(P)}-MMCs will offer significant guidelines to the production engineers to select the optimum values of input process parameters to improve the surface veracity aspects and to execute the subsequent operations to improve the life of the components fabricated utilizing these MMCs.

References

- Azhiri, R. B., Teimouri, R., Baboly, M. G., & Leseman, Z. (2014). Application of Taguchi, ANFIS and grey relational analysis for studying, modeling and optimization of wire EDM process while using gaseous media. *The International Journal of Advanced Manufacturing Technology*, 71, 279–295. <https://doi.org/10.1007/s00170-013-5467-y>
- Bisaria, H., & Shandilya, P. (2018). Experimental investigation on wire electric discharge machining (WEDM) of nimonic C-263 superalloy. *Materials and Manufacturing Processes*, 34, 1–10. <https://doi.org/10.1080/10426914.2018.1532589>

- Chalisgaonkar, R., & Kumar, J. (2014). Parametric optimization and modeling of rough cut WEDM operation of pure titanium using grey fuzzy logic and dimensional analysis. *Cogent Engineering*, 1, 1–28. <https://doi.org/10.1080/23311916.2014.979973>
- Chua, M. S., Rahman, M., Wong, Y. S., & Loh, H. T. (1993). Determination of optimal cutting conditions using design of experiments and optimization techniques. *International Journal of Machine Tools and Manufacture*, 33, 297–305. [https://doi.org/10.1016/0890-6955\(93\)90081-5](https://doi.org/10.1016/0890-6955(93)90081-5)
- Deng, J. (1982). Control problem of grey system. *Systems and Control Letters*, 5, 288–294. [https://doi.org/10.1016/S0167-6911\(82\)80025-X](https://doi.org/10.1016/S0167-6911(82)80025-X)
- Deng, J. (1989). Introduction to grey system theory. *The Journal of Grey System*, 1, 1–24. <https://doi.org/10.5555/90757.90758>
- Design-Expert® help manual. (n.d.). Retrieved March 20, from 2015, http://www.statease.com/dx8_man.html.
- Dey, A., & Pandey, K. M. (2017). Wire electrical discharge machining characteristics of AA6061/cenosphere as cast aluminum matrix composites. *Materials and Manufacturing Processes*, 33, 1346–1353. <https://doi.org/10.1080/10426914.2017.1388517>
- Dey, A., & Pandey, K. M. (2018). Selection of optimal processing condition during WEDM of compocasted AA6061/cenosphere AMCs based on grey based hybrid approach. *Materials and Manufacturing Processes*, 33, 1549–1558. <https://doi.org/10.1080/10426914.2018.1453154>
- Ekmekci, B. (2009). White layer composition, heat treatment and crack formation in electrical discharge machining process. *Journal of Materials Processing Technology*, 40, 70–81. <https://doi.org/10.1007/s11663-008-9220-0>
- Gaitonde, V. N., Karnik, S. R., & Davim, J. P. (2009). Some studies in metal matrix composites machining using response surface methodology. *Journal of Reinforced Plastics and Composites*, 28, 2445–2457. <https://doi.org/10.1177/2F0731684408092375>
- Garg, S. K. (2015). *Optimization of wire electric discharge machining parameters of Al/ZrO₂(P) metal matrix composite*. PhD thesis, NIT, Kurukshetra, India.
- Garg, R. K., Singh, K. K., Sachdeva, A., Sharma, V. S., et al. (2010). Review of research work in sinking EDM and WEDM on metal matrix composite materials. *International Journal of Advanced Manufacturing Technology*, 50, 611–624. <https://doi.org/10.1007/s00170-010-2534-5>
- Garg, S. K., Manna, A., & Jain, A. (2012). An experimental investigation and parametric optimization for wire EDM of Al-5% ZrO₂ particulate reinforced metal matrix composite. *International Journal of Mechanical and Materials Engineering*, 7, 136–145. <https://doi.org/10.4018/ijmmme.2012100103>
- Garg, S. K., Manna, A., & Jain, A. (2013). An experimental investigation for optimization of WEDM parameters during machining of fabricated Al/ZrO_{2(p)}-MMC. *Arabian Journal for Science and Engineering*, 38(12), 3471–3483. <https://doi.org/10.1007/s13369-013-0657-3>
- Garg, S. K., Manna, A., & Jain, A. (2014). An investigation on machinability of Al/10% ZrO_{2(p)}-metal matrix composite by WEDM and parametric optimization using desirability function approach. *Arabian Journal for Science and Engineering*, 39, 3251–3270. <https://doi.org/10.1007/s13369-013-0941-2>
- Garg, S. K., Manna, A., & Jain, A. (2016). Experimental investigation of spark gap and material removal rate of Al/ZrO_{2(p)}-MMC machined with wire EDM. *Journal of the Brazilian Chemical Society*, 38, 481–491. <https://doi.org/10.1007/2Fs40430-015-0394-5>
- Goswami, A., & Kumar, J. (2014). Investigation of surface integrity, material removal rate and wire wear ratio for WEDM of Nimonic 80a alloy using GRA and Taguchi method. *International Journal of Engineering, Science and Technology*, 17(4), 173. <https://doi.org/10.1016/j.jestch.2014.05.002>
- Habib, S., & Okada, A. (2016). Study on the movement of wire electrode during fine wire electrical discharge machining process. *Journal of Materials Processing Technology*, 227, 147. <https://doi.org/10.1016/j.jmatprotec.2015.08.015>
- Jadam, T., Datta, S., & Masanta, M. (2019). Study of surface integrity and machining performance during main/rough cut and trim/finish cut mode of wedm on ti-6al-4v: Effects of wire material.

- Journal of the Brazilian Society of Mechanical Sciences and Engineering*, 41(3), 151. <https://doi.org/10.1007/S40430-019-1656-4>
- Jun, M., Wuyi, M., Jinguang, D., Hao, H., et al. (2018). Integrated optimization model in wire electric discharge machining using Gaussian process regression and wolf pack algorithm approach while machining SiCp/Al composite. *Advanced Mechanical Engineering*, 10, 1–17. <https://doi.org/10.1177/1687814018787407>
- Kandpal, B. C., Kumar, J., & Singh, H. (2017). Optimization and characterization of EDM of AA6061/10%Al₂O₃ AMMC using Taguchi's approach and utility concept. *Production & Manufacturing Research*, 5, 351–370. <https://doi.org/10.1080/21693277.2017.1389315>
- Khanna, R., & Singh, H. (2014). Comparison of optimized settings for cryogenic treated and normal D-3 steel on WEDM using grey relational theory. *Proceedings of the Institution of Mechanical Engineers, Part L: Journal of Materials: Design and Applications*, 1–14. <https://doi.org/10.1177/1464420714565432>
- Kumar, M., & Singh, H. (2016). Multi response optimization in wire electrical discharge machining of inconel X-750 using Taguchi's technique and grey relational analysis. *Cogent Engineering*, 1–14. <https://doi.org/10.1080/23311916.2016.1266123>
- Kumar, S. D., Kanthababu, M., Vajjiravelu, V., Anburaj, R., et al. (2011). Investigation of wire electrical discharge machining characteristics of Al6063/SiC_p composites. *International Journal of Advanced Manufacturing Technology*, 56(9–12), 975–986. <https://doi.org/10.1007/s00170-011-3242-5>
- Kumar, A., Abhishek, K., Vivekananda, K., & Upadhyay, C. (2018a). Experimental study and optimization of process parameters during WEDM taper cutting. *Soft Computing for Problem Solving*, 721–736. https://doi.org/10.1007/978-981-13-1595-4_57
- Kumar, H., Manna, A., & Kumar, R. (2018b). Modeling of process parameters for surface roughness and analysis of machined surface in WEDM of Al/SiC-mmc. *Transactions of the Indian Institute of Metals*, 71(1), 231. <https://doi.org/10.1007/s12666-017-1159-x>
- Kuriakose, S., & Shunmugam, M. S. (2005). Multi-objective optimization of wire-electro-discharge machining process by non-dominated sorting genetic algorithm. *Journal of Materials Processing Technology*, 170, 133–141. <https://doi.org/10.1016/2Fj.jmatprotec.2005.04.105>
- Ma, J., Ming, W., Du, J., Huang, H., He, W., et al. (2018). Integrated optimization model in wire electrical discharge machining using Gaussian process regression and wolf pack algorithm approach while machining SiCp/Al composite. *Advances in Mechanical Engineering*, 1–17. <https://doi.org/10.1177/1687814018787407>
- Maher, I., Sarhan, A. A. D., Marashi, H., Barzani, M. M., & Hamdi, M. (2016). White layer thickness prediction in wire EDM using CuZn coated wire electrode-ANFIS modeling. *The International Journal of Surface Engineering and Coatings*, 94, 204–210. <https://doi.org/10.1080/00202967.2016.1180847>
- Nag, A., Srivastava, A. K., Dixit, A. R., Mandal, A., Das, A. K., et al. (2018). Surface integrity analysis of wire-EDM on in-situ hybrid composite A359/Al₂O₃/B₄C. *Materials Today*, 5(11), 24632. <https://doi.org/10.1016/j.matpr.2018.10.261>
- Patil, N. G., & Brahmankar, P. K. (2010). Some studies into wire electro-discharge machining of alumina particulate-reinforced aluminum matrix composites. *The International Journal of Advanced Manufacturing Technology*, 48(5–8), 537–555.
- Pawade, R. S., & Joshi, S. S. (2011). Multi-objective optimization of surface roughness and cutting forces in high-speed turning of Inconel 718 using Taguchi grey relational analysis. *International Journal of Advanced Manufacturing Technology*, 56, 47–62. <https://doi.org/10.1007/s00170-011-3183-z>
- Pramanik, A. (2014). Developments in the non-traditional machining of particle reinforced metal matrix composites. *International Journal of Machine Tools and Manufacture*, 86, 44–61. <https://doi.org/10.1016/j.ijmactools.2014.07.003>
- Pramanik, A., & Littlefair, G. (2016). Wire EDM mechanism of MMCs with the variation of reinforced particle size. *Materials and Manufacturing Processes*, 31, 1700–1708. <https://doi.org/10.1080/10426914.2015.1117621>
- Pramanik, A., Islam, M. N., Boswell, B., Basak, A. K., et al. (2016). Accuracy and finish during wire electric discharge machining of metal matrix composites for different reinforcement size and

- machining conditions. *Proceedings of the Institution of Mechanical Engineers, Part B: Journal of Engineering Manufacture*, 232, 1068–1078. <https://doi.org/10.1177/0954405416662079>
- Raj, S. O. N., & Prabhu, S. (2016). Modeling and analysis of titanium alloy in wire cut EDM using grey relation coupled with principle component analysis. *Australian Journal of Mechanical Engineering*, 15, 198–209. <https://doi.org/10.1080/14484846.2016.1251077>
- Ramamurthy, A., Sivaramakrishnan, R., Muthuramalingam, T., & Venugopal, S. (2015). Performance analysis of wire electrodes on machining Ti-6Al-4V alloy using electrical discharge machining process. *Machining Science and Technology*, 19, 557–592. <https://doi.org/10.1080/10910344.2015.1085314>
- Rao, M. S., & Venkaiah, N. (2016). Experimental investigation on surface integrity issues of inconel-690 during wire-cut electrical discharge machining process. *Proceedings of the Institution of Mechanical Engineers - Part B: Journal of Engineering Manufacture*, 232, 1–11. <https://doi.org/10.1177/0954405416654092>
- Saha, P., Singha, A., Pal, S. K., & Saha, P. (2008). Soft computing model based prediction of cutting speed and surface roughness in wire electro-discharge machining of tungsten carbide cobalt composite. *International Journal of Advanced Manufacturing Technology*, 39, 74–84. <https://doi.org/10.1007/s00170-007-1200-z>
- Selvakumar, G., Thirupathi Kuttalingam, K. G., & Ram Prakash, S. (2018). Investigation on machining and surface characteristics of AA5083 for cryogenic applications by adopting trim cut in WEDM. *Journal of the Brazilian Society of Mechanical Sciences and Engineering*, 40, 1678–5878. <https://doi.org/10.1007/s40430-018-1192-7>
- Senkathir, S., Aravind, R., Manoj, S. R., & Arun Raj, A. C. (2018). Optimization of machining parameters of Inconel 718 by WEDM using response surface technology. In K. Vijay Sekar, M. Gupta, & A. Arockiarajan (Eds.), *Advances in manufacturing processes. Lecture notes in mechanical engineering* (pp. 383–392). Springer. https://doi.org/10.1007/978-981-13-1724-8_37
- Shandilya, P., Jain, P. K., & Jain, N. K. (2012). Parametric optimization during wire electrical discharge machining using response surface methodology. *Procedia Engineering*, 38, 2371–2377. <https://doi.org/10.1016/j.proeng.2012.06.283>
- Shanmugam, K., & Sahadevan, R. (2018). Bioceramics—An introductory overview. In *Fundamentals biomaterials: Ceramics*. <https://doi.org/10.1016/B978-0-08-102203-0.00001-9>
- Sharma, A., & Yadava, V. (2012). Modelling and optimization of cut quality during pulsed Nd:YAG laser cutting of thin Al-alloy sheet for straight profile. *Optics and Laser Technology*, 44, 159–168. <https://doi.org/10.1016/j.optlaseng.2012.07.012>
- Sharma, N., Raj, T., & Jangra, K. K. (2015). Parameter optimization and experimental study on wire electrical discharge machining of porous Ni₄₀Ti₆₀ alloy. *Proceedings of the Institution of Mechanical Engineers - Part B: Journal of Engineering Manufacture*, 1–15. <https://doi.org/10.1177/0954405415577710>
- Sharma, P., Chakradhar, D., & Narendranath, S. (2017). Analysis and optimization of WEDM performance characteristics of Inconel 706 for aerospace application. *SILICON*, 10, 921–930. <https://doi.org/10.1007/s12633-017-9549-6>
- Shihab, S. K. (2018). Optimization of WEDM process parameters for machining of friction-stir-welded 5754 aluminum alloy using box-behnken design of RSM. *Arabian Journal for Science and Engineering*, 43, 5017–5027. <https://doi.org/10.1007/s13369-018-3238-7>
- Vijayabhaskar, S., & Rajmohan, T. (2017). Experimental investigation and optimization of machining parameters in WEDM of Nano-SiC particles reinforced magnesium matrix composites. *SILICON*, 11, 1–16. <https://doi.org/10.1007/s12633-017-9676-0>
- Wang, J., Wang, T., & Wu, H. (2017). Experimental study on high speed WEDM finishing in steam waster mist. *The International Journal of Advanced Manufacturing Technology*, 91, 3285–3297. <https://doi.org/10.1007/s00170-017-0005-y>
- Yan, B. H., Tsai, H. C., Huang, F. Y., & Lee, L. C. (2005). Examination of wire electrical discharge machining of Al₂O₃/6061Al composites. *International Journal of Machine Tools and Manufacture*, 45(3), 251. <https://doi.org/10.1016/j.ijmactools.2004.08.015>
- Zhang, J. H., Lee, T. C., Wu, C. L., & Tang, C. Y. (2002). Surface integrity and modification of electro-discharge machined alumina based ceramic composite. *Journal of Materials Processing Technology*, 123, 75–79. [https://doi.org/10.1016/S0924-0136\(02\)00065-1](https://doi.org/10.1016/S0924-0136(02)00065-1)

Chapter 11

Material Characterization of Alloy for Aerospace Application: Effect of Laser Power on the Co-axially Deposited T64 Alloy and Cu



M. F. Erinosh, E. T. Akinlabi, and K. O. Oladosu

1 Introduction

Titanium alloy, a strong and lightweight refractory metal, is useful in the aerospace industry and medical, chemical, sport and military gadgets. However, the aerospace industry uses 80% of this alloy, while 20% of usage goes to other industries (The Balance, n.d.). The alloy has an amazing blend of physical, mechanical and erosion obstruction properties, and this has made its application known in the said industries and many more (Moiseyev, 2006). Around 66% of all titanium metal delivered is utilized in flying machine motors and frames (Miyamoto et al., 1999) and many sporting equipment. Titanium and its alloys exhibit a broad range of phase transformations, and a part of the changes are identified with the α -phase to β -phase allotropic modifications (Joshi, 2006).

On the other hand, copper (Cu) is used as a conductor of heat and electricity. It is used for making marine equipment, coins, strain gauges and thermocouples for temperature estimation (Copper Development Association, 2012). It is one of the most widely used engineering materials, due to its excellent ductility, formability, electrical conductivity and machinability. In addition, because of these properties, Cu is embraced in the automotive, aerospace, power generation, defence and so on (Yadav et al., 2020). It is a beta stabilizer of titanium alloy, and it has been used in many ways to strengthen titanium. There are two ways to improve the mechanical

M. F. Erinosh (✉)

Department of Mechanical and Metallurgical Engineering, University of Namibia,
Ongwediva, Namibia

e-mail: merinosho@unam.na

E. T. Akinlabi

Pan African University for Life and Earth Sciences (PAULESI), Ibadan, Nigeria

K. O. Oladosu

Department of Mechanical Engineering, Kwara State University, Malete, Nigeria

properties of Cu, which are age hardening and integration of hard secondary phases (Lee et al., 2001; Dong et al., 2001). Cu has been proven to improve the microstructure and tribological properties of titanium alloy when reinforced with 0.3 wt% of graphene oxide. The TiC particles and Ti₂Cu precipitates formed have led to excellent hardness and tribological properties (Tian et al., 2021). Thick copper (Cu66V34) filler metal alloy has been used to weld a rolled near- α TA15 alloy and cold-rolled QCr0.8 copper plates using electron beam welding process. Cu solid solution improved the bonding strength at the interface of titanium plate (Han et al., 2019). The electrical conductivity and the mechanical properties of pure Cu were investigated when 1 and 2.6 mass % of titanium were added. The strength and corrosion resistance of the sintered Cu were improved (Eze et al., 2018). Copper has been used with titanium by many authors (Clarizia et al., 2017; Loch & Ehasarian, 2017; Rocha et al., 2014; Sanz-Guerrero & Ramos-Grez, 2008; Lloyd et al., 2010; Liu et al., 2014), for its good enhancement properties, just to mention a few. The different weight percentage of Cu (2, 5, 10 and 25) was sintered and tested with titanium for antibacterial action. The antibacterial tests revealed that the Cu content has a strong influence on the sintered alloy due to the high Cu ion release rate in Ti-Cu alloys (Liu et al., 2014). The structural, morphology and optical properties of TiO₂ thin films were investigated with different Cu contents, 0, 12.5, 25 and 50 wt. %, respectively. In the XRD analysis conducted on a high Cu content sample, Cu was revealed to substitute Ti and formed compound of copper-titanium oxide (Horzum et al., 2019). Due to the cracking and brittle failure that took place between TA15 and Inconel 718, Cu was used as a crack eliminator between the alloys (Shang et al., 2019). Ti was fused into Cu by a deposition process, and the absorbed energy was increased due to subsequent surface layering by plasma flows. The fused surface of Cu-Ti alloy was reported to have improved strength and tribological properties (Cherenda et al., 2019). It was reported by some authors that additive manufacturing of Ti-Cu and Ti-Cu-Al alloys is a prospect in the near-net-shape processing which exhibits a promising balance of mechanical properties. Moreover, due to the strong tendency for segregation during solidification, Cu is a good stabilizer to strengthen titanium alloy (Mantri et al., 2020). Inconel 718 and copper alloy were fabricated using laser engineered net shaping additive manufacturing technique to study the thermal properties for aerospace application. Two methods were chosen in the research work, which are the direct deposition of Cu alloy on Inconel 718 and the compositional gradation of the two alloys. Diffused interfaces with the growing of copper-nickel material across the bimetallic interphase were reported when the compositional gradation method was compared to the direct deposition approach (Onuiké et al., 2018). Some authors revealed the work that was conducted on the selective laser melting of Ti6Al4V to 316 L stainless steel, which was achieved with a Cu alloy interlayer. It was reported that the Cu-rich matrix is distributed at the Cu/stainless steel interface, while the microstructure exhibited at the titanium/Cu interface is comprised of layers of different Cu phases (Tey et al., 2020). The vacuum solid-state diffusion method was used to bond Cu and titanium with an interlayer of CoCrFeMnNi high-entropy alloy. It was reported that FCC-type solid solution is formed in the reaction layer, and the interface of Cu/CoCrFeMnNi was well fused,

while intermetallic Mn_2Ti and Cr_2Ti phases were formed at the interface of $CoCrFeMnNi/Ti$ (Ding et al., 2021).

This chapter aims to conduct a laser deposition on titanium alloy (T64) with 10 weight percentage (wt. %) of pure copper (Cu) on titanium alloy substrate, to improve and enhance the surface integrity of the alloy and also to optimize the material selection of engineering applications. The microstructural analysis was conducted on the laser-deposited samples as well as the Vickers microhardness test to identify the effect of the process parameters. The optimization of the process parameters on the hardness values using the Design-Expert 11 software was also carried out.

2 Experimental Procedures

2.1 Materials

The powders used for this work are titanium alloy (T64) powder and copper (Cu) powder. The T64 alloy powder was supplied by F.J. Brodmann and Co., L.L.C., Louisiana, and TLS Technik GmbH, South Africa, while the Cu powder was supplied by the Industrial Analytical (Pty) Limited, South Africa. Titanium alloy square plate was used as the substrate and the dimensions are $102 \times 102 \times 7.54 \text{ mm}^3$. The plate was purchased from Titanium Metal Supply, United States. The materials used for this research work are T64 alloy and Cu powders at the weight of 90 wt % and 10 wt %.

2.2 Methodology

The deposition was performed on an ytterbium laser system at the Council for Scientific and Industrial Research Centre, CSIR, in Pretoria, South Africa. The T64 alloy substrate used before the deposition was sandblasted and cleaned with acetone. The powders were poured into a separate powder feeder, and the laser metal deposition (LMD) process utilized a laser beam to form a pool of melted T64 + 10 wt.% Cu on the surface of a T64 substrate and later solidified for further characterization. The absorbed metal powders produced a deposit on the surface of the substrate as shown in the schematic diagram of Fig. 11.1.

The T64 alloy powder flows from a hopper with the Cu powder from another hopper and converges at a point in a three-way nozzle, and is melted by the laser beam passing through the centre of the nozzle and solidifies. The process parameters used for the deposition process are shown in Table 11.1.

The laser power was varied from 1000 watts to 1600 watts while keeping other parameters such as scanning speed and powder flow rate constant at 0.5 m/min,

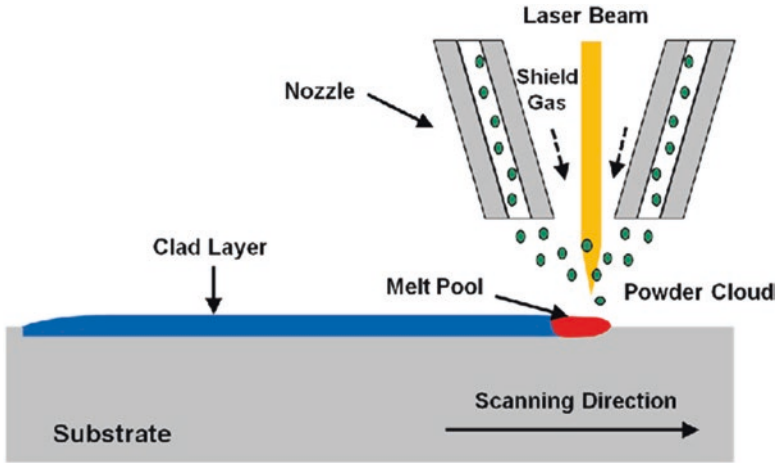


Fig. 11.1 Schematic diagram of LMD process

Table 11.1 Process parameters

Sample designation	Laser power (Watts)	Scanning speed (m/min)	Powder flow rate (rpm)	
			T64	Cu
Sample 1	1000	0.5	1.8	0.2
Sample 2	1200	0.5	1.8	0.2
Sample 3	1400	0.5	1.8	0.2
Sample 4	1600	0.5	1.8	0.2

1.8 rpm for T64 alloy and 0.2 rpm for Cu, respectively. The samples are designated from sample 1 to sample 4. The samples were prepared for lateral surface mounting in a Poly-Fast (resin) via a Struers mounting press. The mounted samples were ground and polished on a grinding and polishing machine. The stages in the grinding process were achieved. The plain (rough) grinding was done using 340#, 500# and 800# grain-size silicon carbide papers attached to a rotary magnetic table on the machine. This process was done with a force of about 40 N under running water for about 5 min at a speed of 300 rpm. The polishing was done using MD-Chem circular disc and OP-S suspension was used as the lubricant and ran for about 8 min at a speed of 300 rpm until a scratch-less mirror-like image on the surface was obtained. All the samples were prepared according to the Struers' note of preparing titanium alloy (Struers Application Note on Titanium, 2013). The Kroll's reagent was prepared for the deposited samples as follows: 100 mL distilled H₂O, 2 mL HF and 4 mL HNO₃ and etched between 15 and 20 s (ATSM E3-11, 2011). The GX41 Olympus microscope was used for the microstructural analyses and observed at low and high magnifications. A Zwick/Roell Vickers hardness machine was used for the

microhardness test. A load of 0.5 kg with a dwell time of 0.25 min was used for the indentation on the cross-sectional surface of both the substrate and the laser-deposited T64 + 10wt. % Cu alloys. This was done according to the ASTM standard (ATSM E384-11e1, 2011). The design of experiment (DOE) was implemented in this chapter to predict the optimum laser powers against the hardness values. Response surface methodology (RSM), a statistical type of experimental design, was used to analyse the experimental variables and to provide an average response to the values of the quantitative variables. The input parameters were laser powers and scanning speed, and these were used to determine the low level and high level of the factors. The number of blocks selected was 2, which are block 1 and block 2, which are proposed for the experiment. The point-type design layout of the experiment was observed for the number of runs, standard orders, the blocks and the response which are the microhardness values to be predicted. The run order is different due to randomization. Fourteen (14) runs were piloted over a 2-day period in two blocks. In the first day period, seven runs were piloted, followed by another seven on the second day.

The relationship between the average microhardness values and the runs is shown in Table 11.2 for day 1 and day 2.

All the 14 runs are included in the table for days 1 and 2, as well as the hardness values for factors 1 and 2. From the table, the microhardness value increases as the laser power was increased.

Table 11.2 Point-type design layout

Std.	Block	Run	Factor 1 A: Laser power (W)	Factor 2 B: Scanning speed (m/min)	Response 1 Microhardness HV
3	Day 1	1	1000	0.5	485
1	Day 1	2	1200	0.5	522
4	Day 1	3	1000	0.5	485
7	Day 1	4	1600	0.5	570
2	Day 1	5	1400	0.5	560
5	Day 1	6	1300	0.5	540
6	Day 1	7	1600	0.5	570
10	Day 2	8	1000	0.5	485
8	Day 2	9	875.736	0.5	463
13	Day 2	10	1200	0.5	522
14	Day 2	11	1300	0.5	540
12	Day 2	12	1400	0.5	560
11	Day 2	13	1600	0.5	570
9	Day 2	14	1724.26	0.5	620

3 Results and Discussion

The section presents the microstructures, microhardness results as well as the design of experimental results. Figure 11.2 shows the micrograph of the lateral section of the T64 alloy substrate.

The micrograph shows the α -phase in the white region and the β -phase in the dark region. The colour of the phases was confirmed by Suprobo et al. (2019). Most of the grains are equiaxed and compressed as a result of the rolled substrate. The microstructures of the laser-deposited T64 + 10 wt. % samples were observed on the optical microscope from the deposit to the heat-affected zone. Figure 11.3(a–f) illustrates the microstructures of the entire deposited samples from sample 1 to sample 4.

Figure 11.3(a) and (b) shows the microstructures of sample 1 deposited at a laser power of 1000 W and scanning speed of 0.5 m/min. Pre-impregnation and formation of Cu particles were formed on the deposit. Little porosities are observed in both the deposit and the heat-affected zone (HAZ) and could be as a result of the entrapped gases. Spongy equiaxed grains were formed immediately after the fusion zone (FZ). The formation could be as a result of the low nucleation rate of the grains and fast cooling rate that exist on sample 1 with the laser power of 1000 W. This can lead to weak boundaries. There is also the formation of Widmanstätten structures, which happened because of the cooling rate during the solidification process of the deposit. The Widmanstätten is a basket-weave-like structure and increases in size when the cooling rate was decreased (Gil et al., 2001). The spongy microstructure

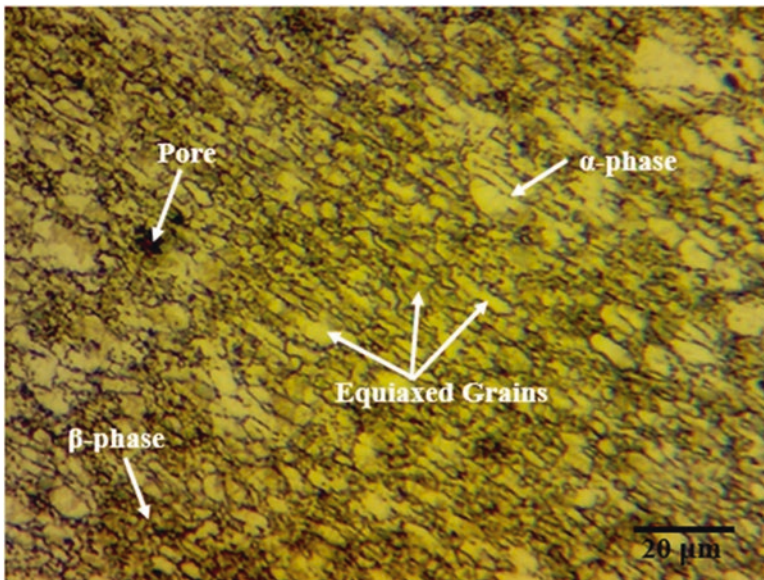


Fig. 11.2 Micrograph of the T64 alloy substrate

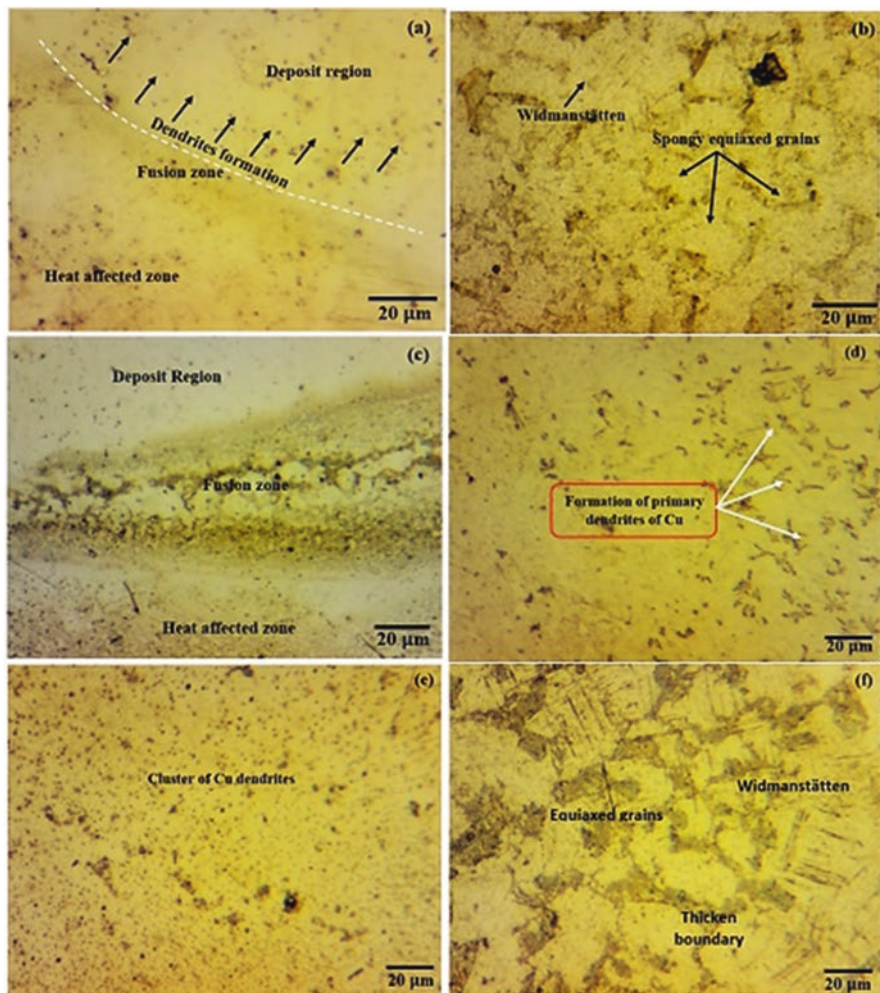


Fig. 11.3 Microstructures of the T64 + 10 wt. % Cu samples deposited at different laser powers: (a) sample 1 at 1000 W, (b and c) sample 2 at 1200 W, (d) sample 3 at 1400 W and (e and f) sample 4 at 1600 W

was extended to sample 2 deposited at a laser power of 1200 W at the immediate dilution zone between the deposit and the HAZ. Primary dendrites of Cu were more obvious in sample 3 deposited at a laser power of 1400 W and scanning speed of 0.5 m/min. The increase in laser power has assisted the discharge of dendrite of Cu. Clusters of Cu were more discharged in the titanium alloy phases as the laser power was increased to 1600 W. It was noticed that as the laser power increases, the density of the dendrites in the deposit increases as well as the size of the dendrites. The size of the FZ and the HAZ also increases with the increase in laser power (Zhao

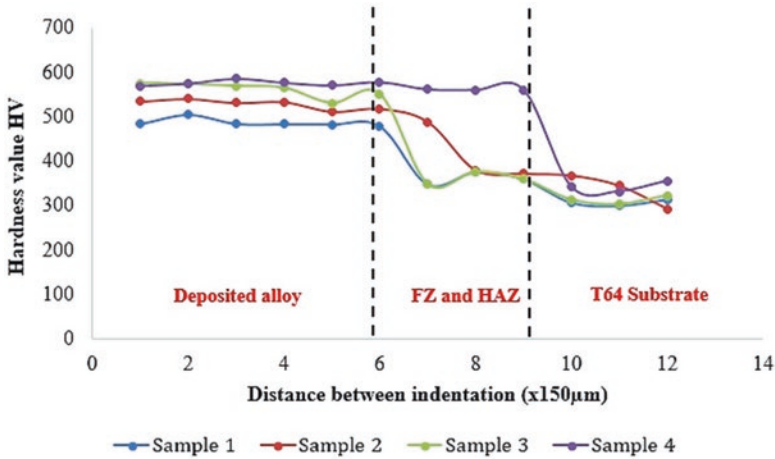


Fig. 11.4 Hardness profiling of laser-deposited T64 + 10 wt. % Cu

et al., 2020) due to the increased melt pool. Basket-weave-like Widmanstätten structures become more and more clear in the HAZ as the laser power was increased.

The Vickers microhardness tests conducted on the deposited samples resulted in the hardness profiling in Fig. 11.4.

The profiling was grouped into three segments to study the behaviour of the alloys at different phases of deposition. The microhardness profiling revealed the changes in the trend of the hardness value from the top of the deposit to the substrate. The hardness values of the entire deposit were increased and decreased in the heat-affected zone, and more decrease was observed in the substrate. Approximate steady values were obtained for sample 4, and the hardness HV values in the deposit were more pronounced than other deposited samples. The average HV values as shown in Fig. 11.5 indicate an increase in the hardness value from samples 1 to 4, as the laser power was increased from 1000 W to 1600 W.

The mean HV between the substrate and sample 1 increased by about 57.3%. Between samples 1 and 2, the mean HV was increased by about 7.4%, while between samples 2 and 3, and 3 and 4 it showed an increase of approximately 7.1% and 2.5%, respectively. All these increments in the HV are as a result of the increase of the laser power. The increase in laser power results in more powder being melted and thus grain boundaries migrate with one another forming new grains. This increases the embrittlement of the material due to the hardness results. At high laser powers, the rate of cooling is slower; and this gives room for structural stability and improves the embrittlement (Erinosho et al., 2014). The highest hardness value is $HV 573 \pm 7$ from sample 4 which was deposited with the laser power of 1600 W and the lowest hardness value is $HV 309 \pm 7$, obtained from sample 1 deposited with the laser power of 1600 W and scanning speed of 0.5 m/min. The addition of Cu has greatly improved the microhardness value of T64 alloy.

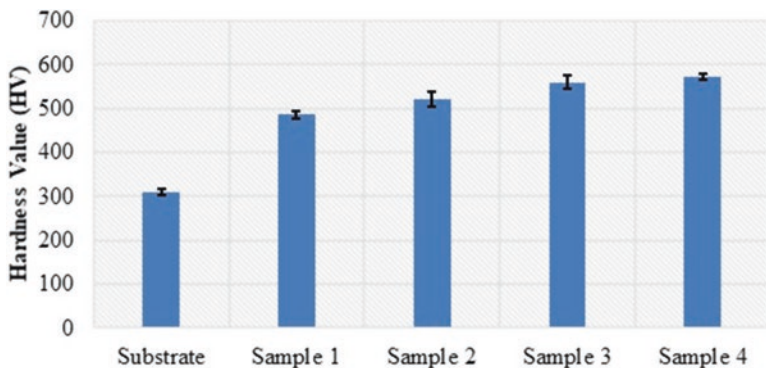


Fig. 11.5 Average hardness of laser-deposited T64 + 10 wt.% Cu

Table 11.3 Sequential model sum of squares

Source	Sum of squares	Df	Mean square	F-value	P-value Prob > F
Mean vs total	4.009E+06	1	4.009E+06		
Block vs mean	56.00	1	56.00		
Linear vs block	24163.13	1	24163.13	265.11	<0.0001(S)
Quadratic vs Linear	79.77	1	79.77	0.8644	0.3744
Residual	922.82	1	92.28		
Total	4.035E+06	14	2.882E+05		

After the design evaluation, the responses are numerically analysed. A fit model is suggested in the analysis. Table 11.3 shows the sequential model sum of the squares.

This shows how the increasing complexity contributes to the total model. The highest p-value and F-value under the quadratic vs linear are 0.3744 and 0.8644 which are aliased. Linear vs block is suggested and significant. Both the values are good for the model. The lack of fit indicates that the model adequately predicts the responses within the design space and all the points are not lurking. The analysis of variance (ANOVA) is a collection of statistical models and their associated estimation procedures and is used to analyse the differences among the group means in a sample. Table 11.4 illustrates the ANOVA for the response surface quadratic model used. The sources in the response surface model include the block, the model, laser power, the residuals, lack of fit and the corrected total.

The model F-value of 431.02 implies the model is significant. P-value is less than 0.0001 which is far less than 0.05, and indicates that the model terms are significant. In the source as indicated, A, A², A³, A⁴ and A⁵ are all significant model terms since they are far less than 0.05. In the model, 75 solutions to optimum desirability of the average microhardness within the response surface model domain are chosen. Figure 11.6(a) and (b) shows the plot of externally studentized residuals versus the predicted values and the plot of residuals versus the experimental run order.

Table 11.4 Analysis of variance for the response surface model

Source	Sum of squares	Df	Mean square	F-value	P-value Prob > F
Block	23.14	1	23.14		
Model	24514.66	5	4902.93	431.02	<0.0001(S)
A-laser power	1159.67	1	1159.67	101.95	< 0.0001
A ²	741.73	1	741.73	65.21	< 0.0001
A ³	171.45	1	171.45	15.07	0.0060
A ⁴	653.90	1	653.90	57.48	0.0001
A ⁵	280.48	1	280.48	24.66	0.0016
Residual	79.63	7	11.38		
Lack of fit	79.63	5	15.93		
Pure error	0.000	2	0.000		
Cor total	24617.43	13			

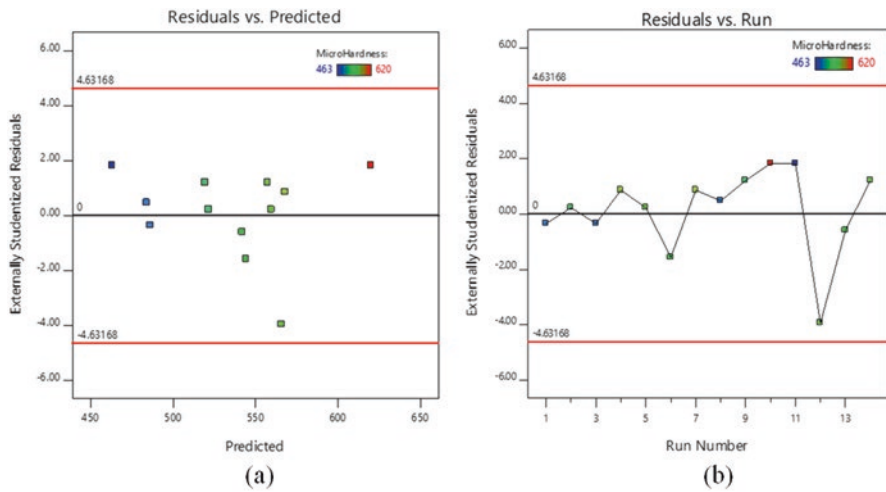


Fig. 11.6 (a) Plot of externally studentized residuals versus the predicted values. (b) Plot of externally studentized residuals versus the experimental run order

There are always control limits on the externally studentized residuals plot to identify the abnormal runs easily. The externally studentized residual test is used for checking whether a run is consistent with the other available runs. In this model, the prediction of the hardness response is given and there is no outlier and the responses fit the model. These plots check for any ignored variables that may have affected the response during the experiment. The trend from the first run to the last runs lies between the upper and lower red lines, and this has shown that there is no outlier and most of the blue bullet points are found close to the zero points of the externally studentized residuals. A green point at the 12th runs on the negative side is close to 4.00 and this shows a little deviation from the other runs.

4 Conclusion

The characterizations were successfully done on the laser-deposited T64 + 10 wt. % Cu. The relevance of T64 alloy in the aerospace, medical and chemical industries is unquestionable. However, despite all the excellent properties, there is a need to improve its surface integrity for prolonged use during service. The improvements of the surface integrity of the T64 alloy were achieved by adding 10 wt% of Cu to the alloy, whose selection was based on its excellent properties. Dendrites of Cu were observed on the deposited samples, and they were found to increase in size and quantity as the laser power was increased. On the design of experiment simulation, the ANOVA model showed a significant result. As the laser power was increased, the formation and growth of Widmanstätten structures occurred and they grew further into the HAZ as the laser power increased. This shows that there are formation of new phases and an increase in embrittlement. The hardness value of the T64 + 10 wt.% Cu alloy was increased as the laser power increases, and the highest hardness value of HV 573 ± 7 from sample 4 was obtained from the highest laser power of 1600 W used. This was a testimony that an increase in laser power increases the microhardness value.

References

- ATSM E3-11. (2011). Standard guide for preparation of metallographic specimens. ATSM International, Accessed 2013 from the database.
- ATSM E384-11el. (2011). Standard test method for Knoop and Vickers hardness of materials. ATSM International Book of Standards, Vol. 03, 01.
- Cherenda, N. N., Basalai, A. V., Uglov, V. V., Laskovnev, A. P., Astashynski, V. M., & Kuzmitski, A. M. (2019). Phase composition and mechanical properties of Cu–Ti alloys synthesized in the surface layer of copper by plasma impact on the Ti/Cu system. *Vacuum*, 167, 452–458.
- Clarizia, L., Vitiello, G., Pallotti, D. K., Silvestri, B., Nadagouda, M., Lettieri, S., Luciani, G., Andreozzi, R., Maddalena, P., & Marotta, R. (2017). Effect of surface properties of copper-modified commercial titanium dioxide photocatalysts on hydrogen production through photoreforming of alcohols. *International Journal of Hydrogen Energy*, 42(47), 28349–28362.
- Copper Development Association. (2012). Retrieved 2013, from <http://www.copperalliance.org.uk/copper-and-its-alloys/alloys/coppers>.
- The Balance. (n.d.). Titanium properties and characteristics. Retrieved January 5, from, 2020 <http://www.thebalance.com/metal-profile-titanium-2340158>.
- Moiseyev, V. N. (2006). *Titanium alloys: Russian aircraft and aerospace applications* (pp. 169–180). CRC Press Taylor & Froes Group.
- Miyamoto, Y., Kaysser, W. A., Rabin, B. H., Kawasaki, A., & Ford, R. G. (Eds.) (1999). *Functionally graded material design, processing and applications*. Materials Technology Series 1999, Springer.
- Joshi, V. A. (2006). *Titanium alloys. An atlas of structures and fracture features* (pp. 1–247). CRC Press Taylor & Francis Group.
- Yadav, S., Paul, C. P., Jinoop, A. N., Rai, A. K., & Bindra, K. S. (2020). Laser directed energy deposition based additive manufacturing of copper: Process development and material characterizations. *Journal of Manufacturing Processes*, 58, 984–997. <https://doi.org/10.1016/j.jmapro.2020.09.008>
- Lee, Y. F., Lee, S. L., Huang, C. H., & Lee, C. K. (2001). Effects of Fe additive on properties of Si reinforced copper matrix composites fabricated by vacuum infiltration. *Powder Metallurgy*, 44(4), 339–343. <https://doi.org/10.1179/pom.2001.44.4.339>

- Dong, S. R., Tu, J. P., & Zhang, X. B. (2001). An investigation of the sliding wear behavior of Cu-matrix composite reinforced by carbon nanotubes. *Materials Science and Engineering, A*, 313, 83–87.
- Tian, N., Dong, L. L., Wang, H. L., Fu, Y. Q., Huo, W. T., Liu, Y., Yu, J. S., & Zhang, Y. S. (2021). Microstructure and tribological properties of titanium matrix nanocomposites through powder metallurgy using graphene oxide nanosheets enhanced copper powders and spark plasma sintering. *Journal of Alloys and Compounds*, 867, 159093.
- Han, K., Wang, T., Tang, Q., Zhang, B., & Feng, J. (2019). Effect of Cu66V34 filler thickness on the microstructure and properties of titanium/copper joint by electron beam welding. *Journal of Materials Processing Technology*, 267, 103–113.
- Eze, A. A., Jamiru, T., Sadiku, E. R., Durowoju, M. O., Kupolati, W. K., Ibrahim, I. D., Obadele, B. A., Olubambi, P. A., & Diouf, S. (2018). Effect of titanium addition on the microstructure, electrical conductivity and mechanical properties of copper by using SPS for the preparation of Cu-Ti alloys. *Journal of Alloys and Compounds*, 736, 163–171.
- Loch, D. A. L., & Ehtasarian, A. P. (2017). Study of the effect of RF-power and process pressure on the morphology of copper and titanium sputtered by ICIS. *Surface and Coatings Technology*, 327, 200–206.
- Sanz-Guerrero, J., & Ramos-Grez, J. (2008). Effect of total applied energy density on the densification of copper–titanium slabs produced by a DMLF process. *Journal of Materials Processing Technology*, 202(1-3), 339–346.
- Lloyd, J. C., Neubauer, E., Barcena, J., & Clegg, W. J. (2010). Effect of titanium on copper–titanium/carbon nanofibre composite materials. *Composites Science and Technology*, 70(16), 2284–2289.
- Liu, J., Li, F., Liu, C., Wang, H., Ren, B., Yang, K., & Zhang, E. (2014). Effect of Cu content on the antibacterial activity of titanium–copper sintered alloys. *Materials Science and Engineering: C*, 35, 392–400.
- Horzum, S., Gürakar, S., & Serin, T. (2019). Investigation of the structural and optical properties of copper–titanium oxide thin films produced by changing the amount of copper. *Thin Solid Films*, 685, 293–298.
- Shang, C., Guojian, X., Wang, C., Yang, G., & You, J. (2019). Laser deposition manufacturing of bimetallic structure from TA15 to inconel 718 via copper interlayer. *Materials Letters*, 252, 342–344.
- Mantri, S. A., Alam, T., Zheng, Y., Williams, J. C., & Banerjee, R. (2020). Influence of post deposition annealing on microstructure and properties of laser additively manufactured titanium copper alloys. *Additive Manufacturing*, 32, 101067.
- Onuikwe, B., Heer, B., & Bandyopadhyay, A. (2018). Additive manufacturing of Inconel 718—Copper alloy bimetallic structure using laser engineered net shaping (LENS™). *Additive Manufacturing*, 21, 133–140.
- Tey, C. F., Tan, X., Sing, S. L., & Yeong, W. Y. (2020). Additive manufacturing of multiple materials by selective laser melting: Ti-alloy to stainless steel via a Cu-alloy interlayer. *Additive Manufacturing*, 31, 100970.
- Ding, W., Liu, N., Fan, J., Cao, J., & Wang, X. (2021). Diffusion bonding of copper to titanium using CoCrFeMnNi high-entropy alloy interlayer. *Intermetallics*, 129, 107027.
- Struers Application Note on Titanium. (2013). http://www.struers.com/resources/elements/12/104827/Application_Note_Titanium_English.pdf. (Accessed from the website).
- Erinosho, M. F., Akinlabi, E. T., & Pityana, S. (2014). Laser metal deposition of T64 + 10wt.% Cu composite: A study on the effect of laser power on the evolving properties. *World Congress of Engineering (WCE), London*, 2, 1203–1208.
- Suprobo, G., Park, N., & Baek, E. R. (2019). Effect of double stage solution treatment on the volume fraction of massive phase (α_m) as a new method to obtain a fine lamellar α/β in Ti–6Al–4V alloy. *Intermetallics*, 113, 106581.
- Zhao, Y., Mingyuan, L., Fan, Z., Huang, S., & Huang, H. (2020). Laser deposition of wear-resistant titanium oxynitride/titanium composite coatings on Ti-6Al-4V alloy. *Applied Surface Science*, 531, 147212.
- Gil, F. J., Ginebra, M. P., Manero, J. M., & Planell, J. A. (2001). Formation of α -Widmanstätten structure: Effects of grain size and cooling rate on the Widmanstätten morphologies and on the mechanical properties in Ti6Al4V alloy. *Journal of Alloys and Compounds*, 329(1–2), 142–152.

Chapter 12

Optimization of Reinforcement Parameters and Turning Conditions for Improving Surface Quality of Hybrid Al-SiC-Red Mud Composite for Automotive and Aerospace Components



Amit Chauhan, Jaswinder Singh, and Saroj Bala

1 Introduction

1.1 Machining of Aluminium Matrix Composites (AMCs)

The demand for AMCs is continuously increasing in automotive sector due to increasing fuel prices and environmental emissions. This may be attributed to low weight and high strength and stiffness of these materials that enhance their load bearing ability (Mistry & Gohil, 2016; Taha, 2001). Therefore, AMCs possess higher abrasion resistance and strength in comparison to monolithic materials (metals and alloys). Due to this, these materials are used to design various automotive components, thereby reducing fuel consumption and emissions of greenhouse gases (GHGs) in the transportation sector. Actually, addition of hard ceramic phase (reinforcements) in the AMCs results in increase in the value of elastic modulus and strength that further improves the working performance of these composites (Bains et al., 2016; Surappa, 2003). However, selection of optimum values of reinforcement parameters, i.e. volume fraction and particle size, is a key area of interest for the researchers. Actually, AMCs may exhibit different mechanical and wear characteristics at different magnitudes of reinforcement parameters. Currently, hard ceramic reinforcements have been considered to be most compatible for developing

A. Chauhan (✉)

Department of Mechanical Engineering, UIET, Panjab University, Chandigarh, Punjab, India
e-mail: drchauhan98@pu.ac.in

J. Singh

Department of Mechanical Engineering, UIET, Panjab University Regional Centre, Hoshiarpur, Punjab, India

S. Bala

PG Department of Physics, SGGGS College, Chandigarh, Punjab, India

high-performance Al composites. However, machining response of the AMCs is considerably deteriorated due to the presence of hard ceramic particles (Muthukrishnan et al., 2007; Sathish Kumar et al., 2015). Therefore, it becomes imperative to find the solution to machining challenges related to the AMCs for widespread use of these materials in the various engineering sectors.

The machining characteristics of the AMCs have been investigated and reviewed by various authors, and it has been revealed that machinability of the AMCs can be improved by evaluating optimum combination of reinforcement parameters and cutting conditions (Behera & Sutradhar, 2012; Das et al., 2014; Hiremath et al., 2016). Hiremath et al. (2016) have studied the turning characteristics (machining forces and surface quality) of the Al6061/B₄C composites using polycrystalline crystal diamond (PCD) tools. It was found that the cutting forces reduced with increasing reinforcement ratio due to the presence of micro-voids and pores. The machinability of the developed composites was reduced with increasing values of cutting parameters (feed rate and depth of cut) and decreasing value of turning speed. Das et al. (2014) have discussed various issues regarding the tool wear of Al/ceramic composites during turning operations. It was revealed that the PCD tools exhibit longer life in comparison to other tool materials as far as machining response of these composite was concerned. The results also indicate that tool wear is increased with increase in the values of the reinforcement parameters (percentage and particle size) and the turning conditions. Further, the depth of cut has the lowest influence on the tool wear during turning operations. Behera and Sutradhar (2012) have found that surface finish of the LM6/SiC composites decreases with an increase in SiC content due to increase in the magnitudes of cutting forces. The machining operations were carried out at different cutting speeds (30–103 m/s) and depth of cuts (0.5–1.5 mm) for the same feed rate (0.05 mm/rev). The machining response of the AMCs was found to be dependent upon the magnitude of cutting parameters. The size of chip was also reduced with an increase in reinforcement content, which was an indication of reduction in ductility of the AMCs.

1.2 Hybrid AMCs (HAMCs) and Their Machining Response

During the last decade, the development of the hybrid HAMCs has attracted attention of the researchers due to their low density and superior mechanical performance and machinability (Rajmohan et al., 2012; Singh, 2016; Singh & Chauhan, 2014, 2016a, 2016b). Actually, lubricating properties of secondary reinforcements improve wear and machining response of the hybrid composites. Currently, researchers are focusing on development of high-performance HAMCs for various engineering applications. According to Priyadarshi and Sharma (2016), process parameters for turning of Al6061-based hybrid composites can be optimized for improved machining response. It has been observed that feed rate and cutting depth are significant parameters having identical influence on machining response of the composites. The cutting speed has been found to exhibit minimal influence on the

cutting force, while the surface quality is improved with an increase in the value of cutting speed. Kumar and Chauhan (2015) have evaluated the surface roughness response of Al-based hybrid composites (Al/SiC/Gr) and ceramic-reinforced composites (Al/SiC) composites under dry turning conditions. The surface roughness of hybrid composites has been found to be lower than that of the SiC-reinforced composites under all combinations of cutting parameters. The feed rate has been found to be the most influential factor regarding surface quality of the hybrid composites. Also, a lower value of feed rate is required to obtain minimum surface roughness for these composites. Bajavarajappa (2009) has found that the Al2219/SiC/Gr hybrid composites exhibit improved machining performance compared with Al/SiC composites. The addition of graphite particles reduces tool wear of developed composites due to reduction in friction coefficient between the tool and the composite. Premnath et al. (2012) have performed experimental investigations to study the milling characteristics of the hybrid Al/Al₂O₃/Gr composites processed by stir casting route under the influence of control parameters. The authors have also found optimum values of various process variables such as feed rate (50 mm/min), speed (4500 rpm), depth of cut (0.1 mm) and Al₂O₃ content (15 wt.%) for enhanced machining response of these composites. The optimum values of cutting force and surface finish were obtained as 132.8 N and 0.28 µm, respectively. It has also been revealed that feed rate is a dominant parameter that controls the cutting mechanism in the machining process. However, a number of scratches and marks were also observed on the machined surface at higher magnitudes of the feed rate.

1.3 Optimization Techniques for Machining Response

It has been observed that machinability of the Al composites can be assessed by investigating various response characteristics such as tool wear, cutting force and surface roughness. Among these, surface roughness of the materials is an important parameter for designing automotive components for wear-resistant applications such as engine components, bearings, clutches and brakes (Bajavarajappa, 2009; Kumar & Chauhan, 2015). It has been revealed that surface quality obtained during machining determines the ability of the materials to withstand severe wear conditions. Moreover, surface texture of the product significantly influences the reliability and appearance of the product. A number of techniques can be used for optimization of selected variables such as reinforcement ratio, cutting speed and depth and feed rate for obtaining minimum roughness value in a machining process (El-Gallab & Sklad, 1998; Suresh et al., 2012). Currently, response surface methodology (RSM) technique has been widely used to analyse experimental data and develop mathematical model for multi-response optimization of machining characteristics of Al composites (Bhushan, 2013; Kant & Sangwan, 2014; Srinivasan et al., 2012). Here, experimental data is obtained by employing design of experiment (DOE) approach, while mathematical model for optimum process parameters can be obtained by using statistical techniques. Further, a comparative analysis

between measured and predicted response can also be made for error estimation and to check the validity of the developed model. Bhushan (2013) has used RSM technique to study the influence of the cutting parameters in CNC turning of Al7075/15%SiC composites. Also, multi-objective optimization has been successfully achieved via desirability-based approach. It has been found that power consumption and tool wear are reduced by 13.55% and 22.12%, respectively. Srinivasan et al. (2012) have also applied desirability-based RSM technique for optimization of machining characteristics such as cutting force, tool wear and surface roughness during machining of LM25/10%Al₂O₃ composites. Kant and Sangwan (2014) have optimized cutting parameters for optimization of the surface roughness and the power consumption. Results of all these studies indicate that the RSM technique is quite suitable for optimization of output response for machining operation of the AMCs. Focused techniques of extracting micro- and nanocellulose, treatment and modification of cellulose, and classification and applications of cellulose are presented by Abdoulhdi A. Borhana Omran. In addition, the work looked into how the reinforcement of micro- and nanocellulose can yield a material with improved performance. Their work highlights performances, limitations and possible areas of improvement to accommodate the broader range of engineering applications (Omran et al., 2021). Suriani et al. (2021b) had presented the limitations of natural fibres such as high moisture absorption, due to repelling nature; low wettability; low thermal stability; and quality variation, which lead to the degradation of composite properties. In this work, a combination of a few common manufacturing defect types illustrating the overview of the impact on the mechanical properties encountered by most of the composite manufacturing industries is presented. Norizan Mohd Nurazzi et al. (2021) have unveiled the successful development related to CNT accompanied polymer composites. The work highlights the mechanical, thermal and electrical performances of a CNT polymer (both single walled and multi-walled). Their work is a crucial pivot in our current understanding of the altered polymer structure after the addition of CNT.

In recent years the eagerness towards learning of biopolymers and growing concerns related to the depletion of resources gave the idea of using PLA (polylactic acid), a biopolymer to be manufactured globally. Therefore, the effectiveness of natural polymers along with PLA is represented in the works of Ilyas et al. (2021). This research provides an insight to the recent works in PLA-derived bio-composite, its synthesis and biodegradation and its properties, processes, challenges and prospects. Suriani et al. (2021a) have conducted several tests at different concentrations of PET yarn and magnesium hydroxide as a reinforcement material. The results for horizontal burning test, tensile test and scanning electron micrographs (SEM) revealed at what concentrations the samples were best to be used for various purposes. It was summarized that the flammability and tensile properties of OPEFB fibre-reinforced fire-retardant epoxy composites could be reduced while using the fibre volume contents in a manner up to an optimal loading of 20%, with the values of 11.47 mm/min and 4.29 KPa, respectively (Suriani et al., 2021a). Nurazzi et al. (2021) has presented a study of natural fibres in the application of ballistics and bulletproof vests and helmets. The article also focuses on the effect of layering and

sequencing of natural fibre fabric in the composites to advance the current armour structure system. Alsubari et al. (2021) has reviewed the drawbacks of loading conditions while using the natural fibres, countered to fibre treatment and hybridization. This study shows the uses of sandwich structure, in a combination of two or more individual components with different properties, which when joined together can give a better performance. The study also shows the application of natural fibre composites in sandwich structures to be minimal. Therefore, their work shines a light on the possibility of using a natural fibre composite in sandwich structure applications. It addresses the mechanical properties and energy-absorbing characteristics of natural fibre-based sandwich structures tested under various compression loads. The results and potential areas of improvement in engineering applications were discussed.

1.4 Novel HAMCs and Objectives of the Study

Although a number of investigations are available for machining characteristics of the AMC's, limited research is available on the investigation of the surface roughness of the HAMCs reinforced with industrial waste materials. However, various types of waste materials like fly ash (FA), red mud (RM), rice husk ash (RHA), etc. have been used for development of lightweight, low-cost and high-performance HAMCs (Rajmohan et al., 2012; Singh & Chauhan, 2016a). The use of these materials can overcome the problem of disposal of waste materials produced in large quantities while reducing the cost of the developed composites. The RM powder is available in abundance at processing sites of the aluminium (available from bauxite ore). Currently, it is being disposed in open land leading to water, soil and air pollution. It is also used in a number of applications such as extraction of metallic elements and cement industry. But, disposal of this waste product in a sustainable manner is still a challenge for the researchers and the scientists. The RM contains oxides of different elements like Fe, Al, Si, Ti, Na and Ca (Singh & Chauhan, 2017a). The results of previous studies indicate that the addition of RM powder results in improvement in mechanical and wear properties of HAMCs (Kumar & Megalingam, 2017; Singh & Chauhan, 2017b, 2018, 2019). However, machining of SiC- and RM-filled Al composites is not investigated till date. Therefore, Al/SiC/RM composites are developed in this study and their turning behaviour has been investigated using CNC lathe machine. Also, optimum values of reinforcement and cutting parameters have been obtained for minimum roughness (improved surface finish) of the developed composite. The influence of process variables (reinforcement parameters and cutting conditions) on machinability response (surface roughness) of HAMCs has also been studied by using RSM technique. The composites are produced via liquid metallurgy route, and dry turning operations are carried out to study the surface quality of the developed composites using Taguchi's approach. The influence of variables on the surface quality of the developed composites has

been studied by using statistical analysis of experimental results and examination of the chips formed during machining of the composites.

2 Materials and Methods

2.1 Materials

In this work, Al2024 was used as a matrix alloy due to its widespread use in the automotive and aerospace industries. The main constituents of this alloy are Al (more than 90%), Cu (about 4%) and Mg (nearly 1.5%) (Rahimi et al., 2015). This alloy was purchased from the local market in the form of thin sheets that can be converted into liquid form at a temperature of 700 °C. The second reinforcement used for fabrication of Al2024 alloy-based hybrid composites was the red-mud powder that is a waste material obtained during production of alumina from the bauxite ore (during Bayer's process). It has been noted that about 1–2 tons of red mud are produced for each ton of the alumina production. Therefore, a million tons (more than 4 million tons) of red mud is produced on daily basis in India that is either stored (for metal recovery or other uses) or released to the waste land. The disposal of this material ultimately leads to soil, water and atmospheric pollution. Therefore, an effective waste disposal of this material will not only reduce the harmful environmental impact, but it will also lead to reduction in the storage/disposal cost. The major elements present in the red-mud powder are Na, Al, Si, Ca, Ti, Fe, S and K with some traces of radioactive elements. The red mud used in the present investigation was brought from aluminium refinery of Hindalco located at Renukoot, Uttar Pradesh, India. It can be observed that the red-mud powder mainly consists of oxides of various elements such as Fe, Al, Si, Ti, Na and Ca that indicates the red mud can be used as a sustainable reinforcement in the Al composites.

2.2 Method

In the present study, casting process was designed in such a way as to reduce particle clustering and porosity in the developed composites. Also, SiC and RM particles were incorporated in the alloy matrix using stir casting set-up. Although stir casting has been found to be an economic and reliable technique, process variables (stirring and casting variables) are required to be selected carefully so as to produce nearly homogeneous composites (Ramanathan et al., 2019; Singh, 2016; Singh & Chauhan, 2018). The reinforcements were incorporated in the alloy matrix using an electric furnace and a mechanical impeller. The former was used to heat the alloy above melting temperature, while the latter created the vortex motion required for mixing of the molten alloy and the reinforcements. Figure 12.1 shows various components

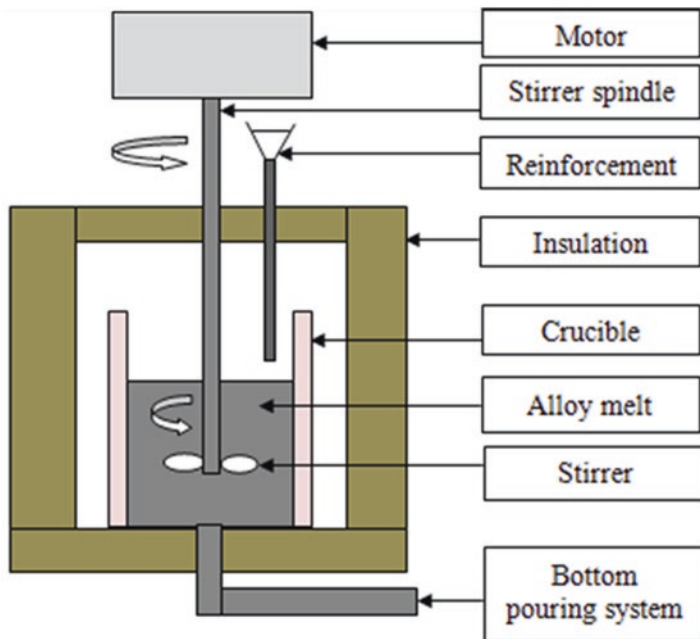


Fig. 12.1 Components of casting machine used for fabrication of composites

Table 12.1 Parameters for the process parameters used for fabrication of composites

Parameter	Value
Melting temperature in the furnace (°C)	750
SiC fraction (%)	5 (fixed)
Red-mud fraction (%)	5–20 (variable)
Mg fraction (%)	1
Preheating temperature of reinforcements (°C)	200
Stirring velocity (rpm)	200–250
Stirring time (min)	30
Preheating temperature of moulds (°C)	400

of casting machine used for fabrication of the composites. Also, various process parameters selected for fabrication of composite specimens have been presented in Table 12.1. The mixing of the molten alloy and the reinforcements was carried out in the graphite crucible of the furnace. Further, 1 wt.% of Mg was also added in the alloy melt in order to minimize the particle agglomeration in the composite specimens. After mixing of all the constituents, composites were casted in the preheated steel moulds (cylindrical shape) through the bottom pouring system. The composite specimens were then subjected to heat treatment under T6 conditions for obtaining

adequate microstructural properties of the composites. In this process, solution treatment of the specimens was done at a temperature of 500 °C for a time period of 2 h. Thereafter, the specimens were quenched in cold water followed by age hardening at 150 °C for 20 h.

2.3 *Microstructural Characterization of the Composites*

The scanning electron micrographs (SEM) of SiC and RM particles are shown in Fig. 12.2, indicating that the shape of RM particles is nearly spherical, while SiC particles have sharp edges. Further, SEM image of the Al composites is presented in Fig. 12.3(a), indicating that both types of reinforcement particles are present in the composite specimens. The microstructure of composites has been observed to be nearly uniform. This may be due to the optimum conditions selected for casting of the specimens. The agglomeration of particles is also visible at some places that may be attributed to the higher fraction (20 wt.%) of RM particles. Similarly, various constituent particles like Al, Cu, Mg, O, F, Ca, etc. present in the composites are confirmed by electron dispersive spectrum (EDS) analysis as indicated in Fig. 12.3(b).

2.4 *Machining of Composite Samples*

The cylindrically extruded cast samples were machined on a CNC lathe machine (Ace Micromatic; model: LT-20XL450) with self-centred three-jaw chuck. The maximum diameter and length of the samples that can be turned on the machine are 190 mm and 224 mm, respectively. The CNC turning lathe used to conduct experiments has a range of spindle speed as 40–4000 rpm. The turning process was designed in accordance with the recommendations of previous investigations

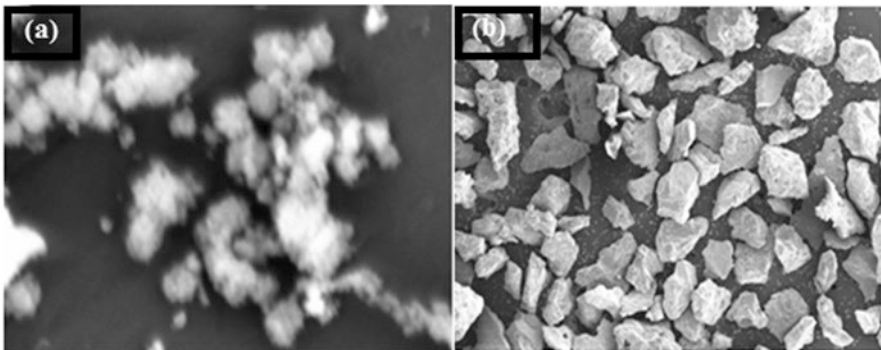


Fig. 12.2 SEM images of the SiC and RM particles

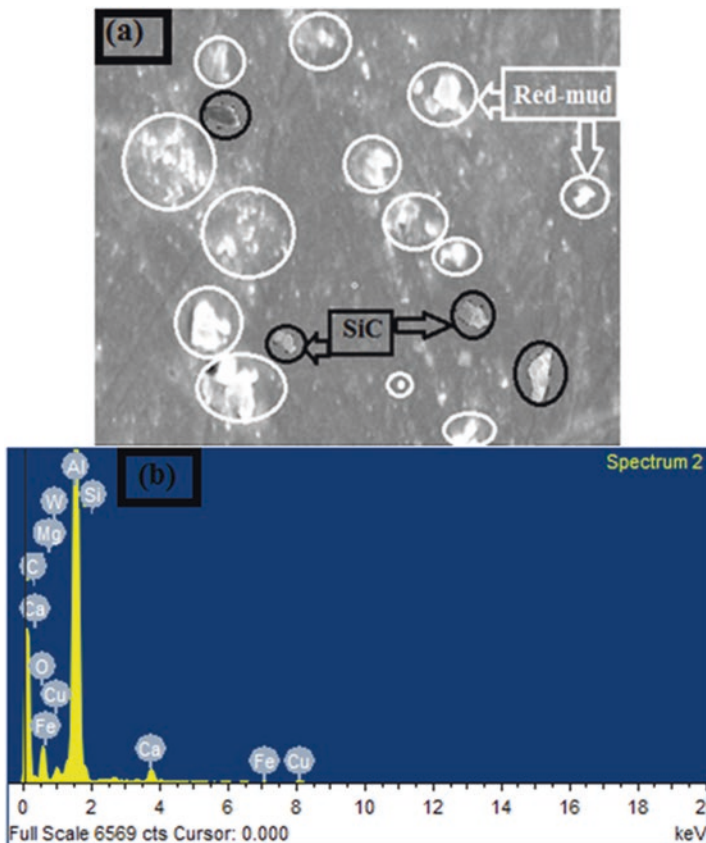


Fig. 12.3 (a) SEM image and (b) EDS spectrum of developed composites at a RM fraction of 5 wt.%

(Pramanik et al., 2008). For this, tungsten-coated carbide medium cutting insert (CCMT 09T304 MT) having the following geometry has been used: positive 80° rhombic with 7° clearance angle. The cost of machining with these inserts is considerably lower in comparison to other inserts like PCD inserts. It has also been found that dry sliding machining is a very popular method due to environmental hazards related to the use of cutting fluid (Goindi & Sarkar, 2017; Sreejith & Ngoi, 2000). Therefore, machining operations were performed under dry tuning conditions on a CNC lathe machine. These carbide inserts were fixed tightly in the tool holder for turning operations. There were four edges on each insert and each turning operation was carried out with a new edge. The experimental set-up used for turning operations has been shown in Fig. 12.4(a), while the machined samples of the developed composites have been shown in Fig. 12.4(b). In this study, the diameter and length of each specimen were prepared as 12 mm and 50 mm, respectively. Three cutting parameters, i.e. depth of cut (0.05–0.2 mm), cutting speed (400–1600 rpm) and feed

Fig. 12.4 (a)
Experimental set-up for
CNC lathe machine used
for turning of the
specimens and **(b)**
machined samples



rate (0.2–0.8 mm/rev), have been selected to investigate the turning behaviour of the hybrid composites. The average roughness (R_a value) of the composite's surface was evaluated using Mitutoyo SS220 roughness tester, which can evaluate roughness value up to 0.01 μm .

3 Experimental Design and Mathematical Modelling

RSM is a statistical tool of mathematical modelling for optimization of the output response for machining of the materials. Therefore, it can be used to evaluate relationship for the output response in terms of input variables. The RSM technique involves three steps (Makadia & Nanavati, 2013; Song et al., 2019):

- In the first stage, experiments are conducted to evaluate the output response using experimental design approach. This approach uses minimum number of experiments for evaluating the output response, thereby reducing cost involved in the experimental phase of investigations.

- Thereafter, mathematical models are developed based on the outcome of the experiments. The relationship between the process variables is defined and the output response has been expressed as a polynomial equation.
- In the last stage, various statistical techniques like response plots and analysis of variance (ANOVA) have been applied to evaluate the optimum combination of process variables.

Many researchers have used Taguchi’s technique of experimental design to investigate machining processes such as drilling, turning and milling since it is economic and less time consuming (Ghani et al., 2005; Radhika et al., 2014b). Here, investigations for the surface roughness have been performed under ‘smaller the better’ category. The signal-to-noise (*S/N*) ratio for has been obtained from the following relation (Ross, 1996; Roy, 1990; Taguchi et al., 1989):

$$\frac{S}{N} = -10 \log \frac{1}{n} (\sum y^2) \tag{12.1}$$

where ‘*n*’ stands for number of experimental outputs and ‘*y*’ represents the observed data.

In the present study, five variables (RM fraction and size, cutting depth, feed rate, and cutting speed) have been selected to study the turning behaviour of the hybrid composites. For precise assessment, more than two levels of parameters are required to be selected. In this study, four levels of the process parameters have been selected and details of the parameters have been shown in Table 12.2.

Based on the selected parameters, L16b plan has been used for evaluating roughness output of the turning process. The turning operations have been conducted as per parametric conditions shown in Table 12.3. The results for the surface roughness along with *S/N* ratios have also been shown in Table 12.3. Each experiment was performed two times at two different geometric locations, and average values have been taken for further analysis.

Based on experimental results, RSM model has been developed for the surface roughness of composite specimens as a polynomial equation. It has been observed in previous studies that higher-order interactions are insignificant in engineering problems. Thus, these are not considered in the present case, and surface roughness equation can be written as first-order polynomial equation as follows:

Table 12.2 Variables for investigating machining characteristics of Al/SiC/RM composites

Parameter	Variable code	Level			
		1	2	3	4
Red-mud contents (wt.%)	A	5	10	15	20
Red-mud size (µm)	B	125	88	75	37
Depth of cut (mm)	C	0.05	0.1	0.15	0.2
Feed rate (mm/rev)	D	0.2	0.4	0.6	0.8
Cutting speed (rpm)	E	400	800	1200	1600

Table 12.3 Experimental layout and results for output response (surface roughness)

S. No.	Factor code					Surface roughness (Ra)			S/N ratio (dB)
	A	B	C	D	E	R1	R2	Average	
1	5	125	0.05	0.2	400	0.47	0.55	0.510	5.8486
2	5	88	0.10	0.4	800	1.19	0.91	1.050	-0.4237
3	5	75	0.15	0.6	1200	2.43	2.51	2.470	-7.8539
4	5	37	0.20	0.8	1600	1.88	1.91	1.895	-5.5521
5	10	125	0.10	0.6	1600	1.42	1.28	1.350	-2.6066
6	10	88	0.05	0.8	1200	0.96	1.02	0.990	0.08730
7	10	75	0.20	0.2	800	1.17	1.05	1.120	-0.9843
8	10	37	0.15	0.4	400	1.34	1.08	1.210	-1.6557
9	15	125	0.15	0.8	800	0.97	1.09	1.030	-0.2567
10	15	88	0.20	0.6	400	1.30	1.33	1.315	-2.3785
11	15	75	0.05	0.4	1600	0.71	0.73	0.720	2.8553
12	15	37	0.10	0.2	1200	0.42	0.58	0.500	6.0206
13	20	125	0.20	0.4	1200	0.92	1.02	0.970	0.2645
14	20	88	0.15	0.2	1600	0.80	0.81	0.805	1.4116
15	20	75	0.10	0.8	400	1.37	1.13	1.250	-1.9382
16	20	37	0.05	0.6	800	0.50	0.58	0.540	5.3521

$$SR = b_o + \sum_{i=1}^k b_i X_i + \sum_{j=1}^k \sum_{l=1}^k b_{ij} X_i X_j + e \tag{12.2}$$

where:

SR is the output response.

b_o , b_i and b_{ij} are the regression coefficients.

X_i and X_j represents process variables for i th and j th terms.

e is the experimental error.

The regression coefficients can be obtained from statistical analysis of the experimental data presented in Table 12.3. Further, ANOVA has been used to evaluate the significant terms in CNC machining of the developed composites. The value of coefficient of determination (R^2) was determined to validate the mathematical model. As the value of R^2 approaches unity, the better is the fitness of the developed model. The regression correlation developed for the surface roughness in terms of significant parameters (main effects and interaction terms) is given below:

$$ASR = 0.9322 - 0.003608A - 0.000146B + 0.2234C + 0.2485D + 0.000029E - 0.000799BD + 0.000001BE - 0.000144DE \tag{12.3}$$

The values of all the coefficients of significant terms have been evaluated using Minitab-17 software, and Eq. (12.3) presents the final relation between the average surface roughness (ASR) and significant factors. The value of R^2 has been found to be greater than 90%, indicating that mathematical model is adequate for evaluating the output response. Here, a correlation graph (between measured and predicted response) and normal probability plot (for residuals) have also been drawn using Minitab-17 software for validating the developed model for surface roughness of the hybrid composites as shown in Fig. 12.5. Figures 12.5(a) and (b) show that all the data points in these graphs are found to be close to the fitted lines with a few exceptions. This shows that the developed model for surface quality of the composites adequately fits the investigated range of parameters.

4 Analysis of Experimental Results

4.1 Ranking of Parameters

The S/N ratio data has been used to obtain the influence of input variables. The analysis of S/N ratio has been done by evaluating the average data for various levels of input variables. The ranks of input variables have been obtained using delta statistics that represents the difference between the highest and lowest values of S/N ratio related to each variable. The input variable with maximum value of delta is given first rank. Further, the minimum value of delta indicates the lowest rank for a variable. Table 12.4 presents results regarding S/N ratio response for surface roughness of the composites. The delta has been found to be highest for depth of cut (C) parameter. Therefore, the depth of cut has been ranked first regarding surface roughness of the composites. Further, cutting speed (E) exhibits minimum value of delta, indicating its lowest rank. In order to evaluate the optimum process conditions, response plots are plotted for S/N ratio. Here, larger value of S/N ratio is required for minimum variance of output near the desired response. Figure 12.6 presents main effect plots for S/N ratio for roughness value of the composites indicating variations in the S/N ratio with respect to different levels of the parameters. The S/N ratio has been found to be maximum at a RM fraction (A) of 15 wt.%, RM size (B) of 37 μm , cutting depth (C) of 0.05 mm, feed rate (D) of 0.2 mm/rev and cutting speed (E) of 800 rpm. Therefore, optimum combination for obtaining minimum value of surface roughness is found to be A3-B4-C1-D1-E2.

4.2 Significance of Parameters

Here, ANOVA analysis has been performed for the experimental data for surface roughness with a confidence level of 95% for evaluating the individual contributions of the parameters. All the candidate terms (main and interaction) are analysed

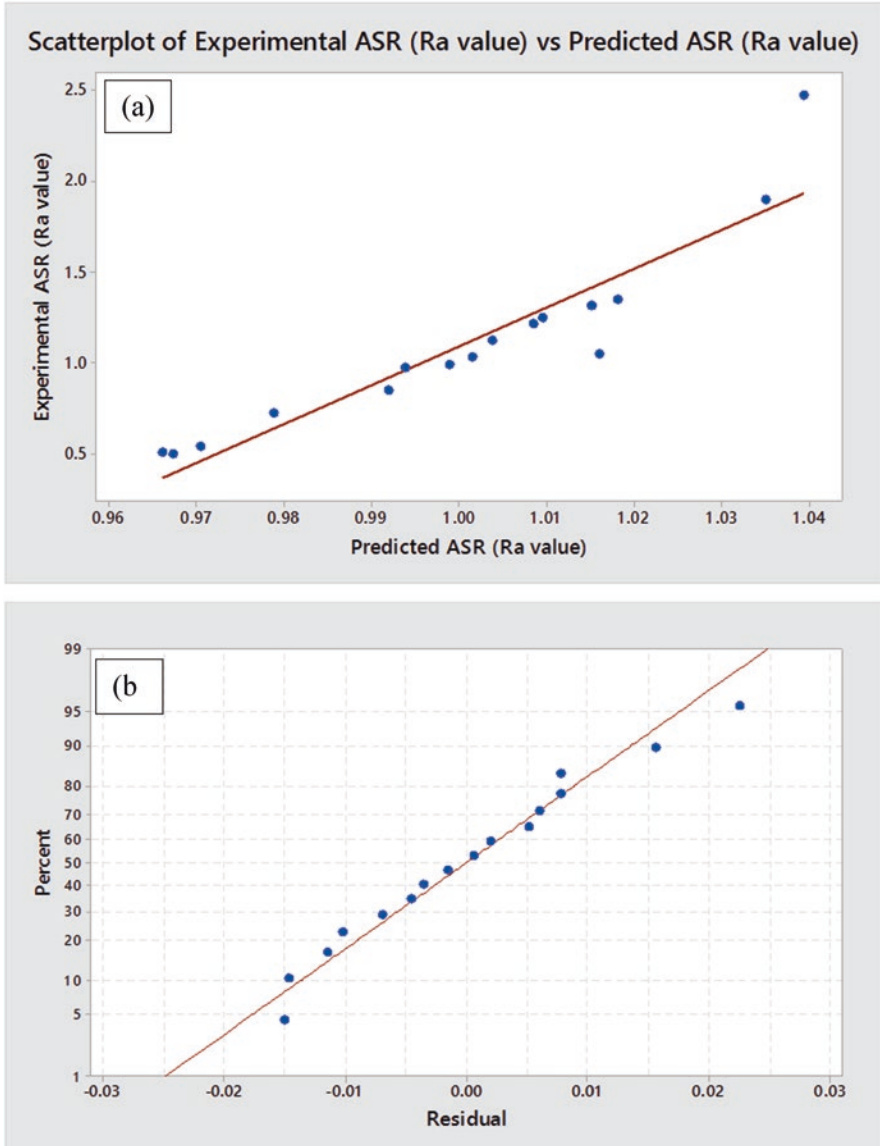


Fig. 12.5 (a) Correlation and (b) normal probability plots for the developed model for surface roughness of hybrid composites

for a significant contribution in the surface roughness response. The p -values have been evaluated for all of the candidate terms. The terms with p -value lower than 0.05 are significant terms regarding surface roughness values of the composites. Table 12.5 presents the results of ANOVA modelling with a value of R^2 as 0.9589,

Table 12.4 *S/N* ratio response for roughness value smaller-is-better

Level/factor	A	B	C	D	E
1	-1.99533	1.04121	3.53534	3.07411	-0.03096
2	-1.28986	-1.98079	0.26298	0.25961	0.92181
3	1.55967	-0.32585	-2.08869	-1.87175	-0.37037
4	1.27253	0.81244	-2.16262	-1.91496	-0.97347
Delta	3.55500	3.02200	5.69797	4.98907	1.89528
Rank	3	4	1	2	5

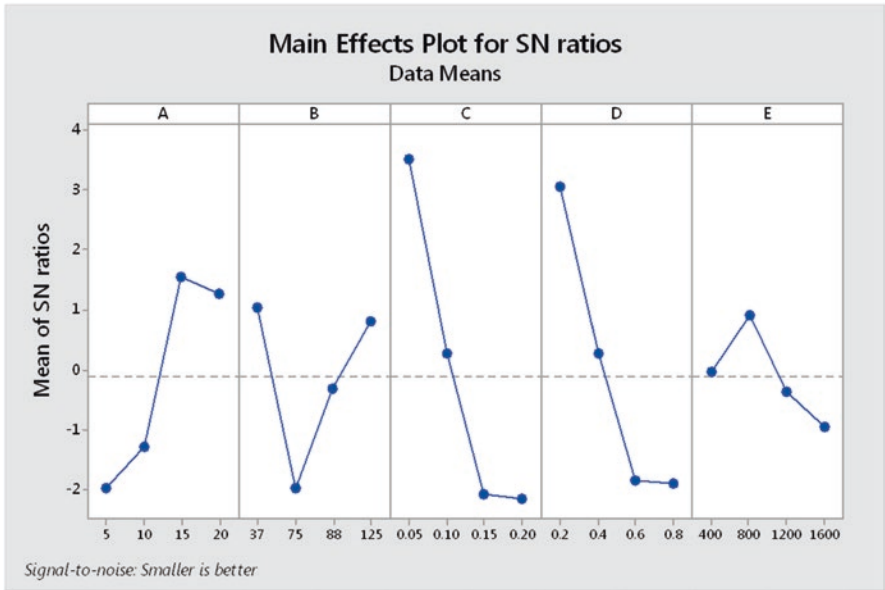


Fig. 12.6 Response plots for *S/N* ratio for surface roughness for Al2024/SiC/red-mud composites

indicating that the model provides excellent fit for parametric influence on surface roughness of the composites.

The results presented in Table 12.5 also indicate that RM wt.% (A), depth of cut (C) and feed rate (D) are main factors with significant contributions in machining characteristics of the composites since their *p*-values are lower than 0.05. Further, *p*-values of other main factors, i.e. RM size (B) and cutting speed (E), are found to be 0.942 and 0.157, respectively. Therefore, these parameters are considered to be insignificant for machining response of hybrid composites. Further, *p*-values of B*D, B*E and D*E (interaction terms) are obtained as 0.025, 0.004 and 0.003, respectively. Therefore, these interaction terms are considered to have significant effect on the machining response of developed composites. Table 12.6 presents the individual contribution of all the significant parameters (main and interaction effects). Here, cutting depth (C) has maximum contribution of 35.30% on the roughness value. Further, contributions of RM wt.% (A) and feed rate have (D) been

Table 12.5 Results for ANOVA analysis for surface roughness value

Source	DF	Adj SS	Adj MS	F-value	P-value	Contr. regression
	8	0.007065	0.000883	20.40	0.000	–
A	1	0.002085	0.002085	48.16	0.000	28.65%
B	1	0.000000	0.000000	0.01	0.942	0
C	1	0.002494	0.002494	57.62	0.000	33.84%
D	1	0.001958	0.001958	45.24	0.000	26.57%
E	1	0.000109	0.000109	2.51	0.157	1.04%
B*D	1	0.000351	0.000351	8.11	0.025	4.76%
B*E	1	0.000734	0.000734	16.96	0.004	9.96%
D*E	1	0.000838	0.000838	19.37	0.003	11.37%
Error	7	0.000303	0.000043			4.11%
Total	15	0.007368				100%

Model summary for transformed response: $S = 0.0065792$, $R^2 = 95.89$, $R^2(\text{adj}) = 91.19$

Table 12.6 Contribution of significant main factors and the interaction effects for Al2024/SiC/red-mud composites

Factor code	A	C	D	B*D	B*E	D*E
Contribution (%)	29.51	35.30	27.71	4.96	10.38	11.86

found as 29.51% and 27.71%, respectively. Further, interaction effect of feed rate and cutting velocity (D*E) has a contribution of 11.86% regarding the machining response of the composites. Also, the interaction effects of particle size with cutting speed and feed rate (B*E and B*D) have contributions of 10.38% and 4.96%, respectively.

4.3 Influence of Parameters on Surface Roughness

In previous reports, it has been revealed that surface roughness of the MMCs depends on the variations in the magnitude of cutting force. However, different types of mechanisms like particle fracture, ploughing and chip formation contribute in variations in the cutting force during machining operations (Kumar & Chauhan, 2015; Priyadarshi & Sharma, 2016). Therefore, variations in surface roughness have been investigated based on the predominant cutting mechanisms in this study. For this, 3D response plots for roughness value w.r.t. RM fraction and other parameters, i.e. particle size, depth of cut, feed rate and cutting velocity, have been generated as shown in Figs. 12.7–12.10.

First of all, it has been observed that surface roughness of composite specimens is reduced with increasing value of RM fraction (5–20 wt.%) irrespective of the magnitude of other parameters. This is an indication that surface finish is improved with an increase in RM fraction in the composites. Actually, RM particles have lubricating characteristics due to which a thin layer is formed at the interface of the

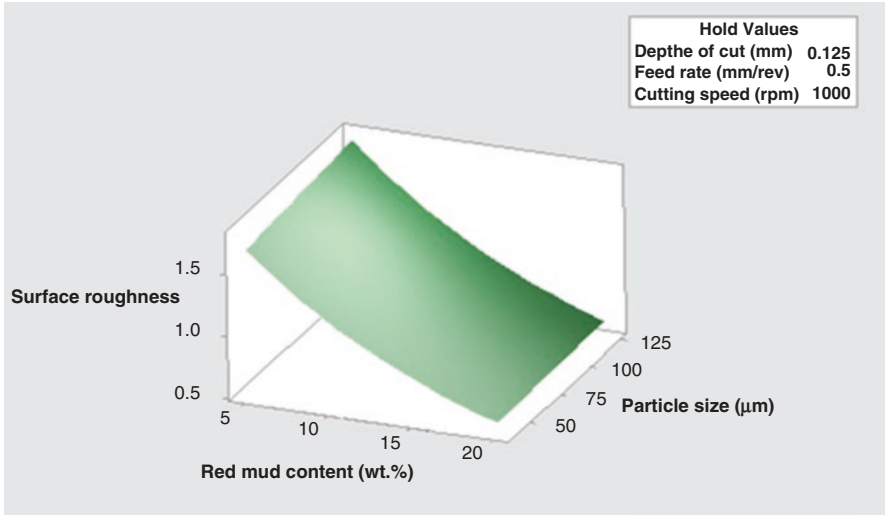


Fig. 12.7 Surface plot for surface roughness vs red-mud content and particle size for the Al2024/SiC/red-mud composites

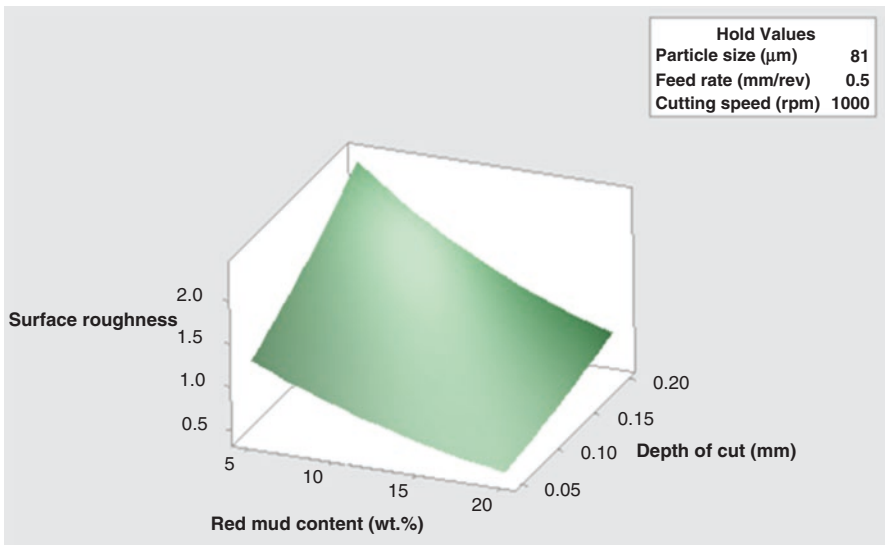


Fig. 12.8 Surface plot for surface roughness vs red-mud content and depth of cut for the Al2024/SiC/red-mud composites

composite sample and the cutting insert (during turning operation) (Roy, 1990). Thus, friction coefficient and heat generated in cutting zone are reduced, which improves the surface quality of the composites with increasing RM fraction. Therefore, the surface finish is significantly improved with an increase in the value

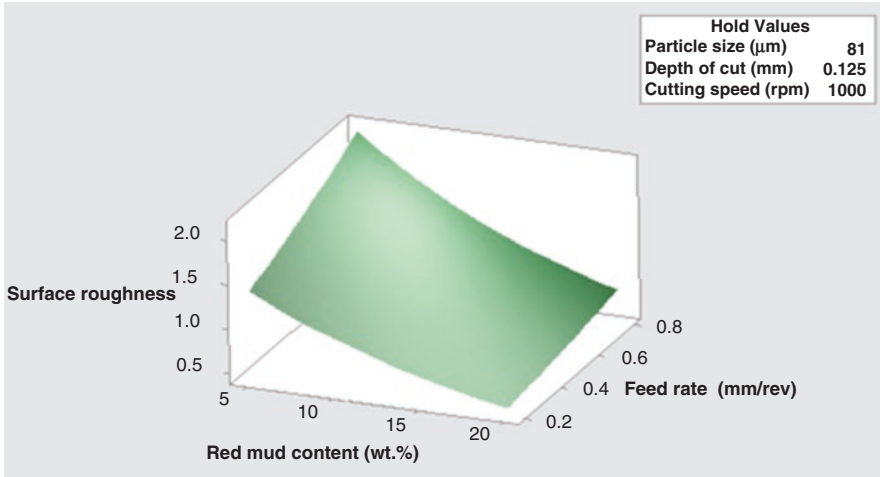


Fig. 12.9 Surface plot for surface roughness vs red-mud content and feed rate for the Al2024/SiC/red-mud composites

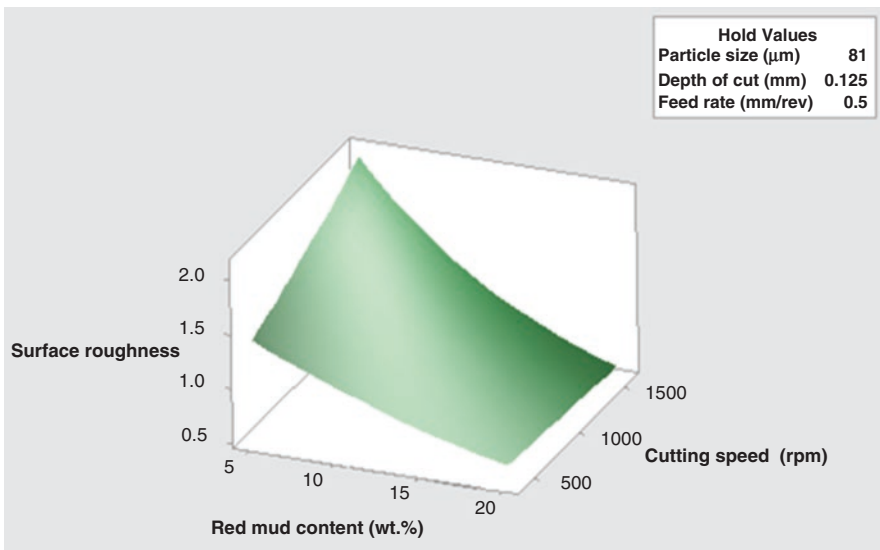


Fig. 12.10 Surface plot for surface roughness vs red-mud content and cutting speed for the Al2024/SiC/red-mud composites

of RM percentage. However, it has also been observed in these plots that this effect has been observed to be reduced at a higher RM fraction (15–20 wt.%). This may be attributed to agglomeration of reinforcement particles at a higher RM percentage (as seen in Fig. 3). This results in particle cracking and debonding during machining operation, ultimately increasing the roughness value of the composites in the

turning process (Sekhar & Singh, 2015). As far as the influence of particle size is concerned, Fig. 12.7 shows that surface roughness is slightly increased with increasing particle size (37–125 μm). This is due to the fact that large particles are easily fractured during machining and debonding occurs resulting in a higher roughness value.

In Figs. 12.8 and 12.9, it has also been revealed that lower values of feed rate (0.2–0.8 mm/min) and cutting depth (0.05–0.20 mm) are required in order to obtain higher surface finish of hybrid composites. The increase in the value of the depth of cut increases the particle debonding and surface resistance at work-tool interface (Priyadarshi & Sharma, 2016). This results in an increase in the magnitudes of cutting and fractional forces along the tool-chip interface leading to reduced surface finish. Similar trends have been observed for variations in the surface roughness with respect to feed rate. The higher feed rate results in increase in the speed of introducing the composite surface to the cutting tool, thereby increasing the resistance force offered by the workpiece to the cutting tool. This ultimately decreases the roughness value for the composites with increasing feed rate. Figure 12.10 also shows that surface roughness is decreased with increasing cutting speed (400–1600 rpm). It has been noticed that a large material flow takes place at a lower cutting speed that increases the frictional force and cutting force at the interface (Kumar & Chauhan, 2015). On the other hand, the deformation of the workpiece is less at a higher cutting velocity. Therefore, frictional force and surface temperature are reduced. Thus, better surface finish of the workpiece is obtained at a higher cutting speed.

In overall, it has been observed in surface plots that surface roughness of the hybrid composites varies significantly with respect to reinforcement percentage, cutting depth and feed rate. On the other hand, roughness value varies slightly with change in the values of cutting speed and particle size. These results are in line with those obtained in the ANOVA analysis. Thus, a higher value of reinforcement percentage and speed and minimum values of particle size, cutting depth and feed rate are required for obtaining the minimum value of surface roughness.

4.4 Analysis of Chip Formation

Figure 12.11 presents the shapes of chips formed during machining of composite samples under different process conditions. To study the influence of machining parameters (cutting depth and feed rate) on chip formation, reinforcement fraction was taken constant (5 wt.%). The analysis shows that size of the chips increases with increasing magnitudes of cutting parameters. At lower magnitudes of feed rate (0.2 mm/rev) and depth of cut (0.05 mm), short and segmented chips are formed during turning of the composites. It has also been observed that the chips formed are long in size and curly in shape at higher values of cutting depth (0.2 mm) and feed rate (0.8 mm/rev). Actually, composites tend to behave in a brittle manner with increase in the values of cutting parameters. Further, thickness and length of the

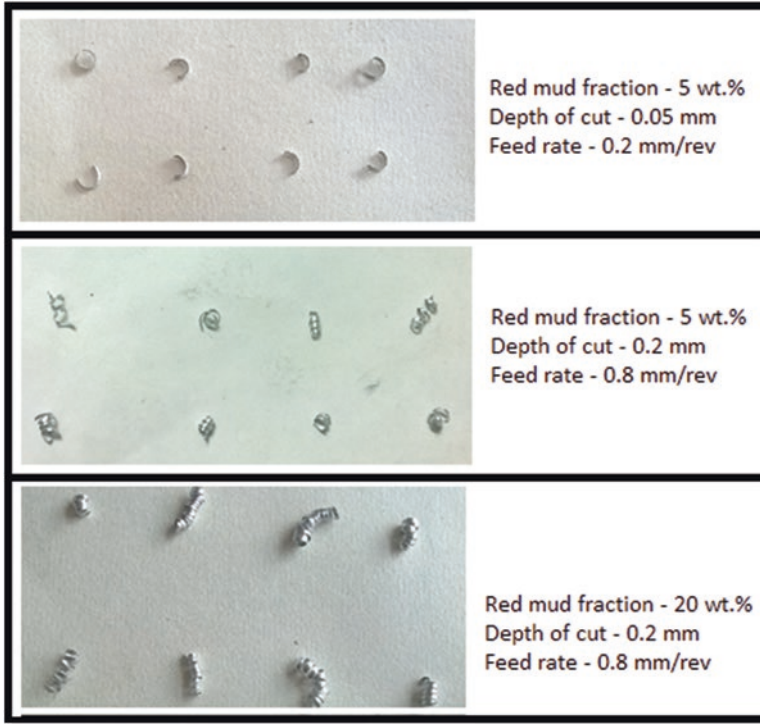


Fig. 12.11 Chip formed during turning of Al/SiC/RM composites under different cutting conditions

chips are increased with increasing RM fraction (from 5 wt.% to 20 wt.%). The chips formed at a RM fraction of 20 wt.% are coil spring type having large length. The surface of chips is also smoother and brighter. This is due to reduced interface temperature and favourable chip-tool interaction. The reduction in the interface temperature is an indication of the reduced cutting forces due to self-lubricating characteristics of RM particles present in the hybrid composites (Priyadarshi & Sharma, 2016).

To study predominant cutting mechanism, SEM images of the chips formed during turning of hybrid composites have been investigated under different parametric conditions. Figure 12.12 presents the micrographs of the chips formed under variable parametric conditions, i.e. feed rate, cutting depth and RM fraction (for the same RM size and speed). At higher values of feed (0.6 mm/min) and depth (0.1 mm) and lower fraction of RM particles (10 wt.%), extensive plastic deformation of the composite surface has been noticed. This extensive surface damage and material flow on the chip surface can be clearly observed in Fig. 12.12(a). Actually, cutting force required under these conditions is comparatively large resulting in higher temperature and increased thermal softening of the composite surface (Dwivedi et al., 2012). Therefore, surface damage is increased and poor surface finish is obtained

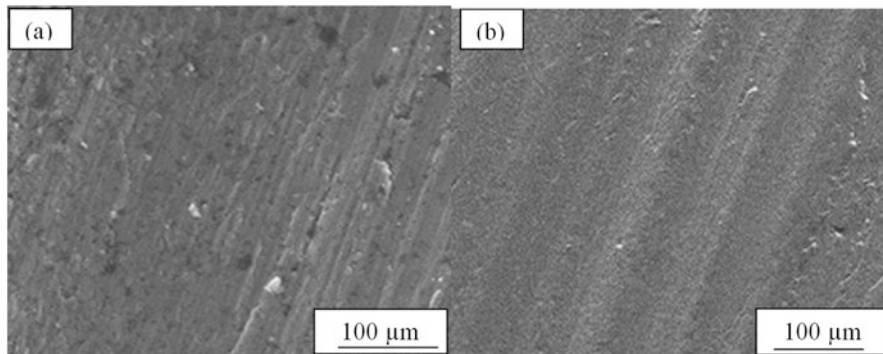


Fig. 12.12 SEM examination of chips formed during turning of specimens at (a) RM fraction of 10 wt.%, cutting depth of 0.10 mm and feed rate of 0.6 mm/rev and (b) RM fraction of 15 wt.%, cutting depth of 0.05 mm and feed rate of 0.40 mm/rev, for a cutting speed of 1600 rpm

under these conditions. Further, decrease in the values of cutting parameters, i.e. feed rate (from 0.6 mm/min to 0.4 mm/rev) and cutting depth (from 0.1 mm to 0.05 mm), and increase in RM fraction (from 10 wt.% to 15 wt.%) reduce damage of the composite surface as indicated in Fig. 12.12(b). This is due to reduced cutting force required to cut the composite samples. Therefore, machined surface exhibits improved surface finish under these conditions. Overall, SEM examination reveals that low values of cutting parameters and higher RM fraction improve surface quality of the composites. Therefore, SEM micrographs agree with statistical analysis, i.e. these input variables significantly control the machining response of the hybrid composites.

4.5 Confirmation Experiment

In this section, results of the conformation experiment are presented to verify the developed model for improved surface quality of the composites. For this purpose, measured and predicted output of the composites has been compared under optimum combination of parameters. The experimental output for the roughness value has been obtained using standard procedure discussed in Sect. 2, while predicted response is calculated using the following equation (Ghani et al., 2005; Radhika et al., 2014a; Suresh Kumar, 2015):

$$N_o = \sum_{i=1}^n (N_i - N_m) + N_m \quad (12.4)$$

where N_m is aggregate mean S/N ratio, N_i is mean obtained at optimum combination of parameters and n is number of main design variables. The results of the confirmation experiment conducted at optimum combination of parameters are presented in

Table 12.7 Comparison of the predicted and observed data for surface roughness of Al2024/SiC/red-mud composites under optimum conditions

Optimum level of parameters	Statistical data		Observed data		Deviation (%)
	Output	<i>S/N</i> ratio	Output	<i>S/N</i> ratio	
A3-B4-C1-D1-E2	0.425	7.432	0.405	7.851	4.17
A3-B4-C2-D1-E3	0.526	5.581	0.500	6.020	5.2
Improvement			23.45%		

Table 12.7. The experimental results are compared with the predicted response and a deviation is obtained up to a level of about 4–5%. Further, a maximum of 6.0202 of *S/N* ratio has been obtained under the investigated conditions. Upon comparing the results under optimum combination of parameters obtained in Table 12.7 (A3-B4-C1-D1-E2) with those obtained in Table 12.3 (A3-B4-C2-D1-E3), it can be observed that a minimum of 23.45% improvement in the *S/N* ratio for roughness value has been obtained by optimization of the various control parameters.

5 Conclusions

The chapter presents the study of surface roughness of the machined surface of Al/SiC/RM composites under sustainable (dry machining) conditions. The composite specimens are produced via liquid metallurgy route, and turning operations have been performed on these specimens under different parametric conditions. Also, Taguchi's technique has been used for conducting experiments and the average value of surface roughness is obtained using MITUTOYO roughness tester. The results are analysed using statistical techniques for significant contributions of parameters in the output response. The conclusions of this study are as follows:

1. The 15 wt.% of RM content, 37 μm of particle size, 0.02 mm of cutting depth, 0.2 mm/rev of feed rate and 88 rpm of cutting speed are the optimum parameters for obtaining minimum surface roughness for the composites.
2. The depth of cut has maximum influence of about 33% in the surface characteristics of the Al composites followed by RM wt.% (28% contribution) and feed rate (26% contribution).
3. Further, influence of the parameters has been studied by RSM technique. The presence of RM particles improves the surface characteristics due to increased lubricating effect of these particles at tool-work interface. It has also been noticed that an increase in cutting depth and feed rate degrades the surface characteristics of hybrid composites since the cutting force required to machine the surface is increased under these conditions.
4. The chip size changes from segmented type to spiral coil type with increase in the values of depth of cut and feed rate. Further, long and coil spring type chips are produced at relatively higher values of RM fraction in the hybrid composites due to the lubricating effect of the RM particles. SEM examination of chips

formed reveals that low values of cutting parameters and higher red-mud contents improve the surface characteristics of the hybrid composites.

5. The confirmation experiment indicates a deviation of 4% in the experimental and the predicted response. A minimum of 23% improvement in the surface quality of the composites is observed under optimum process conditions.
6. Overall, it has been revealed that the addition of RM (an industrial waste material) particles helps in improving the machinability of the hybrid composites under dry turning conditions. The results provide adequate information regarding the machining aspects of HAMCs, which can be used in various industrial applications.

Acknowledgements None.

Declaration of InterestNone.

References

- Alsubari, S., Zuhri, M. Y. M., Sapuan, S. M., Ishank, M. R., Ilyas, R. A., & Asyraf, M. R. M. (2021). Potential of natural fiber reinforced polymer composites in sandwich structures: a review on its mechanical properties. *Polymers*, *13*(3), 423. <https://doi.org/10.3390/polym13030423>
- Arun Premnath, A., Alwarsamy, T., & Rajmohan, T. (2012). Experimental investigation and optimization of process parameters in milling of hybrid metal matrix composites. *Materials and Manufacturing Processes*, *27*, 1035–1044. <https://doi.org/10.1080/10426914.2012.677911>
- Bains, P. S., Sidhu, S. S., & Payal, H. S. (2016). Fabrication and machining of metal matrix composites: a review. *Materials and Manufacturing Processes*, *31*(5), 553–573. <https://doi.org/10.1080/10426914.2015.1025976>
- Bajavarajappa, S. (2009). Tool wear in turning of graphitic hybrid metal matrix composites. *Materials and Manufacturing Processes*, *24*(4), 484–487. <https://doi.org/10.1080/10426910802714431>
- Behera, R., & Sutradhar, G. (2012). Machinability of LM6/SiCp metal matrix composites with tungsten carbide cutting tool inserts. *ARPJ Journal of Engineering and Applied Sciences*, *7*(2), 216–221.
- Bhushan, R. K. (2013). Optimization of cutting parameters for minimizing power consumption and maximizing tool life during machining of Al alloy sic particle composites. *Journal of Cleaner Production*, *389*, 242–254. <https://doi.org/10.1016/j.jclepro.2013.03.049>
- Das, D. K., Mishra, P. C., Singh, S., & Thakur, R. K. (2014). Tool wear in turning ceramic reinforced aluminum matrix composites—A review. *Journal of Composite Materials*, *49*(24), 2949–2961. <https://doi.org/10.1177/0021998314558955>
- Dwivedi, S. P., Kumar, S., & Kumar, A. (2012). Effect of turning parameters on surface roughness of A356/5%SiC composite produced by electromagnetic stir casting. *Journal of Mechanical Science and Technology*, *26*(12), 3973–3979. <https://doi.org/10.1007/s12206-012-0914-5>
- El-Gallab, M., & Sklad, M. (1998). Machining of Al:SiC particulate metal-matrix composites Part I: Tool performance. *Journal of Materials Processing Technology*, *83*, 151–158. [https://doi.org/10.1016/S0924-0136\(98\)00054-5](https://doi.org/10.1016/S0924-0136(98)00054-5)
- Ghani, J., Chodhury, I. A., & Hassan, H. H. (2005). Application of Taguchi method in the optimization of end milling parameters. *Journal of Materials Processing Technology*, *145*, 84–92. [https://doi.org/10.1016/S0924-0136\(03\)00865-3](https://doi.org/10.1016/S0924-0136(03)00865-3)

- Goindi, G. S., & Sarkar, P. (2017). Dry machining: a step towards sustainable machining –challenges and future directions. *Journal of Cleaner Production*, 165(1), 1557–1571. <https://doi.org/10.1016/j.jclepro.2017.07.235>
- Hiremath, V., Auradi, V., & Dundur, S. T. (2016). Experimental investigations on effect of ceramic B 4 C particulate addition on cutting forces and surface roughness during turning of 6061Al alloy. *Transactions of the Indian Ceramic Society*, 75(2), 126–132. <https://doi.org/10.1080/00371750X.2016.1164626>
- Kant, G., & Sangwan, K. S. (2014). Prediction and optimization of machining parameters for minimizing power consumption and surface roughness in machining. *Journal of Cleaner Production*, 83(15), 151–164. <https://doi.org/10.1016/j.procir.2015.02.002>
- Kumar, M., & Megalingam, A. (2017). Tribological characterization of Al6061/alumina/graphite/redmud hybrid composite for brake rotor application. *Particulate Science and Technology*. <https://doi.org/10.1080/02726351.2017.1367747>
- Kumar, R., & Chauhan, S. (2015). Study on surface roughness measurement for turning of Al 7075/10SiC and Al 7075 hybrid composites by using response surface methodology (RSM) and artificial neural networking (ANN). *Measurements*, 65, 166–180. <https://doi.org/10.1016/j.measurement.2015.01.003>
- Lyas, R. A., Sapuan, S. M., Harussani, M. M., Hakimi, M. Y. A. Y., Haziq, M. Z. M., Atikah, M. S. N., Asyraf, M. R. M., Ishak, M. R., Razman, M. R., Nurazzi, N. M., Norraahim, M. N. F., Abrial, H., & Asrofi, M. (2021). Polylactic acid (PLA) biocomposite: Processing, additive manufacturing and advanced applications. *Polymers*, 13(8), 1326. <https://doi.org/10.3390/polym13081326>
- Makadia, A. J., & Nanavati, J. I. (2013). Optimisation of machining parameters for turning operations based on response surface methodology. *Measurement*, 46, 1521–1529. <https://doi.org/10.1016/j.measurement.2012.11.026>
- Mistry, J. M., & Gohil, P. P. (2016). An overview of diversified reinforcement on aluminum metal matrix composites: tribological aspects. *Proceedings of the Institution of Mechanical Engineers, Part J: Journal of Engineering Tribology*, 231(3), 399–421. <https://doi.org/10.1177/1350650116658572>
- Mohd Nurazzi, N., Asyraf, M. R. M., Khalina, A., Abdullah, N., Sabaruddin, F. A., Kamarudin, S. H., Ahmad, S., Mahat, A. M., Lee, C. L., Aisyah, H. A., Norraahim, M. N. F., Ilyas, R. A., Harussani, M. M., Ishak, M. R., & Sapuan, S. M. (2021). Fabrication, functionalization, and application of carbon nanotube-reinforced polymer composite: an overview. *Polymers*, 13(7), 1047. <https://doi.org/10.3390/polym13071047>
- Muthukrishnan, N., Murugan, M., & Rao, K. P. (2007). Machinability issues in turning of Al-SiC (10p) metal matrix composites. *International Journal of Advanced Manufacturing Technology*, 39, 211–218. <https://doi.org/10.1007/s12541-011-0084-x>
- Nurazzi, N. M., Asyraf, M. R. M., Khalina, A., Abdullah, N., Aisyah, H. A., Rafiqah, S. A., Sabaruddin, F. A., Kamarudin, S. H., Norraahim, M. N. F., Ilyas, R. A., & Sapuan, S. M. (2021). A review on natural fiber reinforced polymer composite for bullet proof and ballistic applications. *Polymers*, 13(4), 646. <https://doi.org/10.3390/polym13040646>
- Omran, A. A. B., Mohammed, A. A. B. A., Sapuan, S. M., Ilyas, R. A., Asyraf, M. R. M., Rahimian Koloor, S. S., & Petru, M. (2021). Micro- and nanocellulose in polymer composite materials: a review. *Polymers*, 13(2), 231. <https://doi.org/10.3390/polym13020231>
- Pramanik, A., Zhang, L. C., & Arsecularatne, J. A. (2008). Machining of metal matrix composites: Effect of ceramic particles on residual stress, surface roughness and chip formation. *International Journal of Machine Tools and Manufacture*, 48, 1613–1625. <https://doi.org/10.1016/j.ijmactools.2008.07.008>
- Priyadarshi, D., & Sharma, R. K. (2016). Optimization for turning of Al-6061-SiC-Gr hybrid nanocomposites using response surface methodologies. *Materials and Manufacturing Processes*, 31(10), 1342–1350. <https://doi.org/10.1080/10426914.2015.1070427>

- Radhika, N., Sudhamshu, A. R., & Chandran, G. K. (2014a). Optimization of electrical discharge machining parameters of aluminium hybrid composites using Taguchi method. *Journal of Engineering Science and Technology*, 9(4), 502–512.
- Radhika, N., Sudhamshu, A. R., & Chandran, G. K. (2014b). Optimization of electrical discharge machining parameters of aluminium hybrid composites using Taguchi method. *Journal of Engineering Science and Technology*, 9(4), 502–512.
- Rahimi, B., Khosravi, H., & Haddad-Sabzevar. (2015). Microstructural characteristics and mechanical properties of Al-2024 alloy processed via a rheocasting route. *International Journal of Minerals, Metallurgy, and Materials*, 22(1), 59–67. <https://doi.org/10.1007/s12613-015-1044-8>
- Rajmohan, T., Palanikumar, K., & Kathirvel, M. (2012). Optimization of machining parameters in drilling hybrid aluminium metal matrix composites. *Transactions of Nonferrous Metals Society of China*, 22, 1286–1297. [https://doi.org/10.1016/S1003-6326\(11\)61317-4](https://doi.org/10.1016/S1003-6326(11)61317-4)
- Ramanathan, A., Krishnan, P. K., & Muraliraja, R. (2019). A review on the production of metal matrix composites through stir casting – Furnace design, properties, challenges, and research opportunities. *Journal of Manufacturing Processes*, 42, 213–245. <https://doi.org/10.1016/j.jmapro.2019.04.017>
- Ross, P. J. (1996). *Taguchi techniques for quality engineering: loss function, orthogonal experiments, parameter and tolerance design*. McGraw Hill.
- Roy, K. R. (1990). *A primer on Taguchi method*. Van Nostrand Reinhold.
- Sathish Kumar, M. K., Sravan Kumar, B., & Channankaiiah, et al. (2015). *Manufacturing and machining of aluminium metal matrix composites: An overview*. Paper presented at Conference: ICETS' 15 at Muthayammal Engineering College, June 2015.
- Sekhar, R., & Singh, T. P. (2015). Mechanisms in turning of metal matrix composites: a review. *Journal of Materials Research and Technology*, 4(2), 197–207. <https://doi.org/10.1016/j.jmrt.2014.10.013>
- Singh, J. (2016). Fabrication characteristics and tribological behavior of Al/SiC/Gr hybrid aluminium matrix composites: a review. *Friction*, 4(3), 191–207. <https://doi.org/10.1007/s40544-016-0116-8>
- Singh, J., & Chauhan, A. (2014). Overview of aluminium matrix composites for automotive applications. *International Journal of Applied Engineering Research*, 9(8), 959–966.
- Singh, J., & Chauhan, A. (2016a). Characterization of hybrid aluminum matrix composites for advanced applications: a review. *Journal of Materials Research and Technology*, 5(2), 159–169. <https://doi.org/10.1016/j.jmrt.2015.05.004>
- Singh, J., & Chauhan, A. (2016b). Overview of wear performance of aluminium matrix composites reinforced with ceramic materials under the influence of controllable variables. *Ceramics International*, 42(1), 56–81. <https://doi.org/10.1016/J.CERAMINT.2015.08.150>
- Singh, J., & Chauhan, A. (2017a). Fabrication characteristics and tensile strength of novel Al2024/SiC/red mud composites processed via stir casting route. *Transactions of Nonferrous Metals Society of China*, 27, 2573–2586. <https://doi.org/10.1177/1464420718803126>
- Singh, J., & Chauhan, A. (2017b). Influence of reinforcement parameters and ageing time on mechanical behavior of novel Al2024/SiC/red mud composites using response surface methodology. *JOM*, 69(12), 2471–2479. <https://doi.org/10.1007/s11837-017-2479-3>
- Singh, J., & Chauhan, A. (2018). Investigations on dry sliding frictional and wear characteristics of SiC and red mud reinforced Al2024 matrix hybrid composites using Taguchi's approach. *Proceedings of the Institution of Mechanical Engineers, Part L: Journal of Materials: Design and Applications*. <https://doi.org/10.1177/1464420718803126>
- Singh, J., & Chauhan, A. (2019). A review of microstructure, mechanical properties and wear behavior of hybrid aluminium matrix composites fabricated via stir casting route. *Sadhana*. <https://doi.org/10.1007/s12046-018-1025-5>
- Song, H., Dan, J., Li, J., et al. (2019). Experimental study on the cutting force during laser-assisted machining of fused silica based on the Taguchi method and response surface methodology. *Journal of Manufacturing Processes*, 38, 9–20. <https://doi.org/10.1007/s12633-018-0010-2>

- Sreejith, P. S., & Ngoi, B. K. A. (2000). Dry machining: machining of the future. *Journal of Materials Processing Technology*, 101, 287–291. [https://doi.org/10.1016/S0924-0136\(00\)00445-3](https://doi.org/10.1016/S0924-0136(00)00445-3)
- Srinivasan, A., Arunachalam, R. M., & Ramesh, S. (2012). Machining performance study on metal matrix composites—A response surface methodology approach. *American Journal of Applied Sciences*, 9, 478–483. <https://doi.org/10.3844/ajassp.2012.478.483>
- Surappa, M. K. (2003). Aluminium matrix composites: challenges and opportunities. *Sadhana*, 28, 319–334. <https://doi.org/10.1007/BF02717141>
- Suresh Kumar, S. (2015). Parametric optimization of wire electrical discharge machining on aluminium based composites through grey relational analysis. *Journal of Manufacturing Process*, 20(1), 22–39. <https://doi.org/10.1016/j.jmapro.2015.09.011>
- Suresh, R., Basavarajappa, S., & Gaitonde, V. N. (2012). Machinability investigations on hardened AISI 4340 steel using coated carbide insert. *International Journal of Refractory Metals and Hard Materials*, 33, 75–86. <https://doi.org/10.1016/j.ijrmhm.2012.02.019>
- Suriani, M. J., Radzi, F. S. M., Ilyas, R. A., Petru, M., Sapuan, S. M., & Ruzaidi, C. M. (2021a). Flammability, tensile, and morphological properties of oil palm empty fruit bunches fiber/pet yarn-reinforced epoxy fire retardant hybrid polymer composites. *Polymers*, 13(8), 1282. <https://doi.org/10.3390/polym13081282>
- Suriani, M. J., Rapi, H. Z., Ilyas, R. A., Petru, M., & Sapuan, S. M. (2021b). Delamination and manufacturing defects in natural fiber-reinforced hybrid composite: a review. *Polymers*, 13(8), 1323. <https://doi.org/10.3390/polym13081323>
- Taguchi, G., Sayed, M. E., & Hashing, T. (1989). *Quality engineering and quality system*. McGraw Hill.
- Taha, M. A. (2001). Industrialization of cast aluminium matrix composites (amccs). *Materials and Manufacturing Processes*, 16(5), 619–641. <https://doi.org/10.1081/AMP-100108625>

Chapter 13

Thermal Characterization of Graphitized Carbon Nanotube-Reinforced Ti64 Nanocomposites Synthesized by Field-Assisted Sintering Technique for Fuselage and Wing Box Applications



Adewale Oladapo Adegbenjo, Mary Ajimegoh Awotunde, Tien-Chien Jen, and Johan Herman Potgieter

1 Introduction

Despite their high demand and attractiveness in high-performance, lightweight, and competitive, high-strength applications, titanium (Ti) and its alloys have witnessed immense setback in usage as thermal materials owing to their unimpressive thermal characteristics at room and elevated temperatures (Adegbenjo et al., 2017a; Wang et al., 2015). For example, the thermal conductivity of Grade 1 Ti is typically lower than that anticipated normally for a metal, and alloys of Ti (Ti64 to be specific) most often display significantly lower or inferior thermal conductivities compared to that of the pure grade sample (Adegbenjo et al., 2019a; Işık & Kentli, 2014). Also, due to their low thermal conductivities and poor elastic modulus, the machining of Ti and its alloys becomes very difficult, thereby adversely impacting on tool life as the temperature at the tool and workpiece interface substantially increases while

A. O. Adegbenjo (✉)

Mechanical Engineering Department, Adeseun Ogundoyin Polytechnic, Eruwa, Nigeria

Department of Mechanical Engineering Science, University of Johannesburg, Johannesburg, South Africa

M. A. Awotunde

Centre for Nanoengineering and Tribocorrosion, University of Johannesburg, Johannesburg, Gauteng, South Africa

T.-C. Jen

Department of Mechanical Engineering Science, University of Johannesburg, Johannesburg, South Africa

J. H. Potgieter

School of Chemical and Metallurgical Engineering, University of The Witwatersrand, Johannesburg, South Africa

machining (Li et al., 2020a; Munir et al., 2018). Furthermore, the fields where Ti and its alloys are mostly employed, such as in the aerospace, defense, automotive, and nuclear industries, require that the materials are thermally stable, with high thermal conductivities (Babapoor et al., 2018).

In spite of the above mentioned pitfalls associated with the applications of Ti and its alloys, their demand keeps growing due to excellent compatibility with Carbon Fiber-Reinforced Plastic (CFRP) in respect to corrosion properties and coefficient of thermal expansion. For instance, it is reported that the amount of Ti employed in the low-fuel consumption aircrafts, where a large quantity of CFRP is used, accounts for more than twice the amount used in the conventional aircraft (Inagaki et al., 2014). However, a major problem with the applications of Ti and its alloys at high temperatures is embrittlement arising from oxygen contamination on the surface; hence, they are mostly used at operating temperatures between 500 and 600 °C. Consequently, Ti64 particularly is employed in the fabrication of wing boxes and the fuselage as it offers higher specific strength, competitive weight savings, and excellent fatigue strengths compared to nickel-based alloys. Nevertheless, Wang et al. (2015) opined that adiabatic shear failures are usually experienced in engineering applications where Ti products are required due to the relatively poor heat conduction characteristics of these materials. Hence, the need to enhance their thermal performances become crucial in order to make the best of this class of materials in these identified specialized areas of their applications.

Carbon nanotubes (CNTs) have been described by several researchers as a reliable reinforcing material for metal-based composites due to their superexcellent mechanical and thermal characteristics (Bhat et al., 2011; Chen et al., 2017; Kondoh et al., 2012; Lephuthing et al., 2020; Liu et al., 2020; Munir et al., 2017). MWCNTs display a thermal conductivity in excess of 3000 W/m K, which falls within the range of the quoted values for diamond crystal and in-plane graphite sheets (Munir et al., 2018). Thus, the addition of MWCNTs to Ti matrices is expected to positively affect the thermal characteristics of the resulting Ti-based matrix composites (TMCs) (Kumar et al., 2017; Li et al., 2020a; Munir et al., 2017; Nan et al., 2004). This is in line with the knowledge that TMCs are gaining more acceptances in industrial applications consequent upon their properties of exceptional strength, high stiffness, and low density (Dong et al., 2020; Jiao et al., 2018; Li et al., 2020b). In addition, TMCs reinforced with MWCNTs have been described as new materials with potential opportunities in industry as they offer outstanding low to moderate density and competitively high elastic modulus (Li et al., 2020a; Zhuang et al., 2020). Although the applications of graphite-reinforced metal matrix composites (MMCs) have attracted much attention lately owing to their superior thermal properties and low cost, the development and characterization of MWCNTs-reinforced TMCs have not received much attention from researchers (Wang et al., 2015). This is despite the understanding that CNTs-reinforced MMCs exhibit improved resistance to thermal fatigue (Bakshi et al., 2010b).

Researchers have attributed this gap to the peculiar processing challenges often encountered in the efforts toward achieving a homogeneous dispersion of the MWCNTs reinforcement within the Ti metal matrix (Adegbenjo et al., 2017a,

2017b; Awotunde et al., 2019; Bakshi et al., 2010a; Li et al., 2013a; Munir et al., 2015a). Other reasons are the requirements for use of elevated sintering temperatures to achieve the full densification of TMCs, as well as the associated possibility of interfacial reactions between Ti metal and defective CNTs at the high processing temperatures (Li et al., 2020a; Munir et al., 2018). Although there are some reported studies available in literature on the thermal behavior of pure Ti matrices reinforced with MWCNTs, there are limited studies reported to date on the thermal characteristics of MWCNTs-reinforced Ti64 metal matrix nanocomposites (MMNCs) to the best of the authors' knowledge, as this group of materials have attracted moderate attention from researchers.

Thus, this current work was undertaken to compensate for this knowledge gap by investigating the effect of MWCNTs contents on the thermal diffusivity characteristics of sintered MWCNTs-reinforced Ti64 (MWCNTs/Ti64) fabricated by spark plasma sintering (SPS), a unique field-assisted sintering technique (FAST). This is built on the foundation from previous studies that small additions of MWCNTs into pure Ti matrix can effectively improve the thermal performance of the resulting TMC and capable of positively expanding the applications of Ti and its alloys (Munir et al., 2017, 2018; Nan et al., 2004; Wang et al., 2015). It is perceived that the results of this present study will aid more research efforts into the applications of high-performance TMC materials as probable replacements for the unreinforced Ti64 in the highly demanding, challenging, unpredictable, and harsh application areas wherein they are mostly employed, especially in the aerospace industries.

2 Materials and Methods

2.1 Materials

The MWCNTs-reinforced Ti64 nanocomposites in this work were fabricated from pre-alloyed, spherical-shaped Ti64 (average particle size: $\sim 25 \mu\text{m}$, procured from TLS Technik GmbH & Co., Germany) and MWCNTs (with outside diameter 20–30 nm, 10–30 μm length, ash content $< 1.5 \text{ wt}\%$ and $> 95 \text{ wt}\%$ purity) powders.

2.2 Methods

The as-received MWCNTs were graphitized in a tube furnace (Webb 77 Natick MA, USA) at $1800 \text{ }^\circ\text{C}$ for 5 h in vacuum before their predetermined quantities were dispersed into the Ti64 metal matrices in a high-energy ball milling (HEBM) machine (Retsch PM 400 MA, Germany) for 6 h at 50 rpm and 10:1 ball-powder ratio (BPR). Both the Ti64 and MWCNTs/Ti64 composite powders containing 1, 2, and 3 wt.%, respectively, of the treated MWCNTs reinforcements were

subsequently consolidated into $\text{Ø} 40 \text{ mm} \times 5 \text{ mm}$ thickness disks by SPS (HHPD-25, FCT Germany) at different sintering temperatures of 850–1000 °C. Heating rate, holding time, and applied pressure during SPS synthesis were 50 MPa, 5 min, and 100 °C/min, respectively.

Sixteen $10 \times 10 \times 1 \text{ mm}^3$ test samples for thermal diffusivity experiments were sectioned by precision cutting from the sintered Ti64 and graphitized MWCNTs-reinforced Ti64 nanocomposite disks. The thermal diffusivities of the test samples were measured according to the Laser Flash (LF) (LFA 427 NETZSCH, Germany) method over 50–300 °C temperature range and following the ASTM E1461 procedures. The recorded value for each sample is the mean of three consecutively recorded measurements for each specimen at the specific temperature under consideration. This ensures the reliability, accuracy, and repeatability of all the thermal diffusivity readings collected during the experiments.

As this present study is focused on reporting the influence of added MWCNTs on the thermal characteristics of the sintered bulk MWCNTs-reinforced Ti64 nanocomposites, the details of the parameters used, as well as the processes followed in dispersing MWCNTs into Ti64 metal matrix via HEBM, the subsequent synthesis of the composite powders into bulk composites by SPS, relative density measurements, metallographic preparation, and microstructural analyses of the samples, are not stated in this present paper; these have been adequately reported elsewhere (Adegbenjo et al., 2017b, 2018).

3 Results and Discussion

3.1 *Microstructural Evolution and Densification of the Fabricated Samples*

The microstructural evolution and densification pattern in sintered unreinforced Ti64 and MWCNTs/Ti64 nanocomposites is brought up here in this current study because it will be needed to fully discuss the thermal behavior of the consolidated bulk nanocomposites. The subject has been dealt with in detail elsewhere (Adegbenjo et al., 2017b, 2018). Figure 13.1 shows the secondary electron images (SEI) of the sintered unreinforced Ti64 and MWCNTs/Ti64 nanocomposites consolidated at 1000 °C as observed from the SEM analyses of the samples. The unreinforced Ti64 alloy as seen in Fig. 13.1a shows the typical fully lamellar structure of Ti64 alloy with the characteristic basket weave (Widmanstätten) $\alpha + \beta$ network. However, it was observed that the addition of MWCNTs to Ti64 matrices resulted in transforming this characteristic structure from fully lamellar to equiaxed as could be seen in Fig. 13.1b–d for the sintered nanocomposite samples. All the consolidated samples were sintered to full densification; hence, there were no significant pores observed in the presented images. However, re-agglomerated MWCNTs (shown by black arrows) and TiC (indicated by blue arrows) resulting from the interfacial reaction

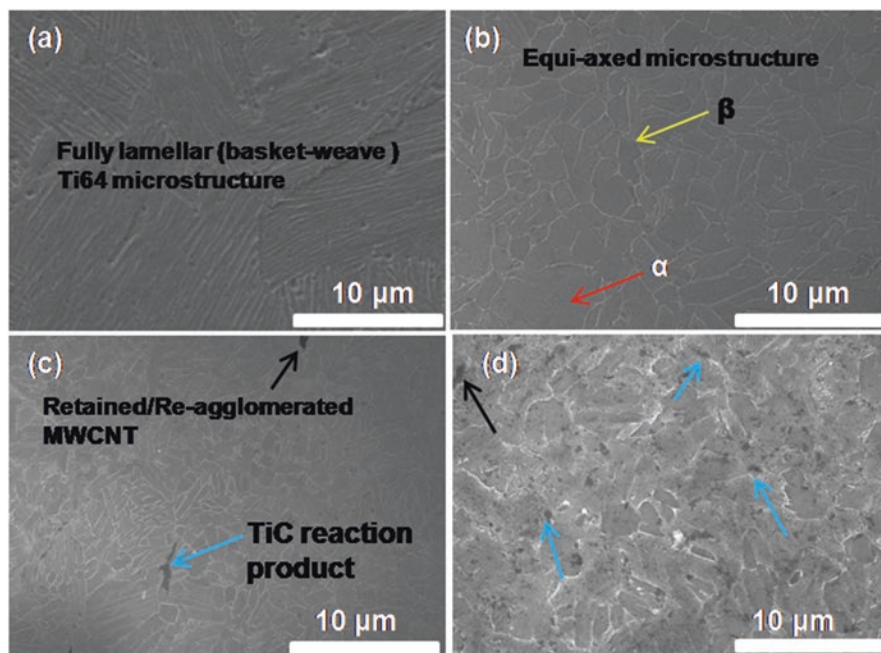


Fig. 13.1 Micrographs of sintered (a) unreinforced Ti64 and MWCNTs-reinforced Ti64 nanocomposites containing varied MWCNTs reinforcements (b) 1 wt.%, (c) 2 wt.%, and (d) 3 wt.%; all consolidated at 1000 °C by SPS

between defective MWCNTs and Ti64 metal particles were observed in the composite samples containing 2 and 3 wt.% MWCNTs, respectively (Fig. 13.1c, d). The 3 wt.% MWCNTs/Ti64 composite exhibited higher TiC content as seen in Fig. 13.1d, which suggests that the composite had more re-agglomerated and damaged CNTs that reacted with Ti64 particles to form the interfacial products (Adegbenjo et al., 2018). This is because the tendency to homogeneously disperse MWCNTs within the alloy matrix becomes increasingly difficult with a higher content of the reinforcement within it (Adegbenjo et al., 2017a, 2019b).

The densification in the unreinforced Ti64 and MWCNTs/Ti64 nanocomposites consolidated by SPS at different sintering temperatures (850–1000 °C) are as shown in Fig. 13.2. Although the unreinforced Ti64 sample reached almost theoretical densities at all the investigated sintering temperatures, it was observed that composite densities reduced steadily with the addition of increasing weight fractions of MWCNTs to Ti64 matrices. Nevertheless, a similar trend of improved densification was seen in both the unreinforced Ti64 and composite samples as the sintering temperature was increased from 850 to 1000 °C. Previous studies have attributed the deteriorating relative densities with the addition of MWCNTs to the presence of re-agglomerated and clustered MWCNTs in the Ti64 metal matrix. Poor interfacial bonding within the composites as a result of insufficient diffusion between Ti64 and

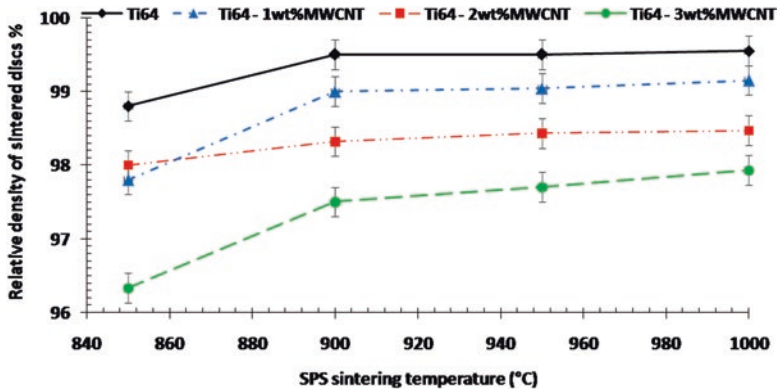


Fig. 13.2 Relative densities of sintered unreinforced Ti64 and MWCNTs reinforced Ti64 nanocomposites at varied sintering temperatures (Adegbenjo et al., 2017b)

the MWCNTs could also cause thermal gradients between the metal matrix and the MWCNTs reinforcement, and this most probably culminated in the declining densification in the composites (Adegbenjo et al., 2017b). On the other hand, the observed enhancements in relative densities with increasing sintering temperatures was attributed to the presumed increased diffusion bonding and atom mobility expectedly with higher sintering temperatures (Adegbenjo et al., 2017b, 2018). These results are in agreement with the outcomes of reported studies on the reinforcement of Al and Ti metal matrices with MWCNTs wherein the authors submitted that even small amounts of CNTs in a metal matrix is sufficient to cause a decline in the relative densities of the resulting composites (Saheb, 2014; Wang et al., 2015). However, the composites with 1 wt.% MWCNTs content had better relative densities compared to the other composites, presumably due to the better dispersion of the MWCNTs in this sample as seen in Fig. 13.1b.

3.2 Thermal Diffusivity Characteristics of Ti64 Alloy and MWCNTs/Ti64 Nanocomposites

The thermal diffusivities of the unreinforced Ti64 and MWCNTs/Ti64 nanocomposites synthesized at varying temperatures are as represented in Fig. 13.3. For the samples consolidated at 850 °C (Fig. 13.3a), the addition of 1 and 2 wt.% MWCNTs, respectively, to Ti64 matrix enhanced the measured thermal diffusivities of the consolidated nanocomposites over that of the virgin Ti64 samples at all the temperatures (50–300 °C) under which the thermal diffusivities were investigated. Considering the two extremes of the testing temperatures, it was observed that at 50 °C, the measured thermal diffusivities of the nanocomposites were improved by 1.7 and 14% with the addition of 1 and 2 wt.% MWCNTs to Ti64, respectively, over the recorded values for the unreinforced alloy, while 4 and 9% improvements were

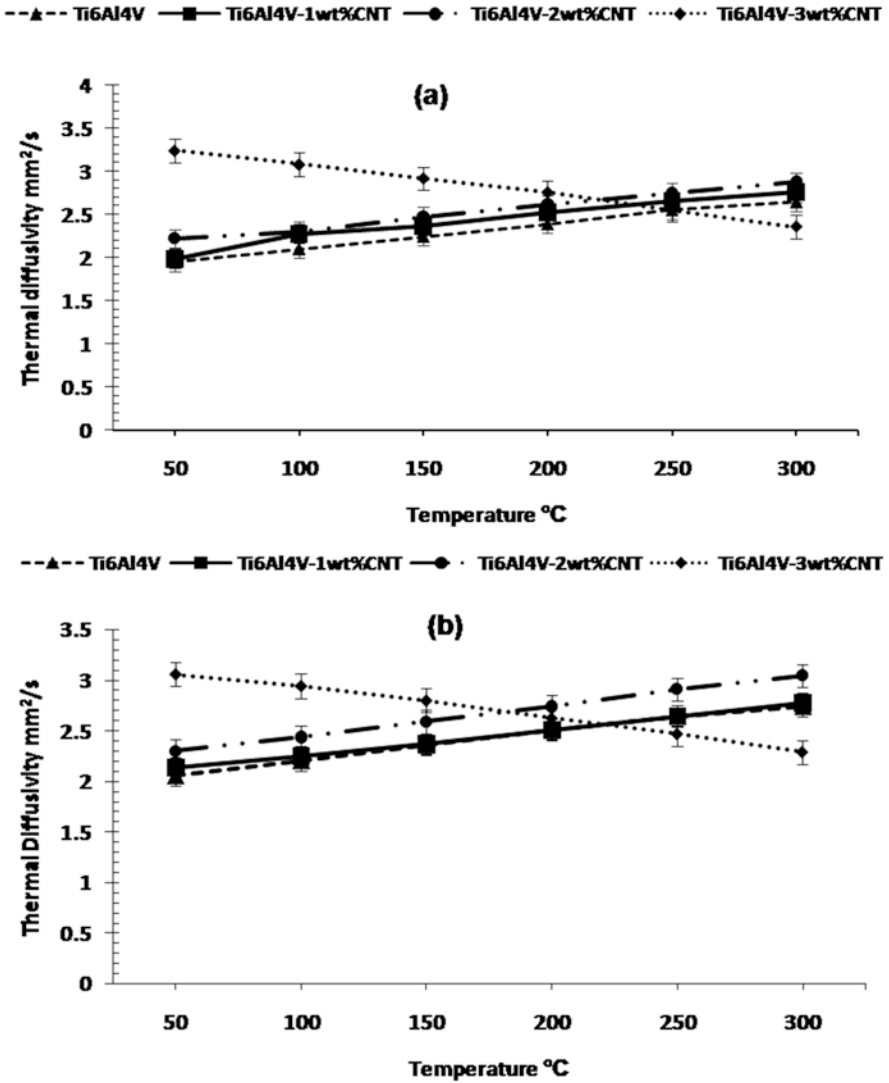


Fig. 13.3 Recorded thermal diffusivities of Ti64 and MWCNTs-reinforced Ti64 nanocomposites sintered at different temperatures (a) 850 °C, (b) 900 °C, (c) 950 °C, and (d) 1000 °C

recorded at 300 °C for the same amounts of MWCNTs added to Ti64 metal matrices, respectively. However, with the addition of 3 wt.% MWCNTs to Ti64, a completely different and opposite trend in the thermal diffusivity behavior of the consolidated nanocomposites was observed. Although the measured diffusivities of the 3 wt.% composites were initially better, compared to the other samples with 1 and 2 wt.% of added MWCNTs reinforcements, respectively, from 50 °C up to

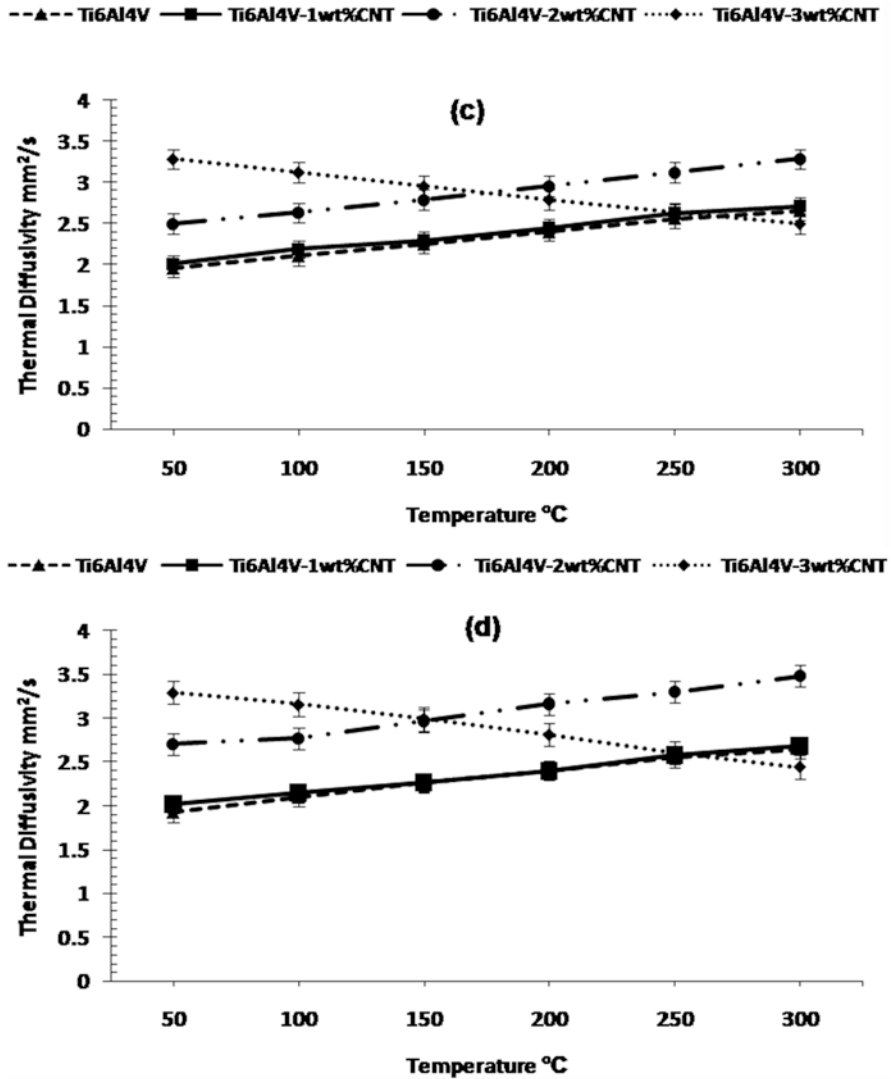


Fig. 13.3 (continued)

200 °C, its recorded thermal diffusivities continued to drop progressively as the testing temperatures investigated were increased. This occurred such that the value recorded for this composite was below that of the unreinforced Ti64 alloy between 250 and 300 °C. Thus, the thermal diffusivities of the 3 wt.% composite deteriorated from 3.24 mm²/s at 50 °C to 2.36 mm²/s at 300 °C, implying 27% degradation in the recorded thermal diffusivity of the composite. However, comparing the 3 wt.% MWCNTs nanocomposite with the unreinforced Ti64 sample, thermal diffusivities

of 3.24 and 1.95 mm²/s, respectively, were recorded at 50 °C while 2.36 and 2.65 mm²/s, respectively, were recorded at 300 °C.

This implies that although the 3 wt.% composite exhibited an enhancement in thermal diffusivity of 66% over unreinforced Ti64 at 50 °C, a depreciation of 11% in the observed diffusivity value was obtained at 300 °C with respect to the unreinforced matrix alloy. In essence, the 3 wt.% composite lost 55% of the enhancement it gained initially at 50 °C over Ti64, as the testing temperature was raised from 50 °C through 300 °C. This shows that despite the fact that the thermal diffusivity performance of the 3 wt.% MWCNTs nanocomposite was the best at lower temperatures compared to the other composites, its performance deteriorates at higher temperatures to the point of falling under that of the unreinforced alloy, which suggests this composite will not be suitable for high-temperature applications. A similar trend in thermal diffusivity behaviors was observed in Fig. 13.3b–d for the other samples sintered at temperatures of 900–1000 °C, respectively, except that the recorded thermal diffusivities of the 3 wt.% MWCNTs composites started to drop below that of the 2 wt.% composite at 200 °C, instead of 250 °C observed earlier at 850 °C sintering temperature.

The noticed decline in the thermal diffusivity behavior of the 3 wt.% MWCNTs composite was attributed to the agglomeration and re-agglomeration of the MWCNTs (i.e., during powder dispersion and sintering, respectively) within the composite arising from the increased difficulty in separating them to achieve their adequate homogeneous dispersion within the Ti64 metal at higher contents of MWCNTs. This difficulty is partly as a result of the high aspect ratio of the MWCNTs, their inherent nano-size dimensions and large surface area. The other factors responsible for this are the tubular morphology of the nanotubes and the strong van der Waals forces in the individual tubes which become predominantly higher with increased contents of the added MWCNTs reinforcement in the metal matrix (Liu et al., 2020; Munir et al., 2015b, 2016; Thostenson et al., 2001). The tendency to losing the positive impact of the MWCNTs reinforcement is also increased at higher contents owing to the amorphization of the MWCNTs which arises from the energy absorbed by them during their dispersion processing by milling, either from the milling balls or friction among the nanotubes and their neighboring Ti particles. This leads to a degeneration of the highly graphitic sp² C-C network into the highly reactive and amorphous sp³ C-C phases in the MWCNTs, which subsequently forms TiC interfacial reaction products, when these defective MWCNTs react with Ti64 particles as seen in Fig. 13.1d (Adegbenjo et al., 2017b; Ferrari & Robertson, 2000; Lespade et al., 1984; Munir et al., 2015c). The channels of defects or damages introduction into carbonaceous materials as identified in literature are via bond angle disorder, bond length disorder, and hybridization, while a three-stage model for a typical amorphization trajectory was put forth as: from graphite to nanocrystalline graphite to amorphous carbon to tetrahedral amorphous carbon (Ferrari, 2007; Ferrari & Robertson, 2000; Lespade et al., 1984).

Hence, the diffusivities of the MWCNTs/Ti64 samples suggest the enhancement in the diffusivity Ti64 is predominantly a contribution of the extent of MWCNTs reinforcement dispersion within its particles. This outcome is in total conformity

with reports of Wang et al., on the diffusivities of pure Ti matrices reinforced with MWCNTs (Wang et al., 2015). They advanced that the observed diffusivities of SPS MWCNTs/Ti samples were enhanced steadily with increase in the fractions of added reinforcement contents in a declining growth rate order. This present investigation also reveals that the diffusivity characteristics of the synthesized nanocomposites is not dependent on the densities of the consolidated samples as the 2 wt.% samples with increased MWCNTs wt.% exhibited improved diffusivities notwithstanding their relatively lower densities compared to the 1 wt.% composites. This is most probably because thermal diffusivity is not only a function of the thickness of the samples and heat diffusion time but also of temperature, which is not dependent on the density of the samples. This explains why the observed thermal diffusivities of the composites in this work were better at higher temperatures, suggesting that the investigated parameter was dependent on thermal transport mechanisms which are based on phonon diffusion in the metal matrix and ballistic transportation in the MWCNTs reinforcement (Wang et al., 2015). It is perceived that this thermal transport must have been hampered in the 3 wt.% composites leading to the observed diminishing thermal diffusivities in these samples at higher temperatures. The inherent pores occurring from increased possibility of nanotubes to get agglomerated as presented in Fig. 13.1d may also be responsible for this, as the pores could act as thermal barriers to effective heat flow in the composites and consequently affect their diffusivities adversely (Song & Youn, 2006; Wang et al., 2013).

The overall thermal diffusivity enhancement in the 2 wt.% MWCNTs composites on one hand is thought to be due to the comparatively lower weight fraction of reinforcement which promoted a relatively better dispersion of the MWCNTs and higher ballistic transportation capacity in the sample. On the other hand, the presence of moderate TiC (Fig. 13.1c) must have contributed positively to the observed improved thermal diffusivity behavior of this sample. This may be supported from the fact that reaction products such as carbides formed during the reaction between defective CNTs, and metal particles are capable of improving the composite wettability through reactive wetting (Bakshi et al., 2009; Laha et al., 2007; Landry et al., 1997). Although the 3 wt.% MWCNTs composite had more TiC reaction products as seen in Fig. 13.1d, these could not positively sustain enhanced thermal diffusivity at higher temperatures due to perceived weak or entirely poor bonding between the TiC and the surrounding Ti64 metal matrix which possibly made the composite structure unstable at the TiC/matrix interface (Li et al., 2020a). This is not far-fetched as a previous study by Bakshi et al. opined that reaction products at composite interfaces may or may not be supportive of a composite's overall thermal properties depending on whether they increase or decrease the CNTs/matrix thermal conductance (Bakshi et al., 2010b).

This perceived varied contribution to thermal diffusivity performance by TiC presence in the consolidated composites from this current study is not strange as the role played (whether positive or negative) by TiC reaction products on the overall bulk TMCs properties has remained a controversial issue and a subject of debate up till date (Adegbenjo et al., 2019b). For instance, some reported studies posited that

TiC formed in situ contributes dispersion strengthening to Ti matrix, while others insisted that the chemical reaction resulting in TiC formation is capable of subsequently damaging the CNTs structure, therefore adversely impacting the properties of the bulk composite (Munir et al., 2015b; Munir & Wen, 2016; Wang et al., 2015). Wang et al. (2015) claimed that TiC's absence in CNTs-reinforced TMCs does not have a specific effect on the interfacial bond strength of the composite, whereas Azarniya et al. (2017) and Kondoh et al. (2012) reported that although TiC phases may aid effective interfacial bonding in MWCNTs/Ti composites at low temperatures, they could adversely affect composite properties at elevated temperatures. A more recent study by Li et al. (2020a) in support of the foregoing also posited that the TiC formed during the SPS processing of CNTs reinforced TMCs can have either a positive or negative influence on the overall property of the TMCs. Furthermore, another much recent study by Li et al. (2020b) in explaining the controversy around the role of TiC reaction products in MWCNTs/TMCs submitted that the process of TiC formation and its position (either on the interface or intragranular) within the composite structure determine whether the formed carbide will play a positive role in the bulk composite or otherwise. They investigated the formation of two types of TiC when 0.25 wt.% CNTs was added to Ti64 matrix powder and consolidated by SPS at 800 °C for 5 min. They attributed the formation of TiC nanoparticles to the in situ interfacial reaction between CNTs and Ti64 metal matrix. It was further stated that a significant amount of the TiC nanoplatelets must have been formed within the grains at 800 °C, suggesting that the inward diffusion of amorphous carbon (a-C) into Ti64 took place long before the occurrence of Ti/CNTs interfacial reaction. Hence, the reported study concluded that the CNTs and the formed TiC nanoparticles were distributed along the grain boundaries while the TiC nanoplatelets were mostly distributed homogeneously within the intragranular microstructure of the bulk composite.

From the foregoing therefore, it may be instructive to submit from this present study that the formed TiCs seen in Fig. 13.1c, d are most plausibly intragranular and interfacial, respectively, based on their presumed roles on the exhibited thermal diffusivities of the synthesized composites. This position conforms to the opinions presented in reported studies that a larger proportion of the carbide reinforcements in TMCs prepared by the powder metallurgy (P/M) route are mostly distributed along the grain boundaries, with a few of them found within the grains, which at times compromises the property enhancement expected of the synthesized bulk composite (Chen et al., 2017; Hayat et al., 2019; Li et al., 2013b; Munir et al., 2015b, 2018; Zheng et al., 2016). This proposition is absolutely in agreement with the reports from the work of Wang et al. (2015) and our previous studies on SPS-processed MWCNTs/Ti64 composites, wherein it was posited that polycrystalline layers of TiC reaction products were formed between Ti64 metal particles and MWCNTs clusters which were mostly situated on the Ti grain boundaries (Adegenjo et al., 2018, 2019b).

3.3 Thermal Conductivity of MWCNTs/Ti64 Nanocomposites

It is a universal understanding that the thermal conductivity behavior of a sample is a reflection of its thermal diffusivity characteristics, as there is a direct relationship between the two quantities. Bakshi et al. (2010b) have established this in their previous study on the thermal conductivity of carbon nanotube-reinforced aluminium (CNTs/Al) composites using the object-oriented finite element method. The universally established and accepted relationship between these quantities is stated in Eq. (13.1), where k is the thermal conductivity, α is thermal diffusivity, ρ is the density of the sample, and C_p is specific heat capacity.

$$k = \alpha \times \rho \times C_p \quad (13.1)$$

Thus, it is presumed from the outcome of this work that the thermal conductivity of the synthesized bulk nanocomposites will generally be better than that of the unreinforced Ti64 matrix alloy because of the added MWCNTs in the composites. It is also expected that the thermal conductivity of the 3 wt.% MWCNTs will deteriorate at higher temperatures in comparison with the other composites in the same pattern as observed for the thermal diffusivity behavior of the nanocomposites. This position is based on the reported outcomes obtained from previous similar studies by different researchers. For instance, Wang et al. (2015), showed that CNTs agglomeration in MWCNTs reinforced pure Ti metal matrices resulted in the degradation of the thermal conductivity of the composites with higher wt.% of MWCNTs. They attributed this to three reasons, which are (1) increased possibility of random nanotubes orientation as a result of aggregating individual tubes into clusters, (2) reduced thermal diffusivity in the composites due to the presence of pores at the MWCNTs-Ti interfaces and among the nanotubes, consequent upon the aggregation of the MWCNTs. These pores were thought to be capable of effectively spreading heat flow, with those pores at the interfaces constituting themselves as thermal barriers, and (3) the thermal conductivity of the composites is adversely impacted with aggregated MWCNTs, due to the reduction in the cleaning effect during SPS processing arising from weakened spark discharge effects, as the cleaning effect not only reduces kinks and twists in MWCNTs but also eliminates impurities and contaminations present in them (Chu et al., 2010b; Kumari et al., 2008; Sivakumar et al., 2007). Other reported works are also in agreement with this position by submitting that agglomeration of CNTs will reduce the heat conduction performance in CNTs-reinforced metal/polymer matrix composites (Song & Youn, 2006; Wang et al., 2013).

The 2 wt.% MWCNTs composite is again expected to exhibit the best thermal conductivity among the composites in this study, notwithstanding the better densification of the 1 wt.% MWCNTs composite (Fig. 13.2), just as the former had better thermal diffusivities as seen earlier. Intuitively, one may want to contest this, especially with the additional understanding that thermal conductivity is a function of the sample's density. However, a reported similar study by Chih-Jong et al., had laid

this contention to rest having shown in their work that the thermal conductivity of graphite-reinforced aluminium matrix composites increased despite decreasing densities of the composites with increasing volume fractions of the graphite reinforcement in the metal matrix (Chih-Jong et al., 2009). The presence of suspected intragranular TiC interfacial products having a healthy and strong bonding with the surrounding Ti particles must have promoted the presumed improvement in thermal conductivity expected of the 2 wt.% MWCNTs composite (Li et al., 2020b), as against the weakly bonded interfacial or grain boundary TiC in the 3 wt.% MWCNTs composite. This is consistent with the fact that a weak interface promotes the formation of porosity which will, of course, adversely affect the conductivity performance of the composite. This is because porosity between individual CNTs results in compromised interfacial heat transfer and consequently reduces the thermal conductivity capacity of the bulk CNTs-reinforced composite (Bakshi et al., 2010b). Furthermore, reported works have also submitted that the interface in CNTs/MMCs plays a crucial part in dictating the properties of the bulk composite as the quality of the interface formed is dependent on the wetting ability of the CNTs, their structural integrity, the prevalent interface reactions, and the extent of carbide formation (Baig et al., 2016). This position was supported by Hamamda et al. (2017) that weak bonds in Cu-CNTs interfaces were responsible for the limited heat flow and reduced thermal conductivity reported in these composites. Hence, the integrity of the interface and its strength is critical for adequate composite strength and exceptional performance (Adegbenjo et al., 2019b; Baig et al., 2016; Ke & Chengchang, 2014). In addition, Chu et al. (2010a) and Hu et al. (2018) agreed that the presence of kinks and twists (due to CNTs clustering, agglomeration, and re-agglomeration), which are unavoidable with higher CNTs weight percents in a metal matrix, is bound to deteriorate the thermal conductivity of the synthesized composite. This was exhibited by the 3 wt.% MWCNTs composites in this current study, which is consistent with the previously reported findings of Song et al. (2006) that smaller CNTs length efficiencies are supportive of improved thermal conductivity, as the effective length of long CNTs are reduced with the presence of kinks and twists, curves, or bends in the nanotubes.

4 Conclusion

This study investigated the influence of added graphitized MWCNTs on the thermal characteristics of carbon nanotube-reinforced Ti64 nanocomposites synthesized by the SPS technique. The addition of MWCNTs to Ti64 improved the thermal diffusivity performance of the synthesized bulk nanocomposites. It was observed that achieving the positive impact of the added MWCNTs was dependent on the extent of MWCNTs dispersion within the metal matrix, the strength and integrity of the composite interface, and the role played by TiC reaction products formed due to the reaction between the Ti metal particles and amorphous carbon (a-C) from defective MWCNTs. Overall, the 2 wt.% MWCNTs composite exhibited the best thermal

characteristics of the synthesized nanocomposites due to the presumed synergistic effects of comparatively homogeneous MWCNTs dispersion and suspected intra-granular TiC which had strong bonding with the surrounding Ti64 particles in this composite. It is expected that the outcome of this study will open new grounds in the application of MWCNTs/Ti64 nanocomposites materials for wing box and fuselage fabrications in the aerospace industries.

Acknowledgments The authors would like to appreciate the University of Johannesburg, South Africa, for the financial support toward this work. The Institute for NanoEngineering Research, Tshwane University of Technology, Pretoria 0001, South Africa, is also appreciated for allowing us to use the Laser Flash equipment for the experiments in the course of this study.

Conflict of Interest The authors declare that there are no conflicts of interest involved in this work.

References

- Adegbenjo, A., Obadele, B., Olubambi, P., Shongwe, M., & Adejuwon, S. (2019a). Thermal diffusivity behaviour of multi-walled carbon nanotube reinforced Ti6Al4V metal matrix composites. *IOP Conference Series: Materials Science and Engineering*, 499, 012002. <https://doi.org/10.1088/1757-899x/499/1/012002>
- Adegbenjo, A. O., Obadele, B. A., & Olubambi, P. A. (2018). Densification, hardness and tribological characteristics of MWCNTs reinforced Ti6Al4V compacts consolidated by spark plasma sintering. *Journal of Alloys and Compounds*, 749, 818–833. <https://doi.org/10.1016/j.jallcom.2018.03.373>
- Adegbenjo, A. O., Olubambi, P. A., Potgieter, J. H., Nsiah-Baafi, E., & Shongwe, M. B. (2017a). Interfacial reaction during high energy ball milling dispersion of carbon nanotubes into Ti6Al4V. *Journal of Materials Engineering and Performance*, 26(12), 6047–6056. <https://doi.org/10.1007/s11665-017-3041-8>
- Adegbenjo, A. O., Olubambi, P. A., Potgieter, J. H., Shongwe, M. B., & Ramakokovhu, M. (2017b). Spark plasma sintering of graphitized multi-walled carbon nanotube reinforced Ti6Al4V. *Materials & Design*, 128, 119–129. <https://doi.org/10.1016/j.matdes.2017.05.003>
- Adegbenjo, A. O., Olubambi, P. A., Westraadt, J. E., Lesufi, M., & Mphahlele, M. R. (2019b). Interface analysis of spark plasma sintered carbon nanotube reinforced Ti6Al4V. *JOM*, 71(7), 2262–2271. <https://doi.org/10.1007/s11837-019-03476-x>
- Awotunde, M. A., Adegbenjo, A. O., Ayodele, O. O., Okoro, A. M., Shongwe, M. B., & Olubambi, P. A. (2019). Interdependence of carbon nanotubes agglomerations, its structural integrity and the mechanical properties of reinforced nickel aluminide composites. *Journal of Alloys and Compounds*, 803, 514–526. <https://doi.org/10.1016/j.jallcom.2019.06.297>
- Azarniya, A., Azarniya, A., Sovizi, S., Hosseini, H. R. M., Varol, T., Kawasaki, A., & Ramakrishna, S. (2017). Physicomechanical properties of spark plasma sintered carbon nanotube-reinforced metal matrix nanocomposites. *Progress in Materials Science*, 90, 276–324.
- Babapoor, A., Asl, M. S., Ahmadi, Z., & Namini, A. S. (2018). Effects of spark plasma sintering temperature on densification, hardness and thermal conductivity of titanium carbide. *Ceramics International*, 44(12), 14541–14546. <https://doi.org/10.1016/j.ceramint.2018.05.071>
- Baig, Z., Mamat, O., & Mustapha, M. (2016). Recent progress on the dispersion and the strengthening effect of carbon nanotubes and graphene-reinforced metal nanocomposites: A review. *Critical Reviews in Solid State and Materials Sciences*, 1–46.
- Bakshi, S., Lahiri, D., & Agarwal, A. (2010a). Carbon nanotube reinforced metal matrix composites—a review. *International Materials Reviews*, 55(1), 41–64.

- Bakshi, S. R., Keshri, A. K., Singh, V., Seal, S., & Agarwal, A. (2009). Interface in carbon nanotube reinforced aluminum silicon composites: Thermodynamic analysis and experimental verification. *Journal of Alloys and Compounds*, 481(1), 207–213. <https://doi.org/10.1016/j.jallcom.2009.03.055>
- Bakshi, S. R., Patel, R. R., & Agarwal, A. (2010b). Thermal conductivity of carbon nanotube reinforced aluminum composites: A multi-scale study using object oriented finite element method. *Computational Materials Science*, 50(2), 419–428. <https://doi.org/10.1016/j.commatsci.2010.08.034>
- Bhat, A., Balla, V. K., Bysakh, S., Basu, D., Bose, S., & Bandyopadhyay, A. (2011). Carbon nanotube reinforced Cu–10Sn alloy composites: Mechanical and thermal properties. *Materials Science and Engineering: A*, 528(22), 6727–6732.
- Chen, B., Shen, J., Ye, X., Jia, L., Li, S., Umeda, J., Takahashi, M., & Kondoh, K. (2017). Length effect of carbon nanotubes on the strengthening mechanisms in metal matrix composites. *Acta Materialia*, 140, 317–325. <https://doi.org/10.1016/j.actamat.2017.08.048>
- Chih-Jong, C., Chih-Hao, C., Jen-Dong, H., & Cheng-Tzu, K. (2009). Thermal characterization of high thermal conductive graphites reinforced aluminum matrix composites. In *2009 4th International Microsystems, Packaging, Assembly and Circuits Technology Conference*, 21–23 Oct. 2009 (pp. 461–464). <https://doi.org/10.1109/IMPACT.2009.5382217>
- Chu, K., Guo, H., Jia, C., Yin, F., Zhang, X., Liang, X., & Chen, H. (2010a). Thermal properties of carbon nanotube–copper composites for thermal management applications. *Nanoscale Research Letters*, 5(5), 868. <https://doi.org/10.1007/s11671-010-9577-2>
- Chu, K., Wu, Q., Jia, C., Liang, X., Nie, J., Tian, W., Gai, G., & Guo, H. (2010b). Fabrication and effective thermal conductivity of multi-walled carbon nanotubes reinforced Cu matrix composites for heat sink applications. *Composites Science and Technology*, 70(2), 298–304. <https://doi.org/10.1016/j.compscitech.2009.10.021>
- Dong, L. L., Lu, J. W., Fu, Y. Q., Huo, W. T., Liu, Y., Li, D. D., & Zhang, Y. S. (2020). Carbonaceous nanomaterial reinforced Ti-6Al-4V matrix composites: Properties, interfacial structures and strengthening mechanisms. *Carbon*, 164, 272–286. <https://doi.org/10.1016/j.carbon.2020.04.009>
- Ferrari, A. C. (2007). Raman spectroscopy of graphene and graphite: Disorder, electron–phonon coupling, doping and nonadiabatic effects. *Solid State Communications*, 143(1–2), 47–57. <https://doi.org/10.1016/j.ssc.2007.03.052>
- Ferrari, A. C., & Robertson, J. (2000). Interpretation of Raman spectra of disordered and amorphous carbon. *Physical Review B*, 61(20), 14095.
- Hamamda, S., Jari, A., Revo, S., Ivanenko, K., Jari, Y., & Avramenko, T. (2017). Thermal analysis of copper-titanium-multiwall carbon nanotube composites. *Nanoscale Research Letters*, 12(1), 251. <https://doi.org/10.1186/s11671-017-2025-9>
- Hayat, M. D., Singh, H., He, Z., & Cao, P. (2019). Titanium metal matrix composites: An overview. *Composites Part A: Applied Science and Manufacturing*, 121, 418–438. <https://doi.org/10.1016/j.compositesa.2019.04.005>
- Hu, W., Zhao-Hui, Z., Zheng-Yang, H., Qi, S., & Shi-Pan, Y. (2018). Interface structure and properties of CNTs/Cu composites fabricated by electroless deposition and spark plasma sintering. *Materials Research Express*, 5(1), 015602.
- Inagaki, I., Takechi, T., & Ariyasu, Y. S. N. (2014). *Application and features of titanium for the aerospace industry*.
- Işik, B., & Kentli, A. (2014). The prediction of surface temperature in drilling of Ti6Al4V. *Archives of Metallurgy and Materials*, 59(2), 467–471.
- Jiao, Y., Huang, L., & Geng, L. (2018). Progress on discontinuously reinforced titanium matrix composites. *Journal of Alloys and Compounds*, 767, 1196–1215. <https://doi.org/10.1016/j.jallcom.2018.07.100>
- Ke, C., & Chengchang, J. (2014). Enhanced strength in bulk graphene–copper composites. *Physica Status Solidi (A)*, 211(1), 184–190. <https://doi.org/10.1002/pssa.201330051>

- Kondoh, K., Threrujirapong, T., Umeda, J., & Fugetsu, B. (2012). High-temperature properties of extruded titanium composites fabricated from carbon nanotubes coated titanium powder by spark plasma sintering and hot extrusion. *Composites Science and Technology*, 72(11), 1291–1297.
- Kumar, M. N., Mahmoodi, M., TabkhPaz, M., Park, S. S., & Jin, X. (2017). Characterization and micro end milling of graphene nano platelet and carbon nanotube filled nanocomposites. *Journal of Materials Processing Technology*, 249, 96–107. <https://doi.org/10.1016/j.jmatprotec.2017.06.005>
- Kumari, L., Zhang, T., Du, G. H., Li, W. Z., Wang, Q. W., Datye, A., & Wu, K. H. (2008). Thermal properties of CNT-Alumina nanocomposites. *Composites Science and Technology*, 68(9), 2178–2183. <https://doi.org/10.1016/j.compscitech.2008.04.001>
- Laha, T., Kuchibhatla, S., Seal, S., Li, W., & Agarwal, A. (2007). Interfacial phenomena in thermally sprayed multiwalled carbon nanotube reinforced aluminum nanocomposite. *Acta Materialia*, 55(3), 1059–1066. <https://doi.org/10.1016/j.actamat.2006.09.025>
- Landry, K., Rado, C., Voitovich, R., & Eustathopoulos, N. (1997). Mechanisms of reactive wetting: the question of triple line configuration. *Acta Materialia*, 45(7), 3079–3085. [https://doi.org/10.1016/S1359-6454\(96\)00372-2](https://doi.org/10.1016/S1359-6454(96)00372-2)
- Lephuthing, S. S., Okoro, A. M., Ige, O. O., & Olubambi, P. A. (2020). Exploring the sintering and densification behaviour of multiwalled carbon nanotube reinforced TiO₂-MnO₂ composites developed by spark plasma sintering. *Journal of Alloys and Compounds*, 835, 155393. <https://doi.org/10.1016/j.jallcom.2020.155393>
- Lespade, P., Marchand, A., Couzi, M., & Cruege, F. (1984). Caraceterisation de materiaux carbonés par microspectrometrie Raman. *Carbon*, 22(4–5), 375–385.
- Li, G., Munir, K., Wen, C., Li, Y., & Ding, S. (2020a). Machinability of titanium matrix composites (TMC) reinforced with multi-walled carbon nanotubes. *Journal of Manufacturing Processes*, 56, 131–146. <https://doi.org/10.1016/j.jmapro.2020.04.008>
- Li, S., Sun, B., Imai, H., & Kondoh, K. (2013a). Powder metallurgy Ti–TiC metal matrix composites prepared by in situ reactive processing of Ti-VGCFs system. *Carbon*, 61, 216–228.
- Li, S., Sun, B., Imai, H., Mimoto, T., & Kondoh, K. (2013b). Powder metallurgy titanium metal matrix composites reinforced with carbon nanotubes and graphite. *Composites Part A: Applied Science and Manufacturing*, 48, 57–66.
- Li, S., Yang, Y., Misra, R. D. K., Liu, Y., Ye, D., Hu, C., & Xiang, M. (2020b). Interfacial/intragranular reinforcement of titanium-matrix composites produced by a novel process involving core-shell structured powder. *Carbon*, 164, 378–390. <https://doi.org/10.1016/j.carbon.2020.04.010>
- Liu, Y., Li, S., Misra, R. D. K., Geng, K., & Yang, Y. (2020). Planting carbon nanotubes within Ti-6Al-4V to make high-quality composite powders for 3D printing high-performance Ti-6Al-4V matrix composites. *Scripta Materialia*, 183, 6–11. <https://doi.org/10.1016/j.scriptamat.2020.03.009>
- Munir, K. S., Kingshott, P., & Wen, C. (2015a). Carbon nanotube reinforced titanium metal matrix composites prepared by powder metallurgy—A review. *Critical Reviews in Solid State and Materials Sciences*, 40(1), 38–55.
- Munir, K. S., Li, Y., Liang, D., Qian, M., Xu, W., & Wen, C. (2015b). Effect of dispersion method on the deterioration, interfacial interactions and re-agglomeration of carbon nanotubes in titanium metal matrix composites. *Materials & Design*, 88, 138–148.
- Munir, K. S., Li, Y., Lin, J., & Wen, C. (2018). Interdependencies between graphitization of carbon nanotubes and strengthening mechanisms in titanium matrix composites. *Materialia*, 3, 122–138. <https://doi.org/10.1016/j.mtla.2018.08.015>
- Munir, K. S., Li, Y., Qian, M., & Wen, C. (2016). Identifying and understanding the effect of milling energy on the synthesis of carbon nanotubes reinforced titanium metal matrix composites. *Carbon*, 99, 384–397.
- Munir, K. S., Qian, M., Li, Y., Oldfield, D. T., Kingshott, P., Zhu, D. M., & Wen, C. (2015c). Quantitative analyses of MWCNT-Ti powder mixtures using Raman spectroscopy: The influ-

- ence of milling parameters on nanostructural evolution. *Advanced Engineering Materials*, 17(11), 1660–1669.
- Munir, K. S., & Wen, C. (2016). Deterioration of the strong sp² carbon network in carbon nanotubes during the mechanical dispersion processing—A review. *Critical Reviews in Solid State and Materials Sciences*, 41(5), 347–366.
- Munir, K. S., Zheng, Y., Zhang, D., Lin, J., Li, Y., & Wen, C. (2017). Improving the strengthening efficiency of carbon nanotubes in titanium metal matrix composites. *Materials Science and Engineering: A*, 696, 10–25. <https://doi.org/10.1016/j.msea.2017.04.026>
- Nan, C.-W., Liu, G., Lin, Y., & Li, M. (2004). Interface effect on thermal conductivity of carbon nanotube composites. *Applied Physics Letters*, 85(16), 3549–3551. <https://doi.org/10.1063/1.1808874>
- Saheb, N. (2014). Sintering behavior of CNT reinforced Al6061 and Al2124 nanocomposites. *Advances in Materials Science and Engineering*, 2014, 1–9.
- Sivakumar, R., Guo, S., Nishimura, T., & Kagawa, Y. (2007). Thermal conductivity in multi-wall carbon nanotube/silica-based nanocomposites. *Scripta Materialia*, 56(4), 265–268. <https://doi.org/10.1016/j.scriptamat.2006.10.025>
- Song, P. C., Liu, C. H., & Fan, S. S. (2006). Improving the thermal conductivity of nanocomposites by increasing the length efficiency of loading carbon nanotubes. *Applied Physics Letters*, 88(15), 153111. <https://doi.org/10.1063/1.2194267>
- Song, Y. S., & Youn, J. R. (2006). Evaluation of effective thermal conductivity for carbon nanotube/polymer composites using control volume finite element method. *Carbon*, 44(4), 710–717. <https://doi.org/10.1016/j.carbon.2005.09.034>
- Thostenson, E. T., Ren, Z., & Chou, T.-W. (2001). Advances in the science and technology of carbon nanotubes and their composites: a review. *Composites Science and Technology*, 61(13), 1899–1912. [https://doi.org/10.1016/S0266-3538\(01\)00094-X](https://doi.org/10.1016/S0266-3538(01)00094-X)
- Wang, F.-C., Zhang, Z.-H., Sun, Y.-J., Liu, Y., Hu, Z.-Y., Wang, H., Korznikov, A. V., Korznikova, E., Liu, Z.-F., & Osamu, S. (2015). Rapid and low temperature spark plasma sintering synthesis of novel carbon nanotube reinforced titanium matrix composites. *Carbon*, 95, 396–407.
- Wang, X., Jiang, Q., Xu, W., Cai, W., Inoue, Y., & Zhu, Y. (2013). Effect of carbon nanotube length on thermal, electrical and mechanical properties of CNT/bismaleimide composites. *Carbon*, 53, 145–152.
- Zheng, Y. F., Yao, X., Su, Y. J., & Zhang, D. L. (2016). Fabrication of an in-situ Ti-2.6vol%TiC metal matrix composite by thermomechanical consolidation of a TiH₂-1vol%CNTs powder blend. *Materials Science and Engineering: A*, 667, 300–310. <https://doi.org/10.1016/j.msea.2016.04.096>
- Zhuang, J., Gu, D., Xi, L., Lin, K., Fang, Y., & Wang, R. (2020). Preparation method and underlying mechanism of MWCNTs/Ti6Al4V nanocomposite powder for selective laser melting additive manufacturing. *Powder Technology*, 368, 59–69. <https://doi.org/10.1016/j.powtec.2020.04.041>

Chapter 14

Hybrid Biocomposites: Utilization in Aerospace Engineering



Emel Kuram 

1 Introduction

Aerospace engineering develops the aircrafts and spacecrafts. Though metals are extensively employed in the building of aerospace structures, new materials such as composites are promising for aerospace engineering.

Wood was the first structural material employed in aircrafts due to its good strength-to-weight ratio and easily shaping into beams for wings, fuselage, and other structures. In 1903, Wright brothers used timber covered with fabric to build the mainframe of their aircraft. Nowadays, wood is not utilized in modern aircraft. However, wood is employed in ribs and spars of the mainframe of small aircraft because of its lightness, toughness, stiffness, and strength. Wood has low density, fracture toughness, Young's modulus, and tensile strength in comparison to other kinds of aerospace materials. Owing to its low density, the specific mechanical properties of wood are like aluminum alloys and most magnesium alloys. Wood has some properties that make it inferior to composites and metals as an aircraft structural material. Disadvantages of wood are given in Table 14.1.

Composition and structure of wood affect the properties of wood used for aircraft material. Greenwood has high water and is not appropriate for aircrafts since it is heavy, soft, and vulnerable to attack from fungi. Therefore, wood must be dried between 2 and 10 years at room temperature. When wood dries, the density decreases owing to evaporation of moisture. The drying of wood causes the increment in the longitudinal stiffness and strength since the cellulose fibrils pack more closely together into space occupied by water molecules (Mouritz, 2012a). The density of timber should be measured prior to building an aircraft to provide the total weight

E. Kuram (✉)

Department of Mechanical Engineering, Gebze Technical University, Gebze, Kocaeli, Turkey
e-mail: kuram@gtu.edu.tr

Table 14.1 Disadvantages of wood

Lower toughness, stiffness, and strength
Anisotropic mechanical properties
Defects causing the reduction in the strength
Hygroscopic nature resulting in shrinking, swelling, and changing density and mechanical properties under atmospheric humidity, which can cause loosening of bolted connections especially propeller flange bolts and warping of the airframe under harsh conditions
Vulnerable to attacking from fungus, insects, and other microorganisms when employed without surface protection and chemical treatment

within the design limit. Employing denser wood in an aircraft is more useful to longitudinal properties than the radial and tangential properties.

Wood in aircraft is often utilized as a laminated plywood made from birch, gabon, mahogany, or spruce to decrease the problems of anisotropy. Timber sheets are bonded with durable and high-strength adhesives. Wood is appropriate for using aircraft structures carrying low loads.

The most significant parameters to be taken into consideration in the design of aircraft interior parts are density, recyclability and reusage potential, energy and other resource need for manufacturing, and toxicity of materials. Selecting of materials used in aircrafts depends on the location and product of usage. For instance, the materials for outer aircraft structure such as wings and nose cone must have excellent fire resistance, while fire resistance is not mandatory requirement for interior structures (Arockiam et al., 2018).

Some properties such as excellent corrosion resistance, high ductility, low cost, and low density make polymers beneficial as aircraft materials. Polymers also are utilized as an adhesive for joining aircraft parts to obtain high strength without utilizing fasteners such as screws and rivets. But polymers cannot be employed alone in structural applications due to their low creep resistance, fatigue life, stiffness, and strength. Another issue for using of polymers in aircraft industry is softening. A polymer for aircraft component should not exceed a temperature of approximately 80% of heat deflection temperature (HDT). HDT is a capability of polymer to resist deformation under load at elevated temperature to prevent distortion.

Polymers and their composites are flammable and release fumes, heat, and smoke when they burn. Therefore, their using is depended on the safety standards in the aircraft industry. In recent years, flame-retardant additives such as halogenated or phosphorus compounds are incorporated into polymers to enable their use in the aircraft industry (Gopi et al., 2017).

Polymerization is the chemical process by which monomers (small molecules) are joined to make macromolecules and can be separated into two kinds: addition and condensation polymerization. Addition polymerization includes the linking of monomers into the polymer chain by a chemical reaction. Condensation polymerization involves two or more different kinds of molecules that generate a molecular chain-done combinations of beginning molecules. Examples of aerospace polymers fabricated by condensation polymerization are epoxy resin, used as matrix phase of carbon fiber composite structures and as structural adhesive and phenolic resin,

used inside aircraft cabins for fire resistance (Mouritz, 2012b). Epoxy resin is the most used thermoset in aircraft components owing to its good durability in hot and wet environment, high strength, and low shrinkage. However, it should not be employed in cabins due to its bad fire performance. Phenolic resin meets fire regulation. Cabin interiors, furniture, and internal fitting in aircraft are made by phenolic resin and glass fiber/phenolic composite.

In composite materials, thermoplastic polymers give some advantages such as higher fracture toughness, better impact resistance, and higher operating temperatures over thermoset polymers. But thermoplastic polymers must be operated at high temperature that make them expensive to fabricate aircraft structures. The most employed thermoplastic polymer group in aircraft structures is polyketones including polyetherketone (PEK), polyetheretherketone (PEEK), and polyetherketoneketone (PEKK) (Mouritz, 2012b). Polymers such as PEEK can be used for the fabrication of composite parts in aeronautical applications at high temperatures (Benyamina et al., 2021). Polycarbonate (PC), polyetherimide (PEI), polyphenylene sulfide (PPS), and polysulfone (PSU) thermoplastic polymers are also utilized in aircraft industry. Impact-resistant, scratch-resistant, tough, and transparent polymers are appropriate for aircraft canopy and window. Acrylic such as polymethyl methacrylate (PMMA) and PC are the most often employed thermoplastics in aircraft windows. Acrylic polymers are lighter, tougher, and stronger than window glass. PC is tougher and stronger than acrylic polymers and is employed as high impact resistance is desired such as canopy and cockpit window due to the hailstones and birds collision risk especially during landing and takeoff. Therefore, PC windows present the flight crew with security against severe impacts.

The using of thermoset polymers in aircraft industry is larger in comparison to the using of thermoplastics. Bismaleimides, cyanate esters, and polyimides thermoset polymers are employed in aircraft structures operating at temperatures above performance limit of epoxy resin (Mouritz, 2012b).

Elastomers are not appropriate for employing in aircraft components due to low strength and stiffness. Using of elastomer is restricted to nonstructural aircraft components that want elasticity, flexibility, and low stiffness such as aircraft tire, gasket, and seal. Elastomers employed for tires include carbon black filler to improve wear resistance and tensile strength. Elastomers can degrade and erode in harsh conditions such as high temperatures, and the most dramatic example of degradation of an elastomer was the space shuttle *Challenger* accident. *Challenger* space shuttle exploded 1 min after takeoff on January 28, 1986, causing seven astronauts dead. The space shuttle is equipped with twice rocket boosters that generate an enormous amount of thrust that throws the main vehicle into space during takeoff. Without boosters, the shuttle would not be able to produce enough thrust to overcome Earth's gravitational force. The boosters are made of hollow metal cylinders, with a joint connecting the cylinders including two O-rings done with an elastomer. The elastomer must form a tight seal to prevent hot gases leakage from the rocket engine during takeoff. Several factors caused the *Challenger* accident; one of the elastomer O-rings in a booster rocket did not form a tight seal because of cold air during takeoff. This resulted in hot combustion gases (above 5000 °F) inside the rocket

engine to rapidly degrade the elastomer O-ring, allowing propellant to escape and ignite, thereby detonating the space shuttle (Mouritz, 2012b).

A structural adhesive is high strength, elastic modulus, and toughness glue employed in aircraft for joining components. Elastomers, thermoplastics, and thermosets possess adhesive properties. Toughening agents such as rubbers are mixed with adhesive to enhance fracture toughness. Structural adhesive must possess low shrinkage when cured to eliminate the residual tensile stress in the joint. Structural adhesive must be resistant to degradation in the environment. Aviation fuel, hydraulic fluid, solvent, and water can attack the bonding; thus, durable adhesives must be utilized. Employing structural adhesives for bonding aircraft structures rather than mechanical fasteners has some advantages. Structural adhesive diminishes the cost and weight of fasteners in aircraft parts. Structural adhesive also reduces fatigue cracking in metal connections due to the elimination of the required drilled holes for fasteners that are areas for the beginning of fatigue cracks. Structural adhesive presents a more uniform stress distribution in the bonding. Bonded joints are lighter than mechanically fastened joints. Bonded joints also cause a smooth surface. Adhesives are present as pastes or films. Film adhesives are employed in bonding aircraft parts since they give higher strength than paste adhesives. Epoxy resin is the most often utilized structural adhesive due to high strength, the capability to adhere to most surfaces, and long-term durability over a wide range of environments and temperatures. Silicone is employed when high toughness is required, while polyimide and bismaleimide are employed when a high-temperature adhesive is wanted. Acrylic resin, inorganic cement, urethane, and phenolic resin are other kinds of adhesives utilized for bonding aircraft components. Hot-melt adhesive is thermoplastic or thermoplastic elastomer that melts when heated, and it is not used in highly loaded aircraft components. Pressure-sensitive adhesive is elastomer that is not cross-linked, and it is not suitable for bonding aircraft structures owing to its low strength.

Radar is employed for aircraft detection and tracking, and it is very important for traffic management in aviation. However, in military operations, it is a problem since they want aircraft must attack its target and escape undetected. Passenger airliners can be detected by radar due to their cylindrical shape and bumps. Metals and composites utilized in aircraft are strong reflectors of electromagnetic waves and thus can be detected by radar. But detection of composite is not as easy as metal. Radar-absorbing material is polymer based employed to the surface of stealth military aircraft to decrease radar cross section, making them difficult for the detection by radar.

Polymer composites are employed in the engine components, airframe, furniture, and internal fittings of aircraft. Polymer composites utilized in aerospace components must meet some requirements such as excellent dimensional stability over a wide range of temperatures, good fatigue performance, high-fracture toughness, high-impact energy to bear sudden impacts of bird strikes, high strength, light weight, and resistance to corrosive environments (fuel and lubricant) and also provide shielding of electromagnetic waves. Good fatigue performance increases the lifetime of aerospace components and safety and decreases the maintenance frequency and cost. Structural health monitoring of damage in the aerospace structures

is important for composites used in aerospace industry so as to perform maintenance on time, which causes the reduction in the maintenance cost and enhancement of the safety of aerospace components (Rana & Figueiro, 2016). Wing box needs high-strength fibers in composite structures. Control surfaces require high-stiffness fibers. Structures requiring both high strength and stiffness such as fuselage and wing need intermediate modulus fibers. Carbon fiber-reinforced polymer composite is suitable for aircraft structures (such as ribs, spars, stringers, wing box) and jet engine parts due to the stiffness of carbon fiber. Carbon fiber-reinforced polymer composite has better corrosion resistance and fatigue properties than metals, and it is employed for doors, fuselage, interior components, tail, and wing in aircrafts (Mouritz, 2012c). Carbon nanotube-reinforced polymer composite is an advanced material that allows a structure to be lightweight, high temperature resistance, and a high strength-to-weight ratio (Nurazzi et al., 2021a). Glass fiber-reinforced polymer composite is utilized rarely in aircraft structures due to its low stiffness. However, its lower cost in comparison to carbon fiber-reinforced polymer composite causes using in some applications at aircraft industry. Therefore, it is mostly used in secondary structures including aircraft fairings, inside cabins for fittings, furnishing, and helicopter structures such as cabin shell. Due to its low dielectric properties, glass fiber-reinforced polymer composite is employed when transparency to electromagnetic radiation is significant such as aerial covers and radomes (Mouritz, 2012c). Radome is dome-shaped components, radar transparent, protecting radar antennas from aerodynamic loading such as impact from bird strike. Materials with high toughness and low dielectric constant are employed for aircraft radome (Haris et al., 2011). Overhead luggage storage containers and partitions are manufactured with glass fiber phenolic resin composite because of its good flammability resistance, low cost, and lightweight. E-glass and S-glass kinds of glass fibers are employed in aircraft applications. E-glass has lower cost and lower strength than S-glass resulting usage in aircraft cabin fittings. Higher strength of S-glass composite causes the use in structural components. Aramid fiber composites are utilized for parts that require impact resistance against high-speed projectiles such as for ballistic protection on military aircraft and helicopter due to absorption of large amount of energy during fracture. Aramid fiber composites are suitable for radomes owing to their good dielectric properties. High vibration damping properties make aramid fiber composites suitable for helicopter engine housings to diminish vibration from the rotor blades reaching the cabin. Aramid fiber composites have high stiffness and strength in tension. However, compression strength of them is low, which is not suitable to use in aircraft components exposed to compression loads (Mouritz, 2012c).

The desire of lightweight materials such as fiber-reinforced polymer composites in aerospace industry is huge due to the rising of gas and oil prices. It is declared that fuel costs about 50% of operational costs and using fiber-reinforced polymer composites in Boeing 787 contributes over 20% more fuel efficiency (Njuguna et al., 2012). Aircrafts with lightweight materials can burn less fuel, thus carrying higher loads or travel longer distances. In summary, polymer composites have an important influence on aerospace structures, by giving cheaper, faster, and safer

transportation. In addition, lower consumption of fuel without compromising the flight performance will cause to drop the greenhouse gases emission. Composite parts utilized in aircraft applications are exposed to impact damage such as bird strike, hailstones, and runway debris causing a drop in load-carrying capability, stability, and structural stiffness.

1.1 Natural Fibers and their Composites

Natural fibers have been used since ancient times; ancient Egyptians mixed wheat straw with Nile River's mud to fabricate brick in order to obtain stronger bricks and to keep their houses cool during summer (Mansor et al., 2019). Natural fibers possess some pros such as abundance, biodegradability, low density, low cost, recyclability (Das et al., 2017; Nurazzi et al., 2021b), nonabrasiveness, renewability, sustainability, and vibration damping. However, most natural fibers are flammable and thermally unstable at low temperature (200–300 °C) releasing fume, heat, and smoke when they burn, limiting their applications in aerospace industry (Chai et al., 2012). Also, they have high moisture absorption, low mechanical properties, and poor dimensional stability. To overcome these weaknesses, several methods such as halogenated and nonhalogenated flame retardants, copolymerization, grafting, layered silicates, nano fillers (Rashid et al., 2021), and synergistic utilize of natural fiber (Rashid et al., 2021; Suriani et al., 2021a) and fire retardant have been employed (Rashid et al., 2021; Suriani et al., 2021b). Therefore, it is mandatory to develop hybrid biocomposites which are thermally stable and flame resistant while simultaneously possessing moderate mechanical properties for aerospace applications. Natural fibers are generally hybridized with glass fiber for enhancing mechanical and physical properties.

Natural fiber-based composites (biocomposites) provide carbon dioxide (CO₂) emission reduction, competitive cost, recycling, and sustainability, and the use of biocomposites in the aerospace industry has been increasing. Environmental problems are rising because of industrialization that directly influences the ecosystem by increasing environmental pollution, fossil fuel costs, greenhouse effects, and global warming problems. Natural fiber-based composites are environmentally friendly and a good alternative to costly materials. Due to this, the demand of natural fiber-based composites in aerospace industry is increasing.

In hybrid composites, two or more kinds of reinforcing materials were added to a polymer matrix to obtain the synergistic influence of all fibers on the overall properties of hybrid composites (Fu et al., 2002). The weakness of one component can be balanced by the properties of another. Hybrid composites of glass fiber/carbon and Kevlar fibers were employed in aircraft components such as engine cowlings, engine pylon fairings and wing-body fairings (Baker et al., 2000). Unidirectional glass-carbon/epoxy hybrid composite was used in helicopter rotor blade (Mouritz,

2012d). Polyetherimide (PEI)/graphene oxide-multiwalled carbon nanotube hybrid nanocomposite films can be integrated into flexible electronic devices for a variety of potential applications in the aerospace and defense industries (Ahmad et al., 2020). It was declared that goat hair and banana fiber-reinforced epoxy hybrid composites laminates fabricated by the hand layup could be used in the aerospace applications (Rao et al., 2020).

This chapter reviewed the application areas of polymers, biocomposites, and hybrid biocomposites in aerospace industry. Some of the used polymers, polymer composites, and hybrid composites in aircraft industry are summarized in this chapter.

2 Components of Aircraft Structure

External shape of an aircraft is determined by fuselage, tail, and wing (Fig. 14.1). Components of aircraft structure are made of a wide variety of materials and are joined with bolts, rivets, screws, and adhesives or welding. Aircraft structural components are designed to resist stress or carry a load.

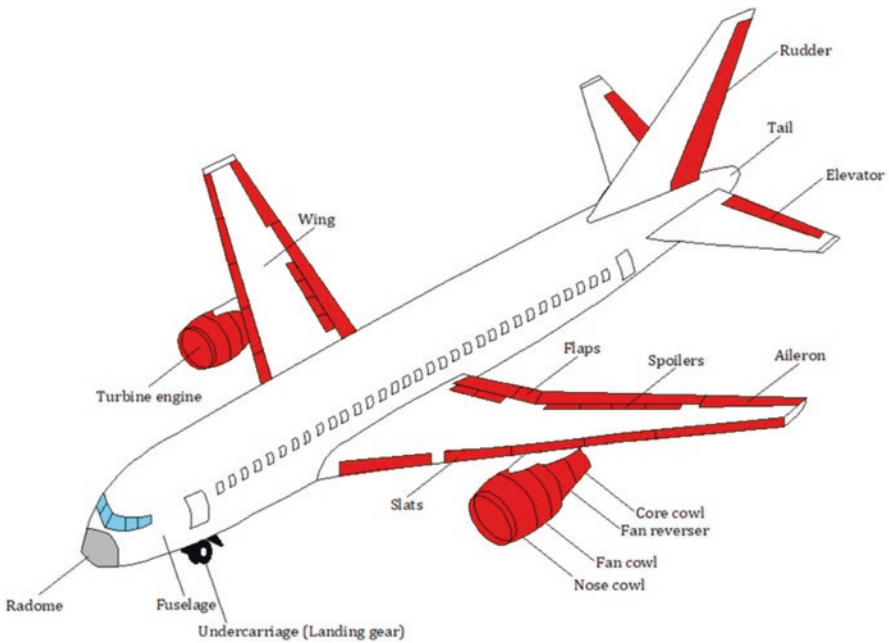


Fig. 14.1 Components of aircraft structure

2.1 Fuselage

Fuselage carries load and all parts are connected to it. Therefore, it must have low weight, must have high stiffness and strength to resist loads, and must be able to withstand bending moments, cabin pressurization, and torsional loads. In transport airplane, the fuselage is near cylindrical or cylindrical, with tail and nose sections, while in modern airplane, the fuselage has a skin attached to the stringers and hoop-shaped frames (Ghori et al., 2018).

2.2 Wing

Wing of an aircraft provides lift and is attached to fuselage by strong bolts. Wings carry loads and act as fuel tank. In most airplane, the wing skin is multifunctional. It determines shape, carries heavy and torsional loads, behaves as a fuel tank, and helps easy inspection and maintenance. Often, the entire airplane wing is fabricated with metal or a mixture of metal and composites (Ghori et al., 2018). Carbon fiber-reinforced plastic is used to make the wing in recent years.

2.3 Tail

Tail provides control and stability in three directions: lateral (left and right), longitudinal (before and after), and vertical (down and up). The horizontal tail with elevator is utilized for lateral axis rotation (pitch) of an aircraft. The vertical fin with rudder is employed for vertical axis rotation (yaw) of an aircraft. Ailerons are utilized for longitudinal axis rotation (roll) of an aircraft. Stability in yaw is provided by the fin. When the airplane needs to yaw, the rudder changes direction. Stability in pitch is provided by the tailplane. When the airplane needs to climb or descend, the elevators change direction. If the position of gravity center changes or the speed of the airplane is varied, the elevator position required to keep level flight will vary. That's why a small extra control surface is added to each major surface to allow the pilot to trim the airplane. Carbon fiber-reinforced plastic is used to make the tail in recent years.

2.4 Undercarriage

Undercarriage (landing gear) provides shock absorbers during landing and provides smooth taxiing; however, it has no function during flight. Therefore, it should be as small and lightweight as possible. Because of heavy weight present in the aft and

fore, large bending moments form in the center. To diminish these bendings, a strong keel beam is installed that decreases the landing gear. During the landing of an airplane, a large amount of heat is occurred, and the shock must be diminished to dissipate this heat. This could be obtained by the existence of disc brakes that increase the friction between the friction material pads (Ghori et al., 2018). Carbon/glass epoxy skins are used to make the landing gear door in recent years.

3 Natural Fiber-Based Composites (Biocomposites)

Biocomposites could be divided into two categories: partially (synthetic polymers + natural fibers or natural polymers + synthetic fibers) and completely (natural polymers + natural fibers) biodegradable composites (Fig. 14.2). Partially biocomposites are prepared from mixing of traditional petro-based nonbiodegradable polymeric materials such as epoxy, polyester, polyethylene (PE), polypropylene (PP), and polystyrene (PS) with natural fibers. Completely biocomposites are developed from natural fibers and natural matrices or synthetic biodegradable matrices such as poly(lactic acid) (PLA). They are completely degradable, sustainable, eco-friendly (Nair et al., 2014), and more environmentally friendly, and they have lower CO₂ footprint (Farg, 2017). They come from the earth, and they can go back into the earth and composted in organic soil with no residue when they are disposed after being utilized (Nair et al., 2014). Completely biocomposites can be prepared by

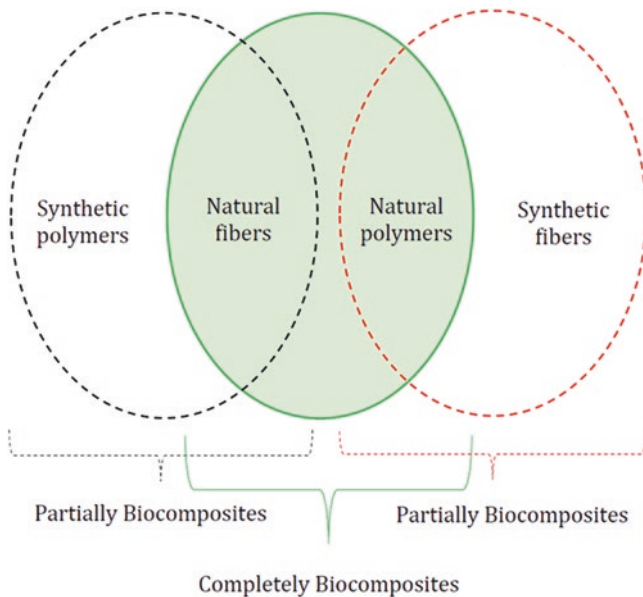


Fig. 14.2 Type of biocomposites

utilizing the traditional manufacturing methods (compounding, compression molding, extrusion, filament winding, hand layup, injection molding, and mixing) that have been employed for composites composed of synthetic fibers and synthetic polymers (Farag, 2017). The possible application of completely biocomposites for aerospace interior parts employing cotton fiber and polyurethane matrix was investigated by Eloy et al. (2015). Results demonstrated that the feasibility of replacing synthetic composites with completely biocomposites in aviation interior applications is to obtain better end-of-life performance and achieve “green airplane” efforts in the future.

Natural fibers such as banana, bamboo, coconut, cotton, hemp, flax, jute, palm, silk, sisal, and wheat are abundant, and they are good and effective reinforcement in polymer matrices (Siva et al., 2012). High specific strength and modulus of natural fiber-based composites can provide use in structural applications such as aircraft and spacecraft (Bharath & Basavarajappa, 2016; Hassan et al., 2010). Natural fibers obtained from animals and plants (Mansor et al., 2019; Omran et al., 2021) have some pros such as biodegradable, high strength-to-weight ratio, low density, low cost, more environmentally friendly, recyclable, renewable (Ilyas et al., 2021; Mansor et al., 2019), and sustainability. Resistance to impact damage is mandatory for composites employed in aerospace applications (Goriparthi et al., 2012). However, low thermal stability of both natural fibers and polymers restricts the application of biocomposites in the areas requiring high thermal stability such as aircraft materials (Sim et al., 2013). Also, low dimensional stability, low mechanical property, and hydrophilic nature of natural fiber give some challenges in the use of polymer composites for higher load-bearing components in aircrafts. To diminish the negative effects of polymer composites with natural fiber, hybridization process is implemented.

Waste of natural fibers is being burnt, affecting the environment negatively. Instead of burning and wasting natural fibers, they could be employed with polymers to develop composites. This endeavor protects the environment and can provide income.

Biocomposites possess low fire resistance; therefore, their safe use in aerospace industry is a question mark (Rashid et al., 2021). Low fire resistance of it is owing to lignin contents of natural fiber in biocomposites (Manfredi et al., 2006). Because flammability is becoming main issue in aviation sector, a new biocomposite that possesses the ability to behave as a self-extinguisher is under investigation. Fire hazard in aviation industry has been known ever since Wrights brother fabricated the aircraft (Karunakaran et al., 2016).

Advantages and disadvantages of employing natural fiber-based composites in aerospace industry are summarized in Table 14.2.

There are some criteria that natural fiber-reinforced composites must meet to employ them for aviation applications (Chandrasekar et al., 2018). These criteria are presented in Table 14.3.

Table 14.2 Advantages and disadvantages of employing natural fiber-reinforced composites in aerospace industry

Advantages	Disadvantages
Density of natural fiber-based composites is lower as compared to synthetic fiber-based composites causing an increment in the load capacity of aircraft structure	The properties of natural fibers are not consistent. Their properties change with harvesting area, harvesting time, intensity of sunlight, rain, and soil type
High specific stiffness and strength of composites can enable more aerodynamic design of complex shapes	Natural fibers have poor compatibility with polymers. Most polymers are nonpolar (hydrophobic); however, natural fibers are polar (hydrophilic)
Corrosion problems are not observed with composites, diminishing the maintenance cost	Moisture sorption tendency of natural fibers causes a drop in mechanical properties
They are fully biodegradable	Natural fibers possess poor thermal stability
Natural fibers have low cost. By adding natural fiber into polymers, the overall fabricating cost of an airplane structure can be decreased.	
Extraction of natural fibers is simple and requires unskilled labor	
Fabricating of natural fiber-based composites does not cause any health problems for the operators	

Table 14.3 Criteria that natural fiber-reinforced composites must meet to employ them for aviation applications

High specific stiffness and strength
Flame retardancy
High moisture resistance
Good interfacial bonding among natural fiber and polymeric matrix to bear different kinds of loads encountered in airplane flight

The main aims of aircraft sector are to decrease carbon dioxide emission, cost, and fuel consumption; hence, the implementation of natural fibers as reinforcement in polymer composites gains more interest in aerospace sector. Aircraft interior parts (such as decking, flooring, seats) and exterior body panels can be manufactured with natural fiber-based polymer composites. Nowadays, biocomposites are used from relatively small, lightly loaded components to heavily stressed structures.

Phenolic resin and woven flax were used to manufacture cabin interiors panels (Anandjiwala et al., 2008). Kenaf fiber gives similar stiffness to glass fiber and low dielectric constant; thus, it is suitable for radome applications (Haris et al., 2011). It was calculated that ramie fiber-reinforced composite reduced the weight of wing box by 12–14% with respect to 7000 series aluminum alloy; however, increment in the weight with flax- and hemp fiber-reinforced composites was found (Boegler et al., 2014).

4 Hybrid Biocomposites

“Hybrid” comes from Greek and Latin (Kaiser et al., 2014). In hybrid composites, two or more kinds of reinforcing materials are added to a polymer matrix (Fu et al., 2002) to obtain the synergistic influence of all fibers on the overall properties of hybrid composites. Weakness of one component can be balanced by the properties of another. Hybridization of synthetic and natural fiber is an environmentally friendly and economically feasible solution (Alsubari et al., 2021; Jawaid & Abdul Khalil, 2011; KC et al., 2018; Panthapulakkal & Sain, 2007). Hybrid composites of two natural fibers are less common in comparison to hybrid composites of natural/synthetic fiber. It was declared that oil palm and sisal fibers were good combination for hybrid composites because of high toughness of oil palm and high tensile strength of sisal (Jacob et al., 2007). It was concluded that palmyra palm leaf stalk fiber/jute fiber-based hybrid polyester composites could be a potential replacement in place of natural/synthetic fiber composites (Shanmugam & Thiruchitrambalam, 2013). Hybrid composites cause excellent impact resistance, good corrosion, and fatigue resistance in aerospace industry. The most important benefit is weight reduction in the range of 20–50% (Jamir et al., 2018). Sisal/banana/coconut sheath fiber-based polyester hybrid composites were developed via compressing molding to determine the mechanical properties (flexural strength, flexural modulus, tensile strength, and tensile modulus) and vibration properties (damping and natural frequency). It was found that stack sequence affected the vibration and mechanical properties. Alkali-treated sisal/coconut sheath/banana combination was the optimal hybrid composite and could be used for interior components of aerospace applications (Senthilkumar et al., 2017).

Two categories for design of hybrid composites are available: interlayer and intra-layer (Fig. 14.3). In intra-layer, both kinds of fibers are mixed in a single layer. In interlayer, each layer is done with a single fiber kind. Interlayer hybrid includes subcategory of skin-core hybrids, which are generally employed in aerospace parts (Shahzad & Choudhry, 2017). In interlayer configuration, layers of two fiber kinds are stacked on top of each other. This is the cheapest and simplest method to

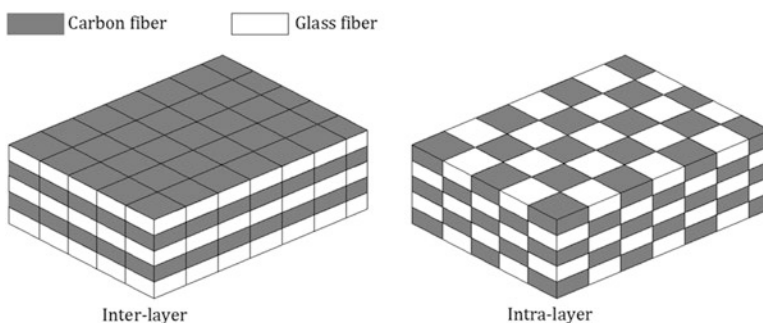


Fig. 14.3 Interlayer and intra-layer hybrid of glass-carbon fibers

produce a hybrid composite. Mixing of different fiber kinds in one layer characterizes intra-layer hybrid composites, causing higher dispersion of fibers as well as a more complex manufacturing process.

5 Manufacturing of Polymer Composites for Aerospace Engineering

Composites for aerospace applications are fabricated with two forms: laminate and sandwich composites (Fig. 14.4). Multiple layers of fiber and resin bonded together create laminates. Carbon fiber epoxy resin laminate composites are employed in heavily loaded aircraft structures (Mouritz, 2012c; Yokozeki et al., 2008) and

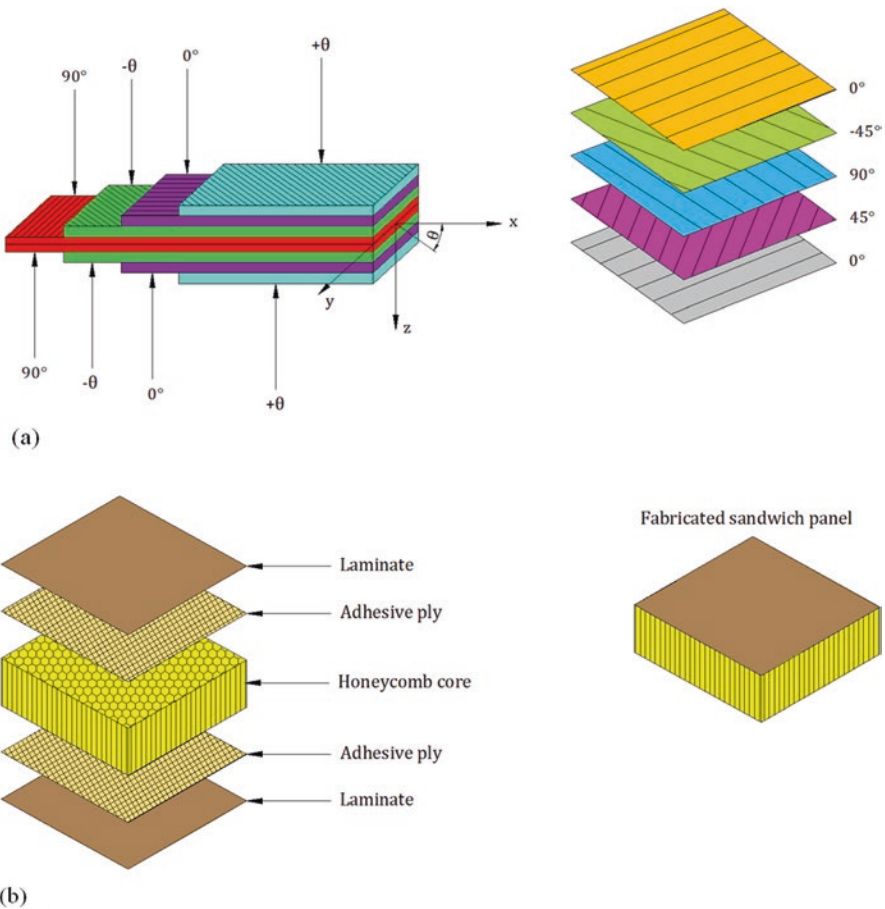


Fig. 14.4 (a) Laminate and (b) sandwich composite

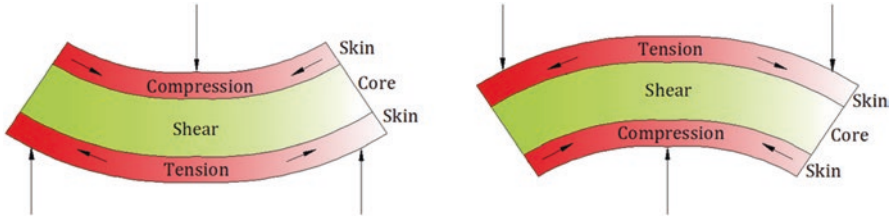


Fig. 14.5 Basic loading of sandwich composite

fuselage. In sandwich composites, thin face skins are bonded to a thick core material with an adhesive film. Under bending, the skins carry compression loads and in-plane tension while the core is exposed to shear (Fig. 14.5). Aluminum honeycomb is the most used core material in aircraft components since it has a lightweight cellular honeycomb structure providing high shear stiffness. Using of polymer foams such as polyetherimide (PEI) and polymethacrylimide (PMI) instead of aluminum honeycomb is rising in the aircraft sector because of their good durability and high temperature properties. Sandwich composites are utilized in lightly loaded aircraft structures requiring high resistance to buckling and bending. Sandwich composites are used for control surfaces (such as ailerons, flaps) and vertical tailplanes.

One of the most common forms of failure for composite materials is delamination. Delamination is a kind of layer deformation in laminated composite materials because of continuous stress and pressure on composite material. This type of failure may cause poor performance during the usage of these materials (Suriani et al., 2021a).

Manufacturing of composite can be separated into two kinds basing on how the polymer is combined with fiber: resin infusion processes such as filament winding (Fig. 14.6), resin film infusion (Fig. 14.7), resin transfer molding (Fig. 14.8), vacuum-bag resin infusion (Fig. 14.9), and prepreg-based processes including autoclave curing (Fig. 14.10), automated fiber placement (Fig. 14.11), and automated tape layup. In filament winding, cylindrical components are manufactured by winding continuous fiber tows over a stationary or rotating mandrel. Drive shafts, missile launch tubes, motor cases, and pressure vessels are fabricated with this process. Resin film infusion is suitable for producing relatively large structures because of its good drapability and near zero void content in comparison to autoclave cured parts (Rout et al., 2021). Moderate size of composite components such as fan blade of engine, rib, and spar for midsection fuselage and empennage is fabricated by resin transfer molding. Resin transfer molding can manufacture high-fiber volume amount composites, resulting them a good candidate for primary aircraft structures that need high fatigue, stiffness, and strength properties. Resin transfer molding is a closed molding process consisting of two molds with inner surfaces possessing the shape of final part. Fabric is placed in cavity between mold and stacked in the desired thickness and direction and then sealed and clamped. It is completely filled with resin injected at low pressure into the mold through a pump. Finally, the mold

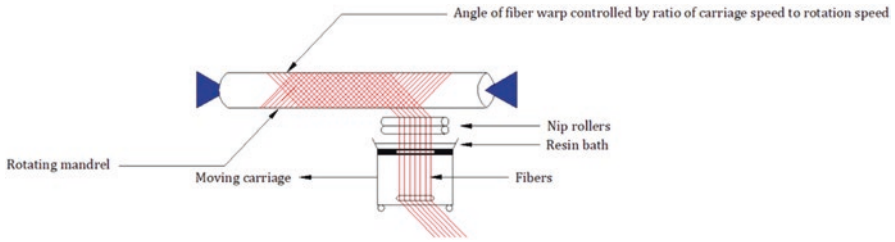


Fig. 14.6 Filament winding

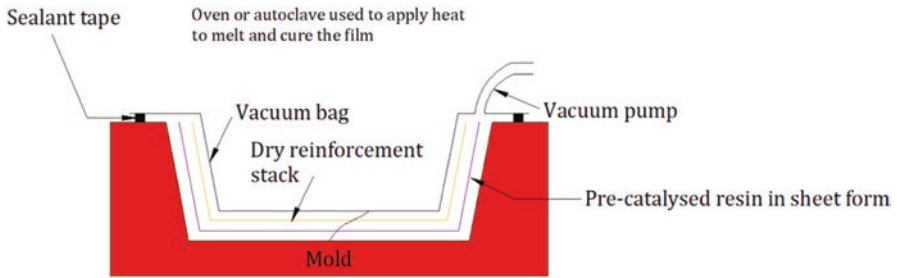


Fig. 14.7 Resin film infusion

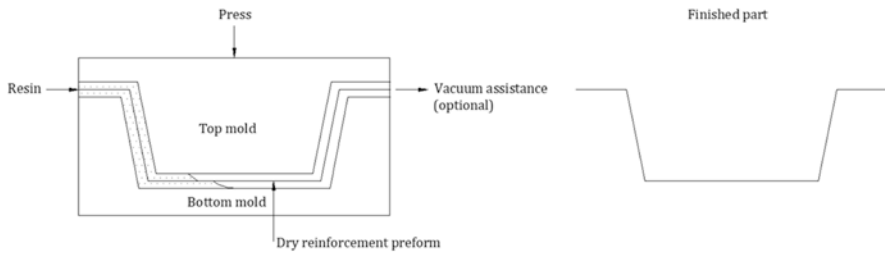


Fig. 14.8 Resin transfer molding

is heated to harden the polymeric matrix to form a solid composite and then trimmed of edge. Vacuum-bag resin infusion fabricates carbon-epoxy structural components. High-quality composites with high fiber amount are obtained with autoclave process which is suitable for primary and secondary parts for helicopters and aircrafts. Automated fiber placement is employed in the automated fabrication of large airplane parts from prepreg such as cowls, ducts, pressure tanks, nozzle cones, fuselage barrels, and spars. Automated tape layup is an automated process utilized to lay up prepreg tape in the manufacturing of composite airplane parts such as carbon-epoxy prepreg components. Near-net shape is obtained by the most manufacturing processes for composites. This is one of the advantages of fabricating with composites instead of metals. After manufacturing, only hole drilling for fasteners or trimming to eliminate excess material from the edges is required (Aisyah et al., 2021; Mouritz, 2012c).

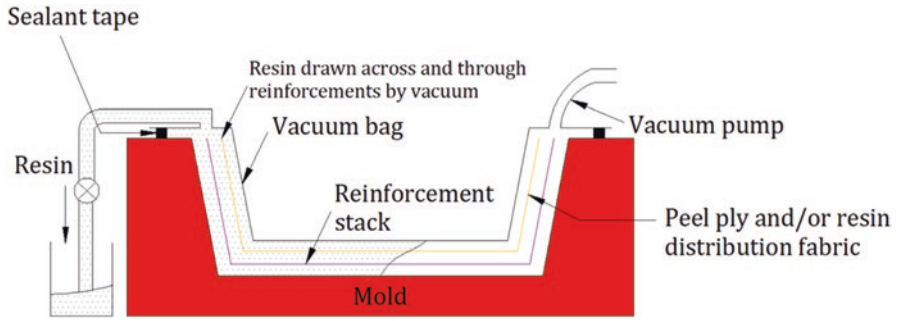


Fig. 14.9 Vacuum-bag resin infusion

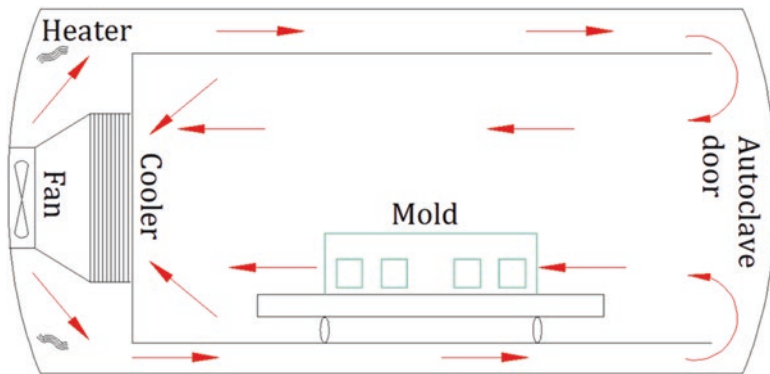


Fig. 14.10 Autoclave curing

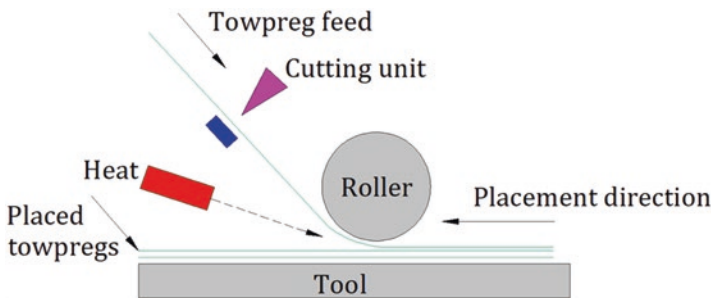


Fig. 14.11 Automated fiber placement

6 Applications of Hybrid Biocomposites in Aerospace Engineering

A wing is a structural beam which is exposed to altering moments and stresses owing to air turbulence, flight maneuver, and its weight and stresses from the gear during takeoff and landing. Moreover, bottom and top surfaces of the wing are

alternately exposed to tension and compression (Mansor et al., 2019). Therefore, wings should be resistant to high forces, and composite materials with high strength can be good choice for these aerospace structures.

The existence of two different fibers caused good wettability, reducing void formation at the fiber-matrix interface and giving hybrid composites with high strength and stiffness (Islam et al., 2017), which could be suitable for the usage in aerospace applications of hybrid biocomposites.

Kenaf fiber-reinforced acrylonitrile butadiene styrene (ABS) with nanoclay hybrid biocomposite is able to self-extinguish and has efficient fire extinction, which can be applied in secondary structures of airplane with advantages such as biodegradable self-extinguishing, lightweight, and cost-effective biocomposite. It was declared that ABS/kenaf fiber (50/50) with 1% nanoclay formulation was applicable for confined spaces in aircraft (Karunakaran et al., 2016).

Impregnation of ceramic sheets into kenaf fiber-reinforced PP biocomposite could improve both inflammability and mechanical properties, causing the use in aerospace applications of hybrid biocomposites (Sim et al., 2013).

Sisal-glass fiber PP biocomposites caused a drop in volumetric coefficient of thermal expansion from 30 to -30 °C and improved moisture resistance showing that hybrid biocomposites expose lower dimensional change when subjected to alternating atmospheric condition (KC et al., 2018). They may be suitable for the use in aerospace applications of hybrid biocomposites.

7 Conclusions

Polymer composites utilized in aerospace components must meet some requirements such as excellent dimensional stability over a wide temperature range, good fatigue performance, high-fracture toughness, high-impact energy to bear sudden impacts of bird strikes, high strength, lightweight, and resistance to corrosive environments (fuel and lubricant) and also provide shielding of electromagnetic waves. Biocomposites have been developed by the researchers in recent years owing to rising pressure on the protection of the environment. Poor interface, moderate to lower mechanical properties, and moisture intake are some drawbacks of biocomposites for partial or full change with synthetic composites. To overcome these drawbacks, hybridizing, blending two or more reinforcements instead of single reinforcement in a polymeric matrix, is widely employed nowadays. Therefore, in this chapter, the works about hybrid biocomposites and their applications in the aerospace industry are reported. Aircraft interior parts (such as decking, flooring, seats) and exterior body panels can be manufactured with natural fiber-based polymer composites.

Acknowledgments There are not enough words to describe how grateful I am to my doctor interventional neurologist Assoc. Prof. Hasan Huseyin Karadeli for giving me a second life after my

brain disease. I am sure that without his operation, I would be unable to do all the things I am able to do now. I am lucky to have him as my doctor. I want to thank him so much for saving my life in August 2019. I also dedicate this chapter to my family and Assoc. Prof. Hasan Huseyin Karadeli.

References

- Ahmad, M. W., Dey, B., Sammar, A. A., et al. (2020). In situ synthesis of graphene oxide in multi-walled carbon nanotube hybrid-reinforced polyetherimide nanocomposites with improved electrical, mechanical and thermal properties. *Advanced Composite Materials*, 29, 529–546. <https://doi.org/10.1080/09243046.2019.1710680>
- Aisyah, H. A., Paridah, M. T., Sapuan, S. M., et al. (2021). A comprehensive review on advanced sustainable woven natural fibre polymer composites. *Polymers*, 13, 471. <https://doi.org/10.3390/polym13030471>
- Alsubari, S., Zuhri, M. Y. M., Sapuan, S. M., et al. (2021). Potential of natural fiber reinforced polymer composites in sandwich structures: A review on its mechanical properties. *Polymers*, 13, 423. <https://doi.org/10.3390/polym13030423>
- Anandjiwala, R. D., John, M. J., Wambua, P., et al (2008). Bio-based structural composite materials for aerospace applications. In *2nd SAIAS symposium, Stellenbosch, South Africa*.
- Arockiam, N. J., Jawaid, M., & Saba, N. (2018). Chapter 6: Sustainable bio composites for aircraft components. In M. Jawaid & M. Thariq (Eds.), (pp. 109–123). Elsevier Science & Technology Books.
- Baker, A. A., Dutton, S., & Kelly, D. (2000). Chapter 12: Aircraft applications and design issues. Composite materials for aircraft structures. *American Institute of Aeronautics and Astronautics*, 435–475.
- Benyamina, B., Mokaddem, A., Doumi, B., et al. (2021). Study and modeling of thermomechanical properties of jute and alfa fiber-reinforced polymer matrix hybrid biocomposite materials. *Polymer Bulletin*, 78, 1771–1795. <https://doi.org/10.1007/s00289-020-03183-7>
- Bharath, K. N., & Basavarajappa, S. (2016). Applications of biocomposite materials based on natural fibers from renewable resources: A review. *Science and Engineering of Composite Materials*, 23, 123–133. <https://doi.org/10.1515/secm-2014-0088>
- Boegler, O., Kling, U., Empl, D., et al. (2014). Potential of sustainable materials in wing structural design. *Deutscher Luft- und Raumfahrtkongress*, 1–6.
- Chai, M. W., Bickerton, S., Bhattacharyya, D., et al. (2012). Influence of natural fibre reinforcements on the flammability of bio-derived composite materials. *Composites: Part B*, 43, 2867–2874. <https://doi.org/10.1016/j.compositesb.2012.04.051>
- Chandrasekar, M., Ishak, M. R., Jawaid, M., et al. (2018). Chapter 14: Low velocity impact properties of natural fiber-reinforced composite materials for aeronautical applications. In M. Jawaid & M. Thariq (Eds.), *Sustainable composites for aerospace applications* (pp. 293–313). Elsevier Science & Technology Books.
- Das, O., Kim, N. K., Sarmah, A. K., et al. (2017). Development of waste based biochar/wool hybrid biocomposites: Flammability characteristics and mechanical properties. *Journal of Cleaner Production*, 144, 79–89. <https://doi.org/10.1016/j.jclepro.2016.12.155>
- Eloy FS, Costa RRC, Medeiros R, et al. (2015) Comparison between mechanical properties of bio and synthetic composites for use in aircraft interior structures. *Meeting on aeronautical composite materials and structures, São Paulo, Brazil*.
- Farag, M. M. (2017). Chapter 5: Design and manufacture of biodegradable products from renewable resources. In V. K. Thakur, M. K. Thakur, & M. R. Kessler (Eds.), *Handbook of composites from renewable materials* (Vol. 2, pp. 111–131). Wiley.

- Fu, S.-Y., Xu, G., & Mai, Y.-W. (2002). On the elastic modulus of hybrid particle/short-fiber/polymer composites. *Composites: Part B*, *33*, 291–299. [https://doi.org/10.1016/S1359-8368\(02\)00013-6](https://doi.org/10.1016/S1359-8368(02)00013-6)
- Ghori, S. W., Siakeng, R., Rasheed, M., et al. (2018). Chapter 2: The role of advanced polymer materials in aerospace. In M. Jawaid & M. Thariq (Eds.), *Sustainable composites for aerospace applications* (pp. 19–34). Elsevier Science & Technology Books.
- Gopi, S., Balakrishnan, P., Sreekala, M. S., et al. (2017). Chapter 11: Green materials for aerospace industries. In D. Ray (Ed.), *Biocomposites for high-performance applications: Current barriers and future needs towards industrial development* (pp. 307–318). Woodhead Publishing.
- Goriparthi, B. K., Suman, K. N. S., & Nalluri, M. R. (2012). Processing and characterization of jute fiber reinforced hybrid biocomposites based on polylactide/polycaprolactone blends. *Polymer Composites*, *33*, 237–244. <https://doi.org/10.1002/pc.22145>
- Haris, M. Y., Laila, D., Zainudin, E. S., et al. (2011). Preliminary review of biocomposites materials for aircraft radome application. *Key Engineering Materials*, *471–472*, 563–567. <https://doi.org/10.4028/www.scientific.net/KEM.471-472.563>
- Hassan, A., Salema, A. A., Ani, F. N., et al. (2010). A review on oil palm empty fruit bunch fiber-reinforced polymer composite materials. *Polymer Composites*, *31*, 2079–2101. <https://doi.org/10.1002/pc.21006>
- Ilyas, R. A., Sapuan, S. M., Harussani, M. M., et al. (2021). Polylactic acid (PLA) biocomposite: Processing, additive manufacturing and advanced applications. *Polymers*, *13*, 1326. <https://doi.org/10.3390/polym13081326>
- Islam, M. S., Ramlı, I. B., Hasan, M. R., et al. (2017). Effect of kenaf and EFB fiber hybridization on physical and thermo-mechanical properties of PLA biocomposites. *Fibers and Polymers*, *18*, 116–121. <https://doi.org/10.1007/s12221-017-6208-x>
- Jacob, M., Thomas, S., & Varughese, K. T. (2007). Biodegradability and aging studies of hybrid biofiber reinforced natural rubber biocomposites. *Journal of Biobased Materials and Bioenergy*, *1*, 118–126. <https://doi.org/10.1166/jbmb.2007.013>
- Jamir, M. R. M., Majid, M. S. A., & Khasri, A. (2018). Chapter 8: Natural lightweight hybrid composites for aircraft structural applications. In M. Jawaid & M. Thariq (Eds.), *Sustainable composites for aerospace applications* (pp. 155–170). Elsevier Science & Technology Books.
- Jawaid, M., & Abdul Khalil, H. P. S. (2011). Cellulosic/synthetic fibre reinforced polymer hybrid composites: A review. *Carbohydrate Polymers*, *86*, 1–18. <https://doi.org/10.1016/j.carbpol.2011.04.043>
- Kaiser, M. R., Anuar, H., & Razak, S. B. A. (2014). Improvement in thermomechanical properties of injection molded nano-modified hybrid biocomposite. *Journal of Thermoplastic Composite Materials*, *27*, 992–1009. <https://doi.org/10.1177/0892705712461518>
- Karunakaran, S., Majid, D. L., & Tawil, M. L. M. (2016). Flammability of self-extinguishing kenaf/ABS nanoclays composite for aircraft secondary structure. *IOP Conf Series: Materials Science and Engineering*, *152*, 012068. <https://doi.org/10.1088/1757-899X/152/1/012068>
- KC, B., Tjong, J., Jaffer, S. A., & Sain, M. (2018). Thermal and dimensional stability of injection-molded sisal-glass fiber hybrid PP biocomposites. *Journal of Polymers and the Environment*, *26*, 1279–1289. <https://doi.org/10.1007/s10924-017-1033-2>
- Manfredi, L. B., Rodríguez, E. S., Wladyka-Przybylak, M., et al. (2006). Thermal degradation and fire resistance of unsaturated polyester, modified acrylic resins and their composites with natural fibres. *Polymer Degradation and Stability*, *91*, 255–261. <https://doi.org/10.1016/j.polyimdegradstab.2005.05.003>
- Mansor, M. R., Nurfaizay, A. H., Tamaldin, N., et al. (2019). Chapter 11: Natural fiber polymer composites: Utilization in aerospace engineering. In D. Verma, E. Fortunati, S. Jain, & X. Zhang (Eds.), *Biomass, biopolymer-based materials, and bioenergy: Construction, biomedical, and other industrial applications* (pp. 203–224). Elsevier Science & Technology Books.
- Mouritz, A. P. (2012a). Chapter 17: Wood in small aircraft construction. In *Introduction to aerospace materials* (pp. 411–427). Elsevier Science & Technology Books.

- Mouritz, A. P. (2012b). Chapter 13: Polymers for aerospace structures. In *Introduction to aerospace materials* (pp. 268–302). Elsevier Science & Technology Books.
- Mouritz, A. P. (2012c). Chapter 14: Manufacturing of fibre-polymer composite materials. In *Introduction to aerospace materials* (pp. 303–337). Elsevier Science & Technology Books.
- Mouritz, A. P. (2012d). Chapter 15: Aerospace applications of fibre-polymer composites. In *Introduction to aerospace materials* (pp. 338–393). Elsevier Science & Technology Books.
- Nair, A. B., Sivasubramanian, P., Balakrishnan, P., et al. (2014). Chapter 15: Environmental effects, biodegradation, and life cycle analysis of fully biodegradable “green” composites. In S. Thomas, K. Joseph, S. K. Malhotra, et al. (Eds.), *Polymer composite* (pp. 515–568). Wiley.
- Njuguna, J., Pielichowski, K., & Fan, J. (2012). Chapter 15: Polymer nanocomposites for aerospace applications. In G. Fengge (Ed.), *Advances in polymer nanocomposites: Types and applications* (pp. 472–539). Elsevier Science & Technology Books.
- Nurazzi, N. M., Asyraf, M. R. M., Khalina, A., et al. (2021a). Fabrication, functionalization, and application of carbon nanotube-reinforced polymer composite: An overview. *Polymers*, *13*, 1047. <https://doi.org/10.3390/polym13071047>
- Nurazzi, N. M., Asyraf, M. R. M., Khalina, A., et al. (2021b). A review on natural fiber reinforced polymer composite for bullet proof and ballistic applications. *Polymers*, *13*, 646. <https://doi.org/10.3390/polym13040646>
- Omran, A. A. B., Mohammed, A. A. B. A., Sapuan, S. M., et al. (2021). Micro- and nanocellulose in polymer composite materials: A review. *Polymers*, *13*, 231. <https://doi.org/10.3390/polym13020231>
- Panthapulakkal, S., & Sain, M. (2007). Studies on the water absorption properties of short hemp-glass fiber hybrid polypropylene composites. *Journal of Composite Materials*, *41*, 1871–1883. <https://doi.org/10.1177/0021998307069900>
- Rana, S., & Figueiro, R. (2016). Chapter 1: Advanced composites in aerospace engineering. In S. Rana & R. Figueiro (Eds.), *Advanced composite materials for aerospace engineering: Processing, properties and applications* (pp. 1–15). Elsevier Science & Technology Books.
- Rao, D. N., Mukesh, G., Ramesh, A., et al. (2020). Investigations on the mechanical properties of hybrid goat hair and banana fiber reinforced polymer composites. *Materials Today's Proceedings*, *27*, 1703–1707. <https://doi.org/10.1016/j.matpr.2020.03.586>
- Rashid, M., Chetehouna, K., Cablé, A., et al. (2021). Analysing flammability characteristics of green biocomposites: An overview. *Fire Technology*, *57*, 31–67. <https://doi.org/10.1007/s10694-020-01001-0>
- Rout, D., Nayak, R. K., & Praharaj, S. (2021). Chapter 13: Aerospace and vehicle industry. In C. M. Hussain (Ed.), *Handbook of polymer nanocomposites for industrial applications* (pp. 399–417). Elsevier.
- Senthilkumar, K., Siva, I., Rajini, N., et al. (2017). Chapter 3: Mechanical characteristics of tri-layer eco-friendly polymer composites for interior parts of aerospace application. In M. Jawaid & M. Thariq (Eds.), *Sustainable composites for aerospace applications* (pp. 35–54). Woodhead Publishing.
- Shahzad, A., & Choudhry, R. S. (2017). Chapter 16: Design and manufacturing of natural fiber/synthetic fiber reinforced polymer hybrid composites. In V. K. Thakur, M. K. Thakur, & M. R. Kessler (Eds.), *Handbook of composites from renewable materials* (pp. 411–448). John Wiley & Sons.
- Shanmugam, D., & Thiruchitrambalam, M. (2013). Static and dynamic mechanical properties of alkali treated unidirectional continuous Palmyra palm leaf stalk fiber/jute fiber reinforced hybrid polyester composites. *Materials and Design*, *50*, 533–542. <https://doi.org/10.1016/j.matdes.2013.03.048>
- Sim, I. N., Han, S. O., Jang, Y. H., et al. (2013). Ceramic sheet hybrid Kenaf reinforced polypropylene biocomposites. *Journal of Applied Polymer Science*, *130*, 1917–1922. <https://doi.org/10.1002/app.39367>

- Siva, I., Jappes, J. T. W., & Suresha, B. (2012). Investigation on mechanical and tribological behavior of naturally woven coconut sheath-reinforced polymer composites. *Polymer Composites*, 33, 723–732. <https://doi.org/10.1002/pc.22197>
- Suriani, M. J., Rapi, H. Z., Ilyas, R. A., et al. (2021a). Delamination and manufacturing defects in natural fiber-reinforced hybrid composite: A review. *Polymers*, 13, 1323. <https://doi.org/10.3390/polym13081323>
- Suriani, M. J., Radzi, F. S. M., Ilyas, R. A., et al. (2021b). Flammability, tensile, and morphological properties of oil palm empty fruit bunches fiber/PET yarn-reinforced epoxy fire retardant hybrid polymer composites. *Polymers*, 13, 1282. <https://doi.org/10.3390/polym13081282>
- Yokozeiki, T., Aoki, Y., & Ogasawara, T. (2008). Experimental characterization of strength and damage resistance properties of thin-ply carbon fiber/toughened epoxy laminates. *Composite Structures*, 82, 382–389. <https://doi.org/10.1016/j.compstruct.2007.01.015>

Chapter 15

Molding of Carbon-Epoxy Composite Prepregs for Applications in Aerospace Industries



Raghu Raja Pandiyam Kuppusamy, Santoshi Mohanta, and Swati Neogi

1 Introduction

Fiber-reinforced composites have become an efficient material for the design and development of high-end and complex aerospace applications because of their light-weight which helps in the improvement of aircraft fuel efficiency. These nonmetallic Fiber-Reinforced Polymeric (FRP) composite materials are competing favorably with the advanced metallic materials and new alloys of Al-Li, Al-Cu, Al-Zn, etc., because of their high specific strength, stiffness, easy manufacturing, and tailor-made properties. In aerospace industries, epoxy and carbon fiber-based composites are very frequently preferred over other resin-fiber combinations due to their improved fatigue strength, corrosion resistance, mechanical strength, and higher service temperature (Campbell, 2004; Gay et al., 2002; Gutowski, 1997). Several researchers have reported the use of carbon fiber polymeric composites for manufacturing of various aircraft parts such as flaps, aileron, landing gear doors, etc. (Barile & Casavola, 2019; Schwartz, 1997).

In recent years, prepreg material which is an intermediate material has gained its importance in manufacturing structural composite components as these materials allow to adjust reinforcement positioning, thickness, number of layers, and their orientations in the molding. In general, these composites are manufactured by hand lay-up process; however, other advanced techniques such as resin transfer molding (RTM), autoclave molding, compression molding, etc., are more suitable

R. R. P. Kuppusamy
Department of Chemical Engineering, National Institute of Technology,
Warangal, Telangana, India

S. Mohanta · S. Neogi (✉)
Composite Applications Laboratory, Department of Chemical Engineering, Indian Institute of
Technology Kharagpur, Kharagpur, West Bengal, India
e-mail: swati@che.iitkgp.ac.in

(Kuppusamy, 2018). These advanced techniques require a proper manufacturing technology which includes design of complex mold geometry and other tool parts. Several literature have reported the application of hand lay-up technique for the development of composite products (Elanchezhian et al., 2014; Paiva et al., 2006, 2009). The composite parts manufactured using prepregs are clean, and manufacturing of complex geometries becomes easier. Most of these products usually have a fiber volume fraction greater than 60%. However, composites fabricated by prepregs employing hand lay-up process leads to nonuniform deposition of epoxy resin which eventually affects the final performance of the product (Mohan et al., 2019).

This book chapter focuses on developing carbon-epoxy composite laminates and prepregs through resin transfer and compression molding processes for applications in aerospace industries. At first, selection of process parameters in molding processes is presented. In the following sections, cure processing and practical difficulties during manufacturing of fully and partially cured composite laminates are addressed. Next, the effect of temperature and pressure cycles on physical and cure conditions of composite laminates are reported. In situ offshore transportation handling of semi-cured laminates are further discussed. In the subsequent section, the effect of preprocessed panel cure on post processing of partially cured composite laminates is discussed. Finally, postprocess resin bleeding analysis of partially cured, hot-pressed, and resin transfer-molded composite laminates is presented.

2 Resin Transfer Molding of Carbon-Epoxy Composite Laminates

2.1 Materials

The materials used for manufacturing carbon-epoxy composite laminates by RTM technique are as follows:

Resin: RTM6 resin, mono-component epoxy resin supplied by Hexcel.

Reinforcement: Carbon fiber-woven roven mat of fabric G0926 with 5H satin weave mat architecture, HexForce RGP390-5H, supplied by Hexcel. Six layers of 45° cut were used to manufacture the prepregs.

2.2 Development of RTM Mold

At first, appropriate mold design was developed in accordance with the composite panel dimensions for the manufacturing of semi-cured and fully cured carbon-epoxy composite laminates via resin transfer molding process. Resin flow, mold-cure temperature cycle, mold-injection pressure cycle, i.e., resin flow rates, injection pressure, and cure possible temperatures, were considered for the development of

RTM mold design. The mold was designed for carbon-epoxy composite laminate dimensions 600 mm × 300 mm (L × B) with a varying part thickness from 2 mm to 8 mm.

Initially, to identify the optimized number and spacing of injection ports and air vents, isothermal mold filling simulations were performed using different resin properties, reinforcement properties, and process parameters. Resin properties include the viscosity variations to quantify different available resin grades. Reinforcement properties include permeabilities, areal density, and porosities to quantify different mat architecture. Injection pressure and flow rate were process parameters considered for the isothermal mold filling simulations. From the simulation studies, it was found that the optimized injection strategy was single point injection port at the center and two-point vents at the sides of the mold having port and vent diameter of 4 mm. Also, the optimized injection strategy delivered an acceptable mold fill time with the variations in the resin properties, reinforcement mat properties, and process parameters. The sensitivity of resin properties, reinforcement mat properties, and process parameters on the mold fill time was evaluated.

A complete mold layout was prepared. The mold material was adjudged as the carbon steel. Bottom half thickness of 40 mm and top half thickness of 23 mm were selected to carry the mechanical aspects of the mold. Metal rod cartridge heaters having capacity of 500 W were used to heat the mold to 250 °C. Resin feed cylinder to the mold was designed for 2 L capacity. The resin feed cylinder was designed to maintain the stored contents to 150 °C to keep the epoxy resin fluidity before resin injection to the mold. Seven heaters were placed at the mold bottom half, and six heaters were placed at the mold top half to aid the temperature cycle to cure the resin. Provisions were made for water circulation at both halves of the mold. The mold cooling capability of the circulating water was tested and found to be enough to meet the cooling demands. The heater and cooler points were placed in such a way that the heating and cooling load is uniformly distributed over the mold. Respective temperatures sensors were placed at top and bottom halves of the mold and the resin preheater. All these temperatures were controlled through the respective sensors, and the data acquisition system was installed to capture temperature variations as a function of time. The complete assembly of mold with heating and cooling elements are shown in Fig. 15.1.

2.3 Manufacturing of Fully Cured Carbon-Epoxy RTM Composite Panel

At first, trials were conducted to manufacture 100%, i.e., fully cured, carbon-epoxy composite laminates using RTM6 manufacturer's cure cycle of 180 °C – 2 h. RTM6 epoxy resin was poured to feed storage cylinder and temperature of the cylinder was kept at 80 °C. Also, the resin at the feed cylinder was pressurized to 1 bar pressure

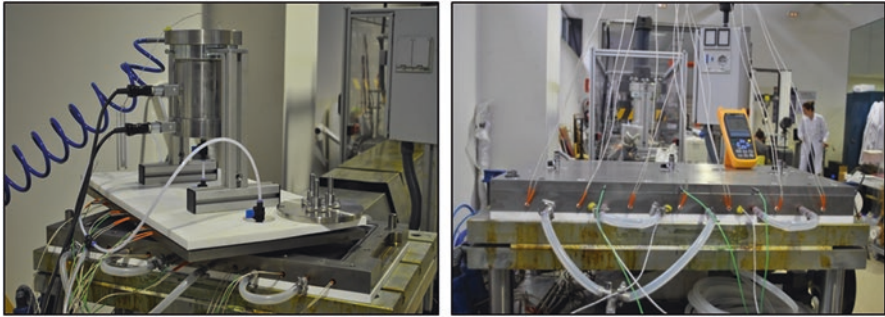


Fig. 15.1 Mold assembly

using compressed air supplied at the upper part of the closed cylinder. Initially, the resin which is at solid state due to cold storage starts melting, and enough time was given to make it low-viscous-flow-able resin. Before resin injection, entry resin port was kept closed and vacuum was applied at both air vents to increase the driving force for resin injection. The mold was preheated to 120 °C, and it was maintained at 120 °C until the completion of resin mold fill process.



The resin injection was started by opening the valve placed in the resin tube connecting feed cylinder and mold injection port. Resin flows with a driving force of 1 bar pressure summed with vacuum applied at both vents. RTM5 epoxy resin was injected through six layers of carbon-woven roven reinforcement mats at 45° architecture. The injection was held until a clear resin free of air bubbles flown out of the vents. Then, mold temperature was increased to 180 °C using a ramp of 3 °C/min for the resin curing. The resin was allowed to cure under 180 °C for 2 h as per the resin manufacturer's cure cycle. The results of the fully cured carbon-epoxy composite panels are presented in Table 15.1.

2.4 Manufacturing of Semi-Cured Carbon-Epoxy RTM Composite Panel

For manufacturing of semi-cured prepregs, four trials were performed at 140 °C by varying time starting from 30 min to 2 h with a time interval of 30 min. The main objective of these trials was to find out the resin cure evolution to the applied temperatures. The results of the developed RTM semi-cured panels are tabulated in Table 15.2, and the RTM mold cure evolution is shown in Fig. 15.2.

From Fig. 15.2, it can be seen that the development of carbon-epoxy composite laminate cure in RTM mold increases with cure time. By comparing the cure of pure resin, hot press laminates, and RTM laminates, it can be observed that the RTM laminates cure slower to the cure development in the other two cases. These differences may be attributed to the difference in resistances contributed by different

Table 15.1 RTM fully cured carbon-epoxy composite panels

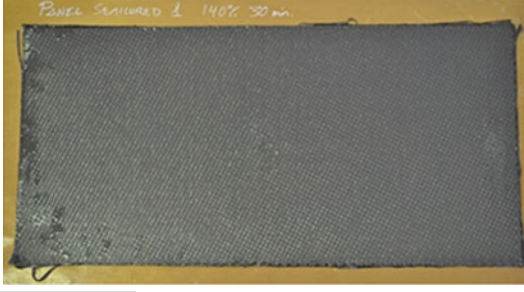
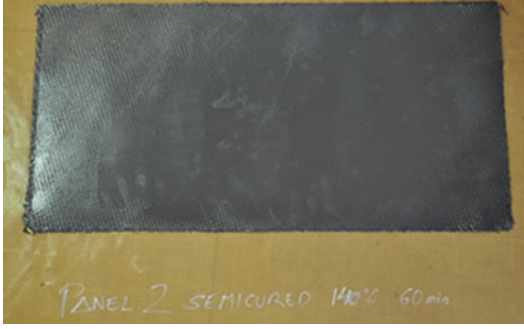


RTM fully cured panel-1 Cure cycle: 180 °C for 120 min Degree of cure: 99% Panel thickness: 2.62 mm	
RTM fully cured panel-2 Cure cycle: 180 °C for 120 min Degree of cure: 99% Panel thickness: 2.55 mm	

heating and cooling load, applied pressure, sample size, etc. Hence, it is required to scan the cure evolution of laminates needed to be tested at every processing site, processing method, and processing conditions.

2.5 Practical Challenges During RTM Processing

- It is required to cure the composite panel to a minimum degree of cure, say to the least of 30% curing. Otherwise, the extraction of panel from the mold becomes difficult. Extraction of under-cured panels using forcible means can lead to the panel damage and alteration in panel dimensions.
- Proper mold sealing and sealing thickness should be ensured. Bubbles get entrapped due to proper sealing and product thickness increase with increased sealing thickness.
- The composite panel cure may differ to the different trials of same cure cycle, if the resin preheating and mold filling time differs. Hence, care should be taken to ensure the idealistic resin preheating and mold filling time at each trial. Also, uniform resin conditions have to be maintained during storage and preheating stages.
- RTM fully-cured composite panels of dimension 600 mm × 300 mm were manufactured using the cure cycle 180 °C for 120 min.
- RTM semi-cured composite panels of dimension 600 mm × 300 mm to the several degrees of cure were manufactured using different cure cycles, and the effect of cure cycle on the degrees of cure was measured.

Table 15.2 RTM semi-cured carbon-epoxy composite panels

<p>RTM semi-cured panel-1 Cure cycle: 140 °C for 30 min Degree of cure: 15% Panel thickness: 2.6 mm</p>	
<p>RTM semi-cured panel-2 Cure cycle: 140 °C for 60 min Degree of cure: 21% Panel thickness: 2.55 mm</p>	
<p>RTM semi-cured panel-3 Cure cycle: 140 °C for 90 min Degree of cure: 30% Panel thickness: 2.65 mm</p>	
<p>RTM semi-cured panel-4 Cure cycle: 140 °C for 120 min Degree of cure: 38% Panel thickness: 2.6 mm</p>	

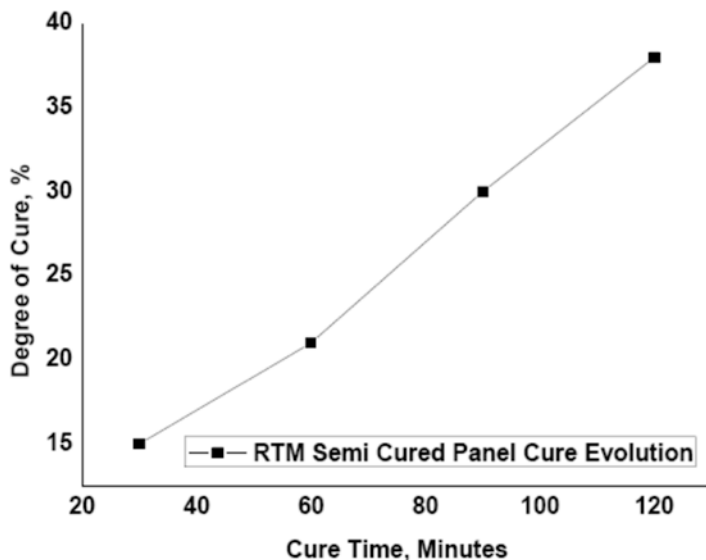


Fig. 15.2 RTM carbon-epoxy composite panel cure evolution

3 Compression Molding of Carbon-Epoxy Composite Laminates

Prior to the development of the semi-cured composite laminates through RTM process, trials were attempted to make out the prototypes of semi-cured composite laminates through hot press/compression molding, using the cure cycles of raw RTM6 resin. If RTM process and product are developed through full-scale trial and error experiments, it may consume more raw material and time, and it may lead to suboptimum process and product parameter. Hence, small-scale prototypes of laminate dimensions 10 cm × 10 cm were tested with resin cure cycles to understand the cure evolution in the composite panel. Hence, these hot press semi-cured composite prototypes avoid the bulk raw material requirement at the initial phase of the process and product development. Also, these prototype studies helped in judging the cure cycle to the actual semi-cure panel development through RTM process. It aided several simpler trials to test possible cure cycles to determine the cure evolution at the laminates.

3.1 Materials

The materials used for manufacturing carbon-epoxy composite laminates by compression molding technique are as follows:

Resin: RTM6 resin (Hexcel).

Reinforcement: Carbon fiber-woven roven mat.

Mat architecture: 6 layers at 45°/45°/45°/45°/45°/45°.

Dimension: 100 mm × 100 mm.

3.2 *Manufacturing of Carbon-Epoxy Laminate by Compression Molding Process*

Initially, the reinforcement layers are applied with RTM6 resin until maximum resin-fiber wetting using hand layup method. Then, each resin-drenched reinforcements are arranged to the required mat architecture and kept to the pseudo-mold made by folded Teflon sheets. Finally, this setup is kept under the hot press to initiate the hot press process. The pictures of the hot press machine and the molds used for the prototypes development are shown in Fig. 15.3(a) and (b).

In the hot press, the whole laminating process is programmed with the timely pressure and temperature applications. Application of heat to the process is disintegrated into resin preheat, resin ramp to the cure cycle, cure cycle, and the cooling stages. All the temperature applications at the different cure zones are programmed as a function of time. Two different cure cycles as 160 °C and 140 °C are utilized in this study. The cure evolution at the panels is measured as function of time for the respective cure cycles.

3.3 *Semi-Cured Composite Laminate Prototypes*

In this work, the knowledge related to cure cycle of RTM6 resin obtained from the thermal characterization of resin was randomly applied to the semi-cured laminate in the hot press. The thermal characterizations such as degree of cure is examined using dynamic DSC scan at a heating rate of 10 °C/min in a DSC Q 20 manufactured by TA instruments. The degree of cure for the laminate cure is obtained from the laminate residual heat and using Eq. (15.1), which is given below.

$$\alpha(\text{Semi Cured Laminate}) = 1 - \frac{\text{Residual Laminate Heat}}{\text{RTM6 Total Heat of Reaction}} \quad (15.1)$$

Along with the degree of cure, physical laminate consistency parameters such as tackiness and physical flexibility were also evaluated at these temperatures.

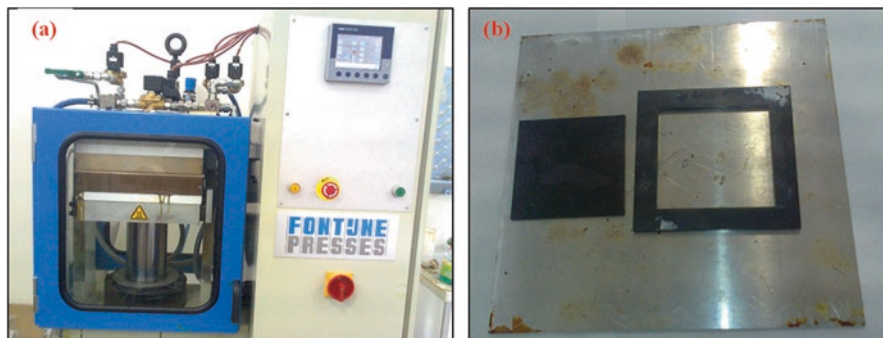


Fig. 15.3 (a) Hot press machine present in laboratory and (b) the mold used for manufacturing of semi-cured composite prototypes

3.4 Cure Cycle – 160 °C

Figure 15.4 as shown below gives the comparisons of raw RTM6 resin and laminate cure evolution at different time interval under 160 °C. It follows the same trend as in the RTM laminate cure. From the graph, it can be inferred that the laminate cures faster compared to the raw resin for the applied cure cycle.

The laminate has the steep rise in the degree of cure compared to the raw resin. The progression of resin cure is measured by DSC dynamic scan, where the heat flow is measured as a function of time, and at every time, the heat evolved from the small sample is absorbed by the nitrogen medium. But in the actual situation (hot press), the laminate is tightly sealed and pressurized, and hence, the exotherm heat increases the resin reactivity and, hence, results in faster curing of laminates as compared to the raw resin (Asim et al., 2017).

3.5 Cure Cycle – 140 °C

Figure 15.5 gives a comparison of raw RTM6 resin and laminate cure evolution at different time intervals while curing at 140 °C. Similar to 160 °C, the laminate cures faster compared to the raw resin for the applied cure cycle at 140 °C. This may be attributed to the exothermal heat built up during curing in closed mold assembly that enhances internal laminate temperature more than mold temperature, and hence, the laminate cure is more compared to DSC measure resin cure at any instant of time. In DSC, exothermal heat that evolves from the sample curing is always removed, and hence, there is no appreciable temperature difference experienced between sample and the pan surface.

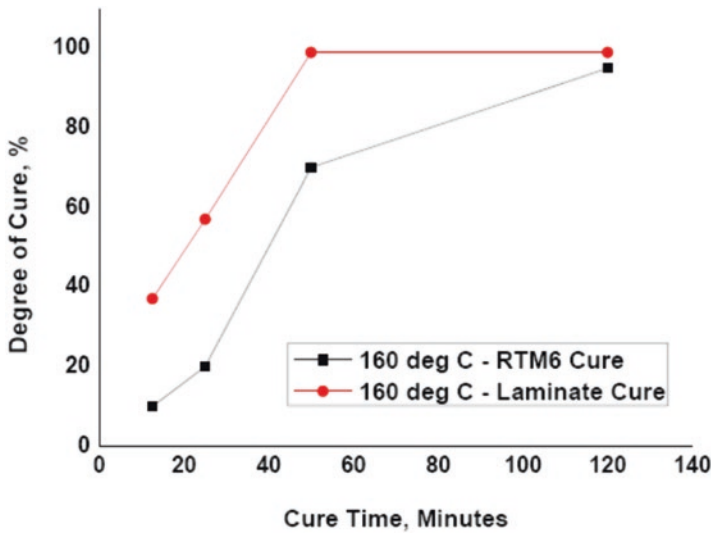


Fig. 15.4 Comparisons of RTM6 resin cure and laminate cure at 160 °C

3.6 Evaluation of Physical Consistency Parameters of Semi-Cured Composite Prototypes

The physical consistency parameters of semi-cured composite laminate such as tackiness, rigidity, and resin gelation are further evaluated and shown in Figs. 15.6–15.8, respectively. Tackiness is the sticky nature of the laminate which is qualitative measure of laminate cure. Rigidity is the physical resistance by the laminate during curing. It was found that the degree of tackiness decreases and rigidity increases as the cure temperature and cure time increase.

From the results, it was found that the laminates with degrees of cure lesser than 40% had more tackiness and flexibility. This may be due to the inadequate cross-linking of prepolymers with applied cure cycle. Semi-cured composite laminates with 30–40% are always preferable because the lower cured laminates can be hot-pressed and co-cured to make thick-sectioned composite laminates. The degree of integration and consolidation will be better if two partially cured composite laminates of laminate cure less than 40% are used to co-cure and consolidate as thick-sectioned composite laminates. The flexibility, tackiness, and rigidity variations of few trials are shown in Figs. 15.6 and 15.7.

The increased tackiness helps the integration of the semi-cured panel and the prepreg, whereas the poor flexibility at the increased tackiness makes it difficult to handle the part. Hence, an offset between tackiness and rigidity is often preferred to enable the semi-cured part in both product integration and storage handling.

Additionally, the degree of cure variation with resin gelation time is shown in Fig. 15.8. This is strongly related to the degree of cure, since a definite amount of

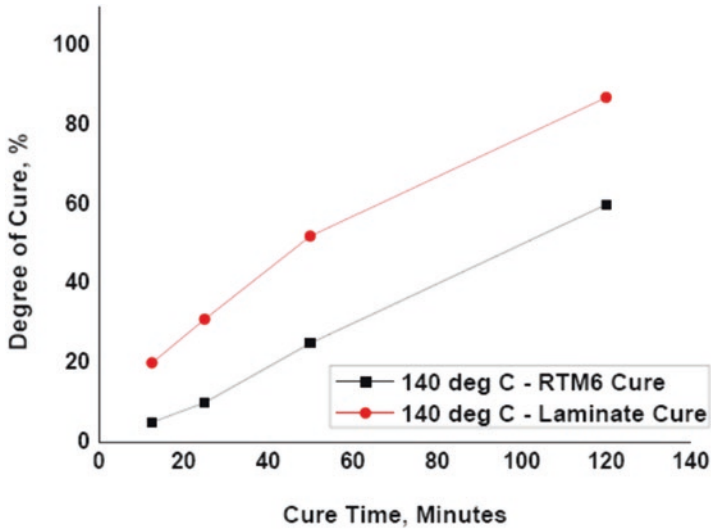


Fig. 15.5 Comparisons of RTM6 resin cure and laminate cure at 140 °C

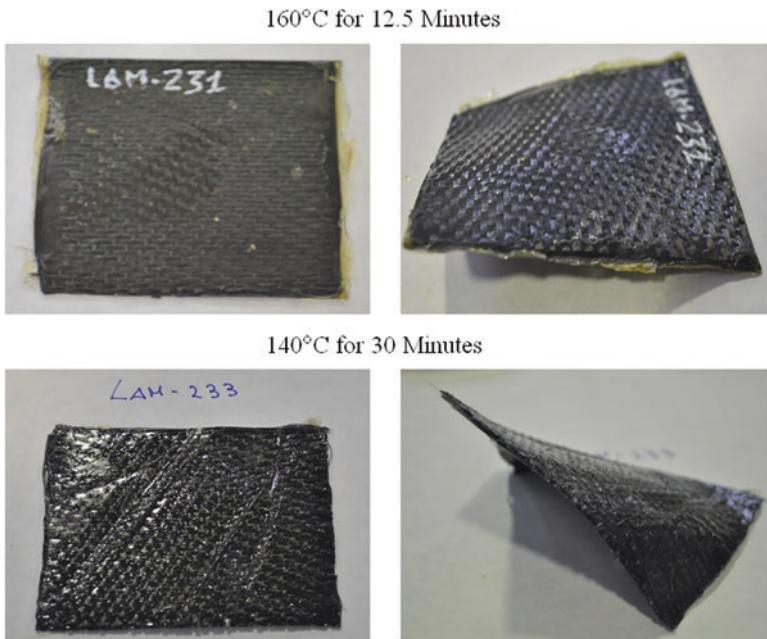


Fig. 15.6 Flexible and tacky semi-cured laminates

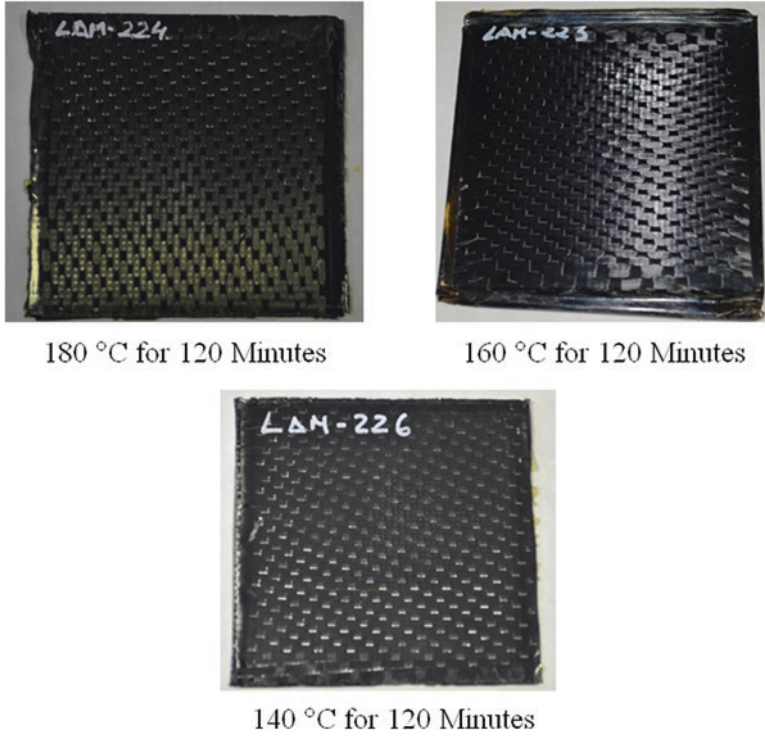


Fig. 15.7 Images of rigid laminates

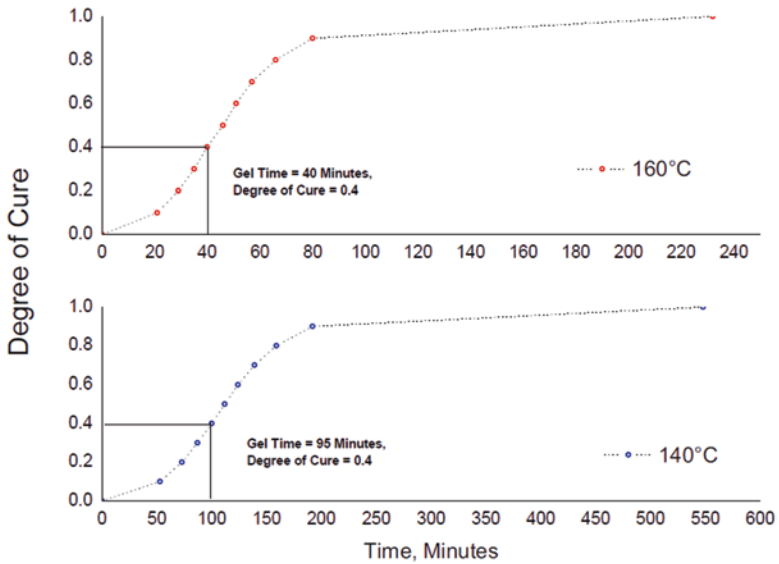


Fig. 15.8 Degree of cure vs. resin gelation

reaction is required to attain the gelation (Mohanta et al., 2020). Though resin cure and laminate cure differ in magnitude, the trend of the laminate rigidity is linear to the resin gelation. It was found from the hot press composite laminate prototypes that the laminate rigidity occurs around 40% of the curing, irrespective of the cure temperature. This may be due to the attainment of minimum cross-linking required to cease free movement of polymer chains. Hence, the gel times are observed to be 40 min and 95 min for 160 °C and 140 °C, respectively, when degree of cure is 40%.

The comparison of resin gel time and degree of cure at different cure temperatures is given in Fig. 15.8. The same trend of degree of cure was observed when the resin gelation is compared to the resin cure percentage. Different cure cycles were imposed on the hot press composite laminates. Finally, the difference between the resin and laminate cures were evaluated at 140 °C and 160 °C for time period less than an hour were judged to be the best suited cure cycles for the laminate curing. These cure cycles are judged based on the consideration of laminate tackiness and rigidity required for multiple laminate integration and storage physical handling.

3.7 Issues Related to Hot Press Processing of Carbon-Epoxy Composite Laminate

In case of hot press method for flat semi-cured composite laminate, the center of the panel was not usually consolidated properly as compared to the edges due to excess resin bleed out. This affects the quality of final products. To address the hot press laminate resin bleed issue, the resin content of the prepreg needs to be analyzed. In the present study, the resin bleed out was determined by taking the weight ratio of layup before and after consolidation according to ASTM D792–13 standard (Kumar et al., 2014). The schematic of process steps is shown in Fig. 15.9, and the detailed test procedures are discussed as follows. At first, six layers of mat were wetted with resin using hand layup method. Weights of resin and fiber used were measured. Then these laminates were covered with breather clothes, and the whole contents were again weighed. Next, these laminates with breather cloth were hot pressed. The breather cloth weights before and after hot press were measured. The resin bleed can be estimated from the difference in the weights of breather cloth before and after hot press process. The details of the constituent materials and the observations made are tabulated in Tables 15.3 and 15.4, respectively.

From the observation tables, the amount of bleed resin can be found out by taking the difference in weight of breather cloth before and after the hot press process, which is $15.5 - 4.2 = 11.3$ g. Similarly, the amount of resin bleed based on wet laminate and hot press laminate is 11.7 g (40.5–28.8 g). This gives the net resin loss as 0.4 g which comes nearly 3%. For cure cycle of 140 °C, net resin bleed percentage was obtained as 66%. The results are presented in Table 15.5.

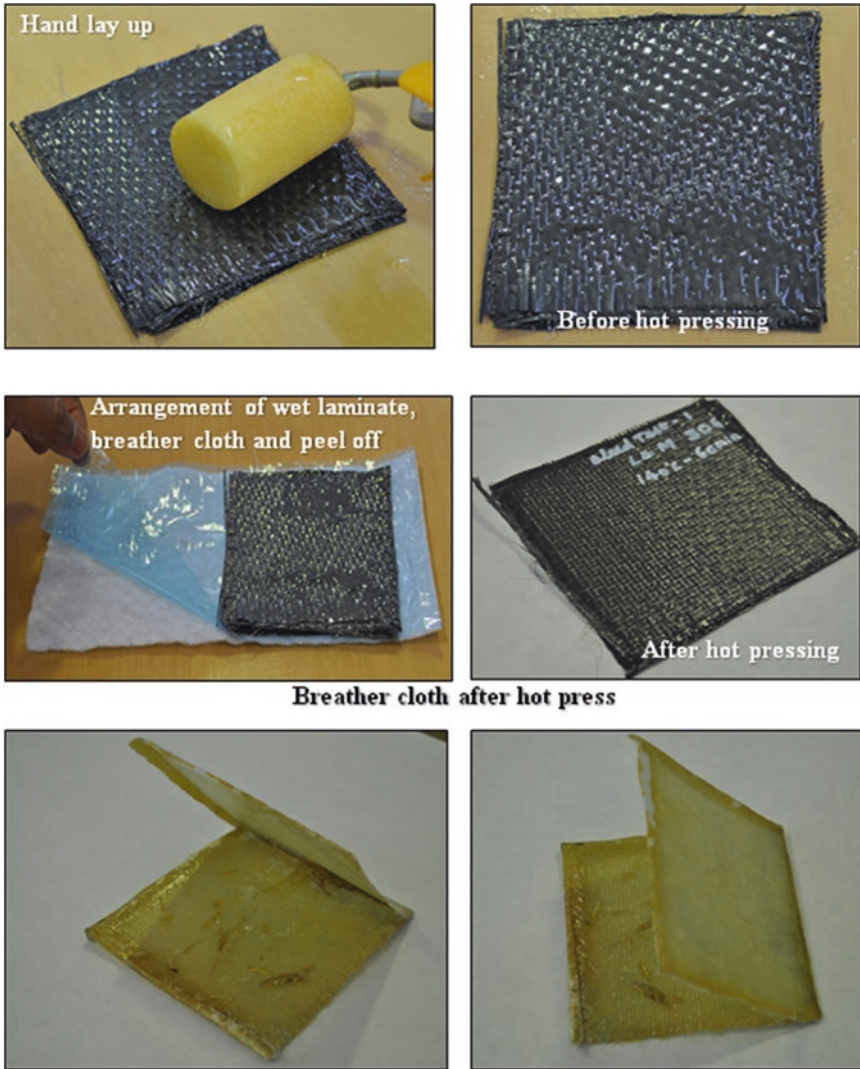


Fig. 15.9 Detailed steps followed to evaluate the resin bleed by taking the weight ratio of carbon-epoxy prepreg layups

Table 15.3 The details of constituent materials

Materials	Properties/grade
Resin	RTM6
Reinforcement	Carbon fiber fabric G0926 with satin weave
Mat architecture	Six layers at 90°/90°/90°/90°/90°/90
Cure cycle	140 °C – 60 min
Pressure cycle	7 bar

Table 15.4 The observations made before and after hot press

Laminate before hot press		Laminate after hot press	
Weight of the breather cloth	4.2 g	Weight of the breather cloth + bleed resin	15.5 g
Weight of the reinforcement layer	22.8 g	Weight of the hot press wet laminate	28.8 g
Weight of the wet laminate	40.50 g	Net resin impregnated	17.7 g
Net resin impregnated	17.7 g	Laminate thickness	1.99 mm
Laminate thickness	3 mm		

Table 15.5 Resin content test results

Cure cycle	Pressure	Degree of cure	Laminate thickness variation	Laminate weight change	Percentage resin bleed
140 °C – 60 minutes	7 bar	54.5%	33.33%	28.89%	66%

4 Conclusions

Epoxy-carbon prepregs are favorable for aerospace applications due to their inherent advantages. Usually, these prepregs are utilized in manufacturing of various aircraft parts by hand layup technique. Other improved techniques such as RTM, autoclave molding, compression molding, etc. are better suited for this purpose. However, due to the limitations associated with the design of complex mold and optimization of process parameters, these manufacturing techniques are not frequently utilized. Therefore, in this chapter, the authors have discussed two of those manufacturing methods such as RTM and compression molding. Detailed design of RTM mold was discussed followed by the manufacturing of semi-cured prepregs. The cure progression (degree of cure) of semi-cured carbon-epoxy prepregs were observed. Similar process was followed for compression molding. Two different cure strategies were adapted to obtain the prepregs, and the best suited cure cycle was judged based on the curing and physical consistency parameters. For the given epoxy-carbon prepregs, a cure time of less than 1 h was selected. Moreover, the problems associated with both the processes are discussed, and the resin bleed was estimated by taking the weight ratio of plies.

References

- Asim, M., Jawaid, M., Saba, N., et al. (2017). Processing of hybrid polymer composites—A review. In V. K. Thakur, M. K. Thakur, & R. K. B. T.-H. P. C. M. Gupta (Eds.), *Hybrid polymer composite materials* (pp. 1–22). Woodhead Publishing.
- Barile, C., & Casavola, C. (2019). Mechanical characterization of carbon fiber-reinforced plastic specimens for aerospace applications. In M. Jawaid & T. M. Saba (Eds.), *Fibre-reinforced com-*

- posites and hybrid composites NBT-M and PT of B. Woodhead Publishing series in composites science and engineering* (pp. 387–407).
- Campbell, F. C. (2004). *Manufacturing processes for advanced composites, Chapter 10* (Thermoplastic Composites: An Unfulfilled Promise).
- de Paiva, J. M. F., dos Santos, A. D. N., & Rezende, M. C. (2009). Mechanical and morphological characterizations of carbon fiber fabric reinforced epoxy composites used in aeronautical field. *Materials Research, 12*, 367–374.
- de Paiva, J. M. F., Mayer, S., & Rezende, M. C. (2006). Comparison of tensile strength of different carbon fabric reinforced epoxy composites. *Materials Research, 9*, 83–90.
- Elanchezian, C., Ramnath, B. V., & Hemalatha, J. (2014). Mechanical behaviour of glass and carbon fibre reinforced composites at varying strain rates and temperatures. *Procedia Materials Science, 6*, 1405–1418.
- Gay, D., Hoa, S. V., & Tsai, S. W. (2002). *Composite materials*. CRC Press.
- Gutowski, T. G. (1997). *Advanced composites manufacturing*. John Wiley & Sons, Inc..
- Kumar, A. A., Dinesh, B. L., & Gaddikeri, K. M., Sundaram, R. (2014). *Challenges in processing of PPS-glass thermoplastic composites*.
- Kuppusamy, R. R. P. (2018). Development of liquid composite moulded thermoset composite automotive parts using process simulations: Liquid composite moulding process simulations. In *Design and optimization of mechanical engineering products* (pp. 24–36). IGI Global.
- Mohan, P. R. K., Kumar, A., & Mohite, P. M. (2019). Development of in-house unidirectional carbon/epoxy prepregs and its characterization for aerospace applications. *Procedia Structural Integrity, 14*, 176–183.
- Mohanta, S., Padarathi, Y., Gupta, J., & Neogi, S. (2020). In-situ determination of degree of cure by mapping with strain measured by embedded FBG and conventional sensor during VIM process. *Fibers and Polymers, 21*, 2614–2624. <https://doi.org/10.1007/s12221-020-1064-5>
- Schwartz, M. M. (1997). *Composite materials. Volume 1: Properties, non-destructive testing, and repair*.

Chapter 16

Recent Advancements in Advanced Composites for Aerospace Applications: A Review



Mohammad Azad Alam, H. H. Ya, S. M. Sapuan, Othman Mamat, Bisma Parveez, Mohammad Yusuf, Faisal Masood, and R. A. Ilyas

1 Introduction

The rapid progress in the aerospace industry provides the momentum for the fast advancement of innovative aircraft materials. The aerospace industry comprises aircraft, spacecraft, and the associated design and production processes. The aerospace

M. A. Alam (✉) · H. H. Ya · O. Mamat
Mechanical Engineering Department, Universiti Teknologi PETRONAS,
Seri Iskandar, Perak, Malaysia
e-mail: azadalam.mech3@gmail.com

S. M. Sapuan
Advanced Engineering Materials and Composites Research Centre (AEMC), Department of
Mechanical and Manufacturing Engineering, Faculty of Engineering, Universiti Putra
Malaysia, Serdang, Selangor Darul Ehsan, Malaysia

Laboratory of Biocomposite, Institute of Tropical Forestry and Forest Products (INTROP),
Universiti Putra Malaysia, Serdang, Selangor, Malaysia

B. Parveez
Department of Manufacturing and Materials Engineering, Faculty of Engineering,
International Islamic University Malaysia, Kuala Lumpur, Malaysia

M. Yusuf
Chemical Engineering, Department, Universiti Teknologi PETRONAS,
Seri Iskandar, Perak, Malaysia

F. Masood
Electrical Engineering, Department, Universiti Teknologi PETRONAS,
Seri Iskandar, Perak, Malaysia

R. A. Ilyas
School of Chemical and Energy Engineering, Faculty of Engineering, Universiti Teknologi
Malaysia, Johor Bahru, Johor, Malaysia

Centre for Advanced Composite Materials (CACM), Universiti Teknologi Malaysia,
Johor Bahru, Johor, Malaysia

and aviation industries have long been pioneers in the development of new innovative materials frameworks and breakthroughs in their production. The utter pace at which this sector has advanced has been remarkable. However, the rising prices of air travel fuel have supervened in greater demand for lighter materials in the aerospace and aviation industries. In the aerospace sector, about 50% of the operating cost is used in fuel consumption. A heavier system needs extra energy to lift in the skies, thus adding up to the overall cost. Thus, the vital driving factors for aerospace materials progress are reduction in weight, application-specific desires, and minimal cost (Alam et al., 2021a; Ghori et al., 2018; Jayakrishna et al., 2018). Though metals, ceramics, and polymers are primarily used in the manufacture of aerospace structural and other components, developments in materials science, notably in composites science and technology, permitted the advancement of favorable modern materials for aerospace engineering. Composites are the materials system which is formed by blending two elements, namely, matrix and reinforcement, to use the valuable attributes of each component. If the reinforcing component in composite material is two or more than two, then it is referred as hybrid composites. Fiber-reinforced composites (FRCs), which are made by various types of matrices (e.g., ceramic, polymeric, metallic, etc.) with fibrous materials, have recently gained a significant attention in the aerospace industry (Rana & Fanguero, 2016). The key advantages of composite materials, due to which they are highly in demand in the aerospace sector, are lightweight, optimum stiffness and strength, high fatigue strength, resistance to corrosion, higher fuel efficiency, and improved performance. One of the most useful characteristics of hybrid composite materials is that they could be sandwiched with multiple layers with the fibers laid in different directions, allowing engineers to assemble the parts that meet strength and other mechanical properties requirements (Mouritz, 2012; Saha, 2016). Composite materials have been utilized in the aerospace sector in essential and secondary underlying parts including aircraft wings, floor beams, landing gear doors, fuselage, antenna dishes, engine cowls, rocket motor castings, center wing boxes, pressure bulkheads, vertical and horizontal stabilizers, etc. Some of these aerospace components such as wings, fuselage, landing gear, etc., are considered safety critical (Mouritz, 2012). Opportunities for global composites as a structural component in aerospace industry is represented in Fig. 16.1.

2 Recent Advances in Aerospace Composites

Demand of composite materials are increasing in both military and commercial aircraft design and manufacturing. Attributes such as escalating air travelers, increase in tourism, rise of low-budget carriers, and rising concern for airplane fuel efficiency remain likely to propel the flea market demand. The manufacturers are seriously investing in exploration and development to revolutionize lightweight and economical composites for aerospace industry with superior strength-to-weight

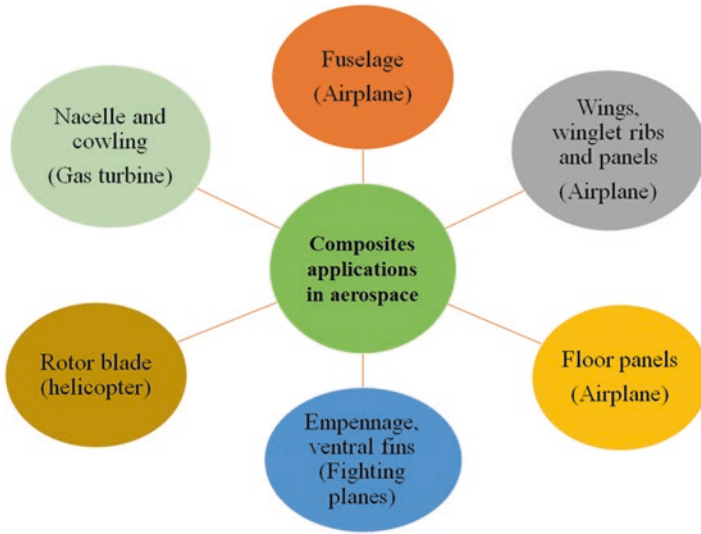


Fig. 16.1 Applications of composite materials in aerospace industry

ratio and outstanding impact strength. Additionally, the fuel costs likely to be nearly 30% of the carrier costs, and the new aircrafts are produced to reduce the fuel costs with improved and fuel-effective aerospace composites. Recent advancements in the composite material have highly influenced the aerospace industry, due to increment in flying performance.

Modern commercial airplanes, such as the Boeing 787 and Airbus A350, used a significant amount of composites to replace heavier metal elements to reduce fuel consumption. As an illustration, Boeing has raised usage of composite materials by a very considerable amount, from 1% (747) to 50% (new 787) of the structural weight of an aircraft (Mouritz, 2012; Zhang et al., 2018). Figure 16.2 depicts the trends in usage of composite materials in Boeing series aircraft.

The composite materials market is estimated to attain an estimated \$39.4 billion by 2025, and it was declined in 2020 due to global financial recession led by COVID-19. However, market witnessed recovery in the year 2021, and it is forecasted to reach an estimate \$39.4 billion by 2025 by a CAGR of 2% to 4% from 2020 to 2025 (Kazmierski, 2011). Figure 16.3 illustrates the trends and forecast for the global composites market. Composites have seen a significant increment material in the latest Boeing models, whereas aluminum-based alloys have seen a drop.

However, the COVID-19 virus outbreak has negatively impacted every industry including aircraft industry, leading to closure of aircraft manufacture and cancellation of fresh orders. The worldwide air traffic dived to nearly standstill in the mid-2020, thus influencing the aerospace industry market. Thus, diminished air traffic combined with the shutdown of airplanes manufacturing services will adversely affect the overall market size.

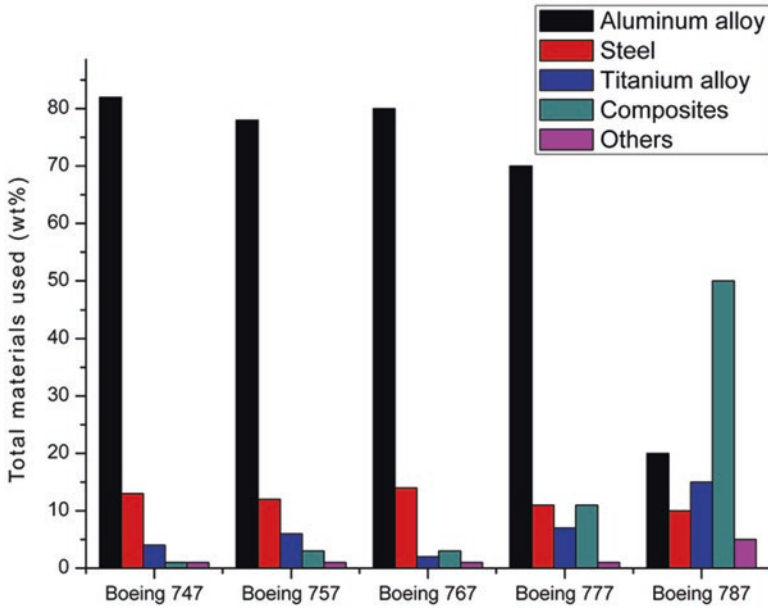


Fig. 16.2 The total amount of materials utilized in the Boeing series airplanes (Zhang et al., 2018)

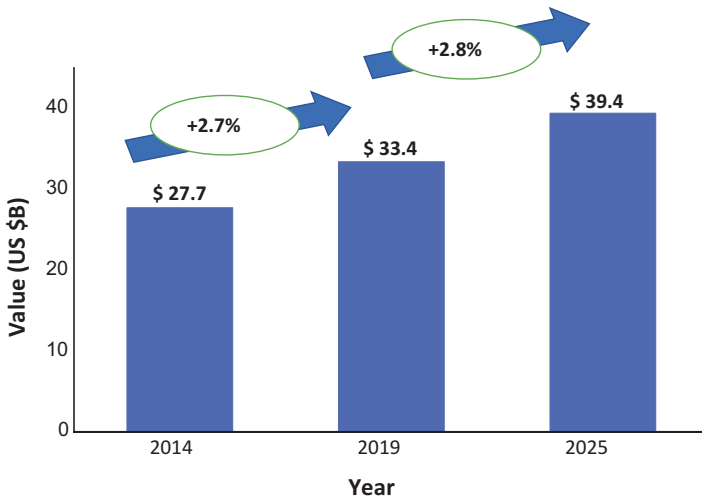


Fig. 16.3 Trends and forecast of global composites for the years 2014 to 2025 (Kazmierski, 2011)

2.1 Polymer Composites in Aerospace Industry

Polymer is a broad term which refers to a wide range of plastics, adhesives, and elastomers. The thermoplastics, thermosets, and elastomers are the three primary types of polymers. The most common thermoplastics-utilized aircraft composite are

polyether ether ketone (PEEK), polyphenylene sulfide (PPS), polysulfone (PSU), polyetherimide (PEI), and polycarbonate. The most widespread use for polymers is as a matrix phase of polymeric composites (Alam et al., 2017, 2020b; Ahmed et al., 2021). Composites for aerospace applications are produced in two fundamental material forms: sandwich and laminate composites. Applications of polymer composite materials are increasing in both military and commercial aircraft design and manufacturing. Polymeric materials have significant pros over the common metallic materials that are utilized in various aerospace components (Al-Oqla & Salit, 2017). One of the vital characteristics of polymer-based composites is being lightweight while offering specific strength, resulting in an overall weight reduction of roughly 20%–50%, and save energy due to lightweight consequently leading toward sustainability (Masood et al., 2021; Yusuf et al., 2021a, 2021b). Other features include the capacity to process materials quickly, meet high dimensional stability requirements, lower thermal expansion, and have good fatigue and fracture resistance (Alam et al., 2015; Begum et al., 2020). Modern air force fighter aircraft have lowered 30% of their weight utilizing polymer composite materials (Khandelwal & Rhee, 2020; Njuguna, 2016). The polymer-based composites contribute up to 80% in advanced launch vehicles designed for satellites and consist of numerous essential satellite components as the honeycomb structures, cylinder support structures, equipment panels, antennas, solar array substrates, etc. The rocket motor housing of the space shuttle's solid booster contains 30 tons of epoxy-graphite composites (Saba et al., 2014).

The use of fiber-polymer composites has been preceded by the passenger and military aircraft, particularly with fighter planes and helicopters. Carbon fiber-epoxy composites have been utilized in the fuselage and wings to improve the structural efficiency and minimize the weight. The 35% composite materials (carbon fiber-poxy and carbon fiber-bismaleimide) were used as structural material in the F-35 Lightning II as depicted in Fig. 16.4. The carbon, aramid fiber, and glass-based composites with improved service life has been used in rotor blades and fuselage of helicopters. A cross-sectional view of sandwiched type composite rotor blade made up of carbon and glass fibers is presented in Fig. 16.5.

The composite material utilized as a structural component in Airbus and Boeing aircraft is summarized in Table 16.1.

Although the application of composites is now common in commercial aircraft. The larger amount of FRPs have been used in the A380 Airplane manufactured by the European Airbus consortium. The panels of the wing trailing edge are composed of carbon and glass fiber-reinforced polymer composites utilizing a modern resin film infusion method (RFI), in which a resin film, layered between carbon and glass fabric layers, as soon as the laminate is laid up, melts once the heat is employed.

Figure 16.6 depicts the composites structural components of A380 airbus. Fiber-metal laminates (FML) are lightweight materials composed of thin bonded sheets of metal and fiber-polymer composite. This combination produces a material which is lightweight, better strength, and the higher fatigue resistant than the monolithic metal and has superior damage tolerance and impact strength than the composite

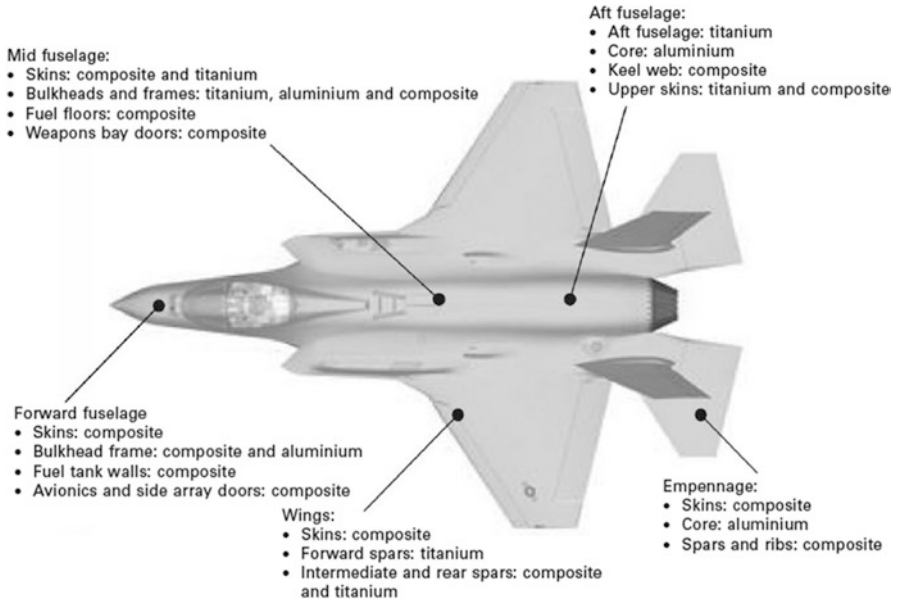


Fig. 16.4 Utilization of composites in the fighter aircraft F-35 Lightning II (Mouritz, 2012)

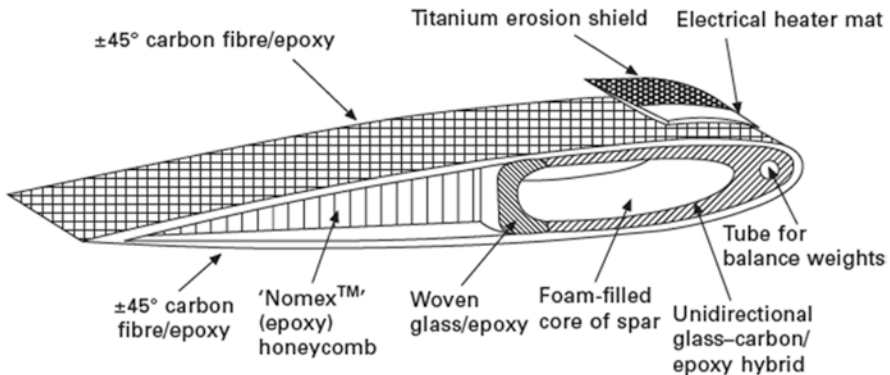


Fig. 16.5 Rotor blade of helicopter made up of sandwich composite material (Mouritz, 2012)

(Vogelansang & Vlot, 2000). The A380 fuselage crown is made up of a hybrid aluminium/glass-reinforced polymer system (GLARE) as shown in Fig. 16.7, which reduces weight, improves damage tolerance, and extends fatigue life (Alderliesten & Benedictus, 2008; Soutis, 2019).

Current civil aviation technologies have focused on replacing secondary structures with fiber composites reinforced with carbon, Kevlar, glass, or a combination of these materials. The matrix material is a thermosetting epoxy system with a 125 or 180 °C curing system and becoming more popular because of its superior resistance to environmental damage. The Boeing 757, 767, and 777, as well as the Airbus

Table 16.1 Airbus and Boeing airliners composite components (Mouritz, 2012)

Composite components	Airbus	Boeing
Fuselage and nose component		
Fuselage	A380	B787
Belly fairing	A380	
Rear pressure bulkhead	A340–600, A380	
Floor beams	A350, A400M	B787
Keel beam	A340–600, A380	
Nose cone	A340–600, A380	B787
Wing and empennage components		
Wing beams	A350, A380	B787
Wing skins	A350, A380	B787
Horizontal stabilizer	A340, A350	B737, B777
Vertical tailplane	A350, A380	B737, B777
Wing box	A380, A400M	B787
Engine components		
Nacelles	A340, A380	B787
Reversers	A340, A380, A350	B787
Reverser details	A380 (gutter fairing) A320 (reverse doors) A380 (reverse doors) A340 (reverse doors)	B787
Fan blades		B787
Cone spinners		B787

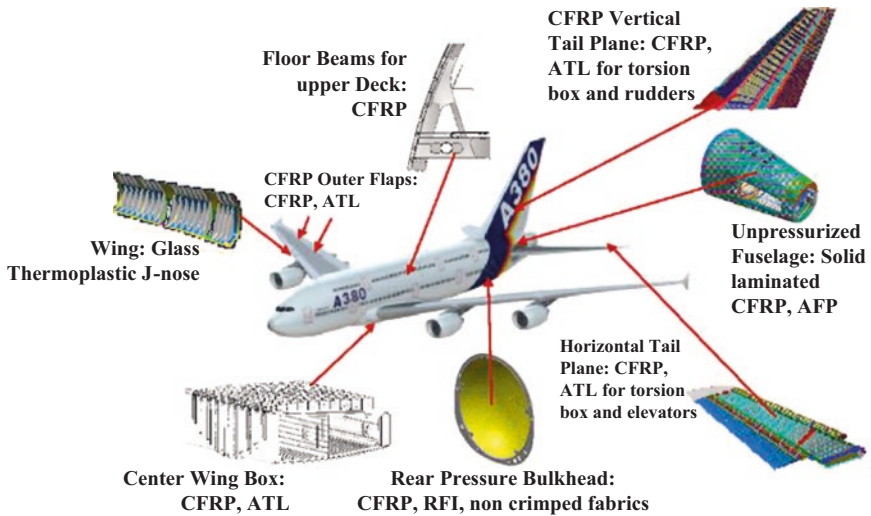


Fig. 16.6 The usage of polymer composites in Airbus A380 (Zhang et al., 2018)



Fig. 16.7 A380 composite tail assembly (empennage) with glare fuselage crown (Soutis, 2019)

A310, A320, A330, and A340 airplanes from Europe, are typical examples of widespread applications of composites in this fashion. The A310 contains a vertical stabilizer (8.3 m high by 7.8 m wide), a major aerodynamic and structural component, manufactured entirely from carbon fiber composite with a total weight savings of nearly 400 kg as compared to the monolithic Al alloy unit previously utilized. Furthermore, the CFRP fin box has only 95 parts (without fasteners) against more than 2000 parts in the metal unit, thus making it much easier to manufacture. The use of CFRP achieved new height with the Airbus model A350 XWB, which retains the usage of composites across the structure with total of 52% by weight. The wing of the aircraft is mostly made up of carbon fiber (CF), that includes the upper and lower covers, gauging 32 m in length and 6 m wide, enabling them among the largest single aircraft parts ever manufactured from CF (Mallick, 2007; De Rosa, et al., 2008). The A320 has increased the usage of composites to the flat stabilizer in addition to the variety of panels and secondary structural parts, resulting in an 800 kg weight reduction over Al alloy skin production. As an indication of the advantage of such weight reduction, it has been projected that 1 kg decrease in weight saves more than 2900 L of fuel each year. Airbus continues to use advanced composites from nose to tail in the A320neo narrow-body airliner, which was deployed by Lufthansa

on January 25, 2016, with enhanced fuel efficiency and significantly decreased noise and emissions (Paiva et al., 2009; Wang et al., 2011; Pimenta & Pinho, 2011).

Similarly, the fuselage, wings, doors, tail, and interior of the new Boeing 787 Dreamliner are made up of nearly 50% composite materials by weight (80 percent by volume). It was the world's first composite airliner due to its all-composite fuselage (its first flight was before the A350). Each fuselage barrel is made in one piece (about 45 feet long), obviating the necessity for more than 50,000 fasteners in traditional airplane construction. However, considerable assembly faults with the composite fuselage portions were identified, resulting in lengthy delays in the aircraft's delivery to the customer. Other technological concerns that needed to be handled are electromagnetic risks such as lightning strikes, because the polymer substance cannot conduct electric energy. Another key concern, primarily for the operator, will be damage assessment, as previously stated, which happens primarily internally and is challenging to detect. Soutis and coworkers have demonstrated the possibility of using a linear array of piezoelectric transducers for the detection of delamination and other modes of damage in composite plates (Diaz Valdes & Soutis, 2000; Diamanti et al., 2004, 2007; Soutis, 2005).

Polymer composites has been utilized in gas turbine engine parts including the front fan case, fan blades, nacelle, outlet guide vanes, nose cone, bypass ducts, spinner, and cowling as depicted in Fig. 16.8. However, the use of polymer composites is limited to engine parts which are required to operate lower temperature (<150 °C) to prevent heat distortion and softening.



Fig. 16.8 Gas turbine engine nacelle and cowling made up of composite material (Mouritz, 2012)

2.2 *Metal Composites in Aerospace Industry*

The aluminum industry has a long history of improving the performance of aerospace alloys and composites. Aluminum alloy serves as matrix in particulate alloy-based metal matrix composites (MMC), and the reinforcements are usually in the form of micron or nanoparticles (Alam et al., 2020a). Aluminum alloy-based composites have always been at the forefront of the research among metal matrix composites, and Al-based composites continued to exist as the most viable candidate to be investigated to make aircraft components sustainable (Ahmed et al., 2021; Alam et al., 2021b; Haider et al., 2015; Shozib et al., 2021; Surappa, 2003). This culminated in the advancement and continuous implementation of high-strength 7XXX alloys in commercial airplanes, for example, 7075, 7150, 7055, and 7449, chronologically as per the order of application (Seshappa & Anjaneya Prasad, 2020; Verma & Vettivel, 2018; Warner, 2006). The 7000 series of aluminum alloys exhibit higher strength relative to other aluminum alloy grades and are chosen for the manufacture of upper wing skins, vertical/horizontal stabilizers, and stringer (Boyer & Padmapriya, 2016; Dursun & Soutis, 2014; Sahu & Sahu, 2020). The fatigue resistance and compressive strength are important factors in the design of structural components of the upper wing (Williams & Starke, 2003). Table 16.2 shows a few of the key materials used in the aircraft's primary and secondary structural components. Because of their high strength-to-weight ratio, good machinability, and comparatively lower cost and higher strength, aluminum alloys like the 7075-T6 are commonly used in aircraft structures. The upper wing skin of the aircraft is made up of 7075-T7751. The aluminum alloys of 7000 series have also been heat treatable, and the Al-Zn-Mg-Cu variants engulf the highest strength to all aluminum alloys (Wanhill, 2013; Zhang et al., 2018). In view of aircraft design factors which is

Table 16.2 Types of major materials for structural and secondary components of aircraft (Saha, 2016)

Aluminum alloys	Titanium	Graphite composites	Fiberglass panels
Wing skin	Main landing gear beam	Floor panels	Rudder
Wing stringers	Inboard carriage	Main deck sidewall panels	Elevators
Wing spar web	Hydraulic tubing	Main deck ceiling panels	Floor panels
Wing spar chords	Lavatory attach fittings	Overhead storage bins	Upper and lower trailing edge panels
Wing ribs	Torque link	Winglet ribs and panels	Wing to body fairing
Wing channel events	APU fire wall		Ailerons
Wing to body chords	Inboard flap fitting		Spoilers
Fuselage skin			Trailing edge flap segments

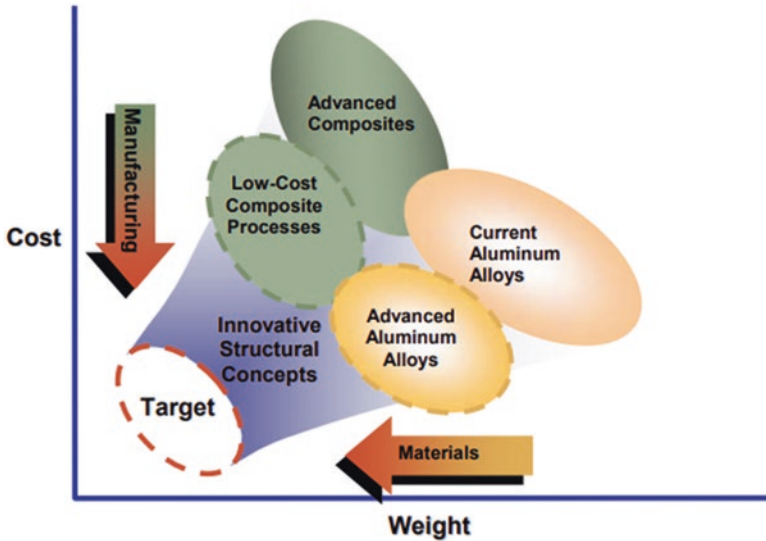


Fig. 16.9 Schematic diagram of cost-weight factors for selection of materials (Warren, 2004)

shown in schematic Fig. 16.9, there seem to be significant cost and weight problems for both aluminum and composites (Warren, 2004).

The applications of composites in the commercial aircraft industry has accelerated. In the 1972, Airbus started utilizing composite materials with considerable success for vertical fins for its A300 series aircraft (Marsh, 2014). In December 2009, a crucial development milestone achieved, as the second largest composite fuselage portion for A350 XWB as shown in Fig. 16.10, was completed in Hamburg, Germany (Marsh, 2010). Airbus Hamburg is liable for fuselage advancement and ultimate assembly, with an associate plant by producing some carbon fiber panels. Center fuselage manufacture takes place at the Aerolia (formerly Airbus) site in Saint-Nazaire, France, applying upper and lower casings offered by Spirit AeroSystems Inc. in North Carolina, USA. Nevertheless, Boeing also progressively made big changes in 2007 in the commercial aircraft industries by utilizing more than 50% composite materials in its new 787 aircraft, with 20% weight saving and better fuel economy (Puttegowda et al., 2018).

The A350 model has a wing and center wing box that significantly consist of composite (nearly 80%) than on earlier Airbus aircraft, and the fabrication arrangements reveal this. With mainstream manufacturing of the wings taking place in the UK, Airbus has increased its capability at Broughton, North Wales, with a new 46,000 square meter plant devoted to A350 XWB wing production. Wing layout and manufacturing go on at the Airbus UK site at Filton, Bristol. Manufacturing of the lower wing shells of the model A350 XWB is depicted in Fig. 16.11.

One notable application is the two ventral fins on the F-16 Fighting Falcon (Mouritz, 2012), which are located on the fuselage just behind the wings as depicted in Fig. 16.12.



Fig. 16.10 Fuselage section made up of composites for the A350 XWB in Hamburg, Germany (Marsh, 2010)



Fig. 16.11 Manufacture of lower wing shells of A350 XWB model (Marsh, 2010)

2.3 *Ceramic Composites in Aerospace Industries*

In aerospace industry, ceramics materials are primarily utilized in engine and exhaust systems, thermal control shields, and frameworks for hyper flying objects. Ceramics and ceramic-based composites that can endure high temperatures like 1600 °C are utilized to produce lightweight turbine elements that prerequisite less cooling air, for example, vanes, nozzles, blades, and combustion liners and components for the exhaust system that improve acoustic reduction and take a long-life recognition to their corrosion and abrasion resistance. Ceramic-based materials for aerospace applications comprise oxides (e.g., alumina), non-oxides (e.g., borides, carbides, and nitrides), glass ceramics, and ceramic matrix composites (e.g., SiC, TiC, Al₂O₃ composites). These materials are described by dimensional permanence



Fig. 16.12 Aluminum-SiC composites utilized in the ventral fins (circled) and fuel access doors of the F-16 Fighting Falcon (Mouritz, 2012)

over a span of temperatures and are improved to have excellent chemical resistance and mechanical strength. Ceramic matrix composites (CMC), for instance, silicon carbide (SiC), titanium carbide (TiC), silicon nitride (Si_3N_4), and aluminum nitride (AlN) matrix composite, have been extensively studied (Arif et al., 2017; Sommers et al., 2010) in current years due to their attractive characteristics, for example, high-temperature steadiness (to survive at higher operating temperature at 1500°C), extraordinary hardness (22 GPa for Al_2O_3 -based composite), and good corrosion resistance. Ceramic matrix composites are typically utilized in high-temperature segments in aircraft like exhaust nozzle. Ceramic matrix composites (CMCs)-containing products were utilized in an aircraft engine named as Leap in the year 2016. This engine was mounted in different aircraft model including the famous Boeing 737 Max. Carbon fiber-reinforced silicon carbide has been explored as an option for aircraft brakes, where the temperatures could approach 1200°C in emergency brake situations (Fan et al., 2016). Despite their advantages, MMCs have been shown to have poor fracture toughness (Walker et al., 2011). To address this shortcoming, some studies (Ahmad et al., 2015; Baig et al., 2018; Liu et al., 2013) have focused on incorporating nanomaterials such as the graphene and carbon nanotubes (CNT) to enhance the fracture toughness of ceramic-based composites. Nevertheless, Ahmad et al. (2015) stated the consequences of CNTs on the fracture toughness of ceramic matrix composite (CMC) are not consistent. The authors deem that graphene nanoplatelets (GNPs) are an effective substitute for CNTs in ceramic composite due to the comparable mechanical properties and well dispersibility to CMC. Walker et al.'s study showed that adding 1.5 vol percent graphene to a Si_3N_4 ceramic composite increased fracture toughness by 235%. The content of graphene platelets, on the other hand, should be limited at a crucial value. For instance, Liu et al. (2013) described the fracture toughness of alumina ceramic

composite improved to $4.49 \text{ MPa m}^{1/2}$ when graphene quantity increased from 0 to 0.38 vol% and subsequently dropped to $3.53 \text{ MPa m}^{1/2}$ when the content of graphene touched up to 1.33 vol%. Other uses of ceramics in the aerospace engineering include bearings, brakes, seals, and other wear-resilient components, automated thermal management structures, armor for helicopters, lightweight optical parts (e.g., silicon carbide mirrors), radiators for deep space vehicles, and windshield coatings. Ceramic components for the aerospace sector frequently have complex shapes, which has prompted the advancement of innovative forming technologies like 3D printing.

3 Challenges in the Development of New Advanced Aerospace Materials

3.1 Corrosion

One of the immense challenges in developing advanced materials for aerospace is corrosion. Corrosion is the chemical degradation of materials because of their reaction to the surroundings (Shaw & Kelly, 2006). Various types of corrosion developed in structural material, for instance, pitting corrosion, uniform corrosion, galvanic corrosion, crevice corrosion, can cause breakdown of parts when the left behind materials cannot sustain the applied loads. Based on the estimate, just up to 30% of the corrosion loss be able to be prevented by corrosion inhibition methods (Kesavan et al., 2012; Khan et al., 2020a). Various researches have examined the corrosion behaviors of various materials, allowing for the simple selection of materials for usage in various adverse environmental conditions. As a result, methods for preventing corrosion of structural materials have been devised, with coating being the most studied (Khan et al., 2020b; Shozib et al., 2021). The purposes of the coating are (1) to offer a regional corrosion barrier, (2) perform as a sacrificial anode, and (3) deliver solute ions (Presuel-Moreno et al., 2008). However, traditional corrosion coating has problem in supplying effective corrosion inhibitors. Therefore, the flaws cannot be protected by the transfer of inhibitor via the liquid corrosive stage (Ilevbare, 2000). Even though some more materials such as cerium sulfate (Kozhukharov et al., 2012), graphene (Chauhan et al., 2020), and oxides of rare earth elements (Chauhan et al., 2020) have been explored to enhance the protective performance, the mechanism of corrosion behavior and prevention method needs to be further studied and explored.

3.2 *Stress Corrosion Cracking (SCC) and Hydrogen Embrittlement (HE)*

Stress corrosion cracking (SCC) is deemed as extremely dangerous failure process as it can trigger gradual crack progression under a secure loading condition. When the size of crack approaches the critical value, the crack caused by SCC under the secure loading can bring about the abrupt breakdown of materials. SCC is caused by tripartite interaction, namely, mechanical stress, corrosive environment, and vulnerable alloy (Winzer et al., 2005). The processes of SCC and HE are pertinent because hydrogen primarily appears at the prongs of cracks in a wet atmosphere (Raja & Shoji, 2011). The department of SCC and HE in some vulnerable metallic materials, like steels (Shu et al., 2012), Mg, and Al-based alloys (Uematsu et al., 2012), have been extensively explored. Mg possesses great intrinsic dissolution propensity, whereas the contaminations and the second phase can behave as the regional cathodes to hasten corrosion by local galvanic, which promotes the vulnerability of Mg-based alloys to SCC. It is established that the separation of Mg along edges of grain can accelerate the hydrogen entry, expedite the transfer of hydrogen, and offer sites for grain border embrittlement by hydrogen chemisorption (Vasudevan & Doherty, 2012). Mg dispersing into Al generates the extremely anodal β phase of Al_3Mg_2 , which may enhance the propensity of Al-based alloys to SCC (Scotto D'Antuono et al., 2014). To avoid HE and SCC, some techniques have been explored in current years to enhance cracking resistance (Shu et al., 2012). Guo (2010) investigated some alloying components in Mg-based alloys and concluded that the Mn element positively affects the increment of SCC resistance. Peng et al. (2011) stated that SCC resistance could be enhanced with the escalation of size and gap between grain boundary precipitates (GBP) by lowering the proliferation rate and the intensity of atomic hydrogen. Analogous techniques like hypothetical and quantum mechanical models, current nano-research, and atomistical inspections have been established to examine the mechanism of SCC and HE.

3.3 *Fretting Wear*

Surface interactions and relative motion between the various engine components are responsible for the fretting wear. Fretting wear is triggered by small-amplitude (<100 μm) oscillatory motion between two contact parts (Tucker & Lindsey, 2002). Fretting wear be able to initiate cracks on the ravaged surface and decrease the fatigue life of the respective components (Tucker & Lindsey, 2002). Fretting wear appears in both aircraft engine parts and structural components such as the bolted connection, bearing shaft, and blade-disc assemblies (Majzoobi et al., 2011). Several researchers have performed tests looking for removal of the undesired fretting wear of aerospace materials. The most extensively studied technique is surface modification, for example, modification in hardness of the surface and adhesion

(Amanov et al., 2012; Zalnezhad et al., 2013). The difference in hardness among two mating duos can significantly influence the fretting wear. Sarhan et al. examined the relation of fatigue life and hardness on a hard anodized Al7075-T6 aerospace alloy. The outcomes revealed that fatigue life of the alloy was improved by improving the surface hardness to 393 HV in lower-stress regions (Sarhan et al., 2013). In another study, it is stated that toughness and bonding strength have more effect as compared to friction factor on fretting wear resistance of graphite-like carbon-coated Ti-based alloys (Du et al., 2014). Even though various materials have been examined for fretting behavior, the general theory explaining fretting behavior and prevention is still in its early stages. Further research should focus on the mechanism of fretting and the development of more effective strategies for reducing fretting resistance.

4 Conclusion and Future Developments

Aerospace materials have a significant impact on design, fabrication, in-service performance, and reliability. Every aspect of the airplane is affected by materials, including price, design selections, weight, performance of the flight, power of the engine and fuel efficacy, maintenance time during service, repair, and recycling and discarding at the end-of-life. The five most important types of structural materials are alloys of aluminum, Al-based composite, fiber-polymer composites (mainly carbon fiber-epoxy), high-strength steels, and titanium alloys. These materials contribute for more than 80% of the structural mass in most military and commercial aircraft. Fiber-metal laminates, magnesium alloys, and ceramic matrix composites are among the other materials utilized in modest amounts in the airframe and engines. In aerospace engineering, choosing the optimum material to meet the desired property requirements of an airplane component is crucial. Many design criteria are considered during materials selection of an aircraft, including whole-of-life ease of production; structure weight; operational efficiency; tolerance against fatigue and damage; electrical, thermal, radar absorption, and electromagnetic properties; and robustness against corrosion and other destructive processes.

The present review demonstrates that significant development has been made in the advancement of both aerospace structural materials and engine materials. For many years, Al-based alloys have been the leading choice in this industry due to their lightweight and well-known mechanical characteristics. The usage of composites (PMCs, MMCs, and CMCs) as an aerospace material has risen in recent years due to improved mechanical properties such as higher stiffness and specific strength as compared to Al-based alloys. However, the normal carbon fiber polymer matrix composites are more prone to suffer as of stress concentration. Furthermore, various obstacles limit the usage of Mg-based alloys, Ti-based alloys, and steels in specific aerospace applications. The decisive factor for aircraft engines necessitates the materials to offer appropriate densities, mechanical properties, and corrosion resistance at elevated temperatures. Ti-based alloys are the dominant materials in the

compressor area, where temperatures range from 500 to 600 degrees Celsius. The high-temperature (1400–1500 °C) turbine portion is made primarily of nickel-based superalloys. Challenges encountered in the advancement of recently advanced composites are corrosion, fretting wear, stress corrosion cracking, and hydrogen embrittlement.

In the outlook, particular mechanical characteristics and challenges such as corrosion, SCC, and fretting wear, will be the key drivers in the advancement and choice of next-generation aircraft structure materials. The airframe materials will be led by several materials, for example, aluminum-based alloys, steels, Ti-based alloys, and advanced composites. The following three areas should be the focus of future aircraft materials research: (i) Develop new advanced composites with excellent mechanical properties by various approaches, including refinement in microstructure, impurities control, and heat treatment processing; (ii) develop novel approaches such as composition alteration, microstructure control, and coating, to meet the challenges of metal alloys and polymers. Adopt more efficient stoppage technique for fretting wear of metal alloys, extra efficient forecast, and prevention approaches for corrosion, HE, and SCC of Mg-based alloys steels and Al-based alloys; (iii) develop hybrid composite materials by reinforcing two or more reinforcement in metal or polymer matrix. The future of aircraft engine materials will be centered on how to survive increased engine temperatures while maintaining adequate mechanical features. The following topics should be the focus of future material development: (i) further improvement in high-temperature resistance of Ti-based alloys by monitoring phases by alloying and heat treatment processing; (ii) develop innovative aerospace composites consuming self-healing polymers and other light metals; (iii) and develop the cutting-edge CMC with high fracture toughness by seeing through the augmented content of fibers and reinforcement like graphene nanoplatelet.

Acknowledgments The authors admirably acknowledge the support of the Mechanical Engineering Department, Universiti Teknologi Petronas, Malaysia, for all the necessary facilities and granting a Ph.D. scholarship under the GA scheme. Authors also would like to thank the Advanced Engineering Materials and Composites Research Center, Department of Mechanical and Manufacturing Engineering, Universiti Putra Malaysia, for informative support during the review.

References

- Ahmad, I., Yazdani, B., & Zhu, Y. (2015). Recent advances on carbon nanotubes and graphene reinforced ceramics nanocomposites. *Nanomaterials*, 5, 90–114.
- Ahmed T, Ya HH, Azeem M, et al (2021) Working of Functional Components in Self-Healing Coatings for Anti-Corrosion Green Tribological Applications. *Green Tribol* 155–172. <https://doi.org/10.1201/9781003139386-6>
- Ahmed, T., Ya, H. H., Mahadzir, S., et al. (2020). An overview: Mechanical and Wear properties of HDPE polymer nanocomposites reinforced with treated/non-treated inorganic nanofillers. *Advanced Manufacturing Engineering*, 231–241.

- Alam, A., Arif, S., & Ansari, A. H. (2017). Mechanical and morphological study of synthesized PMMA/CaCO₃ Nano composites. In *IOP conference series: Materials science and engineering* (p. 12222). IOP Publishing.
- Alam, M. A., Arif, S., & Shariq, M. (2015). Enhancement in mechanical properties of polystyrene-ZnO nanocomposites. *International Journal of Innovative Research in Advanced Engineering*, 6, 122–129.
- Alam, M. A., Sapuan, S. M., Ya, H. H., et al. (2021a). Application of biocomposites in automotive components: A review. In *Biocomposite and synthetic composites for automotive applications*. <https://doi.org/10.1016/B978-0-12-820559-4.00001-8>
- Alam, M. A., Ya, H. H., Ahmad, A., et al. (2021b). Influence of aluminum addition on the mechanical properties of brass/Al composites fabricated by stir casting. *Materials Today: Proceedings*.
- Alam, M. A., Ya, H. H., Azeem, M., et al. (2020a). Modelling and optimisation of hardness behaviour of sintered Al/SiC composites using RSM and ANN: A comparative study. *Journal of Materials Research and Technology*, 9, 14036–14050. <https://doi.org/10.1016/j.jmrt.2020.09.087>
- Alam, M. A., Ya, H. H., Hussain, P. B., et al. (2020b). Experimental investigations on the surface hardness of synthesized polystyrene/zno nanocomposites. In *Advances in manufacturing engineering* (pp. 345–352). Springer.
- Alderliesten, R. C., & Benedictus, R. (2008). Fiber/metal composite technology for future primary aircraft structures. *Journal of Aircraft*, 45, 1182–1189. <https://doi.org/10.2514/1.33946>
- Al-Oqla, F. M., & Salit, M. S. (2017). *Materials selection for natural fiber composites*. Woodhead Publishing.
- Amanov, A., Cho, I. S., Kim, D. E., & Pyun, Y. S. (2012). Fretting wear and friction reduction of CP titanium and Ti-6Al-4V alloy by ultrasonic nanocrystalline surface modification. *Surface and Coatings Technology*, 207, 135–142. <https://doi.org/10.1016/j.surfcoat.2012.06.046>
- Arif, S., Alam, T., Ansari, A. H., et al. (2017). Study of mechanical and tribological behaviour of Al/SiC/ZrO₂ hybrid composites fabricated through powder metallurgy technique. *Materials Research Express*, 4(7), 076511.
- Baig, Z., Mamat, O., Mustapha, M., et al. (2018). An efficient approach to address issues of graphene nanoplatelets (GNPs) incorporation in aluminium powders and their compaction behaviour. *Metals (Basel)*, 8, 1–16. <https://doi.org/10.3390/met8020090>
- Begum, S., Fawzia, S., & Hashmi, M. S. J. (2020). Polymer matrix composite with natural and synthetic fibres. *Advances in Materials and Processing Technologies*, 6, 547–564. <https://doi.org/10.1080/2374068X.2020.1728645>
- Boyer, R., & Padmapriya, N. (2016). Aircraft materials. *Reference Module in Materials Science and Materials*, 1–9. <https://doi.org/10.1016/b978-0-12-803581-8.01934-2>
- Chauhan, D. S., Quraishi, M. A., Ansari, K. R., & Saleh, T. A. (2020). Graphene and graphene oxide as new class of materials for corrosion control and protection: Present status and future scenario. *Progress in Organic Coatings*, 147, 105741.
- Diamanti, K., Hodgkinson, J. M., & Soutis, C. (2004). Detection of low-velocity impact damage in composite plates using lamb waves. *Structural Health Monitoring*, 3, 33–41.
- Diamanti, K., Soutis, C., & Hodgkinson, J. M. (2007). Piezoelectric transducer arrangement for the inspection of large composite structures. *Composites. Part A, Applied Science and Manufacturing*, 38, 1121–1130.
- Diaz Valdes, S. H., & Soutis, C. (2000). Health monitoring of composites using lamb waves generated by piezoelectric devices. *Plast Rubber Compos*, 29, 475–481.
- Du, D., Liu, D., Ye, Z., et al. (2014). Fretting wear and fretting fatigue behaviors of diamond-like carbon and graphite-like carbon films deposited on Ti-6Al-4V alloy. *Applied Surface Science*, 313, 462–469. <https://doi.org/10.1016/j.apsusc.2014.06.006>
- Dursun, T., & Soutis, C. (2014). Recent developments in advanced aircraft aluminium alloys. *Materials and Design*, 56, 862–871. <https://doi.org/10.1016/j.matdes.2013.12.002>
- Fan, S., Yang, C., He, L., et al. (2016). Progress of ceramic matrix composites brake materials for aircraft application. *Reviews on Advanced Materials Science*, 44, 313–325.

- Ghori, S. W., Siakeng, R., Rasheed, M., et al. (2018). The role of advanced polymer materials in aerospace. In *Sustainable composites for aerospace applications* (pp. 19–34). Elsevier.
- Guo, K. W. (2010). A review of magnesium/magnesium alloys corrosion and its protection. *Recent Patents on Corrosion Science*.
- Haider, K., Alam, M. A., Redhewal, A., & Saxena, V. (2015). Investigation of mechanical properties of Aluminium based metal matrix composites reinforced with sic & Al₂O₃. *International Journal of Engineering Research and Applications*, 5, 63–69.
- Ilevbare, G. O. (2000). Inhibition of pitting corrosion on aluminum alloy 2024-T3: Effect of soluble chromate additions vs chromate conversion coating. *Corrosion*, 56, 227–242. <https://doi.org/10.5006/1.3287648>
- Jayakrishna, K., Kar, V. R., Sultan, M. T. H., & Rajesh, M. (2018). Materials selection for aerospace components. In *Sustainable composites for aerospace applications* (pp. 1–18). Elsevier.
- Kazmierski, C. (2011). *Growth opportunities in global composites industry 2011–2016* (pp. 2012–2017). Lucintel, Inc..
- Kesavan, D., Gopiraman, M., & Sulochana, N. (2012). Green inhibitors for corrosion of metals: A review. *Chemical Science Review and Letters*, 1, 1–8.
- Khan, R., Ya, H. H., Pao, W., et al. (2020a). Effect of sand fines concentration on the erosion-corrosion mechanism of carbon steel 90° elbow pipe in slug flow. *Materials (Basel)*, 13. <https://doi.org/10.3390/ma13204601>
- Khan R, Ya HH, Pao W, et al (2020b) Investigation of maximum erosion zone in the horizontal 90 elbow. In *Advances in manufacturing engineering*. Springer, pp. 223–230.
- Khandelwal, S., & Rhee, K. Y. (2020). Recent advances in basalt-fiber-reinforced composites: Tailoring the fiber-matrix interface. *Composites. Part B, Engineering*, 192, 108011. <https://doi.org/10.1016/j.compositesb.2020.108011>
- Kozhukharov, S., Kozhukharov, V., Schem, M., et al. (2012). Protective ability of hybrid nano-composite coatings with cerium sulphate as inhibitor against corrosion of AA2024 aluminium alloy. *Progress in Organic Coatings*, 73, 95–103. <https://doi.org/10.1016/j.porgcoat.2011.09.005>
- Liu, J., Yan, H., & Jiang, K. (2013). Mechanical properties of graphene platelet-reinforced alumina ceramic composites. *Ceramics International*, 39, 6215–6221.
- Majzoobi, G. H., Hojjati, R., & Soori, M. (2011). Fretting fatigue behavior of Al7075-T6 at sub-zero temperature. *Tribology International*, 44(11), 1443–1451.
- Mallick, P. K. (2007). *Fiber-reinforced composites: materials, manufacturing, and design*. CRC press.
- Marsh, G. (2010). Airbus A350 XWB update. *Reinforced Plastics*, 54, 20–24.
- Marsh, G. (2014). Composites and metals—a marriage of convenience? *Reinforced Plastics*, 58, 38–42.
- Masood, F., Nallagownden, P., Elamvazuthi, I., et al. (2021). A new approach for design optimization and parametric analysis of symmetric compound parabolic concentrator for photovoltaic applications. *Sustainability*, 13, 4606.
- Mouritz, A. P. (2012). *Introduction to aerospace materials*. Elsevier.
- Njuguna, J. B. T.-L. C. S. (Ed.). (2016). *Woodhead publishing series in composites science and engineering* (pp. xiii–xvi). Woodhead Publishing.
- Peng, G., Chen, K., Chen, S., & Fang, H. (2011). Influence of repetitious-RRA treatment on the strength and SCC resistance of Al-Zn-mg-cu alloy. *Materials Science and Engineering A*, 528, 4014–4018. <https://doi.org/10.1016/j.msea.2011.01.088>
- Pimenta, S., Pinho, S. T. (2011). Recycling carbon fibre reinforced polymers for structural applications: Technology review and market outlook. *Waste Manag* 31, 378–392. <https://doi.org/10.1016/j.wasman.2010.09.019>.
- Presuel-Moreno, F., Jakab, M. A., Tailleart, N., et al. (2008). Corrosion-resistant metallic coatings. *Materials Today*, 11, 14–23.
- Puttegowda, M., Rangappa, S. M., Jawaid, M., et al. (2018). *Potential of natural/synthetic hybrid composites for aerospace applications*. Elsevier Ltd.

- Raja, V. S., & Shoji, T. (2011). *Stress corrosion cracking: Theory and practice*. Elsevier.
- Rana, S., & Figueiro, R. (2016). Advanced composites in aerospace engineering. In *Advanced composite materials for aerospace engineering* (pp. 1–15). Elsevier.
- Saba, N., Tahir, P. M., & Jawaid, M. (2014). A review on potentiality of nano filler/natural fiber filled polymer hybrid composites. *Polymers (Basel)*, 6, 2247–2273. <https://doi.org/10.3390/polym6082247>
- Saha, P. K. (2016). *Aerospace manufacturing processes*. CRC Press.
- Sahu, M. K., & Sahu, R. K. (2020). Experimental investigation, modeling, and optimization of Wear parameters of B4C and Fly-ash reinforced aluminum hybrid composite. *Frontiers of Physics*, 8, 1–14. <https://doi.org/10.3389/fphy.2020.00219>
- Sarhan, A. A. D., Zalnezhad, E., & Hamdi, M. (2013). The influence of higher surface hardness on fretting fatigue life of hard anodized aerospace AL7075-T6 alloy. *Materials Science and Engineering A*, 560, 377–387. <https://doi.org/10.1016/j.msea.2012.09.082>
- Scotto D'Antuono, D., Gaies, J., Golumbskie, W., & Taheri, M. L. (2014). Grain boundary misorientation dependence of β phase precipitation in an Al-mg alloy. *Scripta Materialia*, 76, 81–84. <https://doi.org/10.1016/j.scriptamat.2014.01.003>
- Seshappa, A., & Anjaneya Prasad, B. (2020). Characterization and investigation of mechanical properties of aluminium hybrid nano-composites: Novel approach of utilizing silicon carbide and waste particles to reduce cost of material. *Silicon*. <https://doi.org/10.1007/s12633-020-00748-z>
- Shaw, B. A., & Kelly, R. G. (2006). What is corrosion? *Electrochemical Society Interface*, 15, 24–27.
- Shozib, I. A., Ahmad, A., Rahaman, M. S. A., et al. (2021). Modelling and optimization of microhardness of electroless Ni–P–TiO₂ composite coating based on machine learning approaches and RSM. *Journal of Materials Research and Technology*, 12, 1010–1025.
- Shu, J., Bi, H., Li, X., & Xu, Z. (2012). The effect of copper and molybdenum on pitting corrosion and stress corrosion cracking behavior of ultra-pure ferritic stainless steels. *Corrosion Science*, 57, 89–98. <https://doi.org/10.1016/j.corsci.2011.12.030>
- Sommers, A., Wang, Q., Han, X., et al. (2010). Ceramics and ceramic matrix composites for heat exchangers in advanced thermal systems—A review. *Applied Thermal Engineering*, 30, 1277–1291.
- Soutis, C. (2005). Fibre reinforced composites in aircraft construction. *Progress in Aerospace Science*, 41, 143–151.
- Soutis, C. (2019). Aerospace engineering requirements in building with composites. In: *Polymer composites in the aerospace industry*. Elsevier, pp. 3–22.
- Surappa, M. K. (2003). Aluminium matrix composites: Challenges and opportunities. *Sadhana*, 28, 319–334. Department of Metallurgy, Indian Institute of Science, Bangalore 560 012, India.
- Tucker, N., & Lindsey, K. (2002). *Introduction to automotive composites*.
- Uematsu, Y., Kakiuchi, T., & Nakajima, M. (2012). Stress corrosion cracking behavior of the wrought magnesium alloy AZ31 under controlled cathodic potentials. *Materials Science and Engineering A*, 531, 171–177. <https://doi.org/10.1016/j.msea.2011.10.052>
- Vasudevan, A. K., & Doherty, R. D. (2012). *Aluminum alloys--contemporary research and applications: Contemporary research and applications*. Elsevier.
- Verma, N., & Vettivel, S. C. (2018). Characterization and experimental analysis of boron carbide and rice husk ash reinforced AA7075 aluminium alloy hybrid composite. *Journal of Alloys and Compounds*, 741, 981–998. <https://doi.org/10.1016/j.jallcom.2018.01.185>
- Vogelansang, L. B., & Vlot, A. (2000). Development of fibre metal laminates for advanced aerospace structures. *Journal of Materials Processing Technology*, 103, 1–5.
- Walker, L. S., Marotto, V. R., Rafiee, M. A., et al. (2011). Toughening in graphene ceramic composites. *ACS Nano*, 5, 3182–3190.
- Wanhill, R. J. H. (2013). *Aerospace applications of aluminum-lithium alloys*. Elsevier.
- Wang, R-M., Zheng, S-R., Zheng, Y. G. (2011). *Polymer matrix composites and technology*. Elsevier.

- Warner, T. (2006). Recently-developed aluminium solutions for aerospace applications. *Materials Science Forum*, 519–521, 1271–1278. <https://doi.org/10.4028/www.scientific.net/msf.519-521.1271>
- Warren, A. S. (2004). Developments and challenges for aluminum—A boeing perspective. In: *Materials forum* (pp. 24–31).
- Williams, J. C., & Starke, E. A. (2003). Progress in structural materials for aerospace systems. *Acta Materialia*, 51, 5775–5799. <https://doi.org/10.1016/j.actamat.2003.08.023>
- Winzer, N., Atrens, A., Song, G., et al. (2005). A critical review of the stress corrosion cracking (SCC) of magnesium alloys. *Advanced Engineering Materials*, 7, 659–693.
- Yusuf, M., Farooqi, A. S., Al-Kahtani, A. A., et al. (2021a). Syngas production from greenhouse gases using Ni–W bimetallic catalyst via dry methane reforming: Effect of W addition. *International Journal of Hydrogen Energy*.
- Yusuf, M., Farooqi, A. S., Alam, M. A., et al. (2021b). Response surface optimization of syngas production from greenhouse gases via DRM over high performance Ni–W catalyst. *International Journal of Hydrogen Energy*.
- Zalnezhad, E., Sarhan, A. A. D., & Hamdi, M. (2013). Investigating the fretting fatigue life of thin film titanium nitride coated aerospace Al7075-T6 alloy. *Materials Science and Engineering A*, 559, 436–446. <https://doi.org/10.1016/j.msea.2012.08.123>
- Zhang, X., Chen, Y., & Hu, J. (2018). Progress in aerospace sciences recent advances in the development of aerospace materials. *Progress in Aerospace Science*, 97, 22–34. <https://doi.org/10.1016/j.paerosci.2018.01.001>

Chapter 17

Flexural and Impact Properties of Flax/ Kevlar and Jute/Carbon Hybrid Fibers-Reinforced PLA Nanocomposites for Aircraft Interior Applications



A. L. A'Liya, S. Nur Aqilah, Norkhairunnisa Mazlan, and R. Natasha

1 Introduction

Many engineering applications widely use composite structures due to their unique properties suitable to replace the traditional metals. Extensive use of composites in industries such as aerospace and military has increased significantly on using advanced composite with improved mechanical properties such as high strength-to-weight ratio, high fatigue and wear resistance, and formability of complex shapes (Banakar et al., 2012; Subramani et al., 2016). For example, most aircrafts nowadays were made of more than 50% of composite materials. The main reason for using composite materials is their lightweight properties, including reducing CO₂ emission and improved fuel consumption. In the meantime, the utilization of nanoscale particles has been taken recently to boost the properties of composite materials. The synergistic combination of functional fillers with the highly processed polymer affects the composite systems, offering various functionalities that

A. L. A'Liya · S. Nur Aqilah
Institute of Nanoscience and Nanotechnology (ION2), Universiti Putra Malaysia,
Serdang, Selangor, Malaysia

N. Mazlan (✉)
Institute of Advanced Technology (ITMA), Universiti Putra Malaysia,
Serdang, Selangor, Malaysia

Aerospace Malaysia Research Center (AMRC), Universiti Putra Malaysia,
Serdang, Selangor, Malaysia

Department of Aerospace Engineering, Faculty of Engineering, Universiti Putra Malaysia,
Serdang, Selangor, Malaysia
e-mail: norkhairunnisa@upm.edu.my

R. Natasha
Institute of Tropical Forestry and Forest Products (INTROP), Universiti Putra Malaysia,
Serdang, Selangor, Malaysia

enlarge their application area (Subramani et al., 2016; Shilpa et al., 2017). Several unique properties of the nanocomposites including high elastic modulus (Alsubari et al., 2021; Kumar et al., 2020; Nurazzi et al., 2021; Omran et al., 2021; Rozilah et al., 2020; Saber-Samandari & Afaghi Khatibi, 2006, 2007), high tensile strength (Saber-Samandari et al., 2007), thermal resistance, flame retardancy, high fracture toughness (Xu & Van Hoa, 2008), dimensional stability and optical properties (Utracki, 2004), and water resistance (Zhou et al., 2008) can be increased by adding a small amount of nanofillers.

There is a significant potential for fiber-reinforced polymers such as lightweight, high strength-to-weight ratio, improved dimensional stabilities, and excellent weathering stabilities (Kendall, 2006). On the other hand, the applications of fiber-reinforced polymer composites were limited to smaller parts such as the bridge deck, reinforcement bars, girders, handrails, or staying cables (Mourit & Gibson, 2006; Qian et al., 2009; Subramanian & Senthilvelan, 2011).

Recently, the use of traditional glass, aramid, or carbon fiber composites has been debated critically because of increased environmental awareness. In addition, the lack of resources on crude oil has escalated the global demand for synthetic-based materials (Ilyas et al., 2019). Hence, this leads to the awareness of global communities to reduce the dependency on synthetic materials, which subsequently urged the plastic manufacturing industry to search for new alternatives and immediate actions (Jaafar et al., 2018). Apart from that, the application of the conventional synthetic-based composite has induced various environmental issues such as waste disposal and environmental sustainability (Merzuki et al., 2019; Sanyang et al., 2018).

Several researchers have proposed necessary actions to engulf this problem, including substituting natural-based material and the application of recycled material from waste products (Nasruddin et al., 2018; Ramli et al., 2018). Recent efforts at research and development have resulted in new, natural resources-based products. The development of natural fiber composites has been a topic of concern because of their efficiency in composite materials (Danso, 2017; Kiran et al., 2019). Furthermore, as a sustainable structural material, natural fibers have excellent potential choices with low density, biodegradability, ability to increase the composite strength, lightweight, low abrasiveness, reduced material cost, and a low environmental impact (Pinto et al., 2014; Seki, 2009). Therefore, a massive range of natural fiber applications in composite materials can be found, for instance, housing construction materials, automotive parts, food packaging, and furniture (Berhanu et al., 2014a, 2014b; Hossain et al., 2014).

More important achievements in research and development (R&D) include natural fiber-reinforced polymers made with natural fiber such as flax, hemp, kenaf, jute, and cotton fibers (Mohanty et al., 2000; Mazlan et al., 2021). The natural fibers themselves are fiber-reinforced structures that influence their mechanical properties by the content of cellulose and microfibril angle (Aisyah et al., 2021; Ilyas et al., 2021a; 2021b; Sanadi et al., 1986). Natural fibers have three types of sources: animals, plants, and minerals. However, plant fiber is the most popular and widely used

because of its availability, variety, and costs. Flax fiber is an example of an alternative to synthetic fiber (Bos et al., 2006). The unique characteristics of renewable natural materials, including environmental efficiencies, extensive availability, cost efficiency, and biodegradability, are desirable for different applications such as the boat and automotive sector as well as infrastructures (Suriani et al., 2021a, 2021b, 2021c, 2021d, 2021e; Ticoalu et al., 2010). Flax fibers produce the mechanical characteristics in which the specific strength of the tension example is comparable to glass fibers (Wambua et al., 2003). Therefore, it makes flax fibers a perfect choice to substitute conventional glass fibers for polymer composite reinforcement (Angelov et al., 2007; Pandey et al., 2010; Rajan et al., 2012). Due to its good mechanical properties, the application of natural fibers as reinforcements in polymer composites has increased over time. Recent developments in natural composites made it more important to enhance the mechanical properties of natural polymers, and the use of woven fibers as a reinforcement is one solution. Woven fibers strengthen the packaging of higher fibers and are stronger by mechanical interlocking (Alavudeen et al., 2011).

Widely used biodegradable polymers are aliphatic polyesters. Examples of aliphatic polyesters are polylactic acid (PLA), polyglycolic acid (PGA), polycaprolactone (PCL), and polyhydroxy butyrate (PHB) (Awal et al., 2015; Hossain et al., 2014; Ilyas et al., 2021a, 2021b; Nazrin et al., 2020; Sairy et al., 2020). PLA was known to have the most significant commercial potential due to its pleasing aesthetic, mechanical strength, better thermal plasticity, biocompatibility, and easy processability in most equipment (Hossain et al., 2014). Polylactic acid (PLA) is extracted from renewable sources by fermentation under controlled conditions of a carbohydrate source, including sugarcane, corn sugar, and potato (Avérous, 2008; Murariu & Dubois, 2016). Du et al. (2014) investigated fabrication of polymer composites with polylactic acid (PLA) and cellulosic natural fibers. The wet-laid fiber sheet method with film stacking composite was used for the fabrication process of the composite. The highest tensile strength result shows were about 121 MPa compared to the neat PLA. Then, a study conducted by Hinchcliffe et al. (2016) has shown improvement in the mechanical properties of natural fiber-reinforced polylactic acid. They observed about 14% and 10% increased for flexural strength and rigidity, respectively, and in addition, about 116% and 62% increased for tensile strength of composite and unreinforced PLA, respectively. Ahsan et al. (2019) observed an improvement of about 59.32% of tensile strength, and 100% of elongation were observed for nano-fibrillated kenaf cellulose (NFKC)-PLA composite, compared to unreinforced PLA. Initially, the nano-fibrillated kenaf cellulose (NFKC) was derived from kenaf fiber after chemical-mechanical treatments. Then, it was introduced into polylactic acid (PLA) as reinforcements to improve the mechanical and morphological properties of the biocomposites. Therefore, it can be concluded that implementing biopolymers such as PLA is an alternative in reducing the dependency on the nonbiodegradable polymer used in various sector applications.

1.1 *Natural Fiber*

1.1.1 **Flax Fiber**

Several applications of composites reinforced by natural fibers have attracted the attention of the composites community in the past years. The properties of natural fiber composites have been considered for a wide range of natural fibers, including flax, jute, hemp, banana, bamboo, pineapple, agave, and rubberwood, in several different studies. In order to achieve better reinforcement of polymer matrix composites, it is crucial to relate their characteristics to the properties of the fiber, such as fiber geometry, fiber orientation, porosity, and mechanical and physical properties.

There are many different types of natural fibers with good mechanical properties, one of which is flax fiber. Murali and Pannirselvam (2011) found that the specific tensile strength of flax fiber is comparable to that of glass fiber. Flax fiber can be used in many forms and configurations such as mats, roving, fabrics, and monofilaments. In term of cost, flax fibers have relatively low cost compared to using glass fibers. There are adverse effects of using glass fibers, as reported by Bos (2004), where the fibers can cause lung cancer, whereas there is no such problem with natural fibers. Thus, flax fiber is suitable fiber to replace conventional glass fiber as reinforcement of composite materials (Pandey et al., 2010; Wu et al., 2016).

Natural fiber like flax has unique properties that are fundamentally different from glass and other synthetic fibers. The properties of flax fiber are majorly influenced by its hydrophilicity. This characteristic leads to poor matrix adhesion and high water absorption due to free hydroxyl and polar groups presence in the fiber itself (Pickering et al., 2016; Yan et al., 2014). The interface and adhesion properties to the polymer matrix can be improved through several various chemical treatments, such as alkaline treatment, silane treatment, benzoylation, acetylation, and enzymatic treatment (Alix et al., 2012; Morrison Iii et al., 2000; Xie et al., 2010; Zhu et al., 2015). Wax is one of the chemical substances in the fiber. The ratio of cellulose will be increased by eliminating the substances with chemical treatment. The mechanical properties of the fiber were found to be improved while the water absorption was found to decrease by chemical treatments (Morrison Iii et al., 2000; Yan et al., 2014). Huner (2018) discovered that fiber treatment with sodium hydroxide (NaOH) improved the properties of epoxy matrix composite. Van de Weyenberg et al. (2006) stated that fiber treatment with NaOH has high fiber swelling compared to treatment with potassium hydroxide (KOH) or lithium hydroxide (LiOH). Nayak et al. (2017) investigated that alkaline treatment for about 1 h not only is successful in removal of pectins and hemicellulose but also managed to improve the tensile strength properties of the flax/polyester composite.

1.1.2 Jute Fiber

The genus *Corchorus*, generally referred to as jute, comprises over 170 species, all of which are annual fibrous plants (Maity et al., 2012). Jute is one of the examples of natural fiber. The jute fiber is obtained from the jute plant's stem. Jute fiber attracts much interest due to its high tensile strength, modulus, and high cellulose content (Danso, 2017). Jute fiber can also be considered an alternative material for replacing synthetic fiberglass and carbon fiber due to its good specific mechanical properties, biodegradability, low cost of production, and low density (Danso, 2017). Berhanu et al.'s (2014a, 2014b) study shows that reinforcement of jute fiber significantly enhanced the mechanical characteristics of composites based on polypropylene. They also observed that as the jute reinforcement is added up to 40 wt.%, the mechanical properties increased significantly. According to Shanmugam (Shanmugam & Thiruchitrambalam, 2013), the alkaline treatment on jute fiber improves its interfacial bonding with polymer matrix and subsequently improves mechanical properties.

The main component that provides high tensile and flexural strength to jute fiber is cellulose. The cellulose content in jute fiber was found to be in the range of 61–71% from overall constituents (Amir et al., 2017; Zafar et al., 2016). With a large number of impurities like pectin, lignin, hemicellulose, oily, and waxy substances that covered the fiber surface, it reduces the compatibility of the hydroxyl groups to react with the hydrophobic polymer matrices. Thus, only mechanical interlocking adhesion can be formed with the nonpolar matrices because the hydroxyl groups could not react with the polar matrices (Seki, 2009). In addition, presence of impurities in the fiber will also lead to poor interactions between fibers and matrix. To overcome this problem, surface treatment was carried out to improve the adhesion of the fiber-matrix while subsequently removing the impurities that covered the fiber surfaces (Zafar et al., 2016).

Gopinath et al. (2014) examined that jute treated with 5 wt.% NaOH performs better tensile strength than jute treated with 10 wt.% NaOH. They concluded that jute fiber treated with low concentrations of NaOH exhibit better mechanical properties as it improved the fiber interactions in the matrix. Gopinath et al. (2014) also added that few factors affected the mechanical properties, such as voids, fiber agglomeration, fiber-matrix adhesion, dispersion, and fiber orientation. In addition, the impurities on jute fibers were found to be eliminated with NaOH treatment (Seki, 2009). Hossain et al., (2014) investigated that Young's modulus of the polymer composite filled with treated jute fiber was higher up to 17% than the untreated jute polymer composite. They suggested that alkali treatment on the jute fiber can leach out the fatty acids and other lignin components, which increased the amorphous region in the jute.

1.2 Synthetic Fiber

1.2.1 Kevlar Fiber

Fiberglass, including E and S glass, carbon fiber, boron, and Kevlar/aramids, are typical synthetic fibers. Kevlar is widely used in military and aerospace applications. High-strength, stiff, and tough Kevlar fiber properties make the fiber a suitable reinforcing fiber composite for aircraft wing and tail. Kevlar is five times stronger than steel, is lighter, and has high thermal stability and impact resistance. In addition, the synthesis fibers are much more durable, strong, easier to maintain, and washable than natural fibers.

1.2.2 Carbon Fiber

Carbon fiber is composed of carbon atoms bonded together to form a long chain. The fibers are incredibly stiff, strong, and light and are used in many processes to create excellent structure materials. Carbon fiber material comes in a variety of “raw” building blocks, including yarns, unidirectional weaves, braids, and several others, which are in turn used to create composite parts. Carbon fiber is strong in which the properties are comparable to steel, and the weight is close to plastic.

Carbon fiber is one of the most common reinforcements for polymer matrix composites. This reinforcing material is well recognized as it has superior properties such as high mechanical strength, high elasticity modulus, good flame resistance, and low density. Therefore, carbon fiber has numerous applications in engineering, for instance, construction, sports equipment, ships, aircraft, and automobile. Carbon fiber has a density of about 1.6 g/cm^3 , and reinforcing in a polymer matrix could notably result in a weight decrease of 40–60% (Das, 2001). However, carbon fiber failed in a brittle manner due to its high strength and modulus properties. Thus, carbon fibers are very susceptible to stress concentration. A strategy to strengthen the carbon fiber weakness as reinforcement in polymer composite is to combine it with ductile fiber. Combining two different fibers or reinforcement materials is called hybridization. Furthermore, the composite processing cost of using carbon fiber solely can be reduced when combined with high strength and cheaper fiber.

Zhang et al. (2012) reported that ideally, a hybrid composite of carbon/glass fiber laminates with 50% carbon fiber reinforcement provides the best flexural characteristics as the carbon fiber layers were placed at the exterior (top or bottom) of the composite. However, experimentally shear stress existed in the specimens, which lead to a slight reduction in flexural properties. They also added that the addition of different fibers with different properties would fail in different manners. Thus, the brittle catastrophic failure of carbon fiber can be avoided, and composite toughness could be enhanced with fiber hybridization.

1.3 *Polylactic Acid (PLA)*

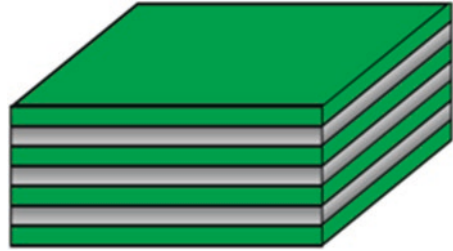
PLA is the aliphatic polyester and biocompatible thermoplastic that is semicrystalline or completely amorphous. PLA, or polylactic acid, or sometimes referred to as polylactide is currently the most promising and popular material with the best choice for growth and green material that is environmentally friendly. PLA provides excellent properties, including high strength and stiffness, and is used in various applications, including food packaging, degradable plastic bags, and automotive applications. Polylactic acid (PLA) is derived from 100% renewable resources of a naturally occurring organic acid, i.e., lactic acid. It is well known as a biodegradable, highly versatile aliphatic polyester (Van de Weyenberg et al., 2006). PLA melts at low temperature, in the range of 180–220 °C, with a glass transition temperature of 60–65 °C. Moreover, the formation of non-harmful and nontoxic compounds from PLA and its composites results from simple hydrolysis of the ester backbones, which can degrade quickly, making PLA degradable. Recycling of PLA to its monomer can be done by using hydrolysis or thermal depolymerization. PLA matrix can quickly be processed by injection molding, casting, extrusion, and spinning. Thus, PLA is an ideal polymeric material for different practical applications worldwide based on its biocompatibility, complete biodegradability, and the non-toxic nature of its degradation products (Drumright et al., 2000).

1.4 *Hybrid Composite*

A hybrid composite is a combination of two or more types that reinforced a prevalent matrix. Although hybrid composites can be generated in many different schemes, most studies on their mechanical characteristics were restricted to settings in which fibers were closely blended or purposely arranged within the matrix. A general rule of mixtures method may be used to quantify a material property concerning the volume concentration of its constituents when assessing the mechanical characteristics of hybrids (Dong et al., 2012; Kushnoore et al., 2019). In several lightweight and high-strength applications, hybrid composite materials effectively replaced traditional materials. The growth of composite materials increases their efficiency by reinforcing two or more fibers in a single polymer, resulting in the advanced material scheme called hybrid composite with a wide variety of material characteristics (Jagannatha & Harish, 2015).

In general, the purpose of the hybridization of two different types of fibers in a composite is to maintain the advantages of both fibers and alleviate some disadvantages. For instance, replacing carbon fibers in the middle of a laminate with cheaper glass fibers can significantly reduce the cost while the flexural properties remain unaffected. If a hybrid composite is loaded in the fiber direction in tension, the brittle fibers will fail before the ductile fibers. This fracture behavior can be used for health monitoring purposes or as a warning sign before final failure. The two types

Fig. 17.1 Interlayer or layer-by-layer



of fibers are typically referred to as low elongation (LE) and high elongation (HE) fibers. The first fiber to fail is usually the LE fiber. The HE fiber does not necessarily have a significant failure strain, but it is always more extensive than LE fiber. The LE and HE fibers can be combined in many different configurations. Interlayer configuration visualized in Fig. 17.1 shows the layers of two fiber types stacked onto each other. This configuration is the simplest and cheapest method for producing a hybrid fiber composite in which the two different fibers were mixed within the layers (Swolfs et al., 2014).

1.5 Nanofiller

The improvement in material properties has attracted significant attention of polymer nanocomposites in industry and academics compared to conventional micro or virgin polymer and macro composites (Bharadwaj, 2001; Liu et al., 2011; Pavlidou & Papaspyrides, 2008; Zeng et al., 2005). The inclusion of high-aspect ratio, nano-size fillers in polymer nanocomposite strongly modifies the polymer's macroscopic properties. Outstanding mechanical properties of polymer nanocomposites are known with minimal addition of nanoparticles comparable to its strength improvement, higher modulus elasticity (Liu et al., 2011; Pavlidou & Papaspyrides, 2008; Zeng et al., 2005), barrier resistance (Bharadwaj, 2001), retardancy of flame (Bourbigot et al., 2000; Laoutid et al., 2009), and others due to the enormous surface area between nanofiller and polymer matrix interaction. Furthermore, nanoparticles have been widely used in polymer matrix composites as reinforcements because of their convenient properties compared to corresponding micro fillers, including ease of processing and advanced materials improvement at 1–5% volume fractions (Sprenger, 2013).

Heydari-Meybodi et al. (2016) reported that the addition of nanoparticles into the polymer matrix could avoid delamination by improving the toughness properties of the polymer matrix. As shown in Fig. 17.2, the crack propagation growth can be delayed with the inclusion of nanoclay. The nanoclay bridging between matrix cracks and toughened the matrix structure. Evolution on the fiber breach, delamination, and matrix cracking can be seen from low-velocity impact analysis. High contact stresses from low impact velocity analysis will initiate matrix cracks. Thus, a

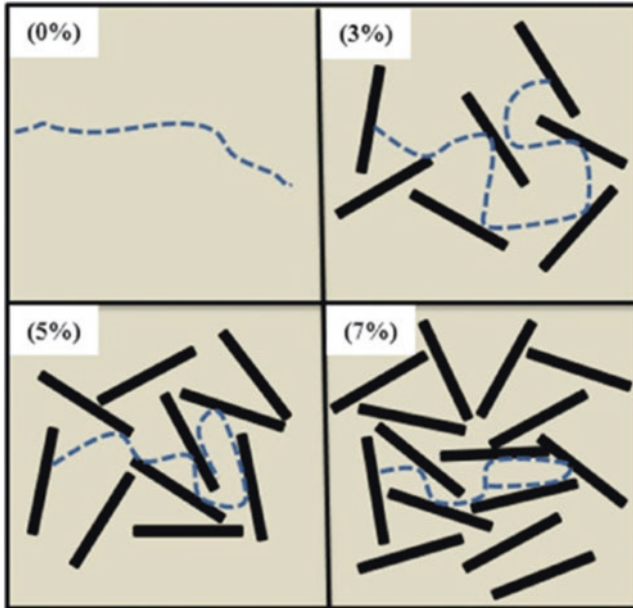


Fig. 17.2 Theoretical picture of more delimited crack propagation with increasing the weight percentage of nanoclay: (a) 0 wt.%, (b) 3 wt.%, (c) 5 wt.%, and (d) 7 wt.% (the crack growth path shows by dotted lines, while the black rectangles show the nanoclays) (Heydari-Meybodi et al., 2016)

pine tree damage propagation through the other plies from the top surface to the bottom can be observed (Silberschmidt, 2016).

The composite's density can be increased by filler concentrations, which will cause the deterioration in properties between the filler and the organic material through interfacial incompatibility. In addition, as the filler content increases, the processability will also decrease. Therefore, in this chapter, the research work is focused on finding the optimum concentration of graphene in jute/flax hybrid PLA nanocomposite.

2 Methodology

In this chapter, woven flax fiber and carbon fiber were used as received from Mecha Solve Engineering. The polylactide acid (PLA) was purchased from NatureWorks LLC product (Ingeo biopolymer 7001D). NaOH was purchased from R&M Chemicals and used for surface treatment onto flax and jute fiber, and chloroform was used as a solvent. Graphene was purchased from BTCorp, India, and used as nanofiller in the hybrid composite. Alkaline treatment was conducted on jute and flax fibers before applying the synthetic fibers (Kevlar or carbon) in PLA nanocomposite.

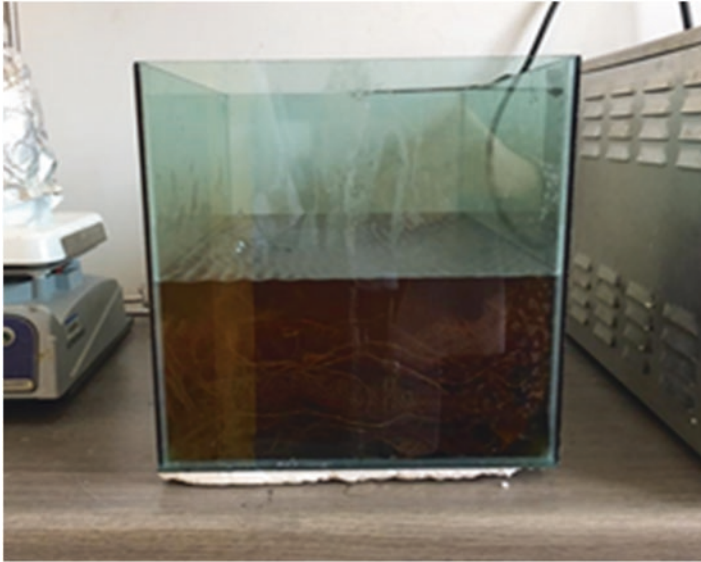


Fig. 17.3 Surface treatment of fibers

2.1 Surface Treatment on Natural Fiber

The woven flax and jute fibers were initially cut into 260×260 mm per piece according to the mold size. The fibers then underwent surface treatment by using alkaline treatment using NaOH solution. The flax and jute fibers were then treated by soaking in 2% and 5% of NaOH solution, respectively, for 2 h, as shown in Fig. 17.3. After undergoing alkaline treatment, the fibers were washed with distilled water until the pH became natural. Next, the flax fibers were dried at room temperature for 48 h. Finally, the dried flax fibers underwent further drying in an oven at 80°C for 24 h to remove excess water while jute fibers dried for 24 h at room temperature, followed by oven drying for 2 h at 100°C .

2.2 Preparation of PLA Thin Film

PLA thin film filled with nanofillers was prepared via solvent casting process. Chloroform was used as solvent with a ratio of PLA to chloroform of about 1:5. First, nanofillers with predetermined weight percentage (1 wt.%, 3 wt.%, and 5 wt.%) were sonicated with chloroform at room temperature with an amplitude of 55% for 30 min to improve the nanofiller dispersibility and reduce agglomerations of the nanofillers. After that, PLA pellets were then added to the solution. The solution was then stirred with a mechanical stirrer for 30 min at about 700 rpm. For the

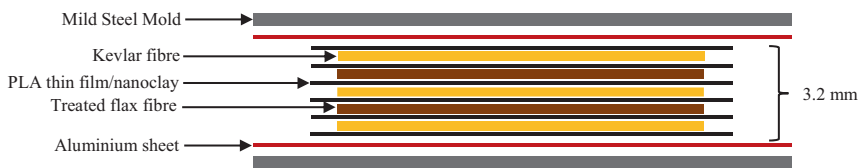
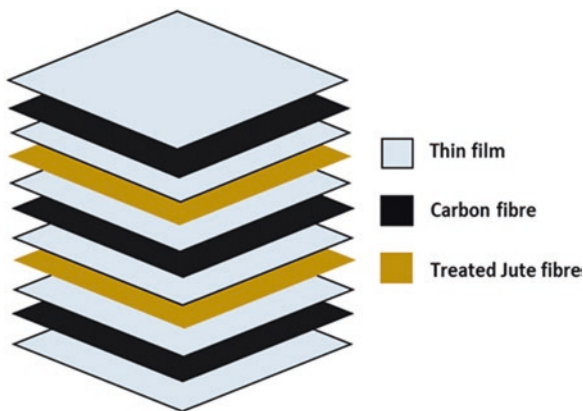


Fig. 17.4 Example of composite layup illustration image

Fig. 17.5 Fiber-reinforced PLA nanocomposite mat arrangement



first 15 min of stirring, the solution was heated at 60 °C and cooled back to room temperature for the next 15 min. Then the nanofiller/PLA solution was casted onto a mold to make a thin film with a thickness of 1 mm. The thin film was then left to cure for 24 h at room temperature. Lastly, the thin film was placed in the oven for a post-curing process at 55 °C for 2 h and 30 min.

2.3 Fabrication of Hybrid Fibers PLA Nanocomposite

The laminated composite was prepared by stacking five layers of fibers with the same arrangement for all samples, as shown in Figs. 17.4 and 17.5 (flax/Kevlar and jute/carbon). The PLA thin film was alternately added between every fiber to bind the woven fibers together. Aluminum sheets were applied on top and bottom of the laminated fibers to avoid sticking on the mild steel mold after the curing process. Woven fibers and PLA thin film were then pressed using a Vecho Vation 40 tonnes compression molding. The fabrication process started with preheat at 190 °C for 15 min and then followed by applying hot press with a pressure of 20 tonnes, while for jute/carbon composites, the preheating temperature was set at 185 °C for 20 min and constantly pressed for about 30 min to obtain the desired thickness.

Table 17.1 Sample abbreviation name for hybrid polymer nanocomposites

Sample abbreviation	Sample name
FK0	Flax/Kevlar/PLA
FK1	1 wt.% of graphene in flax/Kevlar/PLA
FK3	3 wt.% of graphene in flax/Kevlar/PLA
FK5	5 wt.% of graphene in flax/Kevlar/PLA
JC0	Jute/carbon/PLA
JC1	1 wt.% of graphene in jute/carbon/PLA
JC3	3 wt.% of graphene in jute/carbon/PLA
JC5	5 wt.% of graphene in jute/carbon/PLA

Mild steel plates with dimensions of 260 × 260 × 32 mm were used as a mold in the compression molding process. The mold surface was sprayed with a non-silicone mold release agent before the process to prevent the adhesion of composites during the compression molding process. Composites were then cooled and removed from the mold after cured. Table 17.1 shows the designation sample name in this work.

2.4 Characterizations

2.4.1 Flexural Test

Flexural test was conducted to measure the flexural strength and flexural modulus of the composite. The flexural strength is defined as maximum stress at the outermost fiber, either on the compression or tension side of the specimen, while flexural modulus is calculated from the slope of the stress vs. strain deflection curve. These two values can be used to evaluate the sample material's ability to withstand flexure or bending forces. The composites' flexural properties were determined using a three-point flexural bending test according to the ASTM D-790 standard using a Universal Testing Machine (Instron, Model 3365) as shown in Fig. 17.6. Ten specimens were tested for each sample at room temperature with a crosshead speed of 2.0 mm/min and a gauge length (support span) of 60 mm for flax/Kevlar composites. The crosshead speed and support span for jute/carbon composites were 1.28 mm/min and 48 mm, respectively. All specimens were cut following the dimension of rectangular shape, which was 3.5 mm (T) × 12.7 mm (W) × 127 mm (L). Then the flexural test was conducted, as shown in Fig. 17.3.



Fig. 17.6 Three-point bending test on fiber-reinforced PLA nanocomposite

3 Results and Discussion

3.1 Flexural Analysis

The mechanical properties of the hybrid fiber PLA nanocomposite were analyzed by flexural test. Figure 17.7 illustrates the overall flexural behavior for hybrid fiber PLA nanocomposite until fracture. In this research, graphene was added as a reinforcing filler in PLA at various concentrations. Initially, the strength was observed to be increased for all hybrid fiber PLA nanocomposites. However, for hybrid fiber, PLA composite without graphene shows the lowest flexural strength. Earlier good strength occurred on the hybrid fiber/PLA nanocomposite was due to better stress transfer from the PLA/graphene to the hybrid fiber. In addition, graphene forms a network in PLA and increases the microcrack resistance, which enhances the composite strength and stiffness properties. The improvement in composite strength is similar to Lim et al. (2017), which indicates that the inclusion of nanofiller will make the composite stiffer and better stress transfer.

Figure 17.8 shows the flexural properties for jute/carbon hybrid PLA nanocomposite and flax/Kevlar hybrid PLA nanocomposite. Both flexural strength and flexural modulus exhibit a similar trend. For jute/carbon PLA nanocomposite in Fig. 17.8, the flexural strength was observed to be increased with the addition of graphene to 3 wt.%. It was expected that earlier processing of graphene in PLA/chloroform solutions created well-dispersed graphene distributions. Earlier, chloroform was used as a

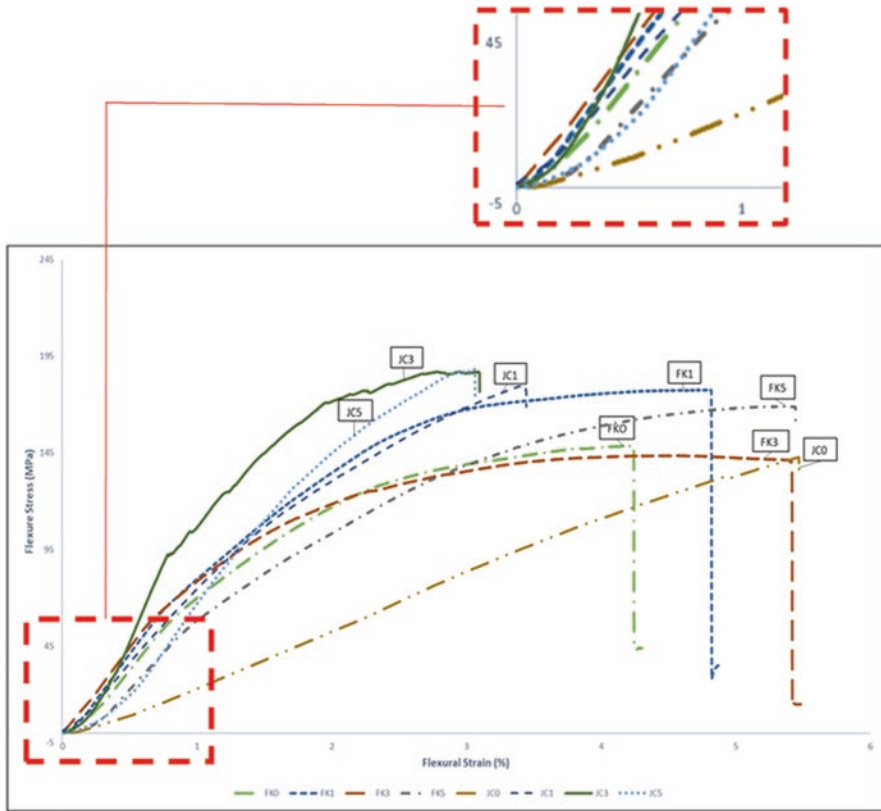


Fig. 17.7 Stress strain behavior of hybrid fiber PLA nanocomposite

solvent to reduce the PLA viscosity and ease the processing of graphene in PLA. Sonication of graphene in the liquid phase will be ideal for breaking the agglomeration or increasing the graphene layer distance (Ciesielski & Samori, 2014). High shear forces and cavitation resulting from the sonication process induce intercalation or exfoliation of graphene platelet. Thus, graphene acts as an obstacle to the PLA composites, which increased the composite strength. Due to the development of a strong interface between matrix, graphene, and fiber, the flexural strength of composites was improved (Seretis et al., 2018). In addition, good contact between PLA and graphene created a significant amount of energy to break the bonding when an external load was applied onto the PLA/graphene. The bending, folding, and scrolling during applied load enhance the matrix mechanical performance (Atif & Inam, 2016). An increase in flexural strength for hybrid fiber PLA nanocomposite filled with graphene can be described in a way that the nanofillers act as load carriers that transfer stresses from PLA through the nanofiller, which leads to the effective and uniform stress distribution (Bhattacharya, 2016). However, further addition of graphene to 5 wt.% in jute/carbon hybrid PLA nanocomposite does not considerably improve the

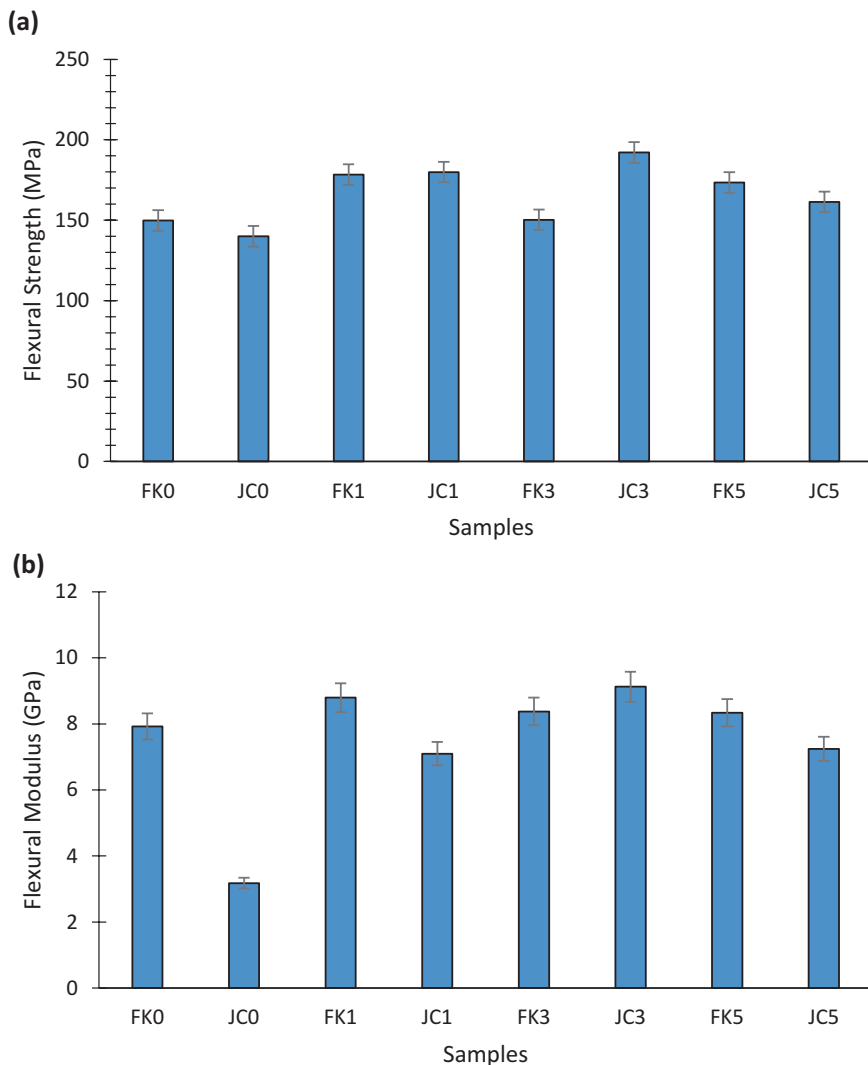


Fig. 17.8 (a) Flexural strength and (b) flexural modulus of hybrid flax/Kevlar and jute/carbon PLA nanocomposites with inclusion of graphene

flexural strength properties. The high graphene concentration was expected to increase the possibility of agglomeration. The particle distance becomes closer, and van der Waals attractions make the graphene have a high tendency to agglomerate (Raghunath et al., 2018). As the graphene agglomerate, the surface area became smaller and reduced the composite's flexural strength. Thus, most of the graphene/PLA nanocomposite interactions will be between graphene-graphene and graphene-PLA. Hence, poor dispersion of the graphene in the matrix results in nonuniform stress distribution across the laminate and exhibits poor mechanical properties.

For flax/Kevlar hybrid PLA nanocomposite, the addition of only 1 wt.% graphene shows high flexural strength of about 178.3 MPa. Presence of graphene acts as a reinforcing agent and resists crack propagation. However, further addition of graphene does not show any significant improvement in flexural strength. Flax fiber has a high surface area. The inclusion of more graphene in PLA seems to reduce the efficiency of the PLA/graphene to react or bind with the flax/Kevlar fibers. Due to lack of fiber-matrix interaction, the flexural strength decreased. Thus, delamination between fibers is much severe due to poor adhesion between flax/Kevlar and PLA/graphene. On the other hand, the flax fiber structure consists of lumens. According to Alimuzzaman et al. (2013), the lumen may act as voids and contain trapped air or gases. Due to uneven PLA distributed on the flax fiber surface, the composite will fail as there is a lack of interaction between two different surfaces. Applying temperature during the compression process of the flax/Kevlar hybrid PLA nanocomposite leads to the presence of voids trapped with gas which is due to the discontinuous PLA disintegrate into the fiber. Moreover, limited fiber-matrix interphase between PLA and hybrid flax/Kevlar leads to earlier composite failure.

3.2 Morphological Analysis

The morphological images on the cross section of the fractured flexural specimen for selected composites were carried out to evaluate the reinforcement filler distribution within the composite structure using SEM. In addition, the origin of crack and its propagation can be observed from the fractured surface appearance. Figure 17.9 shows the fractured surface of PLA thin film. The fractured surface displays cleavage appearance and river line marking of PLA, which indicates the root point of PLA fracture in the composite. Figure 17.10 shows the fractured surface of flax/Kevlar hybrid PLA nanocomposite with 0 and 1 wt.% of graphene. Figure 17.10a(i–ii) shows that most fibers are pulled out due to poor interfacial bonding. The analysis can be compared with the flexural strength analysis, which indicates the insufficient load-carrying capacity of the composite. More fibers were pulled out, and fiber separation was observed due to the composite's poor interfacial bonding, resulting in a decreased load-bearing capability (Bulut, 2017). While Fig. 17.10b(i–ii) shows that some fibers were pulled out, others were fractured into pieces. Fiber fracture indicates possible strong bonding interaction of graphene PLA on the fiber surface, resulting in higher load-carrying capacity when fractured under flexural stress. PLA matrix is weaker than the hybrid fiber. Therefore, the crack starts to initiate in the PLA matrix while graphene may act as a barrier to delay the crack propagation to the fiber layers. Moreover, surface treatment on flax fiber might remove some of the impurities and facilitate the formation of functional groups on the fiber surface. Thus, the unreacted PLA may be attached to the flax surface and improve interfacial bonding.

Figure 17.11 shows the schematic diagram of how graphene's presence in composites may delay crack propagation. When a load is applied to the matrix, the crack

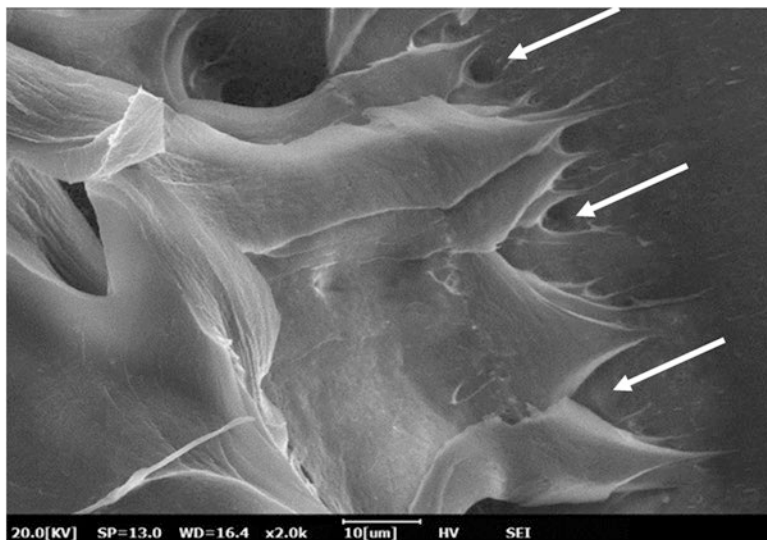


Fig. 17.9 The SEM fracture micrographs image of PLA thin film after flexural test with magnification of $\times 2.0$ k

starts to initiate at a high-stress concentration point. As cracks occurred, the graphene structure will function as a bridge connecting the crack surfaces. At this moment, the matrix load-carrying capability increased while graphene tries to resist the crack propagation. However, when the load is applied further, the graphene may fail, and crack propagates to the matrix until it reaches another graphene layer.

Figure 17.12 shows the adhesion of PLA on the flax fiber surface. The adhesion strongly suggests good interfacial interaction between treated flax and PLA matrix. Chemical treatment on the flax fiber will not only produce functional groups, but the treatment also possibly altered the fiber surface. As a result, the fiber surface became rougher and may also interact with PLA through mechanical interlocking. Thus, good interfacial bonding will effectively improve surface tension, swelling, wetting ability, adhesion, and compatibility with polymeric materials (Mohanty et al., 2001).

Figure 17.13 shows the fractured surface of jute/carbon hybrid PLA nanocomposite. From the morphological image, it can be seen that carbon fiber has a smooth surface and less contact with the PLA matrix. Poor bonding indicates inadequate wetting by PLA (red arrow).

Figures 17.14 shows the fractured surface of the jute/carbon hybrid PLA nanocomposite filled with 3 wt.% of graphene. As discussed earlier in flexural modulus, the addition of 3 wt.% of graphene increased the viscosity of the PLA matrix and makes the composite stiffer. The dark region on the left side shows river marking indicates the brittle failure mark of the sample. In addition, the presence of a gap indicates high local stress concentration and leads to the initiation of crack. Fractured from flexural failure was observed using a scanning electron microscope (SEM), where the rough surface of the composite structure was relatively related to the slow-spreading crack and high-energy absorption in the mixed graphene/PLA matrix.

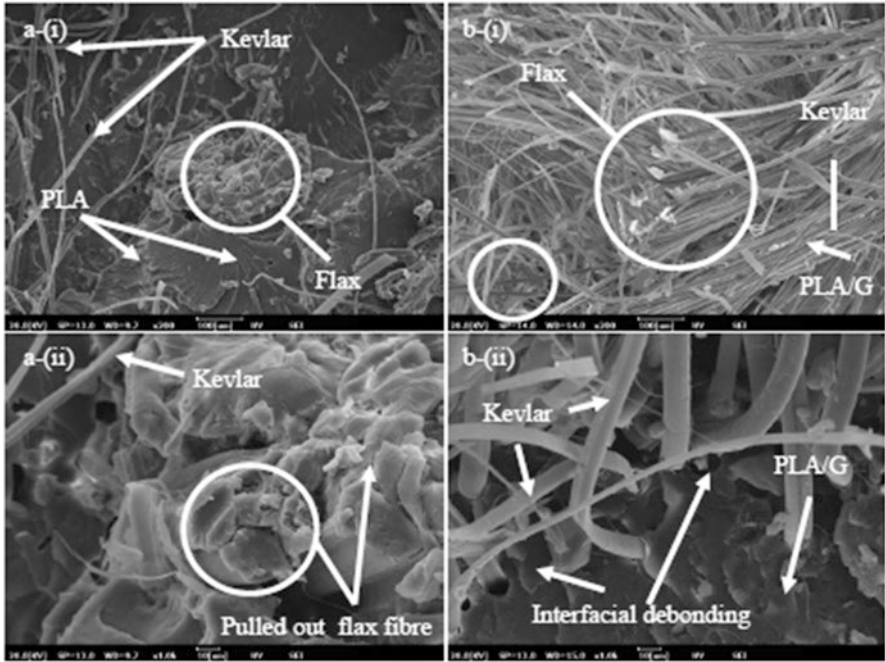


Fig. 17.10 The SEM fracture micrographs image of hybrid nanocomposite (a) FK0 and (b) FK1 after flexural test with magnification of (i) $\times 200$ and (ii) $\times 1.0$ k

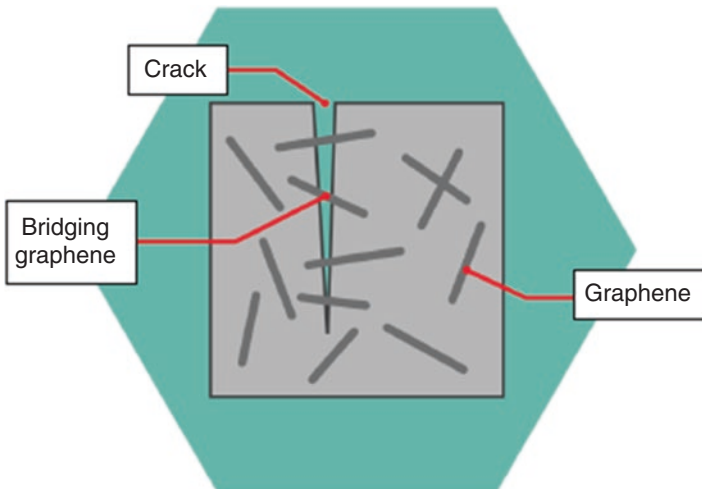


Fig. 17.11 Graphene bridging prevents the crack propagation on polymer nanocomposites

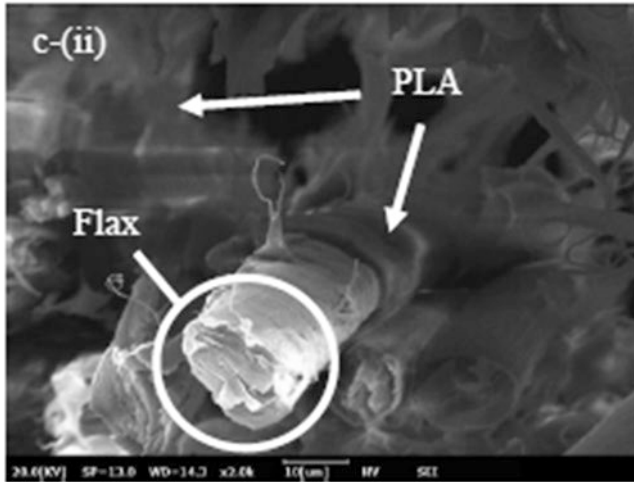


Fig. 17.12 The SEM fracture micrographs image of treated flax after flexural test with magnification of $\times 2.0$ k

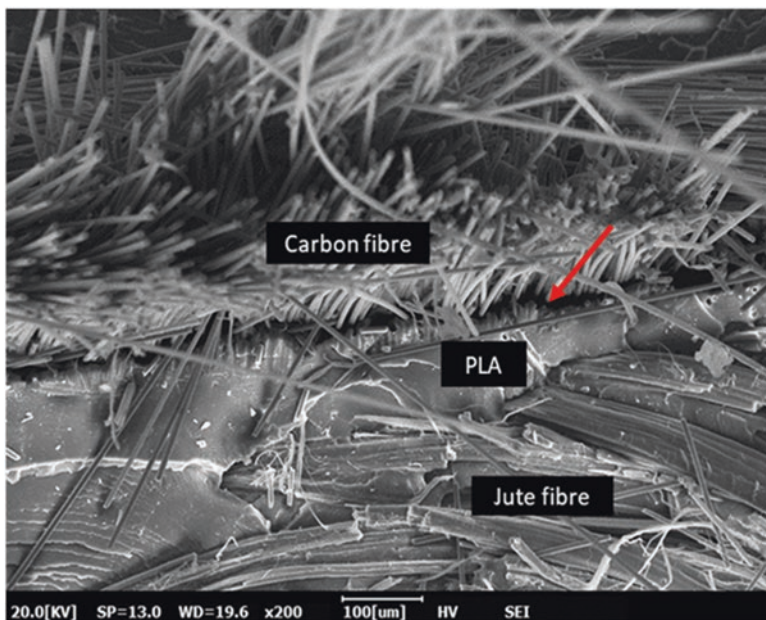


Fig. 17.13 SEM micrograph of PLA/JC composite at $\times 200$ magnification

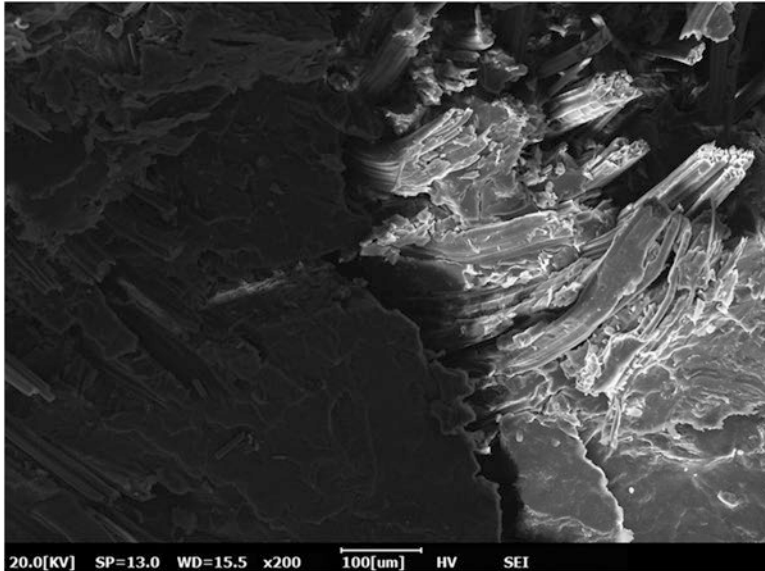


Fig. 17.14 SEM micrographs on the fractured surface of 3 wt.% of graphene jute/carbon hybrid PLA nanocomposite at $\times 200$ magnification

4 Conclusions

When the graphene content increases up to 1 wt.%, the strength and modulus of composite flexure increase up to 178.3 MPa and 8.79 GPa. The graphene increased the composite strength by acting as an obstacle to the deformation of the PLA composites. Composite's flexural strength was also improved due to better interface adhesion between graphene, fiber, and matrix. Alkaline treatment with NaOH on the jute and flax fibers improved the fiber surface properties. The treatment may remove some of the impurities in the fiber structure. Thus, the fiber surface became rough, and functional groups may form linkages with the PLA matrix. Besides that, the sudden risk of failure can be reduced when graphene acts as a bridge to extend the composite's fracture process. The synergistic effects between graphene and fibers in the PLA network show the enhancement between nano and micro properties of the composites. However, increasing the graphene concentration leads to the possibility of graphene agglomeration. Furthermore, the surface area becomes smaller and less bonding occurred with the PLA matrix. In addition, high graphene concentration will make the PLA hybrid composite stiffer and lead to brittle failure.

Acknowledgments The authors would like to thank Universiti Putra Malaysia and Higher Institution Centers of Excellence (HiCoE), Institute of Tropical Forestry and Forest Products (INTROP), for providing research grants for this research (vote: 6369108). Thank you to the Institute of Nanoscience and Nanotechnology (ION2) for providing necessary facilities for this research.

References

- Ahsan, Q., Carron, T. S. S., & Mustafa, Z. (2019). On the use of nano fibrillated kenaf cellulose fiber as reinforcement in polylactic acid biocomposites. *Journal of Mechanical Engineering Science*, 13(2), 4970–4988. <https://doi.org/10.15282/jmes.13.2.2019.15.0412>
- Aisyah, H. A., Paridah, M. T., Sapuan, S. M., Ilyas, R. A., Khalina, A., Nurazzi, N. M., Lee, S. H., & Lee, C. H. (2021). A comprehensive review on advanced sustainable woven natural fibre polymer composites. *Polymers*, 13(3), 471. <https://doi.org/10.3390/polym13030471>
- Alavudeen, A., Thiruchitrabalam, M., Venkateshwaran, N., et al. (2011). Review of natural fibre reinforced woven composite. *Reviews on Advanced Materials Science*, 27, 146–150.
- Alimuzzaman, S., Gong, R. H., & Akonda, M. (2013). Nonwoven polylactic acid and flax biocomposites. *Polymer Composites*, 34(10), 1611–1619. <https://doi.org/10.1002/pc.22561>
- Alix, S., Lebrun, L., Marais, S., et al. (2012). Pectinase treatments on technical fibres of flax: Effects on water sorption and mechanical properties. *Carbohydrate Polymers*, 87(1), 177–185. <https://doi.org/10.1016/j.carbpol.2011.07.035>
- Alsubari, S., Zuhri, M. Y. M., Sapuan, S. M., Ishak, M. R., Ilyas, R. A., & Asyraf, M. R. M. (2021). Potential of natural fiber reinforced polymer composites in sandwich structures: A review on its mechanical properties. *Polymers*, 13(3), 423. <https://doi.org/10.3390/polym13030423>
- Amir, N., Abidin, K. A. Z., & Shiri, F. B. M. (2017). Effects of the fibre configuration on mechanical properties of banana fibre/PP/MAPP natural fibre reinforced polymer composite. *Procedia Engineering*, 184, 573–580. <https://doi.org/10.1016/j.proeng.2017.04.140>
- Angelov, I., Wiedmer, S., Evstatiev, M., et al. (2007). Pultrusion of a flax/polypropylene yarn. *Composites. Part A, Applied Science and Manufacturing*, 38(5), 1431–1438. <https://doi.org/10.1016/j.compositesa.2006.01.024>
- Atif, R., & Inam, F. (2016). Reasons and remedies for the agglomeration of multilayered graphene and carbon nanotubes in polymers. *Beilstein Journal of Nanotechnology*, 7(1), 1174–1196. <https://doi.org/10.3762/bjnano.7.109>
- Avérous, L. (2008). Polylactic acid: Synthesis, properties and applications. In *Monomers, polymers and composites from renewable resources* (pp. 433–450). Elsevier. <https://doi.org/10.1016/b978-0-08-045316-3.00021-1>
- Awal, A., Rana, M., & Sain, M. (2015). Thermorheological and mechanical properties of cellulose reinforced PLA bio-composites. *Mechanics of Materials*, 80, 87–95. <https://doi.org/10.1016/j.mechmat.2014.09.009>
- Banakar, P., Shivanand, H. K., & Niranjana, H. B. (2012). Mechanical properties of angle ply laminated composites: A review. *International Journal of Pure And Applied Sciences*, 9, 127–133.
- Berhanu, T., Kumar, P., & Singh, I. (2014a). Mechanical behaviour of jute fibre reinforced polypropylene composites. In *5th International & 25th all India manufacturing technology, design and research conference (AIMTDR 2014) December 12th–14th*.
- Berhanu, T., Kumar, P., & Singh, I. (2014b). Mechanical behaviour of jute fibre reinforced polypropylene composites. In *5th International & 25th all India manufacturing technology, design and research conference (AIMTDR 2014) December 12th–14th*.
- Bharadwaj, R. K. (2001). Modeling the barrier properties of polymer-layered silicate nanocomposites. *Macromolecules*, 34, 9189–9192. <https://doi.org/10.1021/ma010780b>
- Bhattacharya, M. (2016). Polymer nanocomposites—A comparison between carbon nanotubes, graphene, and clay as nanofillers. *Materials*, 9(4), 262. <https://doi.org/10.3390/ma9040262>
- Bos, H. L. (2004). *The potential of flax fibres as reinforcement for composite materials*. Technische Universiteit Eindhoven. (PhD thesis).
- Bos, H. L., Müssig, J., & van den Oever, M. J. (2006). Mechanical properties of short-flax-fibre reinforced compounds. *Composites. Part A, Applied Science and Manufacturing*, 37, 1591–1604. <https://doi.org/10.1016/j.compositesa.2005.10.011>
- Bourbigot, S., LeBras, M., Dabrowski, F., et al. (2000). PA-6 clay nanocomposite hybrid as char forming agent in intumescent formulations. *Fire and Materials*, 24, 201–208. [https://doi.org/10.1002/1099-1018\(200007/08\)24:4%3C201::aid-fam739%3E3.0.co;2-d](https://doi.org/10.1002/1099-1018(200007/08)24:4%3C201::aid-fam739%3E3.0.co;2-d)

- Ciesielski, A., & Samori, P. (2014). Graphene via sonication assisted liquid-phase exfoliation. *Chemical Society Reviews*, 43(1), 381–398.
- Danso, H. (2017). Properties of coconut, oil palm and bagasse fibres: As potential building materials. *Procedia Eng*, 200, 1–9. <https://doi.org/10.1016/j.proeng.2017.07.002>
- Das, S. (2001). *The cost of automotive polymer composites: A review and assessment of DOE's lightweight materials composites research* (p. 47). Oak Ridge National Laboratory.
- Dong, C., Duong, J., & Davies, I. J. (2012). Flexural properties of S-2 glass and TR30S carbon fiber-reinforced epoxy hybrid composites. *Polymer Composites*, 33(5), 773–781. <https://doi.org/10.1002/pc.22206>
- Drumright, R. E., Gruber, P. R., & Henton, D. E. (2000). Polylactic acid technology. *Advanced Materials*, 12(23), 1841–1846.
- Du, Y., Wu, T., Yan, N., et al. (2014). Fabrication and characterization of fully biodegradable natural fiber-reinforced poly (lactic acid) composites. *Composites Part B: Engineering*, 56, 717–723. <https://doi.org/10.1016/j.compositesb.2013.09.012>
- Gopinath, A., Kumar, M. S., & Elayaperumal, A. (2014). Experimental investigations on mechanical properties of jute fiber reinforced composites with polyester and epoxy resin matrices. *Procedia Engineering*, 97, 2052–2063. <https://doi.org/10.1016/j.proeng.2014.12.448>
- Hassan, M. M., Islam, M. R., Shehrzade, S., et al. (2003). Influence of mercerization along with ultraviolet (UV) and gamma radiation on physical and mechanical properties of jute yarn by grafting with 3-(Trimethoxysilyl) propylmethacrylate (Silane) and acrylamide under UV radiation. *Polymer – Plastics Technology and Engineering*, 42(4), 515–531. <https://doi.org/10.1081/ppt-120023092>
- Heydari-Meybodi, M., Saber-Samandari, S., & Sadighi, M. (2016). An experimental study on low-velocity impact response of nanocomposite beams reinforced with nanoclay. *Composites Science and Technology*, 133, 70–78. <https://doi.org/10.1016/j.compscitech.2016.07.020>
- Hinchcliffe, S. A., Hess, K. M., & Srubar, W. V., III. (2016). Experimental and theoretical investigation of prestressed natural fiber-reinforced polylactic acid (PLA) composite materials. *Composites Part B: Engineering*, 95, 346–354. <https://doi.org/10.1016/j.compositesb.2016.03.089>
- Hossain, K. M. Z., Felfel, R. M., Rudd, C. D., et al. (2014). The effect of cellulose nanowhiskers on the flexural properties of self-reinforced polylactic acid composites. *Reactive and Functional Polymers*, 85, 193–200. <https://doi.org/10.1016/j.reactfunctpolym.2014.09.012>
- Huner, U. (2018). Effect of chemical surface treatment on flax-reinforced epoxy composite. *Journal of Natural Fibers*, 15(6), 808–821. <https://doi.org/10.1080/15440478.2017.1369207>
- Ilyas, R. A., Sapuan, S. M., Asyraf, M. R. M., Dayana, D. A. Z. N., Amelia, J. J. N., Rani, M. S. A., Norrrahim, M. N. F., et al. (2021a). Polymer composites filled with metal derivatives: A review of flame retardants. *Polymers*, 13(11), 1701. <https://doi.org/10.3390/polym13111701>
- Ilyas, R. A., Sapuan, S. M., Harussani, M. M., Hakimi, M. Y. A. Y., Haziq, M. Z. M., Atikah, M. S. N., Asyraf, M. R. M., et al. (2021b). Polylactic acid (PLA) biocomposite: Processing, additive manufacturing and advanced applications. *Polymers*, 13(8), 1326. <https://doi.org/10.3390/polym13081326>
- Ilyas, R. A., Sapuan, S. M., Ibrahim, R., et al. (2019). Sugar palm (Arenga pinnata (Wurmb.) Merr) cellulosic fibre hierarchy: A comprehensive approach from macro to nano scale. *Journal of Materials Research and Technology*, 8, 2753–2766. <https://doi.org/10.1016/j.jmrt.2019.04.011>
- Jaafar, C. A., Zainol, I., Rizal, M. M., et al. (2018) Preparation and characterisation of epoxy/silica/kenaf composite using hand lay-up method. In *I27th Sci. Conf. Microsc. Soc. Malaysia (27th SCMSM 2018)*. Melaka, Malaysia (pp. 2–6).
- Jagannatha, T. D., & Harish, G. (2015). Influence of carbon & glass fiber reinforcements on flexural strength of epoxy matrix polymer hybrid composites. *International Journal of Engineering*, 5(4), 109–112.
- Kendall, D. (2006). *Fiber reinforced polymer composite bridges*. National Composite Network.
- Kiran, Z. S., Babu, V. S., & Shekar, K. S. (2019). Study of the microhardness and erosive wear behavior of organo-modified nanoclay filled glass-epoxy composites and optimization.

- Journal of Mechanical Engineering Science*, 13(2), 4794–4815. <https://doi.org/10.15282/jmes.13.2.2019.03.0400>
- Kumar, T. S. M., Chandrasekar, M., Senthilkumar, K., Ilyas, R. A., Sapuan, S. M., Hariram, N., Rajulu, A. V., Rajini, N., & Siengchin, S. (2020). Characterization, thermal and antimicrobial properties of hybrid cellulose nanocomposite films with in-situ generated copper nanoparticles in Tamarindus Indica. *Nutritional Powder Journal of Polymer Environment*, 1–10. <https://doi.org/10.1007/s10924-020-01939-w>
- Kushnoore, S., Atgur, V., Kanagalpula, P. K. C., et al. (2019). Experimental investigation on thermal behavior of fly ash reinforced aluminium alloy (Al6061) hybrid composite. *Journal of Mechanical Engineering Science*, 13(3), 5588–5603. <https://doi.org/10.15282/jmes.13.3.2019.23.0449>
- Laoutid, F., Bonnaud, L., Alexandre, M., et al. (2009). New prospects in flame retardant polymer materials: From fundamental to nanocomposites. *Materials Science and Engineering R*, 63, 100–125.
- Lim, K. H., Majid, M. S. A., Ridzuan, M. J. M., et al. (2017). Effect of nano-clay fillers on mechanical and morphological properties of Napier/epoxy composites. *Journal of Physics: Conference Series*, 908, 012010. IOP Publishing. <https://doi.org/10.1088/1742-6596/908/1/012010>
- Liu, H. Y., Wang, G. T., Mai, Y. W., et al. (2011). On fracture toughness of nano-particle modified epoxy. *Composites Part B: Engineering*, 42, 2170–2175. <https://doi.org/10.1016/j.compositesb.2011.05.014>
- Maity, S., Chowdhury, S., & Datta, A. K. (2012). Jute biology, diversity, cultivation, pest control, fiber production, and genetics. In *Organic fertilization, soil quality, and human health* (pp. 227–262). Springer. https://doi.org/10.1007/978-94-007-4113-3_9
- Mazlan, N., Chai Hua, T., Sultan, M. T. H., et al. (2021). Thermogravimetric and dynamic mechanical analysis of woven glass/kenaf/epoxy hybrid nanocomposite filled with clay. *Advanced Materials and Processing Technologies*, 7(1), 166–179.
- Merzuki, M. N. M., Rejab, M. R. M., Sani, M. S. M., et al. (2019). Experimental investigation of free vibration analysis on fibre metal composite laminates. *Journal of Mechanical Engineering Science*, 13, 5753–5763. <https://doi.org/10.15282/jmes.13.4.2019.03.0459>
- Mohanty, A. K., Misra, M., & Drzal, M. (2001). Surface modifications of natural fibres and performance of the resulting biocomposites: An overview. *Composite Interfaces*, 8(5), 313–343. <https://doi.org/10.1163/156855401753255422>
- Mohanty, A. K., Misra, M., & Hinrichsen, G. (2000). Biofibres, biodegradable polymers and biocomposites: An overview. *Macromolecular Materials and Engineering*, 276, 1–24. [https://doi.org/10.1002/\(sici\)1439-2054\(20000301\)276:1%3C1::aid-mame1%3E3.0.co;2-w](https://doi.org/10.1002/(sici)1439-2054(20000301)276:1%3C1::aid-mame1%3E3.0.co;2-w)
- Morrison Iii, W. H., Archibald, D. D., Sharma, H. S. S., et al. (2000). Chemical and physical characterization of water- and dew-retted flax fibres. *Industrial Crops and Products*, 12(1), 39–46. [https://doi.org/10.1016/s0926-6690\(99\)00044-8](https://doi.org/10.1016/s0926-6690(99)00044-8)
- Mourit, A. P., & Gibson, A. G. (2006). Fire reaction properties of composites. *Fire Properties of Polymer Composite Materials*, 59–101. https://doi.org/10.1007/978-1-4020-5356-6_3
- Murali, G., & Pannirselvam, N. (2011). Flexural strengthening of reinforced concrete beams using fibre reinforced polymer laminate: A review. *Journal of Engineering and Applied Science*, 6(11), 41–47.
- Murariu, M., & Dubois, P. (2016). PLA composites: From production to properties. *Advanced Drug Delivery Reviews*, 107, 17–46. <https://doi.org/10.1016/j.addr.2016.04.003>
- Nasruddin, N. R. A., Mazlan, N., Basri, M. M., et al. (2018). Thermogravimetric analysis on rice husk ashes-based geopolymer paste. In *IOP conference series: Materials science and engineering* (Vol. 405, p. 012014). IOP Publishing. <https://doi.org/10.1088/1757-899x/405/1/012014>
- Nayak, S. Y., Heckadka, S. S., Kini, U. A., et al. (2017). *Pistachio shell flakes and flax fibres as reinforcements in polyester based* (pp. 17–24). International Conference on Engineering and Information Technology.
- Nazrin, A., Sapuan, S. M., Zuhri, M. Y. M., Ilyas, R. A., Syafiq, R., & Sherwani, S. F. K. (2020). Nanocellulose reinforced thermoplastic starch (TPS), Polylactic acid (PLA), and polybutylene

- succinate (PBS) for food packaging applications. *Frontiers in Chemistry*, 8(213), 1–12. <https://doi.org/10.3389/fchem.2020.00213>
- Nurazzi, M., Norizan, M. R. M. A., Khalina, A., Abdullah, N., Sabaruddin, F. A., Kamarudin, S. H., Ahmad, S.'b., et al. (2021). Fabrication, functionalization, and application of carbon nanotube-reinforced polymer composite: An overview. *Polymers*, 13(7), 1047. <https://doi.org/10.3390/polym13071047>
- Omran, A. A. B., Mohammed, A. A. B. A., Sapuan, S. M., Ilyas, R. A., Asyraf, M. R. M., Kooloor, S. S. R., & Petru, M. (2021). Micro- and nanocellulose in polymer composite materials: A review. *Polymers*, 13(2), 231. <https://doi.org/10.3390/polym13020231>
- Pandey, J. K., Ahn, S. H., Lee, C. S., et al. (2010). Recent advances in the application of natural fibre based composites. *Macromolecular Materials and Engineering*, 295, 975–989. <https://doi.org/10.1002/mame.201000095>
- Pavlidou, S., & Papaspyrides, C. D. (2008). A review on polymer-layered silicate nanocomposites. *Progress in Polymer Science*, 33, 1119–1198.
- Pickering, K. L., Efenfy, M. G. A., & Le, T. M. (2016). A review of recent developments in natural fibre composites and their mechanical performance. *Composites. Part A, Applied Science and Manufacturing*, 83, 98–112. <https://doi.org/10.1016/j.compositesa.2015.08.038>
- Pinto, M. A., Chalivendra, V. B., Kim, Y. K., et al. (2014). Evaluation of surface treatment and fabrication methods for jute fiber/epoxy laminar composites. *Polymer Composites*, 35(2), 310–317. <https://doi.org/10.1002/pc.22663>
- Qian, D., Bao, L., Takatera, M., & Kemmochi, K. (2009). Particle erosion behaviour of unidirectional CF and GF hybrid fiber-reinforced plastic composites. *Journal of Textile Engineering*, 55, 39–44. <https://doi.org/10.4188/jte.55.39>
- Raghunath, S., Kumar, S., Samal, S. K., et al. (2018). PLA/ESO/MWCNT nanocomposite: A study on mechanical, thermal and electroactive shape memory properties. *Journal of Polymer Research*, 25(5), 1–12. <https://doi.org/10.1007/s10965-018-1523-5>
- Rajan, R., Joseph, K., Skrifvars, M., et al. (2012). Evaluating the influence of chemical modification on flax yarn. In *ECCM15–15th European conference on composite materials, Venice, Italy, June (24–28)*.
- Ramli, N., Mazlan, N., Ando, Y., et al. (2018). Natural fiber for green technology in automotive industry: A brief review. In *IOP conference series: Materials science and engineering* (Vol. 368, p. 012012). IOP Publishing. <https://doi.org/10.1088/1757-899x/368/1/012012>
- Rozilah, A., Aiza Jaafar, C. N., Sapuan, S. M., Zainol, I., & Ilyas, R. A. (2020). The effects of silver nanoparticles compositions on the mechanical, physiochemical, antibacterial, and morphology properties of sugar palm starch biocomposites for antibacterial coating. *Polymers*, 12(11), 2605. <https://doi.org/10.3390/polym12112605>
- Saber-Samandari, S., & Afaghi Khatibi, A. (2006). The effect of interphase on the elastic modulus of polymer based nanocomposites. *Key Engineering Materials*, 312, 199–204. <https://doi.org/10.4028/www.scientific.net/kem.312.199>
- Saber-Samandari, S., & Afaghi Khatibi, A. (2007). Evaluation of elastic modulus of polymer matrix nanocomposites. *Polymer Composites*, 28, 405–411. <https://doi.org/10.1002/pc.20322>
- Saber-Samandari, S., Khatibi, A. A., & Basic, D. (2007). An experimental study on clay/epoxy nanocomposites produced in a centrifuge. *Composites Part B: Engineering – Journal*, 38, 102–107. <https://doi.org/10.1016/j.compositesb.2006.03.010>
- Sairy, N. A., Mazlan, N., Ishak, M. R., et al. (2020). Investigation on the flexural properties of nanofillers loading on the jute/carbon/PLA nanocomposites. *Journal of Mechanical Engineering and Sciences*, 14(4), 7424–7433. <https://doi.org/10.15282/jmes.14.4.2020.11.0585>
- Sanadi, A. R., Prasad, S. V., & Rohatgi, P. K. (1986). Sunhemp fibre-reinforced polyester. *Journal of Materials Science*, 21, 4299–4304. <https://doi.org/10.1007/bf01106545>
- Sanyang, M. L., Ilyas, R. A., Sapuan, S. M., et al. (2018). Sugar palm starch-based composites for packaging applications. In *Bionanocomposites for packaging applications* (pp. 125–147). Springer. https://doi.org/10.1007/978-3-319-67319-6_7

- Seki, Y. (2009). Innovative multifunctional siloxane treatment of jute fiber surface and its effect on the mechanical properties of jute/thermoset composites. *Materials Science and Engineering A*, 508(1–2), 247–252. <https://doi.org/10.1016/j.msea.2009.01.043>
- Seretis, G. V., Theodorakopoulos, I. D., Manolakos, D. E., et al. (2018). Effect of sonication on the mechanical response of graphene nanoplatelets/glass fabric/epoxy laminated nanocomposites. *Composites: Part B*, 147, 33–41. <https://doi.org/10.1016/j.compositesb.2018.04.034>
- Shanmugam, D., & Thiruchitrabalam, M. (2013). Static and dynamic mechanical properties of alkali treated unidirectional continuous Palmyra palm leaf stalk fiber/jute fiber reinforced hybrid polyester composites. *Materials and Design*, 50, 533–542. <https://doi.org/10.1016/j.matdes.2013.03.048>
- Shilpa, K. N., Nithin, K. S., Sachhidananda, S., et al. (2017). Visibly transparent PVA/sodium doped dysprosium (Na₂Dy₂O₄) nano composite films, with high refractive index: An optical study. *Journal of Alloys and Compounds*, 694, 884–891. <https://doi.org/10.1016/j.jallcom.2016.10.004>
- Silberschmidt, V. V. (2016). *Dynamic deformation, damage and fracture in composite materials and structures*. Woodhead Publishing.
- Sprenger, S. (2013). Epoxy resins modified with elastomers and surface-modified silica nanoparticles. *Polymer*, 54(18), 4790–4797. <https://doi.org/10.1016/j.polymer.2013.06.011>
- Subramani, N. K., Kasargod Nagaraj, S., Shivanna, S., & Siddaramaiah, H. (2016). Highly flexible and visibly transparent poly (vinyl alcohol)/calcium zincate nanocomposite films for UVA shielding applications as assessed by novel ultraviolet photon induced fluorescence quenching. *Macromolecules*, 49, 2791–2801. <https://doi.org/10.1021/acs.macromol.5b02282.s001>
- Subramanian, C., & Senthilvelan, S. (2011). Joint performance of the glass fiber reinforced polypropylene leaf spring. *Composite Structures*, 93, 759–766. <https://doi.org/10.1016/j.compstruct.2010.07.015>
- Suriani, M. J., Radzi, F. S. M., Ilyas, R. A., Michal, P., Sapuan, S. M., & Ruzaidi, C. M. (2021b). Flammability, tensile, and morphological properties of oil palm empty fruit bunches fiber/pet yarn-reinforced epoxy fire retardant hybrid polymer composites. *Polymers*, 13(8), 1282. <https://doi.org/10.3390/polym13081282>
- Suriani, M. J., Rapi, H. Z., Ilyas, R. A., Petru, M., & Sapuan, S. M. (2021d). Delamination and manufacturing defects in natural fiber-reinforced hybrid composite: A review. *Polymers*, 13(8), 1323. <https://doi.org/10.3390/polym13081323>
- Suriani, M. J., Sapuan, S. M., Ruzaidi, C. M., Nair, D. S., & Ilyas, R. A. (2021c). Flammability, morphological and mechanical properties of sugar palm fiber/polyester yarn-reinforced epoxy hybrid biocomposites with magnesium hydroxide flame retardant filler. *Textile Research Journal*, 1–12. <https://doi.org/10.1177/00405175211008615>
- Suriani, M. J., Sapuan, S. M., Ruzaidi, C. M., Nair, D. S., & Ilyas, R. A. (2021e). Flammability, morphological and mechanical properties of sugar palm fiber/polyester yarn-reinforced epoxy hybrid biocomposites with magnesium hydroxide flame retardant filler. *Textile Research Journal*, 004051752110086. <https://doi.org/10.1177/00405175211008615>
- Suriani, M. J., Zainudin, H. A., Ilyas, R. A., Petru, M., Sapuan, S. M., Ruzaidi, C. M., & Mustapha, R. (2021a). Kenaf fiber/pet yarn reinforced epoxy hybrid polymer composites: Morphological, tensile, and flammability properties. *Polymers*, 13(9), 1532. <https://doi.org/10.3390/polym13091532>
- Swolfs, Y., Gorbatiuk, L., & Verpoest, I. (2014). Fibre hybridisation in polymer composites: A review. *Composites Part A: Applied Science and Manufacturing*, 67, 181–200. <https://doi.org/10.1016/j.compositesa.2014.08.027>
- Ticoalu, A., Aravinthan, T., & Cardona, F. (2010). A review of current development in natural fibre composites for structural and infrastructure applications. In *Proceedings of the southern region engineering conference (SREC 2010)*. Engineers Australia (pp. 113–117).
- Utracki, L. A. (2004). *Clay-containing polymeric nanocomposites* (Vol. 1). iSmithers Rapra Publishing.

- Van de Weyenberg, I., Chi Truong, T., Vangrimde, B., et al. (2006). Improving the properties of UD flax fibre reinforced composites by applying an alkaline fibre treatment. *Composites. Part A, Applied Science and Manufacturing*, 37(9), 1368–1376. <https://doi.org/10.1016/j.compositesa.2005.08.016>
- Wambua, P., Ivens, J., & Verpoest, I. (2003). Natural fibres: Can they replace glass in fibre reinforced plastics? *Composites Science and Technology*, 63, 1259–1264. [https://doi.org/10.1016/s0266-3538\(03\)00096-4](https://doi.org/10.1016/s0266-3538(03)00096-4)
- Wu, C., Lai, W., & Wang, C. (2016). Effects of surface modification on the mechanical properties of flax/ β -polypropylene composites. *Materials*, 9(5), 314. <https://doi.org/10.3390/ma9050314>
- Xie, Y., Hill, C. A. S., Xiao, Z., et al. (2010). Silane coupling agents used for natural fibre/polymer composites: A review. *Composites. Part A, Applied Science and Manufacturing*, 41(7), 806–819. <https://doi.org/10.1016/j.compositesa.2010.03.005>
- Xu, Y., & Van Hoa, S. (2008). Mechanical properties of carbon fiber reinforced epoxy/clay nanocomposites. *Composites Science and Technology*, 68, 854–861. <https://doi.org/10.1016/j.compscitech.2007.08.013>
- Yan, L., Chou, N., & Jayaraman, K. (2014). Flax fibre and its composites: A review. *Composites. Part B, Engineering*, 56, 296–317. <https://doi.org/10.1016/j.compositesb.2013.08.014>
- Zafar, M. T., Maiti, S. N., & Ghosh, A. K. (2016). Effect of surface treatment of jute fibers on the interfacial adhesion in poly (lactic acid)/jute fiber biocomposites. *Fibers and Polymers*, 17(2), 266–274. <https://doi.org/10.1007/s12221-016-5781-8>
- Zeng, Q. H., Yu, A. B., Lu, G. Q., et al. (2005). Clay-based polymer nanocomposites: Research and commercial development. *Journal of Nanoscience and Nanotechnology*, 5, 1574. <https://doi.org/10.1166/jnn.2005.411>
- Zhang, J., Chaisombat, K., He, S., et al. (2012). Hybrid composite laminates reinforced with glass/carbon woven fabrics for lightweight load bearing structures. *Materials and Design*, 36, 75–80. <https://doi.org/10.1016/j.matdes.2011.11.006>
- Zhou, G., Movva, S., & Lee, L. J. (2008). Nanoclay and long-fiber-reinforced composites based on epoxy and phenolic resins. *Journal of Applied Polymer Science*, 108, 3720–3726. <https://doi.org/10.1002/app.27886>
- Zhu, J., Zhu, H., Immonen, K., et al. (2015). Improving mechanical properties of novel flax/tannin composites through different chemical treatments. *Industrial Crops and Products*, 67, 346–354. <https://doi.org/10.1016/j.indcrop.2015.01.052>

Chapter 18

Evolution of Aerospace Composite Materials



Norkhairunnisa Mazlan, T. Chai Hua, S. M. Sapuan, and R. A. Ilyas

1 Introduction

Since the Wright brothers constructed the first airplane over two thousand years ago, there has been a revolution in aerospace materials. The evolution of aeronautical studies on the series development of planes and gilders is inspired by the wings of birds. Natural composite materials such as spruce and wood were employed to construct plane structures during the early stages of aviation development in the 1930s. However, due to a variety of factors such as weather, changes in wood structure, moisture content, wood infections, and flaws, wood structure quickly deteriorates and is difficult to maintain. Then, as time goes on, aircraft materials evolve, shifting from wood to metal. Composite materials, on the other hand, have been created to address concerns about lightweight, corrosion-resistant, and fatigue-resistant materials. To improve payload, agility, takeoff, and landing capabilities, lightweight aircraft constructions are required. Glass fiber-reinforced plastic

N. Mazlan (✉)

Institute of Nanoscience & Nanotechnology (ION2), Universiti Putra Malaysia, Serdang, Selangor, Malaysia

Department of Aerospace Engineering, Faculty of Engineering, Universiti Putra Malaysia, Serdang, Selangor, Malaysia

e-mail: norkhairunnisa@upm.edu.my

T. Chai Hua · S. M. Sapuan

Institute of Tropical Forestry and Forest Products (INTROP), Universiti Putra Malaysia, Serdang, Selangor, Malaysia

R. A. Ilyas

School of Chemical and Energy Engineering, Faculty of Engineering, Universiti Teknologi Malaysia, Johor Bahru, Johor, Malaysia

Centre for Advanced Composite Materials (CACM), Universiti Teknologi Malaysia, Johor Bahru, Johor, Malaysia

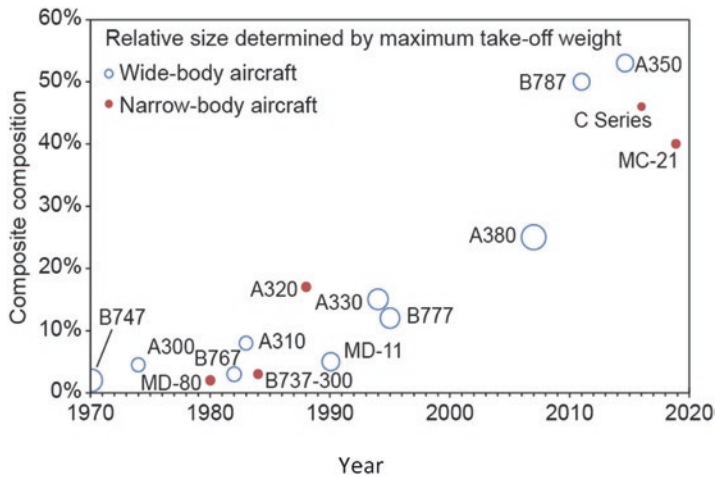


Fig. 18.1 Composite composition in aircraft from 1970 to 2020 (Pierce & Falzon, 2017)

(GFRP) was first used for airplane fairings, noses, and cockpits in the 1940s. Despite its tremendous strength, glass fiber exhibits brittle fracture, which resulted in a catastrophic breakdown. Since then, extensive research has been performed on generating a synthetic polymer appropriate for use with glass fiber, heralding the dawn of the plastic era. GFRP is not only robust and light, but it is also radio frequency transparent, making it ideal for electronic radar equipment in aircraft radomes.

Then as technology advances and demand from the aviation sector grows, composite materials knowledge continues to expand and improve. DuPont invented Kevlar fiber, also known as aramid fiber, in the 1970s. Carbon fiber is being created at the same time, and composite materials are evolving. As indicated in Fig. 18.1, the use of composites in airplanes was formerly limited to less than 10% of the entire structure. Then in the 1990s, composite materials became more popular, with roughly 20% of airplane structures comprised of composite materials. Currently, the Boeing 787 and Airbus A350 use roughly more than 50% composite parts and components in their aircraft.

According to Soutis (2005), Airbus began installing composite vertical fins on A300 and A310 aircraft in 1985. As a result, compared to 2076 parts of original metallic components in aircraft, there is a 95% reduction in parts in aircraft. Surprisingly, the airplane was 400 kg lighter, with lower manufacturing and assembly costs. The dimensions, configurations, aircraft materials, and production procedures of the A350 and Boeing 787 are all identical. Table 18.1 shows the material distribution for current wide-body aircraft such as the Airbus A350 and Boeing 787. The Airbus A350 was discovered to use significantly more composite materials than the Boeing B787.

The use of composite materials has resulted in a 20% reduction in CO₂ emissions by substituting aluminum alloy with a carbon fiber-reinforced polymer (CFRP) composite. As a result, fuel consumption can be reduced while CO₂ and NO_x emissions were reduced (Timmis et al., 2015). As a result of the growing

Table 18.1 Materials distribution between Airbus A350 and Boeing 787

	Airbus A350 (%)	Boeing 787 (%)
Composite	52	50
Steel	7	10
Titanium	14	15
Aluminum/aluminum lithium	20	20
Miscellaneous	7	5

demand from the aerospace industry, more traditional materials such as metals have been substituted by composites. Various forms of composites will be covered in the following sections of this chapter. In addition, environmental impact, end-of-life issues, and future problems for composite materials will be discussed.

2 Composite

2.1 Polymer Matrix Composite (PMC)

Boeing and Airbus are switching from aerospace metal alloys to composite materials in their modern airplanes. In the Boeing 787 Dreamliner, polymer composite is used to the amount of 50%. Eurofighter aircraft, on the other hand, utilized about 70% polymer composites for the outer fuselage, wings, and rudder. In aviation structures, polymer matrix composites are lighter than traditional metallic components. Polymer composite materials are intended to reduce the aircraft's overall weight by 20–40%, allowing it to accommodate more passengers while also increasing its range.

Furthermore, the fabrication of polymer composite materials is less expensive and time-consuming than that of aluminum. PMCs lower overall engine mass and enhance fuel efficiency because they are lightweight (King et al., 2009). A reinforcement phase in fiber or particle and a continuous phase in a binder or matrix make up polymer composite materials. Civil and military aircraft frequently used carbon fiber-reinforced plastic (CFRP) and glass fiber-reinforced plastic (GFRP). Due to covalent bonding and weak van der Waals interactions between layers, the carbon fiber has a high strength and modulus, making it stiff and extremely anisotropic. While glass fiber is extensively utilized as reinforcement because of its high strength-to-weight ratio, dimensional stability, electrical insulation, and inexpensive cost, it is more corrosion resistant. Kevlar fiber, in addition to carbon and glass fiber, is utilized in aircraft construction. Kevlar is five times as strong as steel and has exceptional thermal characteristics. Polymer matrix materials are used as a binder to hold the reinforcing materials together. The resin should be able to transfer load from one fiber to another, for example. Depending on the use on aircraft parts or components, various types of polymer matrix and reinforcement can be employed (Fig. 18.2). Furthermore, diverse fiber insertion and fabrication procedures are used

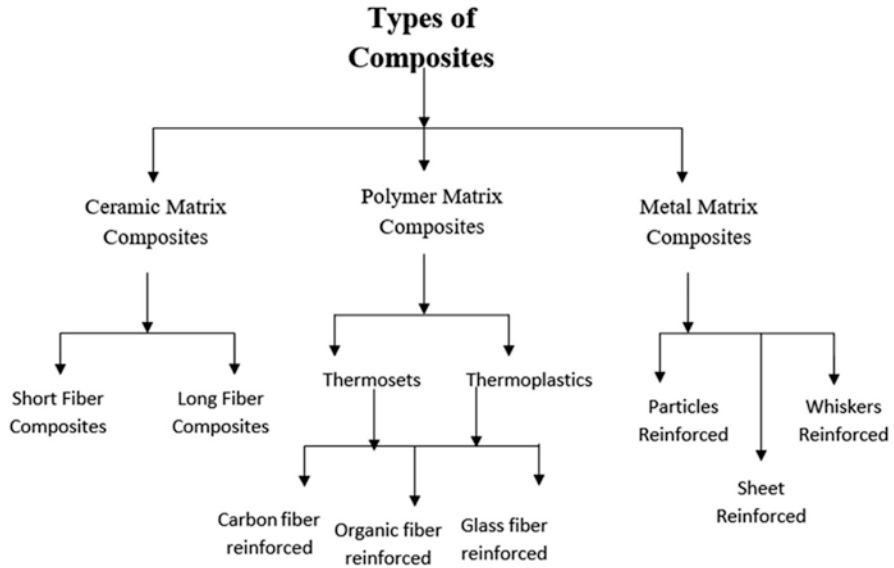


Fig. 18.2 Reinforcement and fabrication process in polymer matrix composite. Adapted with copyright permission from Singh et al. (2020)

Table 18.2 Advantages and disadvantages of different types of polymers (Mouritz, 2012)

Thermoplastic	Thermoset	Elastomer
Advantages		
<ul style="list-style-type: none"> • Non-reacting • Rapid processing • High ductility • High fracture toughness • High impact resistance • Absorbs little moisture • Recyclable 	<ul style="list-style-type: none"> • Low processing temperature • Low viscosity • Good compression properties • Good fatigue resistance • Good creep resistance • Highly resistant to solvents • Good fiber wetting in composite 	<ul style="list-style-type: none"> • Low processing temperature • High ductility and flexibility • High fracture toughness. • High impact resistance
Disadvantages		
<ul style="list-style-type: none"> • High viscosity • High processing temperature (300–400 °C) • High processing pressures • Poor creep resistance 	<ul style="list-style-type: none"> • Long processing time • Low ductility • Low fracture toughness • Low impact resistance • Absorb moisture • Limited shelf life • Non-recycle 	<ul style="list-style-type: none"> • Long processing time • Poor creep resistance • Low Young’s modulus • Low tensile strength

in the fabrication of fiber-reinforced polymer composite materials. The advantages and disadvantages of thermoset, thermoplastic, and elastomer resins utilized in aircraft applications were outlined in Table 18.2.

2.1.1 Thermoset

The thermoset polymer is used to produce the majority of the polymer composite on airplane components. Thermoset is a crosslinked polymer adhesive that cured permanently following a completed chemical reaction. The crosslinking reaction stiffens the polymer and makes it difficult to deform. The backbone structure of thermoset resin can be aromatic or heterocyclic, and it can contain a variety of functional groups to provide effective bonding with reinforcement elements. A curing agent is used in thermoset polymers to increase the covalent bonds between polymer chains. Each epoxy contains distinct functional groups, and the crosslinking reaction varies according to temperature and curing cycle. Epoxy, polyester, phenol-formaldehyde, polyurethane, and other thermoset polymers are utilized in aircraft applications. Epoxy resin is a thermoset polymer that has dominated the aviation market due to its ease of curing using a variety of initiators and curing agents at relatively low cure temperatures. The fuselage of the Boeing 787 Dreamliner, for example, is made of hardened epoxy resin. Glass fiber-reinforced polyester was used to make low-voltage switchgear and control gear assemblies (Halyester). The polyester, which is bonded together with glass fiber and acts as an insulator to protect against high electrical voltage, has excellent mechanical and electrical properties (Bagherpour, 2012).

The development of gigahertz communication technologies necessitated the use of advanced EMI shielding. Lightning discharge, outbound ground-based transmitters, radar monitoring, and onboard communication and entertainment systems can all broadcast electromagnetic (EM) radiation. EMI shielding materials, such as carbon fiber-reinforced epoxy, are used to block undesired EM radiation in aircraft (Tserpes et al., 2020). Sandwich base aviation pallets consisting of epoxy or phenolic-reinforced glass or carbon fiber demonstrate possible weight reduction options as well as good thermal and mechanical performance. A reduction of 1 kg of pallet is anticipated to cost around EUR 163 per year (Al-Fatlawi et al., 2021).

2.1.2 Thermoplastic

Aside from thermoset resin, thermoplastic resin is a high-strength, recyclable matrix that is starting to gain traction in the aerospace industry. The thermoplastic's unique feature is that it can be remelted, providing flexibility and long-term sustainability. Thermoplastics provide better strength and toughness and meet the aircraft's fire/smoke/toxicity (FST) requirements. Furthermore, as compared to high-temperature epoxy thermoset resin, high-temperature thermoplastic resins such as polyetheretherketone (PEEK) and polyphenylene sulfone (PPS) demonstrate outstanding thermal stability. These thermoplastics were employed in aeroengine parts that create constant aerofrictional heating. It was reported that thermoplastic skins-reinforced welded ribs were % lighter than aluminum constructions. About 1000 individual parts in the A380 airframe are built of thermoplastic composite materials, accounting for 7.5% of the overall aircraft composite materials. The cargo floor,

rudder, and elevator tail portion were also fashioned of thermoplastic composite, reducing the overall weight of the aircraft. The aeroengine section's acoustic liner was similarly made of carbon fiber-reinforced polyetherimide (PEI) composite.

2.2 *Metal Matrix Composite*

To build up composite materials, Metal Matrix Composites (MMC) must have at least two elements. Metal serves as the matrix that bonds the reinforcement in MMC. Aluminum, magnesium, iron, cobalt or copper, and titanium are examples of metallic matrix materials (Qin, 2015; Pank & Jackson, 1993). Several oxides in the form of particles, fibers, or whiskers are used to strengthen the MMC (Vijayaram & Baskaralal, 2016). Aluminum and titanium matrix reinforced with oxide, nitride, or carbide are examples of MMCs (King et al., 2009). MMC is used in a variety of aircraft components, including engine components, landing gear, the airframe, and aviation. MMC has a high strength-to-weight ratio, excellent corrosion resistance, outstanding fatigue strength, excellent durability, and weight savings, to name a few. The main disadvantage of MMC is that it is difficult to process, which makes it more expensive than monolithic material.

When a spacecraft leaves the Earth, it passes through around 175,000 thermal cycles with temperatures ranging from 1250 °C to -1250 °C. Similarly, reentry vehicles for Earth and Mars may be exposed to temperatures of more than 1500 °C, putting them under extreme stress during takeoff and orbiting. As a result, spacecraft vehicles must be light and have good dimensional stability, particularly when subjected to varying temperatures in a dynamic environment. As a result, metal matrix composite is an appropriate material that meets the majority of spacecraft material requirements. The space shuttle orbiter's mid-fuselage structure was made of boron/aluminum (B/Al) composite. For each shuttle orbiter, hundreds of B/Al composite tubes were manufactured, resulting in a 45% weight reduction as aluminum (Rawal, 2001).

The use of metal alloy as a binder for metal matrix composite in aviation is due to corrosion concerns. The advancement of alloy material began with the refinement of aluminum alloy. By lowering the overall matrix density, the development of aluminum/lithium alloy has shown significant improvement (1% of lithium reduces the density of aluminum alloy by 3%). Sir Frank Whittles W1, one of the first turbine engines in the German Heinkel He 178, employed the very first superalloy (Piccirillo, 1998). This superalloy is comprised of nickel-chromium, which improves strength and temperature resistance for specialized applications such as turbine blades, discs, seals, rings, and aircraft engine casings. The material is then used in various fields of aerospace engineering, such as composites manufacturing tooling (King et al., 2009; Smith et al., 2001). The development of Vacuum Induction Melting (VIM) adds to the advancement of superalloy. This method allows for greater control over

the composition of superalloys, which improves the material's reliability (King et al., 2009). After then, Airbus and Alcan collaborated to develop alloys with specified qualities, primarily for the Airbus A380 (Lequeu et al., 2007). The goal is to choose the best material for a certain use in an aircraft while keeping the weight as low as possible (Bellonte, 2001). As a result, the airplane uses 61% aluminum alloys, 22% composites, 10% titanium and steel, and 3% fiber metal laminate (Lequeu et al., 2007).

2.3 Ceramic Matrix Composite (CMC)

Another type of composite material utilized in aerospace is ceramic matrix composite (CMC). CMC has a high strength-to-weight ratio, a high temperature capability with high oxidation resistance, a high fracture toughness with minimal thermal expansion, and a high fracture toughness with low catastrophic failure resistance (King et al., 2009; Naslain & Pomeroy, 2016). The matrix of CMC is a highly technological ceramic that outperforms typical ceramic materials. The reinforcement in CMC, on the other hand, can be aramid, graphite, or other ceramic fibers or whiskers that are compatible with the ceramic matrix (Cooke, 1991; Naslain & Pomeroy, 2016). A new class of engineered materials known as ceramic nanocomposites is generated when one or more nanosized phases are combined, having potential uses in a variety of challenging areas (Maitra & Roy, 2018).

CMC's strong thermal stability makes it ideal for use in aircraft, particularly in the hot engine region. Components that could benefit from the CMC coating include turbine disks, combustor liner, turbine airfoils, transition duct convergent flags, and acoustic liners. The turbine inlet temperature is being studied in order to improve material application because fuel efficiency is linked to this section. Interestingly, it was discovered that applying CMC coating increased the turbine inlet temperature by approximately 300 °C above the current temperature of 1200 °C. This considerably improved performance results in a 6% to 8% boost in airplane fuel economy (King et al., 2009). Over the course of an aircraft's entire life, this increase in fuel economy corresponds to a 588 million-liter savings in fuel usage. The amount of fuel consumed is the same as filling 300 of A380s with fuel. As a result, there is a significant benefit in terms of lowering operational aircraft costs, as the cost of jet fuel in 2008 was about quadruple that of 2004 (Ryerson & Hansen, 2013).

2.4 Biocomposite Material

Biocomposite has attracted widespread interest in aerospace as a result of environmental concerns, particularly for interior aircraft panels. Either the reinforcement or the matrix of a biocomposite can be biodegradable, or both reinforcement and

matrix can be biodegradable. In the case of reinforcement, natural fiber can be used to replace synthetic fiber whole or partially. Concerns about depleting petroleum or plastic resources have sparked interest in developing biodegradable materials. Natural fiber is also environmentally friendly because the materials are readily available from a natural resource and are nontoxic, light in weight, and quickly degradable. Hemp, flax, and ramie are examples of high-strength natural fibers that are nearly as strong as glass fiber (Fig. 18.3). The fiber cellulose content and the microfibrillar cellulose fibril angle are the two key factors that influence natural fiber strength.

Due to its inherent fiber structure and qualities, natural fiber has some disadvantages. Depending on the plant’s maturity, the fiber’s geometry may change. Natural fiber is also a hygroscopic material, meaning it absorbs moisture and expands. As a result, adequate fiber treatment is essential to ensure that the natural fiber can transmit its qualities and interact more effectively with the surrounding matrix. Panzera et al. (2020) look at the flax/epoxy fiber composite’s potential for aerospace applications. Flax fiber has the potential to be employed as a sandwich panel in airplanes, according to the researchers. However, there is still potential for growth when it comes to the fiber’s pore structure.

The aviation industry sets high standards for aircraft materials. Gomez-Campos et al. (2021) conducted a life cycle analysis on flax fiber composite materials

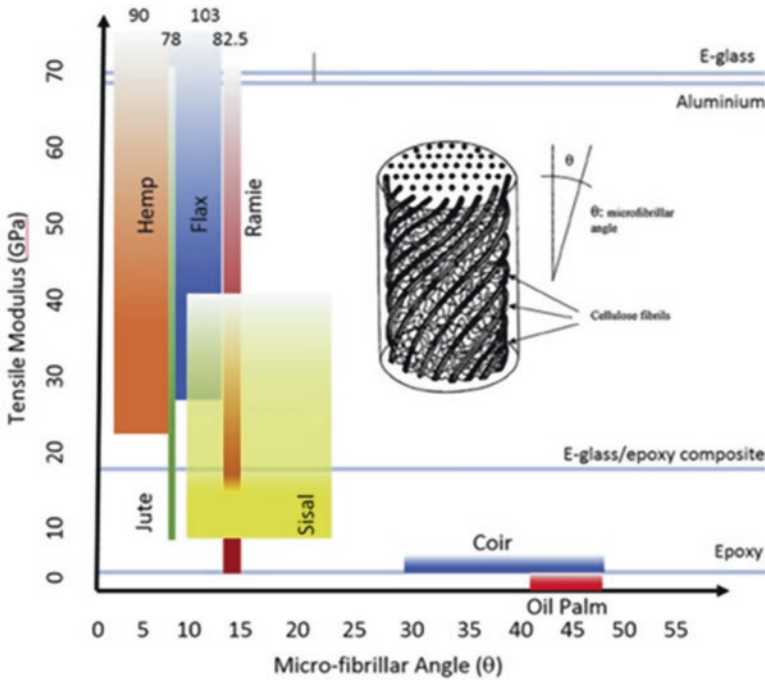


Fig. 18.3 Relationship between microfibrillar angle and tensile modulus on natural and synthetic fibers. Adapted with copyright permission from Lau et al. (2018)

recently. According to their findings, the weight of biocomposite materials is 14% more than that of standard aviation composite materials. Furthermore, the high pore structure of flax fiber necessitated the use of extra resin to create a composite panel. Combining natural and synthetic fibers is one approach to mitigate this issue. In comparison to using natural fiber alone in a composite, the synergistic effect of two reinforcing fibers in a hybrid composite will be beneficial. Amiri et al. (2018), on the other hand, found that resins made from soybean oil and reinforced with flax fiber had potential aircraft structural applications.

2.5 *Nanocomposite Materials*

Nanocomposite materials are gaining attention due to their nanosized fillers. If compared to typical micro and macro fillers (15 vol.%–40 vol.%), these nanofillers require a minimal loading (1 vol. –5 vol percent) for significant improvements in characteristics (Pelin et al., 2012). The present focus of nanocomposites development is on producing sufficient nanoparticles at a cost that is commercially viable (King et al., 2009). Ajmal et al., (2018) reported a cost-effective and environmentally friendly technique to the production of titanium dioxide (TiO_2), as well as the reduction of graphene oxide (GO) utilizing palm oil leaves extract (Amir Faiz et al., 2020).

The zirconia-based nanocomposites meet the need for a high thermal stability coating in gas turbines with higher operating temperatures. These carbon-based nanocomposites are also used as brake disk material and brake lining in military and civil aircraft. Materials for missiles, space shuttles, and reentry vehicles are among the more advanced applications (Milne, 2014). Furthermore, a Yttria-stabilized-zirconia-based ceramic composite was reported to be suitable for use as an abradable coating in a gas turbine for clearance between rotating and stationary parts (Zhao et al., 2012). At high temperatures, the Yttria-stabilized-zirconia nanocomposites can also provide hot corrosion protection (Keshavarz et al., 2013).

2.6 *Shape Memory Composite Materials*

Shape memory materials (SMM) are broadly classified as shape memory polymers (SMP), shape memory ceramics (SMC), shape memory alloys (SMA), and shape memory hydrogels (SMH). Shape memory metals are another name for SMA (Subash & Kandasubramanian, 2020). These materials are well known for their ability to return to their original shape in response to a specific stimulus. The shape memory effect (SME) is the name given to this ability (Huang et al., 2010). Shape memory composites were made by combining a standard composite with a shape memory material. Not only that but certain shape memory materials can be referred to as shape memory composites because they are composed of two or more constituent materials. SMM has been reported numerous times as a potential material

for variable jet intake (Rey et al., 2001; King et al., 2009; Song et al., 2007). The advantages of variable jet intake include reduced noise and fuel consumption. It was commonly reported that approximately 10% of fuel burn is reduced during takeoff and approach, while 2% of fuel burn is reduced during cruise. Furthermore, a 2 dB noise reduction for sidelines and flyovers is possible (Michel, 2011).

The aircraft structure can be optimized throughout the flight performance by adjusting the nozzle diameter during takeoff, cruise, and approach. A larger nozzle diameter is appealing for reducing jet velocity and noise during takeoffs and approaches. A smaller nozzle diameter at cruise, on the other hand, would be preferable to account for varying Mach number and altitude for fan loading optimization and fuel efficiency (Mabe et al., 2008). A hybrid of SMA and self-healing polymer composite have been reported. This hybrid material is appealing for use in synthetic fabrics-reinforced vinyl ester composites with superelastic shape memory NiTi alloy wire. In this study, two types of synthetic fabrics were compared: glass and carbon. The Charpy impact test reveals that SMA-containing composites have higher impact strength than control samples. However, when subjected to repeated impact, SMA/carbon composites showed lower damage tolerance than SMA/glass composites (Bond et al., 2008; Williams et al., 2007).

Self-deployable structures are another sophisticated application of shape memory material. The term “Cold Hibernated Elastic Memory (CHEM)” (Sokolowski et al., 1999; Sokolowski et al., 2004) was commonly used to describe the deployment method upon applied heat stimulus in the early era of shape memory material research (Neogi & Douglas, 1995; Neogi et al., 1998). To date, research on the use of shape memory materials in self-deployable structures is still ongoing (Santo et al., 2014). Hydraulic systems (Quan & Xu, 2015) and morphing variable geometry chevrons are two further conceivable applications of shape memory materials (King et al., 2009).

3 Environmental Impact of Composite Materials

The majority of aircraft deliveries from 1998 to 2018 were in the 175-seat category. From 2019 to 2038, aircraft deliveries of 210-seated aircraft are expected to expand dramatically with 10,396 aircraft, behind only 175-seated aircraft with 11,370 aircraft (Lange, 2019). Air traffic is predicted to expand at a rate of 4.3% per year during the next 20 years, from 2019 to 2038. A total of 39,200 new passenger and freight aircraft are required to meet this demand (Airbus, 2011).

The expansion of aircraft size and number can only mean one thing: more emissions from aircraft engines into the atmosphere. Unless new and better technologies are developed, civil aviation's fuel usage is anticipated to reach 450 tonnes by 2050. Within nearly 60 years of civil aviation operation, this is a tremendous increase of 320 tonnes. With such high fuel use, considerable greenhouse gas emissions are expected (Al-Ghanem, 1999). Over 90% of worldwide aviation emissions are attributed to large aircraft weighing more than 60 tonnes. For example, a typical

A330–200, which accommodates 240 passengers, already weighs 129 tonnes without cargo, passenger, luggage, and fuel (ICAO, 2020).

The emission of greenhouse gases from aircraft can be investigated using a variety of structural, aerodynamics, and propulsion technology innovations. From these options, two basic actions can be made to minimize overall fuel use and improve engine efficiency. Furthermore, the weight of the airplane can be reduced. As a result, composite materials are extremely important. A major weight reduction of 1000 kg on a big turbojet aircraft can significantly reduce fuel consumption by 1.1–1.5 percent. Transitioning from monolithic to composite materials has been shown to successfully reduce aircraft weight without sacrificing strength. Advanced composite materials application within the aircraft structural system can improve engine efficiency while boosting the latter. The use of CMC in turbine engines, which provides improved thermal efficiency, is an outstanding illustration of this (King et al., 2009).

4 Future of Aerospace Materials

The advantages of structurally integrated fiber-optic sensors (SIFORS) over standard mechanical and electrical sensors have piqued researchers' curiosity. Optical fiber sensors are compact and lightweight, allowing them to be easily inserted into composites (Nichols et al., 2007; Murayama et al., 2011; Silva-Munñoz and Lopez-Anido, 2009; Pang et al., 2013; Khat et al., 2010). These properties have sparked interest in using them in structural health monitoring systems for engineering projects around the world, particularly civil infrastructure. SIFORS are critical in the development of future revolutionary materials and strain sensing because they deliver accurate strain measurements to the structure and provide a response regarding the mechanical strain condition (Goossens et al., 2019). The response strain condition would expose the intended structure's structural integrity, reducing the need for routine and regular inspections and maintenance on aircraft structures (García et al. 2015). Continuous monitoring could also be done by delivering a constant load to the investigated structure at any given time to assess its fatigue life (Measures, 1993).

Biomimicry is the study of mimicking nature as an approach to sustainable design. Mimicry can be divided into three levels: the organism level, the behavior level, and the ecosystem level (Aziz & El Sherif, 2015). Da Vinci investigated pigeons for inspiration in human flight. Although he was not successful, he was the pioneer of biomimicry for aviation, which inspired the Wright brothers (Sane, 2016). Likewise, Airbus is keenly looking into biomimicry to gain invaluable insight into making aircraft lighter, faster, and therefore more fuel-efficient. Among their inspiration sources include snow geese, bald eagle, long-eared owl, and white shark (Airbus, 2011). Other bioinspired designs that are being researched include dandelion seeds, maple seeds, and hoppers for mobility in space system design (Menon

et al., 2006), dragonfly for biomimetic drones (Chahl et al., 2021), and lotus leaves for dust-repellant spacecraft surface (Gaier & Jaworske, 2007).

Airbus has been reported to aim to produce a see-through aircraft by 2050. The utilization of bird-skeleton structural material would give rise to the innovation. Bone is a material that has been tailored for a certain application. This is made feasible by its porous interior, which carries tension just where it is needed, allowing it to be both light and strong. As a result, in its use for a see-through airplane, the porous structure would act as the fuselage's panoramic windows. 3D printing is a commonly available technology that may be utilized to manufacture this precise, unique construction material to make this achievable. The material is manufactured using quick layering that builds up the desired design when the drafting is completed on a computer (Rich, 2012).

A decade ago, a notion of growing the material arose, in addition to 3D printing material to satisfy the design of nature-inspired structures. The idea is to reduce waste by developing the material into the exact shape requested, a process known as 3D printing. This is in contrast to the standard design approach, which requires parts to be integrated into a single product (Sargent, 2019). Neri Oxman, regarded as a pioneer in material ecology, claims that eliminating parts and assembling a product brings design closer to nature. Natural materials are used with additive manufacturing technologies to achieve this. 3D printing resembles natural development since it develops an object layer by layer (Jawad, 2019). Another aspect of Airbus's 2050 goal is to equip passengers with organically grown seats that can sense the demands of people and adjust to create the best possible fit. Hybridization with intelligent materials that recall the body's ideal position would enable the response mechanism (Rich, 2012). This hybridization is frequently referred to as 4D printing, which refers to a printed object that can change shape over time (Deshmukh et al., 2020). Cabins would therefore have self-cleaning and self-healing properties, which would allow them to clean and repair themselves (Airbus, 2011).

Translucent wood is a highly possible material to be used alongside the bird-skeleton structure material for the fuselage. Since the latter material already has an optimized structure and strength, translucent wood can fill up the porous spaces and serve as a cabin window. The cellulose in wood has hollow tube structures. Then air trapped in these hollow tubes scatters light which contributes to the materials' transparency. Thus, the initial effort of producing translucent wood was conducted by entirely removing lignin and replacing it with resin. This is because the presence of chromophore light-activated compounds in lignin makes the wood look brown. Complete removal of chromophore involves chemicals that are harmful to the environment, aside from degrading the mechanical strength of wood. Recent advancement of using hydrogen peroxide (Fig. 18.4) enables the modification of chromophores so that wood color is no longer visible. Additional material can be added into transparent wood so that it could absorb, store, and release heat. What makes it even more interesting is that the transparent wood would become cloudier upon the release of stored heat (Eichhorn, 2021).

The increased interest in space exploration necessitates a strategy for producing construction materials on-site. This would lessen the payload by a significant

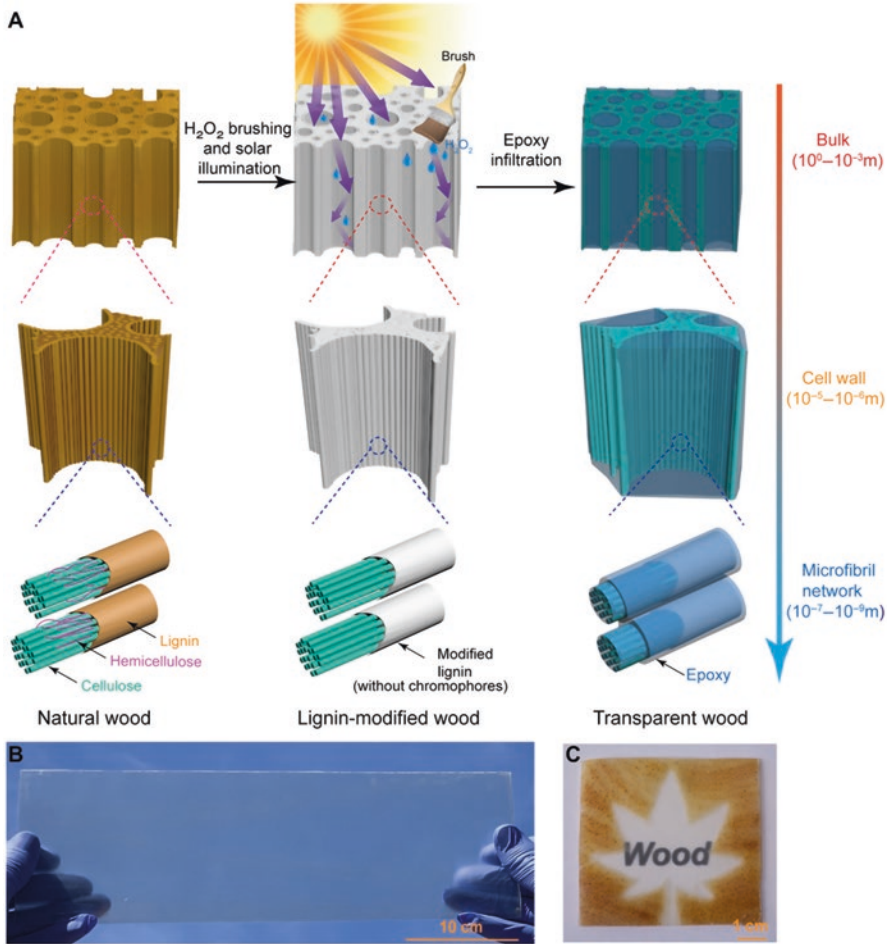


Fig. 18.4 (a) Environmentally friendly method of fabricating translucent wood. (b) A sheet of translucent wood. (c) Translucent wood along the transverse direction (Xia et al., 2021). This Figure is under Attribution-NonCommercial 4.0 International

amount while also saving a significant quantity of fuel and, as a result, money. Earth's new and green construction material, geopolymer concrete, has been widely explored. Lunar and Martian soil have been attracting attention in the aerospace industry because they have the necessary and adequate silica and alumina ingredients for geopolymerization (Alexiadis et al., 2017). Furthermore, alkali metal on the moon could provide the alkaline solution required to complete the process (Matta et al., 2009). Both lunar and Martian soil have stronger compressive and flexural strength than ordinary cement, according to compression and flexural testing. Further investigation finds that Martian soil has a strength comparable to that of traditional building blocks (Alexiadis et al., 2017). Aside from that, urea is currently

being used as a superplasticizer in geopolymer mixes for space exploration. The initial compressive strength of geopolymer samples containing urea was found to be higher than that of typical superplasticizers. Urea is readily available everywhere humans are since it is the second most prevalent component in urine (after water). As a result, these readily available chemicals could be an effective building material for space exploration (Pilehvar et al., 2019).

Because of its potential to mend damaged structures, self-healing material has promise for usage in aircraft structures. This concept is based on biomimicry, which is the study of how living organisms such as plants and animals cure themselves (White et al., 2001). Because the material can repair fracture initiation, this helps to prevent failure due to crack propagation. This provides for lower maintenance costs because certain materials are regarded to nearly self-repair. As a result, the life span of self-healing materials is extended (Das et al., 2016).

There are numerous self-healing mechanisms, the most well known of which are hollow fiber (Pang & Bond, 2005) and encapsulation (Pang & Bond, 2005; Xue et al., 2018). Numerous studies, however, have been conducted to demonstrate the feasibility of using self-healing materials in aircraft. Due to the difficulty of detecting and assessing damage in composites, the use of composites in aircraft requires extensive maintenance. With the growing use of composite materials in aircraft, it is necessary to address this issue (Tan et al., 2008).

Carbon Fiber-Reinforced Polymers (CFRP) are well known in the aerospace industry for their use in aircraft fuselages. To enhance CFRP, the system incorporates self-healing hollow glass. Before allowing the samples to self-heal, they were subjected to quasi-static indentation damage. Following that, the samples were tested to determine their healing efficacy. Flexural strength recovery is 97%, while compressive strength recovery is 92% (Bond et al., 2008). Simultaneously, composites have been reported to have a high rate of successful healing. In the same direction as the fibers were aligned, glass fiber-reinforced epoxy composites were embedded with a series of vascular networks. Lewis acid-catalyzed epoxy was used as the self-healing agent. The composite was found to be completely self-healing and to revert to its original mechanical properties (Coope et al., 2013). Additionally, a hybrid SMA/self-healing polymer composite reinforced with glass and carbon fibers has been reported. It was discovered that the SMA/glass self-healing composite exhibits superior performance when subjected to repeated impact. This suggests that glass fiber could eventually replace carbon fiber as the primary composite material in aircraft (Bond et al., 2008; Williams et al., 2007).

The self-healing concept is not limited to aircraft; it can also be applied to spacecraft. At the moment, spacecraft equipment is protected from space debris impact by an aluminum bumper. We prepared an Ethylene-Methacrylic Acid (EMAA) copolymer with acid groups that were neutralized with sodium ions. The material (now dubbed ionomeric polymer) was compared to aluminum as a spacecraft bumper. Five ionomeric polymers were subjected to impact testing; four of them completely self-healed while one was perforated. When the perforated ionomer polymer was compared to the perforated aluminum bumper, the hole in the ionomer polymer was found to be five times smaller than the hole in the aluminum specimen.

Self-healing polymers were found to be more resistant to impact than aluminum (Francesconi et al., 2013).

The concept of self-healing can also be applied to a coating rather than an entire structure. This would be appropriate for aircraft components that are already considered to be made of a superior material. Aluminum is a well-known material that is frequently used in light aircraft. Due to the fact that aluminum is prone to corrosion, a self-healing coating would be an excellent enhancement for this material. Through chemical conversion of AA2024 aluminum alloy, a self-healing vanadia coating for aerospace-grade aluminum was synthesized. Self-healing was discovered to occur when a thin layer of vanadia oxide forms on aluminum, preventing oxygen from penetrating (Hamdy et al., 2011).

Future aerospace materials are not limited to the invention of new materials; they also include structural improvements to existing materials. Lattice, honeycombs, and foams are all examples of cellular structures. In comparison to honeycombs and foams, the lattice structure is significantly superior because each unit cell can be set as a design variable. This enables the structure to be optimized for the performance of specific custom functions (Pan et al., 2020). Lattice blocks are 15% lighter than the same solid state with identical external dimensions. This is accomplished while maintaining a healthy level of strength. Investment casting is used to shape lattice blocks into pyramidal or tetragonal truss configurations (King et al., 2009).

5 Conclusions

Composite materials are primarily composed of polymer, metal, and ceramic matrixes. The choice of matrix materials and reinforcement is critical for producing a high-performance composite. Composite materials account for approximately 50% of aircraft components. Composite materials used in aerospace applications should be lightweight, have a high strength-to-weight ratio, be resistant to fatigue and corrosion, be durable, and be thermally stable. Glass, carbon, and aramid fibers are frequently used as reinforcement in aerospace composite materials. Additionally, natural fiber has been considered as a future fiber for interior aircraft applications. The biodegradability, availability, and sustainability of natural fiber are well known. Additionally, the addition of a trace amount of nanofiller improves the performance of aerospace composite materials significantly. Apart from advancements in composite development, the aerospace industry has shown interest in innovative composite materials such as self-healing composites and geopolymer composite production.

Acknowledgments The authors would like to express their gratitude to Universiti Putra Malaysia (UPM), particularly the Department of Aerospace Engineering, the Institute of Nanoscience and Nanotechnology (ION2), Institute of Tropical Forestry and Forest Products (INTROP), and Aerospace Malaysia Research Center (AMRC).

References

- Airbus. (2011). *Airbus looks ahead to 2050 and beyond*. Retrieved from <https://www.airbus.com/newsroom/news/en/2011/06/airbus-looks-ahead-to-2050-and-beyond.html>.
- Ajmal, N., Saraswat, K., Afroz Bakht, M., et al. (2018). Cost-effective and eco-friendly synthesis of titanium dioxide (TiO₂) nanoparticles using fruit's peel agro-waste extracts: Characterization, in vitro antibacterial, antioxidant activities. *Green Chemistry Letters and Reviews*, 12(3), 244–254.
- Alexiadis, A., Alberini, F., & Meyer, M. E. (2017). Geopolymers from lunar and martian soil simulants. *Advances in Space Research*, 59(1), 490–495.
- Al-Fatlawi, A., Jármai, K., & Kovács, G. (2021). Optimal design of a fiber-reinforced plastic composite sandwich structure for the base plate of aircraft pallets in order to reduce weight. *Polymers*, 13(5), 834.
- Al-Ghanem, T. M. (1999). Contribution of aviation to global warming. *Intergovernmental Panel on Climate Change (IPCC)*, 1–2.
- Amir Faiz, M. S., Che Azurahaman, C. A., Raba'ah, S. A., et al. (2020). Low cost and green approach in the reduction of graphene oxide (GO) using palm oil leaves extract for potential in industrial applications. *Results in Physics*, 16, 1–7.
- Amiri, A., Burkart, V., Yu, A., et al. (2018). The potential of natural composite materials in structural design. In *Sustainable composites for aerospace applications* (pp. 269–291). Woodhead Publishing.
- Aziz, M. S., & El Sherif, A. Y. (2015). Biomimicry as an approach for bio-inspired structure with the aid of computation. *Alexandria Engineering Journal*, 55(1), 707–714.
- Bagherpour, S. (2012). *Fibre reinforced polyester composites* (pp. 135–166). InTech.
- Bellonte M (2001) Composite materials in the Airbus A380-from history to future. *International conference of composite materials* (pp. 1–5).
- Bond, I. P., Trask, R. S., & Williams, H. R. (2008). Self healing fibre-reinforced polymer composites. *MRS Bulletin*, 33(8), 770–774.
- Chahl, J., Chitsaz, N., McIvor, B., et al. (2021). Biomimetic drones inspired by dragonflies will require a systems based approach and insights from biology. *Drones*, 5(2), 24.
- Cooke, T. F. (1991). Inorganic fibers: A literature review. *Journal of the American Ceramic Society*, 74(12), 2959–2978.
- Coope, T. S., Wass, D. F., Trask, R. S., & Bond, I. P. (2013). Metal triflates as catalytic curing agents in self-healing fibre reinforced polymer composite materials. *Macromolecular Materials and Engineering*, 299(2), 208–218.
- Das, R., Melchior, C., & Karumbaiah, K. M. (2016). Chapter 11: Self-healing composites for aerospace applications. In S. Rana & R. Figueiro (Eds.), *Advanced composite materials for aerospace engineering. processing, properties and applications*. Woodhead Publishing.
- Deshmukh, K., Houkan, M. T., AlMaadeed, M. A., et al. (2020). Chapter 1- introduction to 3D and 4D printing technology: State of the art and recent trends. In K. K. Sadasivuni, K. Deshmukh, & M. A. Almaadeed (Eds.), *3D and 4D printing of polymer nanocomposite materials, processes, applications and challenges*. Elsevier.
- Eichhorn, S. (2021). *Transparent wood is coming, and it could make an energy-efficient alternative to glass*. Retrieved from <https://theconversation.com/transparent-wood-is-coming-and-it-could-make-an-energy-efficient-alternative-to-glass-154981>
- Francesconi, A., Giacomuzzo, C., Grande, A. M., et al. (2013). Comparison of self-healing ionomer to aluminium-alloy bumpers for protecting spacecraft equipment from space debris impacts. *Advances in Space Research*, 51(5), 930–940.
- García, I., Zubia, J., Durana, G., Aldabaldetrek, G., Illarramendi, M. A., & Villatoro, J. (2015). Optical fiber sensors for aircraft structural health monitoring. *Sensors*, 15(7), 15494–15519.
- Gaier, J., & Jaworske, D. A. (2007). Lunar dust on heat rejection system surfaces: Problems and prospects. *NASA STAF*, 26, 1–13.

- Gomez-Campos, A., Vialle, C., Rouilly, A., et al. (2021). Natural fibre polymer composites-a game changer for the aviation sector? *Journal of Cleaner Production*, 286, 124986.
- Goossens, S., De Pauw, B., Geernaert, T., Salmanpour, M. S., Khodaei, Z. S., Karachalios, E., Saenz-Castillo, D., Thienpont, H., & Berghmans, F. (2019). Aerospace-grade surface mounted optical fibre strain sensor for structural health monitoring on composite structures evaluated against in-flight conditions. *Smart Materials and Structures*, 28(6), 1–13.
- Hamdy, A. S., Doench, I., & Moehwald, H. (2011). Intelligent self-healing corrosion resistant vanadia coating for AA2024. *Thin Solid Films*, 520, 5.
- Huang, W. M., Ding, Z., Wang, C. C., et al. (2010). Shape memory materials. *Materials Today*, 13(7–8), 54–61.
- ICAO. (2020). *New ICAO aircraft CO₂ standard one step close to final adoption*. Retrieved from <https://www.icao.int/Newsroom/Pages/New-ICAO-Aircraft-CO2-Standard-One-Step-Closer-To-Final-Adoption.aspx>
- Jawad, M. (2019). *Manufactured by nature: Growing generatively designed products*. Virginia Commonwealth University. (Thesis).
- Keshavarz, M., Idris, M. H., & Ahmad, N. (2013). Mechanical properties of stabilized zirconia nanocrystalline EB-PVD coating evaluated by micro and nano indentation. *Journal of Advanced Ceramics*, 2(4), 333–340.
- Khiat, A., Lamarque, F., Prelle, C., et al. (2010). Two-dimension fiber optic sensor for high-resolution and long-range linear measurements. *Sensors and Actuators A*, 158(1), 43–50.
- King, D., Inderwildi, O., & Carey, C. (2009). Advanced aerospace materials: Past, present and future. *Aviation and the Environment*, 3(9), 22–27.
- Lange B (2019). *Lifting the lid on the global market forecast: Cities, airports & aircraft*. Airbus. 2019.
- Lau, K., Hung, P., Zhu, M., et al. (2018). Properties of natural fibre composites for structural engineering applications. *Composites Part B: Engineering*, 136, 222–233.
- Lequeu, P., Lassince, P., & Warner, T. (2007). Aluminum alloy development for the Airbus A380-part 2. *Advanced Materials and Processes*, 165(7), 41–44.
- Mabe, J. H., Calkins, F. T., & Alkislal, M. B. (2008). Variable area jet nozzle using shape memory alloy actuators in an antagonistic design. In *Industrial and commercial applications of smart structures technologies* (Vol. 6930). International Society for Optics and Photonics.
- Maitra, S., & Roy, J. (2018). Chapter 3: Nanoceramic matrix composites: Types, processing, and applications. In I. M. Low (Ed.), *Advances in ceramic matrix composites*. Woodhead Publishing.
- Matta, M., Smith, S., Baumgardner, J., et al. (2009). The sodium tail of the mood. *Icarus*, 204(2), 409–417.
- Measures, R. M. (1993). Fiber optic sensing for composite smart structures. *Composites Engineering*, 3(7–8), 715–750.
- Menon, C., Ayre, M., & Ellery, A. (2006). Biomimetics: A new approach for space system design. *ESA Bulletin*, 125, 20–26.
- Michel U (2011) The benefits of variable area fan nozzles on turbofan engines. In *Conference: 49th AIAA aerospace sciences meeting including the new horizons forum and aerospace exposition AIAA 2011-0266. Orlando, Florida*.
- Milne, S. (2014). *Nanocomposites in aerospace*. Retrieved from <https://www.azonano.com/article.aspx?ArticleID=3258>
- Mouritz, A. P. (2012). Chapter 13: Polymers for aerospace structures. In A. P. Mouritz (Ed.), *Introduction to aerospace materials*. Woodhead Publishing.
- Murayama, H., Kageyama, K., Uzawa, K., et al. (2011). Strain monitoring of a single-lap joint with embedded fiber-optic distributed sensors. *Structural Health Monitoring*, 11(3), 325–344.
- Naslain, R. R., & Pomeroy, M. R. (2016). Ceramic matrix composites: Matrices and processing. *Reference Module in Materials Science and Materials Engineering*, 1060–1066.
- Neogi, D., Douglas, C., & Smith, D. R. (1998). Experimental development of self-deployable structures. *International Journal of Space Structures*, 13(3), 157–169.

- Neogi, D., & Douglas, C. D. (1995). Design and development of a self deployable structural element. *International Journal of Space Structures*, 10(2), 77–87.
- Nichols, J. M., Trickey, S. T., Seaver, M., et al. (2007). Use of fiber-optic strain sensors and holder exponents for detecting and localizing damage in an experimental plate structure. *Journal of Intelligent Material Systems and Structures*, 18(1), 51–67.
- Pan, C., Han, Y., & Lu, J. (2020). Design and optimization of lattice structures: A review. *Applied Sciences*, 10, 1–36.
- Pang, C., Yu, M., Gupta, A. K., et al. (2013). Investigation of smart multifunctional optical sensor platform and its application in optical sensor networks. *Smart Structures and Systems*, 12(1), 23–39.
- Pang, J. W. C., & Bond, I. P. (2005). Hollow fibre reinforced polymer composite encompassing self-healing and enhanced damage visibility. *Composites Science and Technology*, 65(11), 1791–1799.
- Pank, D. R., & Jackson, J. J. (1993). Metal-matrix composite processing technologies for aircraft engine applications. *Journal of Materials Engineering and Performance*, 2(3), 341–346.
- Panzer, T. H., Jeannin, T., Gabrion, X., et al. (2020). Static, fatigue and impact behaviour of an autoclaved flax fibre reinforced composite for aerospace engineering. *Composites Part B: Engineering*, 197, 108049.
- Pelin, C., Ion, D., Stefan, A., et al. (2012). Nanocomposite as advanced materials for aerospace industry. *Incas Bulletin*, 4(4), 57–72.
- Piccirillo, A. (1998). Heinkel and the turbojet engine-origin of the first jet fighter. In *AIAA and SAE, 1998 world aviation conference (5598)*.
- Pierce, R. S., & Falzon, B. G. (2017). Simulating resin infusion through textile reinforcement materials for the manufacture of complex composite structures. *Engineering*, 3(5), 596–607.
- Pilehvar, S., Arnhof, M., Pamies, R., et al. (2019). Utilization of urea as an accessible superplasticizer on the moon for lunar geopolymer mixtures. *Journal of Cleaner Production*, 247, 1–9.
- Qin, Q. H. (2015). Chapter 1: Introduction to the composite and its toughening mechanisms. In Q. Qin & J. Ye (Eds.), *Toughening mechanisms in composite materials*.
- Quan, D., & Xu, H. (2015). Shape memory alloy in various aviation field. *Procedia Engineering*, 99, 1241–1246.
- Rawal, S. P. (2001). Metal-matrix composites for space applications. *The Journal of Minerals, Metals & Materials Society (TMS)*, 53(4), 14–17.
- Rey, N., Tillman, G., Miller, R. M., et al. (2001). Shape memory alloy actuation for a variable area fan nozzle. In *Proceedings of the SPIE 4332, smart structures and materials 2001: Industrial and commercial applications of smart structures technologies (14 June 2001)*. <https://doi.org/10.1117/12.429677>
- Rich, S. C. (2012). *Aircraft design inspired by nature and enabled by Tech*. Retrieved from <https://www.smithsonianmag.com/arts-culture/aircraft-design-inspired-by-nature-and-enabled-by-tech-25222971/>
- Ryerson, M. S., & Hansen, M. (2013). Capturing the impact of fuel price on jet aircraft operating costs with Leontief technology and econometric models. *Transportation Research Part C: Emerging Technologies*, 33, 282–296.
- Sane, S. P. (2016). Bioinspiration and biomimicry: What can engineers learn from biologist? *Journal of Applied Sciences*, 19(1), 1–6.
- Santo, L., Quadri, F., Accettura, A., et al. (2014). Shape memory composites for self-deployable structures in aerospace applications. *Procedia Engineering*, 88, 42–47.
- Sargent, G. (2019). *From tree to chair without the carpentry: UK couple grows furniture*. Retrieved from <https://www.reuters.com/article/us-britain-furniture-sustainability-idUSKBN1W80R0>
- Silva-Munñoz, R. A., & Lopez-Anido, R. A. (2009). Structural health monitoring of marine composite structural joints using embedded fiber Bragg grating strain sensors. *Composite Structures*, 89(2), 224–234.
- Singh, B., Kumar, R., & Chohan, J. S. (2020). Polymer matrix composites in 3D printing: A state of art review. *Materials Today: Proceedings*, 33, 1562–1567.

- Smith, R. J., Lewi, G. J., & Yates, D. H. (2001). Development and application of nickel alloys in aerospace engineering. *Aircraft Engineering and Aerospace Technology*, 73(2).
- Sokolowski, W. M., Chmielewski, A. B., Hayashi, S., et al. (1999). *Cold hibernated elastic memory (CHEM) self-deployable structures*. NASA jet Propulsion Laboratory JPL, pp. 1–7.
- Sokolowski, W. M., Tan, S. C., & Pryor, M. K. (2004). Lightweight shape memory self-deployable structures for gossamer applications. In *45th AIAA/ASME/ASCE/AHS/ASC Structures, structural dynamics and materials conference, 19–22 April 2004, Palm Springs, CA*.
- Song, G., Ma, N., Lee, H., et al. (2007). Design and control of a proof-of-concept variable area exhaust nozzle using shape-memory alloy actuators. *Smart Materials and Structures*, 16(4), 1342.
- Soutis, C. (2005). Fibre reinforced composites in aircraft construction. *Progress in Aerospace Science*, 41(2), 143–151.
- Subash, A., & Kandasubramanian, B. (2020). 4D printing of shape memory polymers. *European Polymer Journal*, 134, 1–17.
- Tan, W. C., Kiew, J. C., Siow, Z. R., et al. (2008). Self healing of epoxy composite for aircraft's structural applications. *Solid State Phenomena*, 136, 39–44.
- Timmis, A. J., Hodzic, A., Koh, L., et al. (2015). Environmental impact assessment of aviation emission reduction through the implementation of composite materials. *The International Journal of Life Cycle Assessment*, 20(2), 233–243.
- Tserpes, K., Tzatzadakis, V., & Bachmann, J. (2020). Electrical conductivity and electromagnetic shielding effectiveness of bio-composites. *Journal of Composites Science*, 4(1), 28.
- Vijayaram, T. R., & Baskaralal, V. P. M. (2016). A review on the processing methods, properties and applications of metal matrix composites. *International Journal of Engineering Research and Technology*, 45–51.
- White, S. R., Sottos, N. R., Geubelle, P. H., et al. (2001). Autonomic healing of polymers composites. *Nature*, 409, 794–797.
- Williams, G., Trask, R., & Bond, I. (2007). A self-healing carbon fibre reinforced polymer for aerospace applications. *Composites Part A: Applied Science and Manufacturing*, 38(6), 1525–1532.
- Xia, Q., Chen, C., Li, T., et al. (2021). Solar assisted fabrication of large-scale, patternable transparent wood. *Science Advances*, 7(5), 1–8.
- Xue, C., Li, W., Li, J., et al. (2018). A review study on encapsulation-based self-healing for cementitious materials. *Structural Concrete*, 20(1), 198–212.
- Zhao, M., Zhang, L., & Pan, W. (2012). Properties of Yttria-stabilized-zirconia based ceramic composite abrasion coatings. *Key Engineering Materials*, 512–515, 1551–1554.

Chapter 19

Cooling Curve Thermal Analysis of Al-20% Mg₂Si-xB₄C Hybrid Composites for Aerospace Applications



Kee Heng Raymond Ling, Hamidreza Ghandvar, Tuty Asma Abu Bakar,
and Ying Ci Wee

1 Introduction

In recent decades, aluminum matrix composites (AMCs) play a significant role in many applications such as automotive, aerospace, and structural applications due to their low density and high specific strength (Alsubari et al., 2021; Amirkhanlou et al., 2011; Ilyas et al., 2021; Moses et al., 2016; Vajd & Samadi, 2019). Among them, high performance of hypereutectic Al-Mg₂Si in situ composite illustrates promising features to meet the demand for many applications due to improvements in mechanical properties. The Mg₂Si intermetallic phase being the in situ formed in the Al- matrix possesses high hardness, high melting point, high Young's modulus, low density, and low coefficient of thermal expansion (Amado & Daroqui, 2015; Zainon et al., 2016). However, the coarse and dendritic morphology of primary Mg₂Si particles has been thought to deteriorate the mechanical properties of the in situ composite. Hence, controlling the morphology and size of primary Mg₂Si is essential to enhance the mechanical properties of the composites.

There are numerous approaches that introduced to modify the undesired form of primary Mg₂Si structure in hypereutectic Al-Mg₂Si. Generally, the refinement of Mg₂Si particles was mainly by addition of elements into Al-Mg₂Si composite such as bismuth, antimony, strontium (Nordin et al., 2013), boron (Azarbarmas et al., 2011), yttrium (Liu et al., 2018), gadolinium (Sukiman et al., 2019), and more. It also can be achieved by addition of ceramic particles into Al-Mg₂Si composite such as YSZ (Ghandzar et al., 2019), TiB₂ (Gao et al., 2015), SiC (Yuguang et al., 2014), and so on. Among the additive additions, boron carbide (B₄C) particle has good potential for enhancement of mechanical and thermal properties of AMCs. It is a

K. H. R. Ling · H. Ghandvar · T. A. Abu Bakar (✉) · Y. C. Wee
Department of Materials, Manufacturing and Industrial Engineering, School of Mechanical
Engineering, Faculty of Engineering, Universiti Teknologi Malaysia, Skudai, Johor, Malaysia
e-mail: tuty@utm.my

superior ceramic reinforcement material with lower density compared to other commercial reinforcing particles such as SiC, TiB₂, and Al₂O₃ (Harichandran & Selvakumar, 2016; Ipekoglu et al., 2017; Shirvanimoghaddam et al., 2016). Many studies show that the addition of B₄C particles into AMCs can improve the mechanical properties of the composite (Harichandran & Selvakumar, 2016; Ipekoglu et al., 2017; Shirvanimoghaddam et al., 2016). The formation of boron-rich compounds such as Al₃BC and AlB₂ can also be observed in the B₄C-reinforced AMCs (Li et al., 2015; Syahril & Pratama, 2020). Some studies also show the presence of agglomeration of particles, porosities, and clustering in the composite when the concentration of B₄C particles exceeds certain level (Harichandran & Selvakumar, 2016; Ipekoglu et al., 2017; Shirvanimoghaddam et al., 2016). These problems will decrease the yield and ultimate tensile strength of the composites.

Limited research work has been reported on Al-Mg₂Si in situ composite reinforced with B₄C particles. Most of studies only concentrated on the reaction between aluminum and B₄C particles. Hence, the purpose of this study is to investigate the effect of various concentration of B₄C addition on the solidification behavior of Al-20%Mg₂Si in situ composite. The computer-aided CCTA technique is a powerful tool for determining the characteristic parameters of the primary Mg₂Si phase during solidification (Farahany et al., 2013). The results in terms of thermal analysis and microstructures properties will be observed and analyzed accordingly.

2 Materials and Methods

2.1 Materials

Pure Al, pure Mg, pure Si, and B₄C ceramic particles with the size of 10–30 μm supplied by Stanford Advanced Materials (CA 92630, USA) were used as initial materials to prepare Al-20%Mg₂Si-xB₄C ($x = 2.5, 5$ and 10 wt.%) hybrid composites.

2.2 Methods

2.2.1 Composite Fabrication

A resistance furnace (AT6952) was utilized to melt the Al-20%Mg₂Si ingot inside a silicon carbide crucible at 750 °C temperature. When the alloy were melted, B₄C powder was introduced. The supposed addition levels were 0, 2.5, 5, and 10 wt.% B₄C. Stirring action with constant speed was applied for complete homogenization and dissolution.

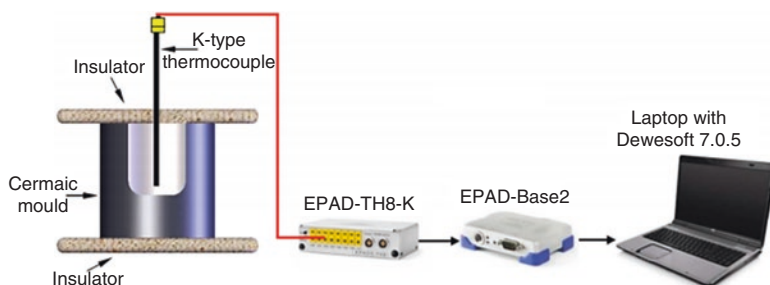


Fig. 19.1 Schematic illustration of experimental setup for thermal analysis

2.2.2 Thermal Analysis

The samples for thermal analysis were achieved by pouring of the molten alloy into a cylindrical ceramic mold that owned the dimension of 40, 40, and 7 mm for outer diameter, height, and wall thickness, respectively, in which the mold was preheated for 15 min at 750 °C. As seen in Fig. 19.1, thermal analysis was conducted by placing a K-type thermocouple in the middle, 15 mm above the bottom of the preheated ceramic mold. The temperature-time data were obtained using EPAD-TH8-K and EPAD-BASE module connected to a computer with DEWESoft 7.0.5. FlexPro 2019 data analysis software was utilized for extracting the recorded data, smoothing the curves, and plotting the cooling curve, first and second derivative curves in order to extract the characteristic data.

2.2.3 Microstructure Characterization

The metallography procedure including the standard grinding and polishing were used to prepare the microstructure samples. Microstructural examinations were carried out via OM (Nikon-MIDROPHOT-FXL) and SEM (Hitachi S-3400 N) equipped with EDS.

3 Result and Discussion

3.1 Microstructural Evolution

Figure 19.2 shows the optical images of Al-20%Mg₂Si composite microstructures with different B₄C concentrations. Consequently, Fig. 19.3 illustrates the XRD patterns of Al-20%Mg₂Si and Al-20%Mg₂Si-5%B₄C composites which indicate presence of Al, Mg₂Si, and B₄C in the composites. The primary Mg₂Si particles for unmodified composite exist as coarse and often in dendritic morphology enclosed with eutectic Mg₂Si cells, as shown in Fig. 19.2(a). With introducing of 2.5 wt.%

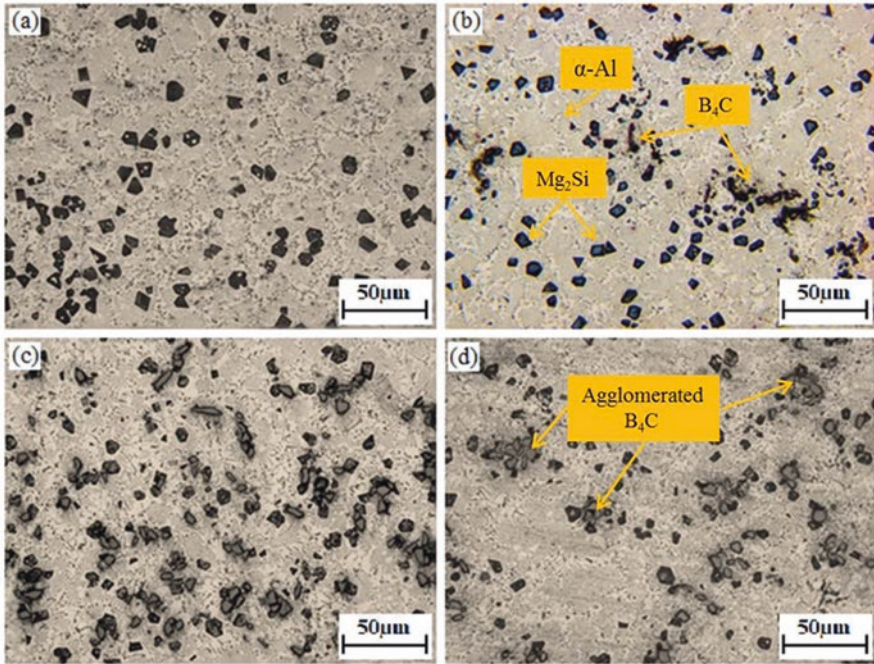


Fig. 19.2 Micrograph of Al-20% Mg_2Si composite added with various addition of B_4C : (a) 0 wt.%, (b) 2.5 wt.%, (c) 5 wt.%, and (d) 10 wt.%

B_4C into the composite, the shape of primary Mg_2Si transformed to regular polygon shape and reduced in size as depicted in Fig. 19.2(b). In addition, there are some Mg_2Si particles with a white hole at the center. As a result of nucleation of $\alpha-Al$ on Mg_2Si particle, the $\alpha-Al$ filled this hole as reported (Ghandvar et al., 2018). When the composite was treated with 5 wt.% B_4C , the shape of primary Mg_2Si altered into a polygonal and further decrease in size, as illustrated in Fig. 19.2(c). Addition of 10 wt.% of B_4C particles depicts the most refined primary Mg_2Si particles. However, more agglomeration of particles, porosities, and clustering were observed in the composite with addition of 10 wt.% B_4C , as illustrated in Fig. 19.2(d).

A similar behavior of the increased porosity with increased B_4C reinforcement content was observed in Al MMCs by the other papers (Harichandran & Selvakumar, 2016; Ipekoglu et al., 2017; Shirvanimoghaddam et al., 2016).

3.2 Quantitative Analysis of Microstructure

Figure 19.4 shows the variations in average particle size, aspect ratio, and particle formation per unit area (density) correspond to the various B_4C additions. The results are match well with microstructure observation in Fig. 19.5, in which with

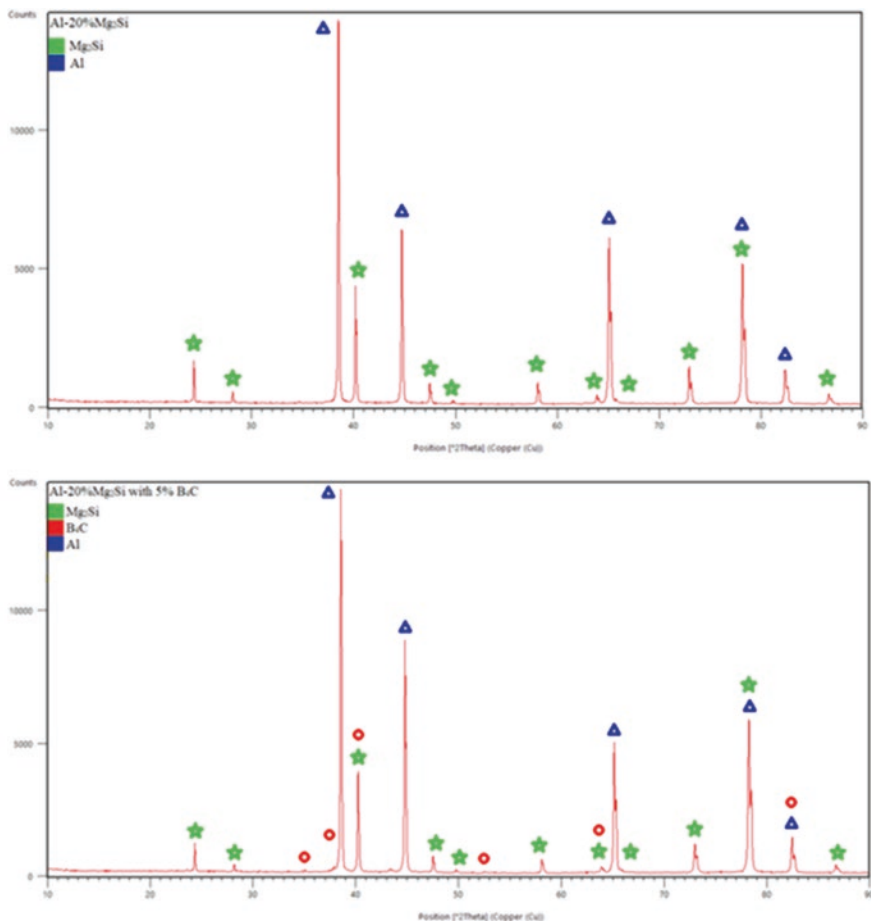


Fig. 19.3 XRD results of Al-20%Mg₂Si composite in unmodified and modified with 5 wt.% B₄C

2.5 wt.% B₄C additions, the average particle size reduced by 7% from 46.9 μm to 43.6 μm , the aspect ratio reduced by 3.7% from 1.34 to 1.29, and the density also decreased by 24% from 135 to 102.5 particle/mm². The reduction in size and aspect ratio of primary Mg₂Si particles as a result of B₄C addition can be associated to the role of B₄C particles to restrict the growth of Mg₂Si particles during solidification. Based on the particle pushing mechanism, the solidification front rejects the B₄C particles and finally entrapped in the grain boundary areas (Nagarajan et al., 1999). In addition, decreasing the density of Mg₂Si particles after addition of B₄C particle to Al-20%Mg₂Si composite is due to the formation of B-rich compound which consumes the existed Mg in the melt and caused reduction of Mg₂Si particles formation (Azarbasmas et al. 2011). With addition of 5 wt.% B₄C to Al-20%Mg₂Si composite, the particles size, aspect ratio, and density of primary Mg₂Si further decreased to 38.8 μm , 1.27, and 84 particle/mm². However, as observed in Fig. 19.5 with further

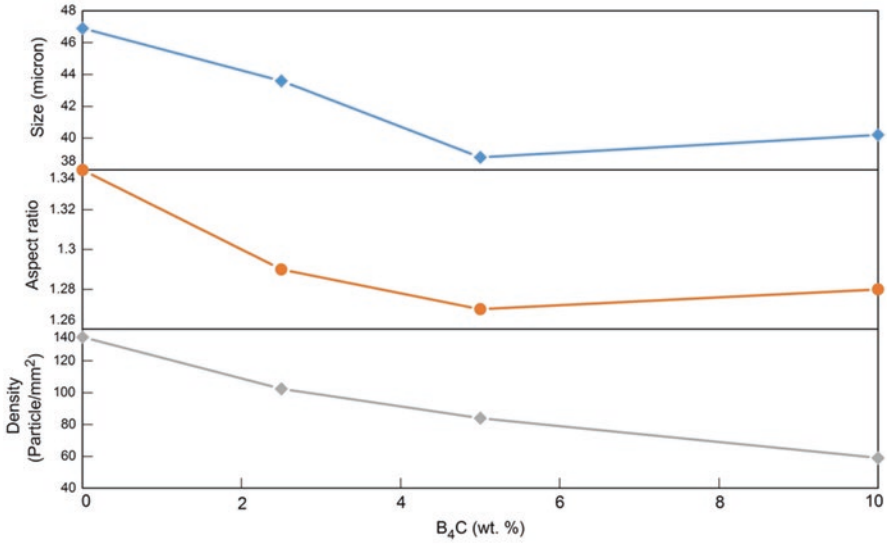


Fig. 19.4 Primary Mg₂Si particles characteristics in Al-20%Mg₂Si composite treated with various content of B₄C

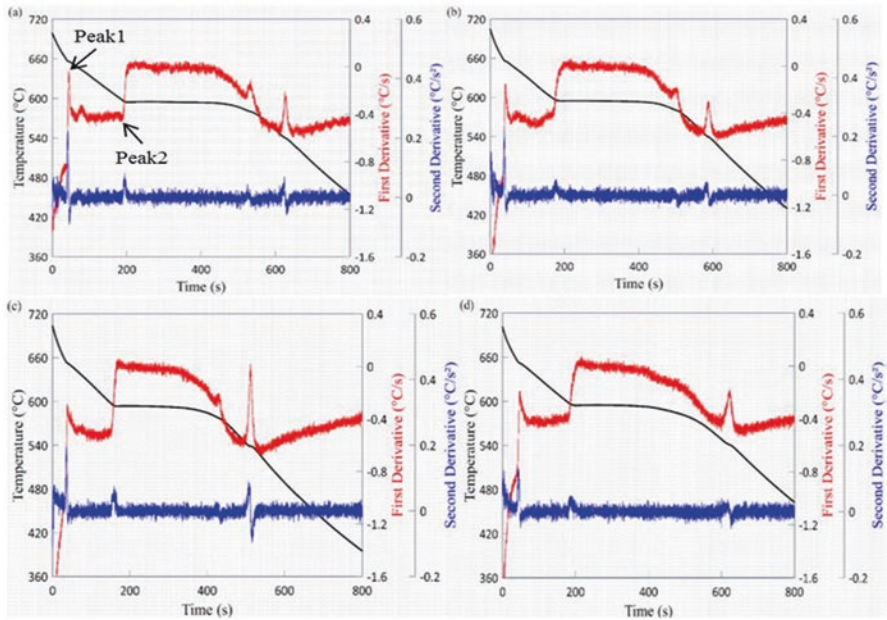


Fig. 19.5 Cooling curves related with first and second derivative curves for the Al-20%Mg₂Si composite with various addition of B₄C: (a) 0, (b) 2.5, (c) 5, and (d) 10 wt. %

addition of B₄C to 10 wt.%, the mean size and aspect ratio of primary Mg₂Si increased to 40.21 μm and 1.28, respectively. Nevertheless, the density decreased to 59 particle/mm². The reason for increasing the mean size and aspect ratio of primary Mg₂Si is agglomeration of B₄C particles in the composite matrix (Fig. 19.2(d)) as B₄C particles are not uniformly distributed throughout of the composite area and hence cannot hinder the growth of primary Mg₂Si particles in their preferred growth directions. As with further increasing the B₄C content in Al-Mg₂Si composite, the formation of B-rich compounds increased as well. Hence, more Mg content will be consumed and results in further decreasing of primary Mg₂Si particles. It has been reported that with addition of SiC and YSZ ceramic particles to Al-Mg₂Si composite, the average size of Mg₂Si reduced with increasing the content of the particles (Moktar et al., 2020; Sukiman et al., 2019).

3.3 Influence of B₄C Addition on Cooling Curves

The calculated cooling rate was at around 0.7 °C s⁻¹. Figure 19.5 illustrates the Al-20%Mg₂Si composite cooling curve with first and second derivative curves with various concentrations of B₄C. The first two peaks of the first and second derivative curve represent two distinct phase transformations that occurred during solidification. According to the binary phase diagram of Al-20%Mg₂Si, the first phase is the primary Mg₂Si phase (Peak 1), while the second phase is the formation of eutectic Al-Mg₂Si phase (Peak 2). With combining of all cooling curves of primary Mg₂Si formation segment with different levels of B₄C addition tested are shown in Fig. 19.6. As observed, addition of B₄C instigated an alteration in solidification behavior of the Al- 20%Mg₂Si composite which is associated with the optical micrograph of the microstructure observed in Fig. 19.2. The similar result is reported in the study carried out by Nordin et al. (2013).

Figure 19.7 shows the correlation exists between the first and second derivative curves used for determining the solidification parameters. The nucleation temperature (T_N) is the point that the d^2T/dt^2 increases abruptly from the zero line. The minimum temperature (T_{Min}) is the point at the summit on the second derivative curve. The growth temperature (T_G) is the point that the second derivative curve shifts down and then shifts up and catches the zero line again (Farahany et al., 2013). Figure 19.8 shows the nucleation temperature (T_N) and growth temperature (T_G) of primary Mg₂Si phase associated to the various B₄C additions. The plotted graph of T_N has the same pattern as for T_G of primary Mg₂Si, indicating the identical influence of these B₄C for these temperatures. Based on the result, it is observed that the T_N of primary Mg₂Si decreased when the B₄C addition was introduced from 2.5 to 10 wt.%. Same trend of graph is also observed for the T_G of primary Mg₂Si phase. From the temperature of 659 °C for unmodified Al-20%Mg₂Si composite, T_N of primary Mg₂Si decreased to 659 °C, 657 °C, and 656 °C after 2.5, 5, and 10 wt.% B₄C addition, respectively. The similar finding about the decreasing of the

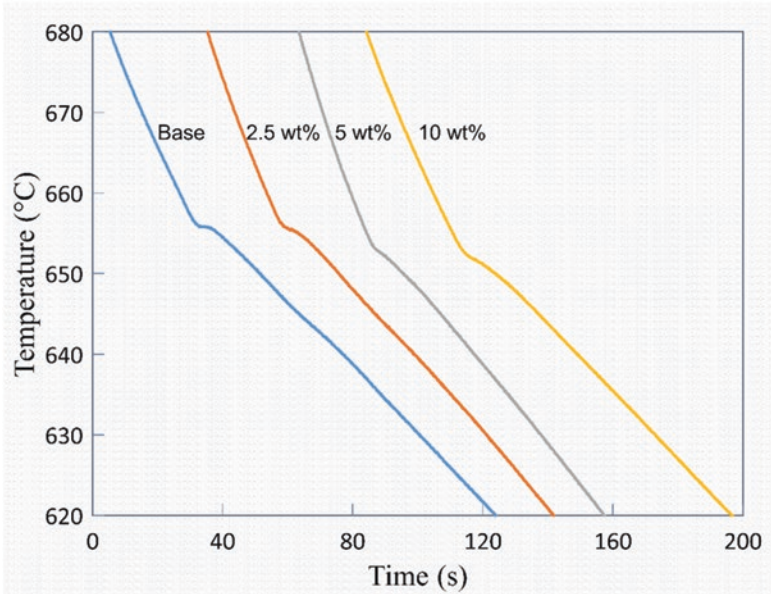


Fig. 19.6 Primary Mg_2Si formation segment corresponds to various concentrations of B_4C addition; 0, 2.5, 5, and 10 wt.% solidified at ceramic mold

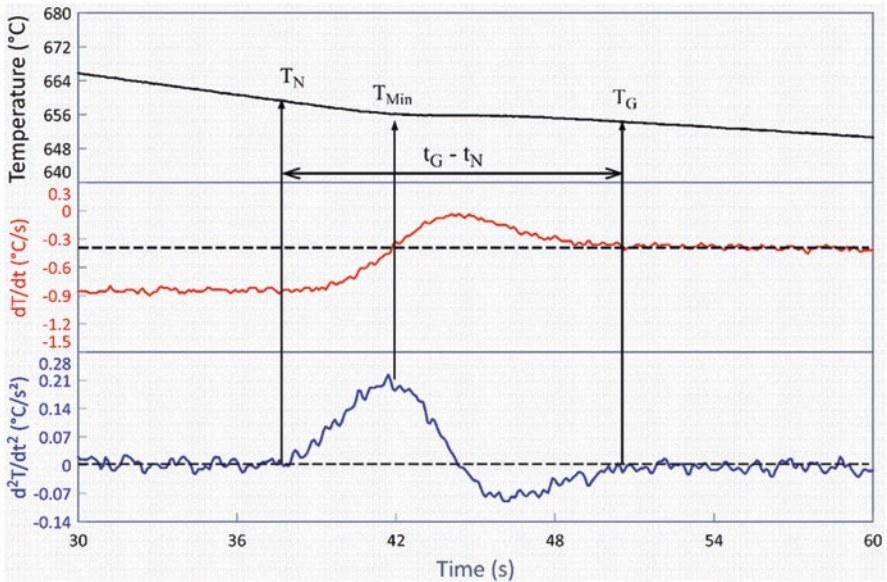


Fig. 19.7 Relationship between first and second derivative curve in the formation of primary Mg_2Si region displaying the points of interest

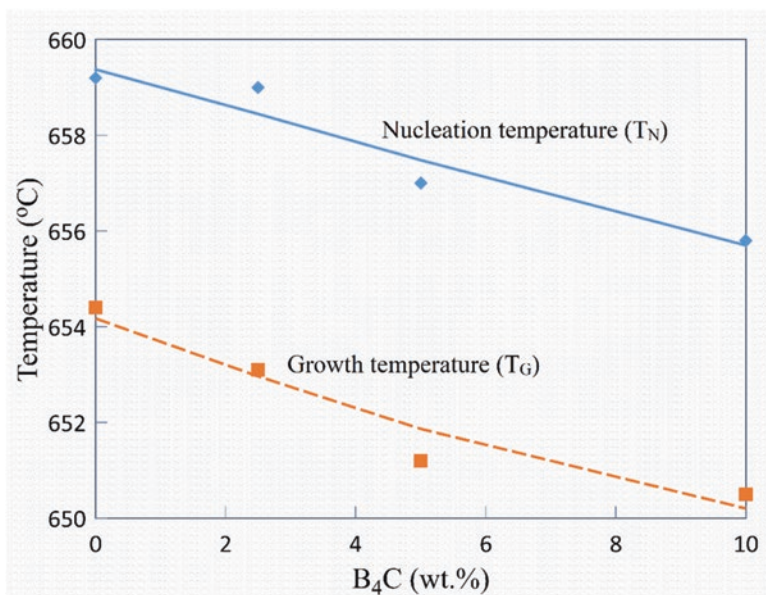


Fig. 19.8 Nucleation temperature (T_N) and growth temperature (T_G) of primary Mg_2Si phase with various content of B_4C addition

nucleation temperature (T_N) of primary Mg_2Si with addition of SiC particles up to 15 wt.% in Al-20% Mg_2Si composite was reported by Moktar et al. (2020).

Figure 19.9 shows the duration (Δt) of primary Mg_2Si particles formation. The $t_G - t_N$ Mg_2Si was used to indicate the time needed for the primary Mg_2Si to nucleate and grow until complete solidification prior to the start of the eutectic cells. In the untreated composite, the primary Mg_2Si duration to grow is about 13.82 s. The time is increased to 12.59 s as the composite was reinforced with 2.5 wt.% B_4C . The duration of primary Mg_2Si particles formation then further decreased with 5 wt.% B_4C and increased again with 10 wt.% B_4C particles. The difference between the duration is small which no more than 3.5 s. It is probably because of the important role of B_4C particles in controlling the growth of Mg_2Si particles which results in alteration of the particles size. The duration of 5 wt.% B_4C addition is lower than the other contents of B_4C . Hence, the best concentration of B_4C for refinement effect is 5%. In the study conducted by Ghandvar et al. (2018), they found that the duration of the Mg_2Si particles for nucleation and growth for 1.0 wt.% Gd addition is lower than other concentrations of Gd.

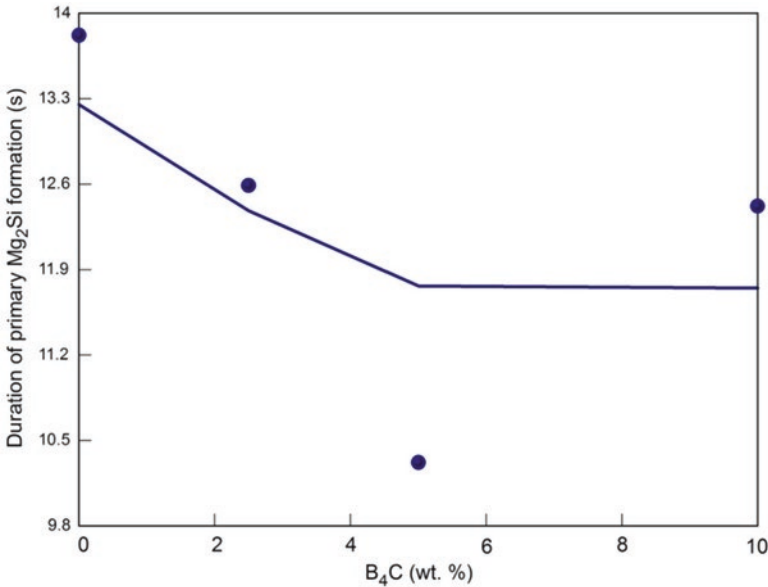


Fig. 19.9 Primary Mg₂Si particles duration for nucleation and growth as a function of addition of B₄C

3.4 Modification Mechanisms of B₄C Addition

3.4.1 Nucleation

The results clearly show that addition of B₄C to the untreated composite caused Mg₂Si particles refinement. Thermal analysis in Fig. 19.10 also depicted that with addition of B₄C, the nucleation temperature reduced, which may designate that the refining influence of B₄C is possibly associated to the stage of nucleation rather than growth. The most desired refinement has been obtained with addition of 5 wt.% B₄C. Most of the research shows that one of the major mechanisms in refinement of primary Mg₂Si particles is heterogeneous nucleation, in which modifier elements or their compounds act as nucleation sites, attributing to more effective heterogeneous nuclei for the primary Mg₂Si phase (Azarbarmas et al., 2011; Gao et al., 2015; Ghandzar et al., 2019; Nordin et al., 2013; Yuguang et al., 2014). Analysis is required to find out whether B₄C could perform as a nucleation substrate for primary Mg₂Si formation.

The crystal structures of B₄C and Mg₂Si are shown in Fig. 19.11. The crystal structures of Mg₂Si and B₄C were obtained from the software PTCLab with their corresponding Crystallographic Information File (CIF). Mg₂Si has face-centered cubic (FCC) crystal system with a lattice parameter of $a = 0.639$ nm and angle of $\alpha = \beta = \gamma = 90^\circ$ and belongs to space group Fm-3 m [225] (Persson, 2015). B₄C has rhombohedral crystal system with a lattice parameter of $a = b = 0.56$ nm,

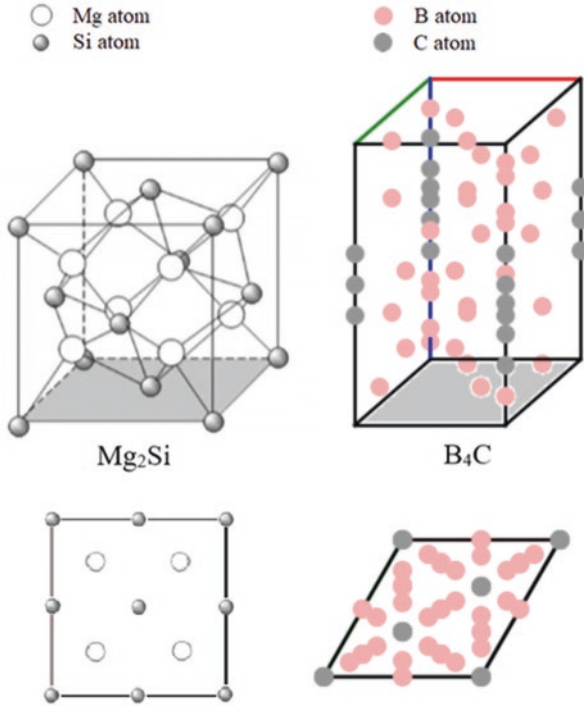


Fig. 19.10 Crystal structures and plane (0 0 1) of Mg₂Si and B₄C (Persson, 2015, 2016)

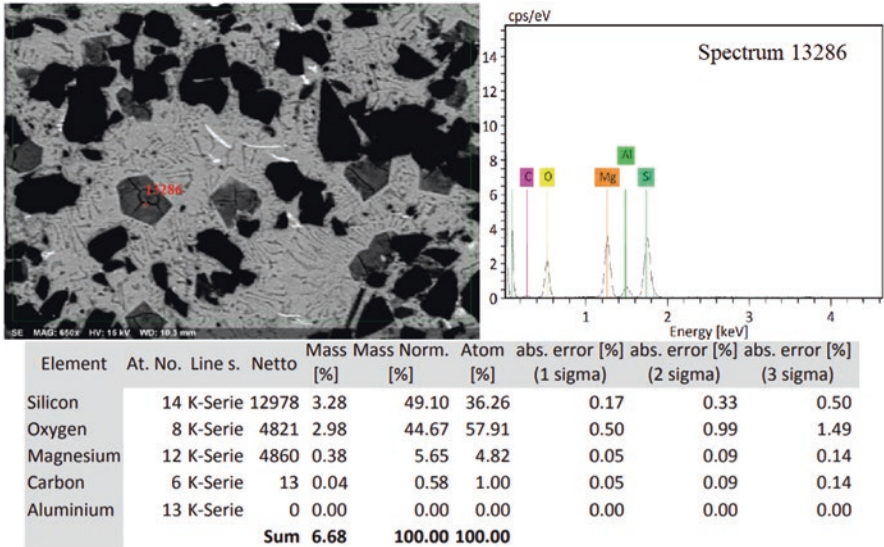


Fig. 19.11 SEM micrograph of Al-20%Mg₂Si composite with 10 wt.% B₄C addition and EDS analysis

$c = 1.212$ nm, angle of $\alpha = \beta = 90^\circ$, and $\gamma = 120^\circ$ and belongs to space group R-3 m [166] (Persson, 2016).

It can clearly see that the distribution of atoms on the B_4C and Mg_2Si planes is in a different manner. The lattice mismatch between different crystal structures cannot be calculated based on Bramfitt's two-dimensional lattice misfit theory (Chen & Li, 2014; Sukiman et al., 2019). The lattice mismatch between these two crystals shows that B_4C particles are not likely heterogeneous nucleation substrates for primary Mg_2Si . Besides, based on microstructural observations as shown in Fig. 19.1, there is no proof that B_4C may provide favorable substrates for Mg_2Si particles precipitation. That is why the primary Mg_2Si particles do not cling and grow up on the surface of B_4C particles. Therefore, B_4C is ineffective heterogeneous nucleation site for primary Mg_2Si particles.

The decrease in nucleation temperature of primary Mg_2Si may be related to the oxide compound, causing the decrease of Mg concentration in the composite (Nordin et al., 2013). The addition of B_4C may cause the decreasing of Mg, resulting to the move in the composition of the alloy to the eutectic point. Figure 19.11 demonstrates the SEM image of Al-20% Mg_2Si composite with 10% B_4C addition with corresponding EDS analysis.

The analysis proved that there is a presence of O atom in the composite. This might be due to the mixing of B_4C powder in the molten Al- Mg_2Si composite done by manual stir casting process. The B_4C powder was added little by little into the melt to prevent the agglomeration of particles. As the addition of B_4C powders increases, the time required for the stirring process increases. The longer the stirring process, the longer the time the melt exposed to the environment, the higher the possibility of moisture and oxygen absorption, the more the oxide compounds can be formed during the process and mixed into the composites. The Mg content will decrease and cause the change in the composition of the alloy to the eutectic point. Hence, the nucleation temperature of primary Mg_2Si decreases as the addition of B_4C increases.

3.4.2 Growth

Similar behavior of the depression in T_N and T_G as shown in Fig. 19.8 is also observed with the addition of different content elements such as bismuth, antimony, and strontium as reported by Nur et al. (2013). The refinement of Mg_2Si is probably related to the adsorption and poisoning mechanisms of boron element. According to Shirvanimoghaddam et al. (2016), Anne et al. (Syahrial & Pratama, 2020), and Li et al. (2015), some B containing compounds are detected in the various B_4C -reinforced aluminum composites. Even though the composites used for the studies are not Al-20% Mg_2Si composite, it is expected that some B elements are "dissolved" from B_4C particles into the liquid-solid interface. Elemental mapping results in Fig. 19.12 indicated that the microstructure contains Al, Mg_2Si , and B_4C particles. It is obvious that there is the presence of B element (B-KA: light-blue

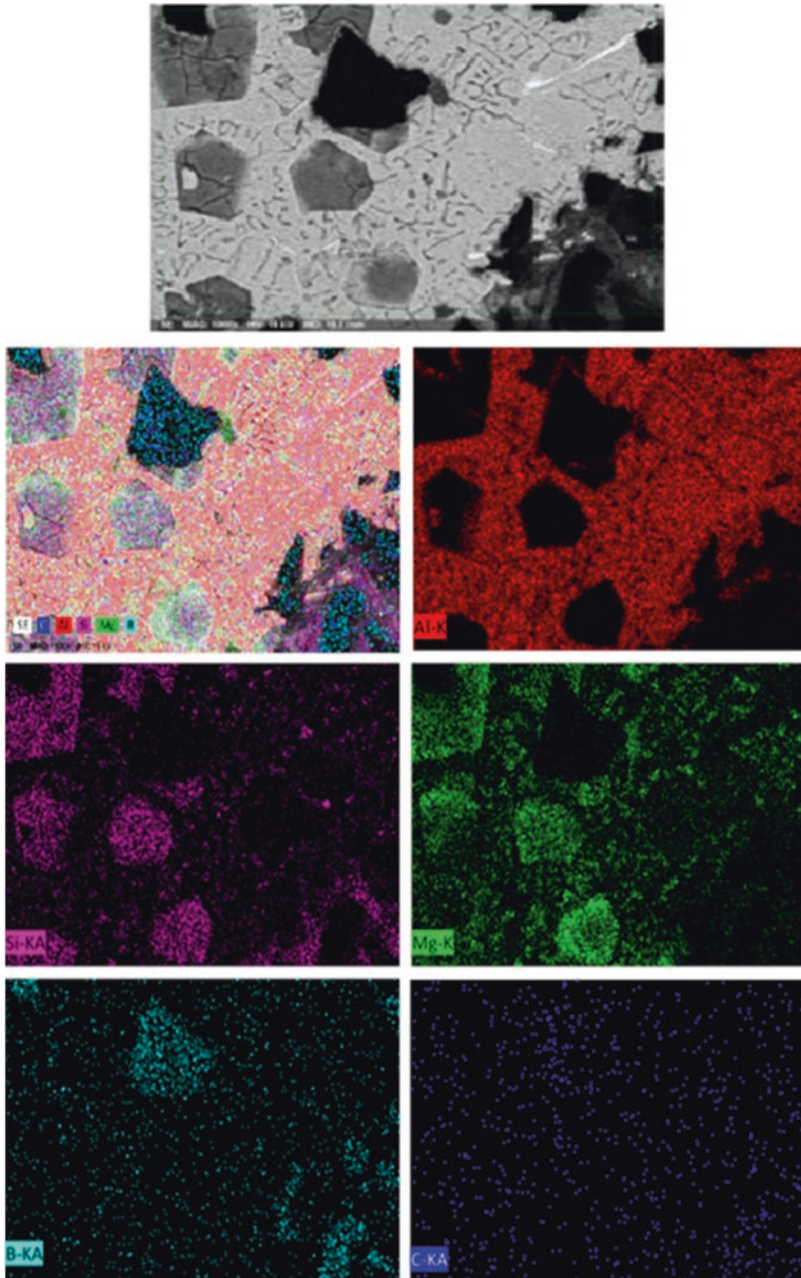


Fig. 19.12 SEM image and related elemental mapping of Al-20%Mg₂Si composite added with B₄C addition

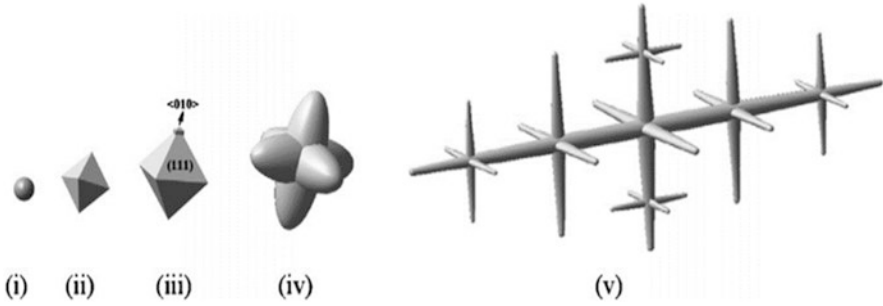


Fig. 19.13 Schematic design of primary Mg_2Si growth manner from a core to dendritic morphology (Wang et al., 2008)

dots) outside the B_4C particles. Hence, the elemental mapping proved that small amounts of B element are “dissolved” from B_4C particles in the Al-20% Mg_2Si composite. It is likely that B elements from B_4C particles play an important role in controlling the growth of primary Mg_2Si phases as reported by Azarbasmas et al. (2011).

According to Azarbasmas et al. (2011), the presence of B element in hypereutectic Al- Mg_2Si composite can change the Mg_2Si surface energy and the morphology of the Mg_2Si particles. The primary Mg_2Si morphology altered from irregular polygonal to a cubic shape. The refinement effect can be attributed to the inhibition of Mg_2Si crystal growth by B element. During solidification of composite, farther to the segregation of boron on the interface between solid and liquid, some B atoms also adsorbed on the growth front and changed the Mg_2Si surface energy (Azarbasmas et al., 2011). The Mg_2Si anisotropic growth will be suppressed by the adsorption and the poisoning effect of B. Figure 19.13 shows the schematic diagram of the growth steps of Mg_2Si particles. The process of unmodified primary Mg_2Si crystal will start from nucleation [Stage (i)] to octahedron and then to dendritic shape [Stage (v)] (Wang et al., 2008).

The lattice of Mg_2Si belongs to face-centered cubic (FCC). According to the Wulff’s theorem, the favored FCC growth direction along $[1\ 0\ 0]$ direction and the $(1\ 0\ 0)$ plane has higher growth rate as compared to the dense $(1\ 1\ 1)$ plane of Mg_2Si crystal. Hence, in equilibrium solidification condition, the steady-state growth shape of Mg_2Si should be octahedron and then to the dendritic morphology along $[1\ 0\ 0]$ (Chen et al., 2017). However, with addition of B_4C particles into the composite, the growth of $(1\ 0\ 0)$ plane is extremely hindered by modifier elements. The final shape of primary Mg_2Si crystal can be confined to Stage (ii) or (iii).

Nonetheless, addition of B_4C particles in the levels more than the best concentration has the opposite effect in refinement of primary Mg_2Si . Beyond the content from 5 wt.% B_4C to 10 wt.% also origin the possibility to agglomeration of particles, porosities, and clustering in the composite as shown in Fig. 19.14. This effect can be attributed to the growth of B_4C surface area. Large surface-to-volume ratio, low wettability, gas entrapment, and the bounding gas layer surface across the B_4C

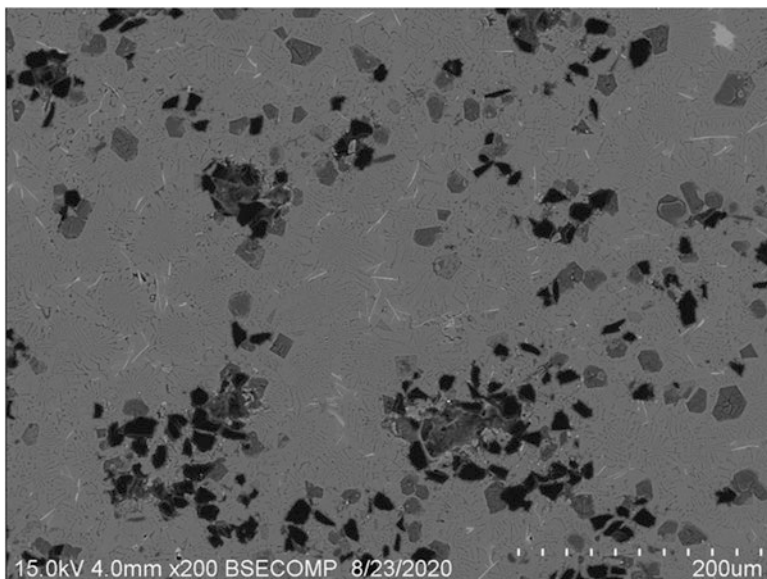


Fig. 19.14 Agglomeration of particles, porosities, and clustering in Al-20%Mg₂Si composite with 10 wt.% B₄C

are supreme areas for heterogeneous pore nucleation (Harichandran & Selvakumar, 2016; Ipekoglu et al., 2017; Shirvanimoghaddam et al., 2016). This problem can decrease the tensile properties of the composite. Hence, the hardness of the Al-20%Mg₂Si composite with 10 wt.% B₄C addition is lower than 5 wt.% B₄C addition. Similar behavior of particles agglomeration is also observed with YSZ addition in Al-Mg₂Si composites as reported by Sukiman et al. (Ghandzar et al., 2019).

4 Conclusions

The influence of different content of B₄C particles on microstructure alteration and solidification parameters of Al-20%Mg₂Si composite was examined. The main conclusion is as follows:

1. The best B₄C content is 5 wt.% as this concentration has the best effect in primary Mg₂Si particles refinement in the composite.
2. The refinement of primary Mg₂Si effect can be attributing to the adsorption and poisoning mechanisms of boron atoms from B₄C particles.
3. The shape of the primary Mg₂Si altered from dendritic to a polygonal shape with a reduction in the particle size, density, and aspect ratio by 7%, 24%, and 3.7%, respectively, with addition of 5 wt.% B₄C.

4. CCTA revealed that the nucleation temperature (T_N) of primary Mg_2Si reduced with B_4C addition due to the formation of oxide compound and decrease of Mg concentration in the composite, causing the shift in composition of the alloy to the eutectic point.

Acknowledgments The authors wish to thank Universiti Teknologi Malaysia (UTM) for provision of research facilities and financial support under the research grants 05E88 and 06G22 (TDR Grant).

References

- Alsubari, S., Zuhri, M. Y. M., Sapuan, S. M., Ishak, M. R., & Ilyas, R. A. (2021). Potential of natural fiber reinforced polymer composites in sandwich structures: A review on its mechanical properties. *Polymers*, *13*(3), 423. <https://doi.org/10.3390/polym13030423>
- Amado, M. N., & Daroqui, F. (2015). Revision of the solvus limit of Al-Mg₂Si pseudo binary phase diagram. *Procedia Materials Science*, *8*, 1079–1088. <https://doi.org/10.1016/j.mspro.2015.04.171>
- Amirkhanlou, S., Jamaati, R., Niroumand, B., & Toroghinejad, M. R. (2011). Using ARB process as a solution for dilemma of Si and SiCp distribution in cast Al-Si/SiCp composites. *Journal of Materials Processing Technology*, *211*, 1159–1165. <https://doi.org/10.1016/j.jmatprotec.2011.01.019>
- AzARBarmas, M., Emamy, M., Karamouz, M., Alipour, M., & Rassizadehghani, J. (2011). The effects of boron additions on the microstructure, hardness and tensile properties of in situ Al-15%Mg₂Si composite. *Materials & Design*, *32*, 5049–5054. <https://doi.org/10.1016/j.matdes.2011.05.036>
- Chen, K., & Li, Z. (2014). Effect of co-modification by Ba and Sb on the microstructure of Mg₂Si/Mg-Zn-Si composite and mechanism. *Journal of Alloys and Compounds*, *592*, 196–201. <https://doi.org/10.1016/j.jallcom.2013.12.041>
- Chen, L., Wang, H.-Y., Liu, K., Cheng, W., Luo, D., & Jiang, Q.-C. (2017). Growth of Mg₂Si crystals shaped by {100} and {111} facets from Al-Mg-Si melts in the presence of calcium. *CrystEngComm*, *19*, 3058–3062. <https://doi.org/10.1039/C7CE00404D>
- Farahany, S., Ourdjini, A., Idris, M. H., & Shabestari, S. G. (2013). Computer-aided cooling curve thermal analysis of near eutectic Al-Si-Cu-Fe alloy. *Journal of Thermal Analysis and Calorimetry*, *114*, 705–717. <https://doi.org/10.1007/s10973-013-3005-7>
- Gao, Q., Wu, S., Lü, S., Duan, X., & Zhong, Z. (2015). Preparation of in-situ TiB₂ and Mg₂Si hybrid particulates reinforced Al-matrix composites. *Journal of Alloys and Compounds*, *651*, 521–527. <https://doi.org/10.1016/j.jallcom.2015.08.162>
- Ghandvar, H., Idris, M. H., Ahmad, N., & Emamy, M. (2018). Effect of gadolinium addition on microstructural evolution and solidification characteristics of Al-15%Mg₂Si in-situ composite. *Materials Characterization*, *135*, 57–70. <https://doi.org/10.1016/j.matchar.2017.10.018>
- Ghandzar, H., Abubakar, T., & Wee, Y. C. (2019). Microstructure characterization and tensile properties of Al-15%Mg₂Si-xYSZ hybrid composite. *Malaysian Journal of Microscopy*, *15*.
- Harichandran, R., & Selvakumar, N. (2016). Effect of nano/micro B₄C particles on the mechanical properties of aluminium metal matrix composites fabricated by ultrasonic cavitation-assisted solidification process. *Archives of Civil and Mechanical Engineering*, *16*, 147–158. <https://doi.org/10.1016/j.acme.2015.07.001>
- Ilyas, R. A., Sapuan, S. M., Harussani, M. M., Hakimi, M. Y. A. Y., Haziq, M. Z. M., Atikah, M. S. N., Asyraf, M. R. M., Ishak, M. R., Razman, M. R., Nurazzi, N. M., Norrahim, M. N. F., Abrial, H., & Asrofi, M. (2021). Polylactic acid (PLA) Biocomposite: Processing, additive

- manufacturing and advanced applications. *Polymers*, 13(8), 1326. <https://doi.org/10.3390/polym13081326>
- Ipekoglu, M., Nekouyan, A., Albayrak, O., & Altintas, S. (2017). Mechanical characterization of B₄C reinforced aluminum matrix composites produced by squeeze casting. *Journal Of Materials Research*, 32, 599–605. <https://doi.org/10.1557/jmr.2016.495>
- Li, Y. Z., Wang, Q. Z., Wang, W. G., Xiao, B. L., & Ma, Z. Y. (2015). Interfacial reaction mechanism between matrix and reinforcement in B₄C/6061Al composites. *Materials Chemistry and Physics*, 154, 107–117. <https://doi.org/10.1016/j.matchemphys.2015.01.052>
- Liu, T., Li, Y., Ren, Y., & Wang, W. (2018). The microstructure and mechanical characterization of Al-30%Mg₂Si composite with Y inoculation addition. *Materials Research Express*, 5, 076512. <https://doi.org/10.1088/2053-1591/aad033>
- Moktar, M. S., Ghandvar, H., & Abu Bakar, T. A. (2020). Microstructural and tensile properties of Al-20%Mg₂Si-xSiCp hybrid metal matrix composite. *Encyclopedia of Renewable and Sustainable Materials*, 5, 54–63.
- Moses, J. J., Dinaharan, I., & Sekhar, S. J. (2016). Prediction of influence of process parameters on tensile strength of AA6061/TiC aluminum matrix composites produced using stir casting. *Transactions of Nonferrous Metals Society of China*, 26, 1498–1511. [https://doi.org/10.1016/S1003-6326\(16\)64256-5](https://doi.org/10.1016/S1003-6326(16)64256-5)
- Nagarajan, S., Dutta, B., & Surrappa, M. K. (1999). The effect of SiC particles on the size and morphology of eutectic silicon in cast A356/SiCp composites. *Composites Science and Technology*, 59, 897–902.
- Nordin, N. A., Farahany, S., Ourdjini, A., Bakar, T. A. A., & Hamzah, E. (2013). Refinement of Mg₂Si reinforcement in a commercial Al–20%Mg₂Si in-situ composite with bismuth, antimony and strontium. *Materials Characterization*, 86, 97–107. <https://doi.org/10.1016/j.matchar.2013.10.007>
- Persson, K. (2015). *Materials data on Mg₂Si (SG:225) by materials project*.
- Persson, K. (2016). *Materials data on B₄C (SG:166) by materials project*.
- Shirvanimoghaddam, K., Khayyam, H., Abdizadeh, H., Karbalaee Akbari, M., Pakseresh, A. H., Ghasali, E., & Naebe, M. (2016). Boron carbide reinforced aluminium matrix composite: Physical, mechanical characterization and mathematical modelling. *Materials Science and Engineering: A*, 658, 135–149. <https://doi.org/10.1016/j.msea.2016.01.114>
- Sukiman, N. A., Ghandvar, H., Abubakar, T. A., & Ci, W. Y. (2019). Microstructure characterization and tensile properties of al-15%mg₂sixYSZ hybrid composite. *Malaysian Journal of Microscopy*, 15, 30–37.
- Syahrial, A. Z., & Pratama, M. A. (2020). The influence various boron carbide reinforcement on the microstructure and mechanical properties of ADC12/B₄C composite by stir casting. In *AIP Conference Proceedings* (Vol. 2232, p. 070005). AIP Publishing LLC. <https://doi.org/10.1063/5.0001985>
- Vajd, A., & Samadi, A. (2019). Centrifugal casting of in-situ Al-Mg₂Si(1-x)Snx composites: A study of radial segregation. *International Journal of Cast Metals Research*, 32, 114–121. <https://doi.org/10.1080/13640461.2018.1558561>
- Wang, H.-Y., Wang, W., Zha, M., Zheng, N., Zhen-Hua, G., Dong, L., & Jiang, Q.-C. (2008). Influence of the amount of KBF₄ on the morphology of Mg₂Si in Mg–5Si alloys. *Materials Chemistry and Physics*, 108, 353–358. <https://doi.org/10.1016/j.matchemphys.2007.10.006>
- Yuguang, Z., Xiaobo, L., Yuanyuan, Y., & Tianjun, B. (2014). Effect of SiC particle addition on microstructure of Mg₂Si/Al composite. *China Foundry*, 11(2).
- Zainon, F., Ahmad, K. R., & Daud, R. (2016). The effects of Mg₂Si (p) on microstructure and mechanical properties of AA332 composite. *Advances in Materials Research*, 5, 55–66.

Chapter 20

Microstructural Characterization, Mechanical Properties, and Sliding Wear Behavior of Al-20% Mg_2Si -x B_4C Hybrid Composites of the Aircraft Body



Shu Sin Teh, Nur Shazwani Ghazali, Hamidreza Ghandvar,
and Tuty Asma Abu Bakar

1 Introduction

Aluminum metal matrix composite (MMCs) is a combination of aluminum alloy reinforced with other types of materials that exhibit different mechanical properties depending on the demands of the applications. It has superior physical and mechanical properties such as good strength, strain, hardness, fatigue, and creep and corrosion resistance (Alsubari et al., 2021; Srivastava et al., 2014). According to Asif and Muhammad (2016), increasing the reinforcement ratio and decreasing the reinforcement particle size can improve the mechanical and fatigue properties of aluminum MMCs. Example of reinforcing materials of aluminum MMCs are silicon carbide (SiC), aluminum oxide (Al_2O_3), magnesium silicide (Mg_2Si), boron carbide (B_4C), natural fiber (Ilyas et al., 2021), and so on.

Mg_2Si is a hard intermetallic compound in dark blue or slightly purple color, possessing characteristics of high melting point, high microhardness, low density, and low thermal coefficient of thermal expansion (Zainon et al., 2016). These properties contribute to Mg_2Si as one of the effective reinforcements in aluminum composites. However, the primary Mg_2Si morphology in as-cast condition appeared in coarse dendritic shape with sharp edges and corners that act as crack initiation sites and further propagate. This property deteriorates the mechanical and wear properties of composites. Hence, modifying and refining of the Mg_2Si particles are desired to improve the poor properties in the composites. Studies show that adding elements such as bismuth (Farahany et al., 2016), strontium (Nordin et al., 2013), zirconium, and antimony (Zhu et al., 2018), the dendritic structure of Mg_2Si altered to

S. S. Teh · N. S. Ghazali · H. Ghandvar · T. A. Abu Bakar (✉)
Department of Materials, Manufacturing and Industrial Engineering, School of Mechanical Engineering, Faculty of Engineering, Universiti Teknologi Malaysia,
Johor Bahru, Johor, Malaysia
e-mail: tuty@utm.my

polygonal and, hence, improved the mechanical and wear properties of aluminum composites.

Boron carbide is a black solid with metallic luster in rhombohedral crystal lattice structure with excellent properties of high elastic modulus, low thermal conductivity, low density, and high hardness (Partida & Rana, 2017). Aluminum MMCs reinforced with B_4C particles increased in their hardness due to the B_4C particles that act as nucleates during the addition in melting. This decreased the size of grain boundary and increased the barrier against the plastic deformation. Hence, the material strength, hardness, and brittleness of the composite increased (Singh & Rai, 2018). Study from Devaraju and Pazhanivel (2016) evaluated that well distribution of B_4C particles in aluminum matrix improved the hardness and wear resistance. However, Kumar and Rai (2018) observed the agglomerations of high-quantity B_4C that lead to the particle-free region and increase the porosity that tends to decrease the mechanical properties.

Both Mg_2Si and B_4C particles are proved to enhance the mechanical and wear properties of aluminum MMCs. However, Mg_2Si particles need to be modified to gain a better reinforcement property. Previous study focuses on the in situ reinforcement or ex situ reinforcement in aluminum composites. Study of hybrid composite (reinforcement through in situ and ex situ) in aluminum composite is rather limited. Hence, the current study targets to examine the microstructure, mechanical, and wear properties of Al-20% Mg_2Si composite reinforced with various contents of boron carbide (B_4C).

2 Materials and Methods

2.1 Materials

The initial materials to prepare the hybrid composites were aluminum with 99.9% purity, magnesium with 99.9% purity, silicon with 98.9% purity, and B_4C powder of 10–30 μm with >99.0% purity supplied by Stanford Advanced Materials (CA 92630, USA).

2.2 Methods

2.2.1 Composites Fabrication

To prepare the Al- Mg_2Si ingot, firstly, the aluminum ingot was melted in the induction furnace (INDUCTOTHERM (S/E ASIA) PTY.LTD) at 800 °C. Then, the silicon ingot was introduced to the molten aluminum at the same temperature. The temperature of the melt was reduced to 750 °C, and magnesium ingot was then added to the molten with constant stirring process. The molten MMC was poured

into a cylindrical steel die and allowed to solidify. Next, the reinforcement material was preheated in induction furnace at 800 °C for 2 h. Meanwhile, Al-20%Mg₂Si composite ingot was melted in a graphite crucible using an induction furnace with a melt temperature of 750 ± 10 °C. The preheated B₄C particles were introduced gradually into the Al-Mg₂Si melt at 750 °C with stirring conditions of 500 rpm speed and 15 min time to obtain a uniform distribution of B₄C particles in molten metal. The melt was reheated to 750 ± 10 °C and poured into the preheated cylindrical steel die and allowed to solidify. Al-20%Mg₂Si composite reinforced with mass fraction of B₄C particles, 0 wt.%, 2.5 wt.%, 5.0 wt.%, and 10.0 wt.%, was prepared. The samples used for microstructure characterization, mechanical, and wear tests were machined out from these castings.

2.2.2 Microstructure Observation

The microstructures of the specimens were observed and analyzed using optical microscope equipped with image analyzer (Nikon-MIDROPHOT-FXL) and scanning electron microscope (SEM) equipped with energy dispersive x-ray analyzer (EDX) (XL-40). The mean size, density, and aspect ratio were calculated to detect the Mg₂Si particle characteristics.

2.2.3 Mechanical Tests

The uniaxial tensile test (ASTM E8M) was conducted by a computerized universal testing machine (Instron 600DX) which can bear a max load of 600 KN at a constant crosshead speed of 1 mm/min. To make sure about the results repeatability, the tensile test was conducted on three specimens for each test. The hardness values were measured by Matsuzawa Vickers hardness machine testing machine at an applied load of 5 N for 30s.

2.2.4 Wear Test

Pin-on-disc sliding wear testing machine (TR-20, DUCOM) was utilized to investigate the specimen's wear properties in accordance to the ASTM G99-04a standard, under applied load of 20 N and 40 N, at constant parameters of track diameter 60 mm, sliding speed 200 rpm, and sliding distance 2000 m, against a hardened chromium steel disc (Rc 64). The length and diameter of the pin samples were 25 and 6 mm, respectively. A linear variable differential transformer (LVDT) was used to monitor the height loss of the specimen in order to measure the wear loss in microns. A frictional force sensor was utilized to measure the frictional force generated on the specimen in Newton. For each experimental condition, a set of three samples was tested, and the average values were utilized for further analysis. The

worn surfaces and tensile fracture surfaces were then cleaned with acetone using ultrasonic cleanser and analyzed via SEM.

3 Results and Discussion

Figure 20.1(a) shows that Al-Mg₂Si-B₄C hybrid composite was successfully fabricated using the casting route. Figure 20.1(b) exhibits the EDX line scan to detect the elements of the phase/compounds which were used to fabricate the composite: Al phase and Mg₂Si and B₄C compounds.

The distributions of B₄C particles and changes morphology of Mg₂Si particles are studied using optical microscope and SEM. It can be observed from Fig. 20.2 that the large irregular size of Mg₂Si decreased in their average size. The dark-gray coarse particles are the B₄C, and the whitish-gray coarse particles in irregular shape are the primary Mg₂Si as seen in Fig. 20.2(b). Both particles are enclosed by a layer of α -Al-rich phase and eutectic Mg₂Si cells. From Fig. 20.2d, it is clearly shown the agglomeration characteristics of B₄C particles at 10.0 wt.% due to the poor wettability of B₄C particles and the different density of B₄C particles with aluminum matrix. In fact, as a result of difference of density between Al and B₄C, dispersion of the ceramic particles in the matrix alloy is not uniform, and hence, the particles agglomerated in some areas of the matrix alloy. Similar results of agglomeration of ceramic particles have been reported in fabrication of Al-Mg₂Si-SiC and Al-Mg₂Si-YSZ hybrid composites when 15%SiC and 9%YSZ particles were added to Al-Mg₂Si composites (Moktar et al., 2020; Sukiman et al., 2019).

In addition, Fig. 20.3 shows that when B₄C particles increased up to 5 wt.% in Al-Mg₂Si composites, the average size of Mg₂Si particles reduced from 46.9 μm to 38.8 μm . This owns to the existence of the B₄C particles that act as the physical barrier as they are rejected by the solidification front during the growth of primary Mg₂Si phase. The maximum modification of the primary Mg₂Si particles (5 wt.% B₄C) compared to the unmodified is at 7% only. As the morphology of primary Mg₂Si particles showed no obvious changes, the aspect ratio of Al-Mg₂Si composite before and after boron carbide addition did not alter much too (Fig. 20.3). Moreover, the average number of primary Mg₂Si particles per unit (mm^2) reduced from 135 particle/ mm^2 to 59 particle/ mm^2 when B₄C content increased from 0 wt.% to 10 wt.%. The decreasing amount of Mg₂Si particles can be due to the compound formed and the shifting of the eutectic point toward the Mg₂Si concentration in the Al-Mg₂Si equilibrium diagram (Azarbarmas et al., 2011).

Figure 20.4 shows the average Vickers hardness values which increased from 75.24 HV to 79.06 HV and reached its maximum value of 100.70 HV when B₄C content increased from 0 to 2.5 and 5.0 wt.%. For 10.0 wt.% B₄C, the hardness value decreased to 84.28 HV. The enhancement in the hardness owns to the existence of the hard B₄C particles and finer, hard primary Mg₂Si particles that increased the obstacles to the grain boundary sliding. For 10 wt.% B₄C, the sudden decreased of the hardness is due to nonuniform distribution of B₄C particles throughout the Al

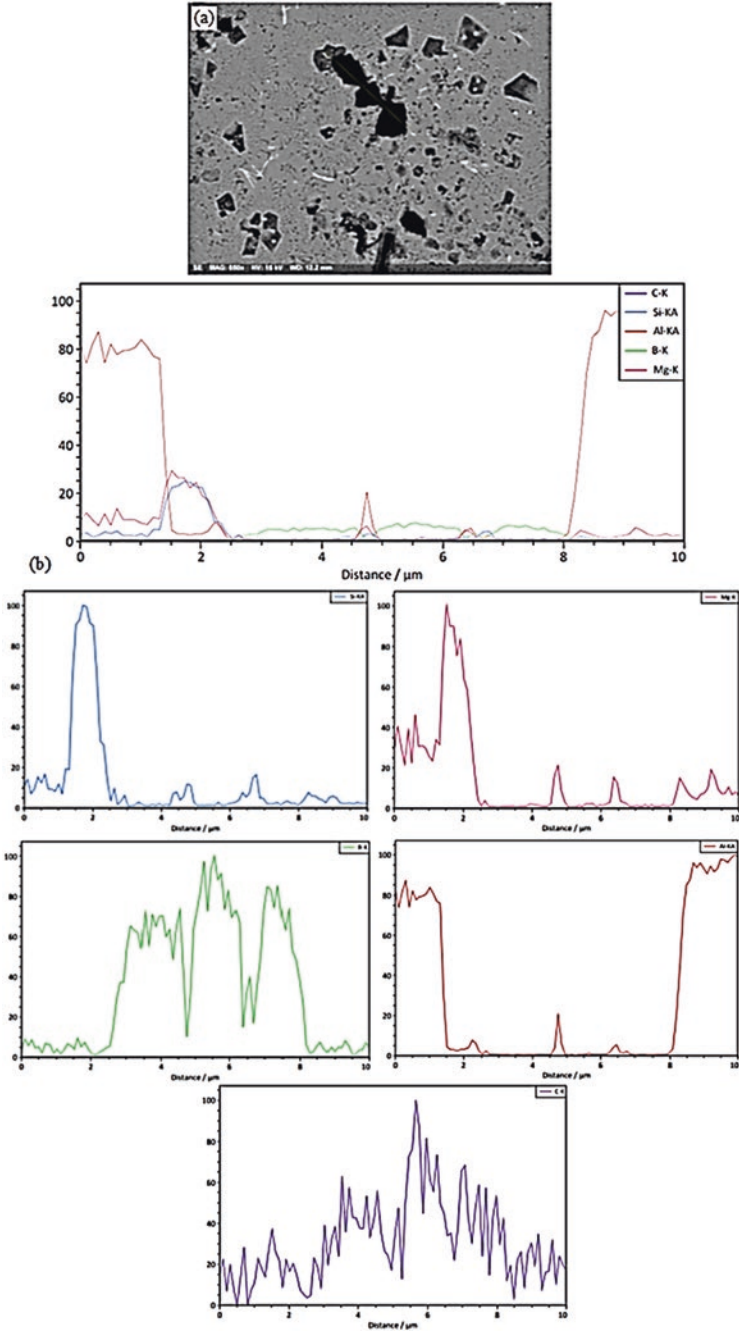


Fig. 20.1 (a) SEM image of Al-20%Mg₂Si-2.5%B₄C hybrid composite and (b) related EDS line scan analysis

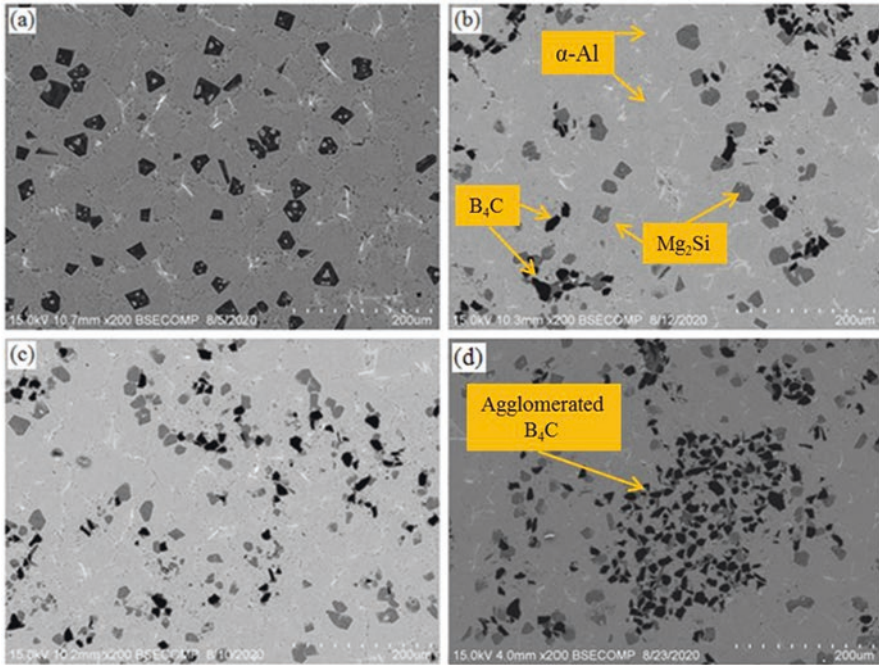


Fig. 20.2 Optical images of Al-Mg₂Si composite samples with various B₄C contents: (a) 0, (b) 2.5, (c) 5.0, and (d) 10.0 wt.%

matrix and hence clustering of B₄C particles. As a result, the number of B₄C particles to resist the applied load during the hardness test decreased which causes the higher exposure of soft aluminum matrix to the indenter and decreasing the average hardness of the composite. Umanath et al. (2011) also reported that addition of SiC and Al₂O₃ reinforcement particles to Al6061 alloy resulted in increasing the microhardness particularly with increasing the particles content due to solid solution hardening of the matrix. Similarly, Uvaraja et al. (2012) claimed that presence of hard SiC and B₄C particles in the matrix alloy caused increasing the hardness of the composite, in which the particles act as barrier to the motion of dislocation.

3.1 Tensile Properties

The ultimate tensile strength (UTS) and percentage elongation (El%) values of fabricated composites are shown in Fig. 20.5(a) and (b), respectively. The Al-20%Mg₂Si-5%B₄C hybrid composite exhibits higher UTS (75.34 MPa) and El% (0.65%) compared to Al-Mg₂Si composite without B₄C particles with UTS and El% of 60.31 MPa and 0.53%, respectively. The high strength value owns to the uniformity distribution of B₄C particles in the matrix material. Dislocation pileup is

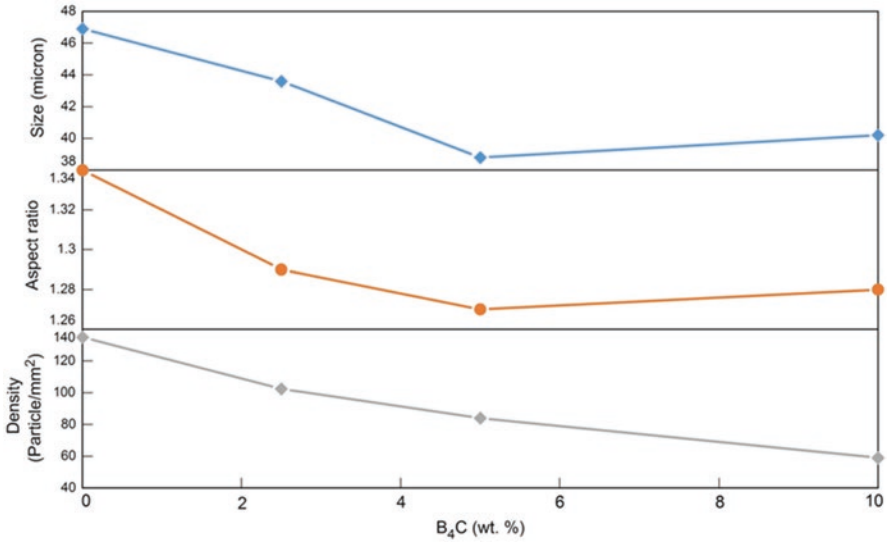


Fig. 20.3 Average sizes, aspect ratio, and average density of primary Mg₂Si particles in Al-Mg₂Si composite reinforced with various amount of B₄C particles

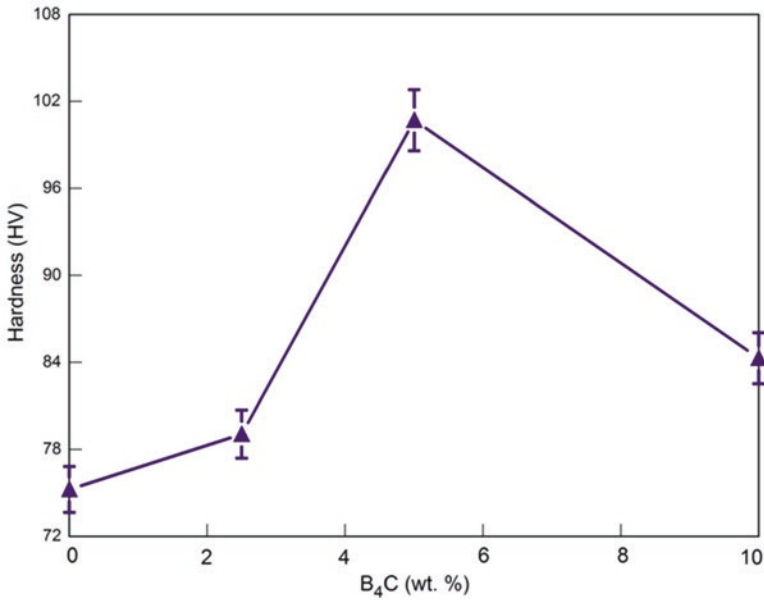


Fig. 20.4 Vickers hardness values of Al-Mg₂Si composite reinforced with different amount of B₄C particles

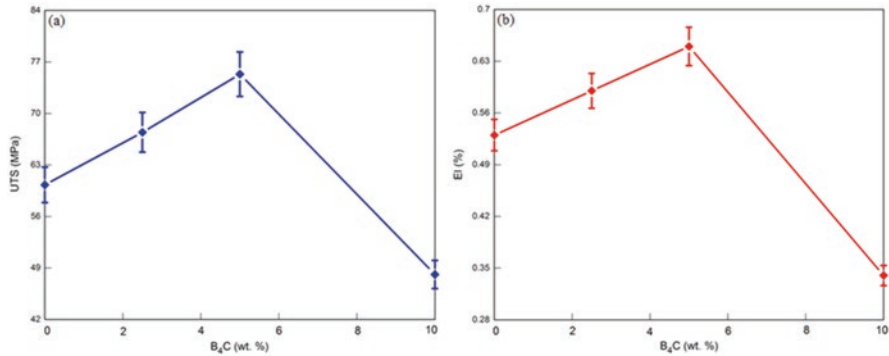


Fig. 20.5 (a) The ultimate tensile strength (UTS) and (b) percentage elongation (EI%) values of Al-Mg₂Si composite with various B₄C contents

generated in the neighbor of B₄C particles due to presence of these particles in Al-Mg₂Si. Hence, the strength of the composite enhanced due to increasing the dislocation density and dislocation interactions in interfaces between the matrix and reinforcement (Ghandvar et al., 2015). The B₄C particles caused to increase the resistance against plastic deformation of composites when subjected to loading. However, the composite reinforced with 10 wt.% B₄C, the UTS and EI% decreased to 48.12 MPa and 0.34%, respectively, which are lower than 5 wt.% B₄C and base Al-Mg₂Si composite. The reduction in tensile properties of Al-Mg₂Si added 10 wt.% B₄C is because of increasing in porosity present in its microstructures due to poor wettability and nonuniform distribution of B₄C as a result of B₄C clustering in Al-Mg₂Si matrix as well as increasing the brittleness feature of the composite which reduces its ductility by adding more B₄C particles to the Al-Mg₂Si. Similar finding has been reported in Al-15%Mg₂Si-xYSZ hybrid composite when the composite was added with various percentages of YSZ ceramic particles. In this study with addition of 6%YSZ, the ultimate tensile strength increased to 85.65 MPa compared to the base material (53.54 MPa) and then decreased to 66.48 MPa when the composite was added with 9% YSZ (Sukiman et al., 2019).

The fracture surfaces of several composite specimens with various tensile strength values were studied by SEM. Figure 20.6 exhibits some micrographs of the fractured surfaces selected from Al-Mg₂Si composites with and without different amounts of B₄C particles after tensile testing at low (a, c, e, and g) and high (b, d, f, and h) magnifications. The fracture surface of Al-20%Mg₂Si composite is illustrated in Fig. 20.6(a, b). As observed, in Al-20%Mg₂Si composite, the primary Mg₂Si particles govern the crack propagation behavior where the propagation of the cracks by the successive cleavage of Mg₂Si particles is alike to the primary Si particles in Al-Si hypereutectic alloy (Sharma et al., 2017). The fracture surface of Al-20%Mg₂Si-5%B₄C hybrid composite is depicted in Fig. 20.6(c, d). It is detected that decohesion occurring at the interface between the matrix and B₄C was rather rare compared to decohesion between Mg₂Si and Al matrix. In fact, B₄C-Al interface is stable and steady, so the cracks start and propagate in the Mg₂Si matrix, not

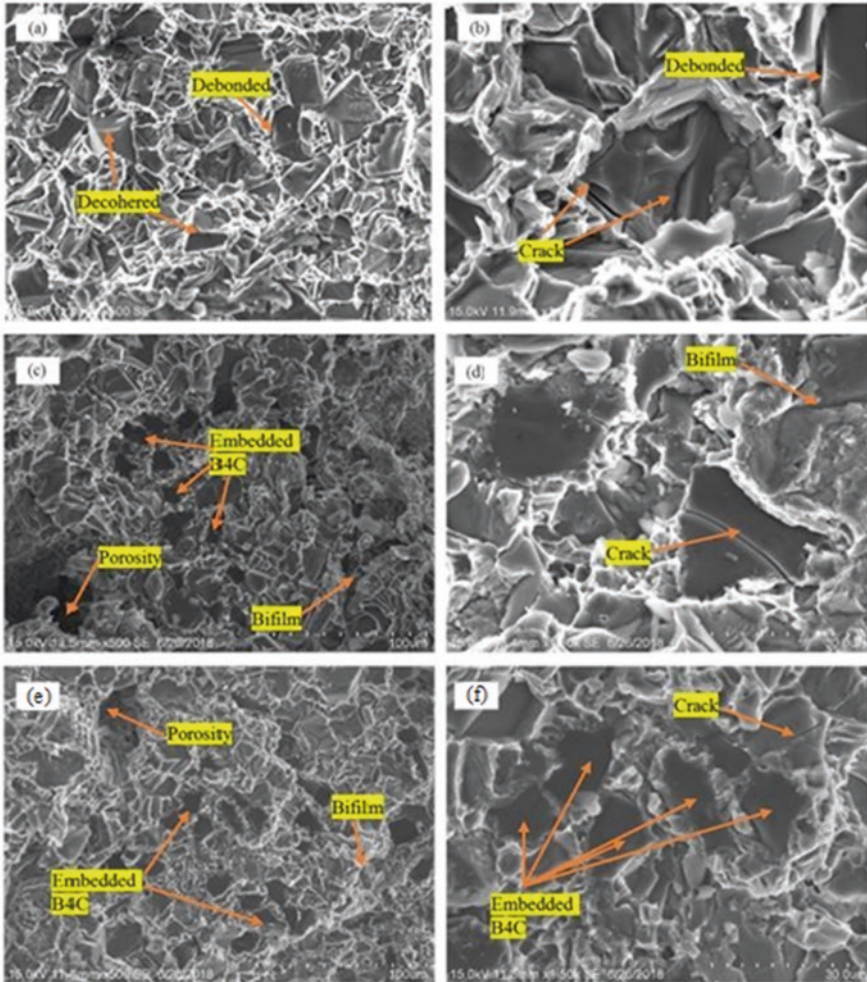


Fig. 20.6 Fractography of Al-20%Mg₂Si tensile samples with various contents of B₄C in low (left) and high (right) magnifications: (a, b) 0, (c, d) 5, and (e, f) 10 wt.% B₄C

on the B₄C-Al interface. In addition, some dimples are seen on the fracture surface of the hybrid composite which indicate ductile mode of fracture. This is because the matrix alloy can be reinforced by uniform distribution of particles due to the effective role of particle-rich alloy as prevention of crack propagation; however, propagation of crack occurred by particle-poor region. Such observation can be associated with higher UTS and E1% values achieved (Fig. 20.5). There are some agglomerations of B₄C particles on the fracture surface in some area as seen in Fig. 20.6(e, f). This is along with the low strength and elongation of hybrid composite as depicted in Fig. 20.5. The local stresses are increased by clustering of the particle, in which proffers sites for nucleation of crack and low-energy propagation paths along the

connected brittle particles. Failure can be defined by higher stresses produced in these areas.

3.2 Wear Behavior

The wear rate of Al-20%Mg₂Si composite with and without various contents of B₄C particles under applied loads of 20 and 40 N is observed in Fig. 20.7. As seen, the wear rate under the applied load of 20 N shows the trend of continuously decreasing from 0.849 mm³/km in base Al-20%Mg₂Si composite to 0.46 mm³/km with the increasing weightage of B₄C content to 5 wt.% due to the changing of material behavior from soft to hard. The decreasing of wear rate is also due to the frictional heating between pin and disc that forms the oxide layer that is harder than the aluminum matrix as well as the segregation of boron that acted as dry lubricant between the sliding surfaces. However, with addition of 10 wt.% B₄C to Al-20%Mg₂Si composite, the wear rate increased which is due to the material removal rate as the agglomerated B₄C particles are pulled out from the matrix and entrapped between pin and disc which in turn results in increasing the wear rate substantially. Nevertheless, it has been reported that with increasing the amount of B₄C, the wear rate decreased (Patidar et al., 2017). In addition, Fig. 20.7 depicts the increased of

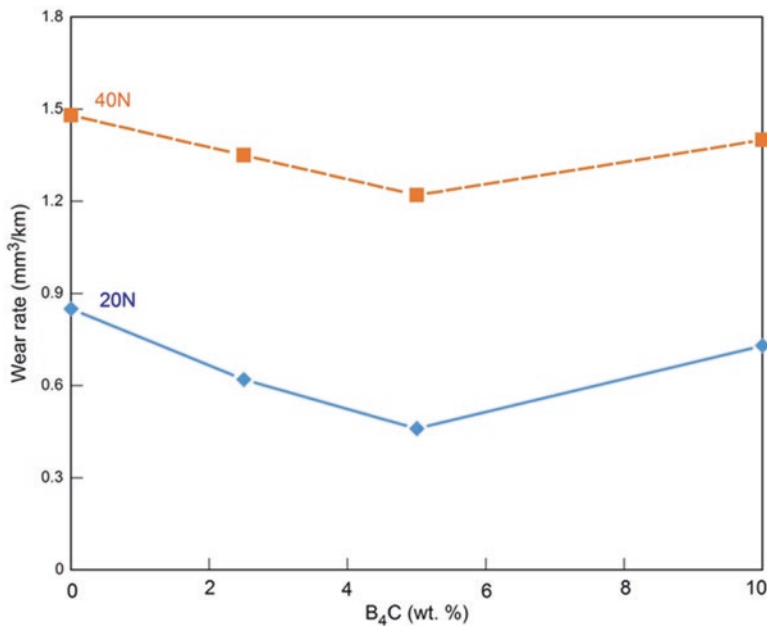


Fig. 20.7 Wear rate of Al-Mg₂Si composite reinforced with different amount of B₄C particles under applied loads of 20 and 40 N

wear rate when the wear rate is increased from 20 N to 40 N. This is expected as the number of contact asperities and the separation of surface asperities increased at the higher loads. Besides, increasing of the applied load also contributed to the gathering of wear debris in the space between the pin and disc that leads to a more serious abrasive wear and, hence, increase the wear rate. It has been claimed that at higher applied load, the frictional heating between the pin and disc promotes the oxidation as well as the softening effect that leads to quick worn of matrix material compared to the metallic oxides. This causes the metallic oxides to contact more with the disc, and when the formation of the oxide layer is faster than the material removal rate, the wear rate decreased (Singh & Rai, 2018).

Figure 20.8 illustrates the coefficient of friction (COF) of Al-20%Mg₂Si composite with and without various percentages of B₄C particles. As seen, under load of 20 N, the COF of the composite with 5 wt.% B₄C is 0.396 which is lower than base Al-20%Mg₂Si composite with COF of 0.464. Nevertheless, with further increase of B₄C reinforcement to 10%, the COF increases to 0.4592. It has been reported that the increasing of the COF is caused by the fragmentation of B₂O₃ layer. This boron oxide layer occurred due to the pullout of B₄C particles that reacts with the atmosphere. Its delamination during the dry sliding forms grooves and scratches on the pin surface and, hence, increased the friction between the pin and sliding disc surface (Prabhakar et al., 2014). For applied load of 40 N, the Al-20%Mg₂Si composite with and without B₄C owns higher COF compared to the 20 N applied load. The COF of Al-20%Mg₂Si composite under applied load of 40 N is 0.55 which reduced

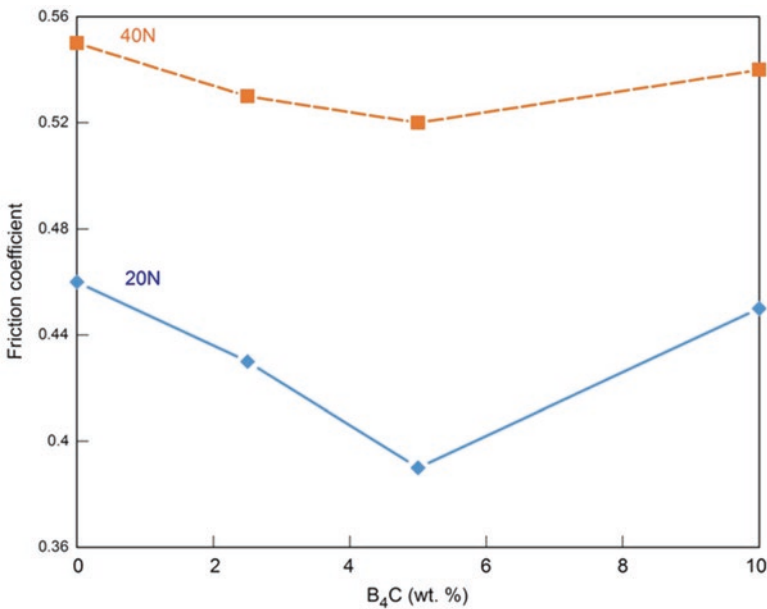


Fig. 20.8 Coefficient of friction of Al-20%Mg₂Si composite reinforced with different amount of B₄C particles

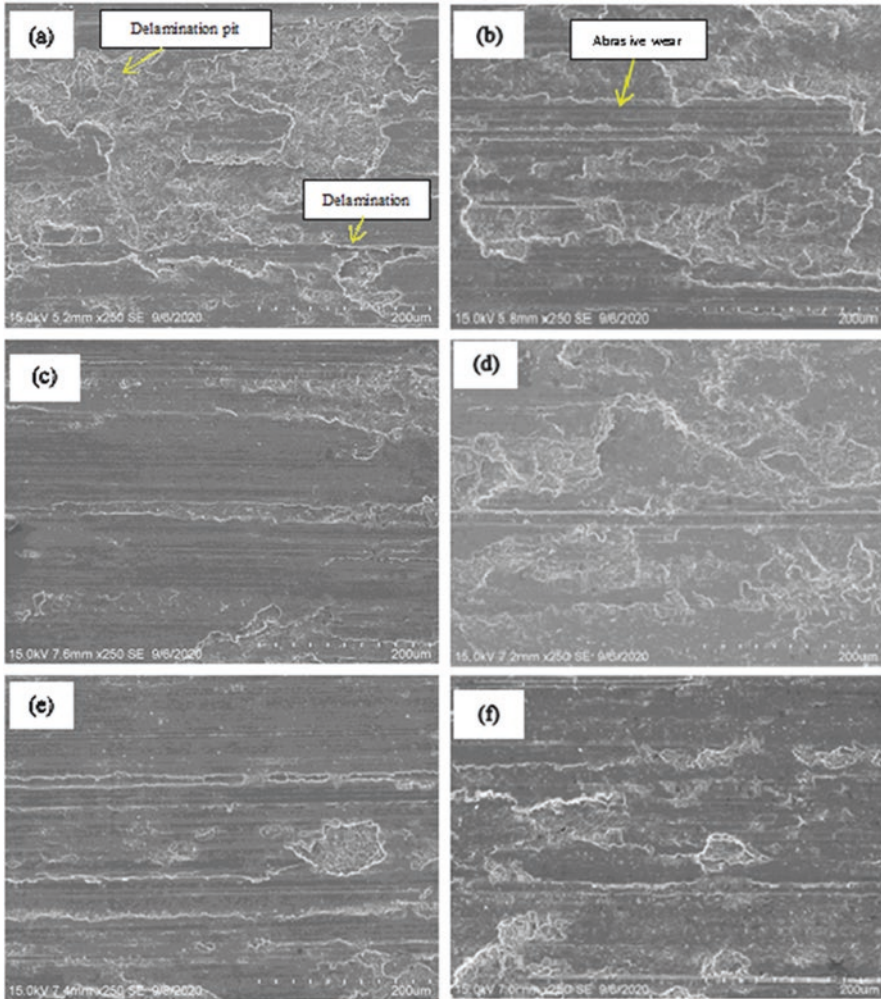


Fig. 20.9 SEM images of the worn surface of Al-Mg₂Si composite samples with various B₄C contents (a, b) 0 wt.%; (c, d) 5 wt.%, and (e, f) 10 wt.% under 20 N (left) and 40 N (right) applied loads

to 0.52 after addition of 5 wt.% B₄C and increased to 0.54 after further addition of 10 wt.% B₄C particles to Al-Mg₂Si composite.

The SEM image of the worn surface of Al-20%Mg₂Si composite under applied load of 20 N is shown in Fig. 20.9(a). Deep and wide plowing grooves parallel to the sliding direction are seen on the worn surface which is indicative of abrasion and delamination as the main wear mechanism. As in base Al-20%Mg₂Si composite the primary Mg₂Si particles are coarse and often in dendritic morphology, the sharp points of the particles are the area for high interlaminar stresses which cause delamination, in which these areas are connected, typically, to the lowest

through-thickness strength (Suriani et al., 2021). The worn surface of Al-20% Mg_2Si -5%B₄C hybrid composite under 20 N applied load shows the decreasing area of delamination pit and decreasing of abrasive wear in quantity and depth (Fig. 20.9(c)). This phenomenon is consistent with the decreasing wear rate result in Fig. 20.7 and decreasing coefficient of friction result in Fig. 20.8. This indicates that the addition of B₄C successfully decreased the amount of material removal of the Al- Mg_2Si composite. Nevertheless, as observed in Fig. 20.9(e) with increasing the B₄C concentration to 10 wt.%, the pits and abrasive areas increased. In fact, the weak bonding of B₄C particles with the matrix led to the pullout of the B₄C particles that resulted in the abrasive wear. This pullout of the particles is due to the weakened adhesion of matrix and the reinforcing particles. As observed in Fig. 20.9, with increasing the applied load from 20 N to 40 N, the flake-like delamination pit areas become wider and deeper. This is due to the accumulation of the pullout particles in the space between the pin and disc surface. This extensive delamination is due to the crack nucleation, crack propagation that source from the fracture and detachment of Mg_2Si particles.

4 Conclusions

In conclusion, the influence of various concentrations of B₄C on the microstructure, mechanical properties, and dry sliding wear behavior of Al-20% Mg_2Si composite was investigated. The addition of 5 wt.% B₄C refined the size of primary Mg_2Si from 46.9 μm to 38.8 μm , altered the aspect ratio at maximum of 5%, and decreased the mean density about 38%. The hardness of the composite increased with the addition of B₄C and reached its maximum value of 100.70 HV at 5.0 wt.% B₄C. Similarly, Al-20% Mg_2Si -5%B₄C hybrid composite shows the highest tensile properties with UTS (75.34 MPa) and El% (0.65) in comparison with other fabricated composites due to refine primary Mg_2Si size as well as the good uniformity distribution of B₄C particles in the matrix. The tensile fracture surface illustrates fine dimples and particles fracturing, indicating ductile mode of fracture. Furthermore, pin-on-disc sliding wear test depicts a drop in wear rate and coefficient of friction for 5.0 wt.% B₄C-added Al-20% Mg_2Si composite under both applied load of 20 and 40 N in which the abrasion wear is considered as the govern wear mechanism under 20 N applied load.

Acknowledgments The authors wish to thank Universiti Teknologi Malaysia (UTM) for provision of research facilities and financial support under the research grants 05E88 and 06G22 (TDR Grant).

References

- Alsubari, S., Zuhri, M. Y. M., Sapuan, S. M., Ishak, M. R., Ilyas, R. A., & Asyraf, M. R. M. (2021). Potential of natural fiber reinforced polymer composites in Sandwich structures: A review on its mechanical properties. *Polymers*, *13*(3), 423. <https://doi.org/10.3390/polym13030423>
- Asif, I., & Muhammad, N. (2016). Effect of the reinforcement on the mechanical properties of aluminium matrix composite: A review. *International Journal of Applied Engineering Research*, *11*(21), 10408–10413.
- Azarbarmas, M., Emamy, M., Karamouz, M., Alipour, M., & Rassizadehghani, J. (2011). The effects of boron additions on the microstructure, hardness, and tensile properties of in situ Al–15%Mg₂Si composite. *Materials & Design*, *32*(10), 5049–5054. <https://doi.org/10.1016/j.matdes.2011.05.036>
- Devaraju, A., & Pazhanivel, K. (2016). Evaluation of microstructure, mechanical and wear properties of aluminium reinforced with boron carbide nano composite. *Indian Journal of Science and Technology*, *9*(20). <https://doi.org/10.17485/ijst/2016/v9i20/84294>
- Farahany, S., Ghandvar, H., Nordin, N., Ourdjini, A., & Idris, M. (2016). Effect of primary and eutectic Mg₂Si crystal modifications on the mechanical properties and sliding wear behaviour of an Al–20Mg₂Si–2Cu–xBi composite. *Journal of Materials Science & Technology*, *32*(11), 1083–1097. <https://doi.org/10.1016/j.jmst.2016.01.014>
- Ilyas, R. A., Sapuan, S. M., Harussani, M. M., Hakimi, M. Y. A. Y., Haziq, M. Z. M., Atikah, M. S. N., Asyraf, M. R. M., Ishak, M. R., Razman, M. R., Nurazzi, N. M., Norrahim, M. N. F., Abrial, H., & Asrofi, M. (2021). Polylactic acid (PLA) biocomposite: Processing, additive manufacturing and advanced applications. *Polymers*, *13*(8), 1326. <https://doi.org/10.3390/polym13081326>
- Kumar, A., & Rai, R. (2018). Fabrication, microstructure and mechanical properties of boron carbide (B₄C_p) reinforced aluminum metal matrix composite - a review. *IOP Conference Series: Materials Science and Engineering*, *377*, 012092. <https://doi.org/10.1088/1757-899x/377/1/012092>
- Moktar, M. S., Ghandvar, H., & Abu Bakar, T. A. (2020). Microstructural and tensile properties of Al-20%Mg₂Si-xSiCp hybrid metal matrix composite. *Encyclopedia of Renewable and Sustainable Materials*, *5*, 54–63.
- Nordin, N., Farahany, S., Ourdjini, A., Abu Bakar, T., & Hamzah, E. (2013). Refinement of Mg₂Si reinforcement in a commercial Al–20%Mg₂Si in-situ composite with bismuth, antimony and strontium. *Materials Characterization*, *86*, 97–107. <https://doi.org/10.1016/j.matchar.2013.10.007>
- Partida, D., & Rana, R. (2017). Effect of B₄C particle reinforcement on the various properties of aluminium matrix composites: a survey paper. *Materials Today: Proceedings*, *4*(2), 2981–2988. <https://doi.org/10.1016/j.matpr.2017.02.180>
- Prabhakar, N., Radhika, N., & Raghu, R. (2014). Analysis of tribological behavior of aluminium/B₄C composite under dry sliding motion. *Procedia Engineering*, *97*, 994–1003.
- Sharma, S. S., Jagannath, K., Prabhu, P. R., Gowri, S., & Harisha, S. R. (2017). Metallography & bulk hardness of artificially aged Al6061-B₄C-sic stir cast hybrid composites. *Kini UA*, *880*, 140–143.
- Singh, R., & Rai, R. (2018). Characterization of B₄C-composite-reinforced. *Aluminum Alloy Composites*. <https://doi.org/10.1063/1.5029649>
- Srivastava, A., Dixit, A., & Tiwari, S. (2014). A review on fabrication and characterization of aluminium metal matrix composite (AMMC). *International Journal of Advance Research and Innovation*, *2*(2), 516–521.
- Sukiman, N. A., Ghandvar, H., Abubakar, T. A., & Wee, Y. C. (2019). Microstructure characterization and tensile properties of Al-15%Mg₂Si-xYSZ hybrid composite. *Malaysian Journal of Microscopy*, *15*, 30–37.

- Suriani, M. J. H., Rapi, Z., Ilyas, R. A., Petru, M., & Sapuan, S. M. (2021). Delamination and manufacturing defects in natural fiber-reinforced hybrid composite: A review. *Polymers*, *13*, 1323. <https://doi.org/10.3390/polym13081323>
- Umanath, K., Selvamani, S. T., & Palanikumar, K. (2011). Friction and wear behaviour of Al6061 alloy (SiCp+ Al₂O₃) hybrid composites. *International Journal of Engineering, Science and Technology*, *3*, 5441–5451.
- Uvaraja, V. C., & Natarajan, N. (2012). Tribological characterization of stir-cast hybrid composite Aluminium 6061 reinforced with SiC and B₄C particulates. *European Journal of Science and Research*, *76*, 539–552.
- Zainon, F., Ahmad, K., & Daud, R. (2016). The effects of Mg₂Si(p) on microstructure and mechanical properties of AA332 composite. *Advances in Materials Research*, *5*(1), 55–56. <https://doi.org/10.12989/amr.2016.5.1.055>
- Zhu, J., Zhou, T., Zha, M., Li, C., Li, J., & Wang, C. (2018). Microstructure and wear behaviour of Al-20Mg₂Si alloy with combined Zr and Sb additions. *Journal of Alloys and Compounds*, *767*, 1109–1116. <https://doi.org/10.1016/j.jallcom.2018.07.032>

Chapter 21

Hybrid Composites for Very Large Lightweight Wind Turbine Blades: Structural and Materials Aspects



Hande Yavuz

1 Introduction

Wind turbines are slender structures and usually constructed by using lightweight laminated polymer composite materials. The structural dimensioning and the life cycle analysis of the wind turbines are affected by the high number of load cycles. Large range of operating conditions induce various detrimental effects on the structural integrity of wind turbine blades which in turn affect the life cycle prediction and operational performance. Wind turbine blades are also specifically vulnerable to vibrations as well as excited by the vast number of excitation mechanisms which particularly applied to high-energy wind turbine plants even at the ideal operating conditions. Hence, it is required to limit the operating speed range to uncritical ranges due to the excitations regardless of the operating environment.

In the wind energy industry, operation, maintenance, and repair costs including the end-of-life (EOL) waste landfill costs are the major considerations. The operators of wind energy power plants are particularly concerned by the reduction of the levelized cost of energy (LCOE) of the investments as well. Hence, the development of very large lightweight wind turbine blades is apparently requiring more intelligent material and structural solutions coupled with improved maintenance strategies including operational and performance monitoring to secure economical concerns and efficiency. The expectations in the advancement of performance monitoring system are related to the enhanced maintenance predictions in various operating conditions. The assessment of damage and the predictions on remaining life cycle and load-bearing capacity prior to failure could be resolved by a combination of various techniques such as intelligent monitoring of rotor blades, advanced

H. Yavuz (✉)

Department of Aerospace Engineering, Faculty of Engineering, OSTİM Technical University,
OSTİM, Yenimahalle, Ankara, Turkey

e-mail: hande.yavuz@ostimteknik.edu.tr

imaging monitoring techniques, automatic modeling of damaged structure, integrated sensor network without excessive cabling, creation of blade-specific finite element models, statistical modeling and analysis for quantification of deviations in weight, and characterization of damage for tomographic error reconstruction.

High competitiveness of the energy market provides the opportunity to integrate novel material and structural solutions in order to develop performant blade structures to concurrently reduce life cycle costs, leveled cost of energy, and end-of-life waste. In this regard, this chapter reviews novel technologies including the potential applications of recently developed nanocomposites with improved mechanical performance for wind turbine blades.

2 Ply Drop-off Concepts in Tapered Composite Laminates

A significant weight saving of the wind turbine blades can be achieved by applying ply drop-off concept. However, material and geometrical discontinuities caused by ply drop in the composite laminates lead to stress concentration problems (Curry et al., 1992). The interlaminar normal and shear stresses developed in the ply drop zones can cause damage even at a load much lower than the final withstand load. For very large turbine blades, there are numerous ply drop zones which is considered as a challenging issue to distinguish the sensitivity regarding the stress concentration. Researchers proposed the potential benefits of ply drop-off concepts to be limited by the ply drop in the strength of the laminate (Varughese & Mukherjee, 1997).

Delamination in composite laminates is one of the important damage modes caused by numerous reasons such as mismatch of Poisson's ratio, large interlaminar stresses, and edge effect which is of great importance (Mukherjee & Varughese, 2001). The delamination mode of failure in the ply drop zone has been studied for decades. In early studies, it was found that composites with internal ply drop zones are about twice as strong as the composites with outer ply drop zones subjected to tensile, bending, and torsion (Daoust & Hoa, 1989). Botting et al. observed 16% improvement in interlaminar stress by changing the ply drop configuration in tensile tests performed in a total of 48 ply drop samples with different configurations made of glass fiber/epoxy (Botting et al., 1996). Agastra and Mandell applied static and cyclic loadings on composite samples with a ply drop zone and obtained the schematic damage geometry in the ply drop zone by using those tested samples (Agastra & Mandell, 2010). Weiss et al. used a series of samples containing a reduction from 20 layers to 12 layers (Weiss et al., 2010). The thick zone, thin zone, and ply drop zone are 90 mm, 90 mm, and 16 mm long, respectively. The ply drop zone is at an angle of 7° with respect to horizontal axis. Fatigue tests of those samples, which have fiber orientations of 0° , $\pm 45^\circ$, and 90° with respect to 0° fiber axis, were compared with the results of finite element analysis. They showed that the delamination occurred in the first two ply drops close to the thin zone in fatigue tests of carbon fiber-reinforced epoxy composite samples with a ply drop zone. Most of their

findings pointed out that the delamination initiates in the side where the interlaminar stresses are the highest in magnitude due to the asymmetric distribution of delamination in the specimen's edges. Moreover, among the studied samples, interlaminar shear stress is found almost four times higher than the interlaminar normal stress. Agastra and Mandell performed the total sample length of 101.6 mm and the two-ply drop within 7 mm length (Agastra & Mandell, 2010). They conducted static and fatigue tests on those samples and compared with finite element analysis. Additionally, they performed delamination analysis by using five different resins. According to their findings, delaminated layers are found close to the ply drop zone covering both of the thick and the thin sides of the specimens. Mukherjee and Varughese conducted a wide range of study on the design of ply drop zones (Mukherjee & Varughese, 2001). They examined ply drops and stepwise ply drops through one direction rather than multiple directions. An increase in normal and shear stresses occurred as the number of layers increased in the ply drop zone. As the number of layers in the drop zone increases, the stress concentration increases. However, as the number of laminates decreases in the drop zone, the stresses spread over a larger area. If the number of plies increased in the ply drop zone, the risk of sudden damage increases accordingly. Fish and Vizzini found that the overlapped dispersed configuration provided the best structural performance rather than staircased-grouped, overlapped-grouped, staircase-dispersed for glass fiber/epoxy composites (Fish & Vizzini, 1992).

Optimization of ply drop zone in wind turbine blades and damage analysis under static/fatigue loads is also an important concern that is studied recently in order to determine the optimum ply order, ply number, and ply drop configuration in the composite laminate of the rotor blade (Albanesi et al., 2018). Hosseiny and Jakobsen studied fatigue damage of ply drop zones in offshore, large wind turbine blades (Hosseiny & Jakobsen, 2016). Fatigue testing is usually conducted edgewise as well as flap-wise for industrial application. Crans et al. examined the strength of ply drop zones in composite laminates under static and fatigue loads using a multi-scale progressive damage analysis method (Crans et al., 2011). Zhang et al. studied damage formation and progression in the ply drop zone both experimentally and computationally (Zhang et al., 2011). They developed a simplified test coupon representing the ply drop zone and examined the performance of various composite fabrics and resins in the ply drop zone. Samborsky et al. studied layer separation damage under fatigue loads in thick ply drops in carbon and glass fiber composites by experimental and numerical simulation (Samborsky et al., 2008). They found that the ply drop thicknesses should be thinner than the glass fiber composite ply drop thickness.

Several researchers examined the effect of nanoparticle reinforcement on ply drop composites as well. By applying nanoparticle reinforcement in the ply drop zone, stress distribution can be achieved in the interphase, and by increasing the stress distribution of the polymer matrix under dynamic load, an improvement in damping properties is achieved (Kabir & Hoa, 2011). An increase in vibration damping indicates an increase in the fatigue life of the structure. Moreover, with the

addition of nanoparticles, significant increase in surface area can be obtained (Helmy et al., 1999). Preventing the agglomeration of nanoparticles by applying surface treatments, nanoparticles dispersed in resin would provide large interphase surface area and positively contribute to fatigue life enhancement in composite structures even at very low concentrations of nanoparticles. Helmy and Hoa examined an addition of 2 wt.% nanoclay reinforcement to a ply drop zone of glass fiber/epoxy composite. However, they found that samples have suffered damage due to delamination (Helmy & Hoa, 2014). Donaldson et al. examined the effects of aramid and carbon nanotube reinforcement on the layer-drop samples made of glass fiber/epoxy with different layer orientations (Donaldson et al., 2012). With the help of carbon nanotube reinforcement, crack onset occurred at 32% higher stress while delamination damage occurred at 30% higher stress. Gouldstone et al. observed an average of 5% improvement in the final load values in samples by adding carbon nanotubes on composite plies undergoing three-point bend test compared to composite structures with ply drop without nano-reinforcement (Gouldstone et al., 2014).

Loos et al. investigated the effect of carbon nanotube (CNT) addition on the fatigue life of epoxy resin (Loos et al., 2012). Especially at high-cycle, low-stress regime, a significant increase in fatigue life is detected. Zhang et al. examined the change of crack propagation rate in 0.5% CNT-reinforced epoxy nanocomposite. Depending on the stress intensity factor, a significant decrease is obtained compared to the neat epoxy (Zhang et al., 2007). In another study of the same group, the fatigue crack growth rate decreased 20 times compared to pure epoxy by optimizing the nanotube diameter, length, and distribution of nanoparticles in epoxy (Zhang et al., 2008). Grimmer and Dharan investigated the effect of carbon nanotube addition on the fatigue life of glass fiber-reinforced epoxy resin (Grimmer & Dharan, 2008). The fatigue life of glass fiber/epoxy composite and CNT-added glass fiber/epoxy nanocomposite with 1% weight ratio are compared. Especially at the high cycle regime, CNT-added nanocomposite material has approximately 2.5 times longer fatigue life compared to glass fiber/epoxy composite. Mechanisms that increase fatigue life in high-cycle, low-stress regime would be related to crack bridging and fiber pullout formations. CNT particles with fibrous structure help to increase the fatigue life at low stresses by reducing the crack propagation upon separating from their grafted surface. However, at low-cycle, high-stress regime, the advantage provided by the use of nanoparticles is found less effective. This may arise due to the fact that CNT addition could not overcome sudden crack propagation in high-stress regime. Hence, in high-stress regime, the effect of CNT addition may not possess the same amount of enhancement in fatigue life compared to low-stress regime. Since the wind turbine blades are subjected to high-cycle, low-stress regime during their operating period, the use of nanoparticles in the turbine blades (Grimmer & Dharan, 2008), especially in the ply drop zones, may provide a positive effect on the fatigue life.

3 Polymer Composite Structures Including Self-Healing Nanomaterials

Synergistic mechanisms usually control the mechanical behavior of the polymer composite rotor blades. The degradation mechanisms are based largely on the service conditions such as relative humidity, UV radiation, and thermal cyclic events such as freezing and thawing, complicating further the prognostication of their life cycle (Gao et al., 2019). Damage of the load-carrying laminates of the blade are compromising, therefore the integrity of the blade. Further damage growth in the load-carrying laminates would take place under the combined effects of mechanical and environmental loads (McGowan et al., 2007). Aerosol, raindrop, and sand impact on the rotating blades at high speeds are the primary causes of surface erosion on the leading edge (Sareen et al., 2014). Moreover, erosion damage becomes significant in a couple of years of service, and the extra coating of the blade may not resist to the raindrop impacts for the lifetime of the blades. Research on erosion of coated samples pointed out that the damage is not only a surface damage but also interface damage through Rayleigh wave propagation. That is why the solution must be searched in improving the core of the blade (Keegan et al., 2013).

Glass fiber-reinforced composites are largely used in the wind industry for the structure of the wind turbine blades. Various designs have been suggested recently for blades to improve structural performance. Nano-enhanced composites have been suggested as a way to prevent the formation of cracks and to reduce their propagation in the matrix phase as well as in the interface, by using carbon nanofibers or graphene oxide, leading to enhanced fracture toughness and increased delamination resistance. However, the small particle size and the secondary bonds such as hydrogen bonds between the carbon-based nanoparticles cause agglomeration, therefore leading to a decrease in the surface area and dispersion problems within the polymeric matrix as well as negatively affecting mechanical and/or thermal or electrical properties (Yavuz et al., 2016; Yavuz & Bai, 2018). Those mechanical properties, especially the delamination properties, may further be researched through parametric and nonparametric tests for polymer composites (Yavuz & Utku, 2021). This would provide clarifications among the beam theory, modified beam theory, and modified compliance calibration methods accordingly.

The majority of polymer composites in blades use thermoset matrices, which are not easily recycled due to their highly cross-linked nature. Moreover, the replacement of conventionally used epoxy resins such as DGEBA (based on bisphenol A which is toxic, endocrine mutagenic, and carcinogenic) by bio-based epoxy resins would reduce the environmental impact and contribute to health and safety issues. Moreover, blades with higher recyclability can both offer a significant advantage at the end-of-life costs considering maintenance planning and damage prediction. Thermoplastic polymers by nature are free from cross-links and therefore can be easily softened and melted or dissolved for recycling. However, they originally

come in solid phase in their raw state, requiring expensive molds for manufacturing, which is a great limitation. In addition, due to their high melt viscosity, the fiber impregnation is hindered, and they may possess lower thermal stability, strength, and resistance to creep compared to thermoset resins. To improve structural performance of the blade structure, the enhancement of the mechanical properties of polymer composites may be realized with the improvement of matrix and interface at the nanoscale under the controlled conditions (Ma & Zhang, 2014; Yavuz & Bai, 2018). With regard to the matrix, the addition of scalable functionalized nanoparticles (i.e., CNT, nanoplatelets) may improve the stiffness and strength of the matrix, while at the same time, it may improve the fracture toughness and interlaminar shear strength (Yavuz & Bai, 2018). Interaction of nanofillers at the nanoscale between the reinforcements, coupled with macroscale enhancement like crack bridging and bifurcation, would effectively lead to stiffer and damage tolerant composite structures (Opelt et al., 2015).

Fiber-reinforced polymer composites, widely utilized in wind turbine blades, still face major issues pertaining to degradation and operational performance, especially in offshore working conditions, while end-of-life blade components are largely incinerated and landfilled (Mishnavesky Jr., 2021; Ramirez-Tajeda et al., 2016). Alternatives could be considered in the frame of manufacturing of composite wind turbine blades by associating anisotropic conductive materials within classical fiber composites processed via thermal molding in order to achieve self-healing properties. The incorporation of nanoparticles in the blade polymer matrix not only improve structural and environmental performance at material level but also induce new features in terms of dual use as self-healing agents within polymeric coatings for the leading-edge protection. The key points for self-healing investigation concerns are the main causes of wind blades damage, which include fatigue due to high loads and accelerated by the environmental loads. Contrarily with the common solutions of self-healing composites, dispersed nanostructures in micrometer thick layers are used as a cross-linked structure of preformed healing agent that would be finally activated till melting for repairing would be an alternative to microcapsules which are ruptured (Matt et al., 2017). Moreover, due to the recycling concerns, natural fiber-reinforced composites may also possess high potential to be integrated in those structural composite applications (Alsubari et al., 2021; Ilyas et al., 2021; Nurazzi et al., 2021a, 2021b; Omran et al., 2021; Suriani et al., 2021a). Here, the important concern is the selection of nano-/micro-powders and additives and check their compatibility with polymer media toward obtaining stable compounds with further healing effect for wind turbine blades. Even though the thermoplastics are significantly repairable compared to thermosets, special attention would be considered on the achievement of local heating in order not to affect whole blade structure while using polymers for healing the cracks.

4 Fracture Mechanics of Polymer Composite and Hybrid Composite Laminates

Fracture mechanics of such large and complex wind turbine blades by using finite element analysis would be performed at different level of accuracy. Beam models are extensively used in the wind turbine analysis (Kim et al., 2013). However, such beam models are not suitable models to study damage initiation and propagation. On one hand, a finite element model consisting of solid elements must be used to predict the initiation and crack propagation in the form of delamination. On the other hand, modeling the entire rotor blade with solid elements is not suitable for preprocessing and processing issues. Hence, damage analysis of sensitive zones would be performed by using global and submodels together (Shah & Tarfaoui, 2016). By creating a detailed finite element model of sensitive regions with sub-modeling approach (Jensen et al., 2006), damage analysis may be performed with high accuracy and in much shorter duration, creating a finite element model of large structures such as wind turbine blades with shell elements, highly efficient in terms of modeling and computational effort compared to the use of three-dimensional solid elements. Júnior et al. compared the global and local structural behavior of a rotor blade modeled by using geometrically exact beam and shell elements (Faccio Júnior et al., 2019). Turbine blades when modeled by using exact beam elements possess almost the same behavior compared to that of shell elements. However, under the extreme loading conditions, local buckling near to trailing edge can be predicted by shell elements rather than exact beam elements.

Working with the correct geometric model and correct material data comes first in the finite element analysis. Most of the engineering constants of composite materials found in the handbooks such as Composite Materials Handbook (CMH-17) and Advanced General Aviation Transport Experiments (AGATE) consider a maximum of 1% air bubble. However, since the presence of air bubbles significantly affects the stress distribution in the ply drop zone(s), finite element analysis may cause the onset of damage to be determined at higher values (Vizzini, 2009). Moreover, air bubbles affect delamination excessively in natural fiber-reinforced composites as well (Suriani et al., 2021b). Therefore, considering that the damage formation, progression, and layer separation studies samples should be examined with a bright field-illuminated light microscope before creating the finite element model (Carroll et al., 2017).

There are several approaches to be used in the finite element analysis of composite structures such as classical laminate theory (CLT) and first-order shear deformation theory (FSDT). Although beam, plate, and shell models are studied in the context of CLT and FSDT, CLT assumes that the plate width/thickness ratio is quite large, since it is an extended version of Kirchhoff's theory developed for homogeneous isotropic plates. In addition, CLT is not always sufficient to determine the stress distribution in the direction of thickness. Moreover, the determination of interlaminar stresses on the laminate free edge is not only an important issue in angle ply laminates but also in unidirectional laminates due to the presence of

broken fibers caused by cutting process (Wisnom, 2000). For this purpose, with the digital image correlation (DIC) system, all strain field can be recorded according to different axial loading conditions, and free edge micro-damage formation and progression can be studied (Carroll et al., 2017). Hence, the effect of the nanoparticle reinforcement on the interlaminar stress could be observed. Since CLT is insufficient for the relatively thicker laminates, it may be necessary to work with higher-order laminate theories accordingly. However, it is hardly recommended to apply high-order theories, such as third-order laminate theories, to the finite element approach. Instead, three-dimensional finite element analysis can be performed in thick plates or in some regions in three-dimensional stress field calculations (Altenbach et al., 2018).

Finite element simulations of sensitive regions can be examined by using interlaminar analysis only, intra-layer damage analyses only, and combined intra-layer damage and delamination analyses. Before moving on to combined analyses, the fact that layer separation analyses and intra-layer damage analyses performed separately may allow one to evaluate the nanomaterial reinforcement in particular. For intra-layer damage criteria, the interactive Tsai-Wu (1971) and Tsai-Hill (Azzi-Tsai, 2006) and semi-interactive Hashin (1980) and Puck (Puck & Schürmann, 2004) are considered frequently. The prediction of damage mode and the evaluation of stress distribution require extensive analysis due to the vast number of effective factors such as orientation, number of plies, as well as the choice of material system (Yavuz, 2019).

Regarding the studies given in the literature, in composites with ply drop zone(s), damage generally occurs in terms of delamination. Interlaminar stress analysis may therefore be modeled with a finite element approach using three-dimensional elements. The issues to be resolved would be in relation to (1) material discontinuity, (2) progressive damage, and (3) deviation of laminate stress-strain from linearity due to geometric discontinuity. The configuration of ply drop zone composite structures occupies an important place in fracture modeling and analysis. The compatibility of models with experimental studies varies depending on the configuration (He et al., 2000). In the context of delamination studies in composite laminates, it was found that strength-based damage analysis approaches are more successfully to determine the onset of layer separation compared to the strain energy release rate approach (Fish & Lee, 1989; He et al., 2000). However, in polymeric composites, it is noted that progressive delamination analysis performed by strain energy release rate approach can be realized more successfully rather than strength-based damage analysis approaches (He et al., 2000; Vizzini & Lee, 1995). In the perfectly oriented unidirectional composite laminates, linear stress-strain behavior is observed when loading is realized in the fiber direction. However, for the laminates including ply drop zones as well as angle ply laminates, this case is not valid. In addition, the discontinuity resulting from matrix damage can be studied by the Newton-Raphson algorithm with nonlinear three-dimensional finite element analysis or by the Newton-Raphson algorithm with viscous regularization (Ullah et al., 2017; Vasiliev & Morozov, 2007). In composite structures including ply drop zone, strength-based damage analysis approaches and fracture mechanics-based approaches are used for

the determination of layer separation onset and progressive layer separation. By evaluating the production tolerance limits on composite samples with ply drop zones, it is emphasized in many sources that the quantity of results may be insufficient when studying layer separation without considering changes in the geometry of the ply drop zone and the angle of ply drop (He et al., 2000; Vizzini, 1992, 2009).

Although most ply drop zone composite structures in the literature agree that the highest interlaminar shear stress is at the beginning of ply drop in numerical simulations, the highest normal interlaminar stress is at the root of ply drop in some studies, and it is reported that may also be located at the beginning of ply drop. In addition, the onset of separation between layers is considered to be at the starting point of ply drop in some studies, while in other studies, it is mentioned that it is at the root of ply drop (He et al., 2000). Therefore, this situation is highly dependent on the laminate configuration and sensitive to possible material discontinuities, although it makes it difficult to classify the locations of stress peaks. Moreover, working with a zero-thickness resin layer can lead to the formation of a stress singularity in the ply drop zone, the resin layer of certain thicknesses in these regions can also be defined based on microscopic observation. Since possible sudden changes in the stress distribution between layers in the ply drop zone may lead to the formation of a stress singularity, this problem can be corrected by stress averaging method (Dhurvey & Mittal, 2013).

5 Conclusions

Relevant factors concerning phenomena related to the very large wind turbines with large rotor blade length are governed by several structural and material constraints as well as mechanical vibrations. Wind turbine blades may suffer from mechanical degradation due to the extreme dynamic loads regarding the large range of operating conditions during their entire service life. Hence, the integration of material solutions should address blade-specific problems. The incorporation of nanofillers with self-healing capability may improve both durability and enhance self-healing features of the blades. Furthermore, it may reduce or at least alleviate the need for costly coating solutions and expensive repairs. Besides, the use of potential material development in wind turbine blades is also interrelated with the integrated active vibration reduction measures. In order to overcome the close values of the natural frequency of large blades to the resonance frequency of the tower, active measures may provide solutions compared to classical passive measures. Accuracy is needed with respect to assembly production and bonding technologies to be designed for very high loads as well. For the computational simulations, creation of blade-specific finite element models for each blade would be considered as a prospective solution in order to quantify deviations such as in weight and/or due to manufacturing defects. Durability and advancements in material and structural solutions should be evaluated with life cycle analysis and life cycle cost analysis. All these advancements would be enabled unless they address environmental aspects including

recyclability, demonstration of the application, risk assessment, quality requirements and market description, life cycle assessment, and life cycle cost.

Acknowledgments Middle East Technical University Center for Wind Energy Structures and Materials Laboratory is gratefully acknowledged for the useful discussions.

References

- Agastra, P., & Mandell, J. F. (2010). Testing and simulation of damage growth at ply drops in wind turbine blade laminates. In *International SAMPE symposium and exhibition, Seattle, USA*.
- Albanesi, A., Bre, F., Fachinotti, V., & Gebhardt, C. (2018). Simultaneous ply-order, ply-number and ply-drop optimization of laminate wind turbine blades using the inverse finite element method. *Composite Structures*, 184, 894–903. <https://doi.org/10.1016/j.compstruct.2017.10.051>
- Alsubari, S., Zuhri, M. Y. M., Sapuan, S. M., et al. (2021). Potential of natural fiber reinforced polymer composites in sandwich structures: A review on its mechanical properties. *Polymers*, 13(423), 1–20. <https://doi.org/10.3390/polym13030423>
- Altenbach, H., Altenbach, J., & Kissing, W. (2018). *Mechanics of composite structural elements*. Springer. <https://doi.org/10.1007/978-981-10-8935-0>
- Azzi, V. D., & Tsai, S. W. (2006). Anisotropic strength of composites. *Experimental mechanics*. <https://doi.org/10.1007/bf02326292>
- Botting, A. D., Vizzini, A. J., & Lee, S. W. (1996). Effect of ply-drop configuration on delamination strength of tapered composite structures. *AIAA Journal*, 34(8), 1650–1656. <https://doi.org/10.2514/3.13285>
- Carroll, J., Xia, S., Beese, A. M., Berke, R. B., & Pataky, G. J. (2017). Fracture, fatigue, failure and damage evolution, Volume 7, in Chapter 9 In-situ observation of damage evolution in QI CFRP laminates. In *Annual Conference on Experimental and Applied Mechanics* (pp. 67–73). <https://doi.org/10.1007/978-3-319-95879-8>
- Crans, G., Paquette, J., Marzocca, P., et al. (2011). *Durability of tapered composite laminates under static and fatigue loading* (Structures structural dynamics and materials conference). Sandia National Lab. (SNL-NM). <https://doi.org/10.2514/6.2011-1757>
- Curry, J. M., Ohnson, E. R., & Tarnes, J. H. (1992). Effect of dropped plies on the strength of graphite-epoxy laminates. *AIAA Journal*, 30(2), 449–456. <https://doi.org/10.2514/3.10938>
- Daoust, J., & Hoa, S. V. (1989). Parameters affecting interlaminar stresses in tapered laminates under static loading conditions. *Polymer Composites*, 10, 374–383. <https://doi.org/10.1002/pc.750100515>
- Dhurvey, P., & Mittal, N. D. (2013). Review on various studies of composite laminates with ply drop-off. *ARPJ Journal of Engineering and Applied Sciences*, 8(8), 595–605.
- Donaldson, S., Stonecash, J. T., & Sih, S. (2012). Transverse cracks at ply drops in fiberglass laminates. *International Journal of Materials Engineering*, 2, 112–117. <https://doi.org/10.5923/j.ijme.20120206.06>
- Faccio Júnior, C. J., Cardozo, A. C. P., Monteiro Júnior, V., et al. (2019). Modeling wind turbine blades by geometrically-exact beam and shell elements: A comparative approach. *Engineering Structures*, 180, 357–378. <https://doi.org/10.1016/j.engstruct.2018.09.032>
- Fish, J. C., & Lee, S. W. (1989). Delamination of tapered composite structures. *Engineering Fracture Mechanics*, 34(1), 43–54. [https://doi.org/10.1016/0013-7944\(89\)90241-5](https://doi.org/10.1016/0013-7944(89)90241-5)
- Fish, J. C., & Vizzini, A. J. (1992). Tailoring concepts for improved structural performance of rotorcraft flexbeams. *Composites Engineering*, 34, 43–54. [https://doi.org/10.1016/0961-9526\(92\)90028-5](https://doi.org/10.1016/0961-9526(92)90028-5)

- Gao, L., Liu, Y., Zhou, W., et al. (2019). An experimental study on the aerodynamic performance degradation of a wind turbine blade model induced by ice accretion process. *Renewable Energy*, *133*, 663–675. <https://doi.org/10.1016/j.renene.2018.10.032>
- Gouldstone, C., Degtiarov, D., & Williams, R. D. (2014). Reinforcing ply drop interfaces using vertically-aligned carbon nanotube forests. In *SAMPE Conference, Seattle, USA*.
- Grimmer, C. S., & Dharan, C. K. H. (2008). High-cycle fatigue of hybrid carbon nanotube/glass fiber/polymer composites. *Journal of Materials Science*, *43*, 4487–4492. <https://doi.org/10.1007/s10853-008-2651-9>
- Hashin, Z. (1980). Failure criteria for unidirectional fibre composites. *ASME Journal of Applied Mechanics*, *42*, 329–334. <https://doi.org/10.1115/1.3153664>
- He, K., Hoa, S. V., & Ganesan, R. (2000). The study of tapered laminated composite structures: A review. *Composites Science and Technology*, *60*, 2643–2657. [https://doi.org/10.1016/S0266-3538\(00\)00138-X](https://doi.org/10.1016/S0266-3538(00)00138-X)
- Helmy, A. K., Ferreira, E. A., & De Bussetti, S. G. (1999). Surface area evaluation of montmorillonite. *Journal of Colloid and Interface Science*, *210*, 167–171. <https://doi.org/10.1006/jcis.1998.5930>
- Helmy, S., & Hoa, S. V. (2014). Tensile fatigue behavior of tapered glass fiber reinforced epoxy composites containing nanoclay. *Composites Science and Technology*, *102*, 10–19. <https://doi.org/10.1016/j.compscitech.2014.05.038>
- Hosseiny SAR, Jakobsen, J (2016) Local fatigue behavior in tapered areas of large offshore wind turbine blades. In IOP Conference Series: Materials Science and Engineering, Vol. 139(1). IOP Publishing. doi: <https://doi.org/10.1088/1757-899X/139/1/012022>.
- Ilyas, R. A., Sapuan, S. M., & Harussani, M. M. (2021). Polylactic acid (PLA) biocomposite: Processing additive manufacturing and advanced applications. *Polymers*, *13*(1326), 1–34. <https://doi.org/10.3390/polym13081326>
- Jensen, F. M., Falzon, B. G., Ankersen, J., et al. (2006). Structural testing and numerical simulation of a 34 m composite wind turbine blade. *Composite Structures*, *76*, 52–61. <https://doi.org/10.1016/j.compstruct.2006.06.008>
- Kabir, A., & Hoa, S. V. (2011). Improvement of vibration damping and flexural fatigue property incorporating Nanoclay into glass/epoxy composite. In *ICAF 2011 structural integrity: Influence of efficiency and green imperatives*. https://doi.org/10.1007/978-94-007-1664-3_12
- Keegan, M. H., Nash, D. H., & Stack, M. (2013). On erosion issues associated with the leading edge of wind turbine blades. *Journal of Physics D: Applied Physics*, *46*, 383001. <https://doi.org/10.1088/0022-3727/46/38/383001>
- Kim, T., Hansen, A. M., & Branner, K. (2013). Development of an anisotropic beam finite element for composite wind turbine blades in multibody system. *Renewable Energy*, *59*, 172–183. <https://doi.org/10.1016/j.renene.2013.03.033>
- Loos, M. R., Yang, J., Feke, D. L., et al. (2012). Enhanced fatigue life of carbon nanotube-reinforced epoxy composites. *Polymer Engineering and Science*, *52*, 1882–1887. <https://doi.org/10.1002/pen.23145>
- Ma, P. C., & Zhang, Y. (2014). Perspectives of carbon nanotubes/polymer nanocomposites for wind blade materials. *Renewable and Sustainable Energy Reviews*, *30*, 651–660. <https://doi.org/10.1016/j.rser.2013.11.008>
- Matt, A. K. K., Beyhaghi, S., Amano, R., et al. (2017). Self-healing of wind turbine blades using micro-scale vascular vessels. *Journal of Energy Resources Technology*, *139*, 051208. <https://doi.org/10.1115/1.4036052>
- McGowan, J., Hyers, J. G., Sullivan, K. L., et al. (2007). A review of materials degradation in utility scale wind turbines. *Energy Materials Science and Engineering for Energy Systems*, *2*, 41–64. <https://doi.org/10.1179/174892407X223902>
- Mishnavesky, L., Jr. (2021). Sustainable end-of-life management of wind turbine blades: Overview of current and coming solutions. *Materials*, *14*(1124), 1–25. <https://doi.org/10.3390/ma14051124>

- Mukherjee, A., & Varughese, B. (2001). Design guidelines for ply drop-off in laminated composite structures. *Composites Part B: Engineering*, 32, 153–164. [https://doi.org/10.1016/S1359-8368\(00\)00038-X](https://doi.org/10.1016/S1359-8368(00)00038-X)
- Nurazzi, N. M., Asyraf, M. R. M., Khalina, A., et al. (2021a). A review on natural fiber reinforced polymer composite for bullet proof and ballistic applications. *Polymers*, 13(646), 1–42. <https://doi.org/10.3390/polym13040646>
- Nurazzi, N. M., Asyraf, M. R. M., Khalina, A., et al. (2021b). Fabrication functionalization and application of carbon nanotube-reinforced polymer composite: An overview. *Polymers*, 13(1047), 1–44. <https://doi.org/10.3390/polym13071047>
- Omran, A. A. B., Mohammed, A. A. B. A., Sapuan, S. M., et al. (2021). Micro- and nanocellulose in polymer composite materials: A review. *Polymers*, 13(231), 1–35. <https://doi.org/10.3390/polym13020231>
- Opelt, C. V., Becker, D., Lepienski, C. M., et al. (2015). Reinforcement and toughening mechanisms in polymer nanocomposites – Carbon nanotubes and aluminum oxide. *Composites Part B: Engineering*, 75, 119–126. <https://doi.org/10.1016/j.compositesb.2015.01.019>
- Puck, A., & Schürmann, H. (2004). Failure analysis of FRP laminates by means of physically based phenomenological models. In *Failure criteria in fibre-reinforced-polymer composites*. Elsevier. <https://doi.org/10.1016/B978-008044475-8/50028-7>
- Ramirez-Tajeda, K., Turcotte, D. A., & Pike, S. (2016). Unsustainable wind turbine blade disposal practices in the United States: A case for policy intervention and technological innovation. *New Solutions: A Journal of Environmental and Occupational Health Policy*, 26, 581–598. <https://doi.org/10.1177/1048291116676098>
- Samborsky, D. D., Wilson, T. J., Agastra, P., et al. (2008). Delamination at thick ply drops in carbon and glass fiber laminates under fatigue loading. *Journal of Solar Energy Engineering*, 130(3). <https://doi.org/10.1115/1.2931496>
- Sareen, A., Sapre, C. A., & Selig, M. S. (2014). Effects of leading edge erosion on wind turbine blade performance. *Wind Energy*, 130, 031001. <https://doi.org/10.1002/we.1649>
- Shah, O. R., & Tarfaoui, M. (2016). The identification of structurally sensitive zones subject to failure in a wind turbine blade using nodal displacement based finite element sub-modeling. *Renewable Energy*, 87, 168–181. <https://doi.org/10.1016/j.renene.2015.09.065>
- Suriani, M. J., Radzi, F. S. M., Ilyas, R. A., et al. (2021a). Flammability tensile and morphological properties of oil palm empty fruit branches fiber/pet yarn-reinforced epoxy fire retardant hybrid polymer composites. *Polymers*, 13(1282), 1–18. <https://doi.org/10.3390/polym13081282>
- Suriani, M. J., Rapi, H. Z., Ilyas, R. A., et al. (2021b). Delamination and manufacturing defects in natural fiber-reinforced hybrid composite: A review. *Polymers*, 13(1323), 1–24. <https://doi.org/10.3390/polym13081323>
- Tsai, S. W., & Wu, E. M. (1971). A general theory of strength for anisotropic materials. *Journal of Composite Materials*, 5, 58–80. <https://doi.org/10.1177/002199837100500106>
- Ullah, Z., Kaczmarczyk, L., & Pearce, C. J. (2017). Three-dimensional nonlinear micro/meso-mechanical response of the fibre-reinforced polymer composites. *Composite Structures*, 161, 204–214. <https://doi.org/10.1016/j.compstruct.2016.11.059>
- Varughese, B., & Mukherjee, A. (1997). A ply drop-off element for analysis of tapered laminated composites. *Composite Structures*, 39, 123–144. [https://doi.org/10.1016/S0263-8223\(97\)00132-3](https://doi.org/10.1016/S0263-8223(97)00132-3)
- Vasiliev, V. V., & Morozov, E. V. (2007). *Advanced mechanics of composite materials*. Elsevier. <https://doi.org/10.1016/B978-0-08-045372-9.X5000-3>
- Vizzini, A. (1992). Strength of laminated composites with internal discontinuities parallel to the applied load. *AIAA Journal*, 30(6), 1515–1520. <https://doi.org/10.2514/3.11095>
- Vizzini, A. (2009). Influence of realistic ply-drop geometries on interlaminar stresses in tapered laminates. *ASTM International*. <https://doi.org/10.1520/stp14030s>
- Vizzini, A. J., & Lee, S. W. (1995). Damage analysis of composite tapered beams. *Journal of the American Helicopter Society*, 40, 43–47. <https://doi.org/10.4050/jahs.40.43>

- Weiss, A., Trabelsi, W., Michel, L., et al. (2010). Influence of ply-drop location on the fatigue behaviour of tapered composites laminates. *Procedia Engineering*, 2, 1105–1114. <https://doi.org/10.1016/j.proeng.2010.03.119>
- Wisnom, M. R. (2000). Test methods, nondestructive evaluation, and smart materials. In A. Kelly & C. Zweben (Eds.), *Comprehensive composite materials*. Pergamon.
- Yavuz, H., Girard, G., & Bai, J. (2016). Dielectric barrier discharge assisted continuous plasma polypyrrole deposition for the surface modification of carbon nanotube-grafted carbon fibers. *Thin Solid Films*, 616, 220–227. <https://doi.org/10.1016/j.tsf.2016.08.028>
- Yavuz, H., & Bai, J. (2018). Plasma polypyrrole coated hybrid composites with improved mechanical and electrical properties for aerospace applications. *Applied Composite Materials*, 25, 661–674. <https://doi.org/10.1007/s10443-017-9644-2>
- Yavuz, H. (2019). Materials selection for aircraft skin panels by integrating multiple constraints design with computational evaluations. *Procedia Structural Integrity*, 21, 112–119. <https://doi.org/10.1016/j.prostr.2019.12.092>
- Yavuz, H., & Utku, D. H. (2021). Parametric and nonparametric tests for the evaluation of interlaminar fracture toughness of polymer composites. *Journal of Reinforced Plastics and Composites*, 40, 450–462. <https://doi.org/10.1177/0731684420973078>
- Zhang, H., Abdi, F., & Paquette, J. (2011). Durability of tapered composite laminates under static and fatigue loading. *Structures Structural Dynamics and Materials Conference*. <https://doi.org/10.2514/6.2011-1757>
- Zhang, W., Picu, R. C., & Koratkar, N. (2007). Suppression of fatigue crack growth in carbon nanotube composites. *Applied Physics Letters*, 91, 193109. <https://doi.org/10.1063/1.2809457>
- Zhang, W., Picu, R. C., & Koratkar, N. (2008). The effect of carbon nanotube dimensions and dispersion on the fatigue behavior of epoxy nanocomposites. *Nanotechnology*, 19, 285709. <https://doi.org/10.1088/0957-4484/19/28/285709>

Chapter 22

Influence of Scanning Speed on the Laser Metal Deposition of Ti-6Al-4V and Mo for Aerospace Application



M. F. Erinosh, E. T. Akinlabi, and K. O. Oladosu

1 Introduction

Titanium is a lightweight, high-strength, low-corrosion structural metal for the production of high-speed aircraft parts. At room temperature, the metal tends to be brittle and becomes malleable and ductile at higher temperatures. Titanium alloy (Ti-6Al-4V), the alpha-beta alloy, is the workhorse alloy in many field since it combines outstanding mechanical strength and low density with excellent corrosion resistance (US Titanium Industry, 2019), well heat treatable (Joshi, 2006), good oxidation resistance, and moderate strength at high temperatures (Sha & Malinov, 2009). The lightness of the alloys and its admirable properties has made them worthwhile for aerospace, biomedical, automobile, sport, and chemical industrial application. The improvement in the properties of the alloy can be achieved by the addition of other alloys (Sen et al., 2010).

On the one hand, molybdenum (Mo) has a very high melting point and is used in steel alloys to increase strength, hardness, electrical conductivity, and resistance to corrosion and wear (Royal Society of Chemistry, 2020). The metal production is hydrostatically compacted and sintered at about 2100 °C from powder using metallurgy techniques. The Mo alloy is mechanically stable at high temperatures, and its high ductility and toughness offer a greater tolerance for failures (International Molybdenum Association, 2020). Additive manufacturing (AM) is the technology

M. F. Erinosh (✉)

Department of Mechanical and Metallurgical Engineering, University of Namibia,
Ongwediva, Namibia

e-mail: merinosho@unam.na

E. T. Akinlabi

Pan African University for Life and Earth Sciences (PAULESI), Ibadan, Nigeria

K. O. Oladosu

Department of Mechanical Engineering, Kwara State University, Malete, Nigeria

of building 3D objects by the addition of a layer-upon-layer of metal, plastic, or concrete material by using a 3D modeling software. The AM facility reads that drawing from the CAD file and builds in a layer-upon-layer manner to produce the 3D image (Amazing, 2020; Sinha, 2020).

Depending on the need, different deposition techniques and process are used such as laser engineered net shaping, stereolithography, selective laser melting, liquid thermal polymerization, fused deposition modeling, etc. (Dehghanhadikolaie et al., 2018). Laser metal deposition is also a technique of additive manufacturing process. It is a deposition technology that creates a metallurgically fused material onto a substrate where the laser beam is used to melt its surface and created a melt pool for powder injection (Graf et al., 2013) and get solidified with high mechanical strength (Ludovico et al., 2010). Numerous works have been done on laser metal deposition of titanium alloy combined with other stabilizing elements or other enhancement compounds (Amado et al., 2019; Graf et al., 2012; Li et al., 2017; Lu et al., 2018; Nyoni & Akinlabi, 2016; Pouzet et al., 2016; Sharman et al., 2018). The functionally graded Ti6Al4V-Mo alloy was produced by laser deposition process. Both the two alloys were alternated with a 25 wt.% rise or decrease in gradient ratio. The microhardness results were reported to increase as a result of increased Mo addition (Schneider-Maunoury et al., 2017). Ti-15Mo alloy was deposited for biomedical application. Response surface methodology technique and ANOVA-based quadratic regression modeling were engaged with the process parameters, and the established result revealed the achievement of low dilution at the highest laser power and low scanning speed as well as the powder feed rate used (Bhardwaj et al., 2019).

Molybdenum disulfide-titania ($\text{MoS}_2\text{-TiO}_2$) nanocomposite oxide was coated on Ti-6Al-4V alloy using plasma electrolytic oxidation (PEO) process. The addition of 4 g/L of MoS_2 particles in the electrolyte was reported to lead to shorter activation time and lower breakdown voltage. In addition, the nanocomposite sample was also discovered to have good wear properties due to the lubricity influence of the 4 g/L MoS_2 particles added under a duty cycle of 50%, and the microstructures were characterized with spark craters and stacks of nanoscale white particles (Chang et al., 2016). On the other hand, MoO_2 is another catalyst with excellent coking resistance and high activity for the partial oxidation of liquid hydrocarbons (Marin-Flores et al., 2011). In order to buttress on the catalytic behavior, Ti-doped MoO_2 was fused to develop the oxygen-to-carbon ratio of MoO_2 for partial oxidation of long-chain hydrocarbons thereby increasing the redox stability of the solid oxide fuel cell process (He et al., 2015). The annealing process and the cooling effect on microstructure and tensile properties of laser-deposited Ti-4Al-1.5Mn titanium alloy were investigated. It was reported that bimodal microstructure of primary α laths and fine lamellar transformed β achieved the cooling processes adopted. In the annealing process conducted at the same temperature, water-quenched samples were revealed to have the highest strength than that of the air-cooled samples (Tian et al., 2014).

The laser surface alloying of Mo on Al 1100 was studied to improve the wear resistance. The microstructure of the laser-deposited samples was characterized by dendrites of Al-Mo intermetallics, and their formation was reported to be attributed to the dilution of Mo in Al. These intermetallics such as Al_8Mo_3 , $AlMo_3$, and Al_5Mo were however revealed to be very hard and difficult to groove and deform plastically during the wear process (Rajamure et al., 2014).

In the literature, there is still scarcity of the deposition process of titanium alloy with Mo reported. The potential of using this LMD technique is immeasurable; nevertheless, it has established a vital response in recent years due to its lingering possibilities for material processing in the industry. However, the aim of this research work is to upgrade the properties of Ti-6Al-4V with the addition of 10 wt.% Mo via laser deposition process, to recognize the impact of varying scanning speed on the deposited alloy through the microstructural analysis and microhardness, and to establish the possibility of Ti-6Al-4V-Mo as being a potential material with a good balance between strength and ductility needed for the aerospace industry.

2 Materials and Methods

99.5% molybdenum powder with the particle size of 170 μm was supplied by Industrial Analytical company from Germany, and the titanium alloy powder with particle size of 45–90 μm was supplied by F.J. Brodmann and Co., LLC, Louisiana, TLS Technik GmbH, South Africa. The titanium alloy square plate (substrate) with the volumetric dimension of $102 \times 102 \times 7.54 \text{ mm}^3$ was purchased from Titanium Metal Supply, United States.

The experiment was conducted on an ytterbium laser system at the Council for Scientific and Industrial Research Centre, CSIR, in Pretoria, South Africa. The deposition procedures for this research are explained in detail as follows: Five (5) samples were produced from the deposition process by varying the scanning speed from 0.5 to 1.5 m/min at an interval of 0.25 while keeping the laser power at 1.7 kW, shielding gas at 15 l/min, and powder flow rate of Ti-6Al-4V alloy and Mo at 3.6 rpm and 0.4 rpm, respectively. The samples were mounted by hot compression mounting method with Multi-Fast on Struers mounting press. Grinding and polishing operations are followed using the emery papers and the grinding and polishing discs with the suspensions for the metallographic preparation of titanium. Metallographic etching was done on the samples to reveal the microstructural details. Kroll's reagent was prepared with 100 ml water, 1–3 ml hydrofluoric acid, and 2–6 ml nitric acid (Taylor & Weidmann, 2016). The optical microscope is used to capture the microstructure, and microhardness test was conducted on each mounted sample using the Zwick Vickers microhardness tester. Response surface model is also applied for the microhardness value using design expert 11 software.

3 Results and Discussion

In this section, microstructural examination, microhardness, and the surface response analysis are presented. Unmelted molybdenum were observed due to the high melting point the Mo exhibited. However, this behavior was explained by Schneider-Maunoury et al. (2017), which is as a result of the insufficient energy density when compared to the high melting temperature of molybdenum.

The β stabilizer molybdenum additions in pre-alloyed Ti6Al4V greatly vary the phase developments with pores (Rajadurai et al., 2021), and elongated grain structures were also detected in the micrograph of the deposited samples. However, these pores could reduce the ductility of the deposit (Rajadurai et al., 2021).

The microstructures of laser-deposited Ti-6Al-4V-Mo alloy from sample 1 to sample 4 are depicted in Fig. 22.1. Widmanstatten structures of laser-deposited Ti-6Al-4V-Mo alloy from sample 1 to sample 4 toward the fusion zone were revealed in Fig. 22.2.

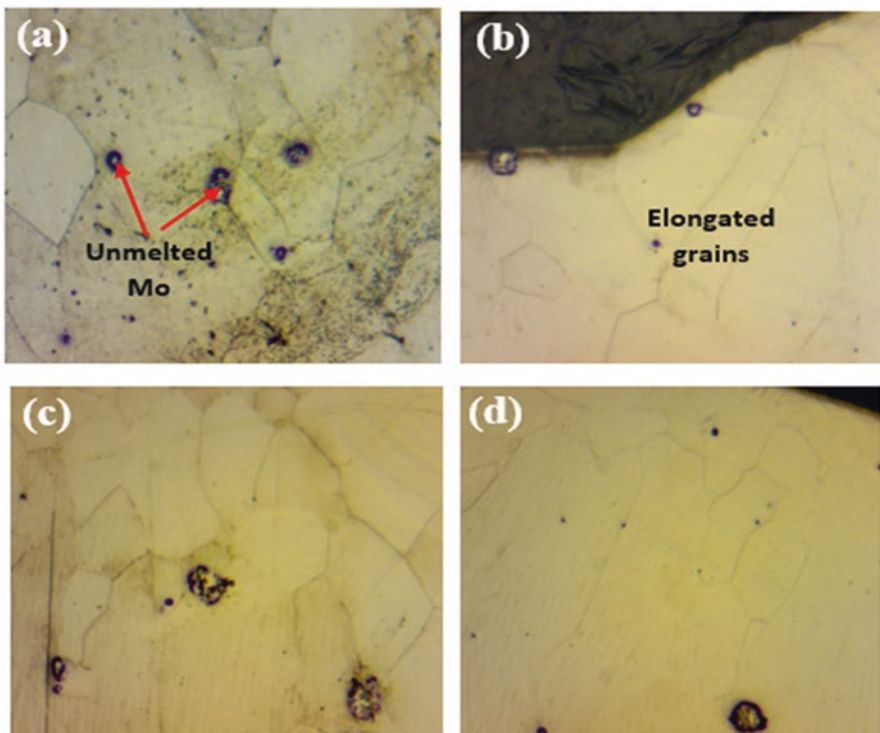


Fig. 22.1 Microstructure of laser-deposited samples. (a) Sample 1 at scanning speed of 0.5 m/min. (b) Sample 2 at scanning speed of 0.75 m/min. (c) Sample 3 at scanning speed of 1.0 m/min. (d) Sample 4 at scanning speed of 1.25 m/min

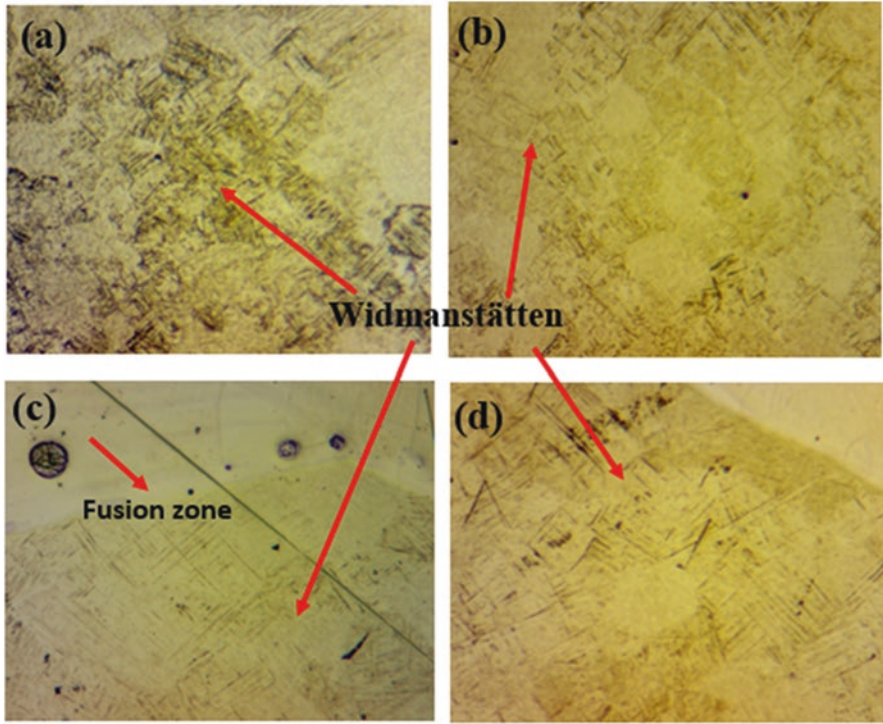


Fig. 22.2 Development of Widmanstätten. (a) Sample 1, (b) sample 2, (c) sample 3, and (d) sample 4

In the entire microstructure, elongated grains were observed as a result of the addition of Mo in the phase of Ti-6Al-4V alloy. Toward the top of the deposit, equiaxed grains were observed before the elongated grains.

The difference in density of the Mo, which is 10.28 g/cm^3 to that of the Ti-6Al-4V alloy, which is 4.42 g/cm^3 , could be the cause of the long grains that were observed in the deposit. The development of Widmanstätten observed in the deposited samples decreases as the scanning speed was increased. The addition of molybdenum has led to the improvement in the β phase of the primary alloy, and this was in agreement with Rajadurai et al. (2021).

The more melt pool created, the more the development of Widmanstätten structures, and they are coarser at low scanning speed and hence the better ductility. The heat-affected zone (HAZ) is found after the fusion zone. It is a non-melted area that has undergone changes in material properties because of its exposure to high temperatures (Twi-global.com, 2019). The level of thermal diffusivity influences the HAZ, and which is dependent on the thermal conductivity, density, and specific heat of a substance. The grain sizes of the deposited samples are also examined. It was deduced that as the scanning speed increases, the average grain size of the samples was found decreasing. Sample 1 deposited at a scanning speed of 0.5 m/min and a

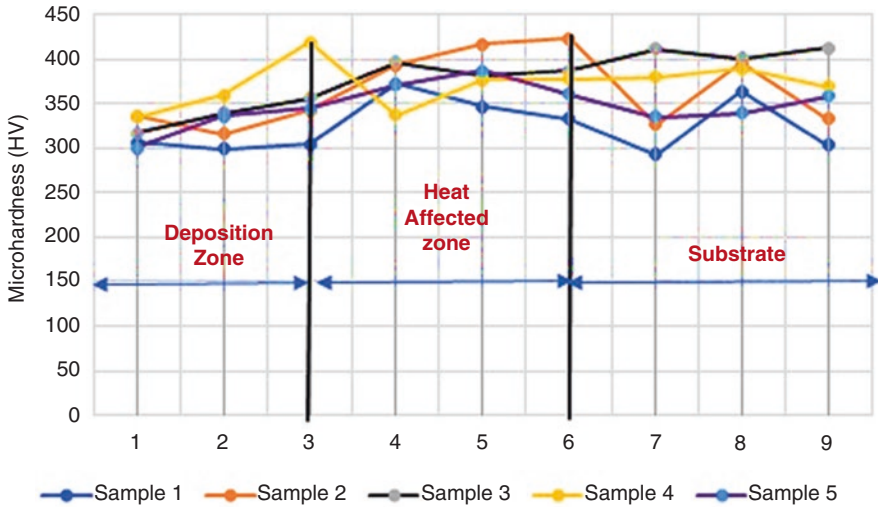


Fig. 22.3 Microhardness profiling

laser power of 1.7 kW exhibited the highest average grain size of 116.89 μm while sample 5 deposited at a scanning speed of 1.5 m/min and a laser power of 1.7 kW exhibited the lowest average grain size of 68.9 μm . The larger grain size according to Hall-Petch relationship of grain size and strength states that the larger the grain size, the greater the ductility. This proves to us that alloying Mo does indeed improve ductility (Rajadurai et al., 2021; Whang, 2011).

Microhardness profiling is plotted as shown in Fig. 22.3, and this depicts the difference in the microhardness on each sample for the different zones: deposit region, heat-affected zone, and substrate.

The average microhardness value of each deposited sample compared to the substrate is shown in Table 22.1.

From the average hardness values, it was found that sample 2 deposited at scanning speed of 0.75 m/min had the highest average hardness value of $\text{HV } 371 \pm 42$, while sample 1 deposited at scanning speed of 0.5 m/min had the lowest value of $\text{HV } 327 \pm 26$. The average hardness values of the samples are more than that of the substrate except sample 1 and sample 5. Although all the hardness values are close to each other. The alloying of Ti-6Al-4V with Mo has shown an improvement in the ductility of the primary Ti-6Al-4V alloy. In general, the microhardness value was increased from sample 1 to sample 2 as the scanning speed was increased and later decreased, although sample 3 showed a slight increase after sample 2. The fluctuating depositing behavior of the Mo during the process as well as the density variation could be responsible for the hardness behavior. However, the slower the scanning speed, the more interaction time between the nozzle and the deposited material and causing a larger melt pool that takes longer time to cool.

The analysis of variance results for the hardness values is depicted in Table 22.2.

Table 22.1 The average microhardness value of the deposited samples

Sample	Sample 1	Sample 2	Sample 3	Sample 4	Sample 5	Substrate
Hardness value (HV)	327 ± 26	371 ± 42	363 ± 28	367 ± 28	350 ± 28	357 ± 41

Table 22.2 Analysis of variance

Source	Sum of squares	Df	Mean square	F-value	p-value	
Block	178.57	1	178.57			
Model	7228.12	3	2409.37	51.47	<0.0001	Significant
A-scanning Speed	254.30	1	254.30	5.43	0.0447	
A ²	2386.84	1	2386.84	50.99	<0.0001	
A ³	1770.38	1	1770.38	37.82	0.0002	
Residual	421.31	9	46.81			
Lack of fit	421.31	4	105.33			
Pure error	0.0000	5	0.0000			
Cor total	7828.00	13				

The **model F-value** of 51.47 implies the model is significant. There is only a 0.01% chance that an F-value this large could occur due to noise. **P-values** less than 0.0500 indicate model terms are significant. In this case, A, A², and A³ are significant model terms. Values greater than 0.1000 indicate the model terms are not significant. If there are many insignificant model terms (not counting those required to support hierarchy), model reduction may improve your model. The generated microhardness values from the design expert for the values from the minimum and maximum of 0.5 and 1.5 m/min are 77 in number of the desirabilities generated by the software. Final equation in terms of coded factors is illustrated in Eq. (22.1).

$$\text{Microhardness} = 366.70 + (-14.10 * A) + (-17.76 * A^2) + (22.85 * A^3) \tag{22.1}$$

The equation in terms of coded factors can be used to make predictions about the response for given levels of each factor. By default, the high levels of the factors are coded as +1 and the low levels are coded as -1. The coded equation is useful for identifying the relative impact of the factors by comparing the factor coefficients. The final equation in terms of actual factors is expressed as Eq. (22.2).

$$\begin{aligned} \text{Microhardness} = & 141.08069 + (662.22835 * \text{scanning speed}) \\ & + (-619.39040 * \text{scanning speed}^2) \\ & + (182.78397 * \text{scanning speed}^3) \end{aligned} \tag{22.2}$$

The equation in terms of actual factors can be used to make predictions about the response for given levels of each factor. Here, the levels should be specified in the original units for each factor. This equation should not be used to determine the relative impact of each factor because the coefficients are scaled to accommodate the units of each factor, and the intercept is not at the center of the design space.

4 Conclusion

In conclusion, the characterizations of the laser-deposited Ti-6Al-4V-Mo were successfully conducted in the laboratory. The microstructures observed in the deposited sample showed elongated grains forming toward the fusion zones. Some unmelted Mo were observed as a result of the high melting point and thermal expansion. Sample 1 deposited at scanning speed of 0.5 m/min and laser power of 1.7 kW has the highest average grain size and coarse Widmanstätten compared to other samples. Sample 2 deposited at scanning speed of 0.75 m/min and laser power of 1.7 kW exhibited the highest average hardness value of HV 371 ± 42 compared to all other deposited samples as well as the substrate. The deposition of Ti-6Al-4V alloy with 10 wt% Mo has improved the ductility of the primary alloy, and this is recommended for aerospace applications.

References

- Amado, J. M., Rodríguez, A., Montero, J. N., Tobar, M. J., & Yáñez, A. (2019). A comparison of laser deposition of commercially pure titanium using gas atomized or Ti sponge powders. *Surface and Coatings Technology*, 374(25), 253–263.
- Amazing. *Additive manufacturing*. Retrieved 09 January, 2020., from <https://additivemanufacturing.com/basics/>.
- Bhardwaj, T., Shukla, M., Paul, C. P., & Bindra, K. S. (2019). Direct energy deposition—Laser additive manufacturing of titanium-molybdenum alloy: Parametric studies, microstructure and mechanical properties. *Journal of Alloys and Compounds*, 787, 1238–1248.
- Chang, F. C., Wang, C. J., Lee, J. W., & Lou, B. S. (2016). Microstructure and mechanical properties evaluation of molybdenum disulfide-titania nanocomposite coatings grown by plasma electrolytic oxidation. *Surface & Coatings Technology*, 303, 68–77.
- Dehghanghadikolaei, A., Namdari, N., Mohammadian, B., & Fotovvati, B. (2018). Additive manufacturing methods: A brief overview. *Journal of Scientific and Engineering Research*, 5(8), 123–131.
- Graf, B., Ammer, S., Gumenyuk, A., & Rethmeier, M. (2013). Design of experiments for laser metal deposition in maintenance, repair and overhaul applications. In *2nd International Through-life Engineering Services Conference, Procedia CIRP* (Vol. 11, pp. 245–248).
- Graf, B., Gumenyuk, A., & Rethmeier, M. (2012). Laser metal deposition as repair technology for stainless steel and titanium alloys. *Physics Procedia*, 39, 376–381.
- He, Q., Marin-Flores, O., Hu, S., Scudiero, L., Ha, S., & Grant Norton, M. (2015). Kinetics of hydrogen reduction of titanium-doped molybdenum dioxide. *Scripta Materialia*, 100, 55–58.
- International Molybdenum Association. Retrieved 09 January, 2020., from <https://www.imoa.info/molybdenum-uses/molybdenum-metal-alloys.php>.
- Joshi, V. A. (2006). *Titanium alloys: An Atlas of structure and fracture features*. CRC Press.
- Li, W., Yan, L., Karnati, S., Liou, F., Newkirk, J., Brown Taminger, K. M., & Seufzer, W. J. (2017). Ti-Fe intermetallics analysis and control in joining titanium alloy and stainless steel by laser metal deposition. *Journal of Materials Processing Technology*, 242, 39–48.
- Lu, M., Mc Cormick, P., Zhao, Y., Fan, Z., & Huang, H. (2018). Laser deposition of compositionally graded titanium oxide on Ti6Al4V alloy. *Ceramics International*, 44(17), 20851–20861.
- Ludovico, A. D., Angelastro, A., & Campanelli, S. L. (2010). Experimental analysis of the direct laser metal deposition process. In *New trends in technologies: devices, computer,*

- communication and industrial systems (pp. 253–272). Polytechnic of Bari, Department of Management and Mechanical Engineering, Italy.
- Marin-Flores, O., Turba, T., Ellefson, C., Scudiero, L., Breit, J., Norton, M. G., & Ha, S. (2011). *Applied Catalysis B: Environmental*, 105, 61.
- Nyoni, E., & Akinlabi, E. T. (2016). Process parameter interaction effect on the evolving properties of laser metal deposited titanium for biomedical applications. *Thin Solid Films*, 620, 94–102.
- Pouzet, S., Peyre, P., Gorny, C., Castelnau, O., Baudin, T., Brisset, F., Colin, C., & Gadaud, P. (2016). Additive layer manufacturing of titanium matrix composites using the direct metal deposition laser process. *Materials Science and Engineering: A*, 677(20), 171–181.
- Rajadurai, M., Muthuchamy, A., Annamalai, A. R., Agrawal, D. K., & Jen, C. (2021). Effect of Molybdenum (Mo) addition on phase composition, microstructure, and mechanical properties of pre-alloyed Ti6Al4V using spark plasma sintering technique. *Molecules*, 26(10), 2894. <https://doi.org/10.3390/molecules26102894>
- Rajamure, R. S., Vora, H. D., Gupta, N., Shivraj, K., Srinivasan, S. G., & Dahotre, N. B. (2014). Laser surface alloying of molybdenum on aluminum for enhanced wear resistance. *Surface & Coatings Technology*, 258, 337–342.
- Royal Society of Chemistry. Retrieved 09 January, 2020., from <https://www.rsc.org/periodic-table/element/42/molybdenum>.
- Schneider-Maunoury, C., Weiss, L., Acquier, P., Boisselier, D., & Laheurte, P. (2017). Functionally graded Ti6Al4V-Mo alloy manufactured with DED-CLAD® process. *Additive Manufacturing*, 17, 55–66.
- Sen, I., Gopinath, K., Datta, R., & Ramamurty, U. (2010). Fatigue in Ti-6Al-4V-B alloys. *Acta Materialia*, 58(20), 6799–6809.
- Sha, W., & Malinov, S. (2009). *Titanium alloys: Modelling of microstructure, properties and application*. CRC, Woodhead Publishing Limited.
- Sharman, A. R. C., Hughes, J. I., & Ridgway, K. (2018). Characterisation of titanium aluminide components manufactured by laser metal deposition. *Intermetallics*, 93, 89–92.
- Sinha, N. *Additive manufacturing*. Retrieved 9th January, 2020. http://home.iitk.ac.in/~nsinha/Additive_Manufacturing%20I.pdf.
- Taylor, B., & Weidmann, E. (2016). *Metallographic preparation of titanium* (pp. 1–6). Struers.
- Tian, X. J., Zhang, S. Q., & Wang, H. M. (2014). The influences of anneal temperature and cooling rate on microstructure and tensile properties of laser deposited Ti–4Al–1.5Mn titanium alloy. *Journal of Alloys and Compounds*, 608, 95–101.
- Twi-global.com. (2019). *What is the heat affected zone (HAZ)?* [online] Retrieved 11 November, 2019, from: <https://www.twi-global.com/technical-knowledge/faqs/what-is-the-heat-affected-zone>.
- U.S. Titanium Industry Inc. *Azom*. Retrieved March 2019., from <https://www.azom.com/article.aspx?ArticleID=1547>.
- Whang, S. (2011). Hall-Petch relationship. *Nanostructured Metals and Alloys*, pp. 787–803.

Chapter 23

Carbon Nanomaterial-Carbon Fiber Hybrid Composite for Lightweight Structural Composites in the Aerospace Industry: Synthesis, Processing, and Properties



Abhishek K. Pathak and Sanjay R. Dhakate

1 Introduction

Carbon fiber-reinforced composites (CFRP) are composite structures where carbon fiber (CF) acts as one of the primary reinforcements in a suitable polymer matrix. In the 1960s, CFRP was first employed in the making of structural parts for aerospace applications. Thereafter, its usage surged, capturing a large market in various technology industries like aircraft, wind turbines, sport, etc. (Pathak et al., 2021a). They have been preferred in space and aviation industries to construct a large number of aircraft components due to their low density, high strength, stiffness, and high fatigue resistance which increases fuel efficiency and leads to a low carbon footprint (Muhammad et al., 2021). The components made of CFRP utilized in airbus are depicted in Fig. 23.1 (Hashish & Kent, 2013). Mainly, the wing cover stringers, spars, and fuselage are constructed using CFRP.

The composite industry has taken a great leap forward by introducing smart polymer matrix and processing methods to achieve actuation, self-healing abilities, and smart properties. Such properties have been realized mainly in the wing structure to make them “morphing or compliant.” The morphing wing structures in aerospace are designed to satisfy the conventional strength, stiffness, and stability and simultaneously be elastic to work on hingeless mechanisms. Advantages include

A. K. Pathak

Department of Aeronautics and Astronautics, The University of Tokyo, Bunkyo-Ku, Tokyo, Japan

e-mail: abhishek.pathak@astr.t.u-tokyo.ac.jp

S. R. Dhakate (✉)

Advanced Carbon Products and Metrology, Advanced Materials and Device Metrology Division, CSIR-National Physical Laboratory, New Delhi, India

e-mail: dhakate@nplindia.org

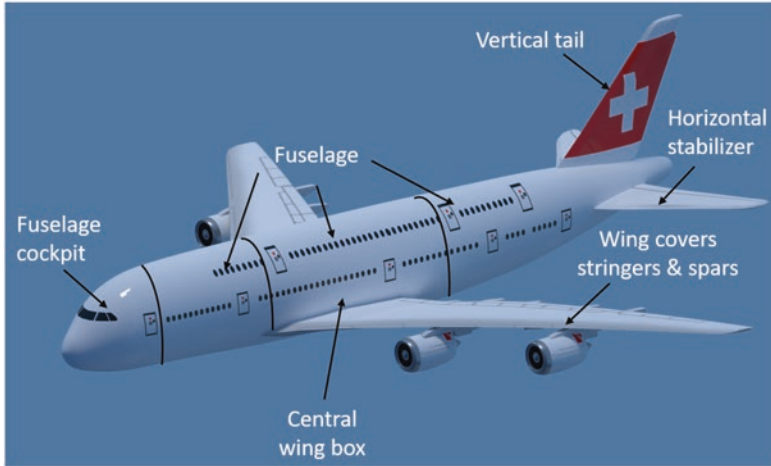


Fig. 23.1 The components of Airbus 350 made from CFRP

superior adaptability, flexibility, and reduced aerodynamic drag posed by discontinuities on the wing surface (Fasel et al., 2020).

A composite assembly for aerospace applications must fulfill high mechanical strength and thermal stability and be electrically conductive for lightning strike protection. For this, it is required to improve the properties of the supporting polymeric matrix. The introduction of nanomaterials for modifying polymeric binder into already matured carbon fiber-reinforced plastics (CFRP) opens the possibility of creating new multifunctional, multiscale materials with optimized mechanical, thermal, and thermal electrical properties. Among different nanomaterials, carbon nanomaterials with different hybridizations are considered ideal reinforcement for modifying the polymer matrix phase at the interface. Diamond and amorphous carbon are one of the tetrahedral carbon systems with sp^3 hybridization used as nanofillers, while intermediate between sp^3 - and sp^2 -hybridized nanomaterial fullerene is also widely used to improve mechanical properties of CFRP. One major drawback of all the materials mentioned above is poor electrical and thermal conductivity, limiting its applications. On the other hand, the electrical and thermal conduction in CFRP is accomplished by incorporating sp^2 -hybridized carbon conductive nanomaterials such as CNT, CNF, graphene, graphene oxide, etc., in CFRP to extend its prominent application in electromagnetic shielding and lightning protection for the aerospace industry (Dunk et al., 2012; Geim, 2009; Hirsch, 2010; Iijima, 1991; Robertson, 2002). Experimental study of this area has focused profoundly on the widely used nano-form carbon nanomaterials synthesis such as CNT, graphene, and CNF. It is not only because of the high aspect ratio but also superior mechanical, thermal, and electrical properties due to its graphitic carbon structure (Pathak et al., 2021c). However, these materials possess high stiffness and defect-free intrinsic carbon structure, making them extremely challenging to reinforce in the polymer. Firstly, CNT and graphene possess very large lateral dimensions (from micrometer to millimeters), and hence, reinforcement is limited to very small concentrations.

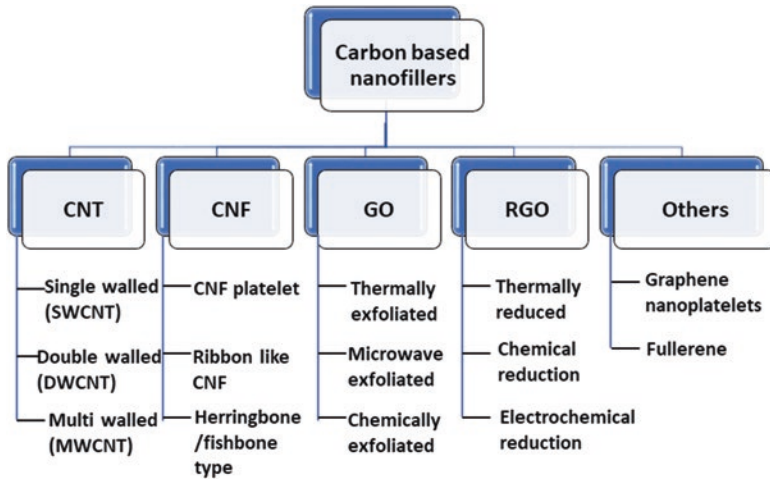


Fig. 23.2 Flowchart depicting various types of carbon-based nanofillers employed in CFRP

These small concentrations are associated with low load-bearing capacity due to agglomeration during composite fabrication using dispersion. Secondly, the surfaces of CNT and graphene are not associated with other functional groups, which inhibit the durable bonding between matrix and fiber, leading to mechanical failure due to poor interfacial interaction (Geim & Novoselov, 2009; Schodek et al., 2009). Many researchers employ the chemical functionalization of CNT and graphene to overcome the poor interfacial interaction of nanofillers and matrix materials (Boukhvalov & Katsnelson, 2008; Englert et al., 2011; Georgakilas et al., 2002; Hirsch & Vostrowsky, 2005; Kuila et al., 2012; Pathak & Dhakate, 2021).

The study of the improvement in mechanical properties of hybrid CFRP composites is rapidly grabbing attention in research groups as well as industries, and thus, an intensive discussion is necessary on these aspects. Therefore, this brings updated information on current fabrication method of hybrid CFRP composites and their mechanics. In detail, the individual properties of nanofillers and their properties, the techniques for their inclusion in the polymer matrix, CFRP fabrication methods and their properties, and automation in manufacturing for speedy and cost-effective production of composite parts will be reviewed. In the end, the future scenario of hybrid CFRP composites with CNT, CNF, and graphene will be covered. The various carbonaceous nanofillers used in CFRP are illustrated in Fig. 23.2.

2 Carbon-Based Nanofillers in CFRP

Carbon is the most abundant and most versatile element of the periodic table with the exceptional atomic properties compared to other elements. It exists in both crystalline and amorphous forms. Diamond, graphene, CNT, and fullerenes are the

crystalline forms of carbon, while charcoal and coal are the amorphous nature carbon material. Carbon atom contains six electrons, and it exists as $1s^2 2s^2 2p^2$ in electronic configuration. The last four electrons (valence electrons) are responsible for making different carbon nanostructures with different bonding affinities (hybridization). The mechanism of filler-reinforced hybrid CFRP composite properties depends upon the size of nanofillers. The improved mechanical properties result from surface interaction, mechanical adhesion, polymer chain restriction, dispersion, etc., dependent upon the size of nanofillers. The electrical properties, catalytic reactivity, polymer adhesion, and chemical reactivity are largely affected when the surface area to volume ratio is high for nano-reinforcement. Other factors such as electromagnetic forces, molecular motion, energy quantization, and quantum confinement also participate at the nanoscale. Consequently, it turns into intermolecular interaction, H-bonding, π - π bonding, and van der Waals interaction. The revival of graphite in the form of carbon nanomaterials like graphene, graphene oxide (GO), reduced graphene oxide (RGO), carbon nanotubes (CNT), carbon nanofibers (CNF), etc., has revolutionized composite manufacturing (Hammel et al., 2004). Their unique physical, mechanical, and thermal characteristics are owing to a high surface to volume ratio. The research and development in dispersing and functionalization have enabled them to exploit their potential as perspective fillers and reinforcement in CFRP. CNF and CNT gain relevance among the various nanofillers due to their exceptional mechanical strength, electrical conductivity, and durability (Fig. 23.3) (Hiremath & Bhat, 2017). GO also does not lag in this race, primarily due to the large number of oxygen functionalities that facilitate the functionalization and easy dispersion in various polymer matrix during the processing of CFRP (Pathak et al., 2016, 2019a).

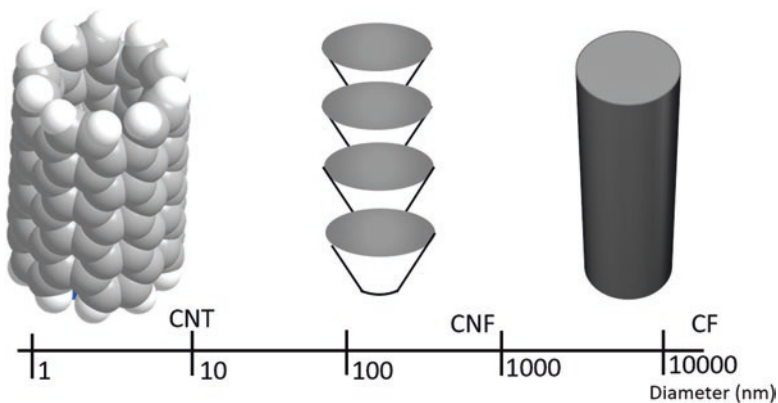


Fig. 23.3 The structure of CNT, CNF, and CF with scale representing the respective diameter of the nanofillers

2.1 Carbon Nanofibers (CNF)

In 1879, Thomas Edison fabricated the CF from cotton and bamboo strands by carbonization process for multiple applications. The application of CNF in structural applications was realized after a morphological study by electron microscope in the 1950s by Soviet scientists Radushkevich and Lukyanovich. Later in 1970, various research groups acted and worked on synthesizing CNF for various structural applications. CNF is quasi-one-dimensional carbon material with a hollow cylindrical fibrous structure of a diameter ranging from 50 to 500 nm (between CNT and CF) and a length of few micrometers (0.5–200 μm), resulting in a high aspect ratio (>100) (Terrones et al., 2001; Zhang et al., 2011). Their structure is formed by parallel alignment of graphene layers along the long axis and is found in different forms such as nonwoven mats, yarns, etc. Depending on the structure, they are classified into three types: (1) platelet CNF, (2) parallel/ribbonlike CNF, and (3) herringbone or fishbone type. They exhibit exceptionally good mechanical and physical properties with Young's modulus ~ 500 GPa, tensile strength ~ 3 GPa, electrical conductivity $\sim 10^3$ S/cm, and thermal conductivity ~ 1900 $\text{Wm}^{-1} \text{K}^{-1}$ (Bal, 2010; Maruyama & Alam, 2002). A decisive factor in retaining and improving the properties of CNF is achieving a perfectly aligned graphitic structure (Ali et al., 2021). This is usually obtained by posttreatment graphitization at a high temperature (<2400 $^{\circ}\text{C}$) during the synthesis and processing of CNFs.

CNF are generally synthesized using electrospinning and catalyst-driven chemical vapor deposition (CCVD) (Gupta & Dhakate, 2012; Inagaki et al., 2012). In CCVD, a carbon feedstock such as acetylene, an appropriate catalyst like Ni and Cu, and a tube furnace is required. The critical controlling parameters are temperature of the furnace (below 700 $^{\circ}\text{C}$) and the surface area of the catalyst on which CNF is grown. Depending on the active area of the catalyst, 2.5 g/m^2 min with approx. 70% conversion of the precursor to nanofibers could be achieved (Xue et al., 2021). CCVD is an excellent method to obtain a high-aspect ratio CNF, with control over thickness and uniformity. Electrospinning is used to obtain continuous, stable, and straight CNF. They are formed from various high carbon content precursors such as polyacrylonitrile (PAN) (Zussman et al., 2005), polyimide (PI) (Park et al., 2014a; Xuyen et al., 2007), polyvinyl alcohol (PVA) (Gupta & Dhakate, 2017), and polybenzimidazole (PBI) (Kim et al., 2004). Here, a particular w/w% solution is prepared in a suitable solvent and electrospun at a 0.1 ml/h flow rate under an applied electric field. A grounded drum collector rotating at a particular speed (2000 rpm) collects the nanofibers, and iodine vapors are passed to stabilize the nanofibers. The fibers are carbonized and graphitized at high temperatures up to 2000 $^{\circ}\text{C}$ to acquire a graphitic structure.

Due to the complexities of these processes, researchers are turning to simple, scalable, and high-yield processes. For example, Ren et al. (2015) used the electrolytic conversion of atmospheric carbon dioxide to CNF. Saavedra and coworkers have achieved the template synthesis of CNF from graphitization of PAN, which is previously polymerized inside the nanosized structural tunnels of microfibrillar silicate sepiolite (Fernández-Saavedra et al., 2004).

2.2 Carbon Nanotubes (CNT)

In 1991, Sumio Iijima got the Nobel Prize for the synthesis of hollow nano-carbon by arc-discharge technique, and after that, the carbon-based nanomaterial was globally recognized (Iijima, 1991). CNT is a cylindrically rolled-up graphene sheet where sp^2 -hybridized carbon atoms are arranged in a hexagonal array. It is the thinnest tubular one-dimension nanostructure ever made by humans. Their diameter varies from ~ 0.4 nm to 3 nm for single-walled CNT (SWCNT) and ~ 1.4 nm to 100 nm for multiwalled CNT (MWCNT), and length is usually in micrometers. They exist in various forms depending on the arrangement of nanotubes: single-walled CNT (SWCNT), double-walled (DWCNT), and multiwalled (MWCNT) as depicted in Fig. 23.4. A strong in-plane bonding exists within all the cylindrical structures. However, in MWCNT and DWCNT, a weak out-of-plane van der Waals interaction is also seen, which gives rise to a concentric periodic interlayered structure. The sp^2 hybridization in CNT confers high tensile strength, which is greater than steel, Kevlar, and even diamond. One of the outstanding features is the elasticity, whereby CNT can return to its original shape after being deformed, such as twist, kink, and bend, through compressive and tensile forces. They are highly chemical as well as thermally stable and hence used in various advanced applications (Bellucci et al., 2007; De Volder et al., 2013; Okan et al., 2015; Sharma et al., 2018a).

Three major methods are usually used for the synthesis of CNT: (1) CVD, (2) laser ablation, and (3) carbon arc discharge (Eatemadi et al., 2014). The electric arc discharge utilizes arcing to consume graphite anode, where carbon evaporates and solidifies on the cathode in a pressurized and heated chamber, while in laser ablation, a graphite block placed in a quartz tube is heated in a furnace via a high-power laser (YAG). A catalyst such as Ni, Co, Fe, or their alloys is also used to synthesize SWCNT. The precursors used in these methods are carbon-based materials such as acetylene, hydrocarbons, and high-quality graphite rods. However, the researchers are also focusing on consumer plastics as a potential source for producing

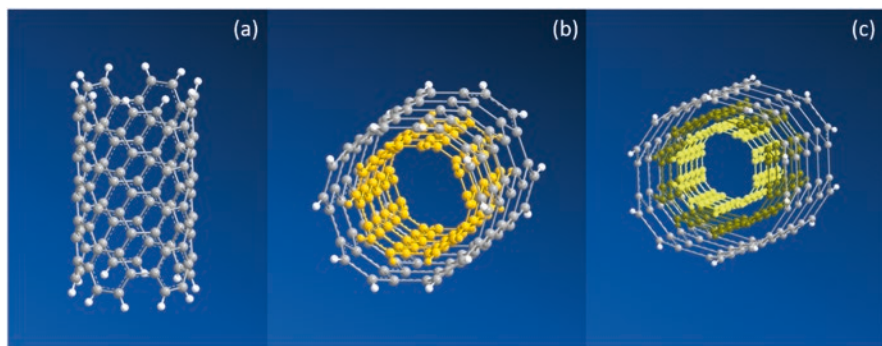


Fig. 23.4 The atomic structure of (a) SWCNT, (b) DWCNT, and (c) MWCNT

high-quality CNTs (Yao et al., 2021). Sugime and group synthesized the longest CNT forest (14 cm) using the CVD technique with iron/gadolinium/aluminum oxide (Fe/Gd/Al₂O_x) as the catalyst (Sugime et al., 2021).

2.3 Graphene and its Derivatives

After discovering graphene in 2010 by Geim and Novoselov, it became global interest due to the thinnest 2D material with exceptional properties. It is one-atom-thick 2D material in which sp² carbon atoms are arranged in a honeycomb array (Geim & Novoselov, 2009). It is a fundamental building block of all the graphitic materials with different dimensions, such as CNT, fullerene, and graphite. The 2D structure of graphene crystal possesses exceptional physical, mechanical, and electron transportation. Graphene has a very high thermal conductivity of ~5000 Wm K⁻¹ along with electron mobility of 250,000 cm² Vs⁻¹. It has a very high specific surface area ~ 2600 m² g⁻¹, elastic modulus 1 TPa, and 240,000 Sm⁻¹ of electrical conductivity (Balandin et al., 2008; Lee et al., 2008; Novoselov et al., 2005). Due to its outstanding properties, it is widely used in a wide range of composite materials for various applications such as strain sensors, aerospace, electrical devices, and supercapacitors (Borah et al., 2017). But the major problem associated with graphene is surface inertness, which inhibits the dispersion in various polymeric materials. The inevitable hydrophobicity of the graphite, graphene, and analogs carbon-based materials has resulted in low solubility in various solvents and often requires dispersing agents. The inclusion of oxygen-based functionalities in the backbone of the carbon framework breaks the strong cohesive force. The controlled oxidation of graphene into graphene oxide generates hydroxyl, carboxyl, and epoxy groups in the edges and middle of the sheet, introducing hydrophilicity in graphene where intercalation of water molecules between the galleries can occur for dispersion in the polymer (Layek & Nandi, 2013). GO is a 2D network of sp²- and sp³-hybridized carbon atoms arranged in a honeycomb pattern. It is an electrical insulator with a finite bandgap (~2.2 eV) responsible for photoluminescence in visible and near IR regions. It was found that the mechanical properties, mainly Young's modulus, vary from 200 to 500 GPa depending on the number of layers and its coverage by oxygen functionalities (Liu et al., 2012). In thermal properties, GO exhibits a negative coefficient of thermal expansion (CTE), which compensates for the positive CTE of the polymer matrix in CFRP and imparts thermal stability to the CFRP. The synthesis of various graphene nanomaterials from graphite is shown in Fig. 23.5. The GO is synthesized using a chemical route by Hummer's and modified Hummer's method. The method utilizes strong oxidizing reagents KMnO₄/NaNO₃ in concentrated H₂SO₄ where graphite is chemically exfoliated and oxidized to achieve various oxygen-containing functional groups in the basal plane of the sheet (Marcano et al., 2010; Pathak et al., 2016). RGO is subsequently obtained by reducing GO through thermal, chemical, and UV irradiation routes (Abdolhosseinzadeh et al., 2015).

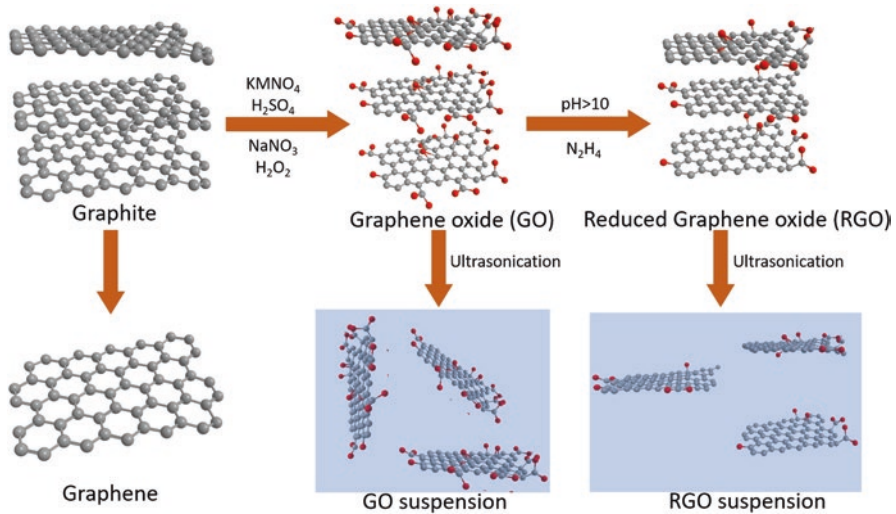


Fig. 23.5 The synthesis scheme of graphene and its derivatives (GO and RGO)

3 CFRP Processing Techniques

3.1 Nanofillers Processing Methods

The properties of nanofillers-incorporated CFRP depend on the homogeneity of nanofillers dispersion. The amount and interaction with reinforcement (CF) and the matrix (epoxy) determine uniformity and their distribution in the composite. The tendency of agglomeration for CNF and CNT is more than GO due to van der Waals and π -stacking. Thus, the initial step of filler dispersion through mechanical processes such as ball milling, shear mixing, ultrasonication, calendaring and high-speed homogenization or chemical means such as functionalization, and polymer/surfactant wrapping is critical in CFRP manufacturing (Cha et al., 2016; Zaccardi et al., 2018). Chakraborty et al. (2011) investigated the role of different dispersing methods such as ultrasonic bath, high shear mixer, three-roll mill, and combination of two of these on the best possible dispersion of CNT in epoxy resin. They found better uniformity with three-roll mill and the addition of dispersing agents. However, the aggregation is seen after the addition of the curing agent. Rana et al. (2011) studied the dispersion behavior of CNF in epoxy. The combination of ultrasonication and high-speed mechanical stirring has proven to be suitable to achieve uniform dispersion without the breakage of CNF. The use of solvent and surfactant is vital at lower concentrations of CNF (up to 0.1 wt.%). Thus, physical factors such as temperature, viscosity, and the amount of curing agent play a part in the formation of premixes with polymer. To overcome the issue of poor dispersion of CNTs, Kim et al. (2021) proposed the use of CNT fibers, which are aligned along the fiber axis.

This would take into account the low volume fraction of CNT, poor dispersion, and low alignment.

A dispersion state is generally assessed using microscopic techniques such as optical microscopy, scanning electron microscopy (SEM), transmission electron microscopy (TEM), and atomic force microscopy (AFM). However, these methods can scan only a tiny portion, while Raman spectroscopy and DSC could also be used to visualize the macroscale cross-linking between the polymer and nanofillers (Zaccardi et al., 2018). Recently, a thin film binarization method was developed by Chou et al. (2021) to assess the dispersibility of graphene nanomaterials in various polymer matrices-epoxy and polybenzoxazine. The method relies on the separation of pixels from nanofillers and transparent matrix. Thus, each nanocomposite consists of different light transmission domains, which are easily identified.

Electrophoretic deposition (EPD) is a new advanced method to introduce carbon nanomaterials onto CF to improve its surface roughness to enhance the mechanical, thermal, and electrical performance of CFRP. Guo and Lu (2012) showed the role of EPD for CNT deposition onto CF surface using ethanol and claimed it as a futuristic dispersion process. Similarly, EPD is also used to disperse other nanomaterials such as CNF and graphene onto fiber surface to improve the interfacial interaction between polymer and fibers (Chen et al., 2016; Chi et al., 2016; Lee et al., 2016; Rodriguez et al., 2010). Although this method is very effective, the major problem associated with this technique is time and the complexity involved in it. Also, for large-scale CF production, the deposition of nanofillers on CF is complicated.

3.2 *CFRP Manufacturing Techniques*

CFRP is manufactured using various techniques. However, a method is found ideal according to the productivity, material cost, high-quality assurance, and flexible approach in terms of the type of matrix, reinforcement, and additives used. The conventional methods comprise open molding, resin transfer molding, compression molding, pultrusion, and filament winding. In addition, new methods such as electrodeposition and 3D printing have been devised to ensure uniformity, time and cost reduction, and bulk production.

3.2.1 **Open Molding**

Open contact molding in one-sided molds is a low-cost, standard process for making fiberglass composite products. Typically used for boat hulls and decks, RV components, truck cabs and fenders, spas, bathtubs, shower stalls, and other relatively large, noncomplex shapes, open molding involves either hand layup or a semiautomated alternative, spray-up.

In an open mold spray-up application, the mold is first treated with mold release. If a gel coat is used, it is typically sprayed into the mold after the mold release has

been applied. The gel coat is then cured, and the mold is ready for fabrication to begin. In the spray-up process, catalyzed resin (viscosity from 500 to 1000 cps) and glass fiber are sprayed into the mold using a chopper gun, which chops continuous fiber into short lengths and then blows the short fibers directly into the sprayed resin stream so that both materials are applied simultaneously. To reduce VOCs, piston pump-activated, non-atomizing spray guns and fluid impingement spray heads dispense gel coats and resins in larger droplets at low pressure. Another option is a roller impregnator, which pumps resin into a roller similar to a paint roller. In the final steps of the spray-up process, workers compact the laminate by hand with rollers. Wood, foam, or other core material may then be added, and a second spray-up layer embeds the core between the laminate skins. The part is then cured, cooled, and removed from the reusable mold.

3.2.2 Compression Molding

This is a thermosetting molding process that employs expensive metal dies but is also durable. This technique is employed in manufacturing bulk quantities. The process involves sandwiching a layer of chopped fiber in between two layers of resin paste. This resin paste was then transferred into a moving film carrier, and fibers were dropped on the film. The second film was placed on this that carried another layer of resin. The rollers are used to compact the sheet by removing excess resin and also entrapped air. Over time, the sheet becomes hard like leather as the viscosity increases.

One of the main disadvantages of conventional processes is the generation of voids and defects. Thus, vacuum-assisted prepreg compression molding (VAPCM) has been devised to avoid the occurrence of such defects. Lee et al. (2019) evaluated the two methods for void content, bending, and tensile strength. Ma et al. (2020) also used vacuum infiltration to form defect-free prepregs before compression molding. As a result, the composite structure was uniform with minimum void content and controlled delamination.

3.2.3 Resin Transfer Molding (RTM)

Resin transfer molding (RTM), also called liquid molding, is a simple process that begins with a two-part matched mold. Dry reinforcement is first placed in the mold, and it is then closed. The resin and catalyst are measured, mixed, and pumped through injection ports to the mold under low to moderate pressures. The viscosity of the resin is kept low during processing so that resin can permeate through thick parts of the fibers. Different resin systems can be used like polyester, vinyl ester, phenolic, and epoxy resins. There are numerous advantages of this method. The dry preform and resin used in this method are less expensive than prepreg materials. The composite obtained from this method has good surface details and finishing (Trofimov et al., 2021; Wang et al., 2013).

3.2.4 Vacuum-Assisted Resin Transfer Molding (VARTM)

Vacuum-assisted resin transfer molding (VARTM) refers to various related processes that represent the fastest-growing new molding technology. The salient difference between VARTM-type processes and RTM is that in VARTM, the resin is drawn into a preform using a vacuum only rather than pumped under pressure. As a result, VARTM does not require high heat or pressure. For that reason, VARTM operates with low-cost tooling, making it possible to inexpensively produce large, complex parts in one shot (Park et al., 2021).

3.2.5 Electrodeposition Resin Molding (ERM)

In most fabrication techniques, void formation during impregnation is unavoidable, affecting the CFRP properties. In some situations, the CF must be particularly arranged along the principal stress direction to obtain high strength and stiffness. Thus, Katagiri and the group developed ERM as a feasible resin deposition around the CF irrespective of the fiber placement (Katagiri et al., 2017a, 2017b). In an electrophoretic cell, the carbon fabric dipped in the polymer solution serves as a cathode, while a stainless steel plate acts as an anode (Fig. 23.6). An electric current applied precisely controls the deposition of epoxy resin on the CF. Since the method neither involves mixing of viscous resin and curing agent nor vacuum, no voids are created (Katagiri et al., 2021).

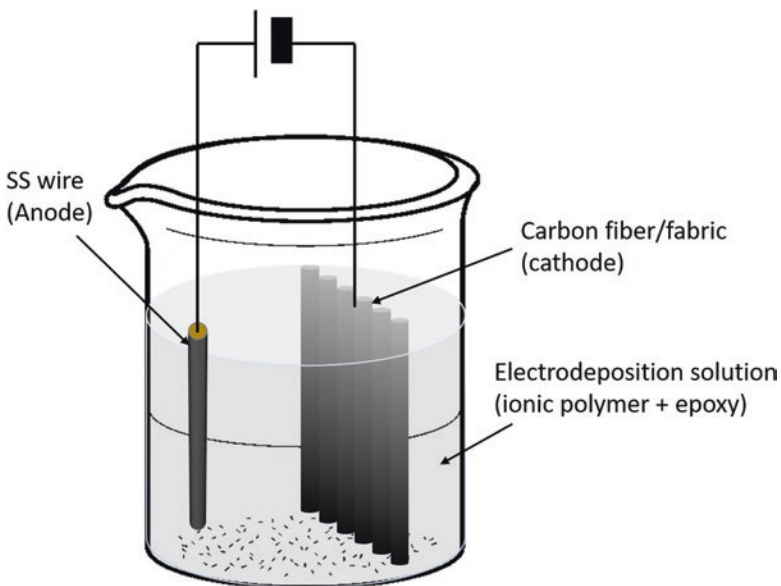


Fig. 23.6 Diagrammatic representation of ERM of CF

3.2.6 Pultrusion

Pultrusion, like RTM, has been used for decades with glass fiber and polyester resins, but in the last decades, the process also has found application in advanced composites applications (Baran et al., 2018). It is a relatively simple, low-cost, continuous process in which the reinforcing fiber (usually roving, tow, or continuous mat) is typically pulled through a heated resin bath and then formed into specific shapes as it passes through one or more forming guides or bushings. The material then moves through a heated die, where it takes its net shape and cures. Further downstream, after cooling, the resulting profile is cut to the desired length. Pultrusion yields smooth-finished parts that typically do not require post-processing. A wide range of continuous, consistent, solid, and hollow profiles are pultruded, and the process can be custom-tailored to fit specific applications. For example, pultrusion is used to obtain open sections and single-/multicelled close-shaped parts like bridges, decks, communication towers, and marine and energy sectors (Vedernikov et al., 2020).

3.2.7 Filament Winding

Filament winding is a continuous fabrication method that can be highly automated and repeatable, with relatively low material costs. A long, cylindrical tool called a mandrel is suspended horizontally between end supports, while the “head,” a fiber application instrument, moves back and forth along the length of a rotating mandrel, placing fiber onto the tool in a predetermined configuration. Computer-controlled filament-winding machines are available, equipped with from 2 to 12 axes of motion. In most thermoset applications, the filament winding apparatus passes the fiber material through a resin “bath” just before the material touches the mandrel. This is called wet winding. However, a variation uses tow prepregs, that is, continuous fiber pre-impregnated with resin. It eliminates the need for an on-site resin bath. In a slightly different process, fiber is wound without resin (dry winding). The dry shape is then used as a preform in another molding process, such as RTM.

3.2.8 Additive Manufacturing (AM)

AM is the process of making 3D objects from their corresponding data files through a layer-by-layer deposition. This technology has enabled the fabrication of complex geometries, shortening the design cycle, enhancing the production and quality that are not attainable by the conventional techniques (Türk et al., 2017). Earlier in AM, only pure plastic parts could be designed; however, after the evolution of fused deposition modeling (FDM) machine with two extrusion nozzles (as shown in Fig. 23.7), it is possible to extrude build material (matrix) and support material (reinforcement) simultaneously (Ning et al., 2015). However, only a few studies reported the fabrication of CFRP parts by FDM. Tekinalp et al. investigated the

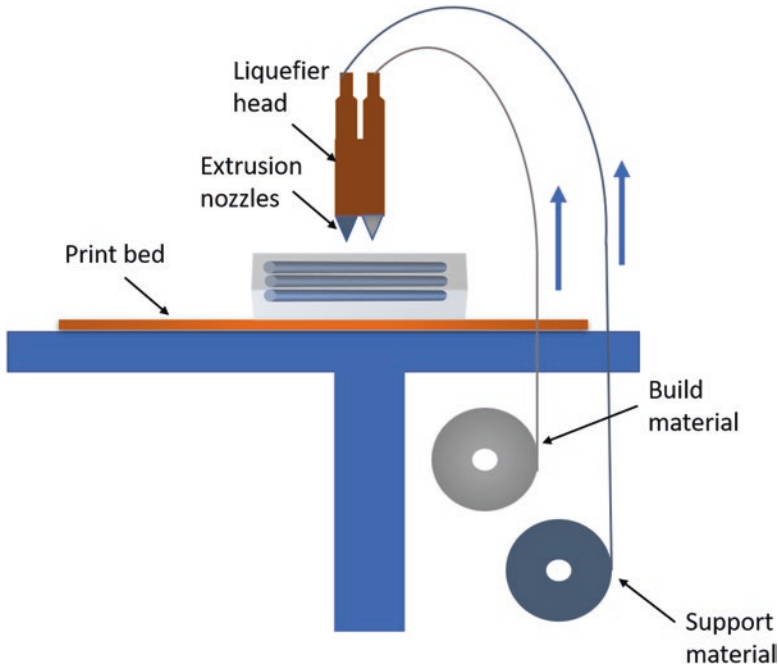


Fig. 23.7 Fused deposition modeling machine (FDM) with two extrusion nozzles for manufacturing of CFRP

mechanical performance of short CF-reinforced ABS composite prepared from 3D printing and compression molding. The results showed a 115% increase in the tensile strength of 3D-printed composite owing to highly oriented CF achieved in printing direction (Tekinalp et al., 2014). Fasel et al. (2020) also reported morphing CFRP structure using AM to increase the mechanical performance due to hingeless mechanisms and reduction in cost. Morphing structures involve a complex design, which is challenging to fabricate through conventional techniques. At present, only a limited number of thermoplastic filaments could be processed in this method, including polycarbonate, ABS, polyamide, and polylactic acid (PLA) (Dudek, 2013).

4 Automation in CFRP Production

Automation in the CFRP aviation industry involves using robots and controlled machines to achieve a defect-free composite structure with increased productivity (Perner et al., 2016). Conventionally, CFRP manufacturing is limited by slow manual procedures. Thus, automation is the need of the hour to accomplish the requirement to produce a large number of aircraft per year. The prepreg layup rate in the manual procedure is far from feasible; hence, automation is expected to scale up

production, maintain reproducibility and consistency, ensure machine efficiency, and reach the manufacturing target. An industrial robot has a comparatively lower price than CNC tools; however, the vibrations produced due to their buildup obstruct the laying process (Krombholz et al., 2012). Thus, a robot-assisted laying process has to conform to a set of standards. The layers must be free from any creased deformations and wrinkles, the deposition of layers should occur with a defined velocity, and the force on the layers must be such that there is no tension in the material (Olsen, 1993; Rabeneck, 2010). The appropriate positioning of each layer is essential to intact the mechanical properties of the final composite structure. In hand layup, there is always the uncertainty of wrongly/misplaced layers, impurities in resin, or prepreg formation, which require examination, making it time-consuming and cost-intensive (Wittig, 2005).

5 Properties

5.1 Mechanical Properties

In CFRP, the CF is the major load-bearing constituent, and the polymer matrix dispels the load to the fibers, maintains the orientation, and protects CF from the external environment. Thus, the in-plane properties are decided by CF, and the polymer dominates out-of-plane properties, which are generally low. In laminated composites, delamination is the predominant cause of crack initiation, growth, and catastrophic failure. This is due to a weak CF-polymer interface, which causes deterioration in interlaminar shear strength (ILSS) and out-of-plane properties (Dhakate et al., 2016). Several strategies have been improvised, such as fiber hybridization/surface modification, matrix toughening, interleaving, Z-pinning, etc., to tackle the in-plane properties (Sun et al., 2017; Vedralnam & Sharma, 2019; Zhao et al., 2020). The nanoscale secondary reinforcement inclusion in CFRP provides a feasible approach for significant improvement due to their high specific surface area. The type of nanomaterial, their dispersion technique, and amount affect the mechanical aspects of composite as compiled in Tables 23.1, 23.2, and 23.3. Different type of CNT (single, double, and multiwalled) possesses different specific surface areas, which directly affects its interaction with the epoxy matrix (Gojny et al., 2005). The functionalization on the CNT surface also alters the interfacial interaction in the interphase. In CNF, the mechanical properties are explained by its structure which consists of truncated conical stacks of graphene where load transfer is effective due to inhibition of lateral sliding of graphene sheets (Iwahori et al., 2005). GO and RGO proved to be a promising filler where interfacial adhesion is improved via functionalization such as silanization, grafting, etc.

Table 23.1 The mechanical properties of CNF-incorporated CFRP

S. no.	CNF type	CNF deposition	Percolation threshold (wt%)	ILSS (MPa)	Bending/compressive strength (MPa)	Reference
1.	Sheets	Interleaving	1.1	55	730	Dhakate et al. (2016)
2.	Bucky paper	Interleaving	10	70	–	Khan and Kim (2012)
3.	Oxidized CNF	EPD	0.67	57.8	406	Rodriguez et al. (2011)
4.	Amidated CNF	EPD	1	58.2	445	
5.	CNF	Dispersion	10	–	789.5	Iwahori et al. (2005)

Table 23.2 The effect of CNT types and their modification on mechanical properties of CFRP

S. no.	Type of CNT	CNT deposition	Percolation threshold (wt%)	ILSS/IFSS (MPa)	Flexural strength (MPa)	Reference
1.	MWCNT	Dispersion	3	98.8	1902	Zhao et al. (2017)
2.	SWCNT	Dispersion	0.3	–	604.9	Burkov and Eremin (2018)
3.	CNT	Spraying	0.75	67	–	Fogel et al. (2017)
4.	Carboxyl MWCNT	Dip coating	5	83.8	–	Xiong et al. (2021)
5.	MWCNT	Ultrasonic dispersion	0.27	8% increase	5% increase	Saadatyar et al. (2021)
6.	Amino MWCNT	EPD	–	58.5	–	Yan et al. (2019)
7.	Carboxyl CNT	Coating	–	35	–	Li et al. (2013)

5.2 Thermal Properties

CFRP used in aerospace and interplanetary missions undergoes rigorous space thermal cycling, including extreme temperature changes, vacuum, and humidity. Thus, evaluation of thermal properties of CFRP under space cyclic conditions and methods to improve the same is critical. A sudden change in temperature leads to the expansion/contraction of the polymer matrix. Nanoscale fillers such as GO, CNT, and CNF have a negative CTE, which normalizes the highly positive CTE of the polymer matrix to attain nearly zero CTE in CFRP (Shirasu et al., 2017). The combined effect of their significant negative CTE and high Young's modulus reduces the

Table 23.3 Mechanical properties of different graphene nanomaterials-reinforced CFRP

S. no.	Graphene nanomaterial type	Deposition	Percolation threshold (wt%)	ILSS/IFSS (MPa)	Flexural strength (MPa)	Reference
1.	GO	Dispersion	0.3	55.7	1178	Pathak et al. (2021b)
2.	GO	Grafting assisted by pyrene	–	75.1		Yan et al. (2021)
3.	Silanized GO	Coating CF	0.5	83.4	1160	Chen et al. (2014)
4.	Triazine functionalized GO	Sizing CF + dispersion	1	71.3	1202	Ma et al. (2019)
4.	GO	Dispersion	2	~80	1180	Rodríguez-García et al. (2020)
5.	Graphene nanoplatelet				1250	
6.	RGO				1230	
7.	Hydrazine reduced RGO	Dispersion	0.2	43	–	Adak et al. (2018)
8.	Thermally reduced RGO	Dispersion	0.3	90	350	Jenkins et al. (2019)
9.	RGO	Dispersion	0.05 g	–	610	Wang et al. (2018)

residual thermal stresses, increasing the nanocomposite's thermal stability (Ghasemi et al., 2015). Thus, the proper dispersion of the nanofillers and polymer and their interfacial adhesion have significant implications on the thermoelastic properties of CFRP. Vartak et al. (2021) evaluated the tensile strength of the neat CFRP and CNT/CFRP after thermal shock and thermal cycling in a vacuum. While thermovacuum increased the tensile strength in both CFRP, the thermal shock enhanced strength in CNT/CFRP. This is ascribed to the stabilization of epoxy with CNT, ceasing the segmental motions in epoxy polymer and shifting the thermal transition to higher temperatures. Similar studies are also conducted with GO as filler to stabilize the curved geometry of CFRP (Pathak et al., 2021b).

Thermal conductivity, which quantifies the heat transfer ability, is an essential factor for high-temperature-resistant parts in spacecraft such as engine nozzle. The CFRP is susceptible to damage in a high heat environment with a significant change in shape, mass loss, and degradation. Thereby, highly thermally conductive materials become crucial in aerospace parts. Park et al. (2014b) studied the thermal conductivity and ablation resistance in CNT/CF/phenolic composites. The thermal conduction is more in CF/phenolic than neat phenolic composite due to the continuous conduction path in the CF mat. At the same time, the thermal conduction elevated with the addition of CNT due to their high surface area for increasing the carbon-carbon contact points necessary for heat transfer.

5.3 *Electrical Properties*

In aerospace and aviation applications, the electrical conductivity of CFRP is critical for providing lightning current channels to protect composite airframes. This is also useful in EMI shielding and microwave absorption in radar materials. EMI shielding is particularly vital in the space domain to filter the valuable signal from electromagnetic interferences. Pristine CFRP exhibits limited electrical conduction (higher in in-plane than through-thickness direction due to CF placement) due to obstruction in conductive pathways posed by the impregnation of conductive CF by insulating polymer matrix such as epoxy. Thus, conduction is enhanced by using conductive fillers, polymer, or coatings to provide a continuous conduction path for electron transfer (Das et al., 2021). Conventional techniques involve metal coatings like copper, aluminum, etc. However, they are vulnerable to peel off and abrade from the composite surface. Thus, filler inclusion provides a sustainable and cost-effective approach. Among the various nanofillers, CNT and CNF are intrinsically conductive, while GO exhibits very little conduction due to the nonavailability of free electrons in their sp^3 -hybridized carbon network, and RGO exhibits reasonable conductivity due to limited oxygen functionalities (Pathak et al., 2019b). Although some researchers have focused on enhancing the electrical conductivity of GO through the alignment of their dipoles, however, not much difference was realized (Senis et al., 2017, 2020). Therefore, the research is much more focused on RGO and graphene nanoplatelets. GNPs showed a significant improvement compared to oxygen-containing GO and RGO due to forming a percolation structure (Rodríguez-García et al., 2020).

CNT and CNF have been the most attractive filler for enhancing electrical properties while retaining the mechanical integrity of CFRP. MWCNT in the form of bucky paper was investigated by Kumar et al., who interleaved epoxy-impregnated MWCNT bucky paper between CFRP laminates to improve through-thickness conductivity. The composites improved in-plane and through-thickness conductivity by 697% and 643%, respectively, which functioned well against simulated lightning strikes of 40 kA intensity (Kumar et al., 2019). In nanofillers-dispersed polymer, the electrical conduction rises with functionalization on the CNT surface due to more exclusive contact achieved through covalent bonding (Yan et al., 2019). A major problem with the dispersion of fillers is the loading constraint, where a high amount causes re-agglomeration and loss of connection in the matrix network. CNT has also been explored in the form of a film placed in between the axially oriented CF laminates. A considerable rise in conductivity is acquired with just two plies of CNT (Chen et al., 2020). Gaztelumendi et al. (2017) reported a 30% enhancement in conductivity by combining CNT bucky paper and CNT doped resin in CFRP by infusion process. CNF paper of high loading was inserted in an interlayer structure of CFRP (Gou et al., 2010). This is because of the high content of continuous CNT and CNF, resulting in the current free flow. Nowadays, conducting polymer reinforced with nanofillers are advanced new materials for lightning strike applications in aerospace (Hirano et al., 2016; Kumar et al., 2018b). In this regard, a

thermosetting polyaniline-based polymer plays a significant role, and nanofillers like CNT, CNF, and graphene play an essential role (Gou et al., 2010; Gagné & Therriault, 2014; Kumar et al., 2017, 2018a; Sharma et al., 2018a). However, conductive polymer CFRP has one major drawback, low mechanical performance compared to epoxy CFRP, and this challenge still needs to be fixed for implementation in aerospace industries for multifunctional purposes.

6 Nanofillers-Incorporated CFRP Hybrid Composite Mechanism

Figure 23.8 demonstrated the schematic representation of nanofillers-incorporated CFRP hybrid composite. The enhancement in properties of CFRP with the incorporation of nanofillers depends upon the size, types of nanofillers and functionalities on the surface, type of bonding which makes with carbon fiber, and the polymeric matrix. The improvement in CFRP properties generally is due to interaction with epoxy polymer via van der Waals force. There is no chemical interaction present between CFRP and CNF in hybrid composite due to the absence of polar functional groups on CNF, which further depends upon the final processing temperature of CNF. The mechanical properties improvement extent in CNF CFRP hybrid composite also depends on the alignment of CNF in hybrid composite, and aligned CNF-incorporated CFRP hybrid composite possesses higher mechanical properties than the randomly oriented CNF-incorporated CFRP composite. In terms of mechanical properties, aligned short CNF assume as continuous CNF, and hence, the improvement in mechanical properties of hybrid CFRP is significant, while in the case of CNTs or functionalized CNT, the nanofillers act as a bridging agent, and it improves the interfacial cross-linking via H-bonding, van der Waals interactions, and π - π bonding (Sharma et al., 2018b). The extent of physical interaction of CNT is significantly greater than the CNF because of the availability of the carbon-carbon π network. In some cases, chemical bonding has been achieved by functionalizing CNT and matrix via in-situ functionalization of epoxy polymer, and more remarkable improvement in the mechanical properties of the hybrid composite than dispersed CNT hybrid composite has been seen. In the case of GO-incorporated CFRP, GO tends to bind both with matrix and CF in hybrid composite, and consequently, the interfacial interaction is higher than CNF and CNT hybrid CFRP. The GO contains oxygen-based polar functional groups, and these functional groups enhance cross-linking and lower the activation energy of chemical cross-linking of polymer and hardener. Hence, due to the increment in cross-linking density, the mechanical properties of the GO hybrid composite affect significantly. GO and functionalized GO can bind with the chemical bond with both polymer and CF, such as ether bond (after substitution reaction between a carboxylic group of CF and hydroxyl group of GO). Apart from this, it also interacts with H-bonding, π - π bonding, and van der Waals forces. In short, the overall performance of hybrid CFRP is mainly dependent upon the type of nanofillers and functional groups present on it. The higher the

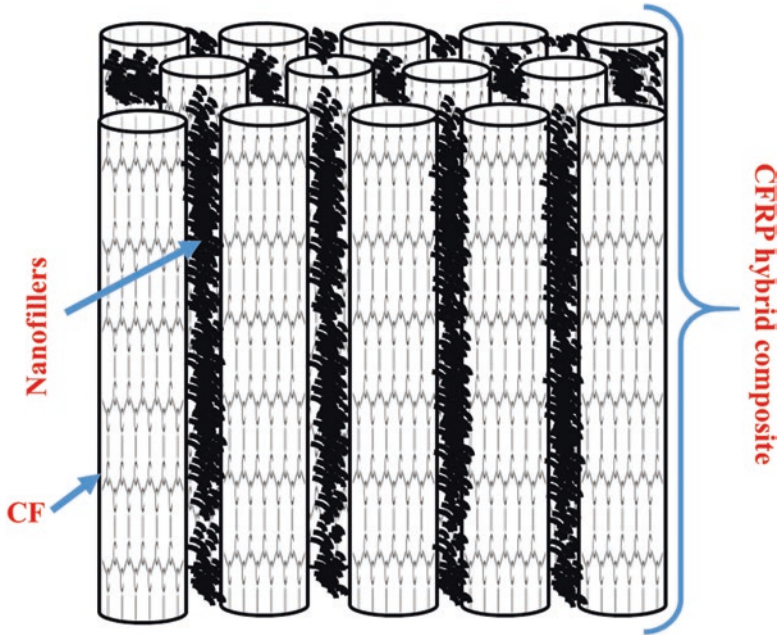


Fig. 23.8 Schematic representation of nanofillers-incorporated CFRP hybrid composite

functional groups, the extent of interaction between polymer matrix and nanofillers will be great, and hybrid composite properties will change (Pathak et al., 2016; Pathak & Dhakate, 2021).

7 Conclusions

The carbon fiber-reinforced polymer composites have been explored for more than decades in the aerospace sector due to their extremely low weight and high resistance to fatigue, chemical, and environmental factors. However, its low mechanical strength and poor electrical and thermal properties limit its usage for long-term service. The emergence of natural/synthetic additives such as carbon-based nanomaterials, particularly CNF, CNT, and graphene derivatives, has brought new insights to their usage. The fabrication of these functional hybrid CFRP at an industrial scale demands sophisticated yet feasible processes such as additive manufacturing, electrodeposition, and automated production, which are still at the infancy stage and require optimization to achieve defect-free, high-yield CFRP. The adaptation of hybrid CFRP nanocomposite materials has significantly improved the structural capabilities of specific components and meets the rigid material and manufacturing demands of the aerospace industry.

Acknowledgments All the authors are thankful to CSIR-National Physical Laboratory, New Delhi, India, and the University of Tokyo, Japan, to provide Internet and software facilities to write the current chapter.

References

- Abdollahseinzadeh, S., Asgharzadeh, H., & Seop Kim, H. (2015). Fast and fully-scalable synthesis of reduced graphene oxide. *Scientific Reports*, 5, 10160. <https://doi.org/10.1038/srep10160>
- Adak, N. C., Chhetri, S., Kuila, T., et al. (2018). Effects of hydrazine reduced graphene oxide on the inter-laminar fracture toughness of woven carbon fiber/epoxy composite. *Composites. Part B, Engineering*, 149, 22–30. <https://doi.org/10.1016/j.compositesb.2018.05.009>
- Ali, A. B., Slawig, D., Schlosser, A., et al. (2021). Polyacrylonitrile (PAN) based electrospun carbon nanofibers (ECNFs): Probing the synergistic effects of creep assisted stabilization and CNTs addition on graphitization and low dimensional electrical transport. *Carbon N Y*, 172, 283–295. <https://doi.org/10.1016/j.carbon.2020.10.033>
- Bal, S. (2010). Experimental study of mechanical and electrical properties of carbon nanofiber/epoxy composites. *Materials and Design*, 31, 2406–2413. <https://doi.org/10.1016/j.matdes.2009.11.058>
- Balandin, A. A., Ghosh, S., Bao, W., et al. (2008). Superior thermal conductivity of single-layer graphene. *Nano Letters*, 8, 902–907. <https://doi.org/10.1021/nl0731872>
- Baran, I., Straumit, I., Shishkina, O., & Lomov, S. V. (2018). X-ray computed tomography characterization of manufacturing induced defects in a glass/polyester pultruded profile. *Composite Structures*, 195, 74–82. <https://doi.org/10.1016/j.compstruct.2018.04.030>
- Bellucci, S., Balasubramanian, C., Micciulla, F., & Rinaldi, G. (2007). CNT composites for aerospace applications. *Journal of Experimental Nanoscience*, 2, 193–206. <https://doi.org/10.1080/17458080701376348>
- Borah, M., Pathak, A. K., Singh, D. K., et al. (2017). Role of limited hydrogen and flow interval on the growth of single crystal to continuous graphene by low-pressure chemical vapor deposition. *Nanotechnology*, 28, 075602. <https://doi.org/10.1088/1361-6528/aa527e>
- Boukhalov, D. W., & Katsnelson, M. I. (2008). Chemical functionalization of graphene with defects. *Nano Letters*, 8, 4374–4379. <https://doi.org/10.1021/nl802234n>
- Burkov, M., & Eremin, A. (2018). Hybrid CFRP/SWCNT composites with enhanced electrical conductivity and mechanical properties. *Journal of Materials Engineering and Performance*, 27, 5984–5991. <https://doi.org/10.1007/s11665-018-3695-x>
- Cha, J., Jin, S., Shim, J. H., et al. (2016). Functionalization of carbon nanotubes for fabrication of CNT/epoxy nanocomposites. *Materials and Design*, 95, 1–8. <https://doi.org/10.1016/j.matdes.2016.01.077>
- Chakraborty, A. K., Plyhm, T., Barbezat, M., et al. (2011). Carbon nanotube (CNT)-epoxy nanocomposites: A systematic investigation of CNT dispersion. *Journal of Nanoparticle Research*, 13, 6493–6506. <https://doi.org/10.1007/s11051-011-0552-3>
- Chen, J., Lekawa-Raus, A., Trevarthen, J., et al. (2020). Carbon nanotube films spun from a gas phase reactor for manufacturing carbon nanotube film/carbon fibre epoxy hybrid composites for electrical applications. *Carbon N Y*, 158, 282–290. <https://doi.org/10.1016/j.carbon.2019.08.078>
- Chen, J., Wu, J., Ge, H., et al. (2016). Reduced graphene oxide deposited carbon fiber reinforced polymer composites for electromagnetic interference shielding. *Composites. Part A, Applied Science and Manufacturing*, 82, 141–150. <https://doi.org/10.1016/j.compositesa.2015.12.008>
- Chen, L., Jin, H., Xu, Z., et al. (2014). A design of gradient interphase reinforced by silanized graphene oxide and its effect on carbon fiber/epoxy interface. *Materials Chemistry and Physics*, 145, 186–196. <https://doi.org/10.1016/j.matchemphys.2014.02.001>

- Chi, Y., Chu, J., Chen, M., et al. (2016). Directly deposited graphene nanowalls on carbon fiber for improving the interface strength in composites. *Applied Physics Letters*, *108*, 211601. <https://doi.org/10.1063/1.4952593>
- Chou, T. Y., Wang, J., Tsai, H.-Y., et al. (2021). A novel thin-film image binarization method to detect nanofiller dispersibility for improving the mechanical performance of epoxy/polybenzoxazine laminate nanocomposites. *Composites Science and Technology*, *208*, 108778. <https://doi.org/10.1016/j.compscitech.2021.108778>
- Das, S., Sharma, S., Yokozeki, T., & Dhakate, S. (2021). Conductive layer-based multifunctional structural composites for electromagnetic interference shielding. *Composite Structures*, *261*, 113293. <https://doi.org/10.1016/j.compstruct.2020.113293>
- De Volder, M. F. L., Tawfick, S. H., Baughman, R. H., & Hart, A. J. (2013). Carbon nanotubes: Present and future commercial applications. *Science (80-)*, *339*, 535–539. <https://doi.org/10.1126/science.1222453>
- Dhakate, S. R., Chaudhary, A., Gupta, A., et al. (2016). Excellent mechanical properties of carbon fiber semi-aligned electrospun carbon nanofiber hybrid polymer composites. *RSC Advances*, *6*, 36715–36722. <https://doi.org/10.1039/C6RA02672A>
- Dudek, P. (2013). FDM 3D printing technology in manufacturing composite elements. *Archives of Metallurgy and Materials*, *58*, 1415–1418. <https://doi.org/10.2478/amm-2013-0186>
- Dunk, P. W., Kaiser, N. K., Hendrickson, C. L., et al. (2012). Closed network growth of fullerenes. *Nature Communications*, *3*, 1–9. <https://doi.org/10.1038/ncomms1853>
- Eatemadi, A., Daraee, H., Karimkhanloo, H., et al. (2014). Carbon nanotubes: Properties, synthesis, purification, and medical applications. *Nanoscale Research Letters*, *9*, 1–13. <https://doi.org/10.1186/1556-276X-9-393>
- Englert, J. M., Dotzer, C., Yang, G., et al. (2011). Covalent bulk functionalization of graphene. *Nature Chemistry*, *3*, 279–286. <https://doi.org/10.1038/nchem.1010>
- Fasel, U., Keidel, D., Baumann, L., et al. (2020). Composite additive manufacturing of morphing aerospace structures. *Manufacturing Letters*, *23*, 85–88. <https://doi.org/10.1016/j.mfglet.2019.12.004>
- Fernández-Saavedra, R., Aranda, P., & Ruiz-Hitzky, E. (2004). Templated synthesis of carbon nanofibers from polyacrylonitrile using sepiolite. *Advanced Functional Materials*, *14*, 77–82. <https://doi.org/10.1002/adfm.200305514>
- Fogel, M., Parlevliet, P., Olivier, P., & Dantras, É. (2017). Manufacturing of conductive structural composites through spraying of CNTs/epoxy dispersions on dry carbon fiber plies. *Composites. Part A, Applied Science and Manufacturing*, *100*, 40–47. <https://doi.org/10.1016/j.compositesa.2017.04.020>
- Gagné, M., & Theriault, D. (2014). Lightning strike protection of composites. *Progress in Aerospace Science*, *64*, 1–16. <https://doi.org/10.1016/j.paerosci.2013.07.002>
- Gaztelumendi, I., Chapartegui, M., Seddon, R., et al. (2017). Enhancement of electrical conductivity of composite structures by integration of carbon nanotubes via bulk resin and/or buckypaper films. *Composites. Part B, Engineering*, *122*, 31–40. <https://doi.org/10.1016/j.compositesb.2016.12.059>
- Geim, A. K. (2009). Graphene: Status and prospects. *Science (80-)*, *324*, 1530–1534.
- Geim, A. K., & Novoselov, K. S. (2009). The rise of graphene. In *Nanoscience and technology* (pp. 11–19). Co-Published with Macmillan Publishers Ltd.
- Georgakilas, V., Kordatos, K., Prato, M., et al. (2002). Organic functionalization of carbon nanotubes. *Journal of the American Chemical Society*, *124*, 760–761. <https://doi.org/10.1021/ja016954m>
- Ghasemi, A. R., Mohammadi, M. M., & Mohandes, M. (2015). The role of carbon nanofibers on thermo-mechanical properties of polymer matrix composites and their effect on reduction of residual stresses. *Composites. Part B, Engineering*, *77*, 519–527. <https://doi.org/10.1016/j.compositesb.2015.03.065>
- Gojny, F., Wichmann, M., Fiedler, B., & Schulte, K. (2005). Influence of different carbon nanotubes on the mechanical properties of epoxy matrix composites – A comparative study. *Composites Science and Technology*, *65*, 2300–2313. <https://doi.org/10.1016/j.compscitech.2005.04.021>

- Gou, J., Tang, Y., Liang, F., et al. (2010). Carbon nanofiber paper for lightning strike protection of composite materials. *Composites. Part B, Engineering*, 41, 192–198. <https://doi.org/10.1016/j.compositesb.2009.06.009>
- Guo, J., & Lu, C. (2012). Continuous preparation of multiscale reinforcement by electrophoretic deposition of carbon nanotubes onto carbon fiber tows. *Carbon NY*, 50, 3101–3103. <https://doi.org/10.1016/j.carbon.2012.02.044>
- Gupta, A., & Dhakate, S. R. (2012). *Electro-spinning: A practical approach to nanofibers new era of research*. LAP LAMBERT Academic Publishing.
- Gupta, A., & Dhakate, S. R. (2017). Development of structurally stable electrospun carbon nanofibers from polyvinyl alcohol. *Materials Research Express*, 4, 045021. <https://doi.org/10.1088/2053-1591/aa6a89>
- Hammel, E., Tang, X., Trampert, M., et al. (2004). Carbon nanofibers for composite applications. *Carbon NY*, 42, 1153–1158. <https://doi.org/10.1016/j.carbon.2003.12.043>
- Hashish, M., & Kent, W. A. (2013). Trimming of CFRP aircraft components. In *WJTA-IMCA conference and Expo*.
- Hirano, Y., Yokozeki, T., Ishida, Y., et al. (2016). Lightning damage suppression in a carbon fiber-reinforced polymer with a polyaniline-based conductive thermoset matrix. *Composites Science and Technology*, 127, 1–7. <https://doi.org/10.1016/j.compscitech.2016.02.022>
- Hiremath, N., & Bhat, G. (2017). High-performance carbon nanofibers and nanotubes. In *Structure and properties of high-performance fibers* (pp. 79–109). Elsevier.
- Hirsch, A. (2010). The era of carbon allotropes. *Nature Materials*, 9, 868–871. <https://doi.org/10.1038/nmat2885>
- Hirsch, A., & Vostrowsky, O. (2005). Functionalization of carbon nanotubes. In *Topics in current chemistry* (pp. 193–237). Springer.
- Iijima, S. (1991). Helical microtubules of graphitic carbon. *Nature*, 354, 56–58. <https://doi.org/10.1038/354056a0>
- Inagaki, M., Yang, Y., & Kang, F. (2012). Carbon nanofibers prepared via electrospinning. *Advanced Materials*, 24, 2547–2566. <https://doi.org/10.1002/adma.201104940>
- Iwahori, Y., Ishiwata, S., Sumizawa, T., & Ishikawa, T. (2005). Mechanical properties improvements in two-phase and three-phase composites using carbon nano-fiber dispersed resin. *Composites. Part A, Applied Science and Manufacturing*, 36, 1430–1439. <https://doi.org/10.1016/j.compositesa.2004.11.017>
- Jenkins, P., Siddique, S., Khan, S., et al. (2019). Influence of reduced graphene oxide on epoxy/carbon fiber-reinforced hybrid composite: Flexural and shear properties under varying temperature conditions. *Advanced Engineering Materials*, 21, 1800614. <https://doi.org/10.1002/adem.201800614>
- Katagiri, K., Honda, S., Nakaya, S., et al. (2021). Tensile strength of CFRP with curvilinearly arranged carbon fiber along the principal stress direction fabricated by the electrodeposition resin molding. *Composites. Part A, Applied Science and Manufacturing*, 143, 106271. <https://doi.org/10.1016/j.compositesa.2021.106271>
- Katagiri, K., Sasaki, K., Honda, S., et al. (2017a). Resin molding by using electro-activated deposition for efficient manufacturing of carbon fiber reinforced plastic. *Composite Structures*, 182, 666–673. <https://doi.org/10.1016/j.compstruct.2017.09.064>
- Katagiri, K., Sasaki, K., Honda, S., et al. (2017b). CFRP manufacturing method using electrodeposition resin molding for curvilinear fiber arrangements. *Composites. Part A, Applied Science and Manufacturing*, 102, 108–116. <https://doi.org/10.1016/j.compositesa.2017.07.006>
- Khan, S. U., & Kim, J.-K. (2012). Improved interlaminar shear properties of multiscale carbon fiber composites with bucky paper interleaves made from carbon nanofibers. *Carbon NY*, 50, 5265–5277. <https://doi.org/10.1016/j.carbon.2012.07.011>
- Kim, C., Park, S.-H., Lee, W.-J., & Yang, K.-S. (2004). Characteristics of supercapacitor electrodes of PBI-based carbon nanofiber web prepared by electrospinning. *Electrochimica Acta*, 50, 877–881. <https://doi.org/10.1016/j.electacta.2004.02.071>
- Kim, T., Shin, J., Lee, K., et al. (2021). A universal surface modification method of carbon nanotube fibers with enhanced tensile strength. *Composites. Part A, Applied Science and Manufacturing*, 140, 106182. <https://doi.org/10.1016/j.compositesa.2020.106182>

- Krombholz, C., Perner, M., Bock, M., & Röstermundt, D. (2012). Improving the production quality of the advanced automated fiber placement process by means of online path correction. In *28th congress of the International Council of the Aeronautical Sciences* (pp 3922–3931).
- Kuila, T., Bose, S., Mishra, A. K., et al. (2012). Chemical functionalization of graphene and its applications. *Progress in Materials Science*, *57*, 1061–1105. <https://doi.org/10.1016/j.pmatsci.2012.03.002>
- Kumar, V., Sharma, S., Pathak, A., et al. (2019). Interleaved MWCNT buckypaper between CFRP laminates to improve through-thickness electrical conductivity and reducing lightning strike damage. *Composite Structures*, *210*, 581–589. <https://doi.org/10.1016/j.compstruct.2018.11.088>
- Kumar, V., Yokozeki, T., Goto, T., et al. (2017). Irreversible tunability of through-thickness electrical conductivity of polyaniline-based CFRP by de-doping. *Composites Science and Technology*, *152*, 20–26. <https://doi.org/10.1016/j.compscitech.2017.09.005>
- Kumar, V., Yokozeki, T., Goto, T., et al. (2018a). Scavenging phenomenon and improved electrical and mechanical properties of polyaniline–divinylbenzene composite in presence of MWCNT. *International Journal of Mechanics and Materials in Design*, *14*, 697–708. <https://doi.org/10.1007/s10999-017-9397-y>
- Kumar, V., Yokozeki, T., Okada, T., et al. (2018b). Effect of through-thickness electrical conductivity of CFRPs on lightning strike damages. *Composites. Part A, Applied Science and Manufacturing*, *114*, 429–438. <https://doi.org/10.1016/j.compositesa.2018.09.007>
- Layek, R. K., & Nandi, A. K. (2013). A review on synthesis and properties of polymer functionalized graphene. *Polymer (Guildf)*, *54*, 5087–5103. <https://doi.org/10.1016/j.polymer.2013.06.027>
- Lee, C., Wei, X., Kysar, J. W., & Hone, J. (2008). Measurement of the elastic properties and intrinsic strength of monolayer graphene. *Science (80-)*, *321*, 385–388. <https://doi.org/10.1126/science.1157996>
- Lee, J. M., Kim, B. M., & Ko, D. C. (2019). Development of vacuum-assisted prepreg compression molding for production of automotive roof panels. *Composite Structures*, *213*, 144–152. <https://doi.org/10.1016/j.compstruct.2019.01.092>
- Lee, J. U., Park, B., Kim, B. S., et al. (2016). Electrophoretic deposition of aramid nanofibers on carbon fibers for highly enhanced interfacial adhesion at low content. *Composites. Part A, Applied Science and Manufacturing*, *84*, 482–489. <https://doi.org/10.1016/j.compositesa.2016.02.029>
- Li, M., Gu, Y., Liu, Y., et al. (2013). Interfacial improvement of carbon fiber/epoxy composites using a simple process for depositing commercially functionalized carbon nanotubes on the fibers. *Carbon NY*, *52*, 109–121. <https://doi.org/10.1016/j.carbon.2012.09.011>
- Liu, L., Zhang, J., Zhao, J., & Liu, F. (2012). Mechanical properties of graphene oxides. *Nanoscale*, *4*, 5910–5916. <https://doi.org/10.1039/c2nr31164j>
- Ma, L., Zhu, Y., Feng, P., et al. (2019). Reinforcing carbon fiber epoxy composites with triazine derivatives functionalized graphene oxide modified sizing agent. *Composites. Part B, Engineering*, *176*, 107078. <https://doi.org/10.1016/j.compositesb.2019.107078>
- Ma, Y., Wang, J., Zhao, Y., et al. (2020). A new vacuum pressure infiltration CFRP method and preparation experimental study of composite. *Polymers (Basel)*, *12*(2), 419. <https://doi.org/10.3390/polym12020419>
- Marcano, D. C., Kosynkin, D. V., Berlin, J. M., et al. (2010). Improved synthesis of graphene oxide. *ACS Nano*, *4*, 4806–4814. <https://doi.org/10.1021/nn1006368>
- Maruyama, B., & Alam, K. (2002). Carbon nanotubes and nanofibers in composite materials. *SAMPE Journal*, *38*, 59–70.
- Muhammad, A., Rahman, M. R., Bains, R., & Bin Bakri, M. K. (2021). Applications of sustainable polymer composites in automobile and aerospace industry. In *Advances in sustainable polymer composites* (pp. 185–207). Elsevier.
- Ning, F., Cong, W., Qiu, J., et al. (2015). Additive manufacturing of carbon fiber reinforced thermoplastic composites using fused deposition modeling. *Composites. Part B, Engineering*, *80*, 369–378. <https://doi.org/10.1016/j.compositesb.2015.06.013>
- Novoselov, K. S., Geim, A. K., Morozov, S. V., et al. (2005). Two-dimensional gas of massless Dirac fermions in graphene. *Nature*, *438*, 197–200. <https://doi.org/10.1038/nature04233>

- Okan, B. S., Zanjani, J. S. M., Letofsky-Papst, I., et al. (2015). Morphology-controllable synthesis and characterization of carbon nanotube/polypyrrole composites and their hydrogen storage capacities. *Materials Chemistry and Physics*, 167, 171–180. <https://doi.org/10.1016/j.matchemphys.2015.10.027>
- Olsen, H. B. (1993). Automated composite tape lay-up using robotic devices. In *Proceedings—IEEE International Conference on Robotics and Automation* (pp. 291–297). IEEE.
- Park, D. C., Yu, T., Park, S. J., et al. (2021). Improvement of impregnation quality on out-of-autoclave processed CFRP aircraft wing spar through resin flow simulation. *Funct Compos Struct*, 3, 025001. <https://doi.org/10.1088/2631-6331/abf480>
- Park, D. W., Noh, H. S., Nojima, H., et al. (2014a). *Method for manufacturing polyimide-based carbon nanofiber electrode*.
- Park, J. M., Kwon, D. J., Wang, Z. J., et al. (2014b). Effects of carbon nanotubes and carbon fiber reinforcements on thermal conductivity and ablation properties of carbon/phenolic composites. *Composites. Part B, Engineering*, 67, 22–29. <https://doi.org/10.1016/j.compositesb.2014.06.022>
- Pathak, A. K., Borah, M., Gupta, A., et al. (2016). Improved mechanical properties of carbon fiber/graphene oxide-epoxy hybrid composites. *Composites Science and Technology*, 135, 28–38. <https://doi.org/10.1016/j.compscitech.2016.09.007>
- Pathak, A. K., & Dhakate, S. R. (2021). Validation of experimental results for graphene oxide-epoxy polymer nanocomposite through computational analysis. *Journal of Polymer Science*, 59, 84–99. <https://doi.org/10.1002/pol.20200442>
- Pathak, A. K., Garg, H., Singh, M., et al. (2019a). Enhanced interfacial properties of graphene oxide incorporated carbon fiber reinforced epoxy nanocomposite: A systematic thermal properties investigation. *Journal of Polymer Research*, 26, 23. <https://doi.org/10.1007/s10965-018-1668-2>
- Pathak, A. K., Garg, H., Subhedar, K. M., & Dhakate, S. R. (2021a). Significance of carbon fiber orientation on thermomechanical properties of carbon fiber reinforced epoxy composite. *Fibers and Polymers*, 22(7), 1–11. <https://doi.org/10.1007/s12221-021-0703-9>
- Pathak, A. K., Garg, H., Yokozeki, T., & Dhakate, S. R. (2021b). Relevance of graphene oxide as nanofiller for geometrical variation in unidirectional carbon fiber/epoxy composite. *Journal of Applied Polymer Science*, 50985. <https://doi.org/10.1002/app.50985>
- Pathak, A. K., Kumar, V., Sharma, S., et al. (2019b). Improved thermomechanical and electrical properties of reduced graphene oxide reinforced polyaniline – Dodecylbenzenesulfonic acid/divinylbenzene nanocomposites. *Journal of Colloid and Interface Science*, 533, 548–560. <https://doi.org/10.1016/j.jcis.2018.08.105>
- Pathak, A. K., Zhou, Y., Lecoindre, L., & Yokozeki, T. (2021c). Polypropylene nanocomposites with high-loading conductive carbon nano-reinforcements for multifunctional applications. *Applied Nanoscience*, 11, 493–503. <https://doi.org/10.1007/s13204-020-01594-6>
- Perner, M., Algermissen, S., Keimer, R., & Monner, H. P. (2016). Avoiding defects in manufacturing processes: A review for automated CFRP production. *Robotics and Computer-Integrated Manufacturing*, 38, 82–92.
- Rabeneck, D. (2010). Boosting composite production, aerotec. In *The engineering and technology magazine for the aerospace industry* (pp. 28–30).
- Rana, S., Alagirusamy, R., & Joshi, M. (2011). Effect of carbon nanofiber dispersion on the tensile properties of epoxy nanocomposites. *Journal of Composite Materials*, 45, 2247–2256. <https://doi.org/10.1177/0021998311401076>
- Ren, J., Li, F. F., Lau, J., et al. (2015). One-pot synthesis of carbon nanofibers from CO₂. *Nano Letters*, 15, 6142–6148. <https://doi.org/10.1021/acs.nanolett.5b02427>
- Robertson, J. (2002). Diamond-like amorphous carbon. *Materials Science and Engineering: R: Reports*, 37, 129–281. [https://doi.org/10.1016/S0927-796X\(02\)00005-0](https://doi.org/10.1016/S0927-796X(02)00005-0)
- Rodriguez, A. J., Guzman, M. E., Lim, C. S., & Minaie, B. (2010). Synthesis of multiscale reinforcement fabric by electrophoretic deposition of amine-functionalized carbon nanofibers onto carbon fiber layers. *Carbon NY*, 48, 3256–3259. <https://doi.org/10.1016/j.carbon.2010.05.018>
- Rodriguez, A. J., Guzman, M. E., Lim, C. S., & Minaie, B. (2011). Mechanical properties of carbon nanofiber/fiber-reinforced hierarchical polymer composites manufactured with multiscale-reinforcement fabrics. *Carbon NY*, 49, 937–948. <https://doi.org/10.1016/j.carbon.2010.10.057>

- Rodríguez-García, V., Gómez, J., Cristiano, F., & Gude, M. R. (2020). Industrial manufacturing and characterization of multiscale CFRP laminates made from prepregs containing graphene-related materials. *Materials Research Express*, 7, 75601. <https://doi.org/10.1088/2053-1591/aba0eb>
- Saadatyar, S., Beheshty, M. H., & Sahraeian, R. (2021). Mechanical properties of multiwall carbon nanotubes/unidirectional carbon fiber-reinforced epoxy hybrid nanocomposites in transverse and longitudinal fiber directions. *Polymers and Polymer Composites*. <https://doi.org/10.1177/0967391120986516>
- Schodek, D. L., Ferreira, P., & Ashby, M. F. (2009). *Nanomaterials, nanotechnologies and design: An introduction for engineers and architects*. Butterworth-Heinemann.
- Senis, E. C., Golosnoy, I. O., Andritsch, T., et al. (2020). The influence of graphene oxide filler on the electrical and thermal properties of unidirectional carbon fiber/epoxy laminates: Effect of out-of-plane alignment of the graphene oxide nanoparticles. *Polymer Composites*, 41, 3510–3520. <https://doi.org/10.1002/pc.25637>
- Senis EC, Vryonis O, Golosnoy IO, et al (2017) *The influence of graphene oxide on the electrical conduction in unidirectional CFRP laminates for wind turbine blade applications*.
- Sharma, S., Kumar, V., Pathak, A. K., et al. (2018a). Design of MWCNT bucky paper reinforced PANI-DBSA-DVB composites with superior electrical and mechanical properties. *Journal of Materials Chemistry C*, 6, 12396–12406. <https://doi.org/10.1039/C8TC04023K>
- Sharma, S., Pathak, A. K., Singh, V. N., et al. (2018b). Excellent mechanical properties of long multiwalled carbon nanotube bridged Kevlar fabric. *Carbon N Y*, 137, 104–117. <https://doi.org/10.1016/j.carbon.2018.05.017>
- Shirasu, K., Nakamura, A., Yamamoto, G., et al. (2017). Potential use of CNTs for production of zero thermal expansion coefficient composite materials: An experimental evaluation of axial thermal expansion coefficient of CNTs using a combination of thermal expansion and uniaxial tensile tests. *Composites. Part A, Applied Science and Manufacturing*, 95, 152–160. <https://doi.org/10.1016/j.compositesa.2016.12.027>
- Sugime, H., Sato, T., Nakagawa, R., et al. (2021). Ultra-long carbon nanotube forest via in situ supplements of iron and aluminum vapor sources. *Carbon N Y*, 172, 772–780. <https://doi.org/10.1016/j.carbon.2020.10.066>
- Sun, J., Zhao, F., Yao, Y., et al. (2017). High efficient and continuous surface modification of carbon fibers with improved tensile strength and interfacial adhesion. *Applied Surface Science*, 412, 424–435. <https://doi.org/10.1016/j.apsusc.2017.03.279>
- Tekinalp, H. L., Kunc, V., Velez-Garcia, G. M., et al. (2014). Highly oriented carbon fiber-polymer composites via additive manufacturing. *Composites Science and Technology*, 105, 144–150. <https://doi.org/10.1016/j.compscitech.2014.10.009>
- Terrones, H., Hayashi, T., Muñoz-Navia, M., et al. (2001). Graphitic cones in palladium catalysed carbon nanofibres. *Chemical Physics Letters*, 343, 241–250. [https://doi.org/10.1016/S0009-2614\(01\)00718-7](https://doi.org/10.1016/S0009-2614(01)00718-7)
- Trofimov, A., Le-Pavic, J., Ravey, C., et al. (2021). Multi-scale modeling of distortion in the non-flat 3D woven composite part manufactured using resin transfer molding. *Composites. Part A, Applied Science and Manufacturing*, 140, 106145. <https://doi.org/10.1016/j.compositesa.2020.106145>
- Türk, D. A., Kussmaul, R., Zogg, M., et al. (2017). Composites part production with additive manufacturing technologies. In *Procedia CIRP* (pp. 306–311). Elsevier B.V..
- Vartak, D., Ghotekar, Y., Deshpande, N., et al. (2021). New horizons of space qualification of single-walled carbon nano tubes-carbon fibre reinforced polymer composite. *Journal of Physics Conference Series*, 1854, 012001. <https://doi.org/10.1088/1742-6596/1854/1/012001>
- Vedernikov, A., Safonov, A., Tucci, F., et al. (2020). Pultruded materials and structures: A review. *Journal of Composite Materials*, 54, 4081–4117.
- Vedrtan, A., & Sharma, S. P. (2019). Study on the performance of different nano-species used for surface modification of carbon fiber for interface strengthening. *Composites Part A: Applied Science and Manufacturing*, 125, 105509.
- Wang, B., Duan, Y., Xin, Z., et al. (2018). Fabrication of an enriched graphene surface protection of carbon fiber/epoxy composites for lightning strike via a percolating-assisted resin film

- infusion method. *Composites Science and Technology*, 158, 51–60. <https://doi.org/10.1016/j.compscitech.2018.01.047>
- Wang, B. C., Zhou, X., & Ma, K. M. (2013). Fabrication and properties of CNTs/carbon fabric hybrid multiscale composites processed via resin transfer molding technique. *Composites. Part B, Engineering*, 46, 123–129. <https://doi.org/10.1016/j.compositesb.2012.10.022>
- Wittig, J. (2005). Process automation for the production of large composite parts. *Reinforced Plastics*, 49, 30–33. [https://doi.org/10.1016/S0034-3617\(05\)00519-9](https://doi.org/10.1016/S0034-3617(05)00519-9)
- Xiong, S., Zhao, Y., Wang, Y., et al. (2021). Enhanced interfacial properties of carbon fiber/epoxy composites by coating carbon nanotubes onto carbon fiber surface by one-step dipping method. *Applied Surface Science*, 546, 149135. <https://doi.org/10.1016/j.apsusc.2021.149135>
- Xue, Z., Xiong, Q., Zou, C., et al. (2021). Growth of carbon nanofibers through chemical vapor deposition for enhanced sodium ion storage. *Materials Research Bulletin*, 133, 111049. <https://doi.org/10.1016/j.materresbull.2020.111049>
- Xuyen, N. T., Ra, E. J., Geng, H. Z., et al. (2007). Enhancement of conductivity by diameter control of polyimide-based electrospun carbon nanofibers. *The Journal of Physical Chemistry B*, 111, 11350–11353. <https://doi.org/10.1021/jp075541q>
- Yan, F., Liu, L., Li, K., et al. (2021). A novel π bridging method to graft graphene oxide onto carbon fiber for interfacial enhancement of epoxy composites. *Composites Science and Technology*, 201, 108489. <https://doi.org/10.1016/j.compscitech.2020.108489>
- Yan, F., Liu, L., Li, M., et al. (2019). One-step electrodeposition of Cu/CNT/CF multiscale reinforcement with substantially improved thermal/electrical conductivity and interfacial properties of epoxy composites. *Composites Part A: Applied Science and Manufacturing*, 125, 105530. <https://doi.org/10.1016/j.compositesa.2019.105530>
- Yao, D., Yang, H., Hu, Q., et al. (2021). Carbon nanotubes from post-consumer waste plastics: Investigations into catalyst metal and support material characteristics. *Applied Catalysis B: Environmental*, 280, 119413. <https://doi.org/10.1016/j.apcatb.2020.119413>
- Zaccardi, F., Santonicola, M. G., & Laurenzi, S. (2018). Quantitative assessment of nanofiller dispersion based on grayscale image analysis: A case study on epoxy/carbon nanocomposites. *Composites. Part A, Applied Science and Manufacturing*, 115, 302–310. <https://doi.org/10.1016/j.compositesa.2018.10.003>
- Zhang, J., Niu, H., Zhou, J., et al. (2011). Synergistic effects of PEK-C/VGCNF composite nanofibres on a trifunctional epoxy resin. *Composites Science and Technology*, 71, 1060–1067. <https://doi.org/10.1016/j.compscitech.2011.03.008>
- Zhao, B., Gao, H., Li, S., et al. (2020). Surface modification of carbon fiber by electropolymerization: Continuous production, thickness control, colorization, and preparation of CFRP. *ACS Applied Polymer Materials*, 2, 2594–2601. <https://doi.org/10.1021/acscapm.0c00232>
- Zhao, Z. J., Zhang, B. Y., Du, Y., et al. (2017). MWCNT modified structure-conductive composite and its electromagnetic shielding behavior. *Composites. Part B, Engineering*, 130, 21–27. <https://doi.org/10.1016/j.compositesb.2017.07.033>
- Zussman, E., Chen, X., Ding, W., et al. (2005). Mechanical and structural characterization of electrospun PAN-derived carbon nanofibers. *Carbon NY*, 43, 2175–2185. <https://doi.org/10.1016/j.carbon.2005.03.031>

Chapter 24

Advanced Composite in Aerospace Applications: Opportunities, Challenges, and Future Perspective



M. R. M. Asyraf, R. A. Ilyas, S. M. Sapuan, M. M. Harussani, H. M. Hariz, J. M. Aiman, Danish Mahmood Baitaba, M. R. Sanjay, M. R. Ishak, Norkhairunnisa Mazlan, Shubham Sharma, Mohammad Azad Alam, and Mochamad Asrofi

1 Introduction

Recently, there has been great interest in high-performance structural designs, such as aerospace applications and advanced composite materials, that are commonly requiring lightweight components with superior mechanical properties to perform in demanding service conditions and supply energy potency. Scientifically and economically, it is now accepted that greenhouse gas emissions as of various

M. R. M. Asyraf
Institute of Energy Infrastructure, Universiti Tenaga Nasional, Jalan IKRAM-UNITEN,
Kajang, Selangor, Malaysia

R. A. Ilyas (✉)
School of Chemical and Energy Engineering, Faculty of Engineering, Universiti Teknologi
Malaysia, Johor Bahru, Johor, Malaysia

Centre for Advanced Composite Materials, Universiti Teknologi Malaysia, UTM,
Johor Bahru, Johor, Malaysia
e-mail: ahmadilyas@utm.my

S. M. Sapuan
Laboratory of Biocomposite Technology, Institute of Tropical Forestry and Forest Products
(INTROP), Universiti Putra Malaysia, Serdang, Selangor, Malaysia

Advanced Engineering Materials and Composites Research Centre (AEMC), Department of
Mechanical and Manufacturing Engineering, Faculty of Engineering, Universiti Putra
Malaysia, Serdang, Selangor, Malaysia

M. M. Harussani · H. M. Hariz · J. M. Aiman
Advanced Engineering Materials and Composites Research Centre (AEMC), Department of
Mechanical and Manufacturing Engineering, Faculty of Engineering, Universiti Putra
Malaysia, Serdang, Selangor, Malaysia

productions have contributed to climate change. Emissions from airplanes are directly discharged into the higher layer and lower layer of ozone, thereby impacting the atmosphere's composition. This emission makes them especially strong relative to other pollutants (Ali et al., 2020a, 2020b, 2021; Rauf et al., 2019; Zainuddin et al., 2019). In Malaysia, the main sources of power generated was crude oil and natural gas which highly contribute to high carbon dioxide emissions as shown in Fig. 24.1. Due to high carbon emission, policy makers such as, International Civil Aviation Organization (ICAO) with aerospace business entities are working together to reduce the greenhouse effect. Thus, implementing new materials such as natural fibre composites to reduce weight loss, advances in aerodynamic and applying new concepts of aircraft are those efforts can be taken to solve this matters (Arockiam et al., 2018; Hamidon et al., 2019; Khan et al., 2018).

Composite advanced materials, which are typically continuous for aerospace use, carbon fibers with a rubber matrix, will provide superior material characteristics than metals, therefore, in order to attain lighter structural structures. Today, as a leading producer of aircraft, substituting modern composite materials with conventional materials, it is possible to harness composites' full capacity by new materials structural layouts. Carbon-reinforced polymer composites are usually used in primary and secondary aircraft construction and system applications (Nayana & Kandasubramanian, 2020). Composites of carbon fiber are typically made in laminate or sandwich shapes for aerospace structural applications (Aisyah et al., 2019;

D. M. Baitaba

Department of Weaving, National Textile University, Faisalabad, Pakistan

M. R. Sanjay

Natural Composites Research Group Lab, King Mongkut's University of Technology North Bangkok (KMUTNB), Bangkok, Thailand

M. R. Ishak

Department of Aerospace Engineering, Faculty of Engineering, Universiti Putra Malaysia, Serdang, Selangor Darul Ehsan, Malaysia

Laboratory of Biocomposite Technology, Institute of Tropical Forestry and Forest Products (INTROP), Universiti Putra Malaysia, Serdang, Selangor, Malaysia

N. Mazlan

Department of Aerospace Engineering, Faculty of Engineering, Universiti Putra Malaysia, Serdang, Selangor Darul Ehsan, Malaysia

S. Sharma

Department of Mechanical Engineering, IK Gujral Punjab Technical University, Main Campus-Kapurthala, Jalandhar, Punjab, India

Department of Mechanical Engineering, Chandigarh University, Chandigarh, Punjab, India

M. A. Alam

Mechanical Engineering Department, Universiti Teknologi PETRONAS, Seri Iskandar, Perak, Malaysia

M. Asrofi

Laboratory of Materials Testing, Department of Mechanical Engineering, University of Jember, Jember, East Java, Indonesia

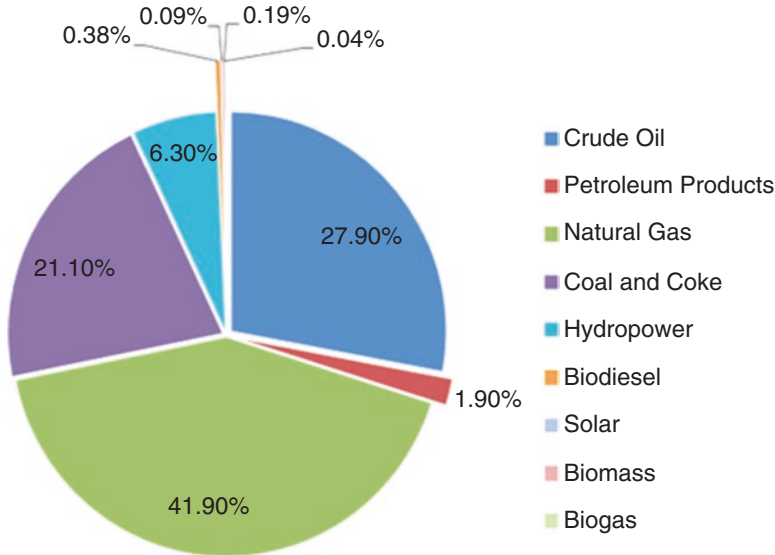


Fig. 24.1 Primary energy supply in Malaysia in 2017 (Ali et al., 2021)

Mohd Nurazzi et al., 2021). Thermoplastic such as epoxy or thermoplastic such as resins is also used to maintain reinforcing fibers as a matrix material (Asyraf et al., 2021d; Ilyas et al., 2020b, 2021c). Although there are pros and cons for the two matrix material forms, thermosetting resins are used widely in aircraft at present fabrication (Soutis, 2019).

Aerospace transport embrace advanced electronics with high energy that generates a number of the foremost dangerous thermal management issues. Such electronic payloads will be burdened by ever-increasing necessities for higher power, higher frequency, more extended periods of operations, inflated complexness, and reduced size of weight (Fairuz et al., 2014; Ilyas et al., 2019). Air-based and space-based vehicles use microelectronic circuitry with integrated management materials thermal loads and the harsh operating condition. These complex systems generate complex systems that produce extreme heat fluxes and produce temperature increases that limit efficiency and require rapid dissipation of heat to escape prompt failure and premature failure of the device. The outcome of these efforts seems to have been disruptive nanotechnologies, including synthetic nanotechnologies, which have led to thermal vias of the diamond and substrates (Schelling et al., 2005), nanocomposite TIMs (Bar-Cohen et al., 2015), on-chip microfluidic heat exchangers (Narayanamurthy et al., 2020), and thermal ground planes (Bar-Cohen et al., 2015).

On the other hand, practical uses of ceramics as coatings in thermal defense systems have been more positive in the past few decades. For the space shuttle, ceramics still gave us valuable lessons on the need for a space shuttle. Flexibility in aircraft structures' design can survive even after their main missions which are cracking during early space mission phases (Novak & Hall, 2003). Nevertheless, the ultimate objective of establishing hypersonic passenger transport vehicles continues to be a

global threat for new and existing planes. These vehicles require composite ceramics that must work reliably under severe conditions of thermal shock conditions (Soboyejo et al., 2015).

In high-performance aircraft and spacecraft structures, fiber-reinforced polymer matrix (FRP) composites are progressively utilized, primarily based on their comparatively high-performance designs and strong specific strength and rigidity derived from their relatively low density (Asyraf et al., 2020e; Heister et al., 2013; Nurazzi et al., 2021a; Suriani et al., 2021a, 2021b, 2021c, 2021d). Delamination may also take place between polymers and fiber layers in the form of fiber/matrix deformation. Thus, dynamic stiffness is located in planes specified by the fiber layout in FRP composites (Alsubari et al., 2021; Amir et al., 2021; Asyraf et al., 2020a; Omran et al., 2021). Residual stresses resulting from manufacturing or initiation sites for delamination are often given add to their engendering and development by material divergences and geometric features, such as edges, holes, and ply droppers. This result has prompted research to boost the resistance to delamination or fracture performance of FRP laminates and the development of test methods for their fracture nature characterization (Asyraf et al., 2020c, 2021a, 2021b). The development rate in strain energy per unit region of delamination controlled by break mechanics tests measuring FRP composites' delamination opposition (Asyraf et al., 2019a, 2021c; Johari et al., 2020a, b). Generally, standardized and established are for the so-called simple modes of loading. It is possible to produce FRP composites as CFRPs or GFRPs or as hybrid reinforcement. These materials may be continuous or short fibers, mostly oriented in a specific direction with the former. Reinforcements of aramid or basalt fiber have been studied but not included in the framework of existing standards. Toward the end, challenges, aviation composite capability, and future viewpoints have been mentioned for future development in the aerospace field.

2 Fiber-Reinforced Polymers (FRPs)

Fiber-reinforced polymers (FRPs) are the composite materials most broadly utilized in aviation structures. For example, their particular properties, superior, lightweight, higher firmness, and improved corrosion resistance, make them an appealing selection for aeronautic applications (Ilyas et al., 2020a; Norizan et al., 2020). It is an incredibly compact and durable fiber-reinforced polymer that incorporates carbon fiber. The reinforcement fibers are typically stiff, tight, and strongly distributed in the composite phases of the matrix. The reinforcement is also the critical load-bearing factor since, in the event of single-fiber breakage, the load can be transferred to other nearby fibers via the matrix. FRPs contain carbon fiber-reinforced polymers (CFRPs), glass fiber-reinforced polymers (GFRPs), and aramid fibers as shown in Fig. 24.2. CFRPs are being used in high-tech applications. GFRP with typical E-glass (electrical) and S-glass (high strength) also has excellent properties.

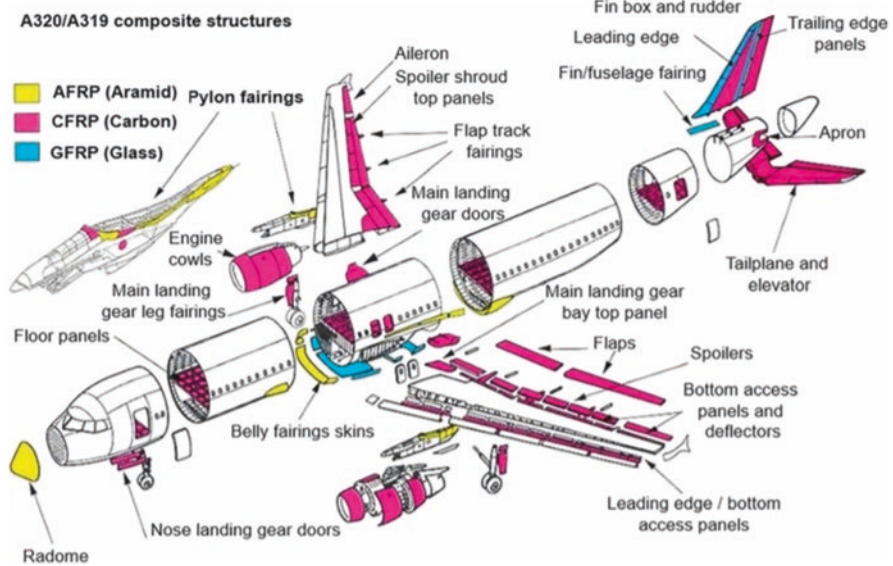


Fig. 24.2 Components made of FRPs used in Airbus (Mouritz, 2012)

3 Challenges and Opportunities in Advanced Composites: Nanocomposites

New advanced engineering materials systems, like organic matrix composites, have a range of applications and aerospace structures, athletic products, superior vehicles, and vessels (Asyraf et al., 2020b; Ilyas et al., 2021b, 2021d). Composite aviation structures likewise have exceptional property details that make the selection of prominent materials frameworks, and for example, nanocomposites become attractive. Nevertheless, there is indeed a clear need to consider the increasing challenges of efficiency, weight, process capability, risk, and life cycle costs in selecting new structural materials (Asyraf et al., 2019b, 2020d; Sapuan et al., 2021). The biggest downside facing nanocomposites is analyzing the degree and efficaciousness of stress transfer through the interaction between nanotubes and polymers in order to assess mechanical strength and stiffness of polymer nanocomposites (Ilyas et al., 2021a; Omran et al., 2021). Table 24.1 shows the summary of approaches and possible applications of nanocomposites in aerospace structural composites.

The integration, control, and usage of nanoparticle-enabled properties inside a ranked, structured composite created using commercially viable process strategies may be a specific challenge for typical composites, as shown in Fig. 24.3, while industrial initiatives continue to explore low-cost methodological approaches for composite manufacturing, the current significant capital expenditure in composite processing equipment (Jusoh et al., 2016).

Table 24.1 Summary of approaches and possible applications of nanocomposites in aerospace structural composites (Kausar et al., 2017)

Property	Common nanocomposite approach	Potential application
Permeability	Inclusion of impermeable, high-aspect ratio silicate or graphite flake in resin	Cryogenic tanks and durability to diffusion species
Outgassing	Inclusion of impermeable, high-aspect ratio silicate or graphite flake in resin	Optical benches, interferometers, and antenna truss structures
Oxidation resistance	Incorporate high-temperature, oxidation-resistant fillers (silicate, CNTs, POSS, etc.) that form passivating layers or slow oxidative erosion in resin or as coating	Thermal protection systems, atomic oxygen resistance, and space structures
Electrostatic dissipation (ESD)	Incorporate high-aspect ratio conductive particles such as CNTs, graphite flake, and metals, as percolated networks in resin between conductive fibers	Charge-dissipating adhesives, coatings, and gap fillers
Electromagnetic interference (EMI)	Create films of highly percolated networks of conductive nanofillers (nickel nanostrand veil, SWNT buckypaper, etc.) that can both absorb and dissipate broadband frequencies	Bus compartment enclosures and electronic enclosures
Lightning strike	Incorporate conductive nanofillers (nickel nanostrands, CNTs, etc.) as highly percolated coatings, appliqués, resins, or veils that can carry large currents and have controlled failure modes	Composite aircraft exteriors

4 Advanced Composite in Aerospace Applications

Aircraft makers have several valid reasons for using composites, and airlines would like composites to be utilized in their industry. Several composite materials come through comparatively more significant strength characteristics than ancient metal-like materials, reducing craft weight and reducing fuel value per rider carried. Composites are more resistant than metal to fatigue from continual takeoff or landing cycles, resulting in fewer pricey inspections over the aircraft's life and longer spent inside the air creating cash.

According to Barile and Cassalova (2018), it was proven that carbon plastics reinforced with high-strength unidirectional fibers are composite materials used in various fields of technology, including aerospace applications. Composite materials accommodate two distinct stages that cause the ultimate properties: the reinforcement and the matrix. The material examined within the initial part of this work was developed by suggesting RFI and handicraft. RFI is quick and economical and generates complicated structures with smart dimensional tolerances than typical ways. This results in increased utilization of composite materials in typical flight and aviation. These mean values of ultimate load and longitudinal modulus were obtained from tensile testing at three temperatures. As for the modulus of elasticity, the cold temperature was rough twice as much as hot temperature and room temperature.

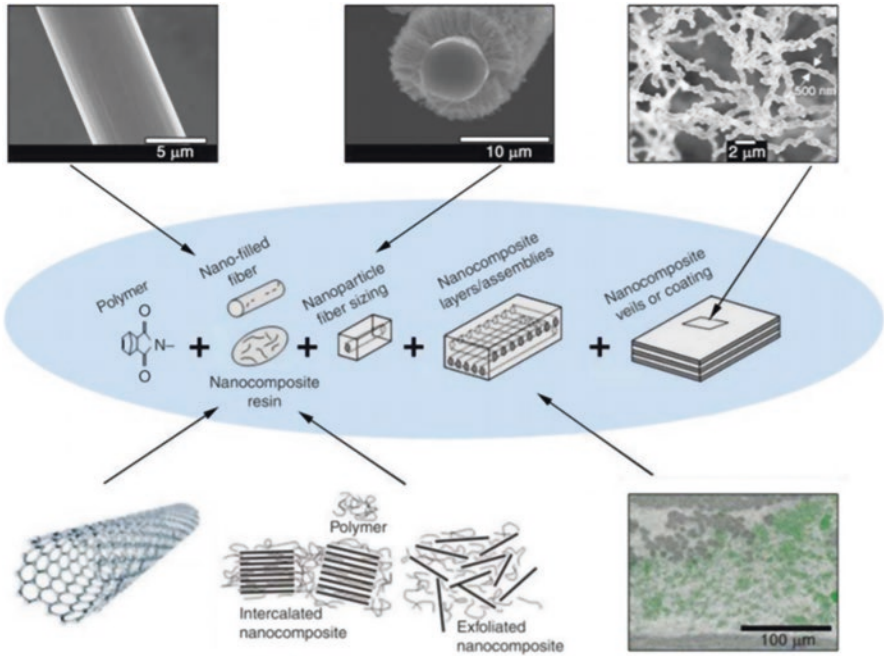


Fig. 24.3 The potential hierarchical integration of nanoparticles within a multiscale composite

The epoxy matrix appeared to become fragile at cold temperatures. Together, these examinations show that practical information demonstrated that the ductile and compressive mechanical properties seemed to improve by diminishing the temperature likely to be correlated with the thermal stability of the carbon fibers. The hole created a discontinuity in the fibers and a localized flaw due to the drilling operation. It influenced the behavior of the composite material; however, in this case, the folds were stitched together. Lowering delamination, in the case of drilled specimens, the mechanical properties declined by about 20%, but the involvement of the fastener cooperated to reduce this effect. Hofstätter et al. (2017) stated in their research on the current state of the art in fiber-reinforced polymers (FRPs) in additive manufacturing (AM). Carbon nanotube was tested for UV-curable resin in a mixture of carbon nanotubes with a weight ratio of 0.1–5%. Having followed the swelling process that requires *N,N*-dimethylacetamide (DMAC) comprising lithium chloride (LiCl), the whiskers were blended with PLA melt during the extrusion process, producing an all-biodegradable composite material with greater strength by 20% and Young’s modulus by 10% with a fiber content of 5%. The evidence presented in this section suggests that existing approaches for additively produced FRPs are uncommon, with many ancient applications utilizing short and long fibers embedded in a very compound matrix, like part, automobile, wind, and medicine engineering.

In a research of impact and delamination failure of multiscale carbon nanotube fiber-reinforced polymer composites by Khan and Kim (2011), fiber-reinforced polymer composites (FRPs) possess highly specific modules and particular strengths and are widely utilized in several structural applications, together with the part, sports product, automotive, civil, and marine structures. Delamination is among the most pervasive life-limiting crack propagation methods in laminate composites. Delamination can lead to a severe decrease in in-plane strength and stiffness, leading to the entire structure's catastrophic failure, and 43% rise in fracture resistance of epoxy resin with 0.5% of amine-operated, double-walled carbon nanotubes (CNTs). The focus of this research is to have a thorough overview of the strategies developed for the manufacture of FRP composites containing CNTs and carbon nanofibers (CNFs) and the implications of the addition of these nanofillers on the impact and delamination resistance of FRP composites.

In a study investigated by Kumar et al. (2013) on the development and characterization of continuous fiber-reinforced polymer-ceramic, it was proven that advanced aerospace structures involve materials capable of performing different purposes. The pursuit for the development of multifunctional materials has contributed to the concept of functionally graded materials (FGMs). Many opposing roles are integrated into a single material, for example, the strength of polymeric materials and ceramics' temperature capability. Toughness associated with the degraded mechanical strength of the hierarchic material can even be improved by utilizing an adequate fibrous reinforcement to accumulate functionally hierarchic composites (FGCs). FGC laminate density was 1.95–2.0 g/cc, whereas category II and VI laminate density were 1.70–1.72 g/cc and 1.85–1.90 g/cc, accordingly. Hence, the principle of homogenous FGM and functionally graded coating has recently been applied to developing ongoing fiber-reinforced functionally graded composites. In a research shown by Naya et al. (2017) on computational micromechanics of the transverse and shear behavior of unidirectional fiber-reinforced polymers including environmental effects, it was established that fiber-reinforced polymers (FRPs) are presently widely utilized in applications where remarkable mechanical characteristics are required in conjunction with lighter weight. With easy transverse tension loading, the method of fracture is regulated by a fiber/matrix debonding interface for each room temperature and dry and warmth or wet conditions. The composite might maintain a considerably higher level of strain throughout transverse compression for fairly high-resistance effects. A quasi-frictionless interface was shown in hot temperature or wet environments in the lack of more accurate results, contributing to an inability to initiate the fiber/matrix interface accompanied by a shear banding at hfr 47%. The studies presented thus far provide evidence that the existing methods of the microconstituents' boundary conditions, such as the fiber/matrix interface and the polymer plastic behavior, were determined experimentally by in situ nano-indentation experiments.

Camli and Binici (2007) proposed in their study on the strength of carbon fiber-reinforced polymers bonded to concrete and masonry that fiber-reinforced polymers (FRPs), that were initially used during defense and aerospace industries, have become common in civil engineering applications since the 1990s increased supply

at lower prices. With growing bonded length, L_{frp} , the load-bearing capacity rose to a certain distance above which there was no increase in power. In an actual building project, when CFRPs are implemented to masonry walls with consistent HCTs built with mortar joints, single HCT failure does not happen and loss may occur due to CFRP rupture. Thus far, the studies presented prove that the bond strength is associated with susceptibility to anchorage length and width than to the concrete or tile compressive strength. In a study experimented by Alderliesten and Benedictus (2008) on Fiber/Metal Composite Technology for Future Primary Aircraft Structures, it was confirmed that the latest developments in the aviation industry indicate a growing need for lower operating and maintenance costs. This transitions into aircraft with longer style life, longer maintenance times, and shorter period maintenance. Despite the attempts being made toward integrated vehicle health management systems, the key to overcoming these strict laws is acknowledging these factors from an initial purpose within the structural style and material choice method. High strength and firmness composite materials, including carbon fiber-reinforced polymers (CFRP), demonstrate failure strains below 2% without ductility. Overall, these studies indicate the production of potential structural materials for region applications remains a substantial distance to travel, considering the possibilities for integrating the different metallic and composite engineering materials.

Rohit and Dixit (2016) explained in their study on future aspect of natural fiber-reinforced composite. For the first time, natural fibers were used 3000 years ago in composite structures in ancient Egypt, where straw and clay were combined to create walls. Thermoplastic materials presently predominate as biofiber matrices; polypropylene, polyethylene, and polyvinyl chloride (PVC) seem to be the most widely used thermoplastics for this purpose, while phenolic, epoxy, and polyester resins are the most commonly used thermoplastic matrices. Given the low density and satisfactory, massive specific properties of natural fibers, composites derived from natural fibers have a sturdy result in the automotive and transport industries. The presence of wood flour in polyester increased the bearing capacity and was also designed to sustain bending. Still, the presence of metakaolin in wood flour polyester composite considerably decreases the durability, flexural modulus, and strength and improves moisture content.

In a study conducted by Al-Lami et al. (2018) on the eco-efficiency assessment of manufacturing carbon fiber-reinforced polymers, it was determined that there is a major opportunity for improving the eco-efficiency of the aerospace manufacturing process in both the ecological and economic aspects of sustainability. An eco-efficiency advantage is critical for introducing carbon fiber-reinforced polymers (CFRPs) in modern commercial aircraft. Life Cycle Assessment (LCA) and Life Cycle Cost Analysis (LCCA) are carried out in the sense of a representative process model built through the application of Business Process Reengineering (BPR). Based on the compiled data review, it is concluded that the carbon footprint is dominated by fiber and energy. The results of the evaluation are tested by conducting a series of validation activities.

A research conducted by Vieira et al. (2017) on strategy and management for the recycling of carbon fiber-reinforced polymers (CFRP) shows that analysis of the

volume of CFRP will have an impact on the present and potential generation of solid waste. Accessible science output has been used to recreate existing ideas and principles to express information from various sources. In this sense, the use of green composites is an alternative to the use of thermoset composites. These items are prepared from nonpetroleum product materials and are preferably made from inexhaustible sources to revisit nature later on. The aviation industry's strategic and operational actions aim to foster a more competitive market that considers the product life cycle between the design and the various post-use stages.

In a report experimented by De Rosa et al. (2008) on EMC impact of advanced carbon fiber/carbon nanotube-reinforced composites for aerospace applications, it was suggested that advanced composite materials are commonly used for both structural and functional applications in the aerospace industry. Five samples of each composite form were tested to minimize the burden of poor homogeneity and low material isotropy by averaging the different effects. It is commonly found that the distribution of measurements differs according to the various forms of composite considered. Overall, this paper indicates that carbon fiber composites' dispersion properties can be better managed by inserting carbon black and multiwall carbon nanotubes rather than increasing the fibers' length.

In general, the application of nanocomposites in aerospace industry has been widely implemented from aerospace vehicle till space station. This material has been well known due to its lightweight with significantly high strength-to-weight ratio. The high-strength, lightweight structure materials vital for aerospace sector are useful to reduce transportation and assembly costs up to billions of dollars. In this case, Table 24.2 displays recent research works reported on advanced composites for aerospace applications.

Various studies have assessed the efficacy of nanocomposite tribological coatings for aerospace applications. Njuguna (2012) collected a comprehensive information on mechanical, thermal, electrical, field emission and optical properties of polymer nanocomposites for advanced aerospace applications. It shows that a type of engineered material that exhibits high strength/weight and modulus/weight ratios compared to some metallic materials is fiber-reinforced composites. Experiments using CNTs on a fully integrated nanotube composite have shown a dramatic improvement in mechanical properties. This study reported that the inorganic layered clay technology, single and multiwalled carbon nanotube technology, carbon nanofiber technology, and metal particle technology can be categorized as nanoscale and microscale particle reinforcement technology.

In a study conducted by Rathod et al. (2017) on the potential of polymer and ceramic matrix composites for aerospace/space vehicle applications, it shows the power to tailor nanoscale materials has opened the likelihood for the subsequent generation to develop multifunctional materials that are appropriate to satisfy the aerospace industry's requirements. Nanoclays are affordable nanofillers that provide high strength, low permeability, and excellent flame-retardant properties suitable for aerospace structures. Composite materials offer chemical stability and fire resistance, apart from the advantage of low operating costs, thanks to their lightweight. Three major disadvantages in most aerospace structures limit composites'

Table 24.2 Recent development of advanced composite materials in aerospace industry

Composites	Primary functions	Additional improvements	References
Glass, graphite, and boron	Types of internal damage	High strength and high stiffness-to-weight ratios	Gdoutos (2020)
Al ₂ O ₃ particle	Porosity ratio	Enhanced the mechanical properties of composite laminate	Tosun et al. (2016)
Aluminum	Changes the microstructural	Improved modulus of elasticity, yield strength, compressive strength, hardness, and ultimate tensile strength	Koli et al. (2015)
Anisogrid (anisotropic grid)	Strong specific strength and modulus of elasticity (with regard to density)	Offer high bending rigidity and resilience during deformation and shear buckling	Vasiliev et al. (2012)
Carbon nanotubes	Electrical resistivity	Decrease the resistivity	Bellucci et al. (2007)
Carbon fiber	Strength and security	Increase in mechanical strength	Barile et al. (2019)
Polyester and epoxy	Flexural strength	Improve bending properties	Gopinath et al. (2014)
Ceramics	Healing ability	Suitable of auto-repairing upon damage evolution	Das et al. (2016)
Auxetic	Higher damping resistance	Enhanced indentation resistance and energy absorbance properties	Wang et al. (2016)
Titanium	Strength-to-weight ratio	Give high corrosion resistance	Peters et al. (2003)
Boron and graphite fiber	Lightweight	Maintain high specific strength and modulus	Cornsweet (1970)
Thermoplastic	Thermosetting adhesive bonding	Higher damage tolerance characteristics	da Costa et al. (2012)
Phenolics	Good smoke and fire resistance	Increase high-temperature resin systems	Campbell (2006)
Ceramic	Static strength	Improve ductility and fracture toughness	Rana and Fangueiro (2016)
Para aramid	Fracture toughness	Improved fracture strength, harm resistance, and strengthened impact characteristics	Yadav et al. (2020)
E-glass fabric	Electrical resistance	Lower in resistance to the fibers	von Klemperer and Maharaj (2009)
Al-cu-based alloys	Yield strength	Higher in resistance to fatigue	Zhang et al. (2018)
Chromium-molybdenum	Tensile strength	Improvements in thermomechanical processing	Boyer et al. (2015)
Softwood craft	Young's modulus	Increase the mechanical bonding of polymers	Balakrishnan et al. (2016)

(continued)

Table 24.2 (continued)

Composites	Primary functions	Additional improvements	References
Carbon nanotubes	Impact and delamination failure	High specific strength and stiffness and impart multifunctionality without substantial weight	Khan and Kim (2011)
Reinforced plastic	Mechanical characterization	It reduces delamination phenomena.	Barile and Casavola (2018)
Carbon fiber	Strength	Significantly improve the ultimate strength of surface-bonded CFRPs both in the presence and absence of plaster finishing	Camli and Binici (2007)
Polymer-ceramic	Thermo-structural application	Enhancing thermal shock resistance and thermal insulation properties	Kumar et al. (2013)
Carbon fiber	Nondestructive evaluation	Enable the production processes to be improved overall by reducing the discarded parts and saving money as a consequence	Meola and Toscano (2012)
Glass fiber	Stiffness and corrosion resistance	Improve the cutting performance	Eqbal et al. (2020)
Fiber/metal composite	Durability	Substantial weight reduction and provide better strength-to-weight ratio	Alderliesten and Benedictus (2008)
Shape-memory polymers	Thermal expansion	Allow for devices with complex shape changes to be imagined and realized	Safranski and Griffis (2017)
Aluminum alloys	Fatigue behavior	Provide combination properties of low density, specific endurance, and ease of processing	Prasad Rambabu et al. (2017)
Beryllium metal matrix	Thermal expansion	Reduced mass, quicker response rates, and increased thermal and mechanical flexibility	Parsonage (2000)
Carbon-epoxy	Fire structural performance	The tensile massive amount power of the material was better compared to the aluminum alloy when subjected to the heat flux.	Grigoriou and Mouritz (2016)
Autoclaved flax fiber	Static, fatigue, and impact behavior	The flexible and shear modules of 3.39 GPa and 1.26 GPa separately in the fire-retardant epoxy polymer used in prepreg The TGA analysis indicates a thermal stability of up to 300 °C, with subsequent significant drop in mass loss from 340 °C to 420 °C	Panzer et al. (2020)
Manufactured textile composites	Damage mechanism	Better out-of-plane characteristics and good resistance to fatigue and implications	Kelkar et al. (2006)

applicability that is more immune to electricity, lower thermal conductivity, and less resistant to impacts, affected by moisture absorption, environmental degradation, and aging over time. During this study, it had been reported that aside from structural and coating applications, nanocomposites are developed as lightweight bearings for aerospace and space applications. These are PMNCs, like PTFE/TiO₂, and CMNC coatings, like WC/DLC/WS₂. The aerospace industry requires repeatable structure features for its certification.

Researchers attempted to evaluate the impact of process optimization of functionalized MWCNT/polyetherimide nanocomposites for aerospace application. In a study conducted by Pitchan et al. (2017) on analyzing optimized extrusion processing condition for manufacturing high-performance PEI/MWCNT nanocomposite for aerospace application, it is found that better preservation of mechanical properties on gamma radiation exposure, lower mass loss under the LEO environment, and PEI/COOH-MWCNT nanocomposite was already equipped by using optimized process criteria that have enhanced mechanical and thermal properties. Thus, the PEI nanocomposite proved to be an excellent candidate for intense spatial conditions. In this study, it was reported that COOH-MWCNTs-reinforced composite showed enhanced thermal and mechanical properties along with better retention of properties upon exposure to gamma irradiation and atomic oxygen.

It is now well established from various studies that nanocomposite and nanostructured tribological materials have a variety of usage for space applications. A “chameleon” tribological coating concept has been developed, and it is found out that WC, WS₂, and diamond-like carbon (DLC) were the first “chameleon” coatings; they offered superior mechanical durability and efficiency in either space or terrestrial environmental cycling (Voevodin & Zabinski, 2005). Ytria-stabilized zirconia (YSZ) was made from the second generation of “chameleon” coatings in a gold matrix with MoS₂- and DLC-encapsulated nanosized reservoirs to address the temperature. In this study, it was reported that nanocomposite tribological coatings were designed to respond to changing environmental conditions by self-adjustment of their surface properties to maintain good tribological performance in any environment. These smart coatings have been dubbed “chameleon” because it is analogous to a chameleon changing its skin color to avoid predators. The coating changes its “skin” chemistry and structure to prevent wear.

To date, several studies have investigated the high-performance, fire-resistant polymeric nanocomposite for aerospace applications. In general, great improvement in thermal stability and fire resistivity thanks to the PBI coating of carbon/epoxy composites. To enhance thermal stability and fire resistance properties, the phenolic fabric-reinforced polymer is then coated with a nanosized calcium silicate-reinforced polybenzimidazole composite. During this study, it had been reported that after air pressure plasma treatment on the polymer, there was a considerable decrease within the contact angle and a big increase within the surface energy of the phenolic composite. After the air pressure plasma application, the concentration of hydrophilic functional groups on the phenolic composite surface increased.

A number of studies have begun to examine the high glass-transition polyurethane-carbon black electro-active form memory nanocomposite for aerospace systems,

synthesizing and demonstrating PU-CB-based thermal/electro-active SMPC with higher glass-transition temperature (Arun et al., 2019). With an increase in CB content, the density of population of the CB particles grew. It was also found that the CB particles were spread evenly inside the matrix and thus decreased the multi gap since the carbon loading increased the contribution. The inclusion of CB particles with a large surface-to-volume ratio increases the surface's energy, resulting in stronger interfacial bonding within a composite matrix packed with particles. This contributes to the creation of voids and eventually results in a loss. The greater the filler's size, the likelihood of the particles being de-wetted from the matrix increases, contributing to shear fracture. It was stated during such a study that according to the available research, the modulated SMPC showed a high glass-transition temperature, including the use of aliphatic isocyanate providing intrinsic stability against ultraviolet rays. The use of CB as a filler increases the adequacy of ultraviolet rays by consuming it and diluting it as heat without influencing the fundamental characteristics of the material.

To date, several studies have investigated the Advanced Composite in Aerospace Applications. The automobile sector is taking a significant glance at composites, and how they can assist the sector soon meets the challenging requirements for fuel efficiency (Yancey, 2016). There are requirements for robust and lightweight materials in both the aerospace and automotive sectors that can work in a rough ecosystem provided by composites. There are numerical methods of optimization available that can help designers work through all the parameters and achieve an optimized weight and output design. The results can generate geometry that is hard to make using conventional methods. With the emergence of additive layered manufacturing or 3D printing techniques, as the authors see, the future brings the possibility of producing genuinely optimized components. Concerning their use of composite materials, there are a few correlations and many distinctions between the spacecraft and automobile industries.

Thus far, a number of studies have found Advanced Composite in Aerospace Applications: Opportunities, Challenges, and Future Perspective. In research of "Integrated nanomaterials for rough thermal management: a perspective for aerospace applications" by Barako et al. (2018), aerospace vehicles have sophisticated high-power electronics that produce several thermal management problems that are most aggressive. The studies demonstrate the development and thermal conductivity of vertically stacked copper nanowires to advance heat through packed components as high-performance thermal interface materials. The authors present a vision for using rationally designed nanomaterial architectures to provide unprecedented property combinations for multiphase heat transfer in heat exchangers and high-power density thermal storage. Despite the relatively high thermal conductivity of commonly used materials, for example, the resistance of the thermal interface between GaN, SiC, and copper components continues to limit the performance of SSPAs. The evidence provided in this section indicates that the temperature control nanotechnology system model will continue to support the transfer of complicated nanoarchitectures with intentional design morphologies and engineered characteristics from dysfunctional nanomaterials including nanocomposites.

Linganiso and Anandjiwala (2016) stated in their research on the fiber-reinforced laminates in aerospace engineering that outstanding structural and functional materials, particularly in the aerospace industry, are the source of advanced composite materials (ACMs), known as advanced composites of the polymer matrix, because they reflect aerospace materials' future. GLARE's benefits include its unique weight, which is around 10% smaller than aluminum. In the future, carbon fiber-reinforced plastics will lead to even more than 50% of an aircraft's structural mass. The findings revealed that the harness of PLAeflex composites was 50% higher than PPefflex composites currently in use. Efforts should be aimed at producing composite-based aerospace components at affordable costs and through easy production methods and establishing precise modeling and simulation strategies for manufacturing and assembly process analysis and product progress monitoring to be competitive with conventional aerospace engineering products.

In research shown by Uyanna and Najafi (2020) on Thermal Protection Systems, the use of thermal protection systems for space vehicles (TPS) includes the protection of space vehicles from severe thermal loads throughout atmospheric entry/reentry. Three different active TPSs, particularly advective cooling, film freezing, and cooling with ventilation, have been studied and tested. The analysis indicates that at the stagnation stage, micro jet arrays' existence contributed to a 50% decrease in the heat flux, by looking at different materials and measurements and the subsequent ultimate surface temperature, an efficient ITPS configuration with minimal mass. They demonstrated that with oxide fiber-reinforced oxide-matrix composites, a mass reduction of 75% could be realized. Although the technology of all three TPS classes has advanced considerably since the beginning of the space programs in the early 1950s, additional investigations are needed at each category in order to ensure the protection and optimum operation of future spacecraft.

In the building of aerospace structures, composite materials are becoming more significant. Fullerene technology itself is the biggest obstacle for the ability to drive volume scale and reduce costs. In the aerospace industry, polymer composites already have tremendous applications. There is a growing practice of integrating polymer composites into the components of the aircraft. For additional property enhancements where polymer composites are lagging, research continues to take place. With their unique properties, polymer nanocomposites are emerging and are potential materials for aerospace industry appliances.

5 Current and Future Aspect of Nanocomposites as Advanced Materials in Aerospace Sectors

Nanocomposites have received much attention over the past decade as researchers search for ways to enhance the properties of engineering polymer composites while retaining its facile processing. Nanocomposites require relatively low dispersant loadings to achieve significant property enhancements, which make them a key

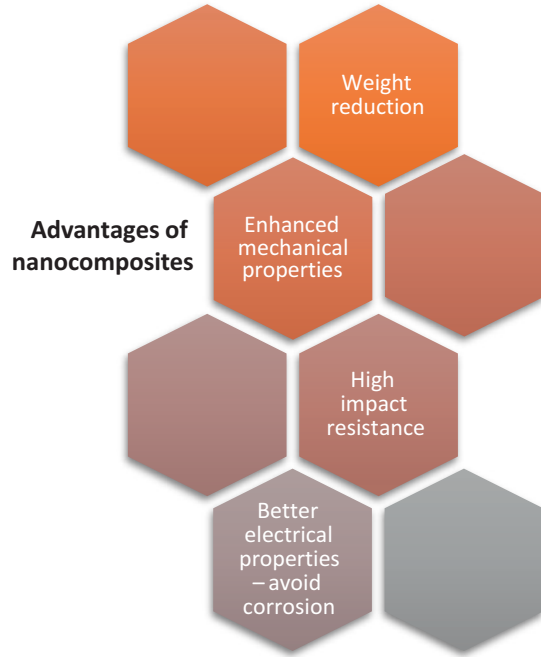
candidate for aerospace applications. Some of these enhancement include increased modulus, enhanced gas barrier properties and atomic oxygen resistance, and better thermal and ablative performance (Alaaeddin et al., 2019; Julkapli et al., 2015; Mohd Nurazzi et al., 2021; Njuguna et al., 2012).

In the aerospace industry, a variety of composites are widely used. During World War II, composites were first used in military aircraft. Nowadays, they are used in the aerospace industry for private planes and advanced commercial aircraft. And it is worth noting that fiberglass, carbon fiber, and aramid fiber are the three most popular types of composites currently available. It also is important to note that each of these categories has subtypes, allowing for a wide range of composites to be developed (Njuguna & Pielichowski, 2003). Fiberglass is a fiber-reinforced polymer composed of a rubber resin reinforced by fine glass fibers. It is also a lightweight, incredibly heavy, and durable fiber (Dwi & Syamsudin, 2019). Although the material has poorer strength properties and is less stiff than carbon fiber, it is usually less porous and the raw materials are less costly. Carbon fiber-reinforced polymer is a fiber-reinforced polymer that incorporates carbon fibers and is incredibly strong and light (Das & Roy, 2018; Harussani et al., 2020; Khalil, 2017). Other fibers, such as aramid (Cheon et al., 2020), Kevlar (Naveen et al., 2018; Nurazzi et al., 2021a), glass fibers (Sanjay & Yogesha, 2017), as well as carbon fibers, can be used in the composite. Aramid fiber is a type of synthetic fiber that is both heat resistant and solid. They are used in aerospace and industrial applications, as well as ballistic-rated body armor fabric and composites, cycling tires, and as an asbestos replacement.

5.1 The Advantages of Nanocomposites in Aviation Industry

Nanocomposite materials are increasingly being used as primary structural materials in commercial, automotive, aerospace, maritime, and recreational structures. Advanced composites do not corrode like steel, and the combination of corrosion and fatigue cracking in aluminum commercial fuselage structures is a serious concern. In the aerospace and defense industries, nano-based composites provide a variety of advantages. With today's escalating fuel costs, an aircraft's resulting fuel efficiency is becoming exceedingly significant. Excellent fatigue and corrosion resistance, as well as strong impact resistance, are other advantages. Composites have become more common in the aerospace and defense industries, with some segments projected to expand rapidly in the next 20 years (Maria, 2013). The overall composite demand is expected to quadruple at a compound annual growth rate of 11.6% in the forthcoming years, increasing USD 53.44 billion by 2027 (Market Study Report, 2021). Nanocomposite technologies have a number of advantages as stated in Fig. 24.4.

Fig. 24.4 Advantages of nanocomposites



5.2 *The Future of Nanocomposites in Aerospace Industry*

Commercial aviation is under constant strain to increase efficiency due to rising fuel prices and environmental campaigning, and weight loss is a crucial factor in the equation. Aside from the day-to-day running costs, part count reduction and corrosion reduction will simplify aircraft maintenance programs. Because of the dynamic nature of the aircraft construction industry, any incentive to lower operational costs is investigated and utilized.

GE Aviation, a global leader in jet engine manufacturing, is engaged in the assembly of massive front fans for jet engines as well as composite component manufacturing. Polymer matrix composites are a special category of composite material. They constructed carbon fiber cloth and silicone resin, and they fabricated cutting-edge manufacturing techniques and machinery (GE Aviation, 2021). HEXCEL is a specialist in lightweight composite, including advanced core parts, HexMC components, and full structures and is a market leader in carbon fiber and composite materials for commercial and defense aircraft, helicopters, and engines. HEXCEL's lightweight structures have a lot of advantages in aircraft construction (HEXCELL, 2021a). A major advantage of carbon fiber-reinforced prepreps over aluminum is the increase in fatigue performance. More than half of the Boeing 787 and Airbus A350XWB airframes are made of carbon fiber composite. The A350 XWB, JSF, F18 E/F, A380, Eurofighter Typhoon, A400M, Boeing 787, and GENX

Engines are among the most sophisticated applications supported by HexTow carbon fiber (HEXCELL, 2021b).

As Rolls Royce learned in the 1960s when the advanced RB211 jet engine with carbon fiber compressor blades collapsed catastrophically due to bird strikes, carbon fiber has a peculiar fatigue behavior and is brittle. Boeing successfully used 1500 composite parts to replace metal features in a helicopter in an experimental program (Maria, 2013). In commercial aviation, the use of composite-based parts in place of metal as part of maintenance cycles is increasingly increasing. Overall, carbon fiber is the most widely used composite fiber in aerospace applications (Khalil, 2017; Norizan et al., 2020, 2021). Blackhawk Composites is a company that makes composites. In the aviation industry, advanced composites play a crucial role. Aircraft operators, both commercial and military, have shown a need for product enhancements, and aftermarket vendors have replied with technologies that improve the durability and reliability of legacy aircraft, frequently using composites. Blackhawk Composites is one of only a few firms that has been licensed to use TORAY carbon epoxy composite material, which is used on commercial jetliners and is preferred by the FAA (Nashua, 2012).

5.3 The Development of New Nanocomposite Materials

New materials are those that have not yet been used in an “as-designed” use in aviation. Some of these materials, especially carbon nanotubes, nanoclays, and graphene-reinforced nanocomposites, have undergone in-flight testing and are on the verge of military use but have yet to achieve widespread approval by OEMs for a variety of reasons.

The amount, dispersion, and surface condition of nanoparticles have a significant impact on the rheological behavior and, by extension, the mechanical properties of nanocomposites in many instances (Dinca et al., 2012). In addition, the impact of the addition on the flexural strength and modulus of carbon fiber-reinforced composites with modified epoxy resin as a matrix are discussed. It is stressed the importance of providing an effective nanofiller dispersion and proper interfacial bonding, all of which are critical in obtaining nanocomposites with enhanced properties due to the nanofillers’ existence. Carbon nanotubes (Nurazzi et al., 2021b; Mohd Nurazzi et al., 2021) and montmorillonite-type nanoclays (Uddin, 2008) are the nanofiller agents used in rheological studies. These compounds were chosen as nanofillers because of their special properties and the benefits they offer to the composite.

Carbon nanotubes have long been anticipated as the next wave of new and innovative technologies. System designers are beginning to see the potential for using this in modern technologies for electronics and insulation in large-scale aircraft. Carbon nanotube manufacturing has many uses in aerospace and defense electronics due to its exhibited EMI shielding characteristics. For example, carbon-based composite aircraft often receives residual current from lightning strikes. Metal is

used to shield the plane; however, residual current is also there. This lightweight composite is used for EMI shielding as well as internal shielding (Shi & Liang, 2008). It provides greater insulation for the weight of a coat of paint and helps you to protect the internals of a carbon fiber-based aircraft. Single-walled carbon nanotubes (SWCNT) have extraordinary mechanical properties, with a tensile strength a hundred times that of steel. All nanotubes should be good thermal conductors along the tube axis, with a property known as “ballistic conduction” (Poncharal et al., 2002), which defined as the transport of electrons in a medium with negligible electrical resistivity due to scattering. Ballistic transport is calculated by semiconductor electronic structure but good insulators laterally to the tube axis. As compared to copper, a metal well known for its strong thermal conductivity, which transmits $385 \text{ Wm}^{-1} \text{ K}^{-1}$ (Pop et al., 2006), it has a thermal conductivity along its axis of around $3500 \text{ Wm}^{-1} \text{ K}^{-1}$. Based on their orientation, carbon nanotubes can be either metallic or semiconducting (geometry). As a result, their thermal and electrical properties are similar to other fiber-type reinforcement agents (graphite, Kevlar, SiC, and alumina fibers). CNT has an order of magnitude higher strength, elastic modulus, and fracture properties than other typical composites used in civilian and military applications. Furthermore, CNT reinforcement has been demonstrated to improve the strength of polymers and composites, allowing them to withstand more impact energy.

Nanoclay additives are useful because of their thixotropic properties; when used as fillers, they can reduce the air permeability of tires and fuel tanks and can be used to replace talc powder and titanium dioxide (Stan et al., 2012). Montmorillonite belongs to the layered silicates nanoclay class, which includes nanoparticles with an anisotropic, platelike, high-aspect ratio morphology, which improves the permeation barrier. The matrix is supposed to have improved dimensional stability at low reinforcement loading by using montmorillonite, a feature that makes it useful in the aerospace and automotive industries. One of the most significant drawbacks of layered silicates is the need for compatibilization with the resin matrix (Guo et al., 2018). Montmorillonite, like all nanoclays in its class, is a hydrophilic compound, which makes it incompatible with polymers (Jeyakumar et al., 2017). It can be altered in a variety of ways to improve its organophilicity.

Graphene is a material more and more manufacturers are incorporating into their design because of the variety of electrical applications. For one, graphene is used in epoxy resins that boost the electrical conductivity of carbon composites in fuselages. Graphene-based carbon material finds numerous applications in aerospace industry such as better barrier performance, surface technology (anti-ice/deice, anti-erosion, health monitoring, damping and protective coating for lightning, graphene sensors for heat management systems, and graphene conductors) (Aftab et al., 2019; Papageorgiou et al., 2015; Sang et al., 2019). Graphene oxide is the functionalized form of graphene which can easily be prepared by the improved Hummer’s method (Marcano et al., 2010). Graphene oxide (GO) possesses several physical and chemical fascinating features such as high stability and large surface area ($\sim 2600 \text{ m}^2/\text{g}$) with several potential applications like the parent material graphene. It is because GO has similar features like graphene with added advantage in functionalized form (Marcano et al., 2010). Graphene can be used in fuel systems of aircrafts, and

graphene oxide membranes have the selectivity for water from other liquids, i.e., as from oils, and have been used to remove the water from the fuel tanks (López-Oyama et al., 2018).

6 Application of 3D Structures in Aircrafts

The aerospace and automotive industry have shown increasing interest in three-dimensional textile composites due to excellent damage tolerance and the ability to produce near-net shape components. 3D woven composites were used to replace the expensive metal alloys resistant to high temperature and decrease 30% to 50% of the weight of rocket engines in the 1960s. Avco Company discussed 3D circular woven carbon-carbon fabric composites for airplane brakes in 1972. 3D woven carbon-carbon and carbon-reinforced silicon carbide composite components occupy an important position in aerospace propulsion systems (nozzles) and combustor for high temperatures because of their high strength at elevated temperatures, low specific mass, and low coefficient of thermal expansion.

3D woven composites are used in air engine nozzles and bracket joint. These composites provide a superior damage tolerance that allows a thin, curved blade to be produced, with consequent aerodynamic benefits. “GE90” produced by General Electric (GE) Company, a world-leading producer of jet engines, uses 3D aerodynamic modeling to evaluate designs that decrease 14 blades to 22 blades (Li & Y.B., 2012). The GE Company uses 3D woven composites for the airframe and fan casing of GE next-generation aeroengine. Boeing 787 and Airbus A350 have used 3D woven composites for the engine. The CFM International Company developed a fan blade named LEAP-X using 3D woven composites in 2012. The internal structures are the 3D woven composites for fan casing preform, including flanges.

3D woven composites provide better through-the-thickness properties and higher postimpact strength compared to the traditional 2D-laminated composites. 3D woven fabrics are given the name 3D because these fabrics have the third dimension, i.e., the prominent thickness of the fabric. Z-direction is also significant in 3D structures as X and Y dimensions. 3D woven structure is produced by the interlacement of three sets of yarns coming from three directions, i.e., longitudinal (X), cross (Y), and vertical (Z), as shown in Fig. 24.5 (Mouritz, 2012).

7 Conclusions

In conclusion, advanced composites have been widely used in aerospace applications because of their unique and influential attributes that are very beneficial to the industry, such as the possibility of substantially strengthening the impact and delamination effectiveness of FRP composites by reinforcing carbon nanotubes to the surface of the fiber/fabric at the expense of a matrix. The beneficial properties of

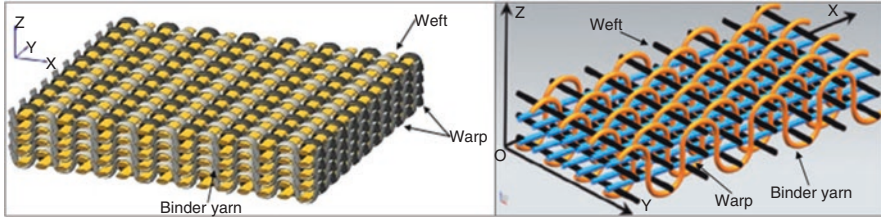


Fig. 24.5 3D woven structures (Mouritz, 2012)

carbon nanotubes that lead to this function involve their very large aspect ratio, outstanding strength and modulus, high failure strain, and special nanoscale reinforcement mechanisms. In addition, the tension and mechanical compression properties tended to improve by lowering the temperature probably associated with the thermal conductivity of the carbon fibers; the hole introduced a discontinuity in the fibers and a localized defect due to the drilling operation; the composite material performance was affected, except in this scenario, the plies were pieced tightly, minimizing the localized defect due to the drilling operation. To date, widely used fiber and matrix substances do not accomplish their full capability, although some immediate advantages are provided by fiber hybridization. However, minimal experimental work and information on how the behavior of impact damage and postimpact stress intensity distinct from impact energy and how the laminate stacking series can affect this behavior. Hybridization measured at the smallest impact energy resulted in a bilinear ductile tensile stress-strain curve and high failure strain. These remarkable findings can positively impact more opportunities and overcome many challenges of the advanced composites in the future perspective of the aerospace application.

Acknowledgments The research has been carried out under program Research Excellence Consortium (JPT (BPKI) 1000/016/018/25 (57)) provided by Ministry of Higher Education Malaysia (MOHE). Besides that, the author would like to acknowledge the support provided by Ministry of Higher Education Malaysia (MOHE) and Universiti Teknologi Malaysia (UTM) through Collaborative Research Grant (CRG), Grant No. 08G30 and CRG 30.3: Retardant coating using graphene/bamboo aerogel mixtures on SAR robotics system, grant number PY/2020/03495-R. J130000.7351.4B534.

References

- Aftab, S. M. A., Shaikh, R. B., Saifullah, B., et al. (2019). Aerospace applications of graphene nanomaterials. In *AIP conference proceedings* (p. 30002). AIP Publishing LLC.
- Aisyah, H. A., Paridah, M. T., Sapuan, S. M., et al. (2019). Thermal properties of woven Kenaf/carbon fibre-reinforced epoxy hybrid composite panels. *International Journal of Polymer Science*, 2019, 1–8. <https://doi.org/10.1155/2019/5258621>
- Alaaeddin, M. H., Sapuan, S. M., Zuhri, M. Y. M., et al. (2019). Physical and mechanical properties of polyvinylidene fluoride - short sugar palm fiber nanocomposites. *Journal of Cleaner Production*, 235, 473–482. <https://doi.org/10.1016/j.jclepro.2019.06.341>

- Alderliesten, R. C., & Benedictus, R. (2008). Fiber/metal composite technology for future primary aircraft structures. *Journal of Aircraft*, 45, 1182–1189. <https://doi.org/10.2514/1.33946>
- Ali, S. S. S., Razman, M. R., & Awang, A. (2020a). The estimation and relationship of domestic electricity consumption and appliances ownership in Malaysia's intermediate city. *International Journal of Energy Economics and Policy*, 10, 116–122. <https://doi.org/10.32479/ijeeep.8358>
- Ali, S. S. S., Razman, M. R., & Awang, A. (2020b). The nexus of population, GDP growth, electricity generation, electricity consumption and carbon emissions output in Malaysia. *International Journal of Energy Economics and Policy*, 10, 84–89. <https://doi.org/10.32479/ijeeep.8987>
- Ali, S. S. S., Razman, M. R., Awang, A., et al. (2021). Critical determinants of household electricity consumption in a rapidly growing city. *Sustain (Switzerland)*, 13, 4441. <https://doi.org/10.3390/su1308444>
- Al-Lami, A., Hilmer, P., & Sinapius, M. (2018). Eco-efficiency assessment of manufacturing carbon fiber reinforced polymers (CFRP) in aerospace industry. *Aerospace Science and Technology*, 79, 669–678. <https://doi.org/10.1016/j.ast.2018.06.020>
- Alsubari, S., Zuhri, M. Y. M., Sapuan, S. M., et al. (2021). Potential of natural fiber reinforced polymer composites in Sandwich structures: A review on its mechanical properties. *Polymers (Basel)*, 13, 423. <https://doi.org/10.3390/polym13030423>
- Amir, A. L., Ishak, M. R., Yidris, N., et al. (2021). Potential of honeycomb-filled composite structure in composite cross-arm component: A review on recent Progress and its mechanical properties. *Polymers (Basel)*, 13, 1341. <https://doi.org/10.3390/polym13081341>
- Arockiam, N. J., Jawaid, M., & Saba, N. (2018). Sustainable bio composites for aircraft components. *Sustainable Composites for Aerospace Applications*, 109–123. <https://doi.org/10.1016/B978-0-08-102131-6.00006-2>
- Arun, D. I., Santhosh Kumar, K. S., Sathesh Kumar, B., et al. (2019). High glass-transition polyurethane-carbon black electro-active shape memory nanocomposite for aerospace systems. *Materials Science and Technology (United Kingdom)*, 35, 596–605. <https://doi.org/10.1080/02670836.2019.1575054>
- Asyraf, M. R. M., Ishak, M. R., Razman, M. R., & Chandrasekar, M. (2019a). Fundamentals of creep, testing methods and development of test rig for the full-scale Crossarm: A review. *Jurnal Teknologi*, 81, 155–164.
- Asyraf, M. R. M., Ishak, M. R., Sapuan, S. M., & Yidris, N. (2019b). Conceptual design of creep testing rig for full-scale cross arm using TRIZ-morphological chart-analytic network process technique. *Journal of Materials Research and Technology*, 8, 5647–5658. <https://doi.org/10.1016/j.jmrt.2019.09.033>
- Asyraf, M. R. M., Ishak, M. R., Sapuan, S. M., & Yidris, N. (2020d). Conceptual design of multi-operation outdoor flexural creep test rig using hybrid concurrent engineering approach. *Journal of Materials Research and Technology*, 9, 2357–2368. <https://doi.org/10.1016/j.jmrt.2019.12.067>
- Asyraf, M. R. M., Ishak, M. R., Sapuan, S. M., & Yidris, N. (2021a). Comparison of static and long-term creep behaviors between balau wood and glass fiber reinforced polymer composite for cross-arm application. *Fibers and Polymers*, 22, 793–803. <https://doi.org/10.1007/s12221-021-0512-1>
- Asyraf, M. R. M., Ishak, M. R., Sapuan, S. M., & Yidris, N. (2021b). Utilization of bracing arms as additional reinforcement in pultruded glass fiber-reinforced polymer composite cross-arms: Creep experimental and numerical analyses. *Polymers (Basel)*, 13, 620. <https://doi.org/10.3390/polym13040620>
- Asyraf, M. R. M., Ishak, M. R., Sapuan, S. M., & Yidris, N. (2021c). Influence of additional bracing arms as reinforcement members in wooden timber cross-arms on their long-term creep responses and properties. *Applied Sciences*, 11, 2061. <https://doi.org/10.3390/app11052061>
- Asyraf, M. R. M., Ishak, M. R., Sapuan, S. M., et al. (2020a). Creep test rig for cantilever beam: Fundamentals, prospects and present views. *Journal of Mechanical Engineering and Sciences*, 14(2), 6869–6887.

- Asyraf, M. R. M., Ishak, M. R., Sapuan, S. M., et al. (2020b). Evaluation of design and simulation of creep test rig for full-scale cross arm structure. *Advances in Civil Engineering*. <https://doi.org/10.1155/2019/6980918>
- Asyraf, M. R. M., Ishak, M. R., Sapuan, S. M., et al. (2020c). Woods and composites cantilever beam: A comprehensive review of experimental and numerical creep methodologies. *Journal of Materials Research and Technology*, 9, 6759–6776. <https://doi.org/10.1016/j.jmrt.2020.01.013>
- Asyraf, M. R. M., Rafidah, M., Azrina, A., & Razman, M. R. (2021d). Dynamic mechanical behaviour of kenaf cellulosic fibre biocomposites: A comprehensive review on chemical treatments. *Cellulose*. <https://doi.org/10.1007/s10570-021-03710-3>
- Asyraf, M. R. M., Rafidah, M., Ishak, M. R., et al. (2020e). Integration of TRIZ, Morphological Chart and ANP method for development of FRP composite portable fire extinguisher. *Polymer Composites*, 41(7), 1–6. <https://doi.org/10.1002/pc.25587>
- Balakrishnan, P., John, M. J., Pothen, L., et al. (2016). Natural fibre and polymer matrix composites and their applications in aerospace engineering. In *Advanced composite materials for aerospace engineering* (pp. 365–383). Elsevier.
- Bar-Cohen, A., Matin, K., & Narumanchi, S. (2015). Nanothermal Interface materials: Technology review and recent results. *Journal of Electronic Packaging, Transactions of the ASME*, 137(4), 040803. <https://doi.org/10.1115/1.4031602>
- Barile, C., & Casavola, C. (2018). Mechanical characterization of carbon fiber-reinforced plastic specimens for aerospace applications. In *Mechanical and physical testing of biocomposites, fibre-reinforced composites and hybrid composites* (pp. 387–407). Woodhead Publishing. <https://doi.org/10.1016/B978-0-08-102292-4.00019-9>
- Barile, C., Casavola, C., & De Cillis, F. (2019). Mechanical comparison of new composite materials for aerospace applications. *Composites. Part B, Engineering*, 162, 122–128. <https://doi.org/10.1016/j.compositesb.2018.10.101>
- Bellucci, S., Balasubramanian, C., Micciulla, F., & Rinaldi, G. (2007). CNT composites for aerospace applications. *Journal of Experimental Nanoscience*, 2, 193–206. <https://doi.org/10.1080/17458080701376348>
- Boyer, R. R., Cotton, J. D., Mohaghegh, M., & Schafrik, R. E. (2015). Materials considerations for aerospace applications. *MRS Bulletin*, 40(12), 1055–1066. <https://doi.org/10.1557/mrs.2015.278>
- Camli, U. S., & Binici, B. (2007). Strength of carbon fiber reinforced polymers bonded to concrete and masonry. *Construction and Building Materials*, 21, 1431–1446. <https://doi.org/10.1016/j.conbuildmat.2006.07.003>
- Campbell, F. (2006). *Manufacturing technology for aerospace structural materials*.
- Cheon, J., Lee, M., & Kim, M. (2020). Study on the stab resistance mechanism and performance of the carbon, glass and aramid fiber reinforced polymer and hybrid composites. *Composite Structures*, 234, 111690.
- Cornsweet, T. M. (1970). Advanced composite materials. *Science (80-)*. <https://doi.org/10.1126/science.168.3930.433>
- da Costa, A. P., Botelho, E. C., Costa, M. L., et al. (2012). A review of welding technologies for thermoplastic composites in aerospace applications. *Journal of Aerospace Technology and Management*, 4, 255–265.
- Das, R., Melchior, C., & Karumbaiah, K. M. (2016). Self-healing composites for aerospace applications. In *Advanced composite materials for aerospace engineering* (pp. 333–364). Woodhead Publishing.
- Das, S. K., & Roy, S. (2018). Finite element analysis of aircraft wing using carbon fiber reinforced polymer and glass fiber reinforced polymer. In *IOP conference series: Materials science and engineering*. (p. 12077). IOP Publishing.
- De Rosa, I. M., Sarasini, F., Sarto, M. S., & Tamburrano, A. (2008). EMC impact of advanced carbon fiber/carbon nanotube reinforced composites for next-generation aerospace applications. *IEEE Transactions on Electromagnetic Compatibility*, 50, 556–563. <https://doi.org/10.1109/TEMC.2008.926818>

- Dinca, I., Ban, C., Stefan, A., & Pelin, G. (2012). Nanocomposites as advanced materials for aerospace industry. *Incas Bulletin*, 4, 73.
- Dwi, A. Z., & Syamsudin, H. (2019). Manufacturing fiberglass-epoxy LSU-03 aircraft propeller using hand lay-up and vacuum assisted resin transfer Moulding (VARTM) methods. In *IOP conference series: Materials science and engineering* (p. 12018). IOP Publishing.
- Equbal, A., Shamim, M., Badruddin, I. A., et al. (2020). Application of the combined ANN and GA for multi-response optimization of cutting parameters for the turning of glass fiber-reinforced polymer composites. *Mathematics*, 8(6), 947. <https://doi.org/10.3390/MATH8060947>
- Fairuz, A. M., Sapuan, S. M., Zainudin, E. S., & Jaafar, C. N. A. (2014). Polymer composite manufacturing using a pultrusion process: A review. *American Journal of Applied Sciences*, 11, 1798–1810. <https://doi.org/10.3844/ajassp.2014.1798.1810>
- Gdoutos, E. E. (2020). Composite materials. In *Solid mechanics and its applications*.
- GE Aviation. (2021). *A driving force for flight*. GE Aviat.
- George, P., Bhowmik, S., Abraham, M., et al. (2019). High-performance fire-resistant polymeric nanocomposite for aerospace applications. *Proceedings of the Institution of Mechanical Engineers, Part L: Journal of Materials: Design and Applications*, 233, 97–108. <https://doi.org/10.1177/1464420716660874>
- Gopinath, A., Senthil Kumar, M., & Elayaperumal, A. (2014). Experimental investigations on mechanical properties of jute fiber reinforced composites with polyester and epoxy resin matrices. *Procedia Engineering*, 97, 2052–2063. <https://doi.org/10.1016/j.proeng.2014.12.448>
- Grigoriou, K., & Mouritz, A. P. (2016). Comparative assessment of the fire structural performance of carbon-epoxy composite and aluminium alloy used in aerospace structures. *Materials and Design*, 108, 699–706. <https://doi.org/10.1016/j.matdes.2016.07.018>
- Guo, F., Aryana, S., Han, Y., & Jiao, Y. (2018). A review of the synthesis and applications of polymer-nanoclay composites. *Applied Sciences*, 8, 1696.
- Hamidon, M. H., Sultan, M. T. H., Ariffin, A. H., & Shah, A. U. M. (2019). Effects of fibre treatment on mechanical properties of kenaf fibre reinforced composites: A review. *Journal of Materials Research and Technology*, 8, 3327–3337. <https://doi.org/10.1016/j.jmrt.2019.04.012>
- Harussani, M. M., Sapuan, S. M., Khalina, A., et al. (2020). Review on green technology pyrolysis for plastic wastes. In *7th Postgraduate seminar on natural fibre reinforced polymer composites 2020* (pp. 50–53).
- Heister, E., Brunner, E. W., Dieckmann, G. R., et al. (2013). Are carbon nanotubes a natural solution? Applications in biology and medicine. *ACS Applied Materials & Interfaces*, 5, 1870–1891.
- HEXCELL. (2021a). HiTape® reinforcements. In [hexcel.com](https://www.hexcel.com).
- HEXCELL. (2021b). Carbon fiber. In [hexcel.com](https://www.hexcel.com).
- Hofstätter, T., Pedersen, D. B., Tosello, G., & Hansen, H. N. (2017). State-of-the-art of fiber-reinforced polymers in additive manufacturing technologies. *Journal of Reinforced Plastics and Composites*, 36, 1061–1073. <https://doi.org/10.1177/0731684417695648>
- Ilyas, R. A., Sapuan, M. S., Norizan, M. N., et al. (2020a). Macro to nanoscale natural fiber composites for automotive components: Research, development, and application. In M. S. Sapuan & R. A. Ilyas (Eds.), *Biocomposite and synthetic composites for automotive applications*. Woodhead Publishing Series.
- Ilyas, R. A., Sapuan, S. M., Asyraf, M. R. M., et al. (2020b). Introduction to biofiller reinforced degradable polymer composites. In S. M. Sapuan, R. Jumaidin, & I. Hanafi (Eds.), *Biofiller reinforced biodegradable polymer composites*. CRC Press.
- Ilyas, R. A., Sapuan, S. M., Asyraf, M. R. M., et al. (2021a). Mechanical and dynamic mechanical analysis of bio-based composites. In S. Krishnasamy, R. Nagarajan, S. M. K. Thiagamani, & S. Siengchin (Eds.), *Mechanical and dynamic properties of biocomposites*. WILEY-VCH GmbH.
- Ilyas, R. A., Sapuan, S. M., Atikah, M. S. N., et al. (2021b). Effect of hydrolysis time on the morphological, physical, chemical, and thermal behavior of sugar palm nanocrystalline cellulose (*Arenga pinnata* (Wurmb.) Merr). *Textile Research Journal*, 91, 152–167. <https://doi.org/10.1177/0040517520932393>

- Ilyas, R. A., Sapuan, S. M., Harussani, M. M., et al. (2021c). Polylactic acid (PLA) biocomposite: Processing, additive manufacturing and advanced applications. *Polymers (Basel)*, *13*, 1326. <https://doi.org/10.3390/polym13081326>
- Ilyas, R. A., Sapuan, S. M., Norizan, M. N., et al. (2019). Potential of natural fibre composites for transport industry: A potential of natural fibre composites for transport industry: A review. In *Proceedings of the Seminar Enau Kebangsaan* (Vol. 2019, pp. 2–11).
- Ilyas, R. A., Sapuan, S. M., Norraahim, M. N. F., et al. (2021d). Nanocellulose/starch biopolymer nanocomposites: Processing, manufacturing, and applications. In F. M. Al-Oqla (Ed.), *Advanced processing, properties, and application of Strach and other bio-based polymer* (1st ed.). Elsevier.
- Jeyakumar, R., Sampath, P. S., Ramamoorthi, R., & Ramakrishnan, T. (2017). Structural, morphological and mechanical behaviour of glass fibre reinforced epoxy nanoclay composites. *International Journal of Advanced Manufacturing Technology*, *93*, 527–535.
- Johari, A. N., Ishak, M. R., Leman, Z., et al. (2020a). Creep behaviour monitoring of short-term duration for fiber-glass reinforced composite cross-arms with unsaturated polyester resin samples using conventional analysis. *Journal of Mechanical Engineering Science*, *14*(4), 7361–7368.
- Johari, A. N., Ishak, M. R., Leman, Z., et al. (2020b). Influence of CaCO₃ in pultruded glass fibre/unsaturated polyester composite on flexural creep behaviour using conventional and TTSP methods. *Polimery*, *65*, 46–54. <https://doi.org/10.14314/polimery.2020.11.6>
- Julkapli, N. M., Bagheri, S., & Sapuan, S. M. (2015). Bio-nanocomposites from natural fibre derivatives: Manufacturing and properties. In *Manufacturing of natural fibre reinforced polymer composites* (pp. 233–265). Springer.
- Jusoh, A. F., Rejab, M. R. M., Siregar, J. P., & Bachtiar, D. (2016). Natural fiber reinforced composites: A review on potential for corrugated Core of Sandwich structures. In *MATEC Web of conferences*.
- Kausar, A., Rafique, I., & Muhammad, B. (2017). Aerospace application of polymer nanocomposite with carbon nanotube, graphite, graphene oxide, and Nanoclay. *Polymer-Plastics Technology and Engineering*, *56*, 1438–1456. <https://doi.org/10.1080/03602559.2016.1276594>
- Kelkar, A. D., Tate, J. S., & Chaphalkar, P. (2006). Performance evaluation of VARTM manufactured textile composites for the aerospace and defense applications. *Materials Science and Engineering: B Solid-State Materials for Advanced Technology*, *132*, 126–128. <https://doi.org/10.1016/j.mseb.2006.02.034>
- Khalil, Y. F. (2017). Eco-efficient lightweight carbon-fiber reinforced polymer for environmentally greener commercial aviation industry. *Sustainable Production and Consumption*, *12*, 16–26.
- Khan, S. U., & Kim, J. K. (2011). Impact and delamination failure of multiscale carbon nanotube-fiber reinforced polymer composites: A review. *International Journal of Aeronautical and Space Sciences*, *12*, 115–133. <https://doi.org/10.5139/IJASS.2011.12.2.115>
- Khan, T., Hameed Sultan, M. T. B., & Ariffin, A. H. (2018). The challenges of natural fiber in manufacturing, material selection, and technology application: A review. *Journal of Reinforced Plastics and Composites*, *37*, 770–779. <https://doi.org/10.1177/0731684418756762>
- Koli DK, Agnihotri G, Purohit R (2015) Advanced Aluminium matrix composites: The critical need of automotive and aerospace engineering fields. In *Materials today: Proceedings*.
- Kumar, S., Murthy Reddy, K. V. V. S., Kumar, A., & Rohini Devi, G. (2013). Development and characterization of polymer-ceramic continuous fiber reinforced functionally graded composites for aerospace application. *Aerospace Science and Technology*, *26*, 185–191. <https://doi.org/10.1016/j.ast.2012.04.002>
- Linganiso, L. Z., & Anandjiwala, R. D. (2016). *Fibre-reinforced laminates in aerospace engineering*. Elsevier Ltd..
- López-Oyama, A. B., Domínguez-Crespo, M. A., Torres-Huerta, A. M., et al. (2018). Dataset on electrochemical reduced graphene oxide production: Effect of synthesis parameters. *Data in Brief*, *21*, 598–603.
- Marcano, D. C., Kosynkin, D. V., Berlin, J. M., et al. (2010). Improved synthesis of graphene oxide. *ACS Nano*, *4*, 4806–4814.

- Maria, M. (2013). Advanced composite materials of the future in aerospace industry. *Incas Bulletin*, 5, 139–150. <https://doi.org/10.13111/2066-8201.2013.5.3.14>
- Market Study Report. (2021). Global aerospace composites market size study, by fiber type (carbon, ceramic, glass, others), manufacturing process (AFP/ATL, lay-up, resin transfer molding, filament winding, others), aircraft type (commercial aircraft, Business & General Aviation, Civi. In *Mark. Study Rep.*
- Meola, C., & Toscano, C. (2012). NonDestructive evaluation of carbon fiber reinforced polymers with Ultrasonics and infrared thermography: An overview on historical steps and patents. *Recent Patents on Materials Science*, 5, 48–67. <https://doi.org/10.2174/1874465611205010048>
- Mohd Nurazzi, N., Asyraf, M. R. M., Khalina, A., et al. (2021). Fabrication, functionalization, and application of carbon nanotube-reinforced polymer composite: An overview. *Polymers (Basel)*, 13, 1047. <https://doi.org/10.3390/polym13071047>
- Mouritz, A. P. (2012). *Introduction to aerospace materials*. Woodhead Publishing Limited.
- Narayanamurthy, V., Jeroish, Z. E., Bhuvaneshwari, K. S., et al. (2020). Advances in passively driven microfluidics and lab-on-chip devices: A comprehensive literature review and patent analysis. *RSC Advances*, 10, 11652–11680. <https://doi.org/10.1039/d0ra00263a>
- Nashua, N. H. (2012). Carbon nanotube technology moves forward. In *Military aerospace electronic system*.
- Naveen, J., Jawaid, M., Zainudin, E. S., et al. (2018). Selection of natural fiber for hybrid kevlar/natural fiber reinforced polymer composites for personal body armor by using analytical hierarchy process. *Frontiers in Materials*, 5, 52.
- Naya, F., González, C., Lopes, C. S., et al. (2017). Computational micromechanics of the transverse and shear behavior of unidirectional fiber reinforced polymers including environmental effects. *Composites. Part A, Applied Science and Manufacturing*, 92, 146–157. <https://doi.org/10.1016/j.compositesa.2016.06.018>
- Nayana, V., & Kandasubramanian, B. (2020). Advanced polymeric composites via commingling for critical engineering applications. *Polymer Testing*, 91, 106774. <https://doi.org/10.1016/j.polymertesting.2020.106774>
- Njuguna, J., & Pielichowski, K. (2003). Polymer nanocomposites for aerospace applications: Properties. *Advanced Engineering Materials*, 5, 769–778.
- Njuguna, J., Pielichowski, K., & Fan, J. (2012). *Polymer nanocomposites for aerospace applications*. Woodhead Publishing Limited.
- Norizan, M. N., Harussani, M. M., Demon, S. Z. N., et al. (2020). Carbon nanotubes: Functionalisation and their application in chemical sensors. *RSC Advances*, 43704–43732.
- Norizan, M. N., Moklis, M. H., Alias, A. H., et al. (2021). Treatments of natural fibre as reinforcement in polymer composites-short review. *Functional Composites and Structures*. <https://doi.org/10.1088/2631-6331/abff36>
- Novak, H. L., & Hall, P. B. (2003). Environmentally compatible vapor-phase corrosion inhibitor for space shuttle hardware. In *5th Conference on aerospace materials* (pp. 1–9).
- Nurazzi, N. M., Asyraf, M. R. M., Khalina, A., et al. (2021a). A review on natural fiber reinforced polymer composite for bullet proof and ballistic applications. *Polymers (Basel)*, 13, 646. <https://doi.org/10.3390/polym13040646>
- Nurazzi, N. M., Harussani, M. M., Zulaikha, N. D. S., et al. (2021b). Composites based on conductive polymer with carbon nanotubes in DMMP gas sensors—an overview. *Polimery*, 66, 85–97.
- Omran, A. A. B., Mohammed, A. A. B. A., Sapuan, S. M., et al. (2021). Micro- and Nanocellulose in polymer composite materials: A review. *Polymers (Basel)*, 13, 231. <https://doi.org/10.3390/polym13020231>
- Panzer, T. H., Jeannin, T., Gabrion, X., et al. (2020). Static, fatigue and impact behaviour of an autoclaved flax fibre reinforced composite for aerospace engineering. *Composites. Part B, Engineering*, 197, 108049. <https://doi.org/10.1016/j.compositesb.2020.108049>
- Papageorgiou, D. G., Kinloch, I. A., & Young, R. J. (2015). Graphene/elastomer nanocomposites. *Carbon N Y*, 95, 460–484.

- Parsonage, T. (2000). Beryllium metal matrix composites for aerospace and commercial applications. *Materials Science and Technology*, 16, 732–738. <https://doi.org/10.1179/026708300101508522>
- Peters, M., Kumpfert, J., Ward, C. H., & Leyens, C. (2003). Titanium alloys for aerospace applications. *Advanced Engineering Materials*, 5(6), 419–427.
- Pitchan, M. K., Bhowmik, S., Balachandran, M., & Abraham, M. (2017). Process optimization of functionalized MWCNT/polyetherimide nanocomposites for aerospace application. *Materials and Design*, 127, 193–203. <https://doi.org/10.1016/j.matdes.2017.04.081>
- Poncharal, P., Berger, C., Yi, Y., et al (2002). *Room temperature ballistic conduction in carbon nanotubes*.
- Pop, E., Mann, D., Wang, Q., et al. (2006). Thermal conductance of an individual single-wall carbon nanotube above room temperature. *Nano Letters*, 6, 96–100.
- Prasad Rambabu, N., Eswara Prasad, V. V. K., & Wanhill, R. J. H. (2017). *Aerospace materials and material technologies* (Vol. 1, p. 586). Springer. <https://doi.org/10.1007/978-981-10-2134-3>
- Rana, S., & Figueiro, R. (2016). Advanced composites in aerospace engineering. In: *Advanced composite materials for aerospace engineering*.
- Rathod, V. T., Kumar, J. S., & Jain, A. (2017). Polymer and ceramic nanocomposites for aerospace applications. *Applied Nanoscience*, 7, 519–548. <https://doi.org/10.1007/s13204-017-0592-9>
- Rauf, R., Munaf, Y., Zarina Syed Zakaria, S., et al. (2019). Analysis of the development on deconcentration in Indonesia. *Journal of Engineering and Applied Science*, 14, 7179–7186. <https://doi.org/10.36478/jeasci.2019.7179.7186>
- Rohit, K., & Dixit, S. (2016). A review - future aspect of natural fiber reinforced composite. *Polymers from Renewable Resources*, 7, 43–60. <https://doi.org/10.1177/204124791600700202>
- Safranski, D. L., & Griffis, J. C. (2017). *Applications of shape-memory polymers*. Elsevier.
- Sang, M., Shin, J., Kim, K., & Yu, K. J. (2019). Electronic and thermal properties of graphene and recent advances in graphene based electronics applications. *Nanomaterials*, 9, 374.
- Sanjay, M. R., & Yogesha, B. (2017). Studies on natural/glass fiber reinforced polymer hybrid composites: An evolution. *Materials Today: Proceedings*, 4, 2739–2747. <https://doi.org/10.1016/j.matpr.2017.02.151>
- Sapuan, S. M., Hemapriya, G., Ilyas, R. A., et al. (2021). Implementation of design for sustainability in developing trophy plaque using green kenaf polymer composites. In *Design for sustainability* (pp. 85–103). Elsevier.
- Schelling, P. K., Shi, L., & Goodson, K. E. (2005). Managing heat for electronics. *Materials Today*, 8, 30–35. [https://doi.org/10.1016/S1369-7021\(05\)70935-4](https://doi.org/10.1016/S1369-7021(05)70935-4)
- Shi, S.-L., & Liang, J. (2008). The effect of multi-wall carbon nanotubes on electromagnetic interference shielding of ceramic composites. *Nanotechnology*, 19, 255707.
- Soboyejo, W. O., Obayemi, J. D., Annan, E., et al. (2015). Review of high temperature ceramics for aerospace applications. *Advances in Materials Research*, 1132, 385–407. <https://doi.org/10.4028/www.scientific.net/amr.1132.385>
- Soutis, C. (2019). Aerospace engineering requirements in building with composites. In P. E. Erving & C. Soutis (Eds.), *Polymer composites in the aerospace industry* (pp. 3–22). Elsevier.
- Stan A, Dinca I, Ban C, et al (2012) Epoxy-layered silicate and epoxy MWCNTs nanocomposites. In: *Applied mechanics and materials*. Trans Tech Publ., pp. 160–169.
- Suriani, M., Sapuan, S., Ruzaidi, C., et al. (2021a). Flammability, morphological and mechanical properties of sugar palm fiber/polyester yarn-reinforced epoxy hybrid biocomposites with magnesium hydroxide flame retardant filler. *Textile Research Journal*, 004051752110086. <https://doi.org/10.1177/00405175211008615>
- Suriani, M. J., Radzi, F. S. M., Ilyas, R. A., et al. (2021b). Flammability, tensile, and morphological properties of oil palm empty fruit bunches fiber/pet yarn-reinforced epoxy fire retardant hybrid polymer composites. *Polymers (Basel)*, 13, 1282. <https://doi.org/10.3390/polym13081282>
- Suriani, M. J., Rapi, H. Z., Ilyas, R. A., et al. (2021c). Delamination and manufacturing defects in natural fiber-reinforced hybrid composite: A review. *Polymers (Basel)*, 13, 1323. <https://doi.org/10.3390/polym13081323>

- Suriani, M. J., Zainudin, H. A., Ilyas, R. A., et al. (2021d). Kenaf fiber/pet yarn reinforced epoxy hybrid polymer composites: Morphological, tensile, and flammability properties. *Polymers (Basel)*, *13*, 1532. <https://doi.org/10.3390/polym13091532>
- Tosun, G., Kurt, M., Fleming, S. P. I., & Scarponi, C. (2016). An overview of magnesium based alloys for aerospace and automotive applications by. *Composites. Part B, Engineering*. <https://doi.org/10.1172/JCI66327>
- Uddin, F. (2008). Clays, nanoclays, and montmorillonite minerals. *Metallurgical and Materials Transactions A: Physical Metallurgy and Materials Science*, *39*, 2804–2814.
- Uyanna, O., & Najafi, H. (2020). Thermal protection systems for space vehicles: A review on technology development, current challenges and future prospects. *Acta Astronautica*, *176*, 341–356. <https://doi.org/10.1016/j.actaastro.2020.06.047>
- Vasiliev, V. V., Barynin, V. A., & Razin, A. F. (2012). Anisogrid composite lattice structures - development and aerospace applications. *Composite Structures*. <https://doi.org/10.1016/j.compstruct.2011.10.023>
- Vieira, D. R., Vieira, R. K., & Chang Chain, M. (2017). Strategy and management for the recycling of carbon fiber-reinforced polymers (CFRPs) in the aircraft industry: A critical review. *International Journal of Sustainable Development and World Ecology*, *24*, 214–223. <https://doi.org/10.1080/13504509.2016.1204371>
- Voevodin, A. A., & Zabinski, J. S. (2005). Nanocomposite and nanostructured tribological materials for space applications. *Composites Science and Technology*, *65*, 741–748. <https://doi.org/10.1016/j.compscitech.2004.10.008>
- von Klemperer, C. J., & Maharaj, D. (2009). Composite electromagnetic interference shielding materials for aerospace applications. *Composite Structures*, *91*(4), 467–472. <https://doi.org/10.1016/j.compstruct.2009.04.013>
- Wang, Z., Zulifqar, A., & Hu, H. (2016) Auxetic composites in aerospace engineering. In *Advanced composite materials for aerospace engineering*.
- Yadav, R., Tirumali, M., Wang, X., et al. (2020). Polymer composite for antistatic application in aerospace. *Defence Technology*, *16*(1), 107–118.
- Yancey, R. N. (2016). *Challenges, opportunities, and perspectives on lightweight composite structures: Aerospace versus automotive*. Elsevier Ltd..
- Zainuddin, S., Mascunra Amir, A., Kibi, Y. R., et al. (2019). Social engineering model of natural resources management of Palu City. *Journal of Engineering and Applied Sciences*, *14*, 275–279. <https://doi.org/10.36478/jeasci.2019.275.279>
- Zhang, X., Chen, Y., & Hu, J. (2018). Recent advances in the development of aerospace materials. *Progress in Aerospace Science*, *97*, 22–34.

Index

A

- AA 6061/cenosphere composite, 198
- ABD stiffness matrix, 152
- Acrylic polymers, 283
- Acrylic resin, 284
- Addition polymerization, 282
- Additive manufacturing (AM), 134, 456, 457, 477
 - LMD, 436
 - 3D object building technology, 435
- Adiabatic shear failures, 264
- Advanced aerospace materials challenges
 - corrosion, 332
 - fretting wear, 333, 334
 - SCC, 333
- Advanced composite materials (ACMs), 485
 - and aerospace applications, 471, 476–485
 - air-based and space-based vehicles, 473
 - carbon-reinforced polymer composites, 472
 - electronic payloads, 473
 - energy supply, 473
 - FRPs, 474, 475
 - greenhouse gas emissions, 471
 - ICAO, 472
 - nanocomposite TIMs, 473
 - thermoplastics, 473
- Advanced composites
 - ACMs (*see* Advanced composite materials (ACMs))
 - advancements, 335
 - in airbus, 326
 - mechanical properties, 335
- Advanced composites of polymer matrix, 485
 - Advanced polymer composite, aerospace engineering applications
 - Airbus A380, 5, 6
 - biobased polymer, 5
 - biocomposites, 10, 12, 13
 - conventional metal alloy replacement, 17
 - conventional metal materials, aircraft structures, 5
 - feature, 17
 - future, 16–17
 - geopolymer, 14–16
 - reinforcing materials, 5
 - synthetic polymer, 5
 - thermoplastics, 9, 10
 - thermoset (*see* Thermoset composite) vibration and thermal properties, 5
 - Aerial vehicle, 141
 - Aerodynamic loading, 285
 - Aerospace applications, 445
 - machining, fibrous composites (*see* Machining of fibrous composites)
 - Aerospace business, 472
 - Aerospace components, 320
 - Aerospace engineering, 281, 320, 372
 - Aerospace industry, 319, 321, 369, 381, 486–488
 - Aerospace materials, 320
 - advancement, 334
 - impact, 334
 - Aerospace polymers, 282
 - Aerospace-grade composites, 122
 - Aerospace structures, 485
 - Aerospace use, 472
 - Agricultural waste fiber, 17

- Air-based and space-based vehicles, 473
- Airbus, 3, 377, 378
- Airbus Hamburg, 329, 330
- Airbus model A350 XWB, 326
- Aircraft, 4, 7, 373, 476
 - elastomers, 283
 - interior parts, 282
 - overhead luggage storage containers and partitions, 285
 - polymers, 282
 - radar, 284
 - structural adhesive, 284
 - structure, 282
 - thermoplastic polymers, 283
 - thermoset polymers, 283
 - wood, 282
- Aircraft components, 372
- Aircraft construction industry, 487
- Aircraft engines, 334
- Aircraft interior parts, 291
- Aircraft materials, 374
- Aircraft operators, 488
- Aircrafts
 - lightweight materials, 285
 - strength-to-weight ratio, 281
 - wood, 281
- Aircraft structure components
 - Fuselage, 288
 - materials, 287
 - stress resistance, 287
 - tail, 288
 - undercarriage, 288, 289
 - wings, 288
- Al 6061/Al₂O₃p MMC, 196
- Al 6063/SiCp MMC, 197
- Al alloy skin production, 326
- Al and Ti metal matrices, 268
- Al composites, 239
- Al/10% wt. ZrO₂(P)-MMC, 211, 215–218
- Al/ceramic composites, 238
- α-phase to β-phase allotropic modifications, 225
- Al/SiC MMCs, 197
- Al/SiC/RM composites, 241
- Al-15%Mg₂Si-xYSZ hybrid composite, 412
- Al-20%Mg₂Si in situ composite, 388
- Al-20%Mg₂Si-xB₄C hybrid composites
 - agglomeration characteristics, 408
 - B₄C addition, cooling curves
 - cooling rate calculation, 393
 - first and second derivative curves, 392–394
 - growth temperature (T_G), 393, 395
 - nucleation temperature (T_N), 393, 395
 - primary Mg₂Si particles
 - formation, 393–396
 - solidification, 393
 - casting route, 408
- EDS line scan analysis, 409
- fractography, 413
- materials, 388, 406
- methods
 - composite fabrication, 388
 - composites fabrication, 406, 407
 - mechanical tests, 407
 - microstructure characterization, 389
 - microstructure observation, 407
 - thermal analysis, 389
 - wear test, 407
- microstructural evolution, 389, 390
- modification mechanisms, B₄C addition
 - clustering, 401
 - crystal structures, 397
 - EDS analysis, 397
 - elemental mapping, 399
 - growth, 398, 400, 401
 - nucleation, 396, 398
 - particles agglomeration, 401
 - porosities, 401
- optical images, 408, 410
- primary Mg₂Si particles, 401, 408
 - aspect ratio, 408, 411
 - average density, 408, 411
 - average sizes, 408, 411
- primary Mg₂Si particles
 - characteristics, 392
- quantitative analysis, microstructure, 390, 391, 393
- refine primary Mg₂Si size, 417
- SEM, 409
- tensile fracture surface, 417
- tensile properties, 410, 412, 413, 417
- UTS, 412
- Vickers hardness values, 408, 411
- wear behavior
 - abrasive wear, 417
 - COF, 415, 417
 - delamination, 417
 - wear rate, 414, 415
 - worn surface, 416, 417
- XRD results, 391
- Al2024/SiC/red-mud composites, 252
- Al2219/SiC/Gr hybrid composites, 239
- Al6061/B₄C composites, 238
- Al6061-based hybrid composites, 238
- Al-based alloys, 333–335
- Al-based composite, 334
- Al-based hybrid composites (Al/SiC/Gr), 239

- Alkaline/acid pre-treatment, 187
 - Alkaline etching, 186
 - Alkaline treatment, 360
 - Alkali-treated sisal/coconut sheath/banana combination, 292
 - Al-Mg₂Si composite, 387
 - Al-Mg₂Si in situ composite, 388
 - Al-SiC composite, 164
 - Aluminium, 186
 - Aluminium alloy (AA 2024), 180, 198–200
 - Aluminium-based FMLs, 181
 - Aluminium matrix composites (AMCs)
 - demand, 237
 - elastic modulus and strength, 237
 - higher abrasion resistance and strength, 237
 - machining characteristics, 238
 - machining response, 238
 - mechanical and wear characteristics, 237
 - Aluminum, 334
 - Aluminum alloy-based composites, 328
 - Aluminum metal matrix composites, 163
 - Aluminum honeycomb, 294
 - Aluminum matrix composites (AMCs), 387
 - Aluminum metal matrix composites, 163
 - B₄C particles, 406
 - mechanical and fatigue properties, 405
 - Mg₂Si, 406
 - physical and mechanical properties, 405
 - reinforcing materials, 405
 - See also* Metal matrix composite (MMC)
 - Aluminum nitride (AlN), 331
 - Amorphization trajectory, 271
 - Analogous techniques, 333
 - Analysis of variance (ANOVA), 233, 247
 - Animal-based fibres, 132
 - Anodising process, 187
 - ANOVA analysis, 255
 - ANOVA-based quadratic regression
 - modeling, 436
 - ANOVA model, 235, 250
 - Aramid, 342
 - Aramid fiber composites, 285
 - Aramid fibre-reinforced aluminium laminate (ARALL), 178, 180, 189
 - Aramid fibers, 368, 474, 486
 - Armor structure system, 24, 241
 - Artificial aging, 200
 - ASTM D792-13 standard, 315
 - ASTM standard, 229
 - Atomic force microscopy (AFM), 453
 - Autoclave curing, 294, 296
 - Autoclave molding, 303, 317
 - Autoclave process, 178, 182
 - Automated fiber placement, 294–296
 - Automated tape layup, 294, 295
 - Automation in CFRP, 457, 458
 - Automobile sectors, 484
 - Automotive applications, 133
 - Average surface roughness (ASR), 249
 - Aviation industries, 5, 320, 374, 486, 487
 - AZ63 magnesium alloys
 - applications, 163
 - ceramic fraction, 163
 - chemical composition, 165
 - CNTs, 165
 - composite materials, 164
 - composite tests
 - double shear, 168, 170–172
 - flexural, 168, 169, 171–173
 - hardness, 167, 170, 171
 - Izod impact, 167, 170
 - tensile, 169, 172, 173
 - compressive force, 164
 - flexural modulus/flexural strength, 164
 - freezing temperature, 163
 - hand layup method, 164
 - impact behavior, fabricated material, 164
 - mechanical properties, 165
 - multi-walled carbon nanotubes, 165
 - SiC, 163, 164
 - specimen preparation
 - materials, 165, 166
 - stir casting, 166
 - stir casting technique, 164, 174
 - strengths, 163
 - tensile properties, magnesium alloys, 164
 - tensile strength, 164
 - tensile test, 164
 - thermal expansion, low coefficient, 163
 - ultrasonic waves, 164
- B**
- Ball milling, 452
 - Ballistic conduction, 489
 - Ballistic transport, 489
 - Ball-powder ratio (BPR), 265
 - Bamboo fibres, 138
 - Banana and pineapple leaf fibres, 132
 - Banana fiber-reinforced epoxy hybrid composites laminates, 287
 - Barely visible impact damage (BVID), 153, 154, 161
 - Basalt fibre, 133
 - Basket-weave-like Widmanstätten structures, 232
 - Bayer's process, 242

- B₄C particles, 388, 390, 400, 406, 412, 413
 Beam models, 427
 B elements, 398, 400
 Bimodal microstructure, 436
 Biobased polymer, 5
 Biocomposite material, 373–375
 Biocomposites
 aerospace applications, 12
 aircraft components, 17
 aircraft interior applications, 13
 aircraft parts, 12
 auxiliary materials, aerospace applications, 12
 aviation interior applications, 290
 biological origin, 11
 categories, 289
 classification, 11, 12, 135, 136
 FST, 12
 glass fiber-reinforced plastic, 13
 hybrid (*see* Hybrid biocomposites)
 low fire resistance, 290
 natural fibers
 chemical compositions, 12
 cost and strength, 12
 properties, 12, 13
 treatment, 13
 PALF, 13
 primary and secondary structures, 12
 raw materials, 11
 renewable materials, 10
 rice husk, epoxy, 13
 silane-treated rice husk-reinforced epoxy composite, 13
 synthetic fibers and polymers, 290
 Biodegradability, 140
 Biodegradable polymers, 343
 Biofiber matrices, 479
 Biomimicry, 377, 380
 Bismaleimide (BMI), 7
 Blackhawk composites, 488
 Boeing 787, 3, 4, 327, 371
 Bone, 378
 Booster blade, 94
 Bramfitt's two-dimensional lattice misfit theory, 398
 Brinell hardness test, 203
 Business Process Reengineering (BPR), 479
- C**
 Calendaring and high-speed homogenization, 452
 Carbon arc discharge, 450
 Carbonaceous nanofillers, 447
 Carbon-based materials, 450
 Carbon-based nanocomposites, 375
 Carbon-based nanofillers
 catalytic reactivity, 448
 chemical reactivity, 448
 CNF, 448, 449
 CNT, 448, 450, 451
 crystalline and amorphous forms, 447
 electrical properties, 448
 filler-reinforced hybrid CFRP composite properties, 448
 GO, 448
 graphene, 448, 451, 452
 mechanical properties, 448
 polymer adhesion, 448
 RGO, 448
 Carbon-carbon π network, 462
 Carbon composites, 2
 compressive and tensile behaviour, 59
 Carbon-epoxy composite laminates, 304
 Carbon-epoxy composite laminates manufacturing, RTM technique
 fully cured carbon-epoxy composite panels, 305, 306
 materials, 304
 mold development, 304–305
 practical challenges, 307
 semi-cured prepregs, 306, 307
 Carbon-epoxy composite laminates, compression molding
 challenges, 315
 cure cycle–140°C, 311
 cure cycle–160°C, 311
 manufacturing, 310
 materials, 309
 physical consistency parameters evaluation, 312, 315
 prototype studies, 309
 resin cure cycles, 309
 semi-cured prototypes, 310
 Carbon-epoxy prepreg layups, 316
 Carbon fiber-based aircraft, 489
 Carbon fiber (CF), 1, 7, 15, 326, 346, 445, 472
 Carbon fiber-epoxy composites, 323
 Carbon fiber epoxy composite prepreg material (IM7-8551), 96
 Carbon fiber polymer matrix composites, 334
 Carbon fiber polymeric composites, 303
 Carbon fiber-reinforced composites, 488
 Carbon fiber-reinforced plastic (CFRP), 16, 111, 264, 285, 368, 369, 380, 474, 478–480, 485, 486
 advantages, 445
 aerospace applications, 445
 automation, 457, 458
 carbonaceous nanofillers, 447

- carbon-based nanofillers, 447–452
- CF acts, 445
- CNT, 446
- components, 445, 446
- electrical and thermal conduction, 446
- electrical properties, 461, 462
- fabrication method, 447
- graphene, 446
- manufacturing (*see* CFRP manufacturing)
- mechanical properties, 446, 447, 458–460
- morphing/compliant, 445
- nanofillers, 452, 453
- nanofillers-incorporated CFRP hybrid
 - composite mechanism, 462, 463
- nano-form carbon nanomaterials
 - synthesis, 446
- nanomaterials, 446
- smart polymer matrix and processing
 - methods, 445
 - thermal properties, 459, 460
- Carbon fibre-reinforced aluminium laminate (CARALL), 180, 184, 187–189
- Carbon fibre-reinforced composites, 59
- Carbon fibre-reinforced polymer (CFRP)
 - composites, 59, 152
- Carbon nanofibers (CNF), 448, 449, 478
- Carbon nanotube reinforcement, 424
- Carbon nanotube-reinforced aluminium (CNTs/Al), 274
- Carbon nanotube-reinforced polymer
 - composite, 285
- Carbon nanotubes (CNT), 264, 331, 424, 446, 448, 450, 451, 477, 488
 - aluminum composite, 165
 - ball milling process, 165
 - chemical functionalization, 447
 - green specimen, 165
 - nano-ferrous composite, 165
 - stir casting, 165
 - structure, 448
- Carbon plastics, 476
- Carbon-reinforced polymer composites, 472
- Carbon-woven roven reinforcement, 306
- Casting process, 242–244
- Catalyst-driven chemical vapor deposition (CCVD), 449
- CB particles, 484
- Cellulose, 136
- Cellulose fibres, 132
- Cellulose nanocrystal (CNC), 137
- Cellulose nanofibre (CNF), 137
- Cellulose nanofibre/random cellulose nanofibre (CNC-CNF)
 - biocomposite, 137
- Cellulosic fibre hybrid composites, 137
- Cellulosic fibres, 136, 137
- Cellulosic/synthetic fibre (hybrid)-reinforced biocomposites, 135–137
- Central composite design (CCD), 204
- Ceramic matrix, 480
- Ceramic matrix composite (CMC), 331, 334, 373
- Ceramic nanocomposites, 373
- Ceramic reinforcement material, 388
- Ceramics composites in aerospace industry
 - components, 330
 - dimensional permanence, 330
 - graphene platelets, 331
 - lightweight turbine elements
 - production, 330
 - materials, 330
 - MMCs, 331
 - windshield coatings, 332
- CFRP aerostructures
 - impact damage, 152, 153
- CFRP fin box, 326
- CFRP laminates
 - BVID, 153, 161
 - drilling-related defects, 160
 - FEA
 - ANSYS, 154
 - boundary conditions, 154, 155
 - hole setups, 154, 155
 - quadratic tetrahedral mesh, 155
 - RH-to-VH distance, 154
 - with no holes, 155, 156
 - holes, 158
 - hole-to-hole interaction, 161
 - mechanical properties, 153
 - repair methods, 153, 154
 - resin-injection method, 161
 - resin-injection protocol, 160
 - RH-to-VH vs. VH-to-VH, 158, 159
 - Saint-Venant's theory, 160
 - stress pattern, 155
 - stress pattern, FEA
 - experimental study, 159
 - failure modes, 160
 - holes, 159, 161
 - hole-to-hole distance, 161
 - 1 RH and 4 VHs, 157, 158
 - 1 RH and 5 VHs, 157, 158
 - 1 RH and 6 VHs, 158, 159
 - RH-to-VH vs. VH-to-VH, 159
 - VHs, 161
 - with 1 RH, 156, 157
 - stress patterns, 155
 - VHs, 161

- CFRP manufacturing
 - AM, 456, 457
 - compression molding, 454
 - ERM, 455
 - filament winding, 456
 - open contact molding, 453, 454
 - pultrusion, 456
 - RTM, 454
 - VARTM, 455
- Challenges, 475–477, 484
- Characteristic basket weave (Widmanstätten)
 - $\alpha+\beta$ network, 266
- Charpy impact test, 376
- Chemical means, 452
- Chemical treatments, 186
- Chip formation, 252
 - composite samples, 255
 - cutting parameters, 255
 - extensive surface damage, 256
 - machined surface, 257
 - parametric conditions, 256
 - RM fraction, 256
 - SEM images, 256
 - SEM micrographs, 257
 - size and depth, 255
- Chip removal mechanisms, fibrous composites
 - cantilever bending, 113, 114
 - composite-related stacks, 116
 - compression stresses, 113
 - cut surface morphologies, 115
 - cutting direction, 113
 - cutting load, 114
 - cutting sequence strategy, 116
 - fiber cutting relation, 115
 - fiber-free surface, 114
 - fiber orientation, 113, 114
 - interfacial debonding, 116
 - interlaminar debonding, 114, 116
 - machined surfaces, 116
 - machining speed, 114
 - metallic alloy benefits, 116
 - microcracks, 114
 - orthogonal cutting, 113–115
 - shear-induced fracture, 114
 - tool rake face, 113–115
 - tool tip attacks, 116
- Chromic-acid anodising (CAA), 187
- Chromic-sulphuric acid etching, 186
- Circular element, 35
- Civil and military aircraft, 369
- Civil aviation technologies, 324
- Classical laminate theory (CLT), 152, 427, 428
- Clay, 26
- Clay dispersion, 40, 52
- Clay/polymer nanocomposites, 55
- Cleavages, 82
- CMNC coatings, 483
- CNC lathe machine, 245, 246
- CNT-added glass fiber/epoxy
 - nanocomposite, 424
- CNT polymer, 240
- CNT-reinforced epoxy nanocomposite, 424
- CNTs/matrix thermal conductance, 272
- CNTs-reinforced composite, 275
- CNTs-reinforced MMCs, 264
- CO₂ emission, 341
- Coated brass wire (CuZn50) electrode, 196
- Coconut coir fibre, 132
- Coefficient of friction (COF), 415, 417
- Coefficient of thermal expansion (CTE), 451
- Coir and kenaf fibres, 129
- Coir fibre, 138
- Cold Hibernated Elastic Memory (CHEM), 376
- Collagen, 132
- Commercial transport aircraft, 3
- Completely biocomposites, 289
- Completely biodegradable/biocomposites, 135
- Complex loading systems, 23
- Composite compressor blade, 94, 95
 - automatic node-to-surface contact, 104
 - bird strike loading, 105
 - cylindrical-shaped object, 103
 - design criterion, 103
 - FEA, 105
 - frontal fan blades, 103
 - gelatin bird impact, 104
 - strain allowable, 105, 106
 - type, 103
 - typical plate-level bird strike analysis, 104
 - use, 106
- Composite fabrication, 388
- Composite fan blade, 93–96
 - camber change, 100
 - characteristic distance, typical notch geometry, 103
 - coupling coefficients optimization, 101
 - design criteria, 96
 - embedded foam inserts, 97–100, 106
 - notches, 106
 - panel-level entitlement, camber, 101
 - passive morphing, 99–101, 106
 - ply drop design, 96–98, 106
 - with wavy edges, 101, 102
- Composite fan platform, 94, 95, 105, 107
- Composite manufacturing industries, 240
- Composite materials, 1, 87, 177, 196, 367
 - A310 elevator, 3

- A320 airframe, 3
 - advancements, 321
 - advantages, 320
 - aerospace applications, 320, 321, 381
 - airbus, 3
 - aircraft, 4, 368
 - aircraft components, 381
 - aircraft construction, 16
 - aircraft fuselage, 4
 - airframe, 4
 - airplanes, 368
 - benefits, 4
 - biocomposite, 373–375
 - Boeing 787, 3, 4
 - Boeing B787, 368
 - CMC, 373
 - commercial transport aircraft, 3
 - definition, 320
 - demand, 320
 - design, 2
 - environmental impact, 376, 377
 - fiber architectures, 4
 - fuel consumption, 368
 - geopolymer composite production, 381
 - hybridisation, 179, 180, 190
 - individual materials, 149
 - laminate composite structure, 4
 - lesser airframe weight, 5
 - light alloy blades *vs.* composite blades, 2
 - market, 321, 322
 - material phases, 149
 - materials distribution
 - Airbus A350 *vs.* Boeing 787, 369
 - matrix, 149
 - mechanical properties, 341
 - military aircraft, 1
 - MMC, 372, 373
 - modern commercial airplanes, 321
 - nanocomposite, 375
 - nanotechnology development, 16
 - natural, 367
 - natural fiber applications, 342
 - PMC (*see* Polymer matrix composite (PMC))
 - properties, 4
 - reduction, fuel consumption, 4
 - reinforcement, 149
 - self-healing composites, 381
 - SMM, 375, 376
 - strength, 4
 - use, 368
 - Composite's density, 349
 - Composites, 255
 - Composites fabrication, 406, 407
 - Compression molding, 26, 28, 303, 317, 454
 - Computer-aided CCTA technique, 388
 - Computer-aided speckle interferometry (CASI), 62
 - Condensation polymerization, 282
 - Conductive nanofillers, 16
 - Continuous fibres, 150
 - Control surfaces, 285
 - Conventional synthetic-based composite, 342
 - Copolymerization, 286
 - Copper (Cu)
 - antibacterial action, 226
 - application areas, 225
 - corrosion resistance, 226
 - electrical conductivity, 226
 - heat and electricity conductor, 225
 - mechanical properties improvement, 226
 - XRD analysis, 226
 - Copper-nickel material across, 226
 - Copper-titanium oxide, 226
 - Corrosion, 332
 - Coupling agent, 187, 188
 - Coupling stiffness matrix, 152
 - COVID-19 virus outbreak, 321
 - Crack propagation, 356
 - Critical thrust force (CTF), 117
 - Cu solid solution, 226
 - Cu66V34 filler metal alloy, 226
 - Cu-rich matrix, 226
 - Curing agent, 371
 - Cu-Ti alloys, 226
 - Cutting depth (C), 251
 - Cutting forces/temperatures, 116, 117, 122
 - Cutting mechanisms, 252
- D**
- Damage formation, 118
 - Data acquisition system, 61
 - Debonding, 255
 - Delamination, 36, 37, 122, 294, 422, 428, 478
 - Delamination area, laminates
 - energy absorption, 42
 - higher resistance, 42
 - impact velocity, 42, 43
 - interlaminar stress, 41
 - nanomaterials, 42
 - nano-reinforcement, 42
 - petal formation, 42
 - projectile perforation, 42
 - resonance frequency levels, 42
 - with clay, 42
 - without clay, 41
 - Delamination damage, 118

- Deposition techniques, 436
- Design criteria, 334
- Design methodologies, composite structures in
 - aircraft engines
 - challenge, 96
 - compressed air, 93
 - compressor blade, 94, 95 (*see also* Composite compressor blade)
 - coupon-level static test results *vs.* blade-level actual test results, 106
 - design lab-level coupons, 96
 - fan blade, 93–96 (*see also* Composite fan blade)
 - fan platform, 94, 95, 105
 - fan sucks, 93
 - FEA, 106
 - fundamental concept, 106
 - loads/boundary conditions, 106
 - Design of experiment (DOE), 229, 239
 - Desirability-based RSM technique, 240
 - Diamond-like carbon (DLC), 483
 - Digital image correlation (DIC) system, 428
 - digital image processing, 61
 - full-field strain measurement, 88
 - non-interferometric optical technique, 61
 - parameters, 63
 - Phantom® V611 camera, 63
 - pixel grey value distributions, 62
 - Digital speckle correlation method (DSCM), 62
 - Digital vernier caliper, 200
 - Diglycidylether of bisphenol A (DGEBA), 60, 68
 - Discontinuous fibres, 150
 - Dispersion mechanisms, 27
 - Double shear test, 168, 170–172
 - Double-walled carbon nanotubes (DWCNTs), 450, 478
 - Drill bits, 117
 - Drilling operation, 120
 - Dry surface treatments, 188, 189
 - Dry turning operations, 241
 - DSC dynamic scan, 311
 - Dynamic loading, 23, 88
 - Dynamic mechanical properties, 87
 - Dynamic tensile studies, 87
- E**
 - Eco-efficiency assessment, 479
 - Eco-friendly, 134, 140
 - EDS spectrum, 245
 - Efficient stoppage technique, 335
 - Elastomers, 283, 284, 322
 - Electric arc discharge, 450
 - Electrical properties
 - CFRP, 461, 462
 - Electrochemical treatment, 187
 - Electrodeposition resin molding (ERM), 455
 - Electromagnetic (EM) radiation, 371
 - Electromagnetic forces, 448
 - Electromagnetic radiation, 285
 - Electromagnetic risks, 327
 - Electromagnetic waves, 284, 297
 - Electron dispersive spectrum (EDS), 244
 - Electronic payloads, 473
 - Electronic speckle photography (ESP), 62
 - Electrophoretic deposition (EPD), 453
 - Electrospinning, 449
 - Embrittlement, 232, 235
 - EMI shielding, 371, 461, 488
 - End-of-life (EOL), 421
 - Energy absorption, 23
 - Energy-dispersive X-ray (EDX) spectrometer, 200, 201, 214–220
 - Energy quantization, 448
 - Energy supply, 473
 - Engineered material, 373, 480
 - Engineering applications, 240, 341
 - Engineering composite, 4
 - Engineering materials, 225
 - Epoxy/clay nanocomposites, strain rate sensitivity
 - brittle fracture, 66
 - deformation, 65
 - drop mass, 64
 - intramolecular configuration, 65
 - load and strain histories, 65, 66
 - quasi-static loading, 64, 65
 - strain contour plots, 65, 67
 - strain–time curves, 64
 - stress–strain responses, 65, 66
 - tensile studies, 64
 - Epoxies, 131, 132
 - Epoxy matrix, 477
 - Epoxy nanocomposites, 56
 - Epoxy resin, 56, 282–284, 371
 - Epoxy tensile properties, clay effects
 - quasi-static loading, 70
 - stress–strain responses, 70
 - tensile modulus, 70, 71
 - tensile strength, 72, 73
 - Epoxy tensile properties, high strain rate effects
 - clay nanocomposites, 69
 - elastic modulus, 68
 - quasi-static, 68
 - tensile modulus, 68

- tensile strength, 68, 69
 - thermosetting resins, 68
 - Epoxy/organoclay mixture, 60
 - Epoxy-based resins, 131
 - Epoxy-carbon prepreps, 317
 - Ethylene-Methacrylic Acid (EMAA) copolymer, 380
 - Excimer laser texturing, 188
 - Extensional stiffness matrix, 152
 - Externally studentized residuals vs. predicted values, 234
- F**
- Fabricate kenaf fibre, 134
 - Face-centered cubic (FCC), 400
 - Fe-CNT metal matrix composite, 165
 - Federal Aviation Administration (FAA), 10, 12, 153, 177
 - fire resistance, 15
 - non-flammable properties, 15
 - Federal Aviation Regulations (FAR), 15
 - Feed rate (D), 251
 - Fiber area analysis, 36
 - Fiber cellulose, 374
 - Fiber hybridization, 346
 - Fiber-matrix interface, 297
 - Fiber metal laminates (FMLs), 111, 323, 334
 - aerospace sectors (*see* FMLs in aerospace sectors)
 - aluminium, 178
 - autoclave process, 178
 - carbon fibre, 178
 - characteristics, 178
 - fatigue and impact properties, 177
 - GLARE, 178
 - natural fibres, 191
 - non-hybrid synthetic fibre-based, 190
 - typical metal layers, 177
 - Fiber-polymer composites, 323, 334
 - Fiber-reinforced composites (FRCs), 320
 - aeroengines, 93
 - aerospace applications, 303
 - aerospace engineering, 93
 - aircraft engine cross section, 93, 94
 - automotive parts, 135
 - cellulosic/synthetic fibre, 135–137
 - critical attributes, 134
 - epoxy and carbon, 303
 - innovation, toughened resins, 93
 - matrix, 134
 - mechanical properties, 135
 - PMCs, 134
 - properties, 93
 - synthetic fibre-reinforced composites, 135
 - Fiber-reinforced geopolymer composite, 16
 - Fiber-reinforced PLA nanocomposite mat arrangement, 351
 - Fiber-reinforced plastics, 4
 - Fiber-reinforced polymer composite materials, 17, 370
 - Fiber-reinforced polymer composites, 285, 342, 426
 - Fiber-reinforced polymer nanocomposites, 42
 - Fiber-reinforced polymers (FRPs), 303, 342, 474, 475, 477, 478
 - Fiber-reinforced thermoset polymer composite, 7, 8
 - Fibres, 150
 - Fibrous polymer composite materials, 17
 - Field-assisted sintering technique (FAST), 265
 - Filament winding, 290, 294, 295, 456
 - Film adhesives, 284
 - Finite element analysis (FEA), 3, 153–155, 157–161
 - Finite element model, 427
 - Fire resistance, 282
 - Fire-resistant geopolymer composite materials, 17
 - Fire-resistant polymeric nanocomposite, 483
 - Fire, smoke, and toxicity (FST), 10
 - First-order shear deformation theory (FSDT), 427
 - Flame-retardant additives, 282
 - Flammability, smoke density, and toxicity (FST), 12
 - Flax fiber, 343
 - fiber treatment, 344
 - vs. glass fibers, 344
 - poor matrix adhesion, 344
 - properties, 344
 - specific tensile strength, 344
 - wax, 344
 - Flax/Kevlar hybrid PLA nanocomposite, 356
 - Flexural modulus, 355
 - Flexural strength, 355
 - Flexural test, 168, 169, 171–173, 352
 - FMLs in aerospace sectors
 - advanced sandwich laminates, 190
 - aluminium alloys, 180, 181
 - ARALL, 178, 180
 - autoclave process, 178
 - CARALL, 180
 - carbon fibre, 178
 - classification, 181
 - composite materials, 180
 - disadvantages, 182
 - environmental awareness, 179

- FMLs in aerospace sectors (*cont.*)
- fatigue and impact properties, 181
 - fatigue crack growth rate, 177
 - fatigue crack resistance, 177, 190
 - fatigue resistance, monolithic metals, 180
 - GLARE, 180
 - manufacturing process, 182–184
 - mechanical properties, 180
 - metallic alloys, 180
 - natural/synthetic fibre-reinforced hybrid composites, 190
 - optimum mechanical performance, 178
 - optimum mechanical properties, 190
 - out-of-autoclave methods, 190
 - plant fibres, 179
 - potential applications, 189, 190
 - surface pre-treatment (*see* Surface pre-treatment, FMLs)
 - synthetic fibre, 190
 - thermoplastic polymer, 182
 - titanium alloys, 181
 - weight reduction, 177
- Fractography
- agglomerations, 83
 - brittle fracture behaviour, 82
 - cleavages, 82
 - failed specimens, 81, 87
 - fibre matrix interaction, 85, 86
 - fibre nanomodified epoxy laminate, 86
 - fractured surfaces, 82, 83
 - HR-SEM, 84
 - massive shear deformation, 84
 - matrix agglomeration, 86
 - microvoids, 84, 87
 - neat epoxy, 84
 - quasi-static loading, 84
 - quasi-static testing, 83
 - SEM micrographs, 85, 87
 - strain rates, 87
 - wettability, 85
- Fracture mechanics
- hybrid composite laminates, 427–429
 - polymer composite, 427–429
- Fretting wear, 333, 334
- Frictional force, 255
- Frictional force sensor, 407
- Functional fillers, 341
- Functionally graded coating, 478
- Functionally graded materials (FGMs), 478
- Functionally graded Ti6Al4V-Mo alloy, 436
- Functionally hierarchic composites (FGCs), 478
- Fused deposition modeling machine (FDM), 456, 457
- Fuselage, 285, 288, 327
- Fusion zone (FZ), 230
- Future aircraft materials research, 335
- Future of aerospace composite materials
- AA2024 aluminum alloy, 381
 - airbus, 377, 378
 - Airbus's 2050 goal, 378
 - alkali metal, 379
 - biomimicry, 377, 380
 - bird-skeleton structural material, 378
 - bone, 378
 - cabins, 378
 - CFRP, 380
 - chromophore light-activated compounds, 378
 - chromophore removal, 378
 - continuous monitoring, 377
 - EMAA, 380
 - hybrid SMA/self-healing polymer composite, 380
 - hybridization, 378
 - investment casting, 381
 - Lewis acid-catalyzed epoxy, 380
 - lunar soil, 379
 - Martian soil, 379
 - mimicry, 377
 - natural materials, 378
 - optical fiber sensors, 377
 - self-foams, 381
 - self-healing materials, 380, 381
 - self-honeycombs, 381
 - SIFORS, 377
 - space exploration, 378
 - translucent wood, 378, 379
 - urea, 379
- Future perspective, 484
- advantages of nanocomposites, 486, 487
 - aerospace industry, 486
 - carbon fiber-reinforced polymer, 486
 - development of nanocomposite, 488–490
 - fiberglass, 486
 - nanocomposites in aerospace industry, 487, 488
- G**
- GE Aviation, 487
- Gel coat, 453
- Genus Corchorus, 345
- Geometric features, 474
- Geopolymer composite, 14–16
- Geopolymer composite curing process, 15
- Geopolymerization process, 14
- Gigahertz communication technologies, 371

- GLARE's benefits, 485
- Glass fiber, 369
- Glass fiber-reinforced composites, 425
- Glass fiber-reinforced epoxy resin, 424
- Glass fiber-reinforced plastic (GFRP), 3, 13, 367–369
- Glass fiber-reinforced polymer (GFRP) composites, 111, 285, 474
- Glass fibers, 178, 285
- Glass fibre-reinforced aluminium laminate (GLARE), 178, 180, 181, 184, 189
- Glass fibre-reinforced composites, 178
- Glass fibres, 129
- Glass/epoxy composites
 - compression and shear properties, 58
 - dynamic response, 58
 - dynamic tensile studies, 59
 - instrumented impact tester, 58
 - tensile modulus, 57
 - tensile strength, 58
- Glass/epoxy hybrid nanocomposites, high strain rates
 - dynamic tensile studies, 72
 - quasi-static loading, 74
 - strain contour plots, 73, 75
 - strain histories, 73, 74
 - strain–time curves, 73
 - stress–strain behaviour, 73
 - stress–strain response, 74, 75
 - tensile properties (*see* Glass/epoxy tensile properties, high strain rate effects)
- Glass/epoxy nanocomposites
 - clay levels, 60
- Glass/epoxy tensile properties, clay effects
 - agglomerations, 80
 - dynamic loading, 80, 81
 - microstructure, 80
 - plastic deformations, 78
 - quasi-static loading, 80, 81
 - stiffness, 80
 - stress–strain responses, 79
 - tensile modulus, 78–80
 - tensile strength, 80–82
- Glass/epoxy tensile properties, high strain rate effects
 - failure strain, 77
 - fibre–matrix interfacial properties, 77
 - GFRP system, 78
 - load histories, 76, 77
 - nanocomposites, 76
 - quasi-static, 76
 - tensile modulus, 76–78
 - tensile strength, 76
- Good fatigue performance, 284
- Grafting, 286
- Grain boundary precipitates (GBP), 333
- Graphene, 360, 446, 448, 451, 452, 489
 - chemical functionalization, 447
- Graphene-based jute/flax hybrid PLA nanocomposite research
 - flexural analysis (*see* PLA flexural analysis)
 - flexural test, 352
 - morphological analysis (*see* PLA morphological analysis)
 - nanocomposites fabrication, 351, 352
 - NaOH, 349
 - surface treatment, natural fiber, 350
 - thin film preparation, 350, 351
- Graphene nanoplatelets (GNPs), 331
- Graphene oxide (GO), 41, 448, 451, 489
- Graphene-reinforced nanocomposites, 488
- Graphitized MWCNTs/Ti64 nanocomposites, thermal characteristics study
 - densification pattern, 266–268
 - HEBM machine, 265
 - materials, 265
 - microstructural evolution, 266–268
 - parameters, 266
 - SPS synthesis, 266
 - SPS technique, 275
 - thermal conductivity (*see* Thermal conductivity, MWCNTs/Ti64 nanocomposites)
 - thermal diffusivity characteristics (*see* Thermal diffusivities, MWCNTs/Ti64 nanocomposites)
 - thermal diffusivity experiments, 266
- Green composites, 128, 480
- Greenhouse gas emissions, 286, 376, 377, 471
- Greenhouse gases (GHGs), 237
- Greenwood, 281
- Grey relational analysis (GRA)
 - grey relational coefficient, 209
 - grey relational grade, 209, 212
 - machining Al/ZrO₂(p)-MMC, 208
 - pre-processing data, 208, 209
 - WireEDM parameters, 208
- Grey relational coefficient, 209
- Grey relational grade, 209, 212
- Grit blasting, 185
- GX41 Olympus microscope, 228

H

- Hall-Petch relationship, 440
- Halogenated and nonhalogenated flame retardants, 286
- Hand lay-up process, 26, 27
- Hand lay-up technique, 304
- Handicraft, 476
- Hardness profiling, 232
- Hardness test, 167, 170, 171, 200, 201, 203, 410
- H-bonding, 448, 462
- Heat-affected zone (HAZ), 230
- Heat deflection temperature (HDT), 282
- Heat treatment process, 16
- Herringbone/fishbone CNF, 449
- Hexachloroethane tablet, 199
- HEXCEL, 487
- High elongation (HE), 348
- High strain rate effects study
 - carbon fibre-reinforced polymer composites, 58
 - DIC, 61–63
 - drop mass tower, 58
 - elastomeric polyurea, tensile properties, 57
 - epoxy/clay (*see* Epoxy/clay nanocomposites, strain rate sensitivity)
 - experimental mechanics, 59
 - glass/epoxy composites, 57
 - glass/epoxy hybrid nanocomposites (*see* Glass/epoxy hybrid nanocomposites, strain rate sensitivity)
 - graphite/epoxy composites, 57
 - HDPE, 57
 - materials, 60
 - microscopic observations, 88
 - optical devices, 59
 - quasi-static and dynamic compression behaviour, 57
 - servo-hydraulic testing apparatus, 58, 61
 - SHTB, 57
 - specimen preparation, 60
 - strain testing apparatus, 57
 - techniques, 57
 - tensile properties, 58
 - testing techniques, 61
- High-energy ball milling (HEBM)
 - machine, 265
- High-intensity stress waves, 58
- High-performance aircraft, 474
- High-performance fibres, 128
- High-performance TMC materials, 265
- High-strength steels, 334
- Homogeneous MWCNTs dispersion, 276
- Hot press molding, *see* Carbon-epoxy composite laminates, compression molding
- HR-SEM (Hitachi model S-4800), 81, 84
- Hummer's method, 489
- Huntsman Advanced Materials (Belgium), 60
- Hybrid Al/Al₂O₃/Gr composites, 239
- Hybrid aluminum/glass-reinforced polymer system (GLARE), 324
- Hybrid AMCs (HAMCs)
 - Al/Al₂O₃/Gr composites, 239
 - Al₂O₃ content, 239
 - development, 238
 - features, 238
 - lubricating properties, 238
 - machining response, 238
 - surface quality, 239
 - surface roughness, 239
- Hybrid biocomposites
 - aerospace applications, 292, 296, 297
 - aerospace industry, 297
 - application, 140, 141
 - carbon fibre composites, 128
 - design categories, 292
 - fibre-reinforced composites, 134–137
 - frequently mentioned natural fibres and fillers, 128
 - green composites, 128
 - high-performance fibres, 128
 - impact resistance, 292
 - interlayer design categories, 292
 - limitations, 141
 - lower dimensional change, 297
 - matrix phase, 131, 132
 - matrix/reinforcing phase, 128
 - natural fibre/synthetic fibre (hybrid)-reinforced polymer composites, 138–140
 - natural fibre-reinforced polymer composite, 132–134
 - natural fibres and fillers, 128
 - natural/synthetic fiber, 292
 - polymer matrix-based composite materials, 127
 - properties, 141
 - reinforcing phases, 129, 130
 - representation, 128, 129
 - synergistic influence, 292
 - tensile strength and modulus, 138
- Hybrid composite laminates, 427–429
- Hybrid composite stacks, 119
- Hybrid composites, 180, 189, 190, 286
 - advanced material scheme, 347

brittle fibers, 347
 CFRP (*see* Carbon fiber-reinforced polymer (CFRP) composites)
 definition, 320
 hybridization, 347
 LE and HE fibers, 348
 mechanical characteristics, 347
 prevalent matrix, 347
 Hybrid fibers PLA nanocomposite fabrication, 351, 352
 Hybrid reinforcement, 474
 Hybrid SMA/self-healing polymer composite, 380
 Hybridisation, 42, 179, 180, 190, 292, 346, 347, 378
 Hydrolysis, 347
 Hydrophobic polymer matrices, 345
 Hypereutectic Al-Mg₂Si in situ composite, 387

I

Impact loading
 gas gun experimental setup, 28
 high-velocity, 55
 kinetic energy, 30
 projectile results, 29
 secondary fibers, 29
 velocities, 29
 In situ offshore transportation handling, 304
 Inconel 718, 226
 Induction-hardened chrome alloy (CK 45), 61
 Industrial Analytical (Pty), 227
 Industrial waste material, 259
 Instrumented impact tester, 58
 Integrated circuit piezoelectric (ICP)-type load sensor, 61
 Interfacial bonding, 273
 Interlaminar analysis, 428
 Interlaminar shear strength (ILSS), 458
 Interlaminar stress analysis, 428
 Interlayer configuration, 292
 Interlayer hybrid, 292
 Intermetallics, 437
 International Civil Aviation the International Organization (ICAO), 472
 International policies, 472
 Intragranular TiC, 276
 Intra-layer hybrid composites, 293
 Ion beam assisted deposition (IBAD), 189
 Ion beam enhanced deposition (IBED), 188, 189
 Izod impact test, 167, 170

J

Jute fiber, 138, 345
 Jute/kenaf/glass fibre-reinforced hybrid composites, 180

K

Kapok and cotton fibres, 132
 Kenaf fiber, 291
 Kenaf fiber-reinforced acrylonitrile butadiene styrene (ABS), 297
 Kenaf fiber-reinforced PP biocomposite, 297
 Kevlar fiber, 346, 369
 Kevlar/*Cocos nucifera* sheath composites, 40
 Kirchhoff's theory, 427
 Kroll's reagent, 228

L

Laminates
 fibre orientation, 151
 lamina layup, 150
 layup, 151
 mechanical properties, 150
 properties, 151, 152
 unidirectional lamina layups, 150
 Laminates energy absorption, above
 ballistic limit
 energy balance, 33
 kinetic energy, 31
 longitudinal and transverse waves, 32
 projectile energy, 31
 projectile mass and initial velocity, 33
 stress and strain, 32
 tensile failure, 32
 transmission factor, 32
 Laminates energy absorption, below
 ballistic limit
 amplitude, 30, 31
 clay dispersion, 40
 critical strain energy release rate, 31
 deflection, 30
 delamination, 39
 energy dissipation, 38
 epoxy resin-reinforced, 41
 impact resistance, 38
 impact velocity, 38, 39
 initial velocity vs. residual velocity, 39, 40
 localized deformation, 30
 matrix crack, 30, 31, 39
 multilayer graphene, 40
 nano-level interlocking mechanism, 38
 potential energy, 30

- Laminates energy absorption, below ballistic limit (*cont.*)
 - projectile energy, 31, 37–39
 - residual velocity, 39–40
 - stiffness, 30
 - stress waves, 30
 - surface-level interactions, 40
 - vibration energy, 37
 - with clay, 39
 - without clay, 37, 39
 - Laminates energy absorption, failure modes
 - delamination, 36, 37
 - elastic deformation, secondary
 - fibers, 35, 36
 - elastic stretching, 47
 - kinetic energy, moving cone, 36
 - matrix crack, 37
 - projectile energy, 46
 - secondary fibers deformation, 47
 - tensile failure, 49
 - tensile failure, primary fibers, 34
 - three-layer laminate, 47
 - with clay, 47
 - without clay, 47, 49
 - Laminating process, 310
 - Laser ablation, 450
 - Laser-deposited samples, 437
 - Laser-deposited T64 characteristics study
 - absorbed metal powders, 227
 - ANOVA, 233
 - applications, 235
 - Cu cluster, 231
 - design evaluation, 233
 - Design-Expert 11 software, 227
 - HAZ, 230
 - materials, 227
 - micrograph, 230
 - microhardness profiling, 232
 - microhardness values, 229, 230, 233
 - microstructural analysis, 227
 - microstructures, 230, 231
 - OP-S suspension, 228
 - point-type design layout, 229
 - process parameters, 227, 228
 - p-value and F-value, 233
 - RSM, 229
 - samples, 228
 - structural stability, 232
 - surface integrity, 227
 - T64 alloy powder, 227
 - ytterbium laser system, 227
 - Laser-deposited Ti-6Al-4V-Mo
 - characterizations
 - actual factors, 441
 - average hardness value, 440, 442
 - average microhardness value, 440, 441
 - coded factors, 441
 - desirabilities, 441
 - fluctuating depositing behavior, 440
 - F-value, 441
 - grain size, 440
 - grinding and polishing operations, 437
 - HAZ, 439
 - hot compression mounting method, 437
 - materials, 437
 - metallographic etching, 437
 - microhardness profiling, 440
 - microstructures, 438, 439, 442
 - P-value, 441
 - response surface model, 437
 - surface response analysis, 438
 - Widmanstatten structures, 438, 439
 - YLS, 437
 - Laser metal deposition (LMD)
 - AM process, 436
 - Ti-6Al-4V, 437
 - titanium alloy, 436
 - LEO environment, 483
 - Levelized cost of energy (LCOE), 421
 - Lewis acid-catalyzed epoxy, 380
 - Life cycle assessment (LCA), 479
 - Life cycle cost analysis (LCCA), 479
 - Lightweight unmanned aerial vehicle, 141
 - Lignocellulosic fibres, 137
 - Linear stress-strain behavior, 428
 - Linear variable differential transformer (LVDT), 407
 - Liquid alkaline activator, 14
 - Liquid molding, 454
 - Lithium chloride (LiCl), 477
 - Lithium hydroxide (LiOH), 344
 - LM6/SiC composites, 238
 - Low elongation (LE), 348
 - Low-velocity impact damage (LVID), 153
 - Low-viscous-flow-able resin, 306
 - Lunar soil, 379
- M**
- Machining composite-related stacks, 122
 - Machining composites, 118
 - Machining metallic-composite stacks, 117
 - Machining of fibrous composites
 - abrasion wear, 123
 - Airbus A380 airplane, 112
 - anisotropic and fiber-orientation-dependent, 122
 - CFRP, 111

- chip removal mechanisms, 113–116
- composite laminate, 110
- conjunction with metallic alloys, 111
- cutting forces/temperatures, 116, 117, 122
- cutting mechanisms, 113
- designing functional cutting tools, 123
- fiber orientation, 111, 122
- fiber-phase reinforcement, 109
- FMLs, 111
- functions, 110
- GFRP, 111
- interlaminar delamination, 112, 119
- lightweight materials, 109
- manufacturing sectors, 123
- material distribution, modern industries, 109
- matrix, 110
- mechanical/physical properties, 109
- modern aerospace applications, 111
- multidirectional fiber-reinforced composites, 110
- multidirectional fibrous composite laminate, 110
- operating wear mode, 123
- properties, 110
- quality, 123
- quality-associated issues, 112
- rapid tool wear, 112
- reinforcing fibers, 110
- secondary manufacturing operations, 112
- sharp cutting edges, 121
- smoothly rounded edges, 121
- stacks, 112
- surface quality characteristics, 112, 117–119, 122
- thermoplastic polymer, 109
- thermoset polymers, 109
- tool failure modes, 123
- tool wear modes, 119–122
- Machining operations, 252
- Machining temperatures, 117, 122
- Magnesium alloys, 334
- Manufacturing techniques, 182–184
- Martian soil, 379
- Material behaviour, 88
- Material divergences, 474
- Mathematical model, 248
- Matrix material, 324
- MD-Chem circular disc, 228
- Mecha Solve Engineering, 349
- Mechanical properties
 - cellulosic fibre hybrid composites, 137
 - CFRP, 458–460
 - economy and environment, 135
 - hybrid composites, 135
 - natural fibres and synthetic fibres, 138, 139
 - natural fibres/composites, 138
 - structural and semi-structural applications, 135
- Mechanical surface treatment, 185
- Mechanical surface-treated aluminium laminates, 185
- Mechanical tests, 407
- Metal alloy, 372
- Metal composites in aerospace industry
 - A300 series aircraft, 329
 - aircraft design factors, 328, 329
 - aluminum alloy, 328
 - center fuselage manufacture, 329
 - commercial aircraft industries, 329
 - F-16 Fighting Falcon, 329
 - fatigue resistance and compressive strength, 328
 - strength-to-weight ratio, 328
 - structural and secondary components, 328
 - wing production, 329
- Metal matrix, 268
- Metal matrix composite (MMC), 196, 264, 328, 372, 373
- Metal mould, 199
- Metal surface pre-treatment, 182
- Mg₂Si, 387
- Mg₂Si particles, 405, 406
- Micro-and nanocellulose, 24, 240
- Microfibrillar cellulose, 374
- Microhardness profiling, 232, 440
- Microhardness values, 235
- Microstructure characterization, 389
- Mimicry, 377
- Mineral materials, 133
- MITUTOYO roughness tester, 258
- Mitutoyo SS220 roughness tester, 246
- Mixtures method, 347
- Modern aerospace industries, 122
- Modified instrumental falling weight drop tower, 58
- Modified montmorillonite clay (GARAMITE®-1958), 60
- Molecular motion, 448
- Molybdenum (Mo)
 - mechanical stability, 435
 - melting point, 435
- Molybdenum disulfide-titania (MoS₂-TiO₂), 436
- Montmorillonite, 489
- Montmorillonite-type nanoclays, 488
- Multidirectional fiber-reinforced composites, 110

- Multiphase heat transfer, 484
- Multi-walled carbon nanotubes (MWCNTs),
 - 165, 450
 - thermal conductivity, 264
 - thermal diffusivity characteristics, 265
 - Ti matrices, 264, 265
 - TMCs, 264
- Multiwalled CNT (MWCNT), 450
- MWCNTs reinforcement, 268
- MWCNTs-reinforced Ti64 (MWCNTs/Ti64), 265
- MWCNTs-reinforced TMCs, 264
- MWCNTs-Ti interfaces, 274

- N
- Nanoclay, 26, 480, 488
- Nanoclay additives, 489
- Nanoclay bridging, 348
- Nanocomposite laminates, energy
 - absorption study
 - analytical methods comparison, 49, 51
 - ballistic limit, 52
 - failure modes (*see* Laminates energy absorption, failure modes)
 - impact loading (*see* Impact loading materials, 24, 26)
 - nanofillers dispersion and specimen fabrication, 26, 27
- Nanocomposite materials, 375
- Nanocomposites, 16, 24
 - advantages, 486, 487
 - aerospace applications, 56
 - approaches and applications, 475, 476
 - in aerospace industry, 480, 487, 488
 - challenges, 475–477
 - definition, 56
 - direct ultrasonication technique, 56
 - development, 488–490
 - dynamic mechanical responses, 56
 - elastic modulus, 342
 - fields, 56
 - future perspective, 485–490
 - nanomaterial, 56
 - nanoscale fillers, 24
 - opportunities, 475–477
- Nano-enhanced composites, 425
- Nano-ferrous composite, 165
- Nano-fibrillated kenaf cellulose (NFKC), 343
- Nanofillers, 23, 40, 179, 342, 452, 453, 478, 480, 488
 - crack propagation, 348, 349
 - dispersibility, 350
 - high-aspect ratio inclusion, 348
 - processability, 349
 - surface area, 348
- Nanofillers-dispersed polymer, 461
- Nanofillers-incorporated CFRP hybrid
 - composite mechanism, 462, 463
- Nano-form carbon nanomaterials
 - synthesis, 446
- Nanoparticle reinforcement, 423, 428
- Nanoscale clay, 24
- Nanoscale fillers, 459
- Nano-sized calcium carbonate, 57
- Nanostructured tribological materials, 483
- Narbon nanotube-reinforced composite
 - application, 24
- Natural composite materials, 1, 367
- Natural fiber-based composites, 286
- Natural fiber-reinforced composite, 427, 479
- Natural fiber-reinforced fire-retardant epoxy composites, 23
- Natural fibers, 11, 12, 374, 381
 - advantages and disadvantages, 290, 291
 - characteristics, 344
 - criteria, 290, 291
 - disadvantage, 286, 290
 - fiber-reinforced structures, 342
 - flax fibers, 344
 - generally hybridized, 286
 - history, 286
 - hybrid biocomposites, 286
 - hybrid composites, 286
 - jute fiber, 345
 - microfibrillar angle vs. tensile modulus, 14
 - potential choices, 342
 - primary chemical compositions, 12
 - properties, 12, 13
 - radome applications, 13
 - reinforcement, 291, 343
 - resistance to impact damage, 290
 - source types, 342
 - treatment, 13
 - types, 290
 - wastes, 290
- Natural fibre/synthetic fibre (hybrid)-reinforced polymer composites, 138–140
- Natural fibres, 129, 179, 190
 - and fillers, 128
 - components, 136
 - epoxy-based resins, 131
 - in matrix, 141
 - in polymer composite, 132
 - types, 129, 132
- Natural fibres application, 240
- Natural fibres limitations, 240

Natural fibre-synthetic fibre hybrid composites, 140

Natural materials, 378

Natural resources-based products, 342

Natural/synthetic fibre-based hybrid FMLs, 190–191

Near-net shape, 295

Newton-Raphson algorithm, 428

Next-generation aircraft structure materials, 335

NFKC-PLA composite, 343

Nickel-based superalloys, 335

Nimonic C-263 super-alloy, 198

Non-destructive testing (NDT) methods, 153

Non-equilibrium inter-diffusion, 189

Non-hybrid composites, 190

Non-renewable materials, 133

Novel HAMCs study

- casting process, 242–244
- composite samples machining, 244–246
- dry turning, 241
- industrial waste materials, 241
- liquid metallurgy route, 241
- machinability response variables, 241
- materials, 242
- mathematical modelling (*see* Response surface methodology (RSM))
- microstructural characterization, 244
- surface roughness (*see* Surface roughness)
- turning behaviour, 241

Novel ramie fabric-reinforced graphene oxide, 42

Nucleation, 396, 398

Nucleation temperature (T_N), 393, 395

O

Oil bath (E3 make), 200

On-chip microfluidic heat exchangers, 473

One-atom-thick 2D material, 451

OPEFB fibre-reinforced fire-retardant epoxy composites, 240

Open contact molding, 453, 454

Opportunities, 475–477, 484

Optical fiber sensors, 377

Optical microscopy, 453

Optimization techniques, machining response, 239

O-rings, 283

Out-of-autoclave (OOA) technique, 10

Out-of-autoclave methods, 190

Out-of-autoclave techniques, 183

Oxygen-based functionalities, 451

P

Parallel/ribbonlike CNF, 449

Partially biocomposites, 289

Partially biodegradable biocomposites, 135

Partially cured composite laminates, 304

Particle agglomeration, 243

Particle-rich alloy, 413

Peel-up delamination, 118

PEI/COOH-MWCNT nanocomposite, 483

PEI/MWCNT nanocomposite, 483

Petroleum-based biodegradable polymers, 136

Phenolic resin, 283, 291

Phosphoric acid anodising (PAA), 187

Photoluminescence, 451

Piezoelectric transducers, 327

Pineapple leaf fiber (PALF) hybrid biocomposite, 13

PLA flexural analysis

- agglomeration, 355
- composite strength, 354
- flax fiber structure, 356
- flax/Kevlar nanocomposite, 353, 356
- graphene, 356
- jute/carbon nanocomposite, 353
- matrix mechanical performance, 354
- mechanical properties, 353
- microcrack resistance, 353
- nanocomposite interactions, 355
- nanofillers, 354
- PLA/chloroform solutions, 353
- reinforcing filler, 353
- stress strain behavior, 354

PLA matrix, 360

PLA morphological analysis

- cleavage appearance, 356
- fiber fracture, 356
- fractured flexural specimen, 356
- graphene, 356, 358
- interfacial bonding, 356, 357
- interfacial interaction, 357
- jute/carbon nanocomposite, 357, 360
- matrix load-carrying capability, 357
- SEM fracture micrographs, 358, 359
- surface treatment, 356

PLA network, 360

PLA synthesis and biodegradation, 24

PLA thin film preparation, 350, 351

Plain (rough) grinding, 228

Plant fibre-based composites, 179

Plant fiber, 179, 342

Plasma electrolytic oxidation (PEO), 436

Plasma-sprayed coatings, 188, 189

Platelet CNF, 449

- Ploughing, 252
- Ply drop design, fan blade, 96–98
- Ply drop-off concepts, tapered composite laminates
 - carbon nanotube reinforcement, 424
 - CNT, 424
 - delamination, 422, 423
 - fatigue testing, 423
 - glass fiber-reinforced epoxy resin, 424
 - interlaminar shear stress, 423
 - interlaminar stress, 422
 - nanoparticle, 424
 - nanoparticle reinforcement, 423
 - nanoparticles, 424
 - optimization, 423
 - static and cyclic loadings, 422
 - stress concentration, 422, 423
- Polyacrylonitrile (PAN), 449
- Polybenzimidazole (PBI), 449
- polycaprolactone (PCL), 343
- Polycarbonate (PC), 283
- Polycrystalline crystal diamond (PCD), 238
- Polyester, 131, 371
- Polyester/TiO₂ nanocomposites, 56
- Polyetheretherketone (PEEK), 283, 371
- Polyetherimide (PEI), 283, 294
- Polyetherketone (PEK), 283
- Polyetherketoneketone (PEKK), 283
- Polyethylene, 479
- Polyglycolic acid (PGA), 343
- Polyhydroxy butyrate (PHB), 343
- Polyimide (PI), 449
- Polyketones, 283
- Polylactic acid (PLA), 240, 343
 - aliphatic polyester, 347
 - biocompatible thermoplastic, 347
 - biodegradability, 347
 - hydrolysis/thermal depolymerization, 347
 - natural fiber-reinforced, 343
 - polymer composites, 343
 - properties, 347
 - reinforcement, 343
 - renewable sources, 343, 347
- Polylactide, 347
- Polymer, 322
 - classification, 5
 - types, 5
- Polymer composite, 16, 284, 427–429
 - aerospace components, 297
 - characteristics, 323
 - contribution, 323
- Polymer composites manufacturing, aerospace engineering
 - Aluminum honeycomb, 294
 - automated fiber placement, 295
 - automated tape layup, 295
 - delamination, 294
 - fiber and resin layers, 293
 - hole drilling, 295
 - resin infusion processes, 294
 - resin transfer molding, 294
 - sandwich composites, 293, 294
 - vacuum-bag resin infusion, 295
- Polymer composites, aerospace applications
 - A380 Airplane, 323, 325
 - F-35 Lightning II, 323, 324
 - fiber-polymer composites, 323
 - FML, 323
 - forms, 323
 - gas turbine engine parts, 327
 - GLARE, 324
 - military and commercial aircraft design/manufacturing, 323
 - modern air force fighter aircraft, 323
 - RFI, 323
 - satellite components, 323
 - structural component, 323, 325
- Polymer foams, 294
- Polymer matrix, 23, 138, 292, 348, 447, 458
- Polymer matrix composite (PMC), 134, 487
 - Boeing 787 Dreamliner, 369
 - civil and military aircraft, 369
 - Eurofighter aircraft, 369
 - fabrication, 369
 - fabrication process, 370
 - glass fiber, 369
 - Kevlar fiber, 369
 - reinforcement, 370
 - reinforcement phase, fiber/particle, 369
 - thermoplastic, 371, 372
 - thermoset polymer, 371
- Polymer nanocomposites, 348, 475, 485
- Polymers
 - composites, 282
 - mechanical properties, 55
 - micro fillers, 56
 - natural/synthetic fillers, 55
 - viscoelastic nature, 56
- Polymethacrylimide (PMI), 294
- Polymethyl methacrylate (PMMA), 56, 283
- Polyphenylene sulfide (PPS), 283, 371
- Polypropylene (PP), 182, 479
- Polysulfone (PSU), 283
- Polyvinyl alcohol (PVA), 449
- Polyvinyl chloride (PVC), 479
- Post-stretching process, 183, 184

- Potassium hydroxide (KOH), 344
 Powder metallurgy (P/M), 273
 Powder-added MMC (PMMC), 196
 Prepreg material, 303
 Prepreg-based processes, 294
 Pressure-sensitive adhesive, 284
 Primary Mg₂Si morphology, 405
 Primary Mg₂Si particles, 387, 389, 396, 408
 Projectile energy, 52
 Projectile velocity, 29
 Protein-based fibres, 132
 PTFE/TiO₂, 483
 PU-CB-based thermal/electro-active SMPC, 484
 Pultrusion, 456
 Push-down delamination, 118
 Push-out delamination modes, 118
 p-values, 251
- Q**
 Quantum confinement, 448
 Quasi-frictionless interface, 478
 Quasi-static loading, 59
 Quenching, 200
- R**
 R² approaches, 248
 Radar, 284
 Radar-absorbing material, 284
 Radio-frequency (RF), 13
 Radome, 285
 Raman spectroscopy, 453
 Ramie fiber-reinforced composite, 291
 Red-mud powder, 242
 Reduced graphene oxide (RGO), 448
 Reinforcement materials, 149
 Renewable natural materials, 343
 Repair methods, 153, 154
 Research and development (R&D), 342
 Research and innovation actions (RIA), 12
 Residual stresses, 474
 Residual velocity of the projectile, 34
 Resin bleeding, 304
 Resin content test, 317
 Resin film infusion (RFI), 294, 295, 323
 Resin injection, 306
 Resin transfer molding (RTM), 294, 295, 303, 454
 Resin-drenched reinforcements, 310
 Resin-injection hole (RH), 153–156, 158, 159, 161
 Resin-injection method, 153
 Response surface methodology (RSM), 436
 Al7075/15%SiC composites, 240
 desirability-based, 240
 DOE approach, 239
 experimental design, 229
 mathematical modelling, 246
 multi-response optimization, 239
 output response optimization, 240
 procedures, 246
 regression coefficients, 248
 selected parameters, 247
 surface roughness, 247
 Taguchi's technique, 247
 variables, 247
 Response surface quadratic model, 233, 234
 Rigidity, 312
 RM fraction, 252, 253
 RM particles, 258
 RM percentage, 254
 RM powder, 241
 RTM fully cured carbon-epoxy composite panels, 305–307
 RTM mold design development
 composite panel dimensions, 304
 cooling capability, 305
 data acquisition system, 305
 material, 305
 optimized injection strategy, 305
 optimized number and spacing, 305
 reinforcement properties, 305
 resin feed cylinder, 305
 resin properties, 305
 RTM semi-cured carbon-epoxy composite panels, 306–308
 RTM5 epoxy resin, 306
 RTM6 epoxy resin, 305
 Rubber matrix, 472
- S**
 Saint-Venant's theory, 160
 Sandwich composites, 294
 Sandwich concept, 177
 Sandwich structure, 24, 241
 Scanning electron microscope (SEM), 59, 200, 202, 240, 357, 453
 Secondary electron images (SEI), 266
 Self-deployable structures, 376
 Self-healing abilities, 445
 Self-healing materials, 380, 381

- Self-healing nanomaterials, polymer composite
 - blade polymer matrix, 426
 - blade structure, 426
 - degradation mechanisms, 425
 - erosion damage, 425
 - fiber impregnation, 426
 - fiber-reinforced polymer composites, 426
 - glass fiber-reinforced composites, 425
 - leading-edge protection, 426
 - load-carrying laminate damage, 425
 - micrometer thick layers, 426
 - nano-/micro-powders, 426
 - nano-enhanced composites, 425
 - nanofillers, 426
 - natural fiber-reinforced composites, 426
 - synergistic mechanisms, 425
 - thermoplastic polymers, 425
 - thermoset matrices, 425
 - wind blades damage, 426
 - wind turbine blades, 426
- Self-healing polymers, 381
- SEM examination, 258
- Semi-cured carbon-epoxy prepregs, 317
- Semi-cured composite laminate prototypes, 310
- Semi-cured prepregs, 317
- Sequential model sum of squares, 233
- Servo-hydraulic tensile testing machine, 57
- S-glass, 285
- Shape memory alloys (SMA), 375, 376
- Shape memory composites, 375
- Shape memory effect (SME), 375
- Shape memory materials (SMM), 375, 376
- Shear mixing, 26, 452
- SHPB apparatus, 61
- Si₃N₄ ceramic composite, 331
- SiC and RM particles, 244
- SiC- and RM-filled Al composites, 241
- SiC-reinforced composites, 239
- Signal-to-noise (S/N)
 - analysis, 249
 - cutting speed, 249
 - input variable, 249
 - relation, 247
 - surface roughness, 249
- Silane, 187
- Silane coupling agent treatment, 188
- Silicon carbide (SiC), 331
 - carbon nanotubes, 165
 - compressive properties, 164
 - flexural test, 174
 - hardness value, 170
 - impact test, 170
 - magnesium alloys, 166
 - mechanical properties, 163
 - semiconductor, 166
 - stir casting technique, 166
 - tensile properties, 164
 - tensile strength, 173
 - tensile test, 173
 - thermal shock resistance, 170
 - yield stress, 173
- Silicon ingot, 406
- Silicon nitride (Si₃N₄), 331
- Silicone, 284
- Silicon-reinforced aluminum alloy
 - impact strength, 164
 - stir casting, 164
- Silk, 132
- Simple modes of loading, 474
- Single-walled carbon nanotubes (SWCNT), 450, 489
- Sintered unreinforced Ti64, 268
- SiO₂/epoxy nanocomposites, 57
- Sisal/banana/coconut sheath fiber-based polyester hybrid composites, 292
- Sisal/glass fibre-reinforced hybrid composites, 180
- Sisal-glass fiber PP biocomposites, 297
- SMA/carbon composites, 376
- SMA-containing composites, 376
- Smart coatings, 483
- Smart properties, 445
- SMPC, 484
- Sol-gel coating, 188
- Solidification, 393, 400
- Solution heat treatment, 199, 200
- Space shuttle, 473
- Spacecraft structures, 474
- Spark plasma sintering (SPS), 265
- Split-Hopkinson pressure bar (SHPB), 57, 87
- Split-Hopkinson tension bar (SHTB), 56, 57, 59
- Spongy microstructure, 230
- SPS MWCNTs/Ti samples, 272
- SPS-processed MWCNTs/Ti64 composites, 273
- Static structural analysis, 105
- Statistical techniques, 258
- Stir casting, 165–166, 174
- Stir casting technique, 164, 166, 174
- Strain energy, 34
- Strength-based damage analysis approaches, 428
- Stress corrosion cracking (SCC), 333

- Stress-strain curve, 34, 35
 - Structural adhesive, 284
 - Structural health monitoring (SHM), 16, 284
 - Structurally integrated fiber-optic sensors (SIFORS), 377
 - Surface characteristics, 258, 259
 - Surface integrity, 235
 - Surface pre-treatment, FMLs
 - chemical treatment, 186
 - classification, 184
 - coupling agent, 187, 188
 - dry surface treatments, 188, 189
 - electrochemical treatment, 187
 - mechanical, 185
 - mechanical properties, 184
 - metal-composite adhesion, 184, 190
 - Surface quality, 117–119, 122
 - Surface resistance, 255
 - Surface response analysis, 438
 - Surface roughness
 - Al/SiC/RM composites, 258
 - ANOVA analysis, 252
 - ASR, 249
 - conformation experiment, 257, 258
 - correlation graph and normal probability plot, 249, 250
 - designing automotive components, 239
 - first-order polynomial equation, 247
 - parameters contributions, 249, 251, 252
 - parameters influence, 252–255
 - regression correlation, 248
 - S/N ratio, 249, 251
 - surface plots, 253–255
 - Surface roughness tester, 200
 - Surface temperature, 255
 - Surface texture, 239
 - Sustainable structural material, 342
 - Synergistic mechanisms, 425
 - Synthetic biodegradable matrices, 289
 - Synthetic fibers, 179, 190, 375
 - carbon fiber, 346
 - Kevlar fiber, 346
 - Synthetic fibre-based FMLs, 189
 - Synthetic polymer, 5
- T**
- Tackiness, 312
 - Taguchi L27 orthogonal array, 196
 - Taguchi's approach, 241
 - Taguchi's technique, 258
 - Tail, 288
 - Tensile failure, 34
 - Tensile test, 164, 169, 172, 173, 203, 204
 - Thermal analysis, 389, 396
 - Thermal conductivity, 439, 460, 489
 - Thermal conductivity, MWCNTs/Ti64 nanocomposites
 - bulk nanocomposites, 274
 - cleaning effect, 274
 - CNTs agglomeration, 274
 - Cu-CNTs interfaces, 275
 - densification, 274
 - graphite-reinforced aluminium matrix composites, 275
 - interfaces, 274
 - intragranular TiC interfacial products, 275
 - object-oriented finite element method, 274
 - porosity, 275
 - structural integrity, 275
 - synthesized composite, 275
 - Thermal depolymerization, 347
 - Thermal diffusivities, MWCNTs/Ti64 nanocomposites
 - agglomeration and re-agglomeration, 271
 - amorphization, 271
 - ballistic transportation capacity, 272
 - CNTs-reinforced TMCs, 273
 - degradation, 270
 - intragranular and interfacial, 273
 - lower densities, 272
 - metal matrix, 271
 - P/M route, 273
 - pores, 272
 - reaction products, 272
 - reinforcement dispersion, 271
 - synthesis, 268
 - temperatures, 269
 - testing temperatures, 269
 - thermal transport mechanisms, 272
 - three-stage model, 271
 - Ti/CNTs interfacial reaction, 273
 - TiC formation, 273
 - TiC interfacial reaction products, 271
 - TiC/matrix interface, 272
 - unreinforced alloys, 268
 - virgin Ti64 samples, 268
 - Thermal ground planes, 473
 - Thermal management, 484
 - Thermal properties
 - CFRP, 459, 460
 - Thermal Protection Systems, 485
 - Thermal protection systems for space vehicles (TPS), 485
 - Thermal shock conditions, 474
 - Thermal stability, 140

- Thermal transport mechanisms, 272
 - Thermoplastic composite, 17, 371, 372
 - advantages, aerospace industry, 10, 11
 - aerospace parts and components, 10
 - aircraft manufacture, future, 9
 - applications in aircraft, 11
 - extreme-temperature plastic, 9
 - high strength-to-weight ratio, 10
 - high-temperature plastic, 9
 - manufacturing, 10
 - OOA technique, 10
 - primary material, aircraft's internal and external structures, 9
 - thermoset composite, 10
 - types, 9
 - utilization, 10
 - Thermoplastic elastomer, 284
 - Thermoplastic materials, 10, 479
 - Thermoplastic polymer, 109, 131, 179, 283, 425
 - polypropylene, 182
 - Thermoplastic resins, 131
 - Thermoplastics, 134, 284, 322, 371, 473
 - Thermoplastics-utilized aircraft composite, 322
 - Thermoset composite, 10, 17
 - aerospace applications, 10
 - aircraft composite materials, 17
 - autoclave, 6, 7, 17
 - BMI, 7
 - CF/BMI composite, 7
 - commercial aircraft structures, 6
 - early wooden framed aircraft, 6
 - engineered fiber types, 7
 - environmental conditions, 6
 - fatigue resistance, 7
 - heat, 7
 - non-reversible hardening and forms, 6
 - properties, 6, 7
 - temperatures, 7
 - tensile and flexural properties, 7, 8
 - uses, 9
 - Thermoset polymer, 109, 283, 371
 - Thermoset resins, 56, 131
 - Thermosets, 322
 - Thermosetting polyaniline-based polymer, 462
 - Thermosetting resins, 473
 - Thick-sectioned composite laminates, 312
 - Thin film binarization method, 453
 - Thixotropic properties, 489
 - Three-dimensional finite element analysis, 428
 - Three-point bending test, 353
 - Ti/CNTs interfacial reaction, 273
 - Ti-15Mo alloy, 436
 - Ti-4Al-1.5Mn titanium alloy, 436
 - Ti6Al4V to 316L stainless steel, 226
 - Ti-based alloys, 334, 335
 - Ti-based matrix composites (TMCs), 264
 - TiC nanoplatelets, 273
 - TiC particles, 226
 - TiC reaction products, 272
 - Timber sheets, 282
 - Titanium (Ti)
 - applications, 264
 - CFRP, 264
 - corrosion resistance, 435
 - fabrication, 264
 - lightweight refractory metal, 225
 - low-corrosion structural metal, 435
 - machining, 263
 - phase transformations, 225
 - properties, 225
 - thermal conductivity, 263
 - thermal materials, 263
 - Titanium alloy (Ti-6Al-4V), 181, 334, 435
 - Titanium carbide (TiC), 331
 - Titanium Metal Supply, 227
 - Titanium/Cu interface, 226
 - Tool wear modes, 119–122
 - Toughening agents, 284
 - Toxic chromate-based treatments, 188
 - Traditional corrosion coating, 332
 - Translucent wood, 378, 379
 - Transmission electron microscopy (TEM), 453
 - Transverse wave, 32, 35
 - Triethylenetetramine (TETA), 60
 - Tungsten-coated carbide medium cutting insert (CCMT 09T304 MT), 245
 - Turbine blades, 427
 - Turbine inlet temperature, 373
 - Types of polymers
 - advantages, 370
 - disadvantages, 370
- U**
- Ultimate tensile strength (UTS), 410, 412, 413, 417
 - Ultrasonic waves, 164
 - Ultrasonication, 452
 - Ultrasonic vibration, 164
 - Uncut fibers, 115, 118, 119, 122
 - Undercarriage (landing gear), 288
 - Unidirectional fiber-reinforced polymers, 478
 - Unidirectional glass-carbon/epoxy hybrid composite, 286
 - Universal tensile testing machine, 200, 202
 - Universal Testing Machine, 352

- Unmelted molybdenum, 438
- Unreinforced Ti64 nanocomposites, 267
- Un-separated clay particles, 24, 25
- Urea, 379
- UV-curable resin, 477

- V**
- Vacuum-assisted prepreg compression molding (VAPCM), 454
- Vacuum-assisted resin transfer molding (VARTM), 178, 455
- Vacuum-bag resin infusion, 294–296
- Vacuum Induction Melting (VIM), 372
- Vacuum solid-state diffusion method, 226
- van der Waals force, 462
- van der Waals interaction, 448
- Vent holes (VHs), 153–155, 157, 158, 160, 161
- Vertical stabilizer, 326
- VIC 2D software, 68
- Vickers hardness methodology, 167
- Vickers hardness number, 168
- Vickers microhardness tests, 227, 232
- Viscoelastic constitutive model, 57
- Void content, 182
- Volatile organic compound (VOC), 10

- W**
- Waste materials, 241
- Water-quenched samples, 436
- WC/DLC/WS2, 483
- Wear behavior, 414–417
- Wear test, 407
- Widmanstätten structures, 230, 235
- Wind energy power plants, 421
- Wind turbine blades, hybrid composites
 - accuracy, 429
 - advancements, 429
 - durability, 429
 - energy market, 422
 - environmental aspects, 429
 - fracture mechanics
 - hybrid composite laminates, 427–429
 - polymer composite, 427–429
 - high-energy wind turbine plants, 421
 - integrated active vibration reduction
 - measures, 429
 - mechanical degradation, 429
 - nanofillers and self-healing capability, 429
 - performance monitoring system, 421
 - ply drop-off concept, composite laminates
 - carbon nanotube reinforcement, 424
 - CNT, 424
 - delamination, 422, 423
 - fatigue testing, 423
 - interlaminar shear stress, 423
 - interlaminar stress, 422
 - nanoclay reinforcement, 424
 - nanoparticle reinforcement, 423
 - nanoparticles, 424
 - optimization, 423
 - static and cyclic loadings, 422
 - static and fatigue loads, 423
 - stress concentration, 422, 423
 - polymer composite
 - self-healing nanomaterials, 425, 426
- Wind turbines, 421
- Wings, 288
- Wire electrical discharge machining, 207
- Wire_{EDM}, 196
- WireEDM of Al/ZrO₂(P)-MMCs
 - AA 6061/cenosphere composite, 198
 - adaptive neuro-fuzzy inference system, 197
 - Al 6061/10% wt. SiCp MMC, 197
 - Al 6063/SiCp MMC, 197
 - Al alloy (AA2024), 198
 - casting, 199
 - coated brass wire (CuZn50) electrode, 196
 - electrical and non-electrical machining
 - parameters, 196
 - experimental design, 205
 - experimental investigation
 - measuring and testing equipment, 200
 - experimental results
 - performance characteristics, 206
 - response surface methodology, 204, 205
 - grey relational analysis, 198
 - hardness test, 201, 203
 - Inconel 706 machining, 197
 - machined surface, 219
 - metallic ion migration, 220
 - Mg matrix composites, 197
 - MRR, 197
 - multi-objective optimization, GRA
 - A5B1C5D4E5F1, 212
 - grey relational coefficient, 209, 210
 - grey relational grade, 209, 210, 212
 - parameters, 208
 - performance characteristics, 212
 - pre-processed data, 210
 - pre-processing data, 208, 209
 - test result, 211
 - test results, 212, 213
 - weight fractions, 208

- WireEDM of Al/ZrO₂(P)-MMCs (*cont.*)
 Nimonic C-263 super-alloy, 198
 non-traditional machining, 197
 optimization techniques, 196
 process parameter range, 204
 reinforced particulates, 197
 sample preparation, testing, 201
 SEM, 202
 solution heat treatment process, 199, 200
 spark gap, 196, 197
 surface veracity and recast layer thickness
 Al/10% wt. ZrO₂(P)-MMC, 215–218
 Al/15% wt. ZrO₂(P)-MMC, 217–220
 Al/5% wt. ZrO₂(P)-MMC, 214, 215
 EDX, 214
 input process parameters, 220
 machined surface, 214
 SEM, 215
 thermal energy, 213
 weight fractions, 213, 220
 tensile tests, 203, 204
 universal tensile testing machine, 202
 universal tensile testing specimen, 202
 weight fractions, 219
- wire deviation, 219
 zirconia (ZrO₂)-reinforced particulate
 properties, 198
- Wood
 aircraft, 282
 composition and structure, 281
 disadvantages, 281, 282
 longitudinal stiffness and strength, 281
 properties, 281
- Woven fibers, 343
 Woven flax, 291
- Y**
 Young's modulus, 59, 451
 Ytterbium laser system (YLS), 437
 Yttria-stabilized zirconia (YSZ), 483
 Yttria-stabilized-zirconia nanocomposites, 375
- Z**
 Zirconia-based nanocomposites, 375
 ZrO₂ particulates, 199
 Zwick/Roell Vickers hardness machine, 228